

THÈSE

En vue de l'obtention du

DOCTORAT DE L'UNIVERSITÉ DE TOULOUSE

Délivré par :

Institut National Polytechnique de Toulouse (Toulouse INP)

Discipline ou spécialité :

Energétique et Transferts

Présentée et soutenue par :

M. CARLOS GARCIA GUILLAMON

le lundi 12 décembre 2022

Titre :

Modélisation de l'injection multipoint de carburant pour la simulation aux grandes échelles de chambres de combustion aéronautiques

---

Ecole doctorale :

Mécanique, Energétique, Génie civil, Procédés (MEGeP)

Unité de recherche :

Centre Européen de Recherche et Formation Avancées en Calcul Scientifique (CERFACS)

Directeur(s) de Thèse :

M. THIERRY POINSOT

M. GABRIEL STAFFELBACH

Rapporteurs :

M. AYMERIC VIE, CENTRALESUPELEC GIF SUR YVETTE

M. GUILLAUME BALARAC, INP GRENOBLE

Membre(s) du jury :

M. FRANÇOIS XAVIER DEMOULIN, UNIVERSITE DE ROUEN, Président

M. JEAN-LUC ESTIVALEZES, TOULOUSE INP, Membre

M. MARCOS CARRERES-TALENS, UNIVERSIDAD POLITECNICA DE VALENCIA, Membre

MME LÉA VOIVENEL, CORIA, Membre

M. RENAUD MERCIER, GROUPE SAFRAN, Membre

M. STEFANO PUGGELLI, GROUPE SAFRAN, Invité(e)

M. THIERRY POINSOT, TOULOUSE INP, Membre

M. VINCENT MOUREAU, CORIA, Invité(e)

Y si fuera
mi vida una escalera
me la he pasado entera
buscando el siguiente escalón

Robe

Parce que, dans le reste de la vie,
personne ne vous demande de chercher
quoi que ce soit,
et on ne risque pas de trouver
puisqu'on ne sait pas
ce qu'on cherche

Fred Vargas

Acknowledgements

Dans *Siddhartha* (Hesse 1922), le passeur de la rivière apprend au protagoniste comment traverser celle-ci. D'abord il l'aide à parcourir cette rivière, jusqu'au moment où le protagoniste arrive à la franchir lui même, apprenant à écouter le fleuve et comprenant son esprit.
Je remercie d'abord mes deux passeurs, Léa Voivenel et Renaud Mercier, qui m'ont guidé pour comprendre et essayer de traverser cette rivière que l'on appelle recherche. Leurs conseils, leur inestimable aide, leur grande disponibilité et leur patience m'ont permis d'aboutir ce projet qui m'a prit tant d'effort et de temps dans les dernières années.

Je dois exprimer ma profonde gratitude à Thierry Poinsot pour avoir dirigé cette thèse et pour m'avoir accueilli au CERFACS les derniers mois de ma thèse. Je le remercie profondément d'avoir pris le temps, malgré son calendrier serré, d'assister aux réunions que m'ont permis d'améliorer ce travail.

Je souhaiterais aussi remercier les membres du jury d'avoir assisté à ma soutenance. Merci d'abord à Aymeric Vié et Guillaume Balarac d'avoir accepté d'être rapporteurs, et d'avoir pris le temps de lire et évaluer ce manuscrit (qui n'est pas le roman le plus amusant du monde...). Merci a François-Xavier Demoulin d'avoir accepté de présider le jury, et à Jean-Luc Estivalèzes, Marcos Carreres, Vincent Moureau et Stefano Puggelli d'avoir évalué mon travail lors de la soutenance. Aussi, merci à Stefano pour nos discussions et sa relecture du manuscrit, et a Vincent pour tous ses conseils.

Maintenant, je voudrais remercier les personnes qui m'ont accompagnés dans cette aventure, en faisant un petit *road trip* qui va du nord de la France au plus sud, de Paris à l'Espagne. A Paris, je souhaiterais remercier d'abord tous les gens que j'ai trouvés à Safran Tech, dans les pôles "Energie et Propulsion" et "Digital Sciences and Technologies". Merci à Melody et à Julien pour tous nos échanges et d'avoir partagé son expérience sur le diphasique et sur YALES2 avec moi. Je souhaiterais remercier aussi tous les membres du project Marie-Curie ANNULIGhT, avec qui on a partagés des bons moments dans différentes villes européennes (comme Toulouse et Munich), et à qui je souhaite le meilleur pour la suite ! Passant au côté personnel, je ne peux que être reconnaissant d'avoir trouvé des gens comme Romain, mon copain d'enjeux diphasiques et des hauts et bas de thèse (et avec qui j'espère pouvoir collaborer dans un avenir proche); Gabriel, compagnon de bureau d'abord, puis pote d'aventures à Paris, Lyon et Barcelone (il nous manque Raz toujours!); Quentin, le "bon breton" avec qui avec qui j'ai affronté des moments difficiles; Clement, le *loco* qui a quitté l'endroit pour aller faire des avions (et qui m'a laissé tout seul les midis dans la salle de sport); Jean-Marie, le master versaillais (car lui, lui il est français) du control et du pilotage; et à Deepali, qui a quitté la region parisienne trop tôt pour faire de l'éolienne dans les champs de tulipes néerlandais (now it's your turn to get that PhD, go kill it!).

Toujours dans la capitale, la Ville Lumière n'aurait pas été aussi charmante sans la compagnie de quelques personnes. I would like to thank then to all the people I met during those three-and-something years, that went from the CiteU to Gentilly with some period in the outskirts (long months though): Miguel (gran amigo, buen compañero de viajes, mejor coloc), Diego (con quien sigo compartiendo cervezas en Barcelona), Pardis (and her invitations to nice gatherings in Villejuif), Javid (congratulations to you too for your recent defense!), Zhila (whose kindness and welcoming are beyond human nature), Jesús (albaceteño en la gran ciudad, y compañero de *parades* y de buenos viajes), Federico (argentino loco, buen compañero de fiestas, mejor profe de salsa), Ana (arquitecta *granaína* ahora más parisina que nadie), Antonio (el catasturiano que nos contagió la moda de las camisas horteras), Gonzalo y Bérangère (que van siempre en pack, ella ya doctora y él quasi-doctor), Laura A. (experta en supervivencia de tesis, y en comprar packs de cerveza para invitarnos a todos), Carmen y Fernando (también en pack, y pronto con alianzas incluidas!), Mar (presente durante el muy principio y el muy final de esta época), Toño (inolvidable compañero de farras, que la providencia ha querido que se sigan dando de vez en cuando) y Jasone (la vasca que más me ha soportado en mi encierro de teletrabajo tras la llegada del pinche virus).

Let's now move souther and stop for a while at *la ville rose*, Toulouse. Despite the few months spent there (and for which most of the time was spent sitted writing this thesis), their human quality was more than excellent. D'abord, je veux remercier les gens du CERFACS pour leur charmant accueil. En particulier, merci à Michèle pour son amabilité et son aide avec les affaires administratives, et à Gérard, Fabrice et Isabelle du équipe CSG pour leur aide avec les affaires techniques. In the personal plane, I can only be grateful for meeting such fantastic people such as Walter (with whom I have shared adventures since the good times at VKI), Abhijeet (also Annulight partner, the kindest indian heart on the planet), Varun (who made me discover the delices of indian food), Patrick (Glück in dein Doktorarbeit mit dem Rotation-Feuer!), Gregory (now a parisian wandering around Châteaufort), Héctor (dele bien a ese amoniaco, algún día conseguirá su sueño de vivir de rentas wey), Sriram (the expert in covid simulations).

Cruzando los Pirineos hacia el sur, me gustaría empezar por agradecer en Barcelona el apoyo moral de mis colegas del BSC y de mi familia de aquí, fundamental en este periodo de correcciones y lectura de tesis que se ha alargado más de lo previsto. Bajando ahora a Valencia, agradezo a mis compañeros de la universidad su amistad y apoyo, a pesar de vernos un par de veces al año (eso tiene la vida, que cada cual sigue su camino, aunque por fortuna estos se siguen cruzando). Y una pequeña mención (aunque no menos importante) a Elena, Loli y Sara, porque lo que Leeds ha unido que no lo separen los años.

Para terminar, acabamos este viaje en Requena, donde empezó todo. Un inmenso gracias a mis amigos por su incondicional apoyo y por estar siempre ahí: Juan el maestro del saxofón, Viseras *Willkommen*, Garban el maestro del basket (y el huevón huevón), Borjeta y nuestras tardes en el perro, Julio y sus *Amunt Valencia nano*, Pepe y sus ironías mordaces, Perelló el *quant* que llega siempre tarde a todas partes, Inés y nuestras interminables charlas y confidencias (apoyo incondicional en los momentos más duros, no cambies nunca rubia), y al desaparecido Torres (¡pronto papá Torres!). A todos vosotros, por tantos años juntos, y por los que nos quedan.

Llegando al final, no puedo sino agradecer a mi familia su incondicional apoyo a lo largo de los años. A mi tío Eloy y a mi abuela Nieves, por todo su cariño desde que era pequeño y pasaba los días de verano en el Rebo. A mi hermano Javi, por todas nuestras conversaciones sobre cualquier tema y sus consejos respecto al noble arte de ir al gimnasio. Y a mis padres José y Gloria, por dármelo todo y apoyar todas mis decisiones a pesar de mi empeño por estar fuera de casa (aunque cada vez más cerca).

Infine, le parole non possono esprimere la mia gratitudine per aver trovato Laura in questo viaggio. Il suo amore, il suo sostegno incondizionato e il suo atteggiamento verso la vita mi hanno fatto superare i momenti brutti (che lei, nonostante gli inconvenienti, ha condiviso con me) e godermi al massimo quelli belli. Spero di poterti ripagare negli anni che passeremo insieme, ovunque ci porti la vita. Grazie anche alla famiglia di Laura per la loro gentilezza e ospitalità nella loro casa nella più grande isola italiana.

Abstract

Modelling of Multipoint Fuel Injection for the Large Eddy Simulation of Aeronautical Combustion Chambers

In the last decades, the aeronautical industry has focused on developing low emission combustion systems to fight climate change. With this objective in mind, aircraft engine manufacturers have developed concepts aimed at burning in lean regimes for reducing pollutant emissions, such as nitrogen oxides (NOx) and carbon monoxide (CO). Lean combustion can be achieved through a proper placement of the liquid phase in the combustion chamber. For this purpose new injection concepts have arisen, such as multi-staged fuel injection (MSFI) systems. The objective of this thesis is the development of a new lagrangian injection methodology for performing dispersed-phase simulations with a realistic prescription of the liquid phase in MSFI systems.

In first place, the lagrangian injection models are developed and validated in an academic kerosene jet in crossflow (JICF) configuration. The theory aspect of the models, named Smart Lagrangian Injectors (SLI), is detailed. SLIs are able to learn spray data from simulations solving for the liquid-gas interface (resolved atomization simulations), and then use these data to prescribe liquid boundary conditions in dispersed-phase computations which model the liquid phase as Lagrangian particles. Furthermore, secondary atomization and momentum exchange between the liquid dense core and the gas are also modeled in the latter. Results from the resolved atomization simulations show that the JICF physical behaviour and topology can be properly retrieved. The spray resolved from these computations is then post-processed to generate the SLI for prescribing liquid boundary conditions in dispersed phase computations. The resulting spray is validated with experimental data, showing a good physical spray behaviour and a correct estimation of fluxes, but an underestimation in the droplets sizes caused by secondary breakup.

Finally, the SLI strategy is applied to the multipoint stage of the BIMER multi-staged combustor, tested at EM2C laboratory, which is more representative of industrial burners. Resolved atomization simulations are performed on one single liquid nozzle. SLIs are built from these simulations and applied to the full multipoint stage, consisting of 10 liquid nozzles, for performing dispersed-phase computations of the burner. These computations show a good agreement with experiments, proving the capability of SLI to prescribe realistic liquid boundary conditions for performing dispersed-phase simulations in MSFI burners.

Résumé

Modélisation de l'injection multipoint de carburant pour la simulation aux grandes échelles de chambres de combustion aéronautiques

Au cours de ces dernières années, l'industrie aéronautique a développé des systèmes de combustion à faibles émissions pour lutter contre le changement climatique. Afin d'atteindre cet objectif, les constructeurs de moteurs aéronautiques ont développé des concepts ciblant la combustion pauvre pour réduire les émissions polluants, notamment les oxydes d'azote (NOx) et le monoxyde de carbone (CO). Ce régime de mélange pauvre peut être obtenu par un placement adéquat de la phase liquide dans la chambre de combustion. Dans cette optique, de nouvelles technologies d'injection de carburant sont apparues, comme les brûleurs à plusieurs étages (MSFI). L'objectif de cette thèse est de développer une nouvelle méthodologie numérique pour la prescription réaliste des sprays modélisés en tant que particules Lagrangiennes, afin de simuler la phase liquide dispersée dans des systèmes MSFI.

Dans un premier temps, les modèles d'injection Lagrangienne sont développés et validés avec une configuration académique de type jet-in-crossflow (JICF). L'aspect théorique de ces nouveaux modèles d'injection, appelés Smart Lagrangian Injectors (SLI), est également détaillé. Les modèles SLI apprennent des données du spray issues de simulations résolues de l'interface liquide-gaz, et utilisent ensuite ces données afin de générer des conditions aux limites concernant les gouttes, qui permettent enfin d'effectuer des simulations Lagrangiennes de la phase liquide dispersée. Par ailleurs, lors de ces simulations de phase dispersée, l'atomisation secondaire des gouttes et l'échange de quantité de mouvement entre le phase dense liquide et le gaz sont également modélisés. Les résultats des simulations d'interface résolue montrent que le comportement physique et la topologie du JICF sont correctement reproduits. Le spray résolu issu de ces simulations est ensuite post-traité pour générer les conditions aux limites de gouttes Lagrangiennes des simulations de phase dispersée. Le spray Lagrangien ainsi produit est comparé à données expérimentales, montrant un comportement physique global satisfaisant et une estimation correcte des débits liquides, mais une sous-estimation de la taille des gouttes causée par le modèle d'atomisation secondaire.

Enfin, la méthodologie SLI est appliquée à l'étage d'injection multipoint du brûleur BIMER, testé au laboratoire EM2C, et plus représentatif des brûleurs industriels. Les modèles SLI sont établis à partir de simulations résolues de l'interface liquide-gaz pour un seul point d'injection, puis appliqués aux simulations de phase dispersée de l'étage multipoint complet, composé de 10 points d'injection. Ces calculs Lagrangiens sont en accord avec les résultats expérimentaux, démontrant la capacité du modèle SLI à générer efficacement des conditions aux limites réalistes pour l'injection liquide afin d'effectuer des simulations liquides dispersées dans des brûleurs MSFI.

Contents

Acknowledgements **v**

Abstract **vii**

Résumé **ix**

Nomenclature **xvi**

List of Figures **xxvi**

List of Tables **xxix**

1 Introduction **1**
1.1 General context . . . 1
1.2 Lean combustion in aeronautical gas turbines . . . 2
1.3 Fuel injection technology . . . 4
1.4 Numerical simulations of fuel injection and combustion . . . 12
1.5 Objective and thesis outline . . . 15
1.6 Acknowledgements . . . 16

I Numerical approaches to model injection systems **17**

2 Numerical methods to simulate resolved atomization **19**
2.1 Introduction . . . 19
2.2 Governing equations . . . 20
2.2.1 Reynolds transport theorem . . . 20
2.2.2 Mass conservation . . . 21
2.2.3 Momentum conservation . . . 24
2.3 Eulerian approaches for dense regime . . . 26
2.3.1 Diffuse interface methods . . . 26
2.3.2 Front-tracking method . . . 27
2.3.3 Volume of Fluid method . . . 28
2.3.4 Accurate Conservative Level Set method . . . 29

3 Numerical methods to simulate dispersed phase **33**
3.1 Introduction . . . 33
3.2 Numerical approaches to model dispersed phase flows . . . 33
3.2.1 Statistical methods . . . 34
3.2.2 Eulerian methods . . . 35
3.2.3 Lagrangian point particle representation . . . 35
3.3 Stage of the art in injection models for MSFI systems . . . 37
3.3.1 Hollow cone spray . . . 38
3.3.2 Airblast spray . . . 41
3.3.3 Liquid jet in crossflow . . . 41
3.4 Conclusions . . . 48

II Building lagrangian injectors from resolved atomization simulations 49

4 Models for lagrangian injection 51
4.1 Introduction . . . 51
4.2 Mathematical description of sprays . . . 51
4.2.1 General formulation . . . 52
4.2.2 Spray formulation in jet in crossflow . . . 52
4.3 Models for lagrangian injection . . . 53
4.4 Lagrangian injectors learning . . . 54
4.4.1 Spray sampling . . . 54
4.4.2 Spray convergence . . . 58
4.4.3 Spatial discretization of sprays . . . 59
4.4.4 Convergence-driven discretization . . . 60
4.4.5 Injectors definition . . . 61
4.5 Dense core blockage effect modeling . . . 63
4.5.1 Actuator Line Method . . . 63
4.5.2 Dense core representation as an actuator . . . 64
4.5.3 Determination of forces . . . 66
4.6 Secondary atomization modeling . . . 67
4.6.1 Taylor Analogy Breakup . . . 68
4.6.2 Enhanced TAB model . . . 70
4.6.3 Gorokhovski stochastic model . . . 71
4.7 Conclusions and perspectives . . . 72

5 Resolved atomization simulations of liquid jet in crossflow 73
5.1 Introduction . . . 73
5.2 Experimental test case . . . 73
5.3 Computational setup . . . 74
5.4 Operating conditions . . . 75
5.5 Gaseous initial conditions . . . 77
5.6 Analysis of JICF simulations . . . 78
5.6.1 Jet evolution . . . 78
5.6.2 Breakup topology . . . 87
5.6.3 Jet trajectories . . . 94
5.6.4 Gaseous perturbations due to liquid core . . . 98
5.6.5 Direct measurement of liquid fluxes . . . 102
5.6.6 Computational performances and costs . . . 108
5.7 SLI building . . . 110
5.7.1 Dense core characterization for ALM . . . 110
5.7.2 Spray characterization . . . 112
5.7.3 Sprays spatial dicretization . . . 120
5.8 Conclusions . . . 128

6 Dispersed-phase simulations of JICF 129
6.1 Introduction . . . 129
6.2 State of the art . . . 129
6.2.1 Experimental results for validation . . . 129
6.2.2 Previous numerical studies . . . 132
6.3 Procedure for parametric study of lagrangian simulations . . . 135
6.4 Influence of gaseous phase . . . 135
6.4.1 Computational setups and boundary conditions . . . 135
6.4.2 Lagrangian jet establishment . . . 145
6.4.3 Analysis of lagrangian spray . . . 147
6.5 Influence of secondary atomization model . . . 152
6.6 Influence of spray injection variables . . . 155
6.6.1 Level-set resolution and injection location . . . 155
6.6.2 Spray velocities . . . 157

6.6.3 Droplets diameters . . . 159
6.6.4 Convergence-driven discretization . . . 160
6.6.5 Operating condition . . . 161
6.7 Artificial delay in secondary breakup . . . 162
6.8 Conclusions . . . 165

III Application to a multipoint injector 167

7 Description and gaseous flow validation 169
7.1 Introduction . . . 169
7.2 Experimental setup . . . 169
7.3 Choice of operating points . . . 171
7.4 Numerical setup . . . 171
7.4.1 Computational geometry . . . 171
7.4.2 Meshes . . . 172
7.4.3 Simulated cases . . . 172
7.5 Physical features of swirled flows . . . 173
7.5.1 Swirl number and vortex breakdown . . . 173
7.5.2 Characteristic time scales . . . 174
7.6 Validation of gaseous field . . . 174
7.6.1 Qualitative validation . . . 176
7.6.2 Quantitative validation . . . 176
7.7 Application operating point . . . 179
7.8 Conclusion . . . 181

8 Resolved atomization simulations of BIMER 183
8.1 Introduction . . . 183
8.2 Computational setup . . . 183
8.3 Operating condition . . . 184
8.4 Analysis of BIMER simulations . . . 187
8.4.1 Jet evolution . . . 187
8.4.2 Breakup topology . . . 189
8.4.3 Jet trajectories . . . 190
8.4.4 Gaseous perturbations due to liquid core . . . 191
8.4.5 Direct measurement of liquid fluxes . . . 195
8.4.6 Computational performances and costs . . . 197
8.5 SLI building . . . 198
8.5.1 Dense core characterization for ALM . . . 198
8.5.2 Spray characterization . . . 199
8.5.3 Sprays spatial discretization . . . 203
8.6 Conclusion . . . 206

9 Dispersed phase simulations in BIMER 209
9.1 Introduction . . . 209
9.2 Computational setup . . . 209
9.3 Experimental results from literature . . . 210
9.4 Boundary condition for liquid phase . . . 210
9.4.1 Multipoint stage injection . . . 210
9.4.2 Pilot stage injection . . . 211
9.5 Boundary condition for gaseous phase . . . 211
9.6 Simulations and results . . . 215
9.6.1 Lagrangian field establishment . . . 216
9.6.2 Qualitative results and experimental comparison . . . 218
9.7 Conclusions . . . 222

IV Conclusions and perspectives **223**

10 Conclusions and perspectives **225**

Bibliography **229**

V Appendices **241**

Appendix A Setup of JICF gaseous inlet profile **243**

Appendix B Gaseous initial conditions for JICF **249**

Appendix C Postprocessing methods for JICF **256**
C.1 Jet trajectory 256
C.2 Direct measurement of liquid fluxes 259
C.3 Dense core breakup point 260

Appendix D Mass conservation in ACLS **264**

Appendix E Convergence of SLI global parameters in JICF **269**

Appendix F Convergence of SLI global parameters in BIMER **272**

Appendix G Calibration of Gorokhovski's breakup model **274**

Nomenclature

Acronyms

ALM Actuator Line Method

BEM Blade Element Momentum

BF Band Flagging

BIMER Banc à Injection Multiple pour les Ecoulements Réactifs

CDF Cumulative Distribution Function

CFD Computational Fluid Dynamics

CM Center of Mass

CRZ Corner Recirculation Zone

DC Dense Core

DCA Direct Coupling Approach

DoE Design of Experiments

DPS Discrete Particle Simulation

EE Euler-Euler

EL Euler-Lagrange

FIM-UR Fuel Injection Model by Upstream Reconstruction

HPC High Performance Computing

IB Interior Boundary

IRZ Inner Recirculation Zone

JICF Jet in Crossflow

LDI Lean Direct Injection

LISA Liquid Injection for Swirled Atomizers

LPP Lagrangian Point Particle

LPP Lean Premixed Prevaporized

MSFI Multi-Staged Fuel Injection

ODE Ordinary Differential Equation

PDA Phase Doppler Anemometry

PDF Probability Density Function

PIV Particle Image Velocimetry

RCT Reduced Computational Time

RMS Root Mean Square

RQL Rich-Burn, Quick-Quench, Lean-Burn

RTT Reynolds Transport Theorem

SCA Statistical Coupling Approach

SLI Smart Lagrangian Injectors

SMD Sauter Mean Diameter

SWJ Swirled Jet

TAPS Twin Annular Premixing Swirler

TKE Turbulent Kinetic Energy

WCT Wall Clock Time

Dimensionless numbers

Oh Ohnesorge number

q Momentum flux ratio

Re Reynolds number

We Weber number

Greek Symbols

α_l	Liquid volume fraction
μ	Dynamic viscosity
ν	Kinematic viscosity
ω	Vorticity
Φ	Evaporation rate
ρ	Density
σ	Standard deviation
σ	Surface tension
τ	Characteristic time

Roman Symbols

$\mathbf{u}$	Velocity vector
$\mathbf{x}$	Position vector
t	Time

inj	Injection
g	Gaseous phase
l	Liquid phase
p	Liquid particle

List of Figures

1.1 Evolution of NO_x emissions with several generations of aircraft engines . . . 2
1.2 NO_x emission forecasts from 2017 to 2040 . . . 2
1.3 Motivation for low-NOx combustion . . . 3
1.4 The TAPS concept . . . 4
1.5 Multipoint injector from Safran Aircraft Engines (SAE) showing the atomization mechanisms present in MSFI systems . . . 4
1.6 Multi-physics phenomena in a reactive jet in crossflow. . . . 5
1.7 Atomization breakup regimes . . . 6
1.8 Primary atomization regimes in jets . . . 7
1.9 Secondary atomization regimes . . . 8
1.10 Experimental images of kerosene JICF breakup . . . 9
1.11 Breakup map for liquid jet in crossflow. Source: Wu et al. (1997) . . . 10
1.12 Primary breakup processes in liquid jet in crossflow . . . 10
1.13 Instantaneous and averages images of a liquid jet in crossflow. Source: Ragucci et al. (2007) . 11
1.14 Effect of q ratio. From left to right: $q = 3, 6, 12, 24$. Fixed values: $d_{inj} = 0.5\ mm$, $u_g = 75\ m/s$, $p_\infty = 4$ bar. Source: Freitag & Hassa (2008). . . . 12
1.15 Effect of air velocity. From left to right: $u_g = 25, 50, 75, 100\ m/s$. Fixed values: $d_{inj} = 0.5\ mm$, $q = 6$, $p_\infty = 4$ bar. Source: Freitag & Hassa (2008). . . . 12
1.16 Direct numerical simulations of primary atomization in liquid jets. . . . 13
1.17 Lagrangian simulations of liquid jets. . . . 14
1.18 Large Eddy Simulation of a Pratt & Whitney combustor. . . . 14
1.19 Schematic of coupled Eulerian–Lagrangian approaches for liquid atomization. . . . 14

2.1 Two-phase systems classification . . . 19
2.2 Numerical methods to simulate two-phase flows. . . . 26
2.3 Comparison of a droplet solved in a 20x20 grid by a diffuse interface method and a sharp-interface VOF method . . . 27
2.4 Illustration of the front-tracking method . . . 28
2.5 Application of VOF method . . . 28
2.6 Representation of distance functions ϕ and ψ in the ACLS methodology . . . 29
2.7 Illustration of dynamic mesh adaptation with AMR . . . 31
2.8 Automatic AMR triggering . . . 31

3.1 Numerical approaches to solve dispersed phase flows . . . 34
3.2 Classification proposed for the state of the art in lagrangian injection modeling. . . . 38
3.3 Pressure-swirl atomizer . . . 38
3.4 FIMUR model for injection in pressure-swirl atomizers . . . 39
3.5 LISA model for injection in pressure-swirl atomizers. Source: Guedot (2015). . . . 40
3.6 Breakup mechanism in an airblast prefilmer spray . . . 41
3.7 Modeling approaches for liquid jet in crossflow proposed by Jaegle (2009). . . . 42
3.8 Contours of instantenous axial velocity and liquid JICF evolution simulated by Apte et al. (2003). . . . 42
3.9 Jet in crossflow simulated with VOF plus lagrangian approach. . . . 43
3.10 Schemes showing numerical models for liquid jets in crossflow . . . 44

3.11 Instantaneous axial gaseous velocity field on the plane y = 0 mm together with the lagrangian droplets. . . . 45
3.12 Jet in crossflow modeling strategy followed by Eckel et al. (2016). . . . 46
3.13 Simulation of jet in crossflow by Eckel et al. (2016). . . . 46
3.14 JICF sprays and penetrations obtained by Fan et al. (2018) with different injected PDFs for the droplets sizes. (a) Uniform distribution (b) χ^2 distribution (c) Nukiyama-Tanasawa distribution (d) Rosin-Rammler distribution. . . . 47
3.15 Simulated jet in crossflow by Fontes et al. (2019). *Left*: close view of the near-jet, showing the resolved dense core with VOF and the perturbation effect on the gaseous field. *Right*: Farfield view of the jet, showing injection point of lagrangian droplets. Droplets are colored by their diameter. . . . 48

4.1 Illustration of SLI spray formulation in a liquid JICF. . . . 53
4.2 Flowchart of the SLI formulation applied to liquid JICF. . . . 54
4.3 Parameters characterizing liquid structures sampled in resolved atomization simulations. . . . 55
4.4 Droplet sampling prodecure. Source: Tropea (2011) . . . 56
4.5 *Left*: Size histogram evolution with accumulation time of droplets. *Right*: comparison of two droplet size histograms from two consecutive time instants. . . . 58
4.6 Evolution of Normalized Mean Squared Error (NMSE) with respect to spray accumulation time. 59
4.7 Schematic of a discrete grid composed of individual spray probes. The zoomed-in probes shows an example of droplets and parameters characterizing the probe and the spray within it that served as injectors. . . . 60
4.8 Convergence-driven discretization of SLI according to a quadtrees structure. . . . 60
4.9 ALM illustration of a velocity triangle and geometrical conventions in an airfoil and mollification of a point force on several nodes of an unstructured grid . . . 64
4.10 Representation of the dense core as an actuator . . . 65
4.11 Force ratio evolution with Re_x. . . . 67
4.12 Taylor analogy breakup between a droplet and a mechanical system with spring and damper. The undeformed droplet is represented by the dashed line, while the thick solid line depicts the droplet after deformation. x is the displacement from the deformed to the undeformed states. . . . 68

5.1 JICF experimental setup . . . 74
5.2 Numerical domain and boundary conditions of the experimental test bench of Becker & Hassa (2002). *Left*: complete domain. *Right*: detailed view of the injection nozzle. All dimensions are in mm. . . . 74
5.3 Baseline JICF mesh, showing magnified views of the near-field and nozzle regions. . . . 75
5.4 Location of simulated operating conditions in the breakup map by Wu et al. (1997) . . . 76
5.5 Profiles of $\overline{u}$ and TKE along the line right upstream the injector for both operating points for mesh resolution $\Delta x_{\text{ups}} = 0.5$ mm. . . . 77
5.6 Instaneous JICF view with mean axial velocity field in symmetry plane $y = 0$ . . . 77
5.7 Lateral view of high We jet at several time instants. . . . 79
5.8 Front view of high We jet at several time instants. . . . 80
5.9 Top view of high We jet at several time instants. . . . 81
5.10 Lateral view of low We jet at several time instants. . . . 82
5.11 Front view of low We jet at several time instants. . . . 83
5.12 Top view of low We jet at several time instants. . . . 84
5.13 Lateral view of meshes and interface contours near the injector at instant $t^* = 16$ for the high Weber operating condition. . . . 85
5.14 Evolution of liquid volume with time in JICF simulations. . . . 86
5.15 Evolution of mesh size with time in JICF simulations . . . 87
5.16 Surface breakup observed in case UG75_DX10 . . . 88
5.17 Column breakup phenomenon in cases UG100_DX10, UG100_DX20 . . . 89
5.18 Resolution of instabilities at windward side of JICF for both resolutions in the high Weber operating point. . . . 90
5.19 y^+ distribution in the nozzle walls for high Weber cases . . . 90
5.20 PDF of y^+ at the nozzle walls for high Weber cases . . . 91

5.21 Mesh element size Δx shown at plane $y = 0$ for instantaneous simulations of cases UG100_DX10, UG100_DX20 . . . 91
5.22 Planes within the injector showing TKE at locations $z = 0, -0.35$ mm for the high Weber case 92
5.23 Profiles of mean vertical velocity, TKE and mean vorticity magnitude at lines located at $y = 0$ along the planes $z = -0.35,\ 0$ mm . . . 92
5.24 Instantaneous vorticity fields for the high Weber operating point. . . . 93
5.25 Vertical velocity profiles at yellow lines depicted in Figure 5.24 . . . 94
5.26 Trajectories and L_2 errors obtained with different methods for case UG100_DX20 . . . 96
5.27 Trajectories and errors obtained with method MEAN_GRAD . . . 97
5.28 Interaction between liquid dense core and gaseous phase. . . . 98
5.29 Jet from case UG100_DX10 showing planes to study the gaseous phase . . . 98
5.30 Mean axial velocity at plane $y = 0$ mm . . . 99
5.31 Mean axial velocity evolution along axial coordinate at locations $z = 1.6, 4$ mm in plane $y = 0$ (lines of Figure 5.30) . . . 99
5.32 Mean axial velocity evolution along vertical coordinate at $x = 1, 2.5, 5, 10, 15$ mm locations of plane $y = 0$ (lines of Figure 5.30) . . . 100
5.33 Mean axial velocity at planes $x = 5, 10$ mm . . . 100
5.34 Mean axial velocity evolution along lateral coordinate at z lines of Figure 5.33 . . . 101
5.35 Mean axial velocity at planes $z = 0.2, 0.8, 16$ mm . . . 102
5.36 Snapshot of a JICF simulation showing the droplets sampling planes (in grey) and the different filming regions . . . 103
5.37 Time evolution of instantaneous liquid flow rates Q_l for case UG100_DX10. . . . 103
5.38 Time evolution of mean and RMS values of Q_l in IBs . . . 104
5.39 Mean flow rates (bars) and RMS (black vertical lines) obtained with IBs for each simulation. 105
5.40 Relative loss of total liquid flow rates loss ΔQ_l with axial distance. . . . 106
5.41 Spatial distributions of volume fluxes obtained from interior boundaries . . . 107
5.42 Cost of the JICF simulations in CPU time and CPU per physical times simulated . . . 109
5.43 Variation with time of the dense core breakup point coordinates $x_\mathrm{b}, z_\mathrm{b}$ and width w. . . . 110
5.44 Evolution of mean geometric parameters of the dense core . . . 111
5.45 Mean values for the dense core geometric parameters . . . 111
5.46 Establishment of SMD and Q_l in JICF sampling planes . . . 113
5.47 Liquid fluxes provided by interior boundaries (solid color bars) and lagrangian tracking (black-dashed color bars). . . . 114
5.48 Evolution of SMD with axial distance for each simulation. . . . 114
5.49 Droplets size (f_0) and volume (f_3) histograms for all cases . . . 116
5.50 Sampled mean liquid velocities for all cases . . . 117
5.51 Scatterplots velocities - diameters for case UG100_DX10 at plane $x = 10$ mm . . . 118
5.52 Mean deformation parameters for all simulations . . . 119
5.53 Scatterplots of deformation parameters α - β for cases UG100_DX10, UG100_DX20 at plane $x = 10$ mm . . . 119
5.54 Spray states at x = 5 mm for case UG75_DX10 . . . 121
5.55 Spray states at x = 10 mm for case UG75_DX10 . . . 121
5.56 Spray states at x = 5 mm for case UG75_DX20 . . . 122
5.57 Spray states at x = 10 mm for case UG75_DX20 . . . 122
5.58 Spray states at x = 15 mm for case UG75_DX20 . . . 122
5.59 Spray states at x = 5 mm for case UG100_DX10 . . . 123
5.60 Spray states at x = 10 mm for case UG100_DX10 . . . 123
5.61 Spray states at x = 5 mm for case UG100_DX20 . . . 124
5.62 Spray states at x = 10 mm for case UG100_DX20 . . . 124
5.63 Spray states at x = 15 mm for case UG100_DX20 . . . 124
5.64 Spray states at x = 5 mm for case UG100_DX20_NT . . . 125
5.65 Spray states at x = 10 mm for case UG100_DX20_NT . . . 125
5.66 Volume flux, arithmetic mean and volume-weighted axial velocities at $x = 5$ mm from case UG100_DX10 . . . 126
5.67 Histograms of droplets diameters D (*left*) and axial velocity u (*center*), and scatterplot $D - u$ (*right*) . . . 127

5.68 Cost savings in SLI development by refining grid resolution 127

6.1 SMD and volume flux maps for the high Weber case obtained experimentally by Becker & Hassa (2002) at a location $x = 80$ mm downstream the liquid injector 130
6.2 Integrated liquid volume flux and SMD profiles by Becker & Hassa (2002) at a location $x = 80$ mm downstream the liquid injector. 130
6.3 Snapshot of instantaneous liquid jet from Becker & Hassa (2002), showing the filming phenomenon 132
6.4 Volume flux maps at $x = 80$ mm for the high Weber operating conditions from experiments (Becker & Hassa 2002) and past computational works on the same configuration and operating condition. The experimental map shows the grid composed of the probes through which the spray is characterized 133
6.5 Integrated SMD and volume flux profiles from experiments and past computational works. Computational fluxes have been obtained through digitalization and are hence not fully reliable 134
6.6 Schematic of parameters involved in SLI simulations and their interactions 135
6.7 Mesh employed for dispersed-phase simulations with ALM 136
6.8 Perturbation effect towards the gaseous phase visualized through the instantaneous velocity magnitude in the plane $y = 0$ 136
6.9 Mean axial velocity field at plane $y = 0$ for resolved case UG100_DX10 and the three actuators tested. The grey cylinder represents the actuator, i.e. the location where body forces are applied137
6.10 Mean axial velocity evolution in ALM and resolved simulations along axial coordinate at locations $z = 1.6, 4$ mm in plane $y = 0$ (lines of Figure 6.9) 138
6.11 Mean axial velocity evolution in ALM and resolved simulations along vertical coordinate at $x = 2.5, 5, 10$ mm locations of plane $y = 0$ (lines of Figure 6.9) 138
6.12 Mean axial velocity field at planes $x = 5, 10$ mm for resolved case UG100_DX10 and gaseous cases with and without ALM 139
6.13 Mean axial velocity evolution along lateral coordinate in ALM and resolved simulations at z lines of Figure 6.12 140
6.14 Location of the reduced domain within the resolved atomization computational setup (in green) and mesh details 141
6.15 Methodology to prescribe mean and RMS velocity fields from resolved simulations in reduced domain for dispersed-phase computation. 142
6.16 Mean axial velocity field at plane $y = 0$ for resolved case UG100_DX10 and prescribed gaseous inlet 143
6.17 Mean axial velocity evolution along axial coordinate at locations $z = 1.6, 4$ mm in plane $y = 0$ 143
6.18 Mean axial velocity evolution along vertical coordinate at $x = 2.5, 5, 10$ mm locations of plane $y = 0$ (lines of Figure 6.19) 143
6.19 Mean axial velocity field at planes $x = 5, 10$ mm for resolved case UG100_DX10 and prescribed gaseous inlet 144
6.20 Mean axial velocity evolution along lateral coordinate at z lines of Figure 6.19 144
6.21 SLI mean volume-weighted (VW) and RMS velocity maps from case UG100_DX10 at $x_{\text{inj}} = 5$ mm 145
6.22 Lagrangian jet establishment in the JICF simulation performed for the ALM optimal and prescribed inlet gaseous phases 146
6.23 Visualization of the breakup cascade from a single lagrangian droplet in case ALM initial illustrating the breakup cascade 147
6.24 Convergence of spray liquid flux (*left*) and SMD (*right*) with time at plane $x = 80$ mm 148
6.25 Evolution of SMD along axial location x for the different gaseous boundary conditions tested 148
6.26 Flux and SMD maps for numerical simulations comparing the effect of gaseous phase modeling with the experimental results 151
6.27 Integrated profiles of flux and SMD maps for numerical simulations comparing the effect of gaseous phase modeling with the experimental results 152
6.28 Flux and SMD maps for numerical simulations comparing the effect of secondary atomization models with the experimental results 153
6.29 Integrated profiles of flux and SMD maps for numerical simulations comparing the effect of secondary atomization models with the experimental results 153
6.30 Evolution of SMD along axial location x for the three atomization models 154

6.31 Integrated profiles of flux and SMD maps for numerical simulations comparing the effect of SLIs obtained with different resolutions and at several injection locations with the experimental results . . . 155
6.32 View of the dispersed spray in simulation UG100_DX20_x05, showing three regions with large droplets along the channel . . . 156
6.33 Evolution of SMD along axial location x with SLIs from two level-set resolutions UG100_DX10, UG100_DX20 at two injection locations . . . 156
6.34 SLI mean arithmetic and VW velocity maps from case UG100_DX10 at $x_{\text{inj}} = 5$ mm . . . 157
6.35 Integrated profiles of flux and SMD maps for numerical simulations comparing the effect of spray velocities with the experimental results . . . 158
6.36 Integrated profiles of flux and SMD maps for numerical simulations comparing the effect of injection diameters $f_0(D)$ with the experimental results . . . 159
6.37 SLI maps from case UG100_DX10 at $x_{\text{inj}} = 5$ mm with and without convergence-driven discretization applied . . . 160
6.38 Integrated profiles of flux and SMD maps for numerical simulations comparing the effect of convergence-driven discretization with quadtrees with the experimental results . . . 161
6.39 Integrated profiles of flux and SMD maps for numerical simulation UG75_DX10 at $x = 5$ mm (low Weber operating condition) . . . 162
6.40 Effect of introducing an atomization delay in space Δx_{atom} in the lagrangian field . . . 162
6.41 Evolution of SMD along axial location x with parameter Δx_{atom} . . . 163
6.42 SMD at $x = 80$ mm for several values of parameter Δx_{atom} . . . 163
6.43 Integrated profiles of flux and SMD maps for numerical simulations comparing the effect of Δx_{atom} with the experimental results . . . 164

7.1 BIMER experimental test bench . . . 170
7.2 Swirled injector of the BIMER test bench . . . 170
7.3 Numerical configuration of BIMER test bench . . . 171
7.4 Details of multipoint injector from BIMER test bench. . . . 172
7.5 View of the meshes employed for the BIMER study at the central plane of the burner. . . . 173
7.6 Ratio between turbulent mean viscosity and mean viscosity in central plane . . . 175
7.7 Mean axial velocities at central plane in BIMER . . . 175
7.8 Qualitative experimental validation . . . 177
7.9 Mean and RMS axial velocity profiles along probes lines at x = 30, 50 mm. . . . 178
7.10 Mean and RMS vertical velocity profiles along probes lines at x = 30, 50 mm. . . . 178
7.11 Mean axial velocity field with streamlines from case APP_FINE . . . 179
7.12 Mean and RMS velocity fields at central plane from case APP_FINE . . . 180

8.1 View of liquid injection point in BIMER . . . 184
8.2 Instantaneous snapshot of liquid injection in BIMER shown the local coordinate system and the location of spray sampling planes . . . 184
8.3 Gaseous state at the vicinity of the liquid injection location . . . 185
8.4 Profiles of mean axial velocity $\overline{u}_c$ and TKE along the vertical line right upstream the liquid injector . . . 186
8.5 Location of simulated operating condition in the breakup map by Wu et al. (1997) . . . 186
8.6 Establishment of BIMER resolved atomization simulations at several time instants . . . 188
8.7 Evolution of liquid volume (*left*) and number of mesh elements (*right*) with time in BIMER resolved simulations . . . 189
8.8 Breakup in BIMER, case DX10. . . . 190
8.9 BIMER trajectories . . . 191
8.10 Interaction between liquid dense core and gaseous phase in BIMER . . . 191
8.11 Jet from BIMER case DX10 showing planes to study the gaseous phase . . . 192
8.12 Mean axial velocity at plane $y = 0$ mm . . . 192
8.13 Mean axial velocity evolution along axial coordinate at locations $z_c = 0.3, 1.5$ mm at plane $y_c = 0$ (lines of Figure 8.12) . . . 193
8.14 Mean axial velocity evolution along vertical coordinate at $x_c = 1, 2, 4$ mm locations of plane $y = 0$ (lines of Figure 8.12) . . . 193
8.15 Mean axial velocity at planes $x_c = 1.5, 3$ mm . . . 194

8.16 Mean axial velocity evolution along lateral coordinate at z_c lines of Figure 8.15 . . . 194
8.17 Mean axial velocity at planes $z = 0.2, 0.8, 16$ mm . . . 195
8.18 Time evolution of instantaneous liquid flow rates Q_l for case DX10 . . . 196
8.19 Time evolution of mean (*top*) and RMS (*bottom*) fluxes in BIMER IBs . . . 196
8.20 Mean flow rates from IBs perpendicular to crossflow in BIMER . . . 197
8.21 Computational CPU costs of BIMER resolved atomization . . . 198
8.22 Time evolution of the BIMER dense core breakup point coordinates $x_\mathrm{b}, z_\mathrm{b}$ and width w. . . . 198
8.23 Evolution of mean geometric parameters of BIMER dense core . . . 199
8.24 Mean values for the BIMER dense core geometric parameters . . . 199
8.25 Establishment of SMD and Q_l in BIMER sprays . . . 200
8.26 Liquid fluxes provided by interior boundaries (solid color bars) and lagrangian tracking (black-dashed color bars). . . . 200
8.27 Evolution of SMD with axial distance for each simulation. . . . 201
8.28 Droplets size (f_0) and volume (f_3) histograms for all BIMER cases . . . 202
8.29 Sampled mean liquid velocities for all cases . . . 202
8.30 Mean deformation parameters for BIMER simulations . . . 203
8.31 Scatterplots of deformation parameters α - β for cases DX10, DX15 at plane $x_c = 2$ mm . . . 203
8.32 Spray states at $x_c = 1.5$ mm for case DX10 . . . 204
8.33 Spray states at $x_c = 2$ mm for case DX10 . . . 204
8.34 Spray states at $x_c = 1.5$ mm for case DX15 . . . 205
8.35 Spray states at $x_c = 2$ mm for case DX15 . . . 205
8.36 Cost savings in SLI development . . . 206

9.1 Experimental maps for for SMD and axial velocity u from Renaud (2015) . . . 210
9.2 Mean axial velocity at plane $y = 0$ mm . . . 212
9.3 Mean axial velocity evolution along axial coordinate at locations $z_c = 0.3, 1.5$ mm at plane $y_c = 0$ (lines of Figure 8.12) . . . 213
9.4 Mean axial velocity evolution along vertical coordinate at $x_c = 1, 2, 4$ mm locations of plane $y = 0$ (lines of Figure 8.12) . . . 213
9.5 Mean axial velocity at planes $x_c = 1.5, 3$ mm for resolved DX10, gaseous unperturbed and gaseous ALM cases. . . . 214
9.6 Mean axial velocity evolution along lateral coordinate at z_c lines of Figure 8.17 . . . 215
9.7 Application of the ALM model to two adjacent injectos in BIMER . . . 215
9.8 Several instants of liquid fuel injection through both pilot and take-off stages for baseline case 217
9.9 Instantaneous views with a established spray for the three disperse-phase computations . . . 218
9.10 Qualitative experimental validation . . . 219
9.11 Contribution of pilot and take-off stages to the resulting spray . . . 220
9.12 Histograms of droplets sizes from Baseline and Evap simulations . . . 221

A.1 Inlet domain and partition into sections for calculation of the gaseous velocity profile in JICF simulations . . . 243
A.2 Parametrization of section 1 (shaded). . . . 244
A.3 Parametrization of section 2 (shaded). . . . 245
A.4 Parametrization of section 3 (shaded). . . . 246
A.5 Parametrization of section 4 (shaded). . . . 246
A.6 Boundary layers in flat plates . . . 247
A.7 Gaseous inlet velocity profiles imposed . . . 248

B.1 Baseline meshes in the region spanning from the inlet to the nozzle injector . . . 250
B.2 Convergence of line-integrated mean axial velocity and TKE with mesh resolution . . . 251
B.3 Instantaneous u' fields from gaseous simulation for the high Weber case . . . 252
B.4 Axial velocity fluctuations and associated frequencies at the sampling probes for the simulations at high Weber number. . . . 253
B.5 Variation in Turbulent Kinetic Energy in probes A and B with upstream mesh resolution. . . . 254
B.6 Profiles of $\overline{u}$ and TKE along the line right upstream the injector. . . . 254

C.1 Illustration of experimental procedure to obtain trajectories. Figures taken from Stenzler et al. (2003) . . . 256
C.2 Methods based on mean trajectories . . . 257
C.3 Procedure to obtain instantaneous trajectories. . . . 258
C.4 Obtention of non-monotonic instantaneous trajectory . . . 259
C.5 Obtention of monotonic instantaneous trajectory . . . 259
C.6 Interior boundaries discretization for obtention of liquid flow rates. . . . 260
C.7 Interior boundaries discretization for obtention of bounded flow rates. . . . 260
C.8 Extraction of dense core from resolved atomization simulations. . . . 261
C.9 Methodology to obtain windward and leeward surfaces of mean dense core from resolved atomization simulations . . . 263

D.1 Regions of mass loss at the end of simulation for (a) case 1 (baseline) and (b) case 3 ($\Delta x_{\min} = 10\ \mu$m). . . . 266
D.2 Evolution of liquid volumes . . . 267
D.3 Liquid volume loss at the end of each run and its contributions . . . 268

E.1 Establishment of mean liquid velocities for each case. . . . 270
E.2 Establishment of RMS liquid velocities for each case. . . . 270
E.3 Establishment of mean deformation parameters for each case. . . . 271
E.4 Establishment of RMS deformation parameters for each case. . . . 271

F.1 Establishment of mean liquid velocities for each case. . . . 272
F.2 Establishment of BIMER RMS liquid velocities for each case. . . . 272
F.3 Establishment of mean deformation parameters for each case. . . . 273
F.4 Establishment of RMS deformation parameters for each case. . . . 273

G.1 Flux and SMD maps for numerical simulations comparing the effect of calibrating the constants from the Gorokhovski model with the experimental results . . . 275
G.2 Integrated profiles of flux and SMD maps for numerical simulations comparing the effect of Gorokhovski's model calibration with the experimental results . . . 276
G.3 Evolution of SMD along axial location x for several values of the Gorokhovski atomization model 276

List of Tables

1.1 Correlations for the jet trajectory of the JICF . . . 11

4.1 Parameters sampled from resolved atomization simulation . . . 55
4.2 Summary of SLI injection parameters . . . 62
4.3 Parameters of an actuator representing the dense core . . . 66

5.1 Nomenclature for resolved atomization simulations . . . 75
5.2 JICF operating points studied . . . 76
5.3 Droplet arrival times to sampling planes $\tau_{\mathrm{dr_x}}$, total physical time simulated t_{ph} and its dimensionless equivalent calculated with Eq. (5.3) in JICF simulations . . . 85
5.4 Summary of methods for computing JICF trajectories . . . 95
5.5 L_2 errors for JICF simulations performed. . . . 97
5.6 Computational cores, mesh cells and total number of droplets present at the domain for JICF simulations at $t^* = 12$ . . . 108
5.7 Computational performances from JICF simulations at $t^* = 12$ . . . 109
5.8 Dense core characterization: geometric and momentum parameters . . . 112
5.9 Total physical t_{ph} and accumulation times t_{acc}, absolute and dimensionless with Eq. (5.3), for each JICF simulation . . . 112
5.10 Number of droplets sampled in JICF simulations: total amount (N_{dr}) and total amount per accumulation time $N_{\mathrm{dr}}/t_{\mathrm{acc}}$ . . . 113

6.1 Experimental SMDs at $x = 80$ mm . . . 131
6.2 Available data from previous numerical studies on experimental validation in the configuration of Becker & Hassa (2002) . . . 133
6.3 Global data obtained at $x = 80$ mm from experiments, previous computational studies and the present work . . . 135
6.4 Parameters of an actuator representing the dense core for the high Weber case . . . 137
6.5 Droplets arrival time to $x = 80$ mm, total physical t_{ph} and accumulation times t_{acc}, absolute and dimensionless with Eq. (6.6), for lagrangian JICF simulations . . . 147
6.6 SMD values at $x = 20, 80$ mm and decay rates λ in the linear region . . . 149
6.7 SMD values at $x = 80$ mm and deviation with the experimental value for different gaseous conditions . . . 149
6.8 SMD values at $x = 80$ mm for simulations with the different secondary atomization models . 154
6.9 SMD values at $x = 80$ mm for simulations with different SLIs . . . 157
6.10 SMD values at $x = 80$ mm for simulations with different prescribed velocities . . . 159
6.11 SMD values at $x = 80$ mm for simulations with different f_0 laws . . . 159
6.12 SMD values at $x = 80$ mm for simulations with and without quadtrees . . . 160
6.13 SMD values at $x = 80$ mm for simulation of the low Weber operating point . . . 161

7.1 Physical properties of dodecane fuel ($C_{12}H_26$) at 20 °C . . . 170
7.2 Operating points for performing non-reactive gaseous simulations . . . 171
7.3 Characteristics of meshes employed in BIMER study . . . 172
7.4 Nomenclature for simulations reported in this chapter . . . 172
7.5 Gaseous fields time scales for each operating point . . . 174

8.1 BIMER operating point to perform resolved atomization simulations . . . 187
8.2 Nomenclature for resolved atomization simulations . . . 187
8.3 Characteristic droplet arrival times to sampling planes $\tau_{\mathrm{dr}_{x_c}}$ [μs] in BIMER simulations . . . 189
8.4 Computational cores, mesh cells and total number of droplets present at the domain for BIMER simulations at $t^* = 4.7$ . . . 197
8.5 Computational performances from BIMER simulations at $t^* = 4.7$ . . . 197
8.6 BIMER dense core characterization: geometric and momentum parameters . . . 199
8.7 Total physical t_{ph} and accumulation times t_{acc}, absolute and dimensionless with Eq. (8.3)n . 199
8.8 Number of droplets sampled in BIMER simulations: total amount (N_{dr}) and total amount per accumulation time $N_{\mathrm{dr}}/t_{\mathrm{acc}}$ . . . 200

9.1 Operating point to perform gaseous and two-phase simulations tested by Renaud (2015) . . . 210
9.2 LISA model setup for pilot injection . . . 211
9.3 Parameters of an actuator representing the BIMER dense core . . . 212
9.4 Dispersed-phase simulations performed for BIMER . . . 215
9.5 Characteristic times for droplets to reach location $x = 35$ mm in the pilot and take-off stages 216
9.6 SMDs obtained compared to experimental one . . . 221

A.1 Parameters obtained characterizing the gaseous inlet velocity profiles . . . 248

B.1 Parameters characterising inflow turbulent fields and flow-through time τ_{ft} in JICF simulations 250
B.2 Configurations tested for the mesh independence study . . . 250
B.3 Estimation of characteristic length and time scales for gaseous phase in JICF simulations . . 255

D.1 Simulations performed to evaluate mass loss due to ACLS . . . 265

G.1 SMD values at $x = 80$ mm obtained with different constants in the Gorokhovski secondary atomization model . . . 274

Chapter 1

Introduction

1.1 General context

In the 20th century, the field of aeronautics has experienced a hectic growth since World War I (1914 - 1919), where airplanes played a fundamental role in aerial battles. The advances in military aviation led to the apparition of the first airlines and the birth of commercial aviation after the war. It was not, however, until World War II (1939 - 1945) that the greatest progresses were made: technological improvements resulted in larger, more efficient aircraft employed for surveillance, in air battles or for bombing purposes. After this period, airplanes used during the war were recycled with civil purposes to transport cargo and passengers. This marked the beginning of a new era for commercial aviation which has continued to grow until nowadays, where air transportation is an essential activity in today's society.

The increasing relevance of commercial aviation has been possible due to advances in aeronautical technologies, from aircraft structures and flight control to propulsion systems. In the case of the latter, the birth of the jet engine in the 1930s supposed a milestone that marked the transition from propelled airplanes working with internal combustion engines to faster aircraft powered by gas turbines. Improvements in propulsion technologies have led to larger, more efficient engines capable to drive airplanes during longer periods of time.

Despite today's propulsion technologies being more efficient than those from its origins, they are not exempt from producing emissions. Chemical species generated during the combustion process in gas turbines include among others CO_2, a greenhouse gas contributing to global warming, and CO and NO_x, considered as pollutant emissions. In this respect, the increasing demand of commercial transportation and a rising general concern about the effects of climate change have placed the need of reducing emissions, as well as noise, as a major constraint for the development of aviation in the decades to come. The Advisory Council of Aeronautic Research in Europe (ACARE) has settled the goal to reduce the emissions per passenger/kilometre of CO_2 by 75 % and of NO_x by 90 % for the year 2050 with respect to the levels of 2000 (ACARE 2017).

Emissions of NO_x are a big concern due to their harmful effect to health and environment (e.g. it is one of the main species producing acid rain). The evolution of aeronautical engines in the last decades have led to higher combustion temperatures and larger Overall Pressure Ratios (OPR), which help to reduce fuel consumption but increase the production of NO_x. Engine manufacturers have worked on mitigating this increasing trend, as shown by the evolution of NO_x emissions with OPR for several generations of engines in Figure 1.1. Certified engines have succeeded in reducing emissions below the ICAO-CAEP regulatory limits. Nevertheless, the NO_x are still expected to grow due to the expanding aerial traffic demand. Figure 1.2 displays the forecasts for several traffic scenarios, where it is visualized the potential effect of technology advances in the emissions at 2040 (lower bounds) with respect to the case where current technologies (of year 2017) would be used (upper bounds). Therefore, in order to maintain the emissions below a certain level and hence accomplish ACARE's goals, substantial efforts are being done. One way of achieving this is by controlling and improving the combustion process, since NO_x are produced at high temperatures. For this purpose, the aeronautical community is working towards new combustion chambers and injection processes aiming at creating **lean combustion**.

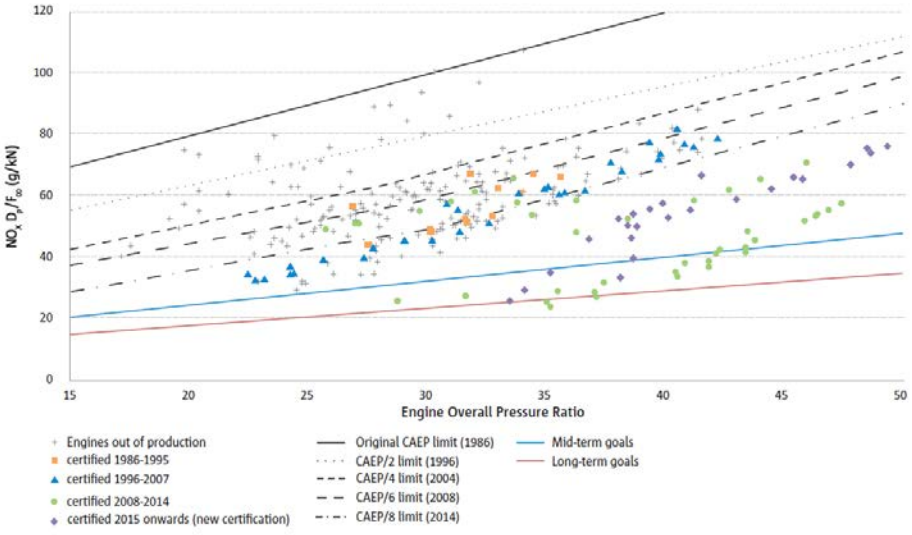

Figure 1.1: Evolution of NO_x emissions with several generations of aircraft engines. Source: EASA (2019)

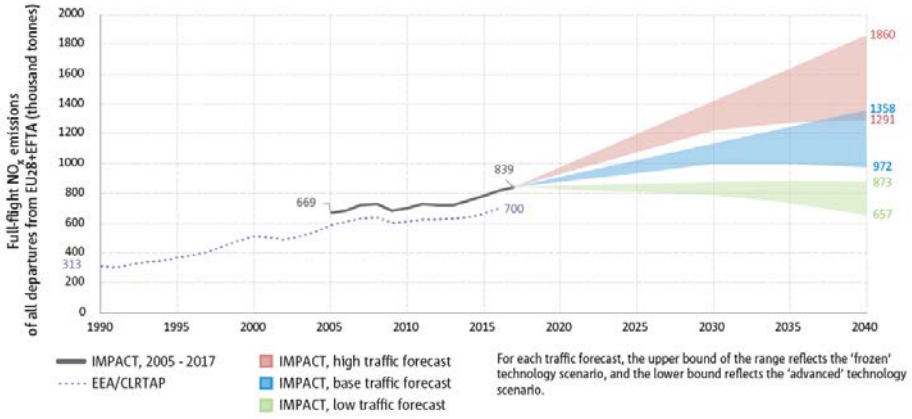

Figure 1.2: NO_x emission forecasts from 2017 to 2040. Source: EASA (2019)

1.2 Lean combustion in aeronautical gas turbines

The motivation for developing lean systems is shown in Figure 1.3 left. At lean regimes (i.e. with an excess of air), the flame temperature is lower and, consequently, NO_x formation is reduced. At the same time, emissions of CO, hydrocarbons (HC) and soot are also diminished at this regime (provided that the air excess is not too high, or the emissions will start to grow again). On the other hand, operating at lean regimes will make the system more prone to thermoacoustic instabilities and will place it closer to the the limit of lean blow-out (LBO), hindering ignition and relight capabilities.

One of the first developed concepts aiming at reducing emissions was the **Rich-Burn, Quick-Quench, Lean-Burn** (**RQL**) (Novick & Troth 1981). RQL systems split the combustion process in three stages. Firstly combustion begins in a fuel-rich primary zone close to the injector, where the NO_x rate is low (see Figure 1.3 left). Then, a quick mixing of the unburnt fuel takes place with fresh air to finally burn in lean conditions. This procedure allows to decrease NO_x emissions as depicted by the low-NO_x route in Figure 1.3 right. However, a fine and complete fuel atomization is needed so that a fast mixing takes place; otherwise, unburnt fuel could produce extra smoke and soot in the rich-burn region (El-Asrag et al. 2007). This hinders the proper operation of RQL chambers in regimes where fuel can hardly be atomized, such as during altitude relight.

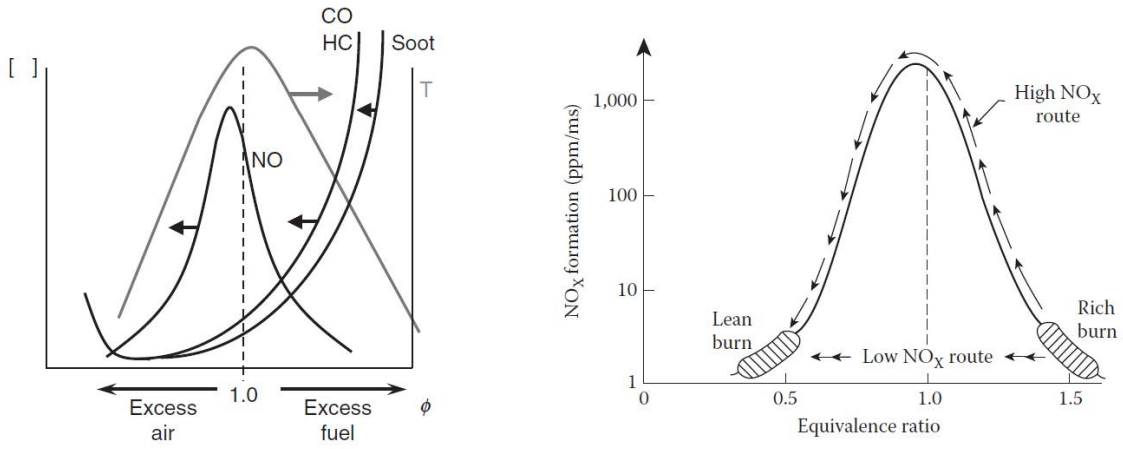

Figure 1.3: Motivation for low-NOx combustion. *Left*: Temperature and species concentration variation with stoichiometric ratio in combustion chambers. Source: Dunn-Rankin (2008). *Right*: NOx formation in Rich-Burn, Quick-Quench, Lean-Burn (RQL) concepts. Source: Lefebvre & Ballal (2010).

The need of reducing NO_x emissions to the levels settled by authorities led to the development of lean combustion strategies, usually referred as low-NO_x (Tacina 1990). In order to foster lean combustion, low-NO_x concepts introduce an excess of air at the vicinity of the injector: around 70 % of air is introduced in the combustion chamber at this location (primary zone), while the rest is injected further downstream for effusion cooling. Compared to conventional combustors, where around 30 % of air is injected in the primary zone and the rest is introduced downstream through dilution holes, this allows to reduce the length of the combustion chamber and hence the residence time of combustion, directly linked to NO_x formation (Lefebvre & Ballal 2010). Furthermore, operating directly at lean regimes will also reduce the formation of soot and CO emissions, which is the main disadvantage of RQL. One of the first lean combustion concepts is the **Lean Direct Injection** (**LDI**) technology (Tacina 1990), where fuel is directly introduced into the reaction zone without previous premixing. Lower peak temperatures and residence times are obtained, hence reducing pollutant formation. Contrarily, LDI concepts can produce a non-uniform combustion if mixing is not complete. In this respect, the **Lean Premixed Prevaporized** (**LPP**) technology appeared to palliate this issue (Bittlinger & Brehm 1999): a premixing length is added before the reaction zone, so that complete evaporation of fuel and mixing can take place before triggering combustion. LPP concepts need, however, a longer combustion chamber to account for the dilution zone, and are more prone to suffer autoignition, flashback and thermoacoustic instabilities.

A good trade-off between both LDI and LPP is obtained with **Multi-Staged Fuel Injection** (MSFI) (Pehanhoat 2006). Fuel is introduced in the combustion chamber through two main stages: a **pilot stage** for flame stabilization purposes, and a **take-off stage** (also called multipoint) where the most of premixing takes place (see Figure 1.4 left). The combination of both injection systems creates a flame that burns in lean conditions and reduces combustion instabilities compared to other low-NO_x concepts (Barbosa et al. 2009). The percentage of fuel introduced through each stage can be controlled in order to optimize the combustion performance depending on the flight phase: this procedure is called staging. Considerable reductions in emissions can be obtained with MSFI in conditions where most of NO_x is produced, such as climb and cruise. Figure 1.4 right shows the improvements in pollution of a multi-staged fuel injector named Twin Annular Premixing Swirler (TAPS) (Foust et al. 2012) compared to a RQL combustor.

MSFI are a promising technology for fuel injection in aeronautical combustors, and manufacturers such as Safran are working on developing these systems for their application in future engines. Since their main characteristic is fuel staging, processes prior to combustion (e.g. injection, atomization and mixing) are fundamental for MSFI performance, and their proper comprehension is paramount to optimize such systems. The next sections makes a review on the two-phase flow physical mechanisms of injection and atomization relevant to these injection systems.

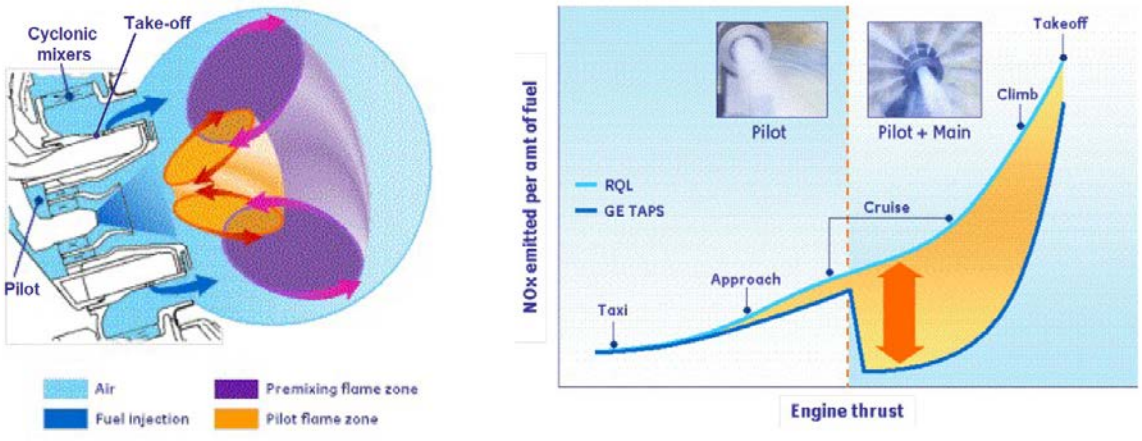

Figure 1.4: The TAPS concept. *Left*: regions in a multi-staged injection system from a TAPS concept. *Right*: effect of multi-staged injection in NO_x emissions from a TAPS concept compared to a RQL system. Source: Foust et al. (2012).

1.3 Fuel injection technology

Figure 1.5 shows a MSFI injector and the atomization mechanisms present in these systems. Fuel is injected through two inlets: a central nozzle (the pilot stage), where a pressure-swirl atomizer delivers a **hollow cone** spray, and the multipoint injectors located in a crown around the central injector (the take-off stage), where liquid atomizes according to a **jet in crossflow** configuration (JICF). As seen in the figure, these two injection systems will produce liquid atomization shortly after the injection location. Furthermore, a third breakup mechanisms is present if the opening angle of the hollow cone is large enough: in such cases, liquid can impinge the walls of the injector and form a film which breaks further downstream due to the interaction between the liquid, aerodynamics and wall, resulting in an **airblast** spray. As a consequence of these three atomization mechanisms, a dispersed spray will be formed further downstream the injection chamber. This dispersed spray will later be able to evaporate, mix with the surrounding air and burn in the combustion process.

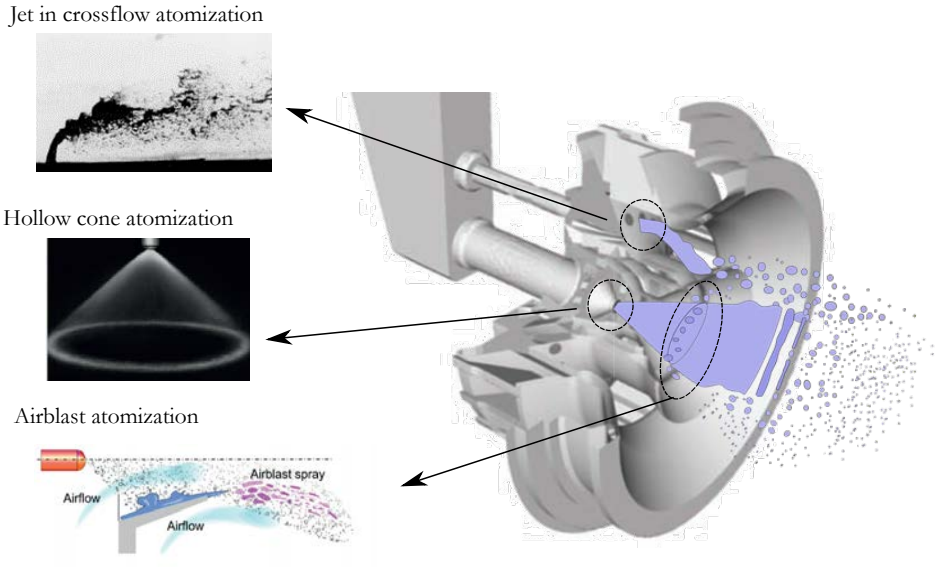

Figure 1.5: Multipoint injector from SNECMA showing the atomization mechanisms present in MSFI systems. Source: Jaegle (2009)

A view of the multiphysical phenomena found within a combustor is shown in Figure 1.6 with an example of reactive liquid JICF. Liquid fuel is injected through the injection nozzle as a coherent jet. Instabilities start taking place after injection and will eventually break the jet into large blobs and ligaments during a process known as **primary atomization** (or primary breakup). Resulting liquid structures will then break into smaller droplets during **secondary atomization** (or secondary breakup) until the droplets are in equilibrium with the surrounding air and reach a small size and a spherical shape. As a consequence of the atomization process, the specific surface of the spray (i.e. the amount of liquid surface which is in contact with the continuous gas) is large and then **evaporation** is promoted. Gaseous fuel can then **mix** with the surrounding air to produce an ignitable mixture that can finally burn in a **combustion** process. Other physical mechanisms are found taking place simultaneously, such as drop-drop interactions, wall-drop interactions and droplet combustion. All these processes are generally found within gas turbines.

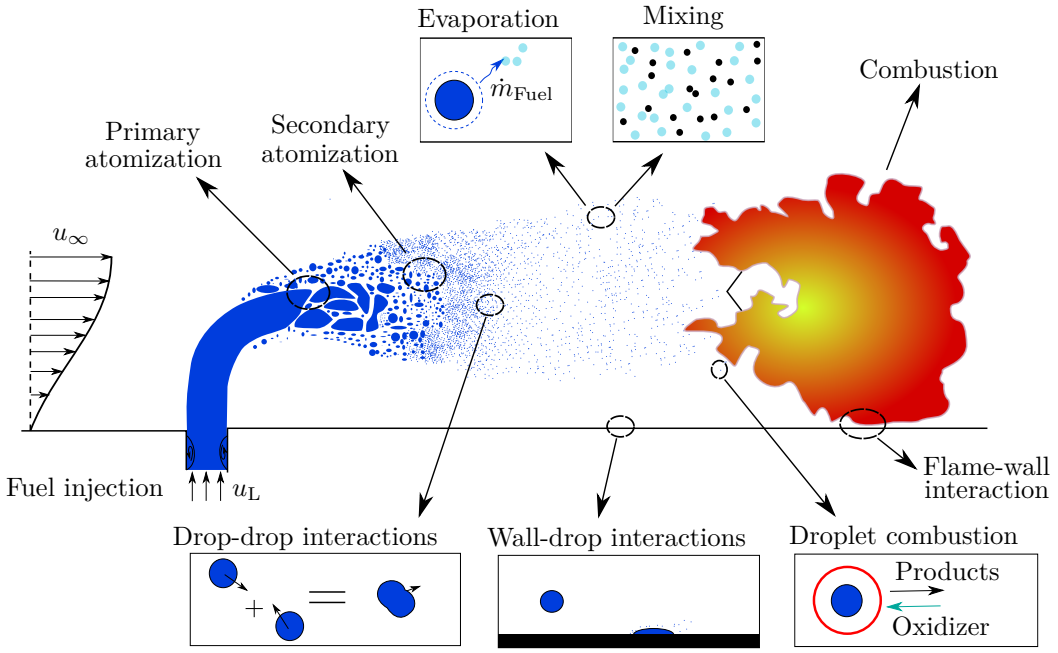

Figure 1.6: Multi-physics phenomena in a reactive jet in crossflow.

As illustrated in Figures 1.5 and 1.6, the atomization process is responsible for the generation of droplets. The size of these droplets should be small enough so that the liquid specific surface is large and fuel can burn efficiently. Otherwise, unburnt fuel and inefficient combustion can increase the production of pollutants such as NO_x and soot. Understanding the driving mechanisms of atomization is therefore essential for the correct design of atomizers and injectors. Atomization involves a wide range of length-scales from the injector size to the diameter of the smallest droplets, with a difference of several orders of magnitude: its study, modeling and simulation are therefore not trivial. The rest of this section is then devoted to introducing the fundamentals of atomization and the jet in crossflow phenomenon, which is of special interest for MSFI systems and constitutes the main application of this thesis.

The atomization process

After liquid injection, atomization is the mechanism through which coherent, dense liquid is fractured into smaller liquid structures. Lefebvre & McDonell (2017) define atomization as "*the process by which a liquid jet or sheet is disintegrated by the kinetic energy of the liquid, by the exposure to high-velocity air or gas, or by mechanical energy applied externally through a rotating or vibrating device* (sic)". Its purpose is to increase the liquid specific surface to allow for fuel evaporation.

Atomization is initially triggered by instabilities which are found naturally in liquids jets. Rayleigh (1878) found that jet breakup into smaller drops is produced due to the growth of small disturbances in the liquid. Instabilities are amplified by the aerodynamic interaction with the surrounding air, enhancing the energy

transfer between both phases. Turbulence in the jet also amplifies these disturbances: if liquid is injected in a high turbulent state, atomization will occur promptly and breakup will be governed by the aerodynamic forces, while if the jet is injected at low speed the breakup will be governed by surface tension and capillary forces, and the breakup morphology will be different. Regimes of atomization are distinguished according to two main dimensionless numbers, the **Reynolds number** Re and the **Weber number** We:

$$Re = \frac{\rho u D}{\mu} \quad ; \quad We = \frac{\rho u^2 D}{\sigma} \tag{1.1}$$

where ρ is density, μ the viscosity, σ the surface tension, u is a characteristic velocity (usually the liquid velocity or the relative velocities between liquid and gas), D a characteristic length (usually the nozzle diameter or the droplet size). The Reynolds number represents the ratio between the aerodynamic forces and the viscous ones: a high Re indicates a high turbulent state and a dominance of inertia as the main breakup mechanism, while a low Re means laminar flow and a predominant role of viscosity. The Weber number defines the relative importance of aerodynamic forces with respect to capillary forces. From these definitions applied to the liquid phase, Re_l and We_l, a third ratio measuring the relative importance between viscous and surface tension forces, called **Ohnesorge number**, can be defined:

$$Oh = \frac{\sqrt{We_l}}{Re_l} = \frac{\mu_l}{\sqrt{\rho_l D \sigma}} \tag{1.2}$$

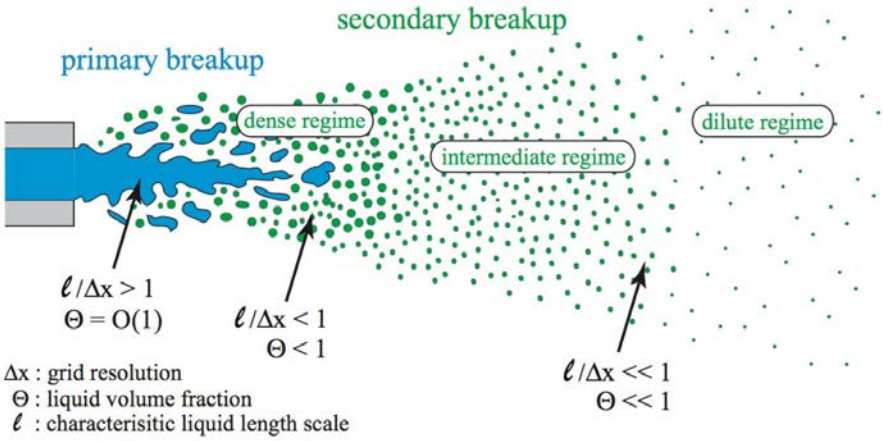

Figure 1.7: Atomization breakup regimes. Source: Herrmann (2003)

Figure 1.7 illustrates liquid jet injection and atomization. The latter is generally divided by the scientific community in two different regimes, which are commonly found in all disintegrations of jets independently of the injection methodology:

- **Primary atomization** is the process by which a liquid jet or sheet breaks from a dense structure into primary structures such as large blobs and ligaments. It is highly dependent on the injector system (pressure-swirl atomizer, jet in crossflow, airblast, etc.), its intrinsic characteristics (internal geometry, discharge coefficient, etc.) and operating conditions (discharge pressure, liquid turbulent state). As shown in Figure 1.7, regions where primary atomization takes place are characterized by high characteristic length scales l (larger than the grid resolution) and high liquid volume fractions, characteristics of the **dense regime**. Numerical methods targeted to solve for primary atomization are addressed in Chapter 2.

  Several regimes of primary atomization are distinguished, classified according to the liquid flow state. These regimes, shown in Figure 1.8, depend on Re_l and Oh based on the liquid velocity and on the injection diameter d_0. As shown, for a fixed value of Oh the governing breakup mechanisms changes if the injection velocity increases (i.e. if Re_l is increases, so turbulence will play a more important role). For the **Rayleigh regime** at low values of Re_l, surface tension is responsible for creating axisymmetric oscillations of the jet with large wavelengths that will make it break into structures larger than the nozzle diameter. Aerodynamic effects are negligible, capillary forces being the leading physical phenomena, and

breakup occurs at several nozzle diameter locations downstream the injection point. As Re_l increases, the relative velocity between the liquid and gas phases is higher and aerodynamic forces cannot be neglected. These ones contribute to the destabilizing waves that create droplets of the size of the nozzle diameter and lead to a faster atomization, yet still occurring at several diameters downstream the injector (**first wind induced regime**). A slightly larger Re_l will swift the dominant breakup role of capillary forces to inertial ones, the wavelenghts of instabilities being amplified by liquid turbulent eddies which break the jet into droplets smaller than the injection nozzle (**second wind induced**). Finally, at even larger values of Re_l capillary forces can be neglected and the breakup is solely governed by aerodynamics, creating small droplets generated right at the nozzle exit (**atomization regime**).

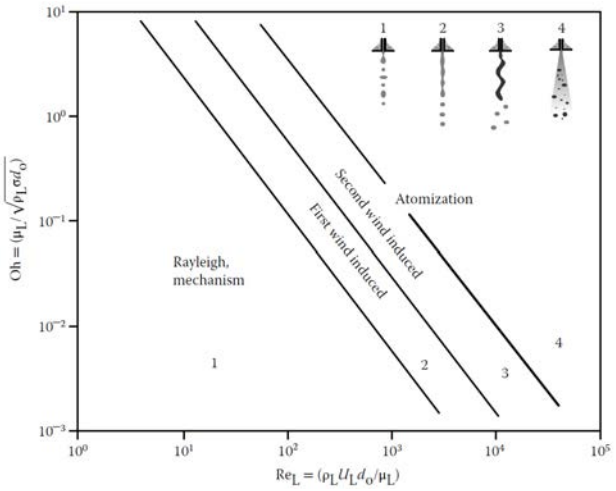

Figure 1.8: Primary atomization regimes in jets. Source: Lefebvre & McDonell (2017)

- **Secondary atomization** occurs after primary atomization, once the main liquid structures have been ejected from the jet and are broken into smaller ones. Injector characteristics and the turbulent state of the coherent liquid do not play a fundamental role anymore: it is the interaction between the liquid structures and the surrounding air that dominates secondary breakup. Figure 1.7 sketches how secondary atomization disintegrates the liquid structures until a developed spray composed of spherical droplets that do not further break. During secondary atomization, the spray undergoes a transition from the dense regime found in primary atomization to a **dilute regime** where the characteristic length scales of liquid (i.e. the droplets diameters) are very small compared to the injector diameter. In this regime, the liquid volume fraction is very low. Between the dense and dilute regimes, an **intermediate regime** can be defined where values of volume fraction and comprised between those of the dense and dilute ones. The lower liquid volume fractions and small sizes (usually smaller than the mesh resolution) found in these regimes require numerical resolution through methods different from those devoted to simulate primary atomization. Such methods are introduced in Chapter 3.

  As the main phenomenon governing secondary atomization is the interaction between the liquid and the gas, this process can be characterized by means of the Weber number based on the relative velocity between phases:

$$We = \frac{\rho_g u_{\text{rel}}^2 r}{\sigma} \tag{1.3}$$

  where $u_{\text{rel}} = |\mathbf{u}_l - \mathbf{u}_g|$ and r is a characteristic length of the liquid structures (the radius for spherical droplets). Different regimes of secondary atomization, universal for any injector geometry and injection system, are depicted in Figure 1.9. For large numbers of We (i.e. high relative velocities and/or large length scales) the breakup is **catastrophic**, and particles are disintegrated into a large number of very small droplets due to shear forces causing stripping. As We decreases the topology of structures found during atomization changes and breakup becomes less aggressive. For small values of We, particles split into a small number of droplets due to **bag** or **vibrational** breakups. For $We < 12$, breakup hardly occurs and droplets are said to be in equilibrium with the surrounding air: atomization is complete. This value is called the **critical Weber number**.

The interactions among droplets (drop-drop) and between droplets and walls (drop-wall), both illustrated in Figure 1.6, also produce secondary atomization with different governing mechanisms than the drop-air interaction. These particular phenomena are not addressed in this thesis and will not be further discussed.

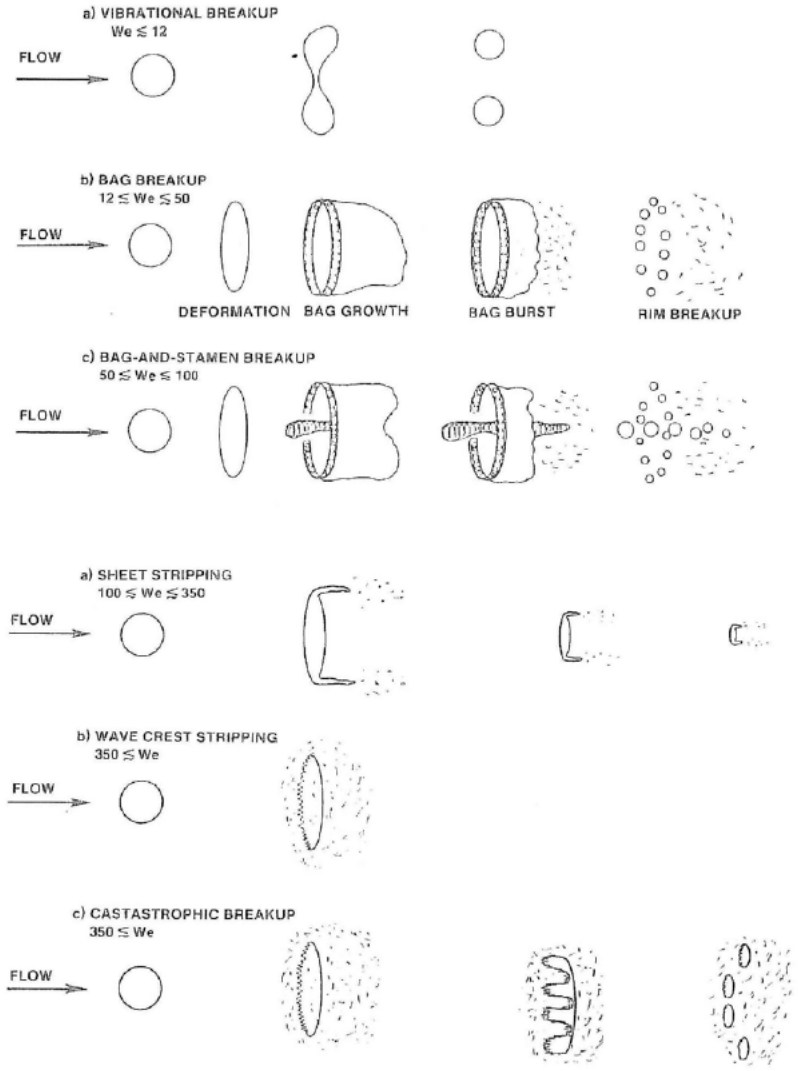

Figure 1.9: Secondary atomization regimes. Source: Pilch & Erdman (1987)

Liquid jet in crossflow

Contrarily to secondary atomization, whose behaviour is not influenced by the injection system, primary atomization is highly dependent on the injector configuration. As a consequence, different liquid structures and characteristic sizes are present in MSFI systems due to the different atomization mechanisms (see Figure 1.5). One characteristic breakup mechanism of MSFI is the one from the take-off stage, which injects fuel in a particular configuration known as liquid jet in crossflow (JICF). In a liquid JICF, a stream of air flows perpendicularly to the direction of liquid injection, as shown in Figure 1.6. The liquid jet leaves the nozzle and bends towards the crossflow direction, undergoing primary and secondary atomization. Consequently, a developed spray is formed further downstream the injection nozzle. The aerodynamic interaction with the surrounding air is of paramount importance: it influences the jet breakup, vertical penetration and the atomization process, which will eventually affect the mixing process prior to combustion in reactive applications.

The atomization process in liquid JICF has been investigated experimentally by several authors (Adelberg 1968, Wu et al. 1997, Becker & Hassa 2002, Ragucci et al. 2007, Freitag & Hassa 2008). These studies have generally identified two main mechanisms of primary breakup:

- **Column breakup**. Surface waves on the liquid column start to grow until the jet breaks into ligaments, which eventually turn into droplets during secondary atomization. An example is shown in Figure 1.10 left, showing the surface waves caused by instabilities. This type of breakup occurs when the aerodynamic interaction is not too strong (low relative liquid-air velocities).
- **Surface breakup**. A strong aerodynamic interaction (large relative liquid-air velocity) produces the disintegration of the liquid jet through shear forces. Small droplets are directly stripped off the sides of the liquid column. Surface breakup can be appreciated in Figure 1.10 right.

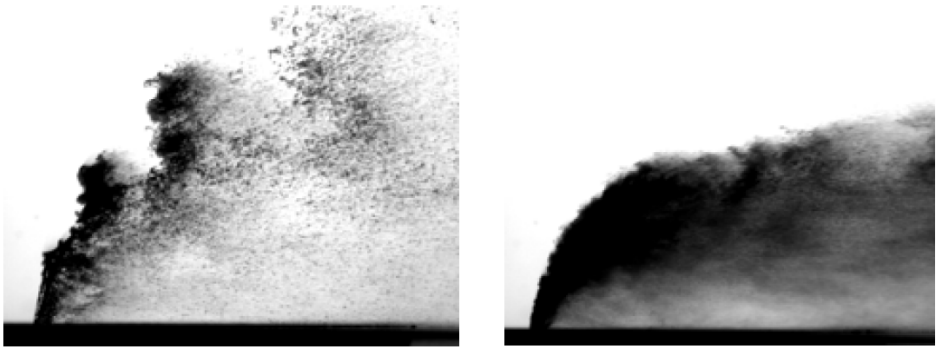

Figure 1.10: Experimental images of kerosene JICF breakup. *Left*: column breakup. *Left*: surface breakup. Source: Freitag & Hassa (2008)

As in any two-phase problem, the physical and breakup characteristics of a JICF can be categorized by means of dimensionless numbers. In liquids jet in crossflow, the main two governing factors are the **momentum flux ratio** q and the **Weber number based on the gaseouos phase** We_g, defined in Eq. (1.4). The former parameter represents the relation between the momentum, or kinetic energies, of the liquid and gaseous phases, while the latter represents the relative contribution of the gaseous phase to capillary forces.

$$q = \frac{\rho_l u_l^2}{\rho_g u_g^2} \quad ; \quad We_g = \frac{\rho_g u_g^2 d_{\text{inj}}}{\sigma} \tag{1.4}$$

The influence of these factors in the breakup process of liquid jets in crossflow has been experimentally studied by Wu et al. (1997), resulting in a breakup map of Figure 1.11. Column and surface breakup, which are the main primary atomization regimes, are separated by the dividing line that indicates the transitional q value between both regimes to be inversely proportional to We_g. For column breakup, several atomization modes appear depending on We_g. Figure 1.12 shows experimental snapshots of these modes. As displayed, for low We_g (capillary and bag regimes) the breakup is dominated by capillary forces and the jet stays coherent until several nozzle diameters downstream the injection point, once the jet has bent and its cross section has been deformed. Waves are clearly observed in the windward side of the jet (i.e. the face in contact with the incoming air), and the wavelength of liquid surfaces λ can be defined as the distance between two nodes. For higher We_g (multimode and shear regimes), instabilities causing breakup are also observed developing along the windward side of the jet, but the stripping of liquid ligaments and droplets at the sides of the jets due to aerodynamic shear is also noticeable . For shear breakup these stripped-off structures appear close to the injection point, hindering the optical access to the jet structure and atomization characteristics further downstream. This was also observed for the surface breakup mode in Figure 1.10 right. Another noticeable characteristic is that the wavelengths λ decrease for larger values of We_g. Sallam et al. (2004) found that the order of magnitudes of the wavelenghts with respect to the injection diameter is $\lambda/d_{\text{inj}} > 1$ for capillary breakup, $\lambda/d_{\text{inj}} \approx 1$ for bag breakup, $0.1 < \lambda/d_{\text{inj}} < 1$ for the multimode regime and $\lambda/d_{\text{inj}} \approx 0.1$ for shear breakup. The main responsible mechanisms of generating these surface waves are either Kelvin-Helmholtz

or Rayleigh-Taylor instabilities. The former ones are said to be the dominating mechanisms for the waves observed in Figure 1.12 (Sallam et al. 2004). It is believed that the prevalence of either one or another mode depends on the density ratio between fluid and gas, the Rayleigh-Taylor being the main dominant mechanism for high density ratios (Ghods 2013). Nevertheless, the appearance and dependence of each instability mode is still not certainly known and remains an open question requiring further research.

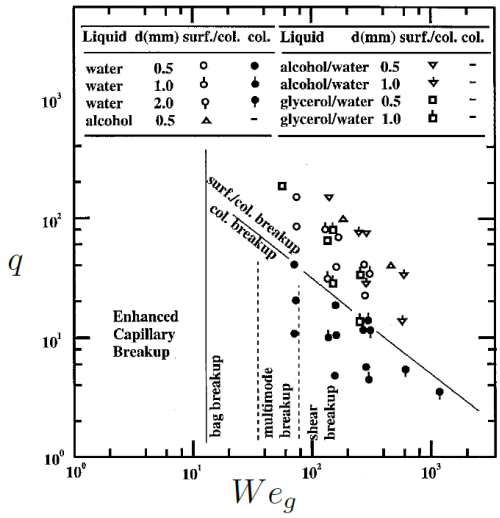

Figure 1.11: Breakup map for liquid jet in crossflow. Source: Wu et al. (1997)

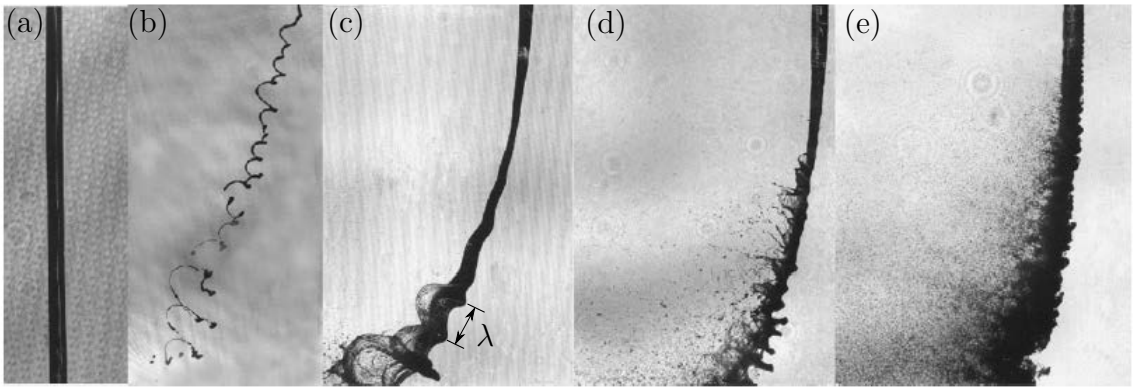

Figure 1.12: Primary breakup processes in liquid jet in crossflow. Air flows from right to left. (a) No breakup, $We_g = 0$. (b) Capillary breakup, $We_g = 3$. (c) Bag breakup, $We_g = 8$. (d) Multimode breakup, $We_g = 30$. (e) Shear breakup, $We_g = 220$. Source: Sallam et al. (2004)

Another relevant characteristic of the liquid jet in crossflow is its penetration, since in real configurations it will determine the region where evaporation and mixing take place and, later, the flame location. The near-field jet penetration can be quantified by means of the **vertical trajectory** of the jet, which is identified as the mean contour of its windward side. This trajectory can be experimentally obtained either from instantaneous snapshots of the jet (Figure 1.13 left) or from average images (Figure 1.13 right), each experimentalist using its own methods. From experimental studies, the trajectory is generally given by correlations relating the vertical trajectory z with the axial coordinate x. Some experimental correlations are shown in Table 1.1, where $We_{ae} = \rho_g u_l^2 d_{\text{inj}}/\sigma$. Figure 1.13 right shows the jet correlation from Ragucci et al. (2007) overlapped with the average jet view.

All the correlations from Table 1.1 show a dependence of the jet trajectory with the injection diameter d_{inj} and the momentum flux ratio q. These are the two main parameters governing the jet penetration. The larger the injection diameter, the further the jet will penetrate. This is attributed to a more coherent jet: if

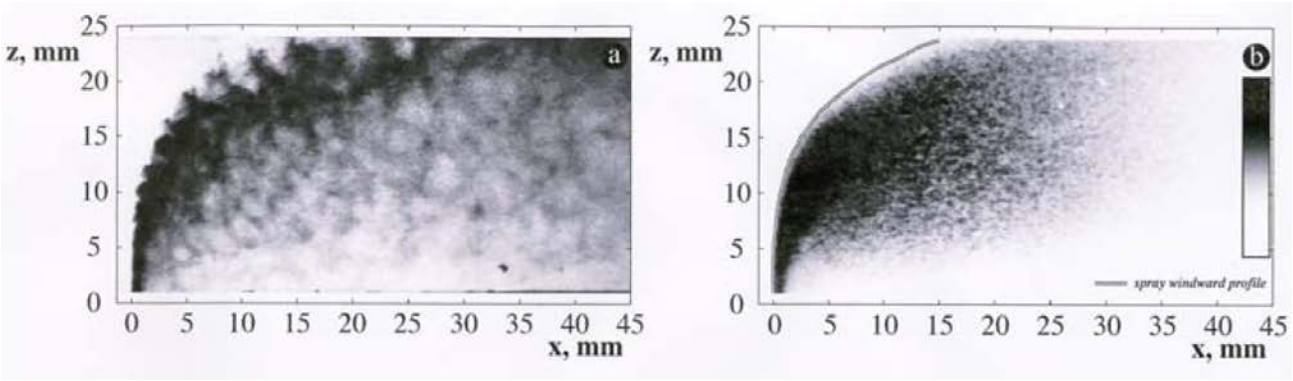

Figure 1.13: Instantaneous and averages images of a liquid jet in crossflow. Source: Ragucci et al. (2007)

Table 1.1: Correlations for the jet trajectory of the JICF

z/d_{inj}	Liquid	Range of validity	Reference
$1.37\sqrt{q\left(\frac{x}{d_{\text{inj}}}\right)}$	Water	$3.4 < q < 185$ $57 < We_{ae} < 1200$	Wu et al. (1997)
$1.57\text{q}^{0.36}\ln\left(1+3.81\frac{x}{d_{\text{inj}}}\right)$	Kerosene	$1 < q < 12$ $90 < We_g < 2120$ $2 < x/d_{\text{inj}} < 22$	Becker & Hassa (2002)
$2.27q^{0.44}We_{ae}^{-0.012}\left(\frac{x}{d_{\text{inj}}}\right)^{0.367}$	Kerosene	$5 < q < 280$ $7 < We_{ae} < 340$	Ragucci et al. (2007)
$1.6q^{0.4}\ln\left(1+3.81\left(\frac{x}{d_{\text{inj}}}\right)\right)$	Kerosene	$3 < q < 24$ $39 < We_{ae} < 3281$ $1.4 < x/d_{\text{inj}} < 50$	Freitag & Hassa (2008)

d_{inj} increases, more liquid mass flow is injected, so the jet carries more momentum and is able to withstand more stiffly the interaction with the airstream. Furthermore, atomization of a thicker jet will produce larger droplets that will travel further due to their ballistic properties. For the momentum flux ratio, increasing its value also increases the jet penetration. This is clearly seen in Table 1.1, as the exponent factor of q is positive in all correlations. Figure 1.14 also illustrates the q effect in the jet penetration. Regarding the influence of the air velocity (or equivalently, We_g), it does not have a direct effect on the jet penetration close to the injection nozzle, as the correlations from Table 1.1 do not show any dependence with We_g. This is observed in Figure 1.15, which shows instantaneous snapshots of a liquid JICF for several values of u_g. The main effect of increasing the gas velocity is the transition from column to surface breakup mechanisms, as given by the breakup map of Figure 1.11. Nevertheless, it is seen that by increasing u_g, the far-field penetration is reduced due to a finer atomization: for low values of u_g, column breakup generates bigger droplets whose ballistic properties allow them to penetrate further in the vertical direction, while higher values of the gas velocity generate smaller droplets both from surface and column breakup mechanisms that will relax faster towards the air velocity and direction. Becker & Hassa (2002) tested a kerosene JICF with several gas velocities and measured the granulometry of the developed spray at a plane located 80 mm downstream the injection nozzle, obtaining the following relation between the Sauter Mean Diameter (SMD) and the kinetic energy of the gas which confirms how the mean droplet size decreases with increasing gas velocity:

$$SMD = 429\left(\rho_g u_g^2\right)^{-0.24} \tag{1.5}$$

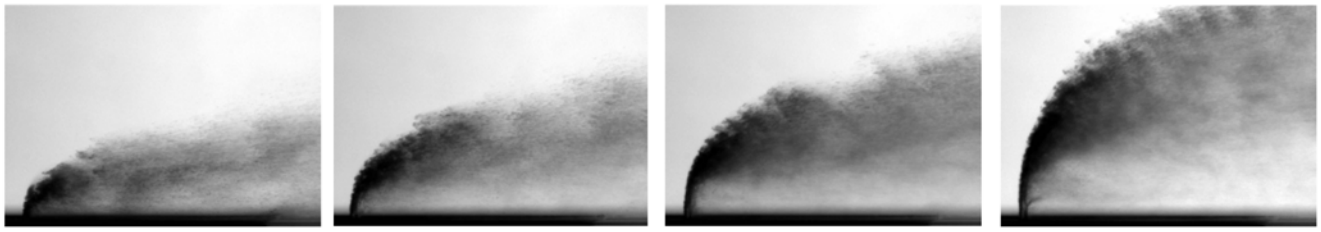

Figure 1.14: Effect of q ratio. From left to right: $q = 3, 6, 12, 24$. Fixed values: $d_{inj} = 0.5\ mm$, $u_g = 75\ m/s$, $p_\infty = 4$ bar. Source: Freitag & Hassa (2008).

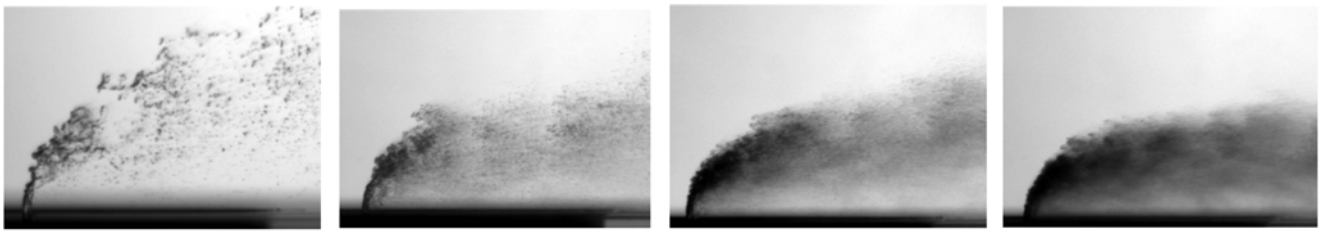

Figure 1.15: Effect of air velocity. From left to right: $u_g = 25, 50, 75, 100\ m/s$. Fixed values: $d_{inj} = 0.5\ mm$, $q = 6$, $p_\infty = 4$ bar. Source: Freitag & Hassa (2008).

1.4 Numerical simulations of fuel injection and combustion

The previous section has illustrated the heterogeneity of phenomena which are found in injection systems relevant to gas turbines, with a special focus on MSFI technology aiming at reducing NO_x formation. The study of these phenomena with experimental facilities is often restricted to academic cases without complex geometries due to difficult optic visualization. Furthermore, experiments do not have access to an operating range representative of realistic conditions.

An alternative to help the study and the design of injection and combustion systems is the use of numerical simulations with Computational Fluid Dynamics (CFD). This tool has gained popularity in the last decades due to the increase in computational performances and the appearance of High Performance Computing (HPC), which allows to perform simulations of complex problems in parallel machines. CFD simulations can provide insightful information on the physical mechanisms and variables of interest, they do not have limitations regarding optical access and are hazard-free. Therefore, numerical simulations have become a powerful tool for the design of combustion systems and the understanding of the underlying fundamental physical phenomena.

In order to resolve a given physical problem, the proper modeling strategy and numerical methods to perform CFD simulations must be chosen. Depending on the required accuracy and the computational resources available, three main approaches exist to resolve numerically the Navier-Stokes equations. From lower to higher accuracy (and equivalently, from lower to higher computational cost), these approaches are:

1. **Reynolds Averaged Navier Stokes** (RANS). The governing equations are averaged and the mean flow field is solved. Extra terms appear in the equations which need additional closure. All the turbulence spectrum, from Taylor to Kolmogorov characteristic length scales, is modeled. RANS methods can provide mean values and is appropriate to characterize pressure drop in certain configurations, but are not suited for solving transient problems.

2. **Large-Eddy Simulations** (LES). A low-pass filter is applied to the Navier-Stokes equations, so that the characteristic length scales below the filter size are modeled while the larger ones are resolved. For the smallest scales, turbulence models accounting for the viscous dissipation are required. One of the most well-known turbulent closures for LES is the Smagorinsky model (Smagorinsky 1963, Germano et al. 1991).

3. **Direct Numerical Simulations** (DNS). In such simulations, all the turbulence characteristic scales are solved and no models are applied. Hence, DNS is an accurate tool for properly resolving turbulence. Nevertheless, its high computational cost limits the application of DNS to reduced geometries and canonical test cases, and nowadays its application to full industrial configurations is out of reach.

These three methodologies are widely used for aerodynamic and hydrodynamic problems involving one fluid phase. Two-phase flow problems also make use of these equations, but they require additional equations and modeling tools to consider the interaction between phases. For cases involving liquid and gas, which are of interest in automotive and aeronautical engines, this interaction is dominated by surface tension σ. In terms of numerical modeling, surface tension creates a discontinuity in pressure and viscosity (as demonstrated later in §2.2) that needs to be dealt with mathematical tools, for instance by adding extra forcing terms in the governing equation for momentum. Furthermore, different methods and modeling methodologies will be used depending on the problem to solve, since the multi-scale, complexity and richness of the physical phenomena in two-phase flows (illustrated in §1.3) does not allow to use a single numerical formalism to solve simultaneously all processes involved.

One large family of numerical methods is the one devoted to resolve accurately atomization. The underlying interest is to capture the dynamics of primary and secondary atomization, its governing physical mechanisms and the interaction with the gaseous phase. For this purpose, the main approach is to perform CFD simulations where the Navier-Stokes equations are resolved for each phase with RANS or LES. Then, additional equations are added in order to determine either the evolution of the interface (e.g. level-set methods) or of the liquid volume fraction (e.g. volume of fluid methods). These simulations are usually denoted as **resolved** or **eulerian**. Figure 1.16 shows two instantaneous jets (diesel and JICF) solved with a resolved atomization approach, where the interface dynamics have been solved with level-set methods. In both cases, ligaments and droplets generated by the atomization process can be clearly appreciated. In this document, Chapter 2 presents numerical methods used nowadays for resolving injection and atomization.

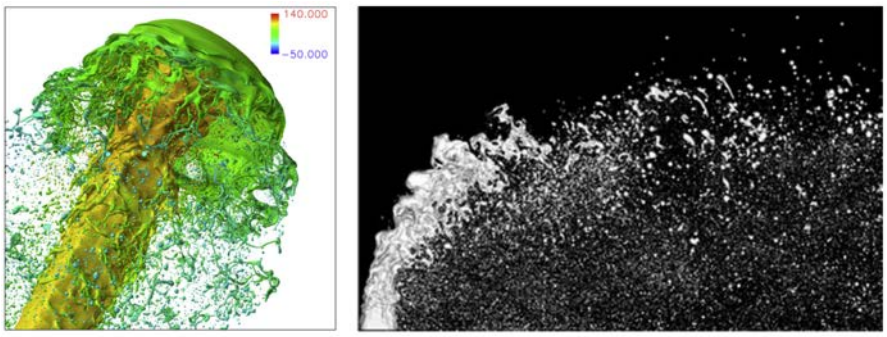

Figure 1.16: Direct numerical simulations of primary atomization in liquid jets. *Left*: diesel jet colored by axial velocity, from Shinjo & Umemura (2010). *Right*: liquid jet in crossflow, from Herrmann (2009).

Methodologies for resolving atomization are envisaged to capture the multi-scale nature of atomization, devoting huge computational resources to solve from the biggest to the smallest scales and the interaction between phases. Nevertheless, the size of the smallest structures and droplets captured are often limited by the grid resolution, and due to their high cost, they cannot be easily coupled with additional physical equations to solve for the evaporation and combustion processes. To tackle these problems, different strategies are used, often circumventing atomization by injecting a spray represented by liquid spherical particles. These particles compose a **dispersed-phase system** where the gaseous phase is resolved by the Navier-Stokes equations and the particles representing the liquid phase evolve according to the dynamics of point-particle systems in **lagrangian simulations**. The coupling between both phases is done through exchange terms of mass, momentum and energy, and hence evaporation and combustion can be easily modeled in these simulations. Figure 1.17 shows also two jets, diesel and jet in crossflow, simulated with lagrangian approaches. Contrarily to the resolved jets of Figure 1.16, here all the liquid phase is represented by means of spherical particles and the dynamics of atomization are not appreciated. In contrast, these simulations are computationally much cheaper than the former ones and can be applied to reactive computations in complex geometries as shown in Figure 1.18, where a full industrial combustor is studied. In lagrangian simulations, the injection process is fundamental and needs to be properly modeled by injecting the right droplets sizes and velocities distributions. Chapter 3 shows the state of the art on several numerical tools to tackle dispersed two-phase flows systems, with special emphasis on their application to liquid jet in crossflow injection.

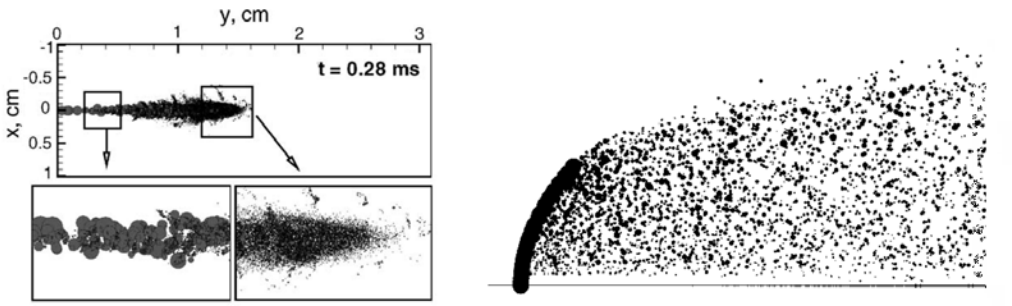

Figure 1.17: Lagrangian simulations of liquid jets. *Left*: diesel jet, from Apte et al. (2003). *Right*: liquid jet in crossflow, from Behzad et al. (2010).

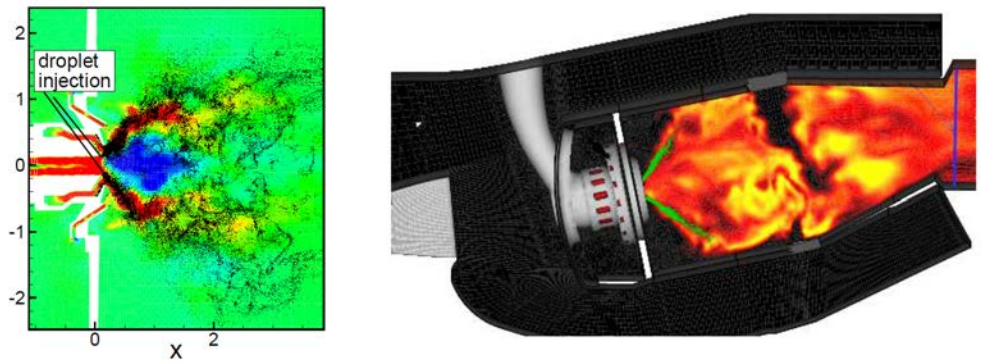

Figure 1.18: Large Eddy Simulation of a Pratt & Whitney combustor. *Left*: fuel spray injection, where liquid phase is represented by lagrangian droplets. *Right*: combustion simulation. Source: Moin & Apte (2006).

Recently, new methodologies representing more accurately the spray by coupling dispersed phase with lagrangian simulations have emerged. Michaelides et al. (2017) divides these coupling methodologies into two main categories: Direct Coupling Approach (DCA) and Statistical Coupling Approach (SCA), shown in Figure 1.19. In DCA, primary atomization is simulated with eulerian approaches, and resolved eulerian droplets are transformed into spherical droplets which are later transported with the lagrangian equations. Conversion criteria based on droplets size and sphericity are used. This approach has been studied by several authors who have demonstrated its capabilities to simulate non-reactive problems (Herrmann 2010, Zuzio et al. 2018, Janodet 2022), but has not yet been applied to combustion cases. In SCA, an eulerian simulation resolves the jet up to a plane after atomization has taken place where droplets are sampled (SC layer in Figure 1.19). Then, the information on the sampled spray is used to inject lagrangian droplets, which are transported further downstream. In this thesis, a new methodology for lagrangian injection multi-staged systems based on SCA is developed. Details on the motivation and organisation of this manuscript are given next.

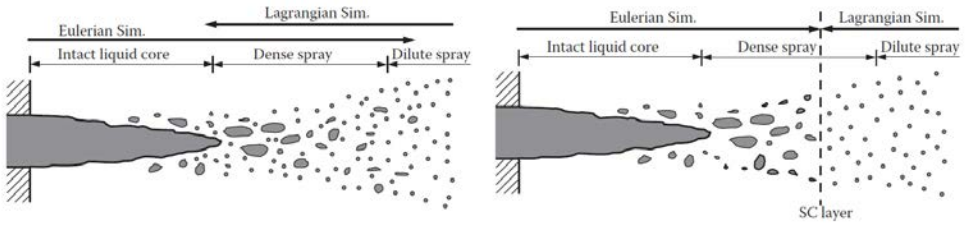

Figure 1.19: Schematic of coupled Eulerian–Lagrangian approaches for liquid atomization. *Left*: direct coupling approach, DCA. *Right*: statistical coupling approach, SCA. Source: Michaelides et al. (2017).

1.5 Objective and thesis outline

Lagrangian simulations have gained great interest in the recent decades due to their capability for modeling multi-physics problems with reduced computational costs. This has made them a useful tool for industrial applications, such as the design of liquid injection systems. At the early stages of injector design, the geometrical parts are not built yet. Design offices first iterate on several numerical concepts to select a few candidate geometries for later manufacturing and experimental testing. Computations are used in this pre-design phase for selecting the best candidates prior to the production of the first prototype, hence removing the need to manufacture all considered geometries. Furthermore, these computations can also be used in later stages of the design process, such as to analyze in depth the test bench results which are not accessible from experimental diagnostics; or during the manufacturing process, when a part shows a quality discrepancy to better assess if it should be kept in the production line. Therefore, it is of interest to improve the reliability of lagrangian computations.

To accurately perform lagrangian simulations, particles need to be properly injected by prescribing droplets sizes and velocities at the right spatial location. This is the role of lagrangian injection models. In some cases, distributions measured experimentally are prescribed in such simulations to recover the dispersed spray obtained further downstream (Jaegle 2009). This requires the availability of experimental test benches representative of the geometry and operating conditions simulated. Other approaches inject directly droplets with the diameter of the injector and the velocity at injection, coupling with secondary breakup models to form a developed spray (Reitz 1987), with the disadvantage that primary atomization is simplified through breakup models which do not account for the same elementary phenomena. Intermediate approaches combine the injection of large droplets with semi-empirical models to take into account more physical phenomena (Eckel et al. 2016), allowing to obtain a more realistic spray but being applicable to a few range of operating conditions. Furthermore, most of the models applicable to reactive simulations do not into account the interaction between the aerodynamic and the liquid, and available models considering this interaction (Arienti et al. 2006, Fontes et al. 2019) combine resolved atomization methods with dispersed phase ones in one simulation, hindering the application to combustion problems. A thorough review of lagrangian injection models in Multi-Staged Fuel Injection (MSFI) systems in done in Chapter 3.

The goal of this thesis is to develop a new methodology to build lagrangian injectors for performing dispersed phase simulations which prescribe a realistic spray in MSFI systems. For this purpose, in first place resolved simulations of an academic liquid Jet In Crossflow (JICF) configuration tested experimentally (Becker & Hassa 2002) are performed with an Accurate Conservative Level Set formalism (Desjardins et al. 2008) to construct a database of atomization representative of MSFI. The methodology uses this database in order to learn the spray state and build the injectors for prescribing the liquid phase in dispersed phase simulations. The developed methodology is similar to the SCA approach reviewed by Michaelides et al. (2017), depicted in Figure 1.19. Apart from the atomization data, the aerodynamic interaction is also taken into account by means of the Actuator Line Method (ALM) (Sørensen & Shen 2002). Then, the methodology is validated by performing dispersed phase simulations in the same configuration. In a second step, the methodology is applied to an academic burner called BIMER which is more representative of industrial MSFI configurations (Renaud 2015).

The manuscript is divided in three main sections as follows:

- **Part I** reviewes the state of the art in numerical methods to simulate two-phase flows. Different strategies are used depending on the atomization regimes as shown in Figure 1.7. Chapter 2 reviews methodologies aiming at resolving atomization, applicable to dense regimes and useful when the atomization dynamics need to be known, but out of scope for reactive simulations including combustion. Chapter 3 reviews existing modeling strategies to simulate dispersed-phase problems, with emphasis on the state of the art in lagrangian methodologies to simulate JICF atomization due to its relevance in MSFI systems. Such modeling approaches are nowadays scarce, specially for jet in crossflow atomizers, for which most models are built on empirical laws. Hence, the objective of this thesis is to propose a new lagrangian injection methodology for multi-staged systems which learns data from a reference spray for a realistic prescription of the liquid phase, and without the need to relying on external data.

- **Part II** describes the design and application of the methodology developed in this thesis. This methodology, which aims at building lagrangian injectors from resolved atomization simulations to prescribed liquid boundary conditions in dispersed phase computations, is thoroughly described in Chapter 4. Then, application of this methodology to build lagrangian injectors in an academic non-reactive kerosene jet in crossflow test case is done in Chapter 5. The obtained injectors are then applied in the same configuration to introduce lagrangian droplets in the dispersed phase simulations of Chapter 6.
- **Part III** focuses on the application of the injection models in an academic MSFI tested at EM2C named BIMER. An introduction to the test bench and simulations of the aerodynamic field are presented in Chapter 7. Then, Chapter 8 describes resolved simulations of the atomization process in BIMER performed for one multipoint injector, from which lagrangian injectors are learnt. Finally, Chapter 9 shows the application of the built injectors to prescribe the liquid phase in dispersed phase simulations of the BIMER burner.

1.6 Acknowledgements

This PhD thesis has been funded by the European Union Horizon 2020 research and innovation program under the Marie Sklodowska-Curie Innovative Training Networks (ITN) Grant agreement No. 765998 in the project ANNULIGhT, granted to Safran Tech. Computer resources provided by GENCI, France, under the allocations A0092B11072 and A0092B10157 are also acknowledged.

Part I

Numerical approaches to model injection systems

Chapter 2

Numerical methods to simulate resolved atomization

2.1 Introduction

Resolution of two-phase flows requires a suitable description for each phase and a careful treatment of the liquid-gas interface. From a numerical point of view, the multi-scale nature of atomization hinders the application of the same methods for resolving atomization accurately and for transporting efficiently a developed spray composed of small droplets, since their characteristic length scales differ by several orders of magnitude. These different characteristic lengths are also related to multiple time scales (Sánchez et al. 2015), which combined make the cost of simulations to increase non-linearly with resolution. Consequently, different numerical methodologies must be chosen according to the targeted problem. Furthermore, if multi-physical phenomena, such as evaporation or combustion, are present, the range of possible models to be applied becomes even narrower.

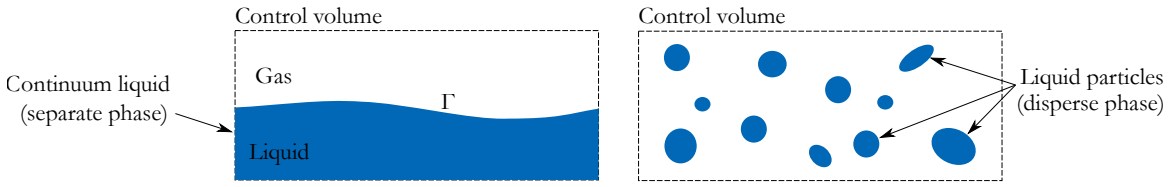

Figure 2.1: Two-phase systems classification. *Left*: separate flow, where both phases are easily distinguished and the interface Γ can easily be tracked. *Right*: dispersed phase flow, where individual fluid particles (disperse phase) are surrounded by the gas (carrier phase). In such systems, the interface can hardly be tracked due to the higher surface-to-volume ratio.

The first step for choosing a proper methodology is to identify the type of regime to solve. One possible classification of two-phase regimes can be done depending on the distribution and topology of the interface. In this respect, one can distinguish between separate and disperse phase (Murrone & Villedieu 2011):

- **Separate phase** flows, also known as dense regime, present a clear definition of the interface and both liquid and gaseous phases can be easily identified (Figure 2.1 left). In such cases, the liquid volume fraction is large and the liquid structures are larger, or at least of the same order, than the cell size, so the atomization dynamics can be captured by the mesh. Within engines, separate phase is found during primary breakup, as shown by the blue regions of Fig. 1.7. Numerical methods devoted to resolve separate phase regimes are tackled in this chapter (§2.3). Generally, these methods are restricted to non-reactive problems and the multi-physics coupling with evaporation and combustion is not yet possible, being currently an emerging research topic (Luo et al. 2019).

- **Dispersed phase** regime is found when the liquid volume fraction is small and the liquid structures cannot be capture by the main grid. The liquid phase is composed by individual liquid particles (usually called droplets) whose high number and small size hinders the tracking of the interface (Figure 2.1 right). Droplets are surrounded by the gaseous phase, also called **carrier phase**. A developed spray produced as a consequence of secondary atomization is an example of dispersed phase systems, illustrated by the intermediate and dilute regimes of Figure 1.7. The same numerical methods used for the separate phase regime cannot be applied, since the characteristic scales are much smaller and the grid resolution required yields the computations unaffordable due to their high cost. Numerical formalisms targeting dispersed phase flows are discussed in Chapter 3. These methods do not resolve the atomization dynamics, but present the possibility to integrate evaporation and combustion.

This chapter gives an overview on the state-of-the-art in numerical methods applicable to resolve separate phase regimes. Section 2.2 introduces the governing equations of non-reactive two phase flows, starting from the Reynolds Transport Theorem and applying it to obtain mass and momentum conservation laws. Then, Section 2.3 presents an overview of existing numerical methodologies for separate phases and reviews a few of them: diffuse interface, front-tracking, Volume of Fluid (VOF), and Accurate Conservative Level-Set coupled with Ghost-Fluid Method (ACLS/GFM). The last one is the methodology used in this thesis for performing resolved simulation atomizations in Chapters 5 and 8.

2.2 Governing equations

2.2.1 Reynolds transport theorem

General form

The starting point for deriving all the conservation equations is the Reynolds transport theorem (RTT). Let's consider a control volume Ω bounded by a control surface $\partial\Omega$. Let's also consider a control mass Ω_m which moves with time to enclose the same amount of mass. This control mass coincides at some time instant with the control volume. The RTT relates the variation of a property $\phi = \phi(\boldsymbol{x}, t)$ in the control mass with its variation in the control volume. In its most general form, it can be expressed as follows (Collado 2007):

$$\frac{d}{dt}\int_{\Omega_m}\phi dV = \frac{d}{dt}\int_{\Omega}\phi dV + \int_{\partial\Omega}\phi\left(\boldsymbol{u}-\boldsymbol{u_c}\right)\cdot\boldsymbol{n}dS \tag{2.1}$$

where $\boldsymbol{u}$ is the flow velocity at the boundaries, $\boldsymbol{u_c}$ is the velocity of the control surface and $\boldsymbol{n}$ is the normal unit vector pointing outwards the surface of the control volume. Bold symbols indicate vectorial quantities.

The first term in the right hand side can be expanded by applying Leibniz's integral rule to a domain with moving boundaries. Following the introduced notation, Leibniz's rule takes the following shape:

$$\frac{d}{dt}\int_{\Omega}\phi dV = \int_{\Omega}\frac{\partial\phi}{\partial t}dV + \int_{\partial\Omega}\phi\left(\boldsymbol{u_c}\cdot\boldsymbol{n}\right)dS \tag{2.2}$$

The latter equation can also be seen as another expression for the RTT particularised for a moving control volume. Introducing it into (2.1) yields:

$$\boxed{\frac{d}{dt}\int_{\Omega_m}\phi dV = \int_{\Omega}\frac{\partial\phi}{\partial t}dV + \int_{\partial\Omega}\phi\left(\boldsymbol{u}\cdot\boldsymbol{n}\right)dS} \tag{2.3}$$

This formulation relates the lagrangian formulation of a system (left hand side, corresponding to the control mass) with the eulerian formulation (right hand side, corresponding to the control volume).

In most of the problems, all the control volumes selected for performing balances are fixed in space, so their boundaries do not move. Consequently, $\boldsymbol{u_c} = 0$ and hence Eq. (2.2) becomes $\frac{d}{dt}\int_{\Omega}\phi dV = \int_{\Omega}\partial\phi/\partial t\, dV$.

Application to two-phase flows

In the particular case of two-phase flows systems comprising gas and liquid phases, denoted respectively by the subscripts g and l, the domain can be decomposed into two subdomains Ω_g and Ω_l. The addition of these two subdomains will make the total domain Ω:

$$\Omega = \Omega_{\mathrm{g}} \cup \Omega_{\mathrm{l}} \tag{2.4}$$

The RTT must hold for each subdomain, so Eq. (2.3) can be applied to each phase separately

$$\frac{d}{dt}\int_{\Omega_{m_{\mathrm{g}}}} \phi \, dV = \int_{\Omega_{\mathrm{g}}} \frac{\partial \phi}{\partial t} \, dV + \int_{\partial\Omega_{\mathrm{g}}} \phi \left(\boldsymbol{u}\cdot\boldsymbol{n}\right) dS \tag{2.5a}$$

$$\frac{d}{dt}\int_{\Omega_{m_{\mathrm{l}}}} \phi \, dV = \int_{\Omega_{\mathrm{l}}} \frac{\partial \phi}{\partial t} \, dV + \int_{\partial\Omega_{\mathrm{l}}} \phi \left(\boldsymbol{u}\cdot\boldsymbol{n}\right) dS \tag{2.5b}$$

The surface integral in the right hand side can be decomposed in two different integrals by considering a common boundary shared by both subdomains: the liquid-gas interface Γ. This interface can be modified with time. Hence, the control boundary $\partial\Omega$ can be expressed as the addition of the following two subdomains:

$$\partial\Omega = \left(\partial\Omega_{\mathrm{g}} \backslash \Gamma\right) \cup \left(\partial\Omega_{\mathrm{l}} \backslash \Gamma\right) \tag{2.6}$$

So the RTT for separate phases can be extended as follows:

$$\frac{d}{dt}\int_{\Omega_{m_{\mathrm{g}}}} \phi \, dV = \int_{\Omega_{\mathrm{g}}} \frac{\partial \phi}{\partial t} \, dV + \int_{\partial\Omega_{\mathrm{g}}\backslash\Gamma} \phi \left(\boldsymbol{u}\cdot\boldsymbol{n}\right) dS + \int_{\Gamma} \phi_{\mathrm{g}} \left(\boldsymbol{u}_{\Gamma}\cdot\boldsymbol{n}_{\Gamma\mathrm{g}}\right) dS \tag{2.7a}$$

$$\frac{d}{dt}\int_{\Omega_{m_{\mathrm{l}}}} \phi \, dV = \int_{\Omega_{\mathrm{l}}} \frac{\partial \phi}{\partial t} \, dV + \int_{\partial\Omega_{\mathrm{l}}\backslash\Gamma} \phi \left(\boldsymbol{u}\cdot\boldsymbol{n}\right) dS + \int_{\Gamma} \phi_{\mathrm{l}} \left(\boldsymbol{u}_{\Gamma}\cdot\boldsymbol{n}_{\Gamma\mathrm{l}}\right) dS \tag{2.7b}$$

where $\boldsymbol{u}_{\Gamma}$ is the velocity at the interface and $\boldsymbol{n}_{\Gamma}$ is the vector normal to the interface pointing outwards its corresponding phase. As the interface is the same but the outward direction is opposed for each phase, an interface normal vector pointing to the liquid phase can be defined:

$$\boldsymbol{n}_{\Gamma} = \boldsymbol{n}_{\Gamma\mathrm{l}} = -\boldsymbol{n}_{\Gamma\mathrm{g}} \tag{2.8}$$

Hence, the RTT for each separate phase can be reformulated as:

$$\frac{d}{dt}\int_{\Omega_{m_{\mathrm{g}}}} \phi \, dV = \int_{\Omega_{\mathrm{g}}} \frac{\partial \phi}{\partial t} \, dV + \int_{\partial\Omega_{\mathrm{g}}\backslash\Gamma} \phi \left(\boldsymbol{u}\cdot\boldsymbol{n}\right) dS - \int_{\Gamma} \phi_{\mathrm{g}} \left(\boldsymbol{u}_{\Gamma}\cdot\boldsymbol{n}_{\Gamma}\right) dS \tag{2.9a}$$

$$\frac{d}{dt}\int_{\Omega_{m_{\mathrm{l}}}} \phi \, dV = \int_{\Omega_{\mathrm{l}}} \frac{\partial \phi}{\partial t} \, dV + \int_{\partial\Omega_{\mathrm{l}}\backslash\Gamma} \phi \left(\boldsymbol{u}\cdot\boldsymbol{n}\right) dS + \int_{\Gamma} \phi_{\mathrm{l}} \left(\boldsymbol{u}_{\Gamma}\cdot\boldsymbol{n}_{\Gamma}\right) dS \tag{2.9b}$$

Finally, a general shape for the RTT in two-phase flows can be obtained by adding Equations (2.9) and applying (2.4) and (2.6):

$$\frac{d}{dt}\int_{\Omega_m} \phi dV = \int_{\Omega} \frac{\partial \phi}{\partial t} dV + \int_{\partial\Omega} \phi \left(\boldsymbol{u}\cdot\boldsymbol{n}\right) dS + \int_{\Gamma} \left(\phi_{\mathrm{l}} - \phi_{\mathrm{g}}\right) \left(\boldsymbol{u}_{\Gamma}\cdot\boldsymbol{n}_{\Gamma}\right) dS \tag{2.10}$$

2.2.2 Mass conservation

General forms

The mass conservation equation for a fluid system is obtained by substituting $\phi = \rho$ in Eq. (2.3):

$$\frac{d}{dt}\int_{\Omega_m} \rho dV = \int_{\Omega} \frac{\partial \rho}{\partial t} dV + \int_{\partial\Omega} \rho \boldsymbol{u}\cdot\boldsymbol{n} dS \tag{2.11}$$

By definition, the control mass is a region of the fluid flow whose mass does not change. Hence, the left hand side of the previous expression is 0 and the **mass conservation in integral form**, or **weak form of mass conservation**, is expressed as follows:

$$\boxed{\int_{\Omega} \frac{\partial \rho}{\partial t} dV + \int_{\partial\Omega} \rho \boldsymbol{u}\cdot\boldsymbol{n} dS = 0} \tag{2.12}$$

The Gauss theorem can be applied to a vectorial field $\boldsymbol{f}$ to transform a surface integral into a volume integral:

$$\int_{\partial\Omega} \boldsymbol{f} \cdot \boldsymbol{n} dS = \int_{\Omega} \nabla \boldsymbol{f} dV \tag{2.13}$$

Applying this theorem considering $\boldsymbol{f} = \rho\boldsymbol{u}$ and substituting into (2.12) yields the general expression for **mass conservation in differential form** or **strong form of mass conservation**:

$$\boxed{\frac{\partial \rho}{\partial t} + \nabla (\rho \boldsymbol{u}) = 0} \tag{2.14}$$

This equation is also known as the **continuity equation in conservative form**. The **non-conservative** form can be obtained by expanding the left-hand side:

$$\frac{\partial \rho}{\partial t} + \nabla (\rho \boldsymbol{u}) = \frac{\partial \rho}{\partial t} + \boldsymbol{u} \cdot \nabla \rho + \rho \nabla \boldsymbol{u} = 0 \quad \rightarrow \quad \frac{d\rho}{dt} + \rho \nabla \boldsymbol{u} = 0 \tag{2.15}$$

where $d/dt = \partial/\partial t + \boldsymbol{u} \cdot \nabla$ is the **material derivative**.

Hereafter, the weak form of mass conservation will be addressed for its application in integral balances.

Global mass conservation in two-phase flows

When two phases are present, mass conservation can be obtained by substituting $\phi = \rho$ into Eq. (2.10):

$$\frac{d}{dt} \int_{\Omega_m} \rho dV = \int_{\Omega} \frac{\partial \rho}{\partial t} dV + \int_{\partial\Omega} \rho \boldsymbol{u} \cdot \boldsymbol{n} dS + \int_{\Gamma} (\rho_\mathrm{l} - \rho_\mathrm{g}) (\boldsymbol{u}_\Gamma \cdot \boldsymbol{n}_\Gamma) dS \tag{2.16}$$

which is a general expression for all two-phase flows in a continuum regime. In this equation, the left hand side represents a sink term which would be finite if mass transfer takes place. For the purposes of this thesis, however, the following hypotheses are stated:

1. Mass transfer at the interface is neglected.
2. Heat transfer at the interface is neglected.
3. Fluids are incompressible.

Assumptions 1 and 2 hold since those phenomena are out of the scope of this work, and their implementation with resolved atomization methods is challenging (Boniou 2022). In real aeroengine conditions, however, the ambient temperature and pressure within the combustion chamber are usually high, and evaporation can take place even shortly after injection (Ghassemi et al. 2006), yielding these hypotheses not valid anymore for the dense liquid phase. Hypothesis 3 (incompressibility) holds since the operating conditions studied in this thesis have low Mach numbers and reactive phenomena (such as combustion) are not approached. Therefore, the sink term from Eq. (2.16) is null and the expression becomes:

$$\int_{\Omega} \frac{\partial \rho}{\partial t} dV + \int_{\partial\Omega} \rho \boldsymbol{u} \cdot \boldsymbol{n} dS + \int_{\Gamma} (\rho_\mathrm{l} - \rho_\mathrm{g}) (\boldsymbol{u}_\Gamma \cdot \boldsymbol{n}_\Gamma) dS = 0 \tag{2.17}$$

It can be noticed that the first two integrals in this expression correspond to the weak form for mass conservation as given by Eq. (2.12). Hence, this expression is simplified to:

$$\int_{\Gamma} (\rho_\mathrm{l} - \rho_\mathrm{g}) (\boldsymbol{u}_\Gamma \cdot \boldsymbol{n}_\Gamma) dS = 0 \tag{2.18}$$

As both ρ_l and ρ_g are always positive, and $\rho_\mathrm{l} > \rho_\mathrm{g}$ for most known applications (including gas turbines and atmospheric two-phase systems), the only possibility for this expression to hold true is when the dot product is zero:

$$\boxed{\boldsymbol{u}_\Gamma \cdot \boldsymbol{n}_\Gamma = 0} \tag{2.19}$$

which implicates that the flow velocity normal to the interface must be zero, i.e. there is no liquid or gas crossing the interface.

Mass conservation in separate phases

Two-phase flows must ensure mass conservation for each phase. This can be done by applying the RTT as given by Eqs. (2.9) to the field $\phi = \rho$. However this formulation introduces the need to deal with the liquid-gas interface, which is often changing in time. A more useful formulation can be developed by the strong form given by (2.12) to each phase separately (Drew & Passman 1999). For applying it properly, it is necessary to introduce before the definition of **volume fraction** for the phase k, α_k:

$$\alpha_k = \frac{V_k}{V} \tag{2.20}$$

This magnitude determines the quantity of a given fluid k that is contained inside a volume V. By definition, it follows that $\sum_{k=1}^{\mathrm{N_{phases}}} \alpha_k = 1$. It can be defined for both gas and liquid phases, α_g and α_l, so then $\alpha_\mathrm{g} + \alpha_\mathrm{l} = 1$.

Once the volume fractions for liquid and gas are introduced, the continuity equation (2.14) can be defined for each phase as follows:

$$\frac{\partial \alpha_\mathrm{g}\rho_\mathrm{g}}{\partial t} + \nabla\left(\alpha_\mathrm{g}\rho_\mathrm{g}\boldsymbol{u}_\mathrm{g}\right) = 0 \tag{2.21a}$$

$$\frac{\partial \alpha_\mathrm{l}\rho_\mathrm{l}}{\partial t} + \nabla\left(\alpha_\mathrm{l}\rho_\mathrm{l}\boldsymbol{u}_\mathrm{l}\right) = 0 \tag{2.21b}$$

The integral balance can be obtained by integrating both expressions over a fixed control volume Ω and applying the Gauss theorem to the divergence term:

$$\frac{\partial}{\partial t}\int_\Omega \alpha_\mathrm{g}\rho_\mathrm{g} dV + \int_{\partial\Omega} \alpha_\mathrm{g}\rho_\mathrm{g}\left(\boldsymbol{u}_\mathrm{g}\cdot\boldsymbol{n}\right) dS = 0 \tag{2.22a}$$

$$\frac{\partial}{\partial t}\int_\Omega \alpha_\mathrm{l}\rho_\mathrm{l} dV + \int_{\partial\Omega} \alpha_\mathrm{l}\rho_\mathrm{l}\left(\boldsymbol{u}_\mathrm{l}\cdot\boldsymbol{n}\right) dS = 0 \tag{2.22b}$$

These equations present two components: a transient term and a surface term. The transient term has an effect when the mass of any phase is changing inside the control volume, e.g. at the first instants of fuel injection, when the fuel mass is increasing with time, or when evaporation takes place. Once a steady-state has been reached, this term becomes 0. The surface term accounts for the mass fluxes entering or leaving the system through its boundaries. From this term, the **mass flow rate** $\dot{m}$ of a flux going though an area A can be defined as:

$$\boxed{\dot{m} = \int_A \rho\left(\boldsymbol{u}\cdot\boldsymbol{n}\right) dS} \tag{2.23}$$

As the normal vector is pointing outwards the control volume, the dot product will be positive in surfaces where both vectors have the same direction, and negative otherwise. Hence, the mass flow rate will be positive in outlets and negative in inlets.

If the transient term in (2.22), which is a source term, is denoted as $\dot{\Omega}_m$, then the mass conservation for separated phases can be written as follows:

$$\dot{\Omega}_{m_\mathrm{g}} = \sum_{i_\mathrm{in}} \dot{m}_{g_i} - \sum_{i_\mathrm{out}} \dot{m}_{g_i} \tag{2.24a}$$

$$\dot{\Omega}_{m_\mathrm{l}} = \sum_{j_\mathrm{in}} \dot{m}_{l_j} - \sum_{j_\mathrm{out}} \dot{m}_{l_j} \tag{2.24b}$$

where into inlet and outlet fluxes are distinguished. Taking again into consideration the hypotheses of no mass transfer and incompressibility, the source terms vanish and the mass conservation equations for each phase turn into:

$$\boxed{\sum_{i_\mathrm{in}} \dot{m}_{g_i} = \sum_{i_\mathrm{out}} \dot{m}_{g_i}} \tag{2.25a}$$

$$\boxed{\sum_{j_\mathrm{in}} \dot{m}_{l_j} = \sum_{j_\mathrm{out}} \dot{m}_{l_j}} \tag{2.25b}$$

2.2.3 Momentum conservation

General forms

The momentum conservation equation for a fluid system is obtained by substituting $\phi = \rho\boldsymbol{u}$ in Eq. (2.3):

$$\frac{d}{dt}\int_{\Omega_m}\rho\boldsymbol{u}dV = \int_{\Omega}\frac{\partial(\rho\boldsymbol{u})}{\partial t}dV + \int_{\partial\Omega}\rho\boldsymbol{u}\left(\boldsymbol{u}\cdot\boldsymbol{n}\right)dS \tag{2.26}$$

The left-hand side term represents the ensemble of forces acting in the control mass. These forces can be separated into volume and surface forces. The volume forces will be denoted by $\boldsymbol{b}$; the surface forces include the pressure p and the viscous stress tensor $\overline{\overline{\boldsymbol{\tau}}}$. With this notation, the **momentum conservation in integral form**, or **weak form**, is defined as:

$$\boxed{\int_{\Omega}\frac{\partial(\rho\boldsymbol{u})}{\partial t}dV + \int_{\partial\Omega}\rho\boldsymbol{u}\left(\boldsymbol{u}\cdot\boldsymbol{n}\right)dS = \int_{\partial\Omega}\left(-p\overline{\overline{\boldsymbol{I}}} + \overline{\overline{\boldsymbol{\tau}}}\right)\boldsymbol{n}dS + \int_{\Omega}\boldsymbol{b}dV} \tag{2.27}$$

where $\overline{\overline{\boldsymbol{I}}}$ is the identity matrix. Applying the Gauss theorem (2.13) with $\boldsymbol{f} = \rho\boldsymbol{u}\boldsymbol{u}$ and operating yields the **momentum conservation in differential form**, or **strong form of momentum conservation**:

$$\boxed{\frac{\partial(\rho\boldsymbol{u})}{\partial t} + \nabla\left(\rho\boldsymbol{u}\boldsymbol{u}\right) = -\nabla p + \nabla\overline{\overline{\boldsymbol{\tau}}} + \boldsymbol{b}} \tag{2.28}$$

This solution is also known as the **conservative form of the momentum equation**. The left-hand side can be further expanded:

$$\frac{\partial(\rho\boldsymbol{u})}{\partial t} + \nabla\left(\rho\boldsymbol{u}\boldsymbol{u}\right) = \boldsymbol{u}\underbrace{\left[\frac{\partial\rho}{\partial t} + \nabla\left(\rho\boldsymbol{u}\right)\right]}_{\substack{\text{Continuity}\\ \text{equation (2.14)}}} + \rho\left[\frac{\partial\boldsymbol{u}}{\partial t} + \boldsymbol{u}\cdot\nabla\boldsymbol{u}\right] = \rho\left(\frac{\partial\boldsymbol{u}}{\partial t} + \boldsymbol{u}\cdot\nabla\boldsymbol{u}\right) = \rho\frac{d\boldsymbol{u}}{dt} \tag{2.29}$$

With this notation, the **non-conservative form** is obtained:

$$\rho\frac{d\boldsymbol{u}}{dt} = -\nabla p + \nabla\overline{\overline{\boldsymbol{\tau}}} + \boldsymbol{b} \tag{2.30}$$

Global momentum conservation in two-phase flows

A global expression for momentum conservation can be obtained by substituting $\phi = \rho\boldsymbol{u}$ into Eq. (2.10):

$$\frac{d}{dt}\int_{\Omega_m}\rho\boldsymbol{u}dV = \int_{\Omega}\frac{\partial\rho\boldsymbol{u}}{\partial t}dV + \int_{\partial\Omega}\rho\boldsymbol{u}\left(\boldsymbol{u}\cdot\boldsymbol{n}\right)dS + \int_{\Gamma}\left(\rho_{\mathrm{l}}\boldsymbol{u}_{\mathrm{l}} - \rho_{\mathrm{g}}\boldsymbol{u}_{\mathrm{g}}\right)\left(\boldsymbol{u}_{\Gamma}\cdot\boldsymbol{n}_{\Gamma}\right)dS \tag{2.31}$$

The left-hand side term can be expressed in the same way as in Eq. (2.27) with a slight modification: another addend must be included to account for the interface, as done in §2.2.1. In this way, this term becomes:

$$\frac{d}{dt}\int_{\Omega_m}\rho\boldsymbol{u}dV = \int_{\partial\Omega}\left(-p\overline{\overline{\boldsymbol{I}}} + \overline{\overline{\boldsymbol{\tau}}}\right)\boldsymbol{n}dS + \int_{\Omega}\boldsymbol{b}dV + \int_{\Gamma}\left[-\left(p_{\mathrm{l}} - p_{\mathrm{g}}\right)\overline{\overline{\boldsymbol{I}}} + \left(\overline{\overline{\boldsymbol{\tau}}}_{\mathrm{l}} - \overline{\overline{\boldsymbol{\tau}}}_{\mathrm{g}}\right) + \overline{\overline{\boldsymbol{\tau}}}_{\sigma}\right]\boldsymbol{n}dS \tag{2.32}$$

In the interface term, a new contribution has been added: surface tension, represented in this equation by the tensor $\overline{\overline{\boldsymbol{\tau}}}_{\sigma}$. Surface tension only contributes at the interface. These terms can now be introduced in the momentum conservation equation:

$$\begin{aligned}\int_{\Omega}\frac{\partial\rho\boldsymbol{u}}{\partial t}dV + \int_{\partial\Omega}\rho\boldsymbol{u}\left(\boldsymbol{u}\cdot\boldsymbol{n}\right)dS + \int_{\Gamma}\left(\rho_{\mathrm{l}}\boldsymbol{u}_{\mathrm{l}} - \rho_{\mathrm{g}}\boldsymbol{u}_{\mathrm{g}}\right)\left(\boldsymbol{u}_{\Gamma}\cdot\boldsymbol{n}_{\Gamma}\right)dS = \\ = \int_{\partial\Omega}\left(-p\overline{\overline{\boldsymbol{I}}} + \overline{\overline{\boldsymbol{\tau}}}\right)\boldsymbol{n}dS + \int_{\Omega}\boldsymbol{b}dV + \int_{\Gamma}\left(-\left(p_{\mathrm{l}} - p_{\mathrm{g}}\right)\overline{\overline{\boldsymbol{I}}} + \left(\overline{\overline{\boldsymbol{\tau}}}_{\mathrm{l}} - \overline{\overline{\boldsymbol{\tau}}}_{\mathrm{g}}\right) + \overline{\overline{\boldsymbol{\tau}}}_{\sigma}\right)\boldsymbol{n}dS\end{aligned} \tag{2.33}$$

Inspecting this equation reveals that the first two terms in both sides make the general integral form of momentum conservation, Eq. (2.27). Therefore, the equation can be simplified:

$$\int_\Gamma (\rho_\mathrm{l}\boldsymbol{u}_\mathrm{l} - \rho_\mathrm{g}\boldsymbol{u}_\mathrm{g})\,(\boldsymbol{u}_\Gamma \cdot \boldsymbol{n}_\Gamma)\,dS = \int_\Gamma \Big(-(p_\mathrm{l} - p_\mathrm{g})\,\overline{\overline{\boldsymbol{I}}} + (\overline{\overline{\boldsymbol{\tau}}}_\mathrm{l} - \overline{\overline{\boldsymbol{\tau}}}_\mathrm{g}) + \overline{\overline{\boldsymbol{\tau}}}_\sigma \Big)\,\boldsymbol{n} dS \tag{2.34}$$

Using now the same hypotheses as previously stated (no heat transfer, no mass exchange, incompressible flows), Eq. (2.19) can then be applied and the left hand side of the previous equation turns 0, hence becoming:

$$\int_\Gamma \Big(-(p_\mathrm{l} - p_\mathrm{g})\,\overline{\overline{\boldsymbol{I}}} + (\overline{\overline{\boldsymbol{\tau}}}_\mathrm{l} - \overline{\overline{\boldsymbol{\tau}}}_\mathrm{g}) + \overline{\overline{\boldsymbol{\tau}}}_\sigma \Big)\,\boldsymbol{n} dS = 0 \tag{2.35}$$

From this relation, it directly follows that:

$$\boxed{(p_\mathrm{l} - p_\mathrm{g})\,\overline{\overline{\boldsymbol{I}}} = (\overline{\overline{\boldsymbol{\tau}}}_\mathrm{l} - \overline{\overline{\boldsymbol{\tau}}}_\mathrm{g}) + \overline{\overline{\boldsymbol{\tau}}}_\sigma} \tag{2.36}$$

As shown by this relation, the effect of surface tension it to introduce a discontinuity in pressure and viscous effects in the interface.

Momentum conservation in separate phases

Following the same procedure of §2.2.2, the volume fraction is used to formulate momentum equations in the strong form. Eq. (2.28) can be applied to each phase for getting separate conservation equations of momentum. However, the **momentum exchange** between both phases must be accounted for through a source term $\dot{\boldsymbol{s}}$. Then, the strong form of momentum conservation equations for each phase take the following form:

$$\frac{\partial\,(\alpha_\mathrm{g}\rho_\mathrm{g}\boldsymbol{u}_\mathrm{g})}{\partial t} + \nabla\,(\alpha_\mathrm{g}\rho_\mathrm{g}\boldsymbol{u}_\mathrm{g}\boldsymbol{u}_\mathrm{g}) = -\nabla\,(\alpha_\mathrm{g}p_\mathrm{g}) + \nabla\left(\alpha_\mathrm{g}\overline{\overline{\boldsymbol{\tau}}}_\mathrm{g}\right) + \alpha_\mathrm{g}\boldsymbol{b}_\mathrm{g} + \dot{\boldsymbol{s}}_\mathrm{g} \tag{2.37a}$$

$$\frac{\partial\,(\alpha_\mathrm{l}\rho_\mathrm{l}\boldsymbol{u}_\mathrm{l})}{\partial t} + \nabla\,(\alpha_\mathrm{l}\rho_\mathrm{l}\boldsymbol{u}_\mathrm{l}\boldsymbol{u}_\mathrm{l}) = -\nabla\,(\alpha_\mathrm{l}p_\mathrm{l}) + \nabla\left(\alpha_\mathrm{l}\overline{\overline{\boldsymbol{\tau}}}_\mathrm{l}\right) + \alpha_\mathrm{l}\boldsymbol{b}_\mathrm{l} + \dot{\boldsymbol{s}}_\mathrm{l} \tag{2.37b}$$

The integral balance can be obtained by integrating both expressions over a fixed control volume Ω and applying the Gauss theorem to the divergence term:

$$\frac{\partial}{\partial t}\int_\Omega \alpha_\mathrm{g}\rho_\mathrm{g}\boldsymbol{u}_\mathrm{g} dV + \int_{\partial\Omega} \alpha_\mathrm{g}\rho_\mathrm{g}\boldsymbol{u}_\mathrm{g}\,(\boldsymbol{u}_\mathrm{g}\cdot\boldsymbol{n})\,dS = \int_{\partial\Omega} \alpha_\mathrm{g}\left(-p_\mathrm{g}\overline{\overline{\boldsymbol{I}}} + \overline{\overline{\boldsymbol{\tau}}}_\mathrm{g}\right)\boldsymbol{n} dS + \int_\Omega \alpha_\mathrm{g}\boldsymbol{b}_\mathrm{g} dV + \dot{\boldsymbol{S}}_\mathrm{g} \tag{2.38a}$$

$$\frac{\partial}{\partial t}\int_\Omega \alpha_\mathrm{l}\rho_\mathrm{l}\boldsymbol{u}_\mathrm{l} dV + \int_{\partial\Omega} \alpha_\mathrm{l}\rho_\mathrm{l}\boldsymbol{u}_\mathrm{l}\,(\boldsymbol{u}_\mathrm{l}\cdot\boldsymbol{n})\,dS = \int_{\partial\Omega} \alpha_\mathrm{l}\left(-p_\mathrm{l}\overline{\overline{\boldsymbol{I}}} + \overline{\overline{\boldsymbol{\tau}}}_\mathrm{l}\right)\boldsymbol{n} dS + \int_\Omega \alpha_\mathrm{l}\boldsymbol{b}_\mathrm{l} dV + \dot{\boldsymbol{S}}_\mathrm{l} \tag{2.38b}$$

where $\dot{\boldsymbol{S}} = \int_{\partial\Omega}\dot{\boldsymbol{s}} dV$. The left hand side of these equations present two terms which are equivalent to the ones in the continuity equations (2.22): a transient term accounting for the momentum variation within the control volume and a surface term accounting for the momentum fluxes entering or leaving the control volume through its boundaries. This term defines the **momentum flow rate**, or **momentum flux**, $\dot{M}$:

$$\boxed{\dot{\boldsymbol{M}} = \int_A \rho\boldsymbol{u}\,(\boldsymbol{u}\cdot\boldsymbol{n})\,dS} \tag{2.39}$$

The right-hand side includes all the contributions from surface and body forces to the change of momentum of the system, plus the source term that will account for the momentum exchange between phases. The surface forces are grouped in the term $\boldsymbol{F}_s$, while the body forces are denoted as $\boldsymbol{F}_b$. If the transient term of the left-hand side is called $\dot{\boldsymbol{J}}$ and the momentum fluxes are separated into inlet and outlet fluxes, then the momentum conservation for separated phases can be written as follows:

$$\boxed{\dot{\boldsymbol{J}}_{m_\mathrm{g}} = \sum_{i_\mathrm{in}} \dot{\boldsymbol{M}}_{g_i} - \sum_{i_\mathrm{out}} \dot{\boldsymbol{M}}_{g_i} + \boldsymbol{F}_{s_\mathrm{g}} + \boldsymbol{F}_{b_\mathrm{g}} + \dot{\boldsymbol{S}}_\mathrm{g}} \tag{2.40a}$$

$$\boxed{\dot{\boldsymbol{J}}_{m_\mathrm{l}} = \sum_{j_\mathrm{in}} \dot{\boldsymbol{M}}_{l_j} - \sum_{j_\mathrm{out}} \dot{\boldsymbol{M}}_{l_j} + \boldsymbol{F}_{s_\mathrm{l}} + \boldsymbol{F}_{b_\mathrm{l}} + \dot{\boldsymbol{S}}_\mathrm{l}} \tag{2.40b}$$

2.3 Eulerian approaches for dense regime

Previously, the governing laws for fluid dynamics have been stated in their weak and strong forms. They have been extended to two-phase flows by introducing the volume fraction into the equations and by distinguishing between phases. It has been proved that surface tension introduces a discontinuity in the momentum equation, something the numerical methods have to deal with. This section presents several interface-capturing methods represented in Fig. 2.2 widely used to solve two-phase flow systems. A thorough classification of existing numerical methods for two-phase flows is shown in Figure 2.2 where the methods discussed in this section are enclosed in red. Models aiming at solving disperse-phase flows use often a two-fluid formulation, since the description of each phase is done with separate equations. On the other hand, methods addressing separate phases are based on a one-fluid formulation, since basically the same governing equations are solved but distinguishing between phases via their different physical properties. This requires a specific treatment of the interface and the jump conditions in pressure due to surface tension, which each method handles differently.

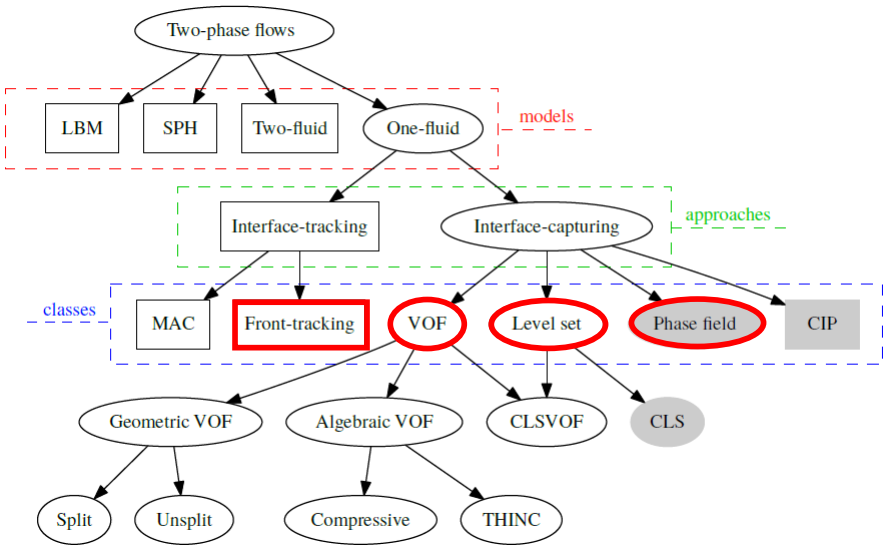

Figure 2.2: Numerical methods to simulate two-phase flows. Ellipses denote interface-capturing methods. Sharp-interface methods are denoted by a white background, while the grey one indicates diffuse-interface methods. Source: Mirjalili et al. (2017)

2.3.1 Diffuse interface methods

Diffuse interface comprises a family of numerical methods in which the interface is not found at a precise spatial location, but is distributed along a transition region where both phases coexist. The volume fraction of gas and liquid phases must add up to 1: $\alpha_l + \alpha_g = 1$. Figure 2.3 displays a droplet solved with a diffuse interface method and a sharp interface (VOF, see §2.3.3) in the same grid, clearly showing how the interface can be easily defined for the latter but not for the former.

A class of diffuse-interface methods arousing recent interest in immiscible, incompressible two-phase flows are the **phase field methods**. Originally, they make use of the Cahn-Hilliard equations (Cahn & Hilliard 1958). Their derivation is based on the minimisation of a free energy functional, which leads to a typical convection-diffusion equation with source terms. This equation presents the main disadvantage that is written in a non-conservative form, and hence it is not suitable for application in immiscible flows (Mirjalili et al. 2020). This issue was later solved by Chiu & Lin (2011), who claimed that the following second order equation can be used with the same purpose and applied to immiscible flows:

$$\frac{\partial \psi}{\partial t} + \nabla \left(\mathbf{u} \psi \right) = \nabla \left[\gamma \left(\epsilon \nabla \psi - \psi \left(1 - \psi \right) \frac{\nabla \psi}{|\nabla \psi|} \right) \right] \tag{2.41}$$

where ϵ is a parameter defining the thickness of the interface, $\gamma = \max(\mathbf{u})$ and ψ is a hyperbolic tangent function representing the distance from the interface, defined later in Eq. (2.48). This equation is transported

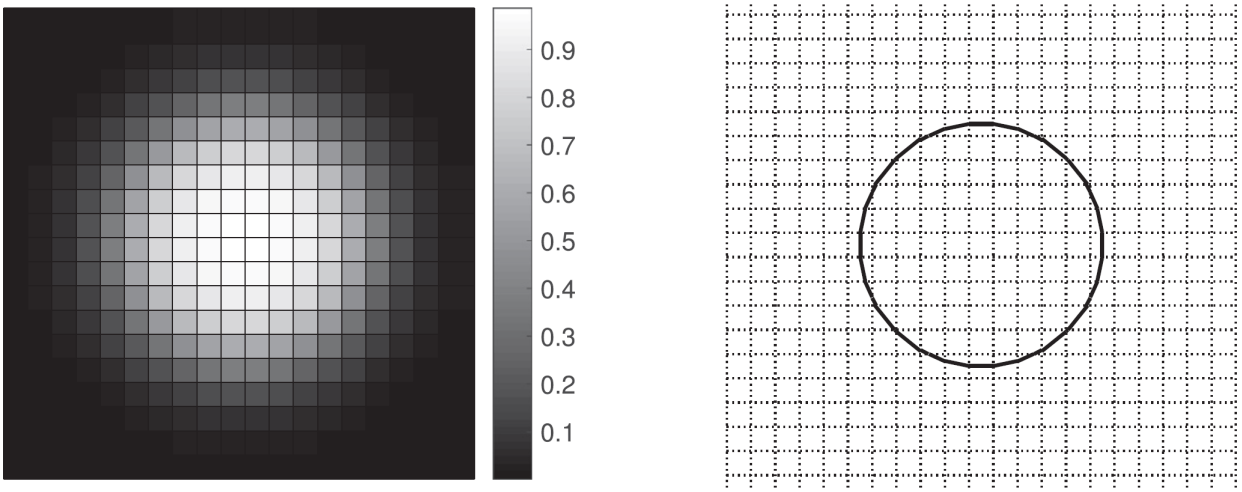

Figure 2.3: Comparison of a droplet solved in a 20x20 grid by a diffuse interface method (*left*) and a sharp-interface VOF method (*right*). Source: Mirjalili et al. (2019)

to obtain the evolution of the interface with time. Then, the velocity fields are obtained from the traditional Navier-Stokes equations with a one-fluid formulation, Eq. (2.28). The density and viscosities are evaluated with the field function ψ:

$$\rho = \psi\rho_l - (1-\psi)\,\rho_g \tag{2.42a}$$
$$\mu = \psi\mu_l - (1-\psi)\,\mu_l \tag{2.42b}$$

Other available diffuse-interface methods have made use of the aforementioned Cahn-Hilliard and applied it to miscible flows (Teigen et al. 2011) and to compressible two-phase systems (Shukla et al. 2010). Diffuse-interface methods find good applicability in particular thermodynamic regimes, like cavitation (Saurel & Pantano 2018) or multicomponent systems at supercritical conditions relevant in rocket engines, where surface tension is non-existent and a proper interface is not present (Dahms & Oefelein 2013, Jofre & Urzay 2021). Their associated challenges currently addressed by the scientific community are mainly related to deal with the multiscale nature of atomization, since small droplets might diffuse when reaching the grid resolution (Saurel & Pantano 2018), and to properly retrieve the thermodynamic properties of fluids around the interface while controlling its thickness (Nayigizente 2021).

2.3.2 Front-tracking method

The front-tracking method is, according to the classification of Figure 2.2, the only method presented in this chapter following an interface-tracking approach (the rest are comprised within the interface-capturing family). It was introduced for the first time by Tryggvason et al. (2001). The interface is modeled as a moving front of lagrangian particles without mass which are explicitly tracked by connected marker points. Particles are convected with the flow field, and their movement is governed according to the kinematic equation:

$$\mathbf{u} = \frac{d\mathbf{x}}{dt} \tag{2.43}$$

where the velocity $\mathbf{u}$ is obtained by solving the flow field. As lagrangian particles are used, the interface is not solved on the same grid as the liquid and gas fields, see Figure 2.4. This makes this method more of a lagrangian nature than an eulerian one in the sense that the interface is resolved separately from the main grid. Yet, both phases are solved with an eulerian formalism in the same grid; hence, this method is categorized as eulerian since it mainly aims at solving separate-phase problems as indicated in Figure 2.1 left. There are indeed interface-tracking methods dealing with the interface from an eulerian perspective, such as the Marker and Cell (MAC) method (McKee et al. 2008).

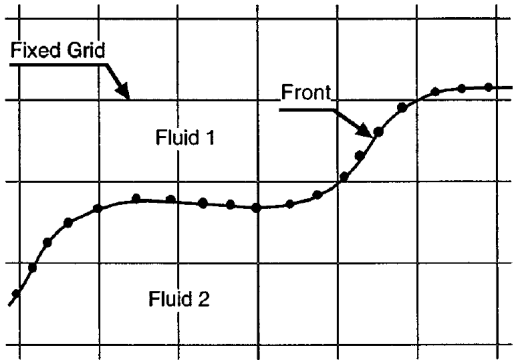

Figure 2.4: Illustration of the front-tracking method: both fluids are solved in the main grid while the interface is represented by a front of particles. Source: Tryggvason et al. (2001)

2.3.3 Volume of Fluid method

The Volume of Fluid method (VOF) was the first numerical methodology developed to solve for liquid-gas interfaces in free surface flows, introduced originally by Hirt & Nichols (1981). It is included among the methods using a **sharp-interface** approach, as opposed to diffuse interface which were succinctly discussed previously. They have been extensively studied in literature, and have been applied for both structured (Scardovelli & Zaleski 1999, Fuster et al. 2009) and unstructured (Jofre et al. 2014, Ivey & Moin 2017) grids. VOF methods identify the liquid regions according to their liquid volume fraction α_l defined in Eq. (2.20). The volume fraction scalar is transported with an advection equation (2.44):

$$\frac{\partial \alpha_l}{\partial t} + \nabla \cdot (\alpha_l \boldsymbol{u}) = 0 \tag{2.44}$$

The material properties, density ρ and viscosity μ, are calculated from the liquid volume fraction:

$$\rho = \alpha_l \rho_l + (1 - \alpha_l)\, \rho_g \tag{2.45a}$$
$$\mu = \alpha_l \rho_l + (1 - \alpha_l)\, \rho_g \tag{2.45b}$$

The biggest advantage of VOF is the mass conservation, as it is ensured when solving Eq. (2.44). On the other side, its main challenge is the difficulty of reconstructing the interface from the transported α_l field, as illustrated in Figure 2.5. According to the approach used to reconstruct the interface, VOF methods can be classified as algebraic or geometric: the first ones indicate methods where the interface does not require geometrical reconstruction, as α_l is transported with analytical functions (Pirozzoli et al. 2019), while in the latter the interface needs to be approximated geometrically through numerical reconstruction (Mirjalili et al. 2017).



Figure 2.5: Application of VOF method, where dark is liquid and white is gas. *Left*: initial flow field. *Middle*: transported α_l field. *Right*: interface reconstruction, where a non-smooth interface can be appreciated. Source: Odier (2006)

2.3.4 Accurate Conservative Level Set method

A well-known class of interface-capturing approaches for two-phase flows are the level set methods. As their own name indicates, these methods identify the interface as a constant value of a scalar level set function. The interface is directly represented and transported using this function, hence its location is always known and no reconstruction needs to be done (as opposed to VOF methods). The level-set method is the formalism used in this thesis for performing resolved atomization simulations, hence it is thoroughly described in the following lines from its fundamentals (Osher & Fedkiw 2003) to the more recent developments by Janodet et al. (2022).

Classical level set methods (Osher & Fedkiw 2003) distinguish between liquid and gaseous phases by introducing the smooth, signed-distance function to the interface $\phi(\mathbf{x}, t)$:

$$\phi\left(\mathbf{x}, t\right) = \pm|\mathbf{x}\left(t\right) - \mathbf{x}_{\Gamma}\left(t\right)| \tag{2.46}$$

According to this definition, the interface is located at $\phi(\mathbf{x}, t) = 0$. Positive values of $\phi(\mathbf{x}, t)$ indicate liquid regions, while negative values denote gas. The interface is then transported with an advection equation:

$$\frac{\partial \phi}{\partial t} + \nabla \cdot (\phi \boldsymbol{u}) = 0 \tag{2.47}$$

When applying the previous expression, the function ϕ will be distorted and its smoothness will be lost. To solve this, the profile of ϕ is reshaped using a reinitialization equation (Sussman et al. 1994). Nevertheless, mass conservation is not ensured after the reinitialization process due to the nature of the distance function ϕ. In this sense, Olsson et al. (2005) tried to reduce the conservation errors by introducing the hyperbolic tangent function ψ:

$$\psi\left(\mathbf{x}, t\right) = \frac{1}{2}\left(\tanh\left(\frac{\phi(\mathbf{x}, t)}{2\varepsilon}\right) + 1\right) \tag{2.48}$$

where ε defines the profile thickness. The function ψ, which is a mapping from the classical signed-distance ϕ, is bounded between 0 and 1, while ϕ is unbounded. The interface Γ is located at the iso-value $\psi = 0.5$; gas phase is given by $\psi < 0.5$, and liquid for $\psi > 0.5$. Figure 2.6 shows a representative view of both distance functions.

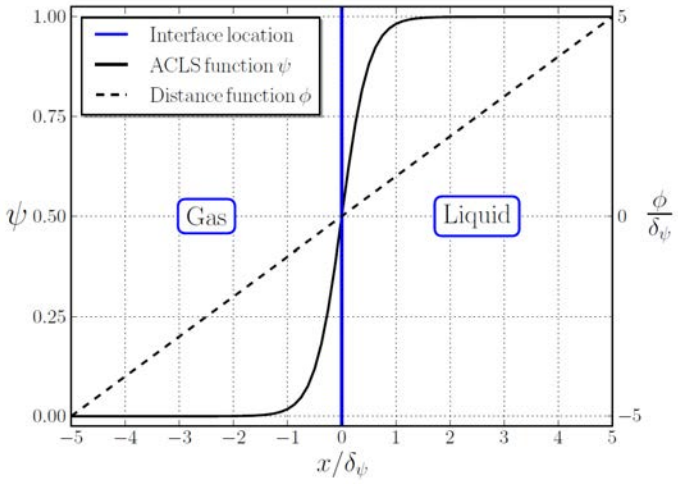

Figure 2.6: Representation of distance functions ϕ and ψ in the ACLS methodology. The signed-distance function ϕ has been normalized by $\delta_\psi = 4\varepsilon$ for visualization. Source: Janodet et al. (2022)

As in the classical level-set method, the hyperbolic tangent profile is also transported via an advection equation:

$$\frac{\partial \psi}{\partial t} + \boldsymbol{\nabla} \cdot (\psi \mathbf{u}) = 0 \tag{2.49}$$

and then reinitialised through resolution of the following equation (Olsson et al. 2007):

$$\frac{\partial \psi}{\partial \tau} = \boldsymbol{\nabla} \cdot \left(\underbrace{\varepsilon (\boldsymbol{\nabla}\psi \cdot \mathbf{n})\mathbf{n}}_{\text{Diffusion}} - \underbrace{\psi(1-\psi)\mathbf{n}}_{\text{Resharpening}} \right) \tag{2.50}$$

where τ is a pseudo-time and $\mathbf{n}$ is the normal vector to the interface, obtained from the signed-distance function ψ:

$$\mathbf{n} = \frac{\nabla \psi}{|\nabla \psi|} \tag{2.51}$$

As indicated in Eq. (2.50), the reinitialization process has two terms: diffusion and resharpening. Both of them are necessary to ensure the smoothness of ψ. The reinitialization equation is then performed for a given number of iterations N_{reinit}, which is a user-defined parameter. With the introduction of ψ and the reinitialization equation, mass conservation errors are reduced, since the smoothness of the profile is better preserved (Olsson et al. 2007): hence, this method is referred as conservative level set. Nevertheless, numerical errors might appear during reinitialisation since small oscillations in ψ can induce big variations in $\mathbf{n}$. To improve the accuracy, Desjardins et al. (2008) proposed an extension to this conservative methodology in which the interface transport is solved with high order schemes and a fast-marching method is used to reconstruct the signed-distance function ϕ. Interface normals are then computed from this function, from which the curvature κ can then be calculated:

$$\mathbf{n} = \frac{\nabla \phi}{|\nabla \phi|} \tag{2.52}$$

$$\kappa = -\nabla \cdot \mathbf{n} \tag{2.53}$$

Desjardins et al. (2008) use a least squares reconstruction to compute κ. This extension to the conservative level set methodology is known as **Accurate Conservative Level Set** (ACLS) method. With these formulations, mass conservation is improved and numerical errors are reduced. ACLS is coupled to the Ghost-Fluid Method (GFM) (Fedkiw et al. 1999) in order to deal explicitly with the pressure jump at the interface:

$$[p]_\Gamma = p_{l,\Gamma} - p_{g,\Gamma} = \sigma \kappa_\Gamma + 2\,[\mu]_\Gamma \mathbf{n}^T \cdot \nabla \mathbf{u} \cdot \mathbf{n} \tag{2.54}$$

where κ_Γ is the interface mean curvature and μ is the dynamic viscosity. Using this formulation, surface tension forces $\sigma\kappa_\Gamma$ are embedded in the pressure jump.

In this work, the more recent extension to the ACLS method by Janodet et al. (2022) is taken. This formulation solves the reinitialization equation introduced by Chiodi & Desjardins (2017):

$$\frac{\partial \psi}{\partial \tau} = \boldsymbol{\nabla} \cdot \left(\frac{1}{4\cosh^2\left(\phi_{\text{map}}/2\varepsilon\right)} \left(|\boldsymbol{\nabla}\phi_{\text{map}} \cdot \mathbf{n}| - 1 \right) \mathbf{n} \right) \tag{2.55}$$

where $\phi_{\text{map}} = \varepsilon \ln\left(\psi/(1-\psi)\right)$ is an analytical signed-distance function mapped for $\psi \in]0;1[$. The equation is solved iteratively for a number of timesteps N_{reinit}, which is often between 3 and 6. This reinitialization equation ensures that the hyperbolic tangent profile ψ is reshaped after transport without introducing significant spurious displacement of the interface. The curvature is then calculated as follows (Goldman 2005):

$$\kappa = \frac{\text{Tr}\left(\boldsymbol{\mathcal{H}}(\phi)\right) - \frac{\boldsymbol{\nabla}\phi^T}{|\boldsymbol{\nabla}\phi|} \cdot \boldsymbol{\mathcal{H}}\left(\phi\right) \cdot \frac{\boldsymbol{\nabla}\phi}{|\boldsymbol{\nabla}\phi|}}{|\boldsymbol{\nabla}\phi|} \tag{2.56}$$

where $\mathcal{H}\left(\phi\right)$ is the Hessian matrix of the distance function. To reduce numerical errors, a Geometric-Projection Marker Method (GPMM) is used to reconstruct ϕ at the nodes in a narrow band around the interface (Janodet et al. 2019). The GFM method is also used to deal with the interface pressure jump. Both phases are solved with a one-fluid formulation by solving Navier-Stokes and evaluating the physical properties at each spatial location with:

$$\rho(\mathbf{x},t) = \rho_g + (\rho_l - \rho_g) H(\psi(\mathbf{x},t) - 1/2) \tag{2.57a}$$

$$\mu(\mathbf{x},t) = \mu_g + (\mu_l - \mu_g)\psi(\mathbf{x},t) \tag{2.57b}$$

where H is the Heaviside function.

Coupling with dynamic mesh adaptation

To better resolve the atomization dynamics and save computational resources, the ACLS/GFM method is coupled to an Adaptive Mesh Refinement (AMR) strategy for increasing the mesh resolution at the liquid-gas interface at an affordable cost (Leparoux et al. 2018). The AMR methodology, illustrated in Figure 2.7, keeps a minimum element size $\Delta x_{\min}$ at the interface and in its surroundings within a band of width $2N_p\Delta x_{\min}$, where N_p is the number of cells with size $\Delta x_{\min}$ at each size of the interface (usually $6 < N_p < 12$). The mesh is dynamically refined throughout the computation with an automatic distance-based triggering ensuring that the interface always remains within this region. In its vicinity, the cell size increases linearly with controlled slope until the baseline cell size Δx_{init}. AMR will be used in all the resolved atomization simulations presented in this thesis. Hence, the full methodology used to performed this simulations will be hereafter referred as ACLS/AMR.

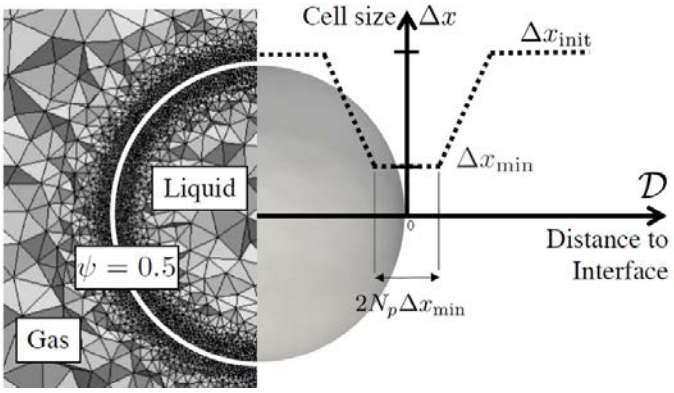

Figure 2.7: Illustration of dynamic mesh adaptation with AMR. Source: Leparoux et al. (2018).

Leparoux et al. (2018) states that ACLS improves liquid mass conservation by propagating and reinitializing the interface given by the contour $\psi = 0.5$. If a uniform mesh is used with sufficient resolution to capture liquid structures, mass conservation is ensured as the level-set profile does not diffuse when transported due to lack of cell size gradients. However, this does not often occur when atomization creates small droplets, as the baseline meshes are not fine enough to capture these small scales. The purpose of AMR is therefore to refine locally and dynamically the mesh to place smaller elements around the interface. However, AMR is not triggered at each timestep, as this would yield very expensive computations. Instead, mesh adaptation is automatically triggered throughout the simulation when the interface propagates and gets closer to the edge of the refined region, see Figure 2.8. For this purpose, a protected distance $|\phi_p| = (N_p/2)\,\Delta x_{\min}$ is defined from the interface (Figure 2.8a), which represents a band called protected region. At each timestep, both the interface and the protected region propagate. At a given time instant (Figure 2.8b), the edge of the protected region will reach the end of the refined area and enter into the gradient zone: at this moment, AMR is triggered. After the remeshing process, a new mesh is produced (Figure 2.8c), and the simulation keeps running.

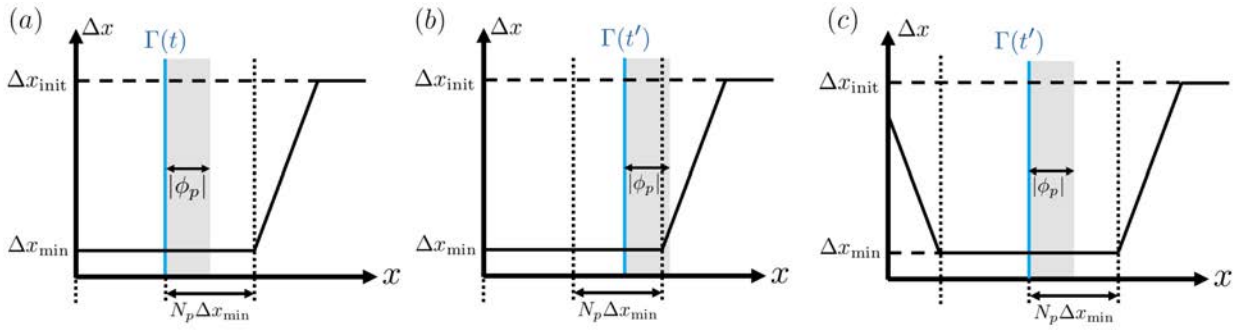

Figure 2.8: Automatic AMR triggering according to a protected distance $|\phi_p|$. (a) Interface Γ after an adaptation process at time t. (b) Interface location at a later time $t' > t$, when the protected region edge falls outside refined area. (c) Mesh after mesh refinement at time instant t'. Source: Janodet (2022).

Chapter 3

Numerical methods to simulate dispersed phase

3.1 Introduction

The previous chapter presented numerical methodologies applicable to separate two-phase flows. Such methods are useful for solving problems where the dynamics of atomization need to be accurately resolved. Nonetheless, these are not suitable to tackle dispersed phase problems due to the high computational costs involved in resolving and transporting a spray composed of many droplets. Furthermore, resolved atomization methods are not able to efficiently solve for multiphysics phenomena relevant in combustion systems such as evaporation, being an ongoing research line nowadays (Boniou 2022). Therefore, dispersed-phase regimes need a different representation of the liquid phase so that: 1) the spray can be transported with acceptable computational costs and 2) more complex physics relevant to reactive problems can be included, such as evaporation and combustion.

In this chapter, numerical strategies to simulate dispersed phase flows are reviewed. Section 3.2 summarizes some of the available formalisms that can be chosen for solving a dispersed phase problem, with special emphasis on the lagrangian point-particle approach which is employed in this thesis. Then, section 3.3 presents the state of the art on lagrangian methods to simulate fuel injection in MSFI systems, which is the starting point of this work.

3.2 Numerical approaches to model dispersed phase flows

The spray generated in the dispersed phase regime is mainly distinguished from liquid in the separate regime by the following features (represented in Figure 1.7):

- The characteristic length scales of the particles. In dispersed phase flows, these ones are usually smaller than the resolution of the main grid.
- The value of the liquid volume fraction α_l. In dispersed phase flows, $\alpha_l < 1$. According its value, one can distinguish between dense regime (moderate values of α_l, particles are close to each other) and dilute regime (lower values of α_l, usually below 10^{-3}, particles are far from each other).

The numerical formalisms to resolve dispersed phase flows will hence depend on these two characteristics. It is also important to consider the interaction with the gaseous phase, since its resolution depends on the main grid. The interaction between the liquid and gaseous phases in dispersed phase flows can be quantified by means of the Stokes number St, defined as the ratio between the characteristic time-scale of a liquid particle τ_p and a characteristic time of the gaseous phase τ_g:

$$St = \frac{\tau_p}{\tau_g} \tag{3.1}$$

A classification of numerical methods to simulate dispersed phase flows based on the volume fraction and the Stokes number has been done by Balachandar (2009), shown in Figure 3.1. As it can be seen, the Stokes

number will depend on the numerical methodology used to resolve the gaseous phase: in DNS, the smallest scales of turbulence with characteristic size η will be resolved and will have a characteristic time τ_k, while in LES the smallest scales resolved ξ will be larger and their time-scales will be different (τ_ξ). Regarding the volume fraction, coupling strategies between liquid particles and gas can be used depending on its value: in the dilute regime particles are far from each other and the interactions among them can be neglected (one and two-way coupling), while in the dense regime the interaction between particles must be taken into account (four-way coupling). The difference between one and two-way coupling depends on if the influence of the liquid phase onto the gas is considered with source terms (two-way coupling) or if it is neglected, so that the gaseous phase will not be perturbed by the particles (one-way coupling).

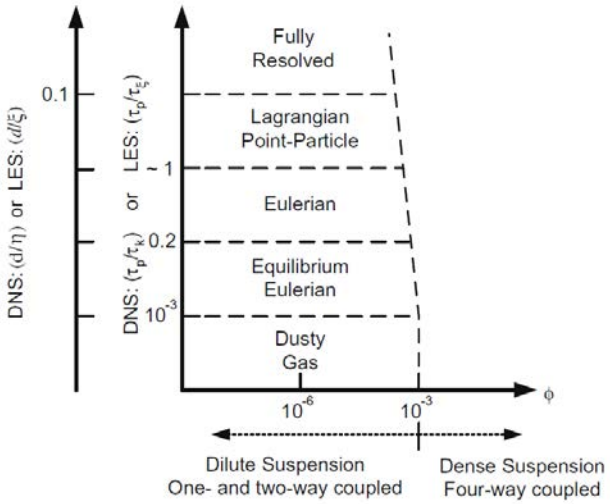

Figure 3.1: Numerical approaches to solve dispersed phase flows. Classification is done with respect to the liquid volume fraction (here defined as ϕ) and to the Stokes number or, equivalently, to the ratio of largest to smallest length scales, which depend on the numerical resolution. Source: Balachandar (2009)

3.2.1 Statistical methods

A spray composed of dispersed droplets can be characterized by means of a number density function f. This function depends on time t, space $\mathbf{x}$, velocity $\mathbf{u}$ and radius r, and can be expressed as follows (Subramanian 2000):

$$f\left(t,\mathbf{x},\mathbf{u},r\right)=\sum_{p=1}^{N_d}\delta\left(\mathbf{x}-\mathbf{x}_p\left(t\right)\right)\delta\left(\mathbf{u}-\mathbf{u}_p\left(t\right)\right)\delta\left(\mathbf{r}-\mathbf{r}_p\left(t\right)\right) \tag{3.2}$$

where N_d is the number of droplets in the spray, and $\mathbf{x}_p$, $\mathbf{u}_p$ and r_p are each individual particles position, velocity and radius respectively. The function f contains all the necessary information to represent the spray. This function is governed by a William-Boltzmann Equation (Williams 1958):

$$\frac{\partial f}{\partial t}+\nabla_{\mathbf{x}_p}\left(\mathbf{u}_p f\right)+\nabla_{\mathbf{u}_p}\left(\mathbf{F}_p f\right)+\frac{\partial E_{S_p} f}{\partial S_p}+\frac{\partial E_{T_p} f}{\partial T_p} \tag{3.3}$$

where $\mathbf{x}_p$, $\mathbf{u}_p$, S_p and T_p are each individual particle's position, velocity, surface and temperature, respectively; $\mathbf{F}_p$ is the force acting on the particle, and E_{S_p} and E_{T_p} are respectively the exchange terms due to mass (evaporation rate) and energy (heat transfer). Statistical approaches aim at determining the function f by solving/approximating Eq. (3.3). Stochastic methods to solve for the dispersed phase include the stochastic lagrangian approach of Dukowicz (1980), eulerian methods considering a monodisperse (Drew & Passman 1999) or a polydisperse spray (Laurent & Massot 2001), and quadrature methods. These methods are out of the scope of the present work and hence are not discussed here.

3.2.2 Eulerian methods

Eulerian methods, also called Euler-Euler formalism (EE), are widely used to model dispersed two-phase flows. The same grid is used for resolving both the carrier and dispersed phases. The carrier phase is solved from the Navier-Stokes equations (§2.2) applied to the gas. For characterizing the dispersed phase, averaged properties and statistical tools are used. These methods present, however, difficulties when dealing with the polydispersion of the spray and when modeling the particles collisions and interactions with the walls (Garcia 2009).

To solve for the dispersed phase, a well-known eulerian formalism is the mesoscopic approach. The particles are described according to the kinetic theory of gases formulated by Chapman & Cowling (1970), so that mesoscopic variables are used to get averaged properties of the spray. In order to develop the equations for the dispersed phase, several assumptions need to be made (Lancien 2018):

1. The atomization process is complete, particles are perfectly spherical and non-deformable.
2. The only force exerted by the carrier phase on the droplets is drag.
3. Temperature is homogeneous inside each droplet.
4. Spray is dilute: $\alpha_l < 10^{-2}$.
5. The interactions between droplets are neglected.
6. The spray is mono-disperse and mono-kinetic: at one point in time and space, the droplets all have the same diameter and velocity.
7. Similarly, at one point in time and space, all droplets have the same temperature.

With these assumptions, the dispersed phase is represented by the following equations based on statistical averages of the spray (Lancien 2018):

$$\frac{\partial \overline{n}_l}{\partial t} + \nabla \left(\overline{n}_l \overline{\mathbf{u}}_l \right) = 0 \tag{3.4a}$$

$$\frac{\partial \rho_l \overline{\alpha}_l}{\partial t} + \nabla \left(\rho_l \overline{\alpha}_l \overline{\mathbf{u}}_l \right) = -\Gamma \tag{3.4b}$$

$$\frac{\partial \rho_l \overline{\alpha}_l \overline{u}_{l,i}}{\partial t} + \nabla \left(\rho_l \overline{\alpha}_l \overline{\mathbf{u}}_l \overline{u}_{l,i} \right) = F_{d,i} - \overline{u}_{l,i}\Gamma + \nabla \overline{\overline{\boldsymbol{\tau}}}_l^{sgs} \tag{3.4c}$$

$$\frac{\partial \rho_l \overline{\alpha}_l \overline{h}_l}{\partial t} + \nabla \left(\rho_l \overline{\alpha}_l \overline{\mathbf{u}}_l \overline{h}_l \right) = -\overline{h}_l \Gamma + \overline{\Phi} \tag{3.4d}$$

where n_l is the number density of the particles, Γ the evaporation rate, F_d the drag force, $\overline{\overline{\boldsymbol{\tau}}}_l^{sgs}$ the subgrid tensor of the liquid phase, $\overline{h}_l$ the liquid enthalpy and $\overline{\Phi}$ the conduction flux term. The exchange between phases is taken into account by the right hand sides of the previous expressions. As it is observed, multiphysics phenomena such as mass exchange due to evaporation and energy transfer can be taken into account with the corresponding exchange terms. This is one of the advantage of the dispersed phase modeling of two-phase flows as opposed to the fully-resolved atomization methods presented in Chapter 2. Other frequently used Eulerian method is the Euler-Lagrange Spray Atomization (ELSA) model (Andreini et al. 2016), which has also been coupled to resolved atomization simulation in the dense phase for solving more accurately atomization (Anez et al. 2019).

3.2.3 Lagrangian point particle representation

Another well-know methodology to simulate dispersed phases systems, broadly employed in aerospace applications, is the lagrangian point particle (LPP) representation. In this formalism, the gas is resolved in the main eulerian grid, but the particles conforming the dispersed phase are tracked individually and represented by a different set of equations. Since the carrier phase is solved in an eulerian grid and the dispersed phase is modeled separately, these method is usually referred as the Euler-Lagrange (EL) formalism. This can make convergence difficult and hinders the introduction of parallelism techniques. As advantages, the resulting the time per iteration is usually lower than for the EE description, and the drop-drop and drop-wall interactions are easier to model.

Dynamics of liquid particles

For describing particles in the lagrangian framework, each particle will be modeled according to the **Discrete Particle Simulation** (DPS) approach. In DPS, liquid particles are completely spherical, robust, and defined spatially as points, so that the location of each parcel can be represented by a single position vector. With these assumptions, the **dynamic equations** for a particle p are (Maxey & Riley 1983):

$$\frac{d\boldsymbol{x}_p}{dt} = \boldsymbol{u}_p \tag{3.5a}$$

$$\frac{d\boldsymbol{u}_p}{dt} = \underbrace{-\frac{3}{4}\frac{\rho_\mathrm{g}}{\rho_p}\frac{C_D}{d_p}|\boldsymbol{v}_r|\boldsymbol{v}_r}_{\substack{\text{Drag}\\ \text{term}}} + \underbrace{\left(1-\frac{\rho_\mathrm{g}}{\rho_p}\right)\boldsymbol{g}}_{\substack{\text{Gravity}\\ \text{term}}} \tag{3.5b}$$

where $\mathbf{x}_p$ and $\mathbf{u}_p$ are the position and velocity of the particle, $\mathbf{v}_r = \boldsymbol{u}_p - \boldsymbol{u}_g$ the relative velocity between the particle and the gas, ρ_g and ρ_p are the gas and liquid particle densities, C_D a drag coefficient, and d_p the particle diameter. Equation (3.5b) is the momentum equation of the droplet and contains the contributions of the two forces considered: the drag forces and the gravitational forces. The first ones are usually the main mechanism of momentum transfer between phases, while the latter are often several orders of magnitude smaller and can usually be neglected (specially at high speeds, where drag dominates the momentum transfer).

The drag coefficient of the particles C_d can be evaluated with the following expression, obtained experimentally by Schiller & Naumann (1935):

$$C_D = \begin{cases} \dfrac{24}{Re}\left(1+0.15Re^{0.687}\right) & \text{if } Re < 1000 \\ 0.44 & \text{if } Re \geq 1000 \end{cases} \tag{3.6}$$

where $Re = \rho_\mathrm{g}|\boldsymbol{v_r}|d_p/\mu_\mathrm{g}$ is the Reynolds number based on the relative velocity and particle diameter.

When considering a lagrangian approach, the influence of the carrier phase on the liquid particles will have a determining effect on their motion. This influence can be quantified by means of the Stokes number defined previously by Eq. (3.1). Its magnitude indicates how the droplet responds to fluctuations of the gas flow. If $St << 1$, the droplet will follow perfectly the fluctuations of the gas flow. On the contrary, if $St >> 1$ the droplets will rather neglect the flow trajectories and follow its own track (ballistic behaviour).

For evaluating the Stokes number, the characteristic timescale for each phase need to be determined. The gaseous timescale can be determined as $\tau_g = d_p/|\mathbf{u}_p|$. Particle timescales can be estimated from the following expression (Maxey & Riley 1983):

$$\tau_p = \frac{d_p^2\rho_p}{18\mu_\mathrm{g}} = \frac{4}{3}\frac{\rho_p}{\rho_\mathrm{g}}\frac{d_p}{C_D|\boldsymbol{v}_r|} = \frac{4}{3}\frac{\rho_p d_{p^2}}{\mu_g ReC_D} \tag{3.7}$$

which can be seen as the relaxation time of the particle; in other words, the time that one particle takes to respond to the fluctuations in the velocity field.

Coupling with mass and energy transfer

As in the EE method, the LPP representation also allows to couple the dynamic equation with exchange terms for mass and energy transfer with the gaseous phase:

$$\frac{dm_p}{dt} = \dot{m}_p = \Gamma \tag{3.8a}$$

$$\frac{dh_p}{dt} = m_p C_{P_\mathrm{g}}\frac{dT_p}{dt} = \Phi \tag{3.8b}$$

where m_p, h_p, T_p and C_{P_g} are respectively the particle mass, enthalpy, temperature and gas specific heat capacity at constant pressure. Γ and Φ are the corresponding source terms for mass and energy. It follows that Equation (3.8a) accounts for the **evaporation** process. If a single component is considered and the uniform temperature model for evaporation is used (Abramzon & Sirignano 1989), then the evaporation term can be expressed as:

$$\Gamma = -\pi d_p Sh\,(\rho_p D_F)\ln(1+B_M) \tag{3.9}$$

where Sh is the Sherwood number, D_F the fuel diffusivity, and B_M the Spalding mass number.

For evaluating the energy transfer in the droplets, the physical processes of **conduction** and **evaporation** are taken into account. Then, the source Φ_p is obtained from the following energy balance.

$$\Phi_p = \underbrace{h_p \pi d_p^2 (T_\mathrm{g} - T_p)}_{\substack{\text{Conduction}\\ \text{term}}} - \underbrace{\dot{m}_p \Delta h_v}_{\substack{\text{Evaporation}\\ \text{term}}} \tag{3.10}$$

where T_g is the gas temperature, h_p is the film coefficient of the gas at the particle surface and Δh_v is the latent heat of vaporization of the particle. Eqs. (3.8) can be solved together with Eqs. (3.5) to obtain the evolution of mass and energy of the droplets with time as they move within the carrier phase.

3.3 Stage of the art in injection models for MSFI systems

Several numerical formalisms for modeling the dispersed phase in two-phase flows have been introduced in the previous section. In this work, the lagrangian representation presented in §3.2.3 is used to model the dispersed phase due to its low computational cost and its applicability to account for polydispersity of the spray.

In all dispersed-phase simulations, the first step is to introduce the lagrangian droplets in the domain with their proper boundary conditions. This is achieved by means of **lagrangian injection models**, which are the main interest of the present work. The fact of using a lagrangian approach for representing the particles has the advantage of allowing the injection of a polydisperse spray from the beginning of the simulation, something which is not possible with other dispersed formalisms such as the eulerian ones. This is of particular interest for performing injection in realistic systems, such as in MSFI configurations presented in §1.3.

This section presents the state of the art in models for lagrangian injection with particular focus on MSFI systems. Figure 3.2 proposes a classification for existing models in literature grouped in a Venn diagram, distinguishing five categories and their interactions. Each research work is located according to the characteristics of the model employed, and the configuration of application within the MSFI models (hollow cone, airblast and JICF) is also specified. Several models are **based on empirical laws** obtained from experimental works, with the main advantage that the physics of the problem are already embedded in these laws, but on the other hand restricted to applications with identical geometry and operating conditions as in the test. Regarding the size of injected droplets, it is found that the **injection of a fully developed spray**, often obtained from experiments providing the spray granulometry further downstream the injection nozzle where atomization is fully complete, is usually performed. In the sense of droplet transport, it is sometimes necessary to consider the **effect of the dense spray on the gaseous phase**: in some configurations (especially in the JICF), coherent structures of the dense regime where primary atomization takes place might perturb the gaseous flow which will consequently affect the convection of droplets further downstream. Since the dense regime is neglected in lagrangian computations, this liquid-gas interaction is not directly taken into account, so the droplet transport might not be well resolved. Furthermore, **secondary breakup of particles** in lagrangian simulations can be considered by means of secondary atomization models. This is specially useful in models which do not inject a developed spray, as the initial droplets will have a larger size than the diameters found in the equivalent real configuration. Independently of evaporation, the decrease of droplets size up to a value which is at equilibrium with the surrounding air can be accounted for with these models.

At last, a category called **reference spray learning** is present in Figure 3.2. It includes models that can use a reference spray to learn its characteristics (droplets sizes, velocity distributions and injection location) and impose realistic spray boundary conditions in dispersed phase simulations. As main advantage, such models could be applied to a wide range of injector configurations and operating conditions. Nevertheless, they require a proper characterization of the spray coming from simulations or experiments. This thesis aims at providing a numerical methodology for developing injection models that are able to follow this reference spray learning process. These models are explained in Chapter 4, so they will not be further discussed in this section. The next lines are then devoted to explain some of the injection models in Figure 3.2 which are of interest for MSFI systems, whose main mechanisms of injection are shown in Figure 1.5.

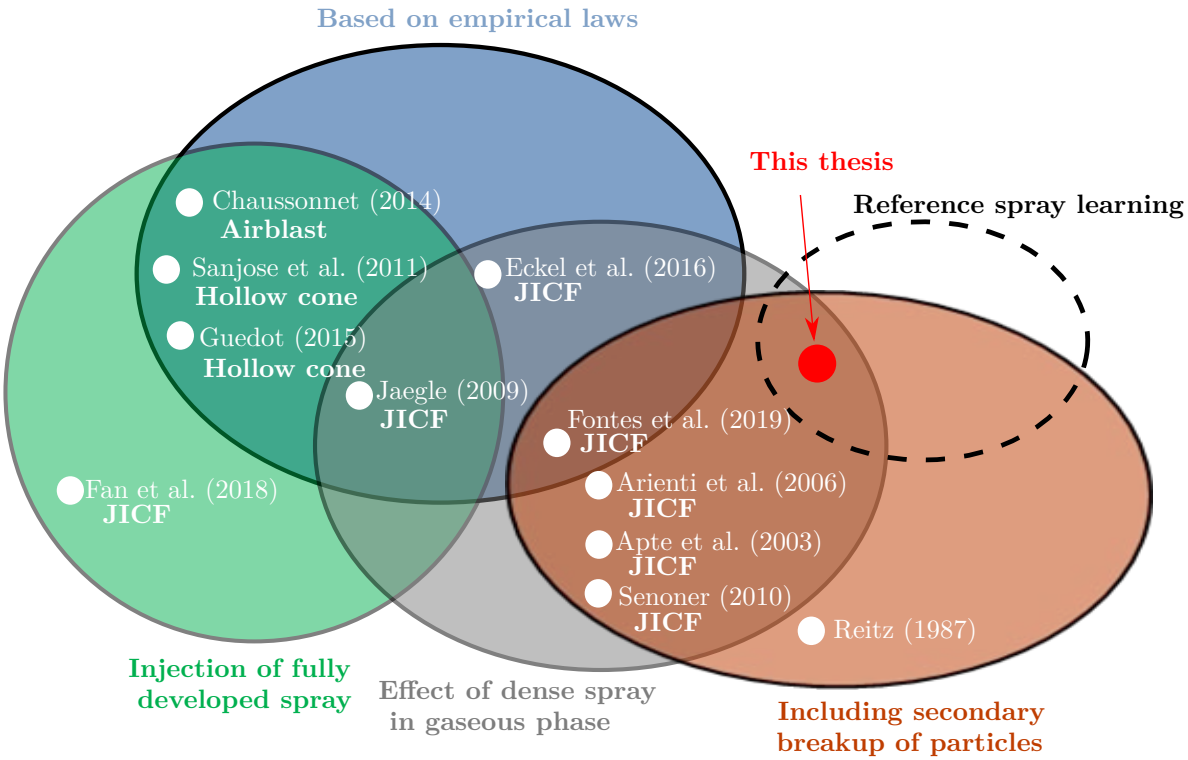

Figure 3.2: Classification proposed for the state of the art in lagrangian injection modeling.

3.3.1 Hollow cone spray

Pressure-swirl atomizers for delivering fuel through the pilot stage in multi-staged injectors will create a hollow cone spray. An example of pressure-swirl injector is shown in Figure 3.3: liquid is injected inside the nozzle with a rotational component (swirl), that will eventually create a hollow cone when the fuel leaves the nozzle. These type of nozzles are widely used and have been extensively studied both experimentally and numerically. Several models exist in literature for modeling the fuel injection in pressure-swirl with lagrangian formalisms. In this section two models are presented: the FIM-UR methodology developed by Sanjose et al. (2011), and the LISA model presented in Guedot (2015).

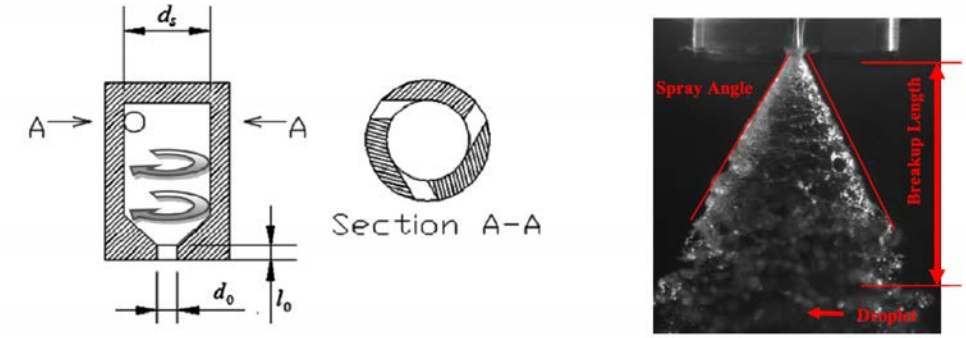

Figure 3.3: Pressure-swirl atomizer. *Left*: schematical view. *Right*: experimental snapshot with key hollow-cone spray features. Source: Wei & Yong (2014).

FIM-UR model

Fuel Injection Model by Upstream Reconstruction (FIM-UR) is an injection model which prescribes a developed spray in pressure-swirl atomizers, neglecting the atomization process. In its original formulation by Sanjose et al. (2011), a monodisperse spray is imposed. The extension to polydisperse sprays has been done by Vié et al. (2013).

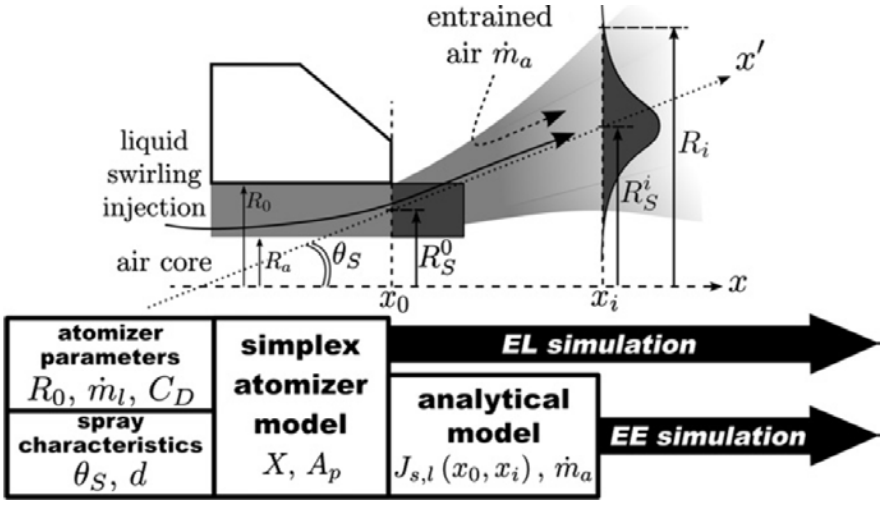

Figure 3.4: FIMUR model for injection in pressure-swirl atomizers. Source: Sanjose et al. (2011).

The principles of FIM-UR are shown in Figure 3.4. The spray is imposed at an injection location x_i, whose boundary conditions are obtained by reconstruction from the properties at the real injection location x_0. FIM-UR can be applied for both EL and EE simulations, with the difference that the latter require additional analytical calculations to determine the momentum transfer and the entrained air mass flow rate. Both cases use the same model inputs: the spray is characterized by the diameter of droplets d and the half-spray mean angle θ_s, and the atomizer is parametrized by its exit radius R_0 and the injected liquid mass flow rate $\dot{m}_l$. Then, empirical formulas for pressure-swirl atomizers are used to calculate the remaining parameters of the model. The ratio X of the air core surface A_a to the discharge orifice surface A_o, called the contraction ratio, is given by Rizk & Lefebvre (1985):

$$X = \frac{A_a}{A_0} = \left(\frac{R_a}{R_0}\right)^2 = \frac{\sin^2\theta_s}{1+\cos^2\theta_s} \tag{3.11}$$

From this formula, the air core radius R_a can be solved. The contraction ratio X can now be used to estimate the discharge coefficient of the atomizer (Lefebvre & McDonell 2017):

$$C_D = 1.17\sqrt{\frac{(1-X)^3}{1+X}} \tag{3.12}$$

which can be used to obtain the tangential-injection surface A_p:

$$A_p = 20.73 C_D^2 A_0 \tag{3.13}$$

With all these parameters known the axial, radial and tangential velocities at the real injection location x_0 can be obtained:

$$u_x^0(\theta, r_0) = \frac{\dot{m}_l}{\rho_l \pi (R_0^2 - R_a^2)} \tag{3.14a}$$

$$u_r^0(\theta, r_0) = 0 \tag{3.14b}$$

$$u_\theta^0(\theta, r_0) = \frac{\dot{m}_l}{\rho_l A_p}\frac{r_0}{R_S^0} \tag{3.14c}$$

Finally, the properties at the numerical injection location x_i are calculated by applying mass and momentum balances between x_0 and x_i (Sanjose et al. 2011):

$$u_x^i(\theta, r_0) = \frac{\pi R_0^2}{\rho_l I_\alpha A_u} \exp\left(-\frac{(r-\mu)^2}{\sigma^2}\right) \tag{3.15a}$$

$$u_r^i(\theta, r_0) = \frac{\dot{m}_l}{\rho_l A_p} \sqrt{1 - \left(\frac{R_S^0}{R_S^i}\right)^2} \frac{r}{R_S^i} \tag{3.15b}$$

$$u_\theta^i(\theta, r_0) = \frac{\dot{m}_l}{\rho_l A_p} \frac{R_S^0}{R_S^i} \frac{r}{R_S^i} \tag{3.15c}$$

where μ, σ are respectively the mean and variance of the gaussian profile of volume fraction at x_i (see Figure 3.4) and $I_\alpha = \sigma^2\left(1 - \exp\left(-R_i^2/\sigma^2\right)\right) + \sigma R_S^i \sqrt{\pi}\,\mathrm{erf}\left(R_i/\sigma\right)$.

LISA model

The main disadvantage of the FIM-UR model is the inability to ensure that the spray opens following the prescribed mean angle θ_s, which is indeed an input to the problem. To solve this issue, Guedot (2015) proposed the Liquid Injection for Swirled Atomizers (LISA) model. This methodology, described in Figure 3.5, follows the same baseline as FIM-UR, but proposes some modifications to keep the mean spray angle constant.

The model inputs are the liquid mass flow rate $\dot{m}_l$, the spray mean angle θ_s and the atomizer exit radius R_0. The principles are identical to FIM-UR: droplets have no radial velocity at injection, and the axial velocity is obtained from mass conservation with the injected flow rate. Hence, both are calculated respectively with Equations (3.14a) and (3.14b). The tangential (or azimuthal) velocity imposed is calculated according to the derivations of Guedot (2015):

$$u_\theta(r) = u_z \frac{r}{R_S^0} \tan\sigma_s \tag{3.16}$$

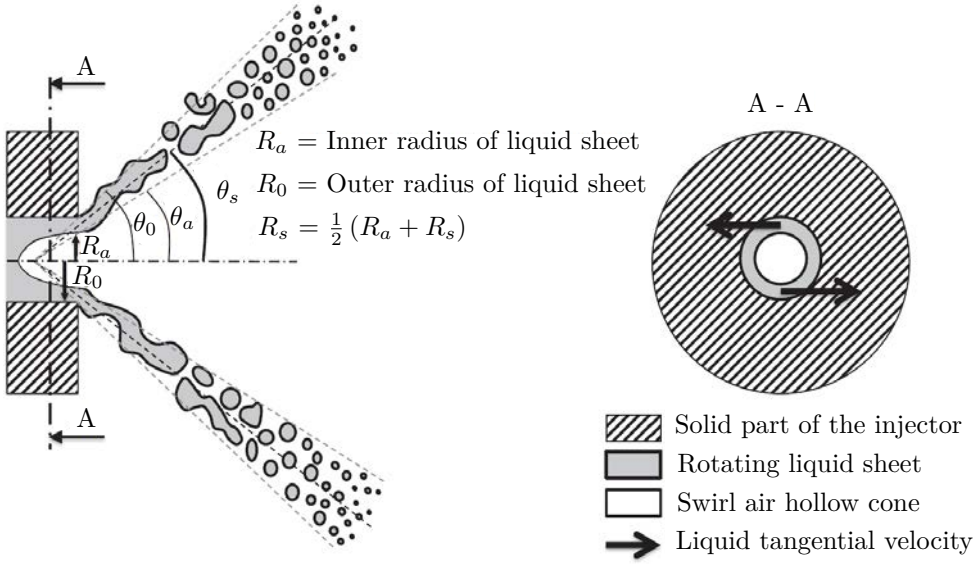

Figure 3.5: LISA model for injection in pressure-swirl atomizers. Source: Guedot (2015).

3.3.2 Airblast spray

In MSFI, at certain operating conditions the liquid injected through the pilot or take-off stages can impinge the walls of the atomizer forming an airblast spray. These have been extensively studied (Lefebvre 1980, Gepperth et al. 2010) and used in industrial burners, found in atomizers of type plain jet or prefilmers (Lefebvre & McDonell 2017).

Regarding numerical approaches to simulate airblast sprays, a phenomenological model was derived by Chaussonnet et al. (2016) called PAMELA (Primary Atomization Model for prEfilming airbLAst injectors). This model uses results obtained in the KIT-ITS airblast experiment by Gepperth et al. (2010) for predicting initial conditions for droplets sizes and velocities. Correlations and laws for droplets sizes are derived by observing the breakup mechanisms found in airblast spray, shown in Figure 3.6. This thesis does not address airblast atomization and hence this model is no longer discussed here: the interested reader is referred to Chaussonnet (2014) and Chaussonnet et al. (2016) for more details into PAMELA model, and to Carmona (2021) for a more recent extention of this model, named Automatic-PAMELA, to a wider range of geometries and operating conditions. Other recent works aim at understanding the spray distribution from resolved calculations

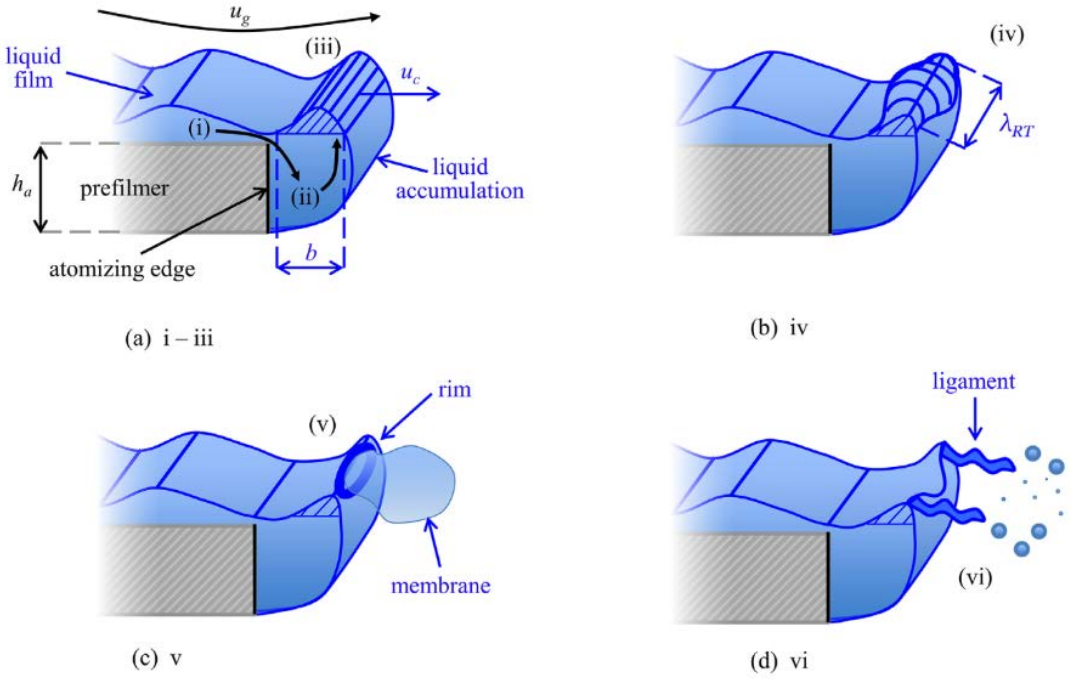

Figure 3.6: Breakup mechanism in an airblast prefilmer spray. Source: Chaussonnet et al. (2016).

3.3.3 Liquid jet in crossflow

Several numerical approaches have been used to study liquid jet in crossflow injection, whose phenomenology has been introduced in §1.3. Figure 3.7 shows four different modeling approaches. Case (a) is the direct simulation of the jet (resolved atomization computation) performed with the methodologies introduced in Chapter 2, which has been used in several works (Herrmann 2009, Pai et al. 2009, Behzad et al. 2016, Li & Soteriou 2018). The other three approaches englobe several ways of tackling JICF simulations from a lagrangian perspective, where droplets are injected. All the categories from Figure 3.7 take into account, one way or another, the liquid column (dense core) and hence its influence on the gaseous phase. This section reviews seven different past works to tackle liquid JICF from a lagrangian perspective. These works, which are all classified in Figure 3.2, are explained in chronological order.

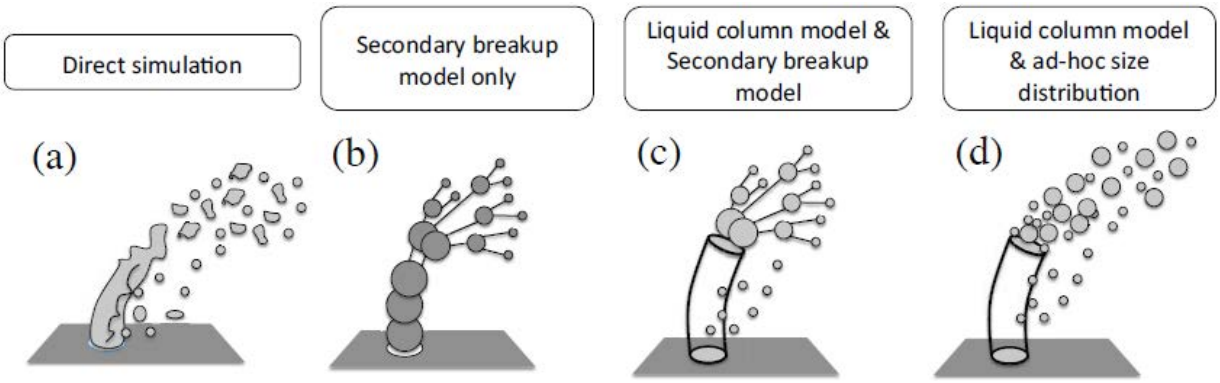

Figure 3.7: Modeling approaches for liquid jet in crossflow proposed by Jaegle (2009).

Blob model combined with secondary atomization (Apte et al. 2003)

Apte et al. (2003) performed simulations of a water JICF. The objective of their work was to test a secondary atomization model in simulations representative of realistic gas-turbine configurations. This breakup model is detailed in §4.6.3 of this document. For liquid injection, droplets with size equal to the nozzle diameter were introduced perpendicularly to the crossflow. Their velocity is the bulk liquid velocity at injection. This methodology is inspired by the blob model developed by Reitz (1987), who simulated diesel jets by injecting droplets with size equal to the nozzle diameter which were later broken by action of an atomization model.

The model by Apte et al. (2003) is included in the (b) category of Figure 3.7. Due to their initial big size, the droplets can easily influence the incoming gaseous flow field by means of two-way coupling between lagrangian particles and gas. Figure 3.8 shows the results obtained by Apte et al. (2003). The jet leaving the nozzle is composed of large droplets. These particles bend towards the crossflow direction due to momentum exchange and break into smaller sizes due to the action of the secondary atomization model. The black and white contours denote the axial gas velocity profile at the central plane, showing the perturbation effect of the liquid onto the crossflow. This model presents the advantages that it is simple, cheap and does not rely on empirical correlations. On the other hand, the liquid column dynamics and breakup are not properly represented through the blob model. Consequently, the liquid-gas interaction is limited to only the two-way coupling and complex turbulent gas structures caused by the dense core are not captured, which could also influence secondary atomization.

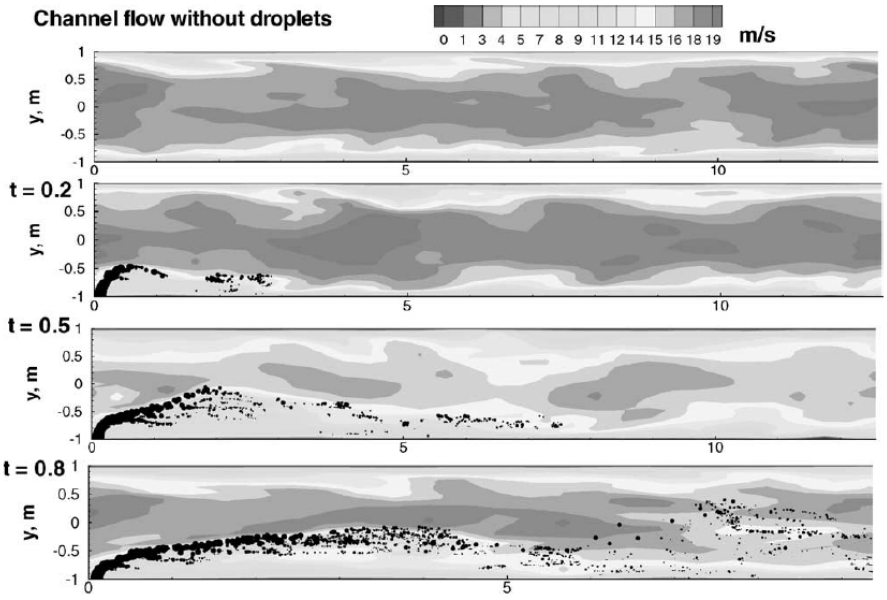

Figure 3.8: Contours of instantenous axial velocity and liquid JICF evolution simulated by Apte et al. (2003).

Modeling the liquid-gas interaction with resolved dense core (Arienti et al. 2006)

Arienti et al. (2006) focused their work on capturing the liquid-gas interaction between the liquid column and the gaseous crossflow. For this purpose, they combined a Volume-of-Fluid (VOF) method (see §2.3.3 for a review on VOF) to solve for the dense core with a lagrangian approach to inject and transport droplets. By properly solving for the continuous liquid phase, the blockage effect is directly taken into account without the need of any extra models. Figure 3.9 left shows front and side views (top and bottom, respectively) of the the dense core resolved by VOF (snapshot a) and of the mean gaseous vector fields at the same planes (snapshot b). Vortices created by the presence of the dense core are captured in both planes with this strategy, hence demonstrating its applicability to model the liquid-gas interaction.

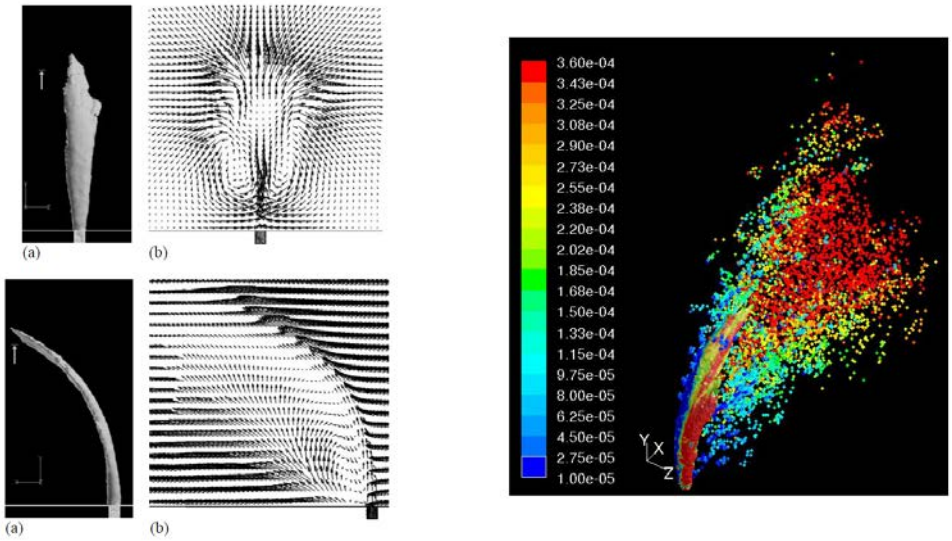

Figure 3.9: Jet in crossflow simulated with VOF plus lagrangian approach. *Left*: dense core view and vector lines showing vortical structures. *Right*: instantaneous snapshot of droplets injected along the dense core. Source: Arienti et al. (2006).

Injection of lagrangian particles is performed at several locations alongside the liquid column, equally spaced between the nozzle exit and the column breakup point. Droplets sizes are obtained from experimental correlations, while the initial velocity is the continuous phase velocity (i.e. from the liquid column) at the same location plus a fluctuating component obtained as the product between a gaussian PDF and the local turbulent velocity from VOF. Figure 3.9 right shows a instantaneous snapshot of the spray, depicting the dense core and the injected droplets colored by their diameter. Additional submodels considered in the computation include dispersion models to account for turbulent fluctuations during droplets transport (Gosman & Ioannides 1983) and the wave secondary atomization model developed by Reitz (1987). This model presents the advantage of directly accounting for the liquid dense core, hence capturing the complex liquid-gas interaction. On the other hand, it relies on empirical correlations to estimate the breakup location (which limits its application to the validity range of the experiments) and is computationally more expensive than a full lagrangian model, as it also solves for the dense core with the resolved method VOF.

Modeling column and shear breakup with empirical laws (Jaegle 2009)

At operating conditions corresponding to surface breakup (Figure 1.11), there are small droplets being torn apart from the liquid column due to the high aerodynamic shear. The quantity of liquid removed by this mechanism is more notorious as q and We are larger. At the same time, there is also the liquid column which undergoes instabilities and breaks first into ligaments (primary atomization) and then into smaller droplets (secondary atomization). Figure 3.10 left shows both mechanisms of droplet generation.

Some numerical methodologies try to predict the size and flow rate of droplets generated by surface breakup, while simultaneously taking into consideration the liquid column. Jaegle (2009) has used this strategy by using empirical laws to predict the liquid column, the size of the injected particles and the flow rate of droplets generated by surface breakup. His approach is illustrated in Figure 3.10 center. Droplets

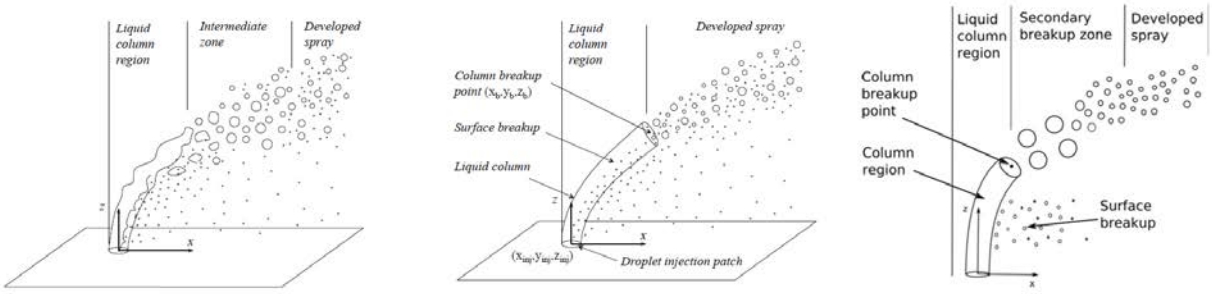

Figure 3.10: Schemes showing numerical models for liquid jets in crossflow. *Left*: classification of different regions of the liquid jet atomization. *Center*: column model considered by Jaegle (2009), neglecting the intermediate zone and secondary breakup. *Right*: column model considered by Senoner (2010).

are injected at the injection patch, which corresponds to the liquid nozzle exit. The liquid column is not resolved, but its region of influence is estimated in order to impose a modified drag law to the droplets that are convected within it. Once these droplets abandon the column region, the drag law is changed to the usual one. At the same time, there are droplets being injected along the liquid column region in the axial direction to model the surface breakup mechanism.

The first step in this model is to estimate the region to modify the drag law. For it, the liquid column is assumed to be cylindrical and to expand from the liquid nozzle exit until the breakup point $(x_\mathrm{b}, y_\mathrm{b}, z_\mathrm{b})$. Its location is estimated from the following experimental expressions by Fuller et al. (2000):

$$\frac{x_b}{d_\mathrm{inj}} = \frac{C_D C_{ab}^2}{\pi} \tag{3.17a}$$

$$\frac{y_b}{d_\mathrm{inj}} = 0 \tag{3.17b}$$

$$\frac{z_b}{d_\mathrm{inj}} = C_{ab} \frac{u_l}{u_\infty} \sqrt{\frac{\rho_l}{\rho_\infty}} \tag{3.17c}$$

where $C_D = 4.39$ is a constant drag coefficient, $C_{ab} = 2.58$ is a breakup coefficient, u_l is the liquid velocity at injection and u_∞ is the gas freestream velocity. The particles travelling in the liquid column region will follow the following modified transport law (Fuller et al. 2000):

$$\frac{du_l}{dt} = \frac{2C_D}{d_\mathrm{inj}\pi} \frac{\rho_l}{\rho_\infty} (u_\infty - u_l)^2 \tag{3.18a}$$

$$\frac{dv_l}{dt} = 0 \tag{3.18b}$$

$$\frac{dw_l}{dt} = 0 \tag{3.18c}$$

Particles are injected at the liquid nozzle exit with velocity u_l and a size sampled from a distribution obtained experimentally by Becker & Hassa (2002). Simultaneously, stripped-off droplets are injected at random locations along the liquid column to account for surface breakup. The mass flow rate $\dot{m}_{l,SB}$ and constant size SMD_{SB} of these droplets are given by the experimental expressions of Ranger & Nicholls (1968) and Chou et al. (1997), respectively:

$$\dot{m}_{l,SB} = \frac{3}{2} l_\mathrm{col} \rho_l \sqrt{\pi d_\mathrm{inj}} A a_l u_\infty \tag{3.19a}$$

$$SMD_{SB} = 0.09 d_\mathrm{inj} \tag{3.19b}$$

$$u_{l,SB} = u_c + 0.37 (u_\infty - u_c) \tag{3.19c}$$

where l_col is the length of the liquid column, u_c is the streamwise velocity of liquid column at the location of surface breakup, and A and a_l are constants obtained from the fluid properties and operating conditions

(Ranger & Nicholls 1968). An example of the simulated lagrangian JICF obtained by Jaegle (2009) is shown in the top of Figure 3.11. This model presents the advantage that it is computationally cheap and, despite directly injecting a developed spray, it models the drag effects created by the liquid column and the shear stripping phenomenon through empirical laws. On the other hand, it is only applicable to the operating condition for which the experimental laws and the prescribed size distribution were obtained (high Reynolds numbers), and does not capture the complex liquid-gas interactions created by the liquid column.

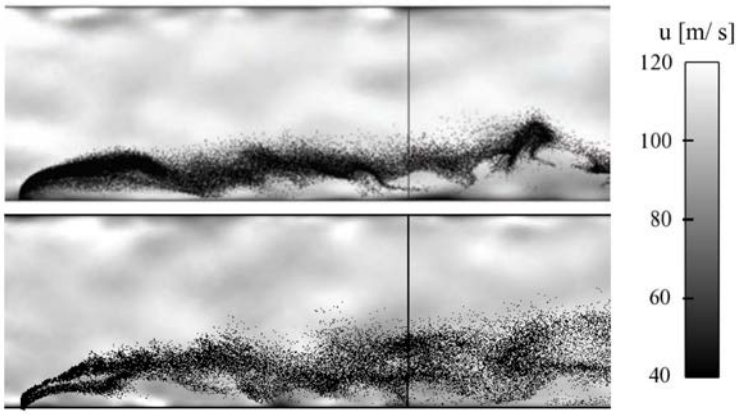

Figure 3.11: Instantaneous axial gaseous velocity field on the plane y = 0 mm together with the lagrangian droplets. q = 6. *Top*: numerical results by Jaegle (2009). *Bottom*: numerical results by Senoner (2010).

Combining shear breakup with blob method and secondary atomization (Senoner 2010)

A similar approach to the previous one has been explored by Senoner (2010). In the same way as Jaegle (2009) (and in the same experimental configuration), the breakup point is calculated from Eqs. (3.17). This location defines then the column region where the modified law of Eqs. (3.18) is applied. Regarding surface breakup, the same methodology employed by Jaegle (2009) (previous model discussed) is followed, where droplets are injected with the properties given in Eqs. (3.19).

The originality of the approach by Senoner (2010) lies on the size of particles at injection. While the previous model injects a developed spray, the current one introduces droplets with constant size through the liquid nozzle. The prescribed droplet's diameter is determined by the following expression:

$$d_{\text{drop}} = \sqrt[3]{\frac{3}{2} d_{\text{inj}} \lambda_s} \tag{3.20}$$

where $\lambda_s \approx 0.15 d_{\text{inj}}$ is the wavelength of the column surface instabilities (Sallam et al. 2004). These droplets will then break into smaller ones through a secondary atomization model (Apte et al. 2003). The present model can be illustrated as in Figure 3.10 right. A snapshot of the lagrangian jet obtained by this methodology is shown in Figure 3.11 bottom. This model has the same advantages as the one by Jaegle (2009) (i.e. computationally cheap, drag effects by dense core are modeled, shear stripping of droplets is considered), plus it accounts for secondary breakup and does not rely on experimental particles size distributions. On the other hand, it also needs empirical laws for modeling particles' drag at the dense core region and the shear stripping phenomenon (valid at high Reynolds number), and it does not capture the complex liquid-gas interactions created by the liquid column.

Semi-empirical model for shear breakup regime (Eckel et al. 2016)

Following the line of modeling shear breakup, Eckel et al. (2016) developed a semi-empirical model for this regime. The numerical strategy is depicted in Figure 3.12. This approach injects cylindrical parcels (a,b) mimicking the dense structures of the liquid column which are tracked with a lagrangian formalism and transported with a modified drag law (c). These cylinders have the same diameter as the injection orifice. As the parcels move, droplets modeling shear breakup are stripped-off the column (d) with properties (mass flow rate, sizes, velocities) given by experimental laws (e). The parcels will then lose mass until they reach a residence time corresponding to the breakup of the liquid column (f), when they are broken into smaller,

spherical droplets representing column breakup (g). This approach is continuously performed to model the jet behaviour (h). Dispersion models are used for enhancing the droplet transport (Gosman & Ioannides 1983). Models to account for secondary breakup are not needed, as the employed approach generates a developed spray. A snapshot of the resulting jet is shown in Figure 3.13, where the difference between the liquid column made of cylindrical parcels and the developed spray zone composed by spherical droplets is clearly visible. The advantages of this method are its low computational cost and its consideration of complex physical phenomena such as liquid column drag, shear stripping, primary and secondary atomization. On the other hand, this model is exclusively built on empirical laws which are valid for Weber numbers (We) corresponding to the shear breakup regime, making it unapplicable to higher We regimes (catastrophic breakup) or lower ones (bag breakup).

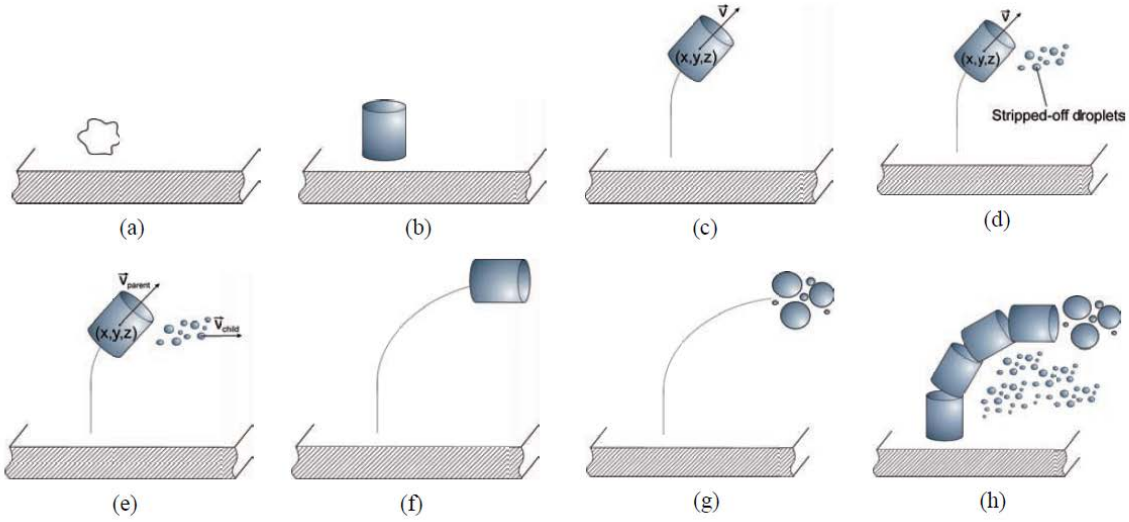

Figure 3.12: Jet in crossflow modeling strategy followed by Eckel et al. (2016).

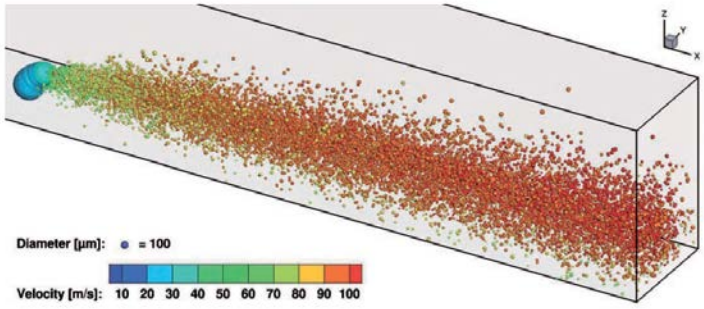

Figure 3.13: Simulation of jet in crossflow by Eckel et al. (2016).

Statistical method for injection of a fully developed spray (Fan et al. 2018)

All the methodologies previously discussed, except for Arienti et al. (2006), performed injection of droplets at the nozzle orifice center with the liquid injection velocity. Furthermore, large droplets of the order of the nozzle diameter were injected in all cases except in the model of Jaegle (2009), who introduced a developed spray. In this line, the work of Fan et al. (2018) explored an approach to inject a developed spray at the nozzle orifice following a statistical method. Each particle is injected with attributes chosen as follows:

- Diameter: sampled from a Probability Density Function (PDF) $f(D)$. Four PDFs for droplet sizes were studied: uniform, χ^2, Nukiyama-Tanasawa and Rosin-Rammler.

- Velocity: randomly chosen from a Gaussian distribution with standard deviation equal to the liquid injection velocity.
- Injection location: at a random point in a circular patch placed at the liquid nozzle exit.

Figure 3.14 shows a lateral view of the sprays and the penetration for four cases, each one injecting a different PDF for the droplet diameter. Each PDF gives a different range of droplet diameters and a different spray penetration, showing the importance of chosen accurately the initial boundary conditions for reproducing sprays with lagrangian formalism. This model presents the advantages of its simplicity (it defines the injection parameters according to mathematical expressions) and its low computational cost. On the other hand, the injection parameters have been calibrated with experimental results, hence this model cannot be applied without data for such calibration, and the liquid-gas interactions created by the liquid column are not modeled.

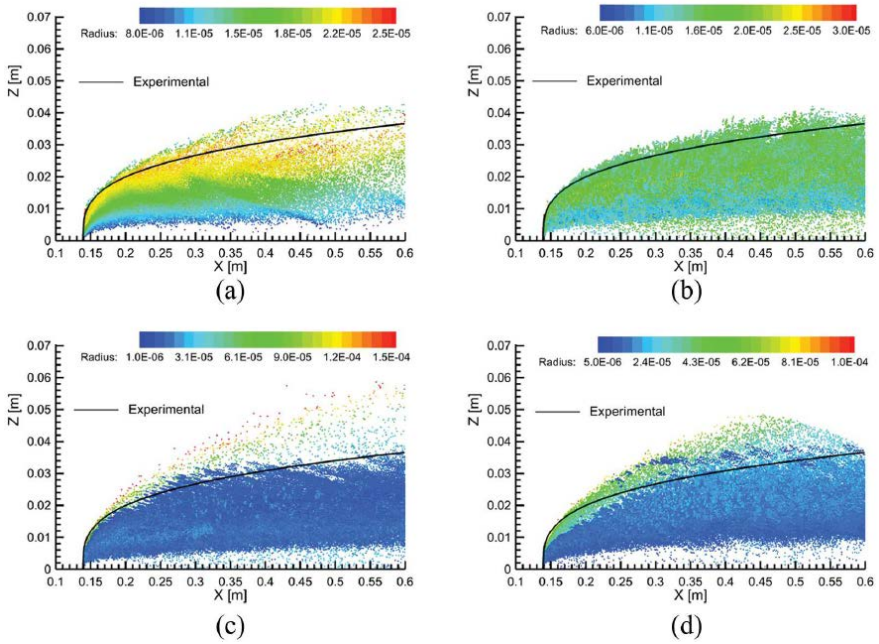

Figure 3.14: JICF sprays and penetrations obtained by Fan et al. (2018) with different injected PDFs for the droplets sizes. (a) Uniform distribution (b) χ^2 distribution (c) Nukiyama-Tanasawa distribution (d) Rosin-Rammler distribution.

Hybrid model for jet in crossflow injection (Fontes et al. 2019)

One of the most recent works (up to date) focused on JICF modeling has been performed by Fontes et al. (2019). As in the study by Arienti et al. (2006), this approach combines a direct resolution method (VOF) for solving the liquid column with an injection procedure for lagrangian droplets. Experimental correlations are used to obtain column breakup location. The liquid-gas interaction due to the dense core presence is therefore taken into account (Figure 3.15 left). Injection of lagrangian droplets is performed at the column breakup location (Figure 3.15 right): their velocity is equal to the liquid eulerian velocity at this point and their size is obtained from experimental correlations. Two operating points at low We were simulated with this methodology, surface breakup was not modeled since it was not present at these conditions. This model presents the main advantage that it accounts for complex physical phenomena: secondary atomization, coalescence and complex liquid-gas interaction. On the other hand, it relies on empirical correlations obtained at low Weber numbers for determining the breakup coordinates, and neglects the shear stripping; hence, it is not suitable for application at high Weber numbers.

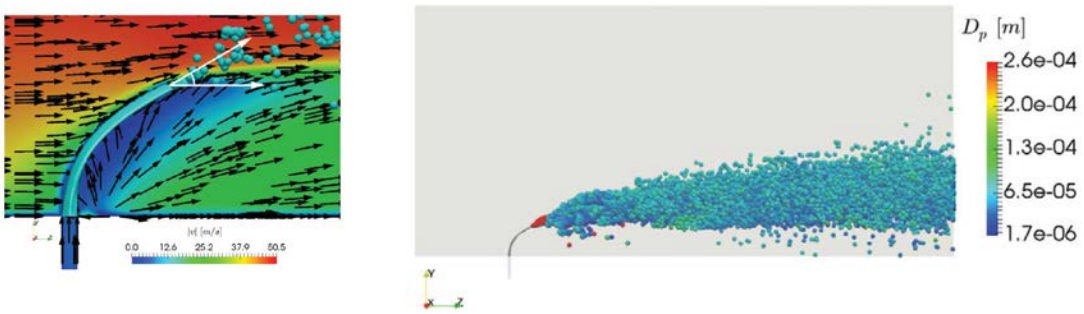

Figure 3.15: Simulated jet in crossflow by Fontes et al. (2019). *Left*: close view of the near-jet, showing the resolved dense core with VOF and the perturbation effect on the gaseous field. *Right*: Farfield view of the jet, showing injection point of lagrangian droplets. Droplets are colored by their diameter.

3.4 Conclusions

This chapter has presented a review on numerical methods for dispersed-phase systems. Several approaches to model dispersed sprays have been introduced, being the lagrangian point particle assumption the most widely used one. Then, the state of the art in modeling Multi-Staged Fuel Injection (MSFI) systems has been reviewed. The three atomization mechanisms present in MSFI have been reviewed, with special emphasis on liquid jet in crossflow (JICF) since they are the subject of this thesis.

Existing models for JICF are scarce, and most of them are built upon experimental correlations and applicable to a narrow range of operating conditions. A more generic modelling framework for JICF systems with a realistic prescription of the liquid phase is still needed. Therefore, the objective of this thesis is to propose a new lagrangian injection methodology for JICF systems which learns data from a reference spray and prescribes realistic liquid boundary conditions in dispersed-phase computations.

Part II

Building lagrangian injectors from resolved atomization simulations

Chapter 4
Models for lagrangian injection

4.1 Introduction

Chapter 3 introduced numerical formalisms to represent dispersed two-phase flows. Special emphasis was given to the lagrangian representation of the fluid phase, as it is widely employed approach in aerospace applications. The reasons are its low computational cost with respect to other formalisms and its ability to account for additional physics such as collisions, evaporation and combustion. The chapter culminated with the presentation of lagrangian methodologies to model fuel injection in Multi-Staged Fuel Injection (MSFI) systems, paying extra attention to the state of the art in methodologies for simulating Jets in Crossflow (JICF).

In this work, a novel numerical methodology to build numerical injectors for performing dispersed phase simulations in MSFI systems has been developed. The injectors built with this methodology have been named Smart Lagrangian Injectors (SLI). Figure 3.2 shows the location of the new method into the proposed classification of existing numerical models for lagrangian injection: SLI are built by learning a reference spray, which can be obtained either experimentally or numerically. In this thesis, the reference spray is obtained through resolved simulations of the atomization process. Computations performed with SLI will also account for the interaction of the dense liquid phase with the surrounding gas (blockage effect in liquid JICF) and secondary atomization models for further breakup of lagrangian particles.

This chapter details the underlying theory of SLI, showing all the key modeling ingredients. Section 4.2 introduces mathematical foundations representing the spray which are used by describing the models in Section 4.3. The learning methodology to build injectors from a reference spray is defined in Section 4.4. Finally, the theory of the models blocks accounting for the blockage effect and secondary atomization models are discussed respectively in Sections 4.5 and 4.6.

4.2 Mathematical description of sprays

In §3.2.1, dispersed sprays resulting from atomization were described by a function f which represented the number density function of droplets. Then, all spray characteristics can be obtained by a proper definition and integration of f. Several methods targeting the determination of f were discussed in Chapter 3, from statistical approaches to the Lagrangian Point-Particle (LPP) representation. Even if only statistical approaches make use of the William-Boltzmann equation to represent f, LPP can be considered as an approximation to this function by considering the point particle approximation. Consequently, since in this work dispersed phase flows use the LPP assumption, a mathematical representation of dispersed sprays based on the function f as given by Eq. (3.2) is used. This section intends to provide some theoretical foundations for the developed models from a generic, mathematical perspective. The rest of the chapter will be dedicated to explain how this formulation is applied in the current work.

4.2.1 General formulation

The spray produced by atomization can be described by a continuous function F:

$$F\left(t, \mathbf{x}, \mathbf{u}, D\right) \tag{4.1}$$

which is defined in the whole spatial domain $\Omega(\boldsymbol{x})$, $\forall \boldsymbol{x} = \{x, y, z\}^T \in R^3$. In SLI, the spray will be characterized in plane surfaces. Therefore, it is of interest to sample the spray crossing a surface $\mathcal{S}$ belonging to the whole spatial domain: $\mathcal{S} \subset \Omega$. The spray sampled in this surface is described by a continuous function f:

$$f\left(t, \mathbf{x}, \mathbf{u}, D\right) = F\left(t, \mathbf{x}, \mathbf{u}, D\right) \ \forall \ \mathbf{x} \in \mathcal{S} \tag{4.2}$$

As f is defined in a surface, it can be spatially represented by only two coordinates. These surface coordinates can be expressed as a vector $\boldsymbol{s} = \{\xi, \eta\}$. They can represent any type of surface, from cartesian to curvilinear. Therefore, the function f can be expressed in terms of $\boldsymbol{s}$ as:

$$f\left(t, \boldsymbol{s}, \mathbf{u}, D\right) \tag{4.3}$$

Since both Eqs. (4.2) and (4.3) are identical, there is an equivalence between $\boldsymbol{x} = \{x, y, z\}$ and $\boldsymbol{s} = \{\xi, \eta\}$. This relation can be expressed mathematically as:

$$h : \boldsymbol{x} \rightarrow \boldsymbol{s} \tag{4.4}$$

where h is a mapping function, or morphism, that will transform from cartesian coordinates $\boldsymbol{x}$ to surface coordinates $\boldsymbol{s}$.

In this work, the variation of the spray characteristics with time will not be considered. Instead, the obtention and study of a stationary, mean spray will be the main objective of SLI. For such purpose, the spray will be sampled in time for a period T which should be large enough in order to obtain a converged spray (see §4.4.2), hence eliminating the dependence with time. Mathematically speaking, this can be represented through integration:

$$f\left(\boldsymbol{s}, \boldsymbol{u}, D\right) = \frac{1}{T} \int_0^T f\left(t, \boldsymbol{s}, \boldsymbol{u}, \right) dt \tag{4.5}$$

Eventually, for a better characterization of the spray, the sampling surface $\mathcal{S}$ will be spatially discretized into several elements, or probes, of size ΔS. In this way, the spray within each probe can be independently study to provide **spatially refined statistics**. The representation of spatially refined statistics can be obtained from f by integrating spatially this function within each probe centered around $(\xi_\mathrm{j}, \eta_\mathrm{k})$:

$$f_{\mathrm{j,k}}\left(\boldsymbol{s}_{\mathrm{j,k}}, \boldsymbol{u}, D\right) = \frac{1}{\Delta\xi\Delta\eta} \int_{\xi_{\mathrm{j}-1/2}}^{\xi_{\mathrm{j}+1/2}} \int_{\eta_{\mathrm{k}-1/2}}^{\eta_{\mathrm{k}+1/2}} f\left(\boldsymbol{s}, D\right) d\xi d\eta \tag{4.6}$$

4.2.2 Spray formulation in jet in crossflow

A more precise, less abstract interpretation for the SLI spray formulation can be obtained by applying the general formulation to a liquid JICF problem, atomization case introduced in §1.3. Figure 4.1 shows a liquid JICF from a resolved atomization simulation. As observed, the liquid leaves the injection nozzle as a coherent jet moving along the z direction and then starts bending towards the x direction. Atomization starts taking place and breaks the jet into firstly ligaments and, subsequently, droplets. The resulting droplets from the atomization process conform a spray that can be analyzed by the SLI strategy. Therefore, to study this spray, first droplets need to be gathered in sampling surfaces. In a geometrically simple JICF problem as the one from Figure 4.1, the sampling surfaces are planes perpendicular to the crossflow direction x denoted in the figure by S. The surface coordinates $\boldsymbol{s}$ aforementioned correspond therefore to the in-plane coordinates in the sampling surface, which in the system of reference depicted in Figure 4.1 yield $\boldsymbol{s} = \{y, z\}$. Therefore the discrete, spatially refined statistics are obtained in probes centered at $(y_\mathrm{j}, z_\mathrm{k})$, and the function $f_{\mathrm{j,k}}$ given generally by Eq. (4.6) can be applied to the proposed JICF formulation as:

$$f_{\mathrm{j,k}}\left(\boldsymbol{s}_{\mathrm{j,k}}, \boldsymbol{u}, D\right) = \frac{1}{\Delta y \Delta z} \int_{y_{\mathrm{j}-1/2}}^{y_{\mathrm{j}+1/2}} \int_{z_{\mathrm{k}-1/2}}^{z_{\mathrm{k}+1/2}} f\left(\boldsymbol{s}, \boldsymbol{u}, D\right) dydz \tag{4.7}$$

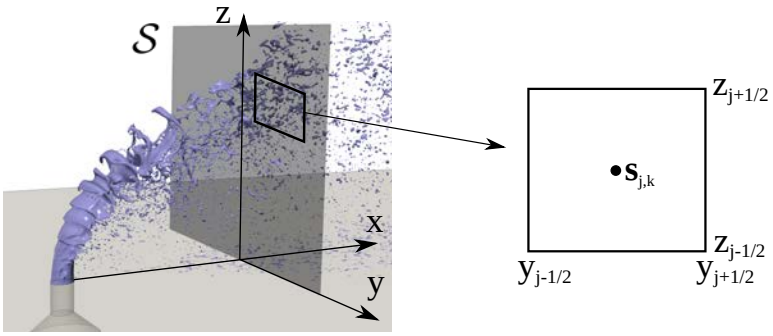

Figure 4.1: Illustration of SLI spray formulation in a liquid JICF.

4.3 Models for lagrangian injection

The objective of the lagrangian injection models is to provide input parameters for prescribing liquid boundary conditions in dispersed phase simulations. These input parameters are intended to represent a realistic spray resulting from primary atomization. Most existing models perform lagrangian injection by neglecting the atomization process due to its complexity, while other rely on experimental data or correlations which are valid for a limiting range of operating conditions (see §3.3 for a discussion on the state of the art in dispersed-phase simulations of MSFI systems).

With this objective in mind and knowing the limitations of the existing approaches, the intention of this work is to develop models that can be fed from primary atomization data to: 1) inject a proper dispersed-phase and 2) model as accurately as possible the momentum exchange due to the liquid-gas interaction in the primary atomization region. The latter has often been neglected in many dispersed phase simulations. To address both points, this thesis relies firstly on **numerical simulations of the resolved atomization process** using an Accurate Conservative Level Set method (details on this methodology given in §2.3.4). These simulations are used to construct a spray database by sampling the droplets passing through planes perpendicular to the crossflow direction and then applying the spray formulation previously presented. The functions $f\left(\boldsymbol{s}, \boldsymbol{u}, D\right)$ of the spray formulation represent therefore the statistical distributions of the spray's size, velocity and fluxes. These distributions are processed in a **lagrangian injectors learning process** to eventually yield the discretized spray $f_{\mathrm{j,k}}\left(\boldsymbol{s}_{\mathrm{j,k}}, \boldsymbol{u}, D\right)$ that is used as lagrangian injector to perform **dispersed-phase simulations**. At the same time, the liquid-gas interaction between the jet dense core and the crossflow is also analyzed and learnt to provide a model that contributes to the liquid-gas **momentum exchange** in the disperse-phase simulations, which a priori is neglected (and which many models do not take into account or circumvent by introducing experimental correlations). In this way, the full methodology only needs data from the resolved atomization simulations for learning injectors and running dispersed-phase computations. Additionally, the learning process could also account for information from external databases for building the injectors, such as experimental data in case these were available. In this thesis, only data from resolved atomization simulations is used, and the consideration of other databases is left for future work. The proposed approach will be called hereafter as Smart Lagrangian Injectors (SLI).

The full approach of SLI is detailed schematically in the flowchart of Figure 4.2. The process is summarized in the following lines:

1. **Resolved atomization simulations** are performed to build a spray (statistical spray distributions) and liquid-gas interaction (momentum exchange) database (Chapter 5).

2. This database is used and processed by the models to **learn the spray state** and build lagrangian injectors (Chapter 4). The learning part consists of the following parts: **spray sampling** (§4.4.1), **spatial discretization** (§4.4.3) and **spray convergence** (§4.4.2) of the injectors. The convergence can be checked either globally in the sampling plane, or locally by dealing with the sprays contained in each discrete, individual probe in order to perform a **converge-driven classification** (§4.4.4).

3. **Dispersed-phase simulations** are run where the liquid phase is prescribed with the injectors developed with this methodology (Chapter 6). Apart from the lagrangian injectors that inject the liquid phase, the two following submodels are also contained in these simulations:

   - **Dense core learning** with the **actuator line model** in order to take into account the perturbation effect of the liquid dense structures (i.e. the liquid dense core in the JICF) in the gaseous phase during lagrangian simulations (§4.5). The information to characterize the dense core is taken from the resolved simulations and later imposed into the lagrangian ones.
   - **Secondary atomization models** to consider further possible breakup of spherical droplets during lagrangian simulations (§4.4.3).

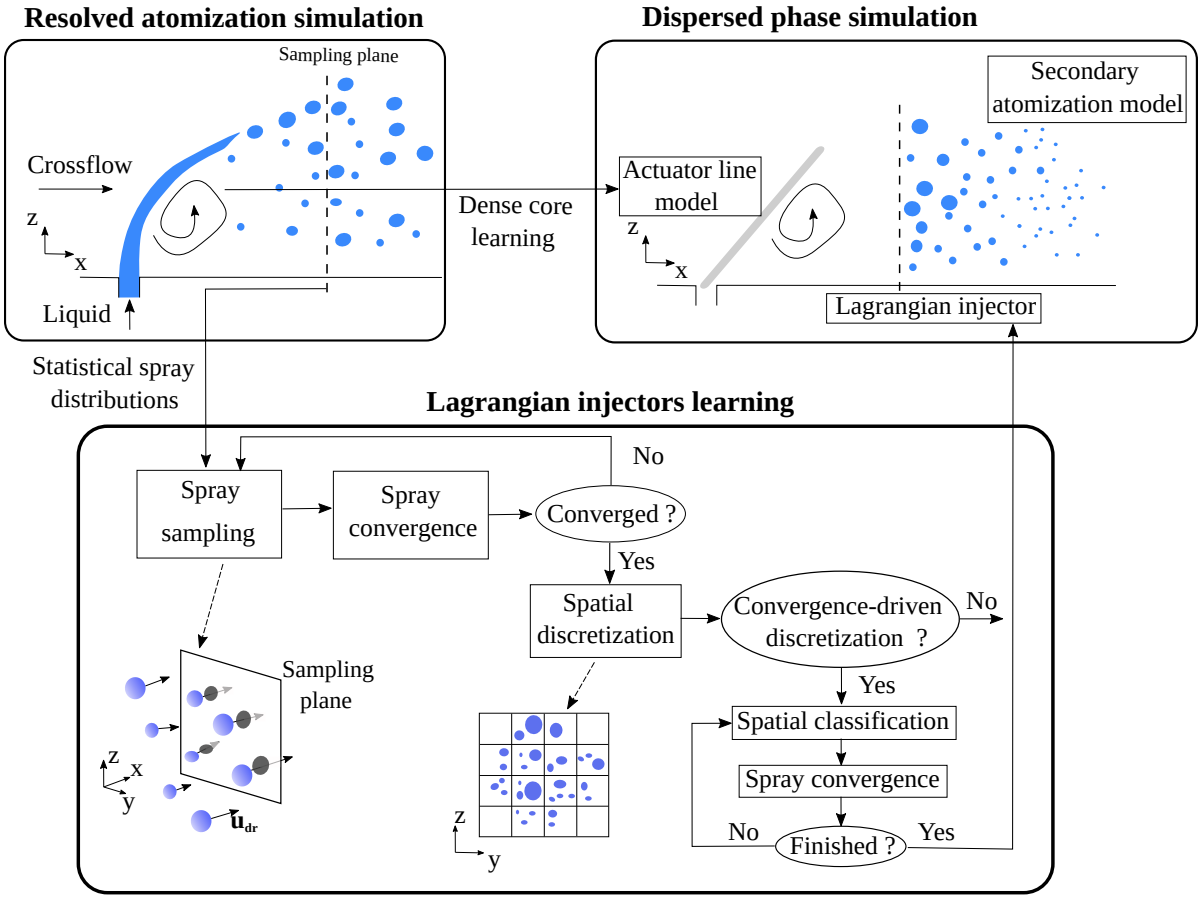

Figure 4.2: Flowchart of the SLI formulation applied to liquid JICF.

4.4 Lagrangian injectors learning

4.4.1 Spray sampling

Identification of liquid structures in resolved simulations

The first step in the learning process is to obtain the spray from resolved atomization simulations. For this purpose, droplets must be identified in space. According to the Accurate Conservative Level Set method (ACLS, §2.3.4), liquid regions are identified by level set values $\psi > 0.5$, and the interface Γ is located at $\psi = 0.5$. It is possible then to identify and tag individual liquid structures as independent closed regions of Γ, whose domain is denoted as Ω_l. Each structure can then be characterized by its volume V_{dr}, its center of mass location $\mathbf{x}_{\mathrm{dr}}$ and velocity $\mathbf{u}_{\mathrm{dr}}$, and maximum and minimum distances from the interface to the center

Table 4.1: Parameters sampled from resolved atomization simulation

Parameter	Definition	Description
V_{dr}	$\int_{\Omega_l} dV$	Volume enclosed by interface
$\mathbf{x}_{\mathrm{dr}}$	$\frac{1}{V}\int_{\Omega_l} \boldsymbol{x} dV$	Location of center of mass
$\mathbf{u}_{\mathrm{dr}}$	$\frac{1}{V}\int_{\Omega_l} \mathbf{u}(\boldsymbol{x})\, dV$	Velocity of center of mass
$r_{\max}$	$\max(\lvert\mathbf{x}-\mathbf{x}_{\mathrm{dr}}\rvert)\, \forall \mathbf{x} \in \Omega_l$	Maximum distance to center of mass
$r_{\min}$	$\min(\lvert\mathbf{x}-\mathbf{x}_{\mathrm{dr}}\rvert)\, \forall \mathbf{x} \in \Omega_l$	Minimum distance to center of mass

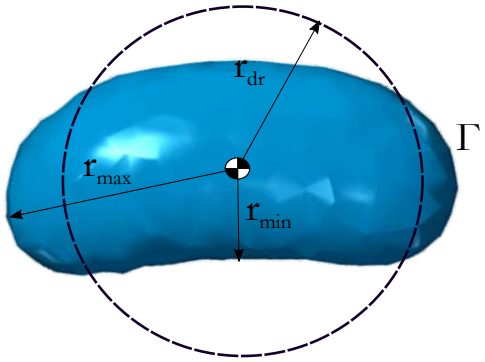

Figure 4.3: Parameters characterizing liquid structures sampled in resolved atomization simulations.

of mass $R_{\max}$ and $R_{\min}$, as depicted in Figure 4.3. The formulas used for calculating these parameters are shown in Table 4.1.

In order to get statistics for spray characterization, it is useful to define a characteristic size of each liquid structure. For this purpose, an equivalent radius r_{dr} is calculated from the liquid volume V_{dr}:

$$r_{\mathrm{dr}} = \sqrt[3]{\frac{3V_{\mathrm{dr}}}{4\pi}} \tag{4.8}$$

which is the radius of a sphere containing the same volume as the liquid structure. The equivalent diameter is then $d_{\mathrm{dr}} = 2r_{\mathrm{dr}}$. In cases where sampled structures are spherical droplets, R_{dr} is the true radius and, therefore, a representative measure of the droplets' size. On the other hand, if liquid structures are not fully spherical (which is often the case after primary atomization), the equivalent radius does not provide full information on their topology. To determine the deviation of the identified liquid structure from a sphere, the radii $r_{\max}$ and $r_{\min}$ can be used to calculate the deformation parameters α and β (Zuzio et al. 2018):

$$\alpha = \frac{r_{\max}}{r_{\mathrm{dr}}} \quad ; \quad \beta = \frac{r_{\min}}{r_{\mathrm{dr}}} \tag{4.9}$$

By definition, $\alpha \geq 1$ and $\beta \leq 1$. A perfect sphere would present $\alpha = \beta = 1$. In this thesis, no distinction between droplets and ligaments has been done to construct the injectors after the learning procedure. The reason was that resolved atomization simulations of JICF could not reach a spatial location where only spherical droplets were present (full atomised spray), due to their high computational costs. Hence, hereafter all liquid structures will be referred as droplets, and the term droplet sampling will be used. Inclusion of distinction between ligaments and droplets (i.e. between non-spherical and spherical structures) could be further taken into account with parameters α and β to, for example, modify drag coefficients in lagrangian simulations at the first steps after injection (Bagheri & Bonnadonna 2016).

Sampling procedure

Droplets are sampled according to their center of mass location. Note that, despite the ACLS methodology being eulerian, liquid structures produced by resolved simulations are being tracked as lagrangian particles

(lagrangian tracking). Two sampling methods based on experimental techniques can be used (Tropea 2011), their main difference being the topology of the sampling regions (see Figure 4.4):

- A control volume (unit volume in Figure 4.4) is defined as the sampling probe. Particles within the control volume are sampled at a particular time instant, producing a **volume distribution**.
- A surface area (unit area in Figure 4.4) or plane is defined as the sampling probe. Droplets crossing this area per unit time are sampled, producing a **flux density distribution**.

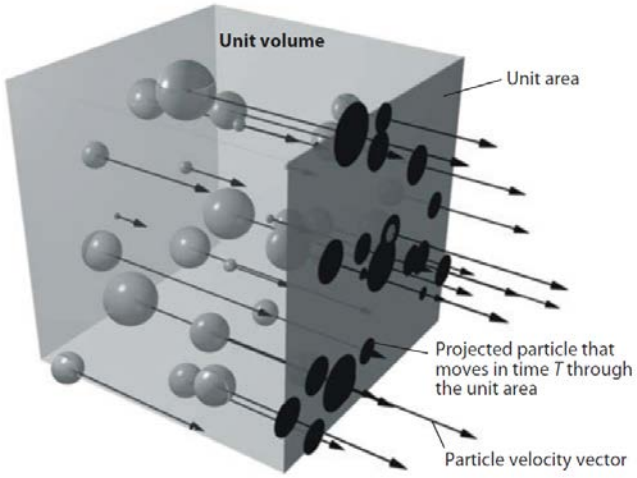

Figure 4.4: Droplet sampling prodecure. Source: Tropea (2011)

In this work, droplets crossing surface areas are sampled, hence obtaining flux density distributions. This method is chosen to be closer to experimental measurements performed in jet in crossflow configurations (Wu et al. 1998, Becker & Hassa 2002). The defined surface areas employed will be hereafter referred as **sampling planes**. To determine when a droplet is sampled, a sampling rate T_{sample} is specified so that the current location and velocities of droplets' center of mass at time t is checked. Then, the location of each droplet at time $t + T_{\text{sample}}$ is estimated by projecting the position of the center of mass with the current velocities. Droplets whose current location at t and projected location at $t + T_{\text{sample}}$ is at different sides of a sampling plane are sampled. This procedure is referred as **lagrangian projection** of droplets. It is computationally cheap, so it can be performed in the resolved and dispersed phase computations without highly increasing their cost. On the other hand, it presents two main disadvantages: some actual crossing droplets might not be sampled, and contrarily, some droplets might be sampled twice. These downcomes of the methodology could be circumvented by including a tag field in the resolved simulations where droplets are assigned an ID number that does not change with time. However, this is not available yet and is difficult to implement, since the atomization process hinders droplet tagging as liquid structures change constantly during primary and secondary breakup.

The sampling rate is chosen so that that all droplets crossing the plane are collected. Droplets are accumulated with time, and then statistics are calculated. Choosing a right sampling rate ensures that at the end of the accumulation process, the mass flow rate in average is the actual rate passing through the sampling plane in the resolved simulations. If the sampling rate is too low, some droplets might be missed and the flow rate captured will not be the right one (aliasing phenomenon on the spray sampling procedure). Another technique to measure flow rates directly in resolved atomization simulations, called interior boundaries, has been applied in this work. This one, detailed in Annex C.2, is later applied in §5.6.5 and compared to the rates obtained from the lagrangian tracking procedure.

Defining statistics for sprays

The resulting accumulated spray is composed of a polydisperse ensemble of droplets, each droplet characterized by parameters from Table 4.1. In order to characterize the spray, it is useful to define averaged

and Root-Mean Squared (RMS) values for the whole spray from the individual droplets parameters. For an arbitraty magnitude f, the arithmetic mean and RMS values would be defined as follows:

$$\overline{f} = \frac{1}{N_{\mathrm{dr}}} \sum_{i=1}^{N_{\mathrm{dr}}} f_i \qquad ; \qquad f_{\mathrm{RMS}} = \sqrt{\overline{f^2} - \overline{f}^2} \tag{4.10}$$

where N_{dr} is the number of accumulated droplets. In the case of polydisperse sprays, where there are several liquid structures with different volumes, it is also useful to define volume-weighted averages in order to give more relevance to the properties of larger droplets. For an arbitrary magnitude f, the volume-weighted mean and RMS can be defined as:

$$\overline{f}_{\mathrm{VW}} = \frac{1}{\sum_{i=1}^{N_{\mathrm{dr}}} V_i} \sum_{i=1}^{N_{\mathrm{dr}}} f_i V_i \quad ; \quad f_{\mathrm{RMS,VW}} = \sqrt{\overline{f^2}_{\mathrm{VW}} - \overline{f}^2_{\mathrm{VW}}} \tag{4.11}$$

where V_i is the volume of each liquid structure. Related to the injectors the definition of mean and RMS values, either arithmetic or weighted-averaged, will be applied to the velocities in the three directions, α and β.

In two-phase flow problems involving disperse-phase sprays, it is useful to define average diameters of droplets with definitions different than the one given by applying Eq. (4.10). since they are better representative of the physical problems involving mass or heat transfer (Lefebvre & McDonell 2017). For combustion applications, the most used averaged diameter is the Sauter Mean Diameter (SMD):

$$\mathrm{SMD} = \frac{\sum_{i=1}^{N_{\mathrm{dr}}} d_i^3}{\sum_{i=1}^{N_{\mathrm{dr}}} d_i^2} \tag{4.12}$$

where d_i is the individual diameter of each droplet. The numerator of this expression is proportional to the cube of the diameter, which is equivalent to the droplet volume. The denominator is dependent to its square, which is related to the droplet liquid surface. Therefore, the SMD represents the relation between the liquid volume and surface in a spray. This is specially useful when evaporation is present (i.e. prior to combustion), since evaporation occurs when the specific liquid surface (the surface of liquid in contact with air) is large: that is, when the SMD is small.

Finally, a last useful magnitude that can be defined for a convecting spray is the liquid flow rate, which is a mean quantity by definition. Considering a sampling surface as in Figure 4.4, the mean liquid flow rate passing through it can be obtained as:

$$Q_l = \frac{dV_l}{dt} \approx \frac{\Delta V_l}{\Delta t} = \frac{\sum_{i=1}^{N_{\mathrm{dr}}} V_i}{t_{\mathrm{acc}}} \tag{4.13}$$

where t_{acc} is the total accumulation time. Q_l is the nominal flux representing the liquid mass per timestep passing through each sampling plane considered. If the sampling plane is discretized in several probes (see §4.4.3) and the fluxes are determined within them, the addition of all probes' fluxes will yield the nominal flux through the whole sampling plane. In these cases, the fluxes from each probe will depend on the probes surface S_{probe}: the smaller S_{probe}, the smaller the nominal flux. Therefore, when dealing with spatially discretized sprays it is useful to express the flux in relation to the probe surface S_{probe}. This yields a surface-weighted flux q_l, commonly named volume flux:

$$q_l = \frac{Q_{l,\mathrm{probe}}}{S_{\mathrm{probe}}} \tag{4.14}$$

The value of q_l converges with the probe size, as opposed to Q_l. Effectively, if the size of the probe $\Delta y \times \Delta z$ is reduced, the liquid flux as defined by Eq. (4.13) will also decrease since less droplets might be sampled in a smaller surface. Nevertheless, the volume flux q_l defined by Eq. (4.14) will we maintaned because, despite the reduction in Q_l, the probe surface is also smaller.

4.4.2 Spray convergence

Simulations using the ACLS/AMR methodology resolve atomization and provide deep insight on the driving physical phenomena. Nevertheless, their main limitation is their cost (see §5.6.6), which increases when more liquid is present in the domain. Consequently, the accumulation time of droplets will be finite and, logically, restricted to the physical time simulated. This can pose a problem for spray characterization, since statistics might not be converged if the number of sampled droplets is not sufficient.

Here, a methodology to evaluate spray convergence is proposed. The objective is to provide a quantitative measure to assess whether enough droplets have been sampled to obtain reliable statistics (Vié et al. 2016). If the spray is converged, then it can be spatially discretized to get local statistics that will conform the injectors (§4.4.3). This convergence criterion is also used to propose another discretization strategy in which refinement is performed following a quadtrees structure (convergence-driven discretization, see §4.4.4).

At each time step t_i of the accumulation process, the spray will be formed by a number of droplets $N_{\mathrm{dr},i}$. This number will increase as more particles are accumulated with time, since all droplets sampled previously are also accounted for (hence the name accumulation). One can see this methodology as obtaining a **time-averaged spray**, since dependence with time is neglected. Statistics representing the spray, such as droplet size histograms, can be calculated on the accumulated spray at each time t_i. Figure 4.5 left shows an illustrated view of the size histogram evolution at several accumulation instants. The histogram indicates the probability $f\left(d_{\mathrm{dr}}\right)$ of finding a droplet of size d_{dr} within a class n: $d_{\mathrm{dr}} \in [d_{\mathrm{dr},n} - \Delta d_{\mathrm{dr}}/2, d_{\mathrm{dr},n} + \Delta d_{\mathrm{dr}}/2]$. Its shape will change with accumulation time until an instant from which it will stay constant if more droplets are sampled. At this point, the spray will be considered to be converged.

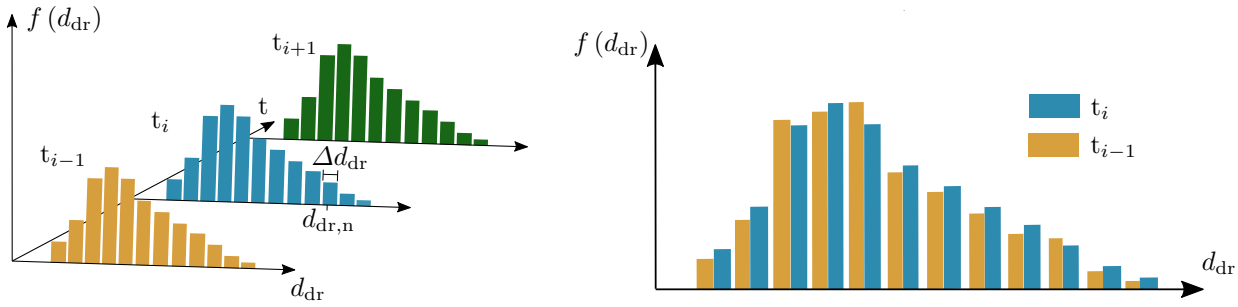

Figure 4.5: *Left*: Size histogram evolution with accumulation time of droplets. *Right*: comparison of two droplet size histograms from two consecutive time instants.

The main issue now is to determine quantitatively when the spray is converged. For this purpose, the histograms are compared in pairs at subsequent time instants, t_i and t_{i-1}, as shown in Figure 4.5 right. The same number and width of droplets classes are used in both histograms. The difference between both histograms is then measured by means of a Mean Squared Error (MSE) function defined as:

$$MSE^{t_i} = \frac{1}{N}\sum_{n=1}^{N}\left(f_n^{t_{i-1}} - f_n^{t_i}\right)^2 \tag{4.15}$$

where N is the total number of classes in the histogram. This criterion is similar to the Cramer-von Mises measure to compare two statistical distributions (Anderson 1962). The MSE can then be calculated at each accumulation time instant and then be normalized by the maximum value obtained, yielding a Normalized Mean Squared Error (NMSE) (Hanna et al. 2004):

$$NMSE^{t_i} = \frac{MSE^{t_i}}{\max_{t_i}\left(MSE\right)} \tag{4.16}$$

The evolution of NMSE can be displayed with time as shown in Figure 4.6. The NMSE decreases with accumulation time until reaching a plateau, where the NMSE does not move significantly. Convergence is achieved at the beginning of this plateau, which is defined for values of the NMSE below a threshold $\varepsilon_{\mathrm{th}}$.

$$NMSE < \varepsilon_{\mathrm{th}} \tag{4.17}$$

where $\varepsilon_{\mathrm{th}}$ is set to 0.03 (i.e. 3%).

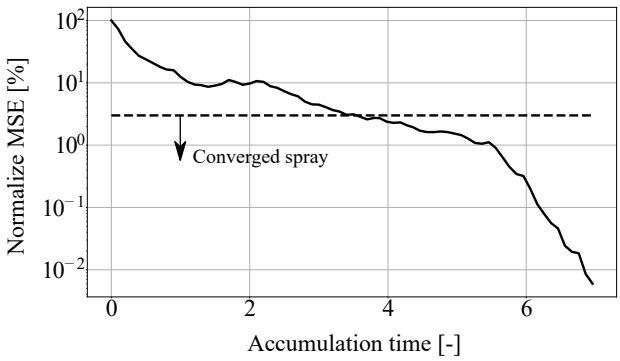

Figure 4.6: Evolution of Normalized Mean Squared Error (NMSE) with respect to spray accumulation time (solid line). The dashed line indicates the chosen threshold of $\varepsilon_{\text{th}} = 3\%$.

It is worth noting that the convergence criterion based on NMSE introduced in this section depends solely on the equivalent droplets size d_{dr}. Future work would include to extend this criterion to other magnitudes fundamental for a proper spray representation, such as velocities and flow rates. Furthermore, a time-independent spray has been considered in all the previous process by accumulating droplets and calculating statistics which do not depend on the time when they were sampled. A perspective in this respect would be to obtain a transient spray in order to create unsteady numerical injectors. This could be useful in systems where thermoacoustic instabilities appear and there are fluctuations in the injected flow rates, such as aeronautical gas turbines (Lieuwen 2012). Further possible improvements could also include the use of information theory techniques for characterizing the convergence state, which have recently been applied and evaluated in sprays (Panao 2012, Panao et al. 2020).

4.4.3 Spatial discretization of sprays

Once the global accumulated spray at the sampling plane is converged according to the NMSE criterion, enough droplets have been sampled to perform a spatial discretization of the spray. The objective is to classify spatially the in-plane accumulated droplets into a grid composed of several rectangular probes so that spray statistics can be calculated within each probe individually. Later on each probe will conform an injector for the dispersed-phase simulations: the SLI is therefore the whole grid composed of all the discrete injectors.

Figure 4.7 shows an example of a discrete spray grid resulting from the spatial discretization process. The grid has dimensions (w_{spray}, h_{spray}), which correspond to its width and height given in the y and z directions respectively. Grid's dimensions can be calculated in three ways: 1) they can be chosen ad-hoc by the user (as long as they englobe the full spray in order not to miss sampled mass); 2) they are calculated automatically as given by the furthest droplets in the y, z directions; 3) they are calculated automatically if the individual probe dimensions (w_{inj}, h_{inj}) are given by the user, in which case the grid size will be calculated accordingly in order to englobe the whole in-plane spray. The sketch at the right in Figure 4.7 shows a magnified view of a single probe of the grid, which composes an individual injector. The probe consists of dimensions (w_{inj}, h_{inj}) and center x_{inj}. Each droplet in the probe is characterized by the parameters from Table 4.1, from which the equivalent droplet diameter d_{dr} is calculated with Eq. (4.8) and the deformation parameters α and β with Eq. (4.9). These parameters are then used to calculate statistics on each probe's spray, which are later used to perform injection. The parameters conforming each injector are later introduced in §4.4.5. The spatially distributed statistics in the sampling grid can be represented in maps of mean and RMS values, which give an idea of the spray shape in terms of diameters, fluxes and velocity distributions.

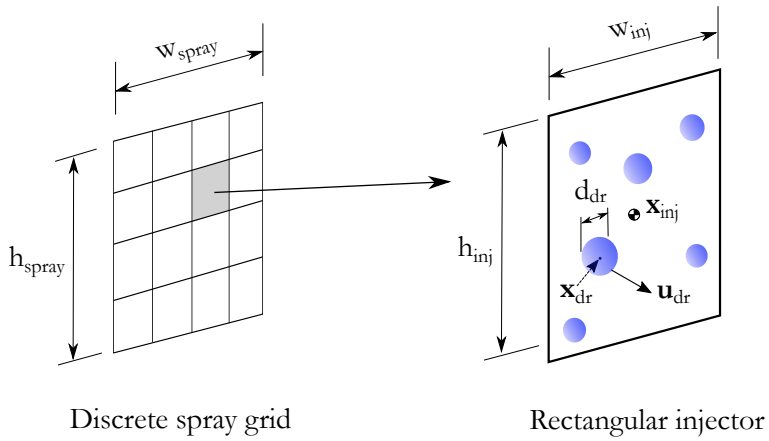

Figure 4.7: Schematic of a discrete grid composed of individual spray probes. The zoomed-in probes shows an example of droplets and parameters characterizing the probe and the spray within it that served as injectors.

4.4.4 Convergence-driven discretization

Among all parameters being calculated in each individual probe, the NMSE is also calculated in the same way as explained in §4.4.2. Then, the local convergence level of each probe's spray is estimated, which gives an idea of the spatial convergence distribution in the SLI. This local convergence can be used to further refine the grid in those probes which present a converged spray, as shown in the flowchart of Figure 4.2. Hereafter, the full spray will be referred as **global spray** and the discretized spray will be named **local spray**.

If convergence-driven discretization is performed, those probes presenting convergence will be further refined by a factor $\times 2$: i.e. the probe will be split into 4 probes of size ($w_{\text{inj}}/2$, $h_{\text{inj}}/2$). This will conform a refined grid with the same global dimensions (w_{spray}, h_{spray}) but containing more elements, and spray statistics will be calculated into each new probe for the spray contained within it. If the refined elements are again converged according to the NMSE criterion and further refinement is wished to be done, the process can be repeated again and as many times as desired. This discretization process, known as **quadtrees**, is therefore base in a tree structure with several levels of refinement, and has been widely used for performing Adaptive Mesh Refinement (AMR) in grids for solving two-phase resolved atomization problems (Popinet 2003, Fuster et al. 2009, Zuzio 2010). Figure 4.8 shows an example of quadtrees refinement in a 2x2 SLI with two refinement levels (left) and the resulting SLI (right).

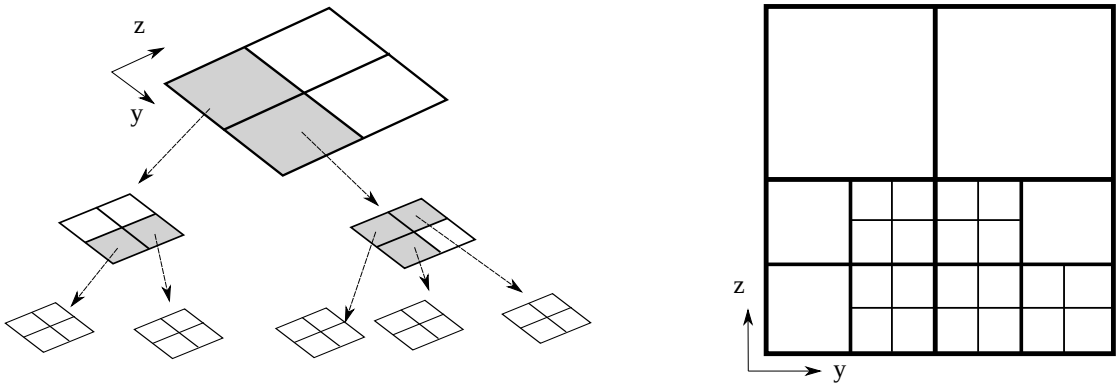

Figure 4.8: Convergence-driven discretization of SLI according to a quadtrees structure. *Left*: quadtree structure with two tree levels, where the converged elements refined are shadowed. *Right*: resulting discretized injector.

4.4.5 Injectors definition

Once a spatially-discretized injector is obtained (either if convergence-driven discretization has been applied or not), an SLI is built. An example of an injectors and the accumulated droplets within it was shown in Figure 4.7. Each injector has then the following characteristics in terms of topology and spray characteristics calculated:

- **Injector topology** defined by its width w_{inj}, height h_{inj} and center $\mathbf{x}_{\text{inj}}$. From the injector dimensions, its injection surface (called probe surface) is calculated as $S_{\text{probe}} = w_{\text{inj}} \times h_{\text{inj}}$. All these parameters are calculated after the spatial discretization process. A lagrangian particle will be injected at a point x_i randomly located within the injection surface: the number of injection points N_{pts} in each probe needs to be specified by the user. Results from dispersed phase simulations have shown not to be sensitive to this value, so if not specified it is set by default to 5.

- **Flow rate** Q_l to be delivered through the injector. This value is calculated with applying Eq. (4.13) to each individual probe. Q_l determines the number of droplets to be injected at each time step. If divided by the probe surface S_{probe}, the volume flux q_l is obtained as given by Eq. (4.13). Nevertheless, this quantity is useful for graphical visualization of the spray with volume flux maps but cannot be specified to perform injection: the nominal flux Q_l needs to be supplied instead.

- **Droplets diameters distribution** $f_0\,(d)$. Since all the information on (equivalent) droplets size sampled and accumulated from resolved atomization simulations are available, the diameter of the injected droplets can be specified to the injector. Three options are possible for the distribution f_0: 1) to provide directly the sampled size histogram from the resolved simulations; 2) provide a size PDF that fits the histogram, such as a lognormal distribution (Lefebvre & McDonell 2017); 3) provide a constant diameter to all the droplets. Each lagrangian droplet injected d_i is therefore either sampled from f_0 when the desired injection size is done according to a histogram of PDF, or constantly set as $d_i = \text{SMD}$ where SMD is calculated with Eq. (4.12).

- **Spray velocities**. As with particle diameters, the velocity components of each sampled and accumulated droplet from resolved atomization simulations is available. These velocities can be treated statistically in order to obtain reliable velocity injection values for the dispersed-phase simulations. However, on the contrary to the injectors, here no velocity distributions are used but instead the mean and RMS velocities are calculated by plugging $f = u$ into Eqs. (4.10) and (4.11) to yield arithmetic and volume-weighted mean and RMS velocities, respectively. Then, injection of a lagrangian particle i is performed according to the following law:

$$\boldsymbol{u}_{\text{i}} = \overline{\boldsymbol{u}} + r\boldsymbol{u}_{\text{RMS}} \tag{4.18}$$

  where $\overline{\boldsymbol{u}}$ is the mean velocity and $\boldsymbol{u}_{\text{RMS}}$ is the RMS one. If volume-weighted velocities are injected, the calculated parameters $\overline{\boldsymbol{u}}_{\text{VW}}$ and $\boldsymbol{u}_{\text{RMS,VW}}$ are used instead. The parameter r is a random number that multiplies the RMS to provide a varying velocity through all the injection process. Three different laws are available to sample random numbers for r, being these ones:

  - **Uniform law**. r follows a uniform distribution: $r \sim \mathcal{U}\left(-\sqrt{3}, \sqrt{3}\right)$, where $-\sqrt{3}$ and $\sqrt{3}$ are the limits of the distribution. Such values are set so that the RMS of the signal from Eq. (4.18) maintains its RMS provided values.
  - **Gaussian law**. r follows a normal distribution $r \sim \mathcal{N}\left(\mu = 0, \sigma^2 = 1\right)$, where μ is the mean and σ^2 the variance. Such values are set so that the RMS of the signal from Eq. (4.18) maintains its RMS provided values.
  - **Zero law**. In this case the RMS are not considered for injection and only constant velocities equal to mean resolved velocities are injected, therefore $r = \mathbf{0}$.

Apart from the spray parameters to perform injection, the following liquid physical properties also need to be specified: density ρ_l, viscosity μ_l and surface tension σ. The density is needed in the dispersed-phase simulations to calculate the dynamics of the droplets according to Eqs. (3.5), while the viscosity and surface tension are used by the secondary atomization models to estimate the breakup time and children radii of lagrangian droplets (§4.6). A summary of all the parameters involved in SLI and the way in which they are calculated is provided in Table 4.2.

Table 4.2: Summary of SLI injection parameters

Group	Parameter	Description	Obtention method
Injector topology	$\mathbf{x}_{\text{inj}}$	Injector center	Calculated through discretization process
	w_{inj}	Injector width	Calculated through discretization process
	h_{inj}	Injector height	Calculated through discretization process
	N_{pts}	Number of injection points in the injector	User-defined
Spray characteristics to calculate the individual particle properties	Q_l	Nominal flux to be injected	Eq. (4.13)
	f_0	Droplet size distribution	Histogram, PDF fit or constant (SMD)
	$\overline{\mathbf{u}}$	Arithmetic mean injection velocities	Eq. (4.10) with $f = \mathbf{u}$
	$\mathbf{u}_{\text{RMS}}$	Arithmetic RMS injection velocities	Eq. (4.10) with $f = \mathbf{u}$
	$\overline{\mathbf{u}}_{\text{VW}}$	Volume-weighted mean injection velocities	Eq. (4.11) with $f = \mathbf{u}_{\text{VW}}$
	$\mathbf{u}_{\text{VW,RMS}}$	Volume-weighted RMS injection velocities	Eq. (4.11) with $f = \mathbf{u}_{\text{VW}}$
	r	Random numbers law to multiply $\mathbf{u}_{\text{RMS}}$	User-defined
Individual particle properties at injection	$\mathbf{x}_{\text{i}}$	Injection location	Randomly chosen from the injection points
	d_i	Drop diameter	Randomly sampled from f_0, or constant if SMD
	$\mathbf{u}_i$	Drop injection velocity	Eq. (4.18)
Liquid properties	ρ_l	Particle's density	User-defined
	μ_l	Particle's viscosity	User-defined
	σ	Surface tension	User-defined

4.5 Dense core blockage effect modeling

One of the biggest advantages of resolved atomization simulations is the resolution of the liquid-gas interaction. This allows capturing the perturbation effect from the liquid jet to the gaseous phase, which creates turbulent structures that affect droplets dispersion. In the jet in crossflow this influence is paramount, since the liquid coherent structures impose a blockage effect to the gaseous phase that creates vortices downstream the liquid injection nozzle (see Figure 3.9 and Chapter 5)

Perturbation effects are not taken into account *a priori* in dispersed phase simulations, since the coherent structures are not present. As illustrated in §3.3, some approaches have succeeded in emulating this interaction between phases by injecting lagrangian big droplets according to the the blob method (Reitz 1987) and adding a two-way coupling between liquid and gaseous phases (Apte et al. 2003, Senoner 2010). Other studies have solved and kept the liquid coherent structures with VOF to capture the interaction, and then performed lagrangian injection and spray transport (Arienti et al. 2006, Fontes et al. 2019).

In this work, the blockage effect is modeled in dispersed phase computations by means of the Actuator Line Method (ALM). This method has been, to the author's knowledge, only used up to date in wind turbine simulations for modeling the turbulent wakes created by the tower and blades. Firstly, a review on the theory and some previous works in ALM is done. Secondly, a simple model for representing the dense core with ALM is proposed. This model will be later fed from the resolved atomization simulations of Chapter 5 and applied to dispersed phase computations in Chapter 6.

4.5.1 Actuator Line Method

A proper modeling of wind turbines and windfarms requires an accurate representation of the wakes generated by the presence and movement of the blades. Since performing DNS is unaffordable due to the wide range of space and time scales found in these problems, LES are often used. For a proper representation of the wakes in these computations, aerodynamic models are added to consider the effect of the moving blades. The first developed model in this research line was the Actuator Disk Method (ADM) (Sorensen & Myken 1992). The moving blades are modeled as a disk which interacts with the incoming air. This perturbation is taken into account by means of body forces in the Navier-Stokes equations that influence the gaseous flow field. The purpose of ADM is the determination and imposition of these forces.

An extension of the ADM was done later by Sørensen & Shen (2002), known as **Actuator Line Method** (ALM). In this case, the moving bodies are not represented by a disk but by lines emulating the rotor blades. Each individual blade is discretized by points which are equally spaced by a length w. A body force is imposed in each blade point. The cross section of a blade has an airfoil shape (see Figure 4.9 left), so the forces imposed by ALM to the flow field can be calculated from Blade Element Momentum (BEM) theory (Hansen 2015):

$$L = \frac{1}{2}\rho_g u_{\text{rel}}^2 c\left(r\right) w C_L\left(r\right) \tag{4.19a}$$

$$D = \frac{1}{2}\rho_g u_{\text{rel}}^2 c\left(r\right) w C_D\left(r\right) \tag{4.19b}$$

where L is lift, D is drag, u_{rel} the relative velocity, $c\left(r\right)$ the chord size at the span direction r, and $C_L\left(r\right)$ and $C_D\left(r\right)$ lift and drag coefficients respectively. With this methodology, the variation of the forces along the span direction can be taken into account through changing chord and coefficients. The chord is given by the blade geometry, while the lift and drag coefficients are tabulated for each airfoil.

In the computational domain, the body forces cannot be directly applied in a single point since it would create a numerical singularity in the Navier-Stokes equations. Therefore, the body source term is applied using a mollifying function η that distributes the body force f from the forces calculated at each blade element:

$$\mathbf{f}\left(\mathbf{x}, t\right) = -\sum_{e=1}^{N} \left(L\mathbf{e}_L + D\mathbf{e}_D\right) \eta\left(\left|\mathbf{r} - \mathbf{r}_e\right|\right) \tag{4.20}$$

where $\mathbf{e}_L$ and $\mathbf{e}_D$ are the unit vectors along the lift and drag directions (Figure 4.9 left), the subscript e refers to each blade element and the mollifying function is defined by Eq. (4.21).

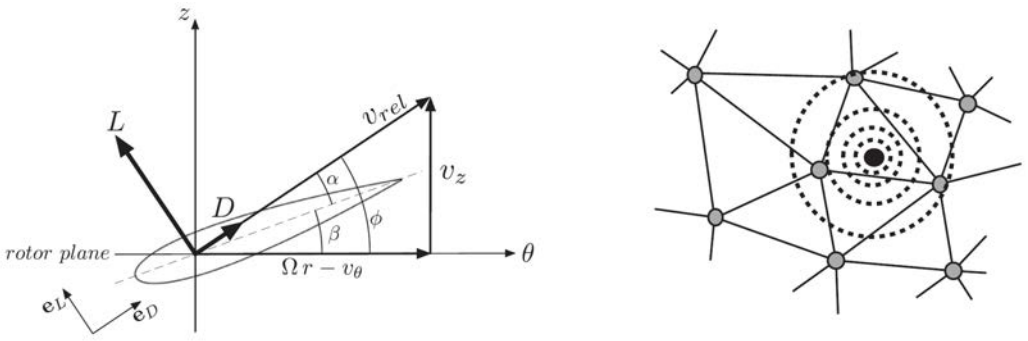

Figure 4.9: ALM illustration of a velocity triangle and geometrical conventions in an airfoil (*left*) and mollification of a point force on several nodes of an unstructured grid (*right*). Source: Benard et al. (2018).

$$\eta(d) = \frac{1}{\epsilon^3 \pi^{3/2}} \exp\left[-\left(\frac{d}{\epsilon}\right)^2\right] \tag{4.21}$$

where $\epsilon = 2w$. The mollification process is depicted in Figure 4.9 right. The simplicity of ALM and its applicability to represent the perturbations created by solid blades have seen its application to model the interaction with other bodies, such as towers in wind turbines Benard et al. (2018), and to use it for generating synthetic turbulence in the grids (Houtin-Mongrolle et al. 2020)).

4.5.2 Dense core representation as an actuator

As depicted in Figure 3.9, the presence of the dense core creates a wake and vortical structures further downstream. This interaction can be captured in resolved atomization simulations (see §5.6.4 of Chapter 5), but not in dispersed phase simulations where the coherent liquid structures are neglected. Since these liquid-gas interactions can have a strong influence on the transport of droplets in the developed spray region, it is of interest to model this effect in dispersed phase simulations. For this purpose, ALM is used.

Figure 4.10 shows the representation of the dense core (top figures) as an actuator line model (bottom figures). Its complex topology is emulated by a frustum with increasing chord from the bottom ($c_0 = d_{\text{inj}}$) to the top ($c_L = W$). The frustum has a length L and an inclination angle θ which are obtained from the breakup point coordinates (x_b, z_b) of the dense core in resolved atomization simulations: $L = \sqrt{x_b^2 + z_b^2}$ and $\theta = \tan^{-1}(z_b/x_b)$. In the resolved simulations, the dense core is obtained as the largest liquid structure in the domain, and its breakup point is estimated as the point at the symmetry plane $y = 0$ located further downstream from the injection location (see Appendix C.3 for a detailed explanation). In the dispersed-phase computations, the actuator points where discrete forces are placed are equally-spaced with a distance w along the center line of the frustum. The number of points N_p also needs to be specified in the ALM model.

Apart from the geometry, the forces applied to the actuator points are also defined. In this model, instead of specifying coefficients as done in wind turbine blades, the forces will be directly imposed in the actuator points. As shown in Figure 4.10c, the force in the actuator will evolve linearly from the bottom to the top in order to take into account the real increasing cross-section of the actuator, which has the effect of increasing drag (Mashayek et al. 2006). The force acts in a direction normal to the axis of the frustum. Therefore, the imposed forces can be decomposed into two components: a drag force D along the x direction and a lift force L along the z direction. Forces are specified at each actuator point with coordinates (x_p, z_p) along the actuator. As the coordinates are automatically calculated according to the number of actuator points N_p and the breakup point (x_b, z_b), the forces will be expressed with respect to the line coordinate $s_p = \left(x_p^2 + z_p^2\right)^{1/2}$ with expresses the distance of each actuator point to its base. Hence, the force decomposition into lift and drag holds as follows:

$$\mathbf{F}(s_p) = D(s_p)\,\mathbf{i} + L(s_p)\,\mathbf{k} \tag{4.22}$$

where $\mathbf{i}$ and $\mathbf{k}$ are the unit vectors in the x and z directions, respectively. To estimate these forces, the net force applied to the dense core $\mathbf{F}_{\text{DC}}$ is obtained from the resolved simulations (see §4.5.3). This force is

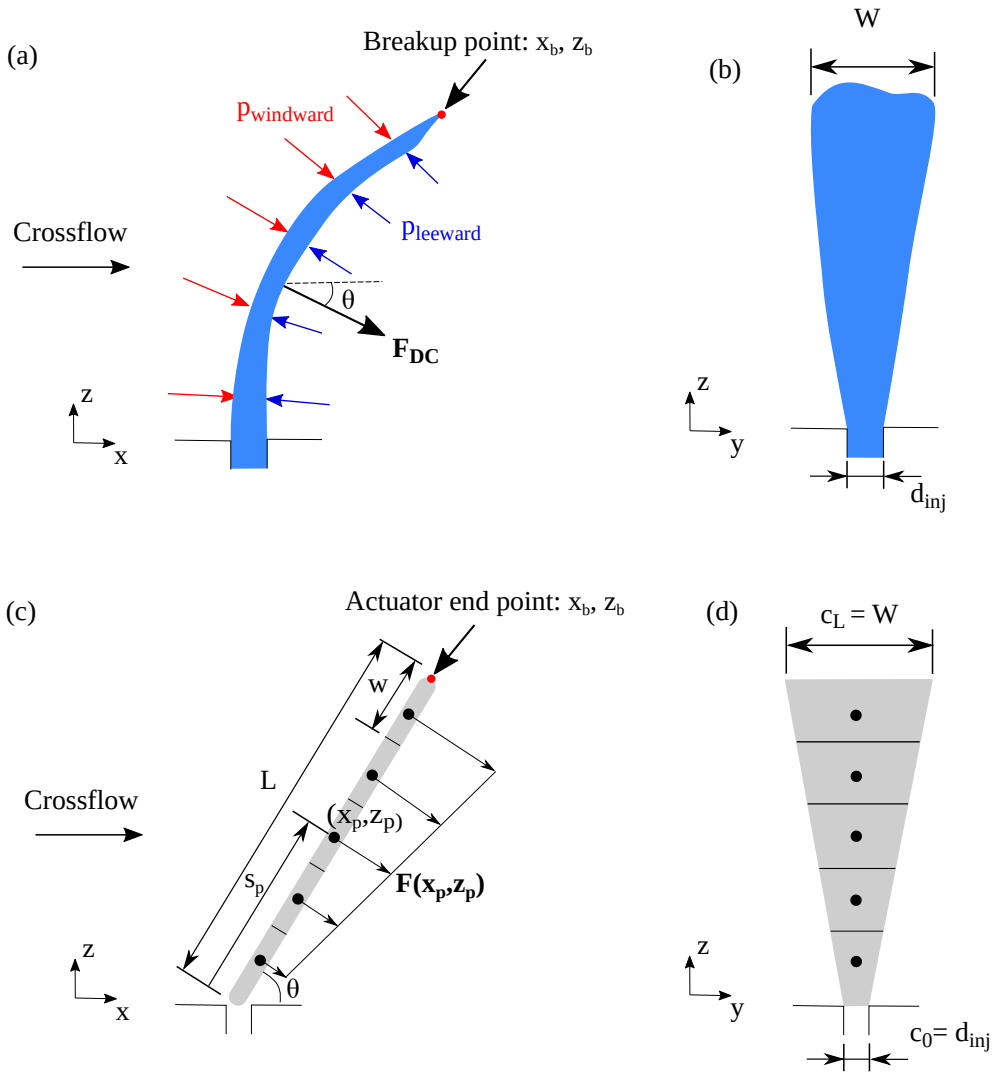

Figure 4.10: Representation of the dense core as an actuator, showing lateral (*left*) and frontal (*right*) views of the jets. *Top*: schematic dense core from a resolved simulation. *Bottom*: actuator line model of the dense core.

assumed to act in the same direction as the forces $\mathbf{F}(s_p)$ from the actuator model, and is repartitioned into the several forces that are applied to the actuator points. Therefore, the following condition must be fulfilled:

$$\sum_{p=1}^{N_p} |\mathbf{F}(s_p)| = |\mathbf{F}_{\mathrm{DC}}| \tag{4.23}$$

As the forces $|\mathbf{F}(s_p)|$ increase linearly along the actuator, its evolution is represented by the following expression accordingly to the vertical coordinates z_p of the actuator points:

$$|\mathbf{F}(s_p)| = |\mathbf{F}_{\mathrm{DC}}| \frac{s_p}{\sum_{p=1}^{N_p} s_p} \tag{4.24}$$

And finally, the drag and lift forces to impose are calculated as follows:

$$L(s_p) = -|\mathbf{F}(s_p)| \cos\theta = -|\mathbf{F}_{\mathrm{DC}}| \cos\theta \frac{s_p}{\sum_{p=1}^{N_p} s_p} \tag{4.25a}$$

$$D(s_p) = |\mathbf{F}(s_p)| \sin\theta = |\mathbf{F}_{\mathrm{DC}}| \sin\theta \frac{s_p}{\sum_{p=1}^{N_p} s_p} \tag{4.25b}$$

Therefore, the forces imposed to the actuator points are parametrized by the dense core net force $|\mathbf{F}_{\mathrm{DC}}|$, the actuator inclination θ and the actuator points. Table 4.3 shows a recap of the parameters used in the proposed model. In this table, the angle θ is not shown since it can be obtained with trigonometry from the initial and end points of the actuator. The number of actuator points N_p is not taken as an input parameter as it has been checked that, if large enough, it does not have an effect of the perturbed flow field: therefore, it has been set to $N_p = 100$ for all cases presented in this thesis.

Table 4.3: Parameters of an actuator representing the dense core

Parameter	Units	Description
x_b, z_b	mm	Actuator end point
$\lvert\mathbf{F}_{\mathrm{DC}}\rvert$	N	Dense core net force

4.5.3 Determination of forces

The forces to impose in the actuator model are learnt from the resolved atomization simulation. For this purpose, they are firstly calculated in these simulations by calculating the corresponding term of the momentum equation (2.27):

$$\boldsymbol{F}_{\mathrm{DC}} = \boldsymbol{F}_p + \boldsymbol{F}_\tau = \int_{\partial\Omega_{DC}} \left(\underbrace{-p\boldsymbol{n}}_{\text{Pressure}} + \underbrace{2\mu\bar{\bar{\epsilon}}\boldsymbol{n}}_{\text{Shear}} \right) dS \tag{4.26}$$

where $\partial\Omega_{DC}$ denotes the dense core surface. $\boldsymbol{F}$ has two contributions: a pressure force term and a shear force term. In a first instance, the shear term is neglected (see next section for details). Therefore, the total force term is reduced to the pressure force:

$$\boldsymbol{F}_{\mathrm{DC}} = \boldsymbol{F}_p = -\int_{\partial\Omega_{DC}} p\boldsymbol{n}dS \tag{4.27}$$

To simplify this expression, the forces in the windward and leeward sides of the dense core are assumed to be constant as indicated in Figure 4.10a by the red and blue arrows, respectively. The surface of the dense core can be approximated according to the actuator model as $\partial\Omega_{\mathrm{DC}} \approx S_{\mathrm{DC}} = \frac{1}{2}(c_0 + c_L)\, L$, being $L = \sqrt{x_{\mathrm{b}}^2 + z_{\mathrm{b}}^2}$ if the actuator initial point is located at the origin of the coordinate system. Therefore, Eq. (4.27) can be reduced to

$$\boxed{|\boldsymbol{F}_{\mathrm{DC}}| = (p_{\mathrm{windward}} - p_{\mathrm{leeward}})\, S_{DC}} \tag{4.28}$$

It must be taken into account that the dense core as a rigid body immersed in a fluid. Its geometry has been approximated by observations of the dense core shape in resolved atomization simulations, and have been taken as constant. In reality, the dense core is a deformable body whose topology (breakup point, inclination, length) changes with time. Future works on deriving more thorough models intending to represent the dense core should take into account these transient properties (Patil & Sahu 2021).

Neglecting the shear force term

For a body immersed in a fluid, the shear force is defined as:

$$\boldsymbol{F}_\tau = \int_{\partial\Omega_{\mathrm{DC}}} 2\mu\bar{\bar{\epsilon}}\boldsymbol{n}dS \tag{4.29}$$

where $\bar{\bar{\epsilon}}$ is the deformation tensor:

$$\bar{\bar{\epsilon}} = \frac{1}{2}\left(\nabla\boldsymbol{u} + (\nabla\boldsymbol{u})^T\right) \tag{4.30}$$

The forces $\boldsymbol{F}_\tau$ cannot be easily calculated with the current methodology. Instead, a more simple expression of the shear forces based on a friction coefficient C_f and a reference surface S is used (Johnston 1984, Soedarmo et al. 2018):

$$\boldsymbol{F}_\tau = \frac{1}{2}\rho_g u_g^2 S C_f \tag{4.31}$$

The friction coefficient C_f is obtained from the following expression (Yang & Sotiropoulos 2017):

$$C_f = 0.37\left(\log Re_x\right)^{-2.584} \tag{4.32}$$

where Re_x is the Reynolds number based on the incoming velocity and the distance along the dense core.

The relative intensity of the force $\boldsymbol{F}_p$ with respect to $\boldsymbol{F}_\tau$ can be measured by dividing expressions (4.28) and (4.31), plugging also Eq. (4.32):

$$r_F = \frac{|\boldsymbol{F}_p|}{|\boldsymbol{F}_\tau|} = \frac{\Delta p}{0.185\rho_g u_g^2\left(\log Re_x\right)^{-2.584}} \tag{4.33}$$

Numerical application to JICF operating conditions

The force ratio from Eq. (4.33) can be estimated for the operating conditions of interest in this thesis. These correspond to the high-pressure jet in crossflow simulated in Chapter 5. The pressure diference for these cases is $\Delta p \sim O\left(10^4\right)$ (see Table 5.8 for specific values). Considering this value, the expression for r_F can be estimated to be:

$$r_F \sim \frac{10^5}{\rho_g u_g^2\left(\log Re_x\right)^{-2.584}} \tag{4.34}$$

In the operating points studied (summarized in Table 5.2), $\rho_g = 7.21$ kg m^{-3} and $u_g = 75; 100$ m s^{-1}. Then, Re_x ranges from 10^3 to 10^5. With these values, r_F is plotted as a function of Re_x in Figure 4.11. As observed, the ratio r_F presents values between 10 to 90 for the Re_x range of interest. These ratios mean that the pressure force $\boldsymbol{F}_p$ is between 10 and 90 times the shear force $\boldsymbol{F}_\tau$. Therefore, $|\boldsymbol{F}_\tau| << |\boldsymbol{F}_p|$ and only the contribution of the pressure force is considered to calculate the dense core net force.

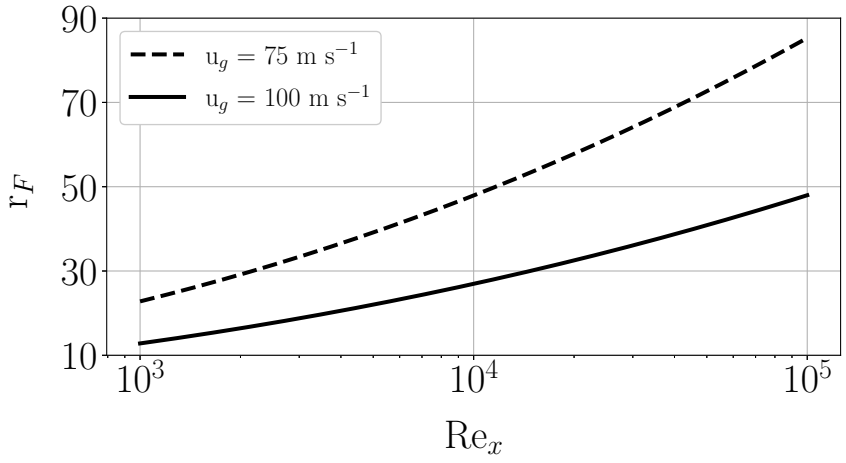

Figure 4.11: Force ratio evolution with Re_x.

4.6 Secondary atomization modeling

In disperse phase simulations, spray is modeled by a set of spherical and rigid particles whose dynamics are governed by the point-particle equations described in §3.2.3. Due to these assumptions, particles will not break by their interaction with the gaseous phase as in the resolved atomization simulations. Nevertheless, further breakup can be taken into account by means of secondary atomization models. The most important parameter governing secondary atomization is the Weber number based on the relative velocities between liquid and gas u_{rel}:

$$We = \frac{\rho_g u_{\text{rel}}^2 r}{\sigma} \tag{4.35}$$

Different mechanisms produce secondary atomization depending on the value of We, see Fig. 1.9. Existing models for secondary atomization have been developed for each particular mode of breakup, such as the WAVE model for high Weber numbers (Reitz 1987) or the Taylor Analogy Breakup (TAB) model for low ones (O'Rourke & Amsden 1987). The former model predicts breakup by following a linear stability analysis considering Kelvin-Helmholtz waves as the governing breakup mechanisms, while the latter makes an analogy between a droplet and a second-order mechanical system. Nevertheless, up to date there is not a model which accounts for all different breakup mechanisms and that can capture all the physical complexity of secondary atomization.

In this work, three atomization models have been implemented and tested: the TAB model, the Enhanced TAB model (Tanner 1997), and the stochastic model of Gorokhovski (2001). They are described in the following sections.

4.6.1 Taylor Analogy Breakup

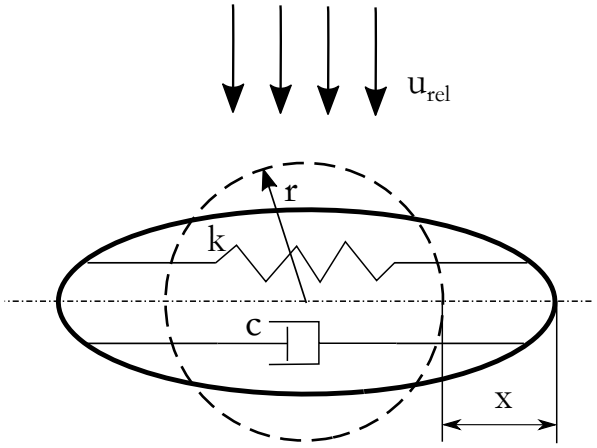

Figure 4.12: Taylor analogy breakup between a droplet and a mechanical system with spring and damper. The undeformed droplet is represented by the dashed line, while the thick solid line depicts the droplet after deformation. x is the displacement from the deformed to the undeformed states.

The Taylor Analogy Breakup (TAB) model is one the first secondary atomization models. Developed by O'Rourke & Amsden (1987), it makes an analogy between a droplet and a mechanical system as shown in Fig. 4.12. Breakup occurrence is estimated by solving the ordinary differential equation (ODE) representing the oscillating dynamics of the mechanical system depicted:

$$m\ddot{x} = F - kx - c\dot{x} \tag{4.36}$$

where x is the displacement from the droplet's equator due to deformation, m is the mass, F is the external force, k is the spring constant and c is the damping coefficient. The Taylor analogy makes a comparison between this mechanical system and the droplet, producing the following relation between constants:

$$\frac{F}{m} = C_F \frac{\rho_g u_{\text{rel}}^2}{\rho_l r} \quad ; \quad \frac{k}{m} = C_k \frac{\sigma}{\rho_l r^3} \quad ; \quad \frac{c}{m} = C_d \frac{\mu_l}{\mu_g r^2} \tag{4.37}$$

where $C_F = 1/3$, $C_k = 8$, $C_d = 5$ are constants, r the droplet radius, ρ the density, σ the surface tension, μ the viscosity, and the subscripts l and g indicate liquid and gases respectively.

The deformation x can be expressed by a non-dimensionless parameter y, hereafter referred as droplet distorsion, whose equivalence is $y = x/(C_b r)$, where $C_b = 0.5$ is a constant. Using the expressions from the Taylor analogy and introducing the change of variable y, the ODE (4.36) becomes:

$$\ddot{y} = \frac{C_F}{C_b}\frac{\rho_g}{\rho_l}\frac{u_{rel}^2}{r^2} - \frac{C_k\sigma}{\rho_l r^3}y - \frac{C_d\mu_l}{\rho_l r^2}\dot{y} \tag{4.38}$$

This expression governs the breakup of droplets, which occurs for $y > 1$ (i.e. when the amplitude of the oscillation x equals the radius of the undeformed droplet). For solving this equation, it is useful to introduce the following parameters:

$$t_d = \frac{2\rho_l r^2}{C_d\mu_l} \tag{4.39a}$$

$$\omega^2 = C_k\frac{\sigma}{\rho_l r^3} - \frac{1}{t_d^2} \tag{4.39b}$$

where t_d is the oscillation damping time and ω is the oscillations frequency. With these definitions, the solution to Eq. (4.38) is:

$$y(t) = We_c + e^{-t/t_d}\left[(y_0 - We_c)\cos(\omega t) + \frac{1}{\omega}\left(\dot{y}_0 + \frac{y_0 - We_c}{t_d}\right)\sin(\omega t)\right] \tag{4.40}$$

where $We_c = \frac{C_F}{C_k C_b}We = We/12$ with the constants previously defined. The distorsion rate can be obtained by differentiating the former expression with time:

$$\dot{y}(t) = \frac{We_c - y(t)}{t_d} + e^{-t/t_d}\left[\left(\dot{y}_0 + \frac{y_0 - We_c}{t_d}\right)\cos(\omega t) - \omega(y_0 - We_c)\sin(\omega t)\right] \tag{4.41}$$

As it can be seen, the previous equations are continuous. For numerical implementation of the algorithm, it is more convenient to express them in their corresponding discrete form:

$$y^{n+1} = We_c + e^{-dt/t_d}\left[(y^n - We_c)\cos(\omega dt) + \frac{1}{\omega}\left(\dot{y}^n + \frac{y^n - We_c}{t_d}\right)\sin(\omega dt)\right] \tag{4.42}$$

$$\dot{y}^{n+1} = \frac{We_c - y^{n+1}}{t_d} + e^{-dt/t_d}\left[\left(\dot{y}^n + \frac{y^n - We_c}{t_d}\right)\cos(\omega dt) - \omega(y^n - We_c)\sin(\omega dt)\right] \tag{4.43}$$

where the subindexes n and $n+1$ indicate two consecutive time instants separated by the timestep dt.

To estimate breakup, firstly ω^2 is calculated with Eq. (4.39b). According to its value, two scenarios are possible:

- If $\omega^2 < 0$, oscillations are not present. Hence, the droplet does not deform and the values for droplets distorsion and distorsion rate are set to 0: $y^{n+1} = y^n = 0$.
- If $\omega^2 > 0$, breakup is possible. In this case, the amplitude of oscillations A is calculated:

$$A = \sqrt{(y^n - We_c)^2 + (\dot{y}^n/\omega)^2} \tag{4.44}$$

Again, the value of A will present two different alternatives:

- If $We_c + A \leq 1$, then $y^n \leq 1$ and droplet will not break. Deformation and deformation rate will then be updated by applying Eqs. (4.42) and (4.43).
- If $We_c + A > 1$, breakup is possible. A breakup timestep dt_{bu} is then calculated as the smallest root of the following equation:

$$We_c + A\cos(\omega dt_{bu} + \phi) = 1 \tag{4.45}$$

where the phase ϕ is obtained from the following:

$$\cos\phi = \frac{\dot{y}^n - We_c}{A} \quad ; \quad \sin\phi = -\frac{\dot{y}^n}{A\omega} \tag{4.46}$$

Breakup will then occur for $dt < dt_{bu}$, or also if updating the deformation it is found that $y^{n+1} > 1$. Once breakup is triggered, the associated droplet (named parent) will divide into one or several smaller particles (named children). The mean size of children droplets r_{32} is obtained through an energy balance between the produced droplets and the parent with radius r, yielding the following relation between both sizes:

$$\frac{r}{r_{32}} = 1 + \frac{8K}{20} + \frac{\rho_l r^3}{\sigma}\dot{y}^2\left(\frac{6K-5}{120}\right) \tag{4.47}$$

where $K = 10/3$ is a constant. Now, radii of children droplets r_{ch} are randomly chosen from a Rosin-Rammler distribution [1] with characteristic diameter r_{32} and factor $q = 3.5$:

$$Q(r) = 1 - \exp\left(-\left(\frac{r}{r_{0.632}}\right)^q\right) \tag{4.48}$$

which can be inverted to obtain r_{ch}:

$$r_{ch} = r_{32}\sqrt[3.5]{-\log(1-Q)} \tag{4.49}$$

where Q is Cumulative Density Function (CDF). To estimate the size of children droplets droplets from this distribution, Q is randomly sampled from a uniform distribution $\in [0, 1]$. The resulting random number is introduced in the previous expression, yielding a value for one children droplet. This procedure is repeated until the volume of all children droplets equals the volume of the parent, hence conserving mass. Children droplets are then randomly located along the surface of the parent droplet. They will all inherit the velocity of the parent droplet, plus a component $v_\perp$ with magnitude:

$$v_\perp = C_v C_b r \dot{y}^n \tag{4.50}$$

where $C_v \approx 1$. The direction of $v_\perp$ is randomly chosen in a plane normal to the relative velocity u_{rel}. Finally, all children droplets all initialised with $y = \dot{y} = 0$.

4.6.2 Enhanced TAB model

The main disadvantage of the TAB model is the underprediction of droplets size. To overcome this problem, an improved version of the TAB model was developed by Tanner (1997) and named Enhanced Taylor-Analogy Breakup (ETAB). Breakup is predicted and triggered in the same way as in TAB, but the size of children droplet is estimated differently. While TAB makes use of an energy balance (O'Rourke & Amsden 1987), ETAB considers that the droplet production rate is proportional to the number of children droplets. Mathematically, this proportionality is expressed by the following exponential decay law:

$$\frac{dm_{\text{ch}}}{dt} = -3K_{\text{br}}m_{\text{ch}} \tag{4.51}$$

where m_{ch} is the mass of children droplets. This law depends on the atomization regime through the breakup constant K_{br}, which depends on We and the oscillation frequency ω:

$$K_{br} = \begin{cases} k_1\omega \text{ if } We \leq We_t \\ k_2\omega\sqrt{We} \text{ if } We > We_t \end{cases} \tag{4.52}$$

where k_1 and k_2 are constants, and We_t is a transition Weber number between bag and stripping breakup regimes, set to 80 (Tanner 1997). The bag breakup k_1 is obtained from the following expression to make a smooth transition between both regimes:

$$k_1 = k_1^*\left[\left(\frac{k_2}{k_1^*}\left(\sqrt{We_t}-1\right)\right)\left(\frac{We}{We_t}\right)^4 + 1\right] \tag{4.53}$$

where $k_1^* = 2/9$. The stripping breakup constant is fixed to $k_2 = 2/9$.
The size of children droplets is calculated by integrating the production law Eq. (4.51):

$$\frac{r_{ch}}{r} = e^{-K_{br}t_{bu}} \tag{4.54}$$

[1] In the original work by O'Rourke & Amsden (1987), a χ^2 distribution is used

where t_{bu} is estimated as in the TAB model, Eq. (4.45). All children droplets generated from a parent with radius r will have identical size r_{ch}. Finally, children will inherit parent's velocity plus a normal component given by:

$$v_{\perp} = C_A C_b r \left(\dot{y}^n\right)^2 \tag{4.55}$$

whose direction is randomly chosen in a plane normal to the relative velocity u_{rel}. In this expression, C_A is a constant determined from an energy balance:

$$C_A^2 = 3\left(1 - \frac{r_{ch}}{r} + \frac{5}{72} C_D We\right)\frac{\omega^2}{\dot{y}^2} \tag{4.56}$$

being C_D is the drag coefficient of the parent droplet, Eq. (3.6). Note that $v_{\perp}$ defined by the ETAB model differs from TAB's Eq. (4.50) by considering C_A to be dependent on the breakup regime.

4.6.3 Gorokhovski stochastic model

Both TAB and ETAB models were derived using the Taylor analogy breakup. The TAB model is known (Tanner 1997, Dahms & Oefelein 2016, Fontes et al. 2019) to underestimate the diameter of the children droplets and to not distinguish between breakup regimes, producing too many droplets when the Weber number is high. Hence, the applicability of TAB is restricted to breakup at low We. ETAB tried to solve this issue by considering an exponential decay law for the size of children droplets which would depend on the breakup regime. Both models are, however, deterministic in the sense that a single range of droplet sizes is considered when breakup is produced.

A different secondary atomization model not based on the Taylor analogy was derived by Gorokhovski (2001). This model circumvents the deterministic approach of the TAB family of models by accounting for a range of children droplet sizes when breakup occurs. This is done by using a stochastic approach based on Kolmogorov's theory of breakup (Kolmogorov 1941). Following this theory, the evolution of droplet's sizes is represented by a Fokker-Planck equation:

$$\frac{\partial T\left(\ln r, t\right)}{\partial t} = -\nu\langle\xi\rangle\frac{\partial T\left(\ln r, t\right)}{\partial\left(\ln r\right)} + \frac{1}{2}\nu\langle\xi^2\rangle\frac{\partial^2 T\left(\ln r, t\right)}{\partial\left(\ln r\right)^2} \tag{4.57}$$

where $T\left(\ln r, t\right)$ is the cumulative distribution of droplets sizes, ν the breakup frequency, and $\langle\xi\rangle$ and $\langle\xi^2\rangle$ are parameters. After some mathematical development (Apte et al. 2003), the cumulative distribution function can be expressed as:

$$T\left(\ln r, t\right) = \frac{1}{2}\left(1 + \operatorname{erf}\left(\frac{\ln r - \ln r_{ch} - \langle\xi\rangle}{\sqrt{2\langle\xi^2\rangle}}\right)\right) \tag{4.58}$$

This function will be later used to obtain the size of children droplets. The previous step is to determine when breakup occurs. In this model, two criteria are used:

- Parent droplets must be larger than a critical radius r_{cr}. This value is determined from a critical Weber number $We_{\text{crit}} = 6$:

$$r_{\text{crit}} = \frac{We_{\text{crit}}\sigma}{\rho_g u_{\text{rel}}^2} \tag{4.59}$$

- The residence time of the particles must be larger than a computed breakup time t_{bu}:

$$t_{bu} = B\sqrt{\frac{\rho_l}{\rho_g}}\frac{r}{u_{rel}} \tag{4.60}$$

where $B = \sqrt{3}$.

If both $r > r_{\text{crit}}$ **and** $t > t_{bu}$, breakup occurs. In this case, size of children droplet is obtained from the cumulative density function $T(\ln r_{ch}, t)$, Eq. (4.58), from which $\ln r_{ch}$ can be solved:

$$r_{ch} = r \exp\left(\langle\xi\rangle + \sqrt{2\langle\xi^2\rangle}\,\text{erf}^{-1}(2T-1)\right) \tag{4.61}$$

The size of children droplets are then obtained by sampling a random value of T from a uniform distribution between 0 and 1, $T \sim \mathcal{U}(0,1)$, and then applying the previous equation. The parameters $\langle\xi\rangle$ and $\langle\xi^2\rangle$ are calculated from the following equations:

$$\langle\xi\rangle = K_1 \ln\left(\frac{We_c}{We}\right) \tag{4.62a}$$

$$-\frac{\langle\xi\rangle}{\langle\xi^2\rangle} = K_2 \ln\left(\frac{r}{r_{crit}}\right) \tag{4.62b}$$

where K_1 and K_2 are model constants, which are of order unity. The constant K_1 controls the mean size of children droplets, while K_2 influences its standard deviation.

Children droplets inherit then a velocity which has two components: the parent particle velocity in the same direction, plus a velocity normal to the parent's direction and magnitude equal to:

$$|\mathbf{u}_{\text{ch,n}}| = \frac{r}{t_{bu}} \tag{4.63}$$

4.7 Conclusions and perspectives

This chapter has introduced and detailed the injection models developed in this thesis. The full process is depicted by the flowchart of Figure 4.2. The learning of the liquid injectors, baptised as SLI, is based on a spray characterization process of droplets resulting from resolved atomization simulations. Such process consists of sampling a flux-density distribution of droplets and evaluating its convergence to then make an in-plane discretization of the spray. Then, the individual sprays of the discrete grid are characterized by average values of fluxes, diameters, and velocities, and by RMS values of velocities. The spray grid can also be further refined through a convergence-driven discretization process. Then, resulting injectors can be used to inject a realistic spray in dispersed phase simulations. The models are then closed by including in the dispersed phase simulations: 1) a modelisation of the dense core perturbance effect towards the gas with Actuator Line Method (ALM), which is based on a learning process from the resolved atomization simulations; and 2) a secondary atomization model that continues breaking the particles in case they are not in equilibrium with the surrounding air. The next chapters are devoted to the two-phase simulations and the application of the models.

For further development of the models, the following perspectives could be considered:

- Include a modified drag coefficient for lagrangian particles which depends on the deformation of the liquid structures sampled in resolved atomization simulations. This would allow for a more accurate transport of the lagrangian spray at the first time instants of injection, which would affect the particle's trajectories and the liquid-gas relative velocity before secondary breakup takes place.
- Consider a transient spray obtained through the accumulation process to develop an unsteady injection model. This would be specially useful in reactive cases where thermoacoustic oscillations play an important role, such as gas turbine and rocket engines.
- Extend the spray convergence criterion, defined as a MSE norm on the droplet diameters, to include other parameters such as liquid velocities.
- Improve the actuator line model developed in this thesis to make a better representation of the resolved dense core, such as by considering a transient behaviour of its topology and its force.

Chapter 5

Resolved atomization simulations of liquid jet in crossflow

5.1 Introduction

The previous chapter has detailed the theory of the Smart Lagrangian Injectors (SLI) models to build injectors for dispersed-phase simulations. These models aim at being generic and applicable to a broad range of operating conditions and injector configurations. In this thesis, they are developed from resolved simulations of an academic kerosene jet in crossflow (JICF) configuration. This chapter details these simulations, performed with the software YALES2 (Moureau et al. 2011), and how SLI can be built from them.

In first place, the experimental bench by Becker & Hassa (2002) is presented in §5.2. The computational setup for the resolved simulations is detailed in §5.3. Two operating conditions to simulate are given in §5.4. Gaseous conditions for initializing the liquid computations are reported in §5.5. Then, results from the resolved atomization simulations are provided in §5.6, where a physical analysis of the JICF simulations is performed. Studied features include the evolution of the liquid jet, the jet breakup process, its vertical trajectories (validated with an experimental correlation), gaseous disturbances due to liquid dense core, and computation of resolved liquid fluxes. Finally, the simulations are processed to provide the necessary data for building SLI in §5.7. These will be later used for dispersed-phase computations in Chapter 6.

Some results from this chapter have been published in Janodet et al. (2022).

5.2 Experimental test case

The experimental configuration of the pressurized JICF tested by Becker & Hassa (2002) is shown in Figure 5.1. Liquid kerosene is injected through the atomizer ports to a quartz glass duct of rectangular cross section 25x40 mm^2. The duct inlet is located at 120 mm upstream the injection port. The boundary layer thickness developing along the bottom of the duct has been measured experimentally just upstream the atomizer, being between 4 and 5 mm. The lateral walls allow for optical access from the atomizer port until a location at 100 mm downstream. Air is introduced through two separate channels, a main one and a supplementary one. The main airflow is injected at the inlet of the quartz duct, while the supplementary one passes around it. Both airflows merge at the end of the duct and leave the domain through a common exit acting as a sonic throttle. The velocity inside the quartz can then be tuned by varying the size of the nozzle and the supplementary air flow rate. In the experiments performed, the range of air velocities goes from $u_g = 50$ to 100 m/s and the range of pressure from $p = 1.5$ to 15 bar, hence allowing the study high-pressure conditions. The air temperature is maintained to $T_g = 290$ K. The fuel tested was kerosene Jet A-1 with density $\rho_l = 795$ kg m^{-3} and surface tension $\sigma = 22 \cdot 10^{-3}$ N m^{-1}.

The liquid injection nozzle can be seen in Figure 5.1 right. It consists of a plain jet nozzle of $d_{\text{inj}} = 0.45$ mm diameter and L/d_{inj} ratio of 1.56 with sharp edges. The average discharge coefficient for the mass flow rates of interest in the experimental studies is 0.6. More details on the test rig can be found in Brandt et al. (1997).

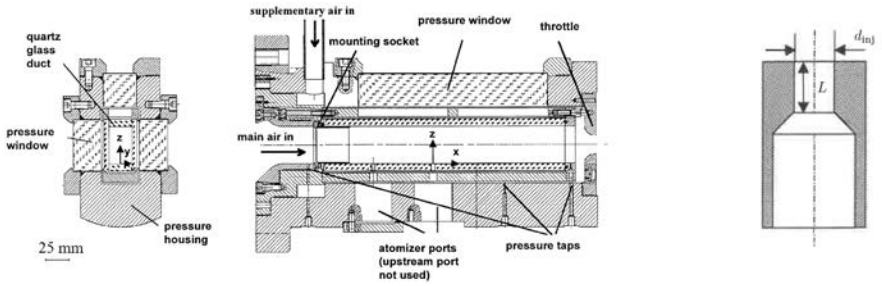

Figure 5.1: JICF experimental setup. *Left*: Test rig. *Right*: liquid nozzle geometry employed in the experimental study. Source: Becker & Hassa (2002)

5.3 Computational setup

Figure 5.2 shows the computational domain developed to replicate the simulations of the test bench from Becker & Hassa (2002). The plenum is modeled as a box with dimensions 25x40x270 mm^3. The hydraulic diameter of the duct cross section, which is used to calculate the gas Reynolds number, is $D_h = 30.8$ mm. A magnified view of the nozzle is also shown, with diameter 0.45 mm and straight section length of 0.7 mm prior to injection to keep $L/D = 1.56$ as in the experiments. The boundary conditions are also indicated. The plenum walls use a wall law of logarithmic type except closer to the domain pressure outlet, which have been set to slip walls to avoid backflow. The nozzle walls are rigid walls. For the liquid inlet, a Poiseuille profile has been specified, while in the gaseous inlet a mean velocity profile has been set in order to recover the boundary layer thickness of between 4 and 5 mm upstream the injection nozzle as described in the experiments (see Appendix A for details). Due to the high Reynolds number at the gaseous inlet ($Re \sim O\left(10^6\right)$, see Table 5.2), synthetic turbulence is added in the liquid inlet.

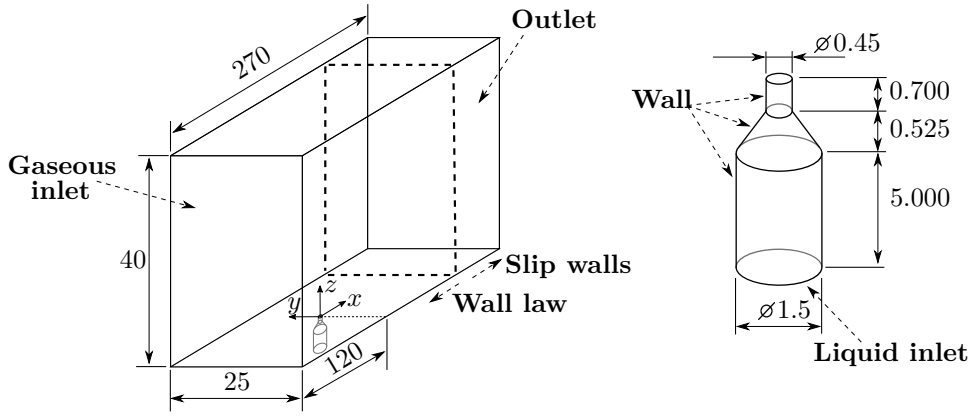

Figure 5.2: Numerical domain and boundary conditions of the experimental test bench of Becker & Hassa (2002). *Left*: complete domain. *Right*: detailed view of the injection nozzle. All dimensions are in mm.

Figure 5.3 shows the baseline mesh, where the symmetry plane $y = 0$ is displayed. It is composed of 66 million tetrahedral cells. The baseline cell size in the channel upstream liquid injection is 0.5 mm, which was chosen after performing a mesh independence study on the gaseous field (results in Appendix B). The cells located in the downstream region have an average size of 3 mm, and the element size within the discharge section of the liquid nozzle is refined to 20 μm. This mesh is used at the beginning of all the simulations performed, which afterwards changes dynamically throughout the simulation as more liquid is introduced in the domain due to the Adaptive Mesh Refinement (AMR) routine. Simulations are performed with the ACLS methodology describe in §2.3.4. Liquid is allowed to penetrate up to a certain x location downstream the injector: at this location, a sponge layer is added to remove liquid artificially for restricting the region inside the plenum containing liquid, thus limiting the cost of the resolved simulations. The location of the sponge layers is detailed in the next section, since it depends on each performed simulation.

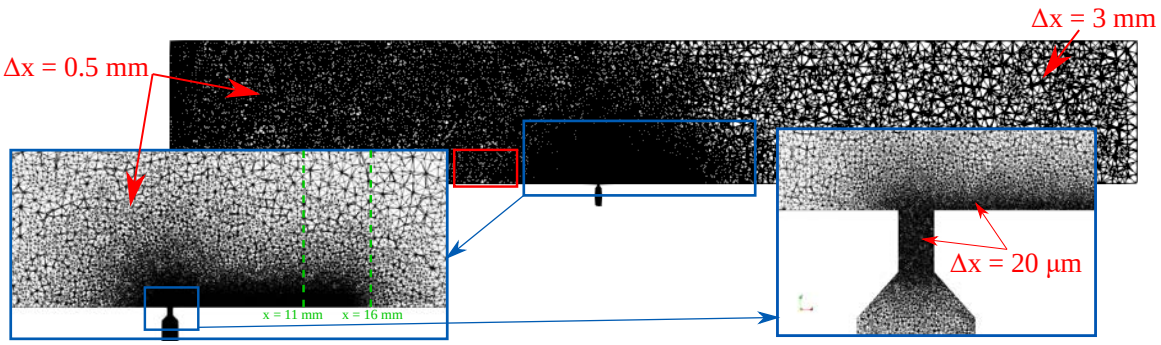

Figure 5.3: Baseline JICF mesh, showing magnified views of the near-field and nozzle regions. The red rectangle is the region where meshes are shown in the mesh convergence study of Appendix B. The dashed green lines show the axial locations where liquid is artificially removed in the simulations for limiting their computational cost (sponge layers)

5.4 Operating conditions

Two operating conditions tested experimentally in Becker & Hassa (2002) have been simulated. Both of them have the same momentum ration $q = 6$ but differ in the Weber number: $We_g = 830$ (low Weber) and $We_g = 1470$ (high Weber), calculated with Eq. (1.1). According to the values of q and We_g, the former condition corresponds to surface breakup dominating regime while the latter is located at the dividing line between column and surface breakup. Figure 5.4 shows the location of both operating points in the breakup map of Wu et al. (1997). The physical magnitudes and dimensionless numbers of both operating points are shown in Table 5.2. Apart from the values q and We_g, the dimensionless numbers in Eq. (5.1) are also calculated: the liquid and gaseous Reynolds numbers Re_l and Re_g respectively, Ohnesorge number Oh, aerodynamic Weber We_{aero}, relative Weber We_{rel} and density ratio r. These numbers have been added since they are defined in several experimental studies (Wu et al. 1997, Becker & Hassa 2002, Ragucci et al. 2007) to characterize the operating points tested.

Computations are performed with the ACLS methodology combined with the AMR routine described in §2.3.4. For each operating condition, two interface cell sizes have been simulated: $\Delta x_{\min} = 20$ μm (coarse case) and $\Delta x_{\min} = 10$ μm (fine case). The levelset band around the interface, which denotes the region where the cell size is $\Delta x_{\min}$, has been set to 12 cells ($N_p = 12$ from Figure 2.7). The nomenclature for each simulation, which is used hereafter in this document, is introduced in Table 5.1: cases indicate the operating point by its gaseous velocity (UG), the level-set resolution (DX), and an additional simulation with no synthetic turbulence (NT) injected has been performed. The coarse cases locate the sponge layer to remove liquid at a downstream distance of $x = 16$ mm, while the fine ones place it at $x = 11$ mm (these locations are indicated by the green lines of Figure 5.3). In such ways, droplets can be sampled up to planes $x = 15$ and 10 mm respectively. The number of steps for the reinitialization equation (2.55) is set to $N_{\text{reinit}} = 6$. This parameter has shown to affect mass conservation in the JICF simulations; its effect and the choice of this value are discussed in Appendix D.

$$
\begin{aligned}
Re_l &= \frac{\rho_l u_l d_{\text{inj}}}{\mu_l} \qquad Re_g = \frac{\rho_g u_g D_h}{\mu_g} \qquad Oh = \frac{\mu_l}{\sqrt{\rho_l \sigma d_{\text{inj}}}} \\
We_{\text{aero}} &= \frac{\rho_g u_l^2 d_{\text{inj}}}{\sigma} \qquad We_{\text{rel}} = \frac{\rho_g \left(u_g - u_l\right)^2 d_{\text{inj}}}{\sigma} \qquad r = \frac{\rho_l}{\rho_g}
\end{aligned}
\tag{5.1}
$$

Table 5.1: Nomenclature for resolved atomization simulations

$\Delta x_{\min}$ [μm]	Turbulence injection ?	**Operating condition**	
		Low We_g	High We_g
10	Yes	UG75_DX10	UG100_DX10
20	Yes	UG75_DX20	UG100_DX20
20	No	-	UG100_DX20_NT

Table 5.2: JICF operating points studied

Parameter	**Symbol**	**Units**	**Low Weber**	**High Weber**
Nozzle diameter	d_{inj}	mm	0.45	0.45
Gas bulk velocity	u_g	m s^{-1}	75	100
Gas flow rate	Q_g	m^3 s^{-1}	0.075	0.1
Liquid bulk velocity	u_l	m s^{-1}	17.5	23.33
Liquid flow rate	Q_l	mm^3 s^{-1}	2783	3710
Ambient pressure	p_{amb}	bar	6	6
Gas temperature	T_g	K	290	290
Liquid temperature	T_l	K	290	290
Gas density	ρ_g	kg m^{-3}	7.21	7.21
Liquid density	ρ_l	kg m^{-3}	795	795
Gas viscosity	μ_g	kg m^{-1} s^{-1}	$1.8162 \cdot 10^{-5}$	$1.8162 \cdot 10^{-5}$
Liquid viscosity	μ_l	kg m^{-1} s^{-1}	$1.5 \cdot 10^{-3}$	$1.5 \cdot 10^{-3}$
Surface tension	σ	kg s^{-2}	0.022	0.022
Momentum ratio	q	-	6	6
Gas Reynolds number	Re_g	-	$0.92 \cdot 10^6$	$1.22 \cdot 10^6$
Liquid Reynolds number	Re_l	-	4170	5560
Gas Weber number	We_g	-	830	1470
Liquid Weber number	We_l	-	5000	8850
Relative Weber number	We_{rel}	-	490	870
Aerodynamic Weber number	We_{aero}	-	45	80
Ohnesorge number	Oh	-	0.017	0.017
Density ratio	r	-	110	110

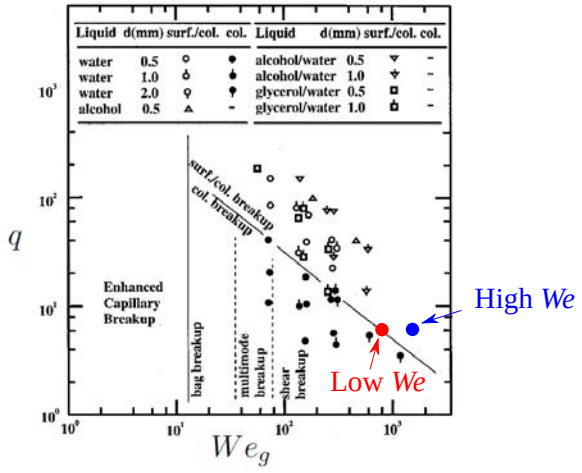

Figure 5.4: Location of simulated operating conditions in the breakup map by Wu et al. (1997)

5.5 Gaseous initial conditions

Prior to liquid injection, a gaseous field must be initialised in the computations. The objective is to obtain an established velocity profile that reproduces correctly the mean profile with a boundary layer thickness δ as observed in the experiments, which is reported to be between 4 and 5 mm (Becker & Hassa 2002). For this purpose, a mean profile is injected at the gaseous inlet shown in Figure 5.2 formed by the combination of a boundary layer and a flat outer profile. The details on this mean profile are given in Appendix A. Furthermore, the gaseous flow is turbulent, as shown by the high gaseous Reynolds number ($>> 10^4$) in the operating points studied (see Table 5.2). Therefore, synthetic turbulence is also injected at the gaseous inlet, hence a random fluctuating velocity component is added to the mean profile. This turbulence requires then a cell size that allows its transport in the mesh. For this purpose, a mesh independence study was performed, from which a mesh resolution $\Delta x = 0.5$ mm from the gaseous inlet until the liquid injection nozzle is chosen. This element size allows for a proper turbulent transport (frequencies and energy content) with a moderable cost. Details on the injection of synthetic turbulence and the mesh independence study are discussed in Appendix B.

Figure 5.5 shows the profiles for gaseous mean axial velocity $\overline{u}$ and Turbulent Kinetic Energy (TKE), calculated as $TKE = \left(\overline{u'^2} + \overline{v'^2} + \overline{w'^2}\right)/2$, for both operating points. As shown, a boundary layer thickness of around 5 mm is captured, reflected in both the $\overline{u}$ and TKE profiles. This agrees with the values reported by Becker & Hassa (2002). Part of the liquid jet is immersed within the boundary layer, as illustrated in Figure 5.6 where the velocity profile is plotted alongside an instantaneous view of a liquid jet from a resolved simulation. Since the TKE values are large within the boundary layer as shown in Figure 5.5b, it is probable that turbulence from the boundary layer plays a role in the jet primary breakup.

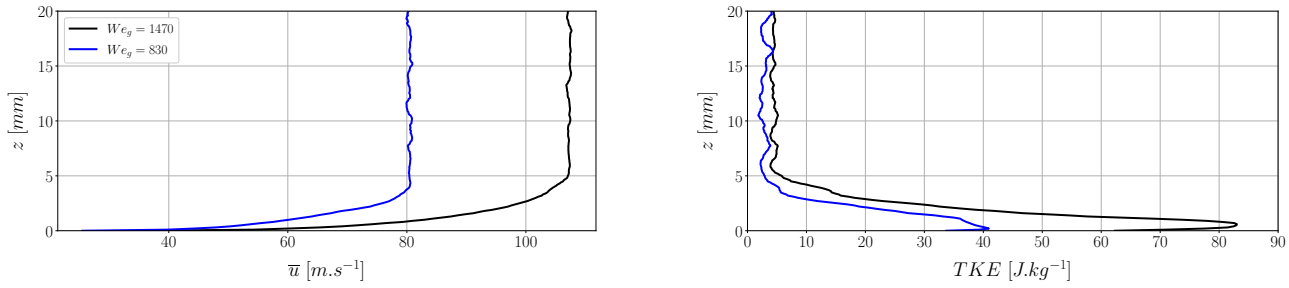

(a) Mean axial velocity

(b) Turbulent Kinetic Energy

Figure 5.5: Profiles of $\overline{u}$ and TKE along the line right upstream the injector for both operating points for mesh resolution $\Delta x_{\text{ups}} = 0.5$ mm.

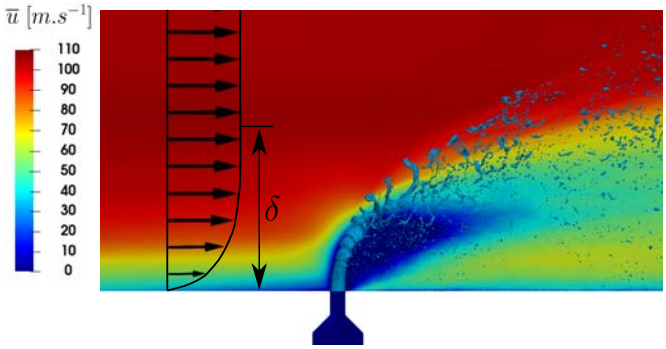

Figure 5.6: Instaneous JICF view with mean axial velocity field in symmetry plane $y = 0$. The vectors represent the velocity profile just upstream the injector, showing the boundary layer thickness $\delta = 5$ mm. The velocity profile has been displaced upstream in the picture for a better visualization.

5.6 Analysis of JICF simulations

This section reports and analyzes several physical features from the JICF configurations, including a validation with an experimental correlation for the jet's vertical trajectory (§5.6.3). The data here presented are of interest to verify the capability of resolved simulations for accurately capturing the physics and dynamics of atomization. The results from this section are, however, not directly used to construct a Smart Lagrangian Injector (SLI): for this purpose, §5.7 is entirely devoted to SLI building, and the interested reader is directly referred to this section.

5.6.1 Jet evolution

Figures 5.7 to 5.12 shows the evolution of the jet for all the simulations in three different view: lateral, front and top. The left column shows the thicker resolution, while the right column shows the finer one. The interface is represented by the iso-value $\psi = 0.5$. The snapshots correspond to the same time instants in all cases, which are expressed in dimensionless units with respect to the liquid inertia timescale τ_{in}:

$$t^* = \frac{t}{\tau_{\text{in}}} \tag{5.2}$$

with $\tau_{\text{in}} = d_{\text{inj}}/u_l$. This timescale is widely used in literature to express the establishment of liquid jets in crossflow (Herrmann et al. 2011). Applying this formula to each operating condition results in values of $\tau_{\text{in}} = 25.72$ and 19.29 μs for the low and high Weber cases, respectively. Since the values for τ_{in} are different for both operating points, the absolute times from injection are not the same for each condition. However, due to the different injection velocities in each case, the introduction of the timescale t^* allows for a proper comparison among jets from different operating conditions.

The lateral view of the jets show that the jet leaves the nozzle in the vertical direction and then bends towards the crossflow. For both operating points and both resolutions, droplets are stripped off the sides of the liquid column shortly after injection (surface breakup) and are convected downstream the crossflow direction. The finer resolution shows more droplets generated by surface breakup than the coarse one. Further downstream, the jet is deformed due to the crossflow impact and momentum exchange, leading to the breakup of the liquid column into big ligaments (column breakup). It is also noticeable in the instantaneous snapshots of Figures 5.7 and 5.10 that the jet vertical trajectory differs with resolution: fine simulations penetrate further vertically than the coarse ones. This is due to the resolution of instabilities, since the ligaments generated in the fine simulation contain more inertia and therefore will travel further than the ones generated in the coarse mesh. The resulting trajectories are quantifed and compared later in §5.6.3, confirming these observations from the qualitative figures. It is also worth to mention that resulting trajectories are not dependent on the operating point simulations (for identical mesh resolutions), which is in line with the experimental observations (see Table 1.1) since the momentum flux ratio $q = 6$ is identical for both simulations and trajectories are believed to be solely dependent on this factor.

Front views of the jets are shown in Figures 5.8, 5.11 for each operating point, while the top views are seen in 5.9, 5.12. The front views show clearly the windward instabilities in the fine case, which extend along all the width of the liquid column. These ones are generated right at the vicinity of the injector, observed through the corrugations at these region which are developed and amplified further downstrea. The top views show the lateral opening of the jet along the crossflow direction: the fine jets show a wider dense core than the coarse ones (a quantitative analysis on the dense core topology is later provided in§5.7.1), and the subsequent spray formed after atomization presents also a larger span in the lateral direction for the former than for the latter.

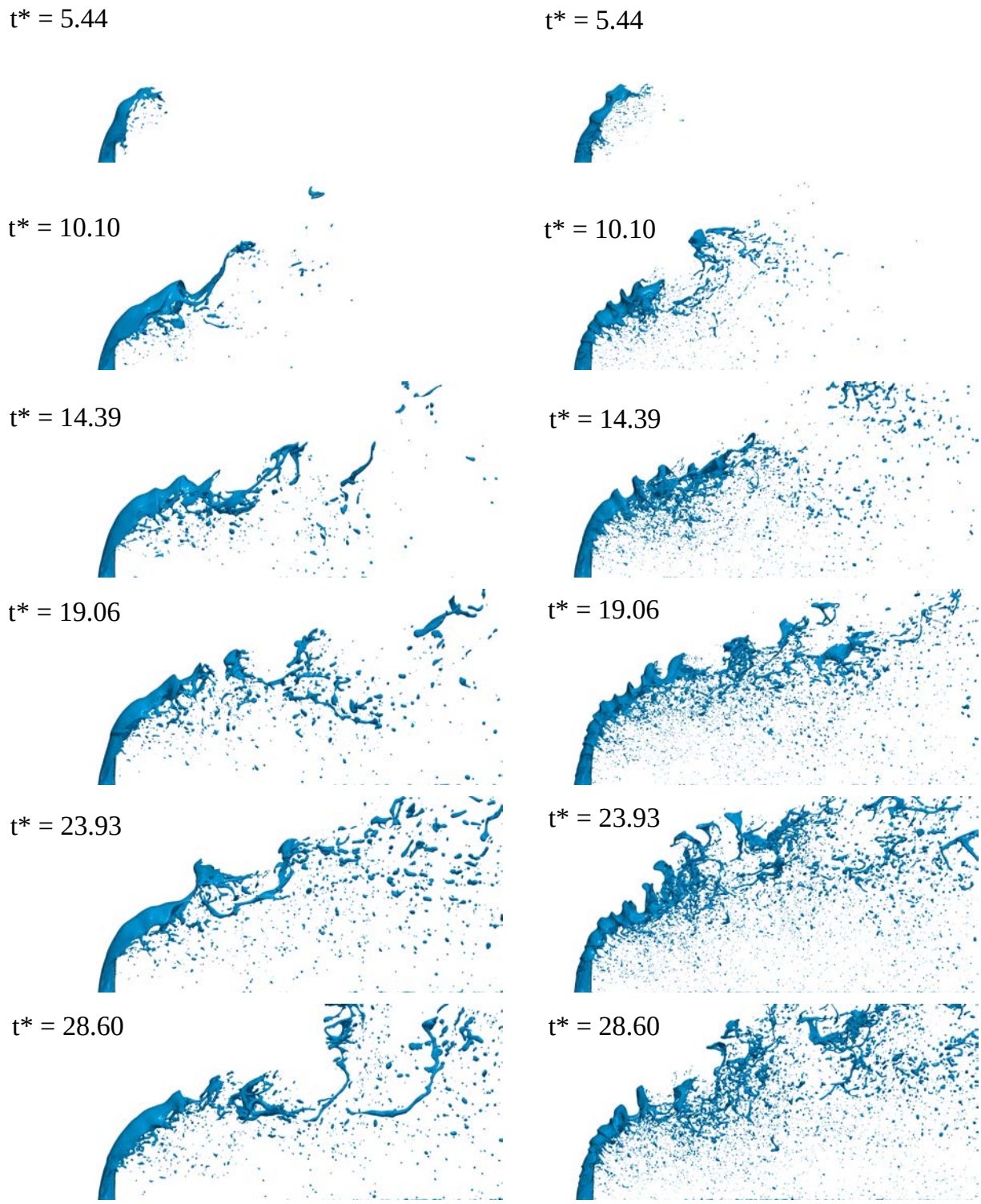

Figure 5.7: Lateral view of high We jet at several time instants. *Left*: UG100_DX20. *Right*: UG100_DX10.

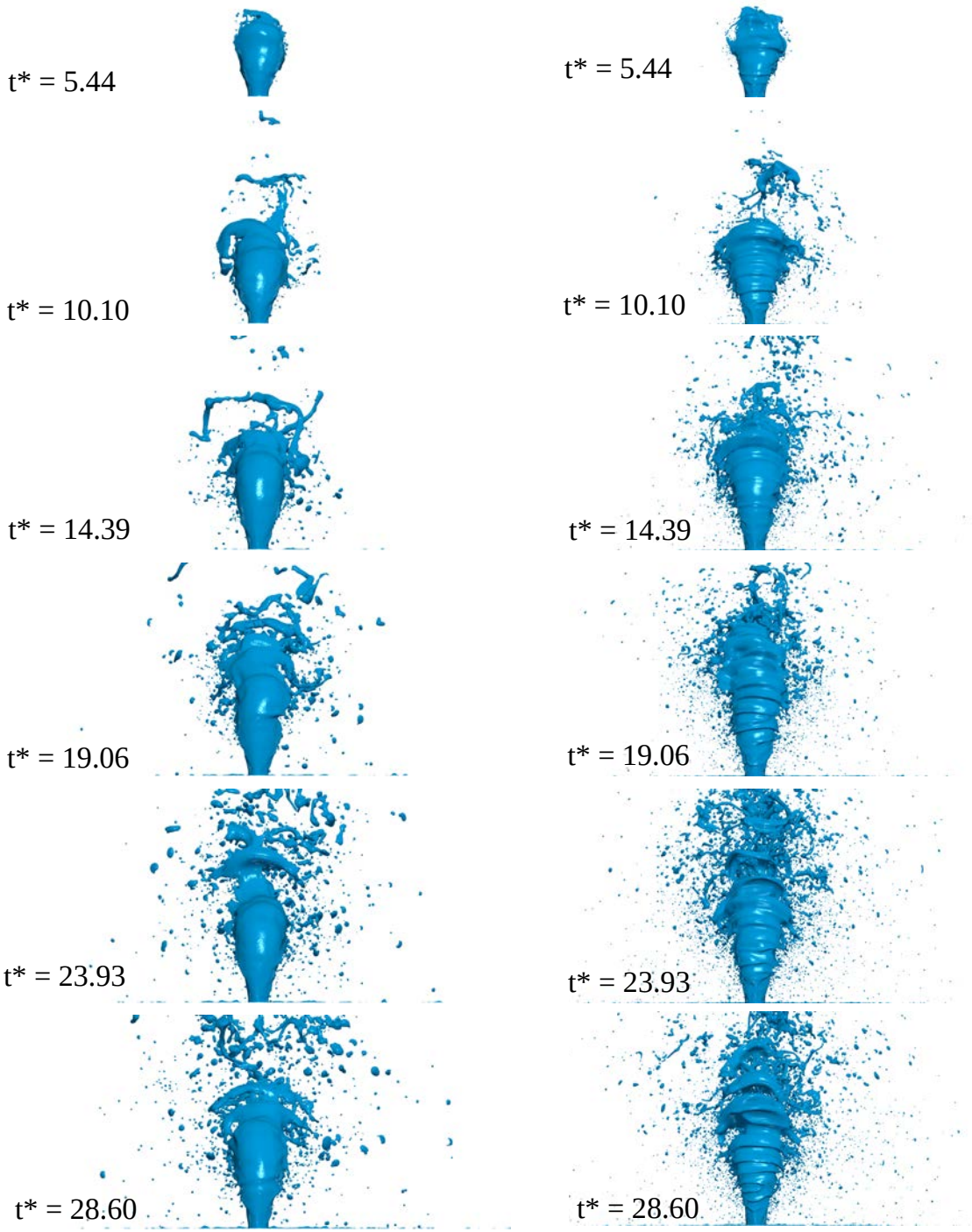

Figure 5.8: Front view of high We jet at several time instants. *Left*: UG100_DX20. *Right*: UG100_DX10.

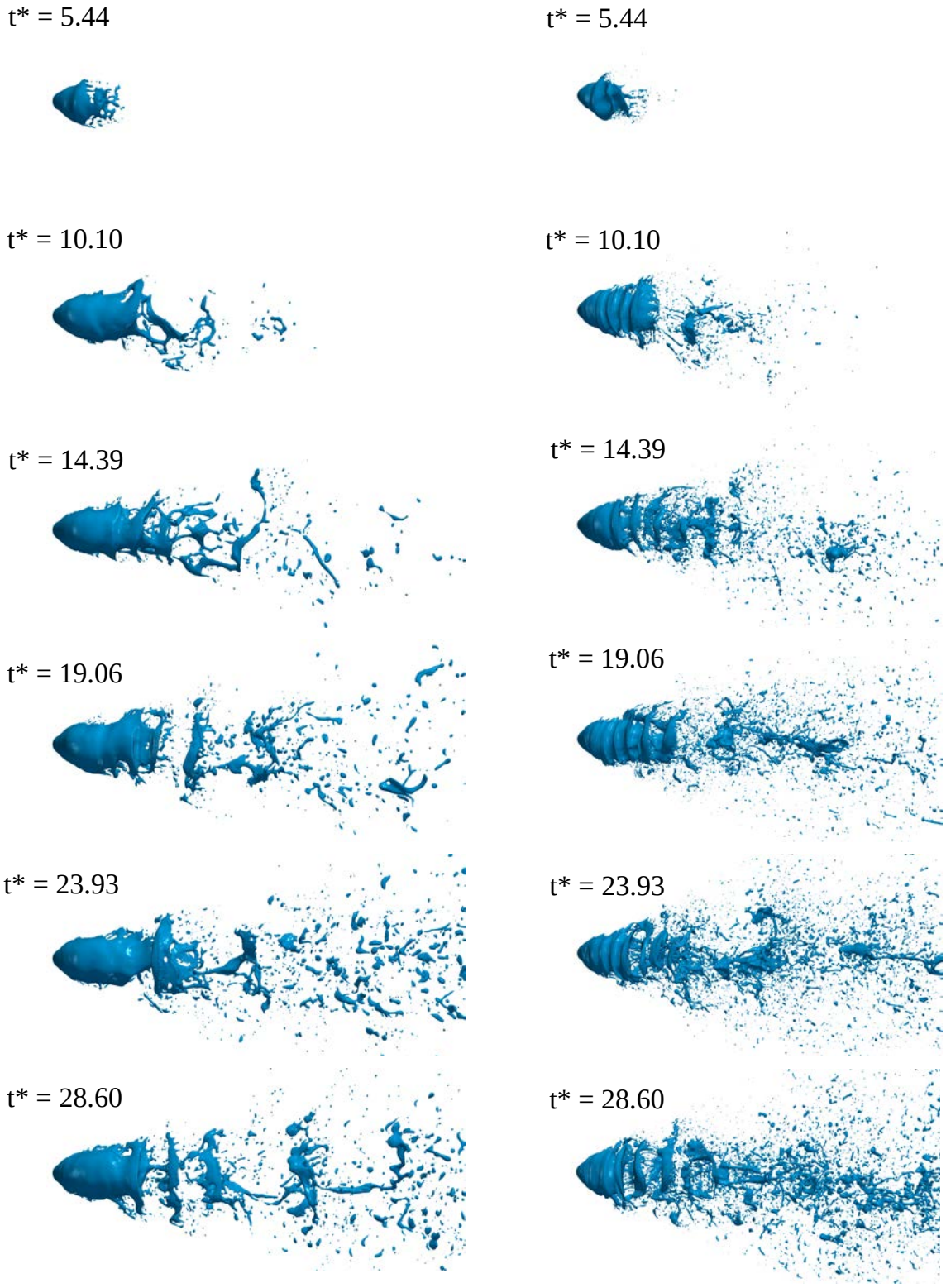

Figure 5.9: Top view of high We jet at several time instants. *Left*: UG100_DX20. *Right*: UG100_DX10.

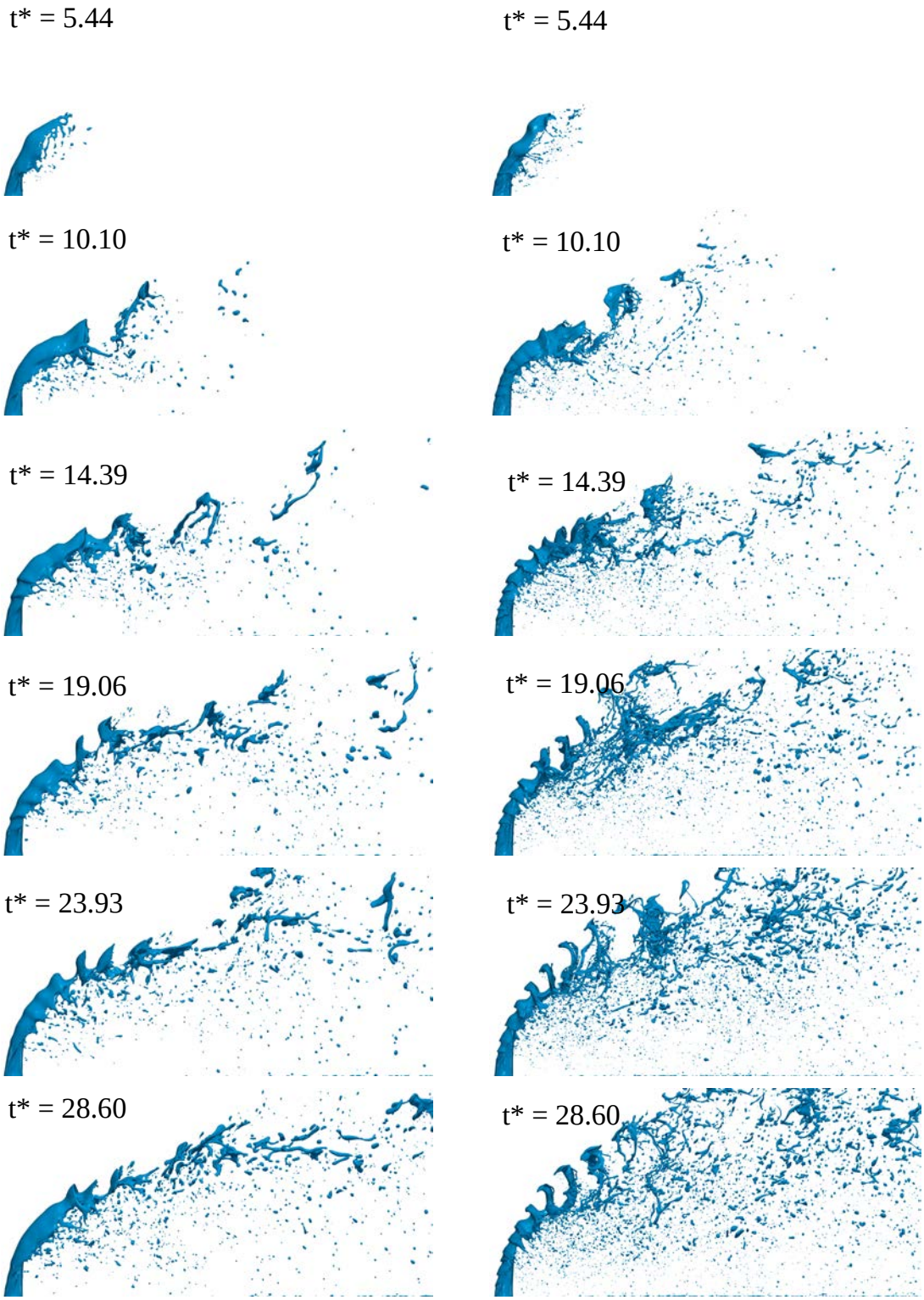

Figure 5.10: Lateral view of low We jet at several time instants. *Left*: UG75_DX20. *Right*: UG75_DX10.

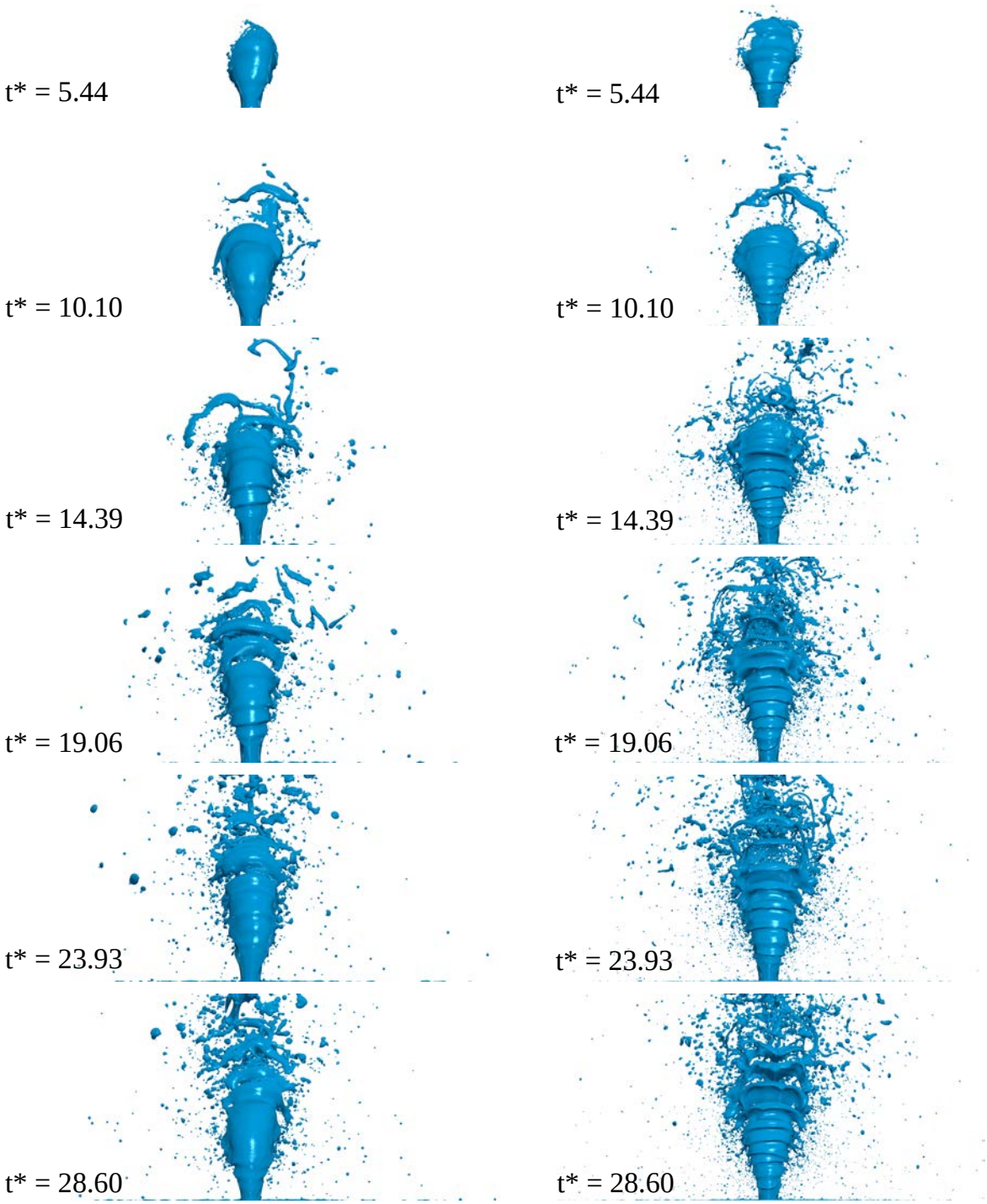

Figure 5.11: Front view of low We jet at several time instants. *Left*: UG75_DX20. *Right*: UG75_DX10.

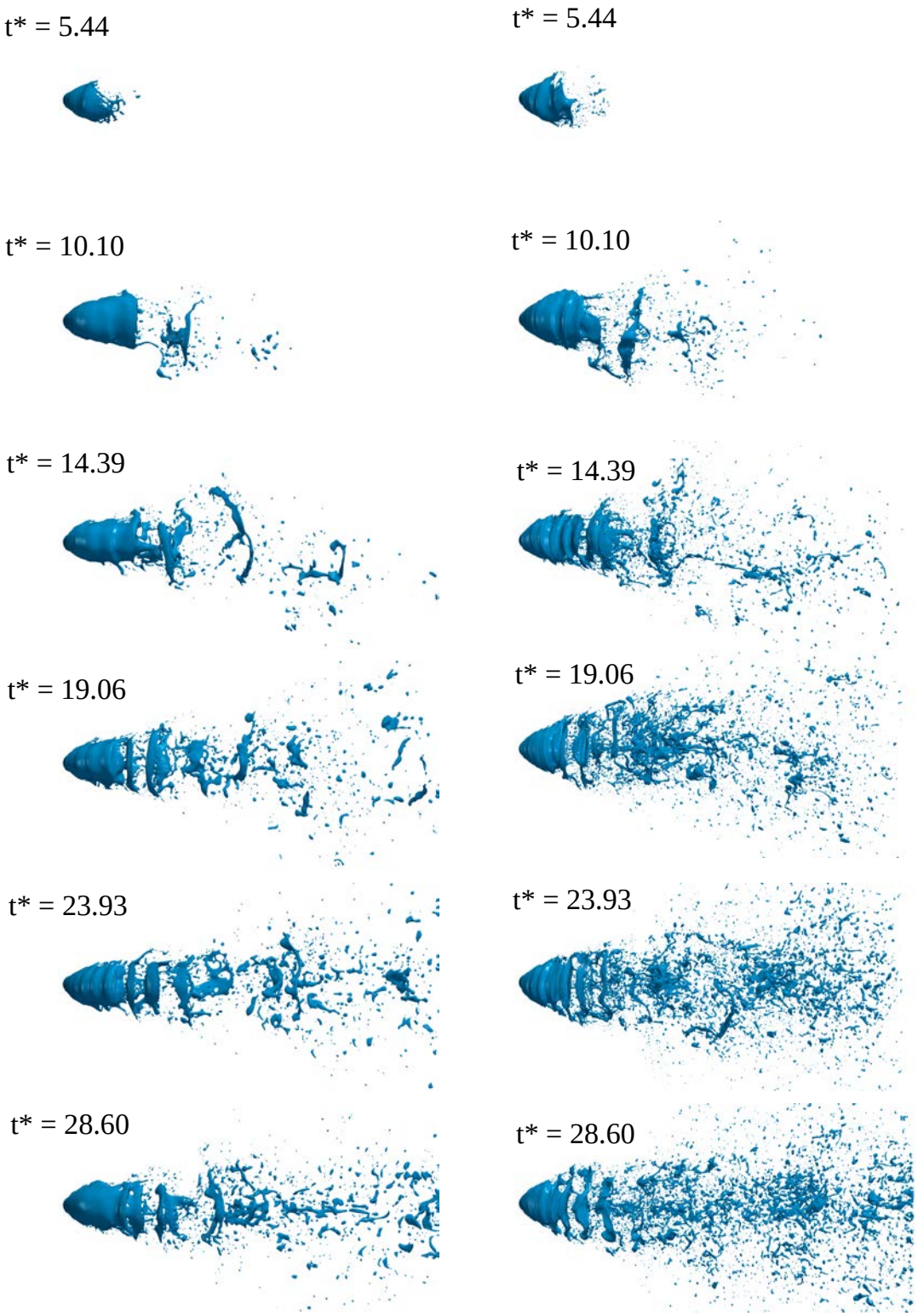

Figure 5.12: Top view of low We jet at several time instants. *Left*: UG75_DX20. *Right*: UG75_DX10.

Liquid establishment

At the early instants of the injection process, the quantity of liquid in the domain increases with time. Then, the jet reaches the axial location where liquid is suppressed to avoid transporting droplets further downstream and hence reducing computational resources (sponge layer): from this time instant onwards, the liquid quantity in the domain remains at a constant value, and the jet is considered to be established. Since dynamic mesh adaptation is used to locate the smallest mesh elements in the liquid-gas interface (as explained in §2.3.4), the mesh size increases with time as the interface surface within the domain is larger. An example of different meshes produced by each interface resolution is shown in Figure 5.13. The physical time instant is the same for both simulations, corresponding to early injection. A cut of the mesh in the plane $y = 0$ is depicted, which shows how the regions where there is liquid contain much more elements than those which do not. The fine jet also shows liquid droplets further downstream that are not generated in the coarse one, hence there are refined spatial regions in the former that are not observed in the later.

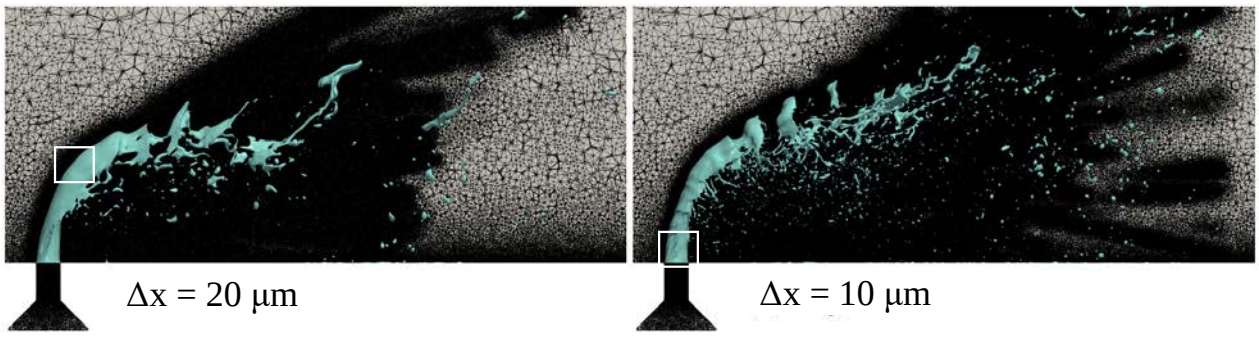

Figure 5.13: Lateral view of meshes and interface contours near the injector at instant $t^* = 16$ for the high Weber operating condition. *Left*: simulation UG100_DX20. *Right*: simulation UG100_DX10. Zoomed-in views of the rectangles are given in Figure 5.18.

To illustrate a qualitative evolution with time of different quantities, the dimensionless time t' is used:

$$t' = \frac{t}{\tau_{\mathrm{dr_{x=10}}}} \tag{5.3}$$

where $\tau_{\mathrm{dr_{x=10}}}$ is the arrival time of the first droplet to the sampling plane at $x = 10$ mm depicted in Figure 5.36. The plane $x = 10$ mm has been chosen because it is the last plane where liquid is sampled before being artificially removed in the fine simulations with $\Delta x_{\mathrm{min}} = 10$ μm, and is a sampling plane common to all simulations performed. Table 5.3 shows the droplets arrival times to the different sampling planes in all simulations, as well as the total physical time simulated (t_{ph}) and its corresponding dimensionless value calculated with Eq. (5.3).

Table 5.3: Droplet arrival times to sampling planes $\tau_{\mathrm{dr_x}}$, total physical time simulated t_{ph} and its dimensionless equivalent calculated with Eq. (5.3) in JICF simulations

Case	$\tau_{\mathrm{dr_x}}$ [μs]			t_{ph} [ms]	t'_{ph}
	$x = 5$ mm	$x = 10$ mm	$x = 15$ mm		
UG75_DX10	192.7	295.2	-	1.08	3.64
UG75_DX20	234.7	355.8	456.7	6.30	17.70
UG100_DX10	143.7	218.7	-	0.78	3.58
UG100_DX20	176.8	258.4	362.8	6.16	23.84
UG100_DX20_NT	167.9	260.2	-	6.10	23.44

In order to check the jet establishment in the domain, firstly the evolution of liquid volume with time is monitorded. This quantity can be obtained by integrating the level-set function ψ in all the domain at each time instant:

$$V_l\left(t\right) = \int_{\Omega} \psi\left(\mathbf{x}, t\right) d\mathbf{x} \tag{5.4}$$

The evolution of V_l for each simulation is shown in Figure 5.14. The volume increases linearly at the first instants in all cases, since the injected liquid flow rate is constant. As indicated in Table 5.2, flow rates are different for each operating point: nevertheless, the zoomed-in view shows that the slope of the t'-V_l is identical among resolutions, but differs among operating points. This is due to the timescales used to define t' from the physical time t: for identical operating condition, the first droplet to reach the sampling plane $x = 10$ mm arrives earlier in the fine case than in the coarse one. For identical resolutions, the droplets will reach the sampling plane earlier in the high Weber point than in the low one: as a consequence, the scaling balances out and the curves are overlapped in the linear region. Shortly after $t' = 1$ (times when the first droplet reach plane $x = 10$ mm), the simulations for which liquid is suppressed after this axial location stabilize towards a constant liquid volume (with variations due to the amount droplets being suppresed, which changes at each time instant). Case UG100_DX20_NT reaches convergence in liquid volume quantity, while cases UG75_DX10 and UG100_DX10 (fine resolution simulations) are on the verge of this liquid stabilizing value, showing that they have reached a steady state. They have not run longer due to their high computational cost (details provided in §5.6.6). Simulations for which liquid is suppressed further downstream at $x = 15$ mm (UG75_DX20, UG100_DX20) achieve a stabilized liquid volume larger than the other cases, and reach this establishment at a later time.

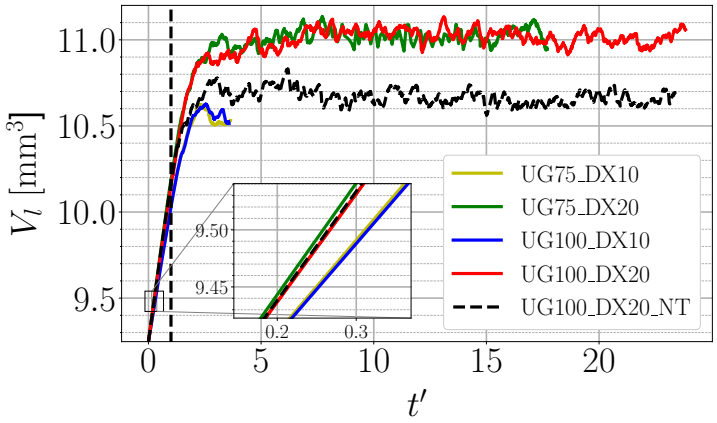

Figure 5.14: Evolution of liquid volume with time in JICF simulations. The dashed, black vertical line corresponds to $t' = 1$, time instant when the first droplet reaches the sampling plane $x = 10$ mm.

The evolution of mesh size with time, given by the number of mesh elements (N_{elements}), is shown in Figure 5.15 for all simulations. For the fine simulations, the final number of elements is larger than in the coarse ones despite liquid being suppressed further upstream. The contrast is notorious, differing by one order of magnitude: for instance, in the high Weber simulations the simulation UG100_DX20 contains $346{\cdot}10^6$ elements while case UG100_DX10 ends at $1815{\cdot}10^6$ elements. By looking at Figure 5.15a, one can see that the number of elements increases slowly at the beginning and then rises exponentially (linearly in the semi-logarithmic plot) until there's enough liquid in the domain and steady-state is reached. The first slow increase, which last for a short time, is associated to the increase of liquid volume due to jet injection prior to its fragmentation; the exponential increase is then associated to the creation of ligaments and droplets due to the atomization process, as the liquid-gas specific surface increases and therefore more elements are generated by the ARM process. Figure 5.15b reveals the transition from the slow increase to the exponential rise in N_{elements} to occur at $t \sim 0.3$ for the fine simulations and at $t \sim 0.5$ for the coarse ones, which agrees with the earlier atomization observed in the fine cases (see for instance Figure 5.7).

The dashed line in Figures 5.15a and 5.15b corresponds to $t' = 1$, which is the instant at which the sampling plane $x = 10$ mm detects the first droplet in each simulation. Figure 5.15b shows that this instant is located in the exponential region. Previously, there is no liquid being artificially removed in the simulations, so the curves increase monotonically (except for some minor decreases due to small droplets that reach the size of mesh resolution and disappear due to the unability of being further propagated in the simulations). After this point, the number of elements continues to increase exponentially up to $t' \sim 1.5$ when the slope starts to decrease and, finally, the number of elements stabilizes. Right after $t' \sim 1.5$ there is a considerable amount of liquid droplets reaching the articifial sponge layer and being removed. Nevertheless, at this stage there are more droplets being generated in the near-nozzle region due to the disturbance effect of the liquid

dense core to the air, which creates gaseous turbulence that helps to atomize ligaments ejected from the dense core. This explains the monotonic increase in the number of elements for $t' > 1$ prior to its establishment around a constant value, which depends on each simulation. The only noticeable difference at $t' = 1$ is for the simulation UG75_DX10, which shows an abrupt reduction. Two reasons might explain this decrease. First, there is not only one droplet, but several ones reaching the last sampling plane, hence these droplets are all simultaneously removed from the simulation. Since the mean diameter of the droplets generated in a liquid JICF is larger when the air dynamic pressure is lower (Becker & Hassa 2002), which is the case for the low Weber operating point, the droplets generated in this case are in general larger than for the high Weber case (this is later shown in §5.7.2), so all these droplets contain more elements than one single droplet from the case UG75_DX10 and the removed amount liquid is larger. The second hypothesis is that, at this time instant, several liquid structures with size comparable to the mesh resolution limit disappear simultaneously when transported to the next timestep (a discussion on droplets disappearing due to this numerical phenomenon is given in Appendix D), causing an overall decrease in the number of elements. The combination of both could also occur, which combined would induce a larger decrease in the number of elements than if every single one acts separately.

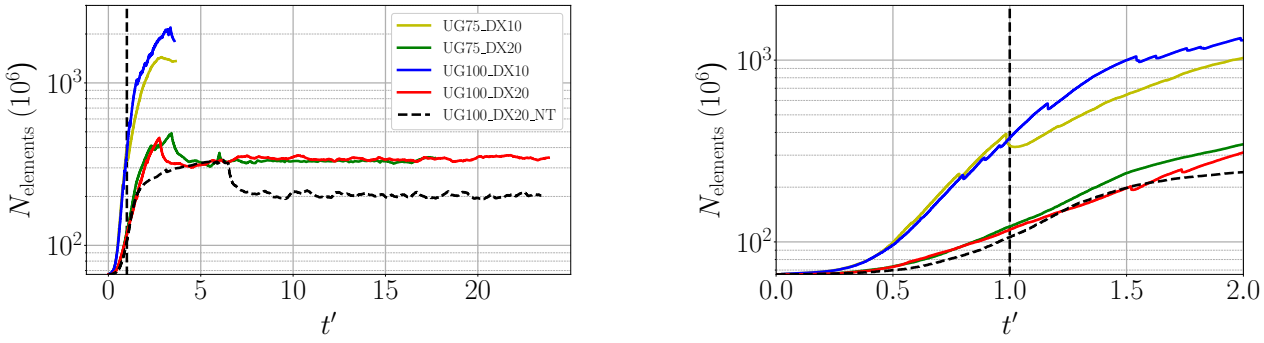

(a) Evolution in simulations

(b) Zoomed-in view of Figure 5.15a in range $t' \in [0, 2]$

Figure 5.15: Evolution of mesh size with time in JICF simulations. The dashed, black vertical line corresponds to $t' = 1$, time instant when the first droplet reaches the sampling plane $x = 10$ mm.

5.6.2 Breakup topology

In a liquid JICF, the most common primary atomization mechanisms are column and surface breakup (see §1.3 for a literature review on the topic). Both mechanisms are also identified in the resolved simulations performed. The **surface breakup** phenomenon is illustrated in Figure 5.16. Two regions are analyzed at the side of the jet: region A shows a zoomed-in view closer to the liquid injector, while region B details surface breakup taking place further downstream. Closer to the injector (region A), surface breakup is caused by lateral instabilities developed as a consequence of the strong shear force exerted by the incoming air, which forms corrugations at the surface (Behzad et al. 2016). Droplets generated in this region do not undergo further breakup since they are very small (see the green and red ellipses, which follow the droplets generated from the corrugations) and, often, of the order of mesh resolution: most of these droplets will disappear when the levelset function is transported in the simulations. This issue is discussed later in §5.6.5. Further downstream (region B), the jet is more deformed and surface breakup generates ligaments that separate from the main core and then undergo classical atomization: enclosed in red, the formation process of a ligament and its breakup into three smaller, different ligaments is depicted. As shown, this process forms liquid structures which are not spherical and can undergo further atomization, even though this one still occurs close to the jet dense core and the formed structures will be in equilibrium with the ambient gas shortly afterwards.

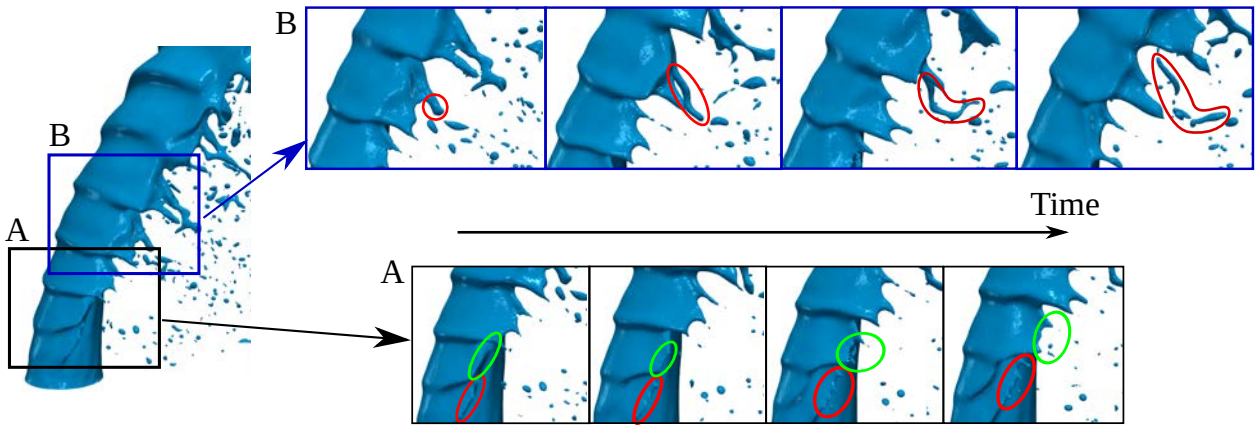

Figure 5.16: Surface breakup observed in case UG75_DX10

Column breakup is depicted in Figure 5.17, where cases UG100_DX20 and UG100_DX10 are shown. Jets are colored by vertical velocity w. This atomization mechanism is mainly caused by the instabilities developed in the windward side of the jet, which are highly dependent on the mesh resolution employed: simulations with the coarse resolution of $\Delta x_{\text{min}} = 20$ μm do not show instabilites until the column is highly deformed far from the injector. On the contrary, the fine resolution $\Delta x_{\text{min}} = 10$ μm resolves windward instabilities closer to the injector: these ones are propagated downstream the jet leading to its breakup. Coarse simulations do not show instabilities close to the injector, but eventually develop interfacial waves further downstream leading also to column breakup. In the fine case, instabilities are formed at the outlet of the liquid nozzle and amplified along the liquid column. Further downstream, they form sheets which are pushed by the air. The red ellipse encloses one of these sheets and follows it with time until it breaks: the sheet starts to separate from the dense core in its central region and forms tiny ligaments that break into small droplets while keeping an annular ligament with high velocity attached to the dense core by its edges. This ligament eventually separates and breaks into smaller ligaments that will continue to undergo atomization further downstream. The coarse simulation shows no instabilities at the beginning of the column, but similar topology of the produced ligaments. Ligaments from the fine simulation have a higher vertical velocity than in the coarse one. As a consequence, the liquid structures in the fine case will penetrate further, which will affect the sprays sampled further downstream. The mean trajectories from the jets, which are discussed in §5.6.3, will also reveal the difference in jet penetration with resolution.

Resolution of instabilities

As aforementioned, surface instabilities are present in the jet's windward side for the fine resolution but not for the coarse one. This can be clearly observed by looking at Figures 5.7 to 5.12. Previous works on resolved simulations of liquid-gas interfaces in injectors have also shown a dependency of the instabilities with the mesh resolution, such as the compound nozzle of Cousin et al. (2012). In this section, some possible causes of the development of windward instabilities are investigated and discussed. Three main hypothesis are thought to play a role in the formation of instabilities:

1. The smallest wavelengths are of the order of the mesh resolution and can be resolved by the fine mesh, but not with the coarse one.

2. The **liquid turbulence** within the nozzle is affected by the interface resolution, causing instabilities for the fine case but not for the coarse one.

3. The **gaseous field** outside the nozzle is affected by the interface resolution, causing instabilities for the fine case but not for the coarse one.

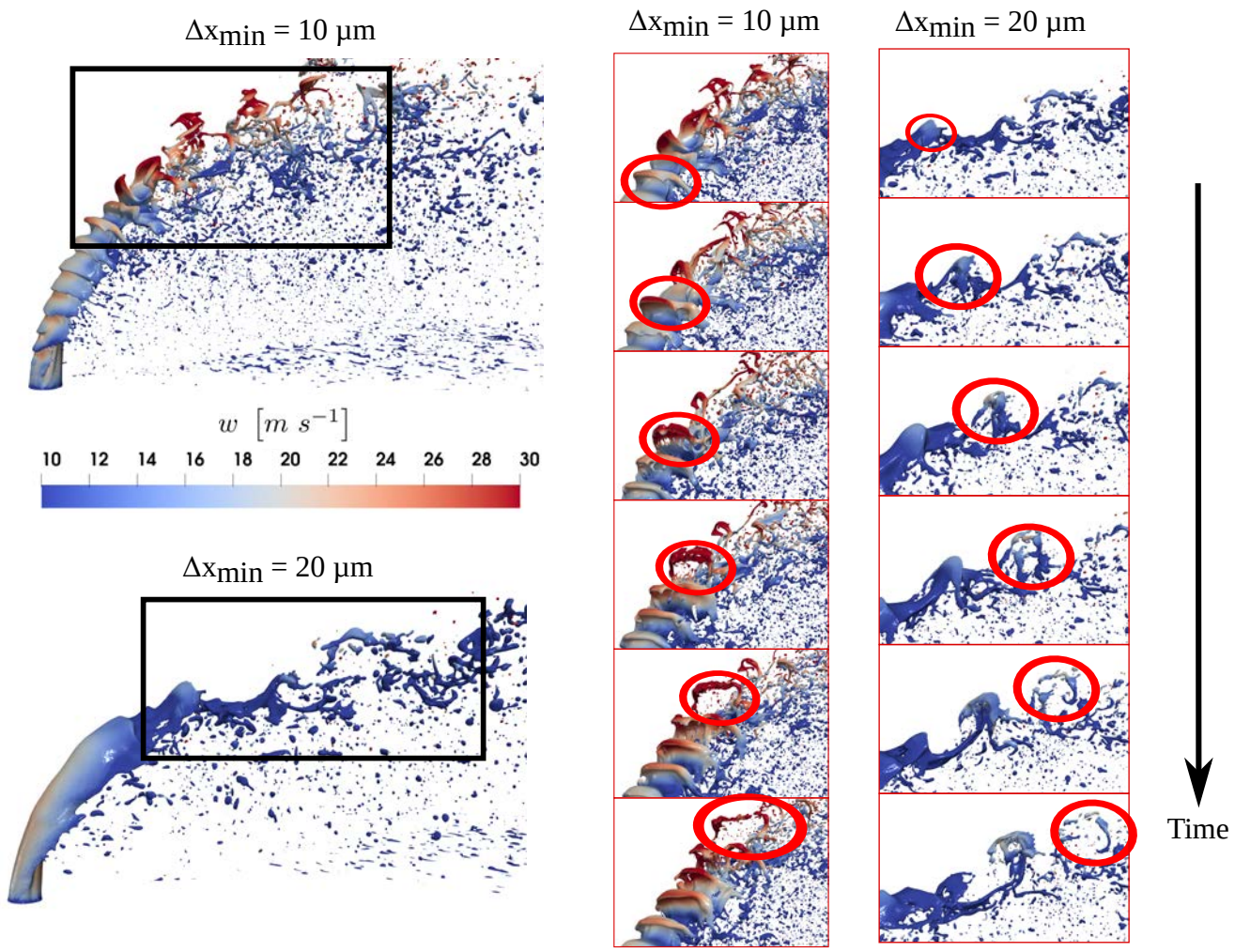

Figure 5.17: Column breakup phenomenon in cases UG100_DX10, UG100_DX20

1) Size of smallest wavelengths

The first hypothesis to be tested for clarifying why the coarse mesh does not resolve these liquid disturbances is that this resolution ($\Delta x_{\text{min}} = 20$ μm) is not fine enough to capture the wavelenghts. To assess this, instantaneous views of the mesh and liquid-gas interface in the plane $y = 0$ mm are shown in Figure 5.18. The spatial domain corresponds to the white rectangles of Figure 5.13. The instability in the coarse mesh is visualized downstream the jet since it is where waves start appearing, while the fine resolution captures the first instabilities evolving in the vicinity of the injector. In both cases, instabilities are present in the windward size of the jet, λ being the size of the shortest wavelengths (i.e. the first instability developed along the jet interface). The measured wavelength is $\lambda \approx 400$ μm for the coarse resolution $\Delta x_{\text{min}} = 20$ μm, which yields a ratio $\lambda/\Delta x_{\text{min}} = 20$. In the case of the fine resolution $\Delta x_{\text{min}} = 10$ μm, the measured instability is $\lambda \approx 160$ μm, corresponding to $\lambda/\Delta x_{\text{min}} = 16$. According to Pairetti et al. (2020), waves can be resolved with at least 4 mesh elements, i.e. $\lambda/\Delta x_{\text{min}} = 4$, so the instabilities are properly resolved in both cases. Indeed, the smallest instability in the fine simulation could also be resolved in the coarse one, since in this case the ratio would be $\lambda/\Delta x_{\text{min}} = 160/20 = 8$. Therefore, the coarse mesh is thin enough to capture the smallest instabilities, and the first hypothesis does not hold true.

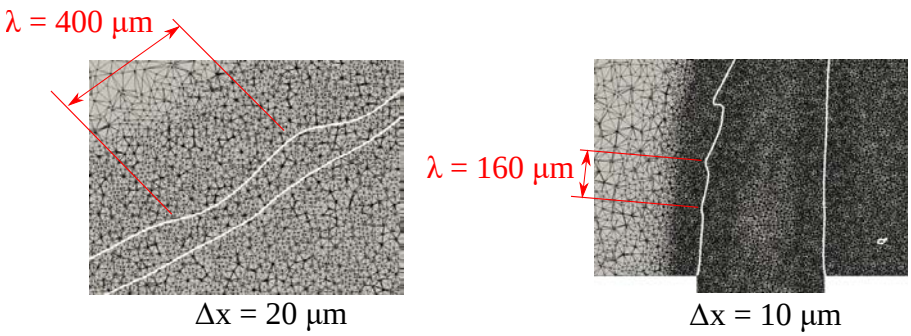

Figure 5.18: Resolution of instabilities at windward side of JICF for both resolutions in the high Weber operating point. The domain depicted corresponds to the white rectangles in Figure 5.13.

2) Liquid turbulence in nozzle

From previous studies, it is believed that the formation of instabilities in injectors is caused by the turbulence within the injection nozzle. This holds in both two-phase problems involving liquid injectors (Wu et al. 1994, Xiao et al. 2014) and in single-phase, mixing problems where one gaseous species is injected into a plenum containing a different gas, such as in gaseous jets in crossflow (Kelso et al. 1996, Karagozian 2014). Wu et al. (1994) studied experimentally a round liquid jet in which they suppressed the boundary layer at the injector exit, finding that interface instabilities are reduced in such case. They concluded then that "*boundary layer effects, such as vorticity or variations of mean velocities from viscous effects, play a dominant role in primary breakup* (sic)".

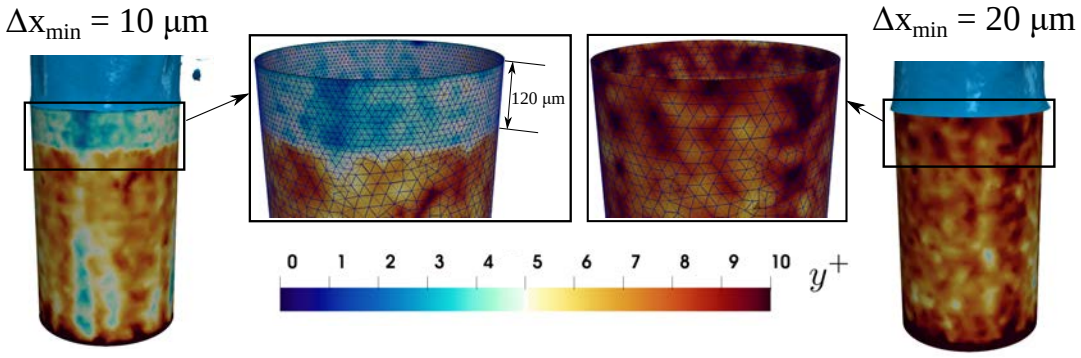

Figure 5.19: y^+ distribution in the nozzle walls for high Weber cases

A view of the nozzle for the high Weber case colored by the dimensionless wall distance $y^+ = y/u_\tau/\mu$, where y is the distance normal to the wall and u_τ the friction velocity, is displayed in Figure 5.19. Both fine and coarse resolutions are shown. The y^+ is a scalar magnitude representing the dimensionless distance from the first cell to the wall, and indicates the level of resolution in the vicinity of the walls: high values ($y^+ > 12$) mean that the boundary layer is poorly resolved and wall functions are needed as boundary conditions, while low values denote good resolution and wall laws can be avoided (Pope 2000). Figure 5.19 shows the y^+ distribution to be low in both nozzles. The PDF of the y^+ at the injector walls for both cases is plotted in Figure 5.20: its magnitude is always lower than 15, hence the wall is properly resolved in both cases and no wall functions are needed, which justifies the choice of non-slip wall boundary condition as indicated in Figure 5.2. The coarse resolution shows the smallest y^+ to be around 4, while the fine one displays values close to 1 and a higher presence of elements with y^+ between 1 and 5. A zoomed-in view of this section in Figure 5.19 shows that the cell is finer in a region spanning 120 μm upstream the nozzle exit: here, the mesh size is 10 μm for the fine case while the coarse simulation contains elements with 20 μm cell size. The reason is that the levelset band has been set to 12 cells from the liquid interface, and the interface is attached to the nozzle edges at the exit of the injector: the refinement extends then up to 12 cells upstream the injection point, creating a region of 120 μm with cells of 10 μm size. For the coarse case, the same applies but with a cell size of 20 μm (and therefore a refinement region of 240 μm length). As a consequence, the y^+ values

are low in the end section of the nozzle for the fine case, yielding cells with $y^+ < 5$ (an $y^+ < 5$ indicates that the viscous sublayer, which is the closest part of the boundary layer close to the wall, is resolved) as shown by the PDF of Figure 5.20 which are not captured by the coarse case.

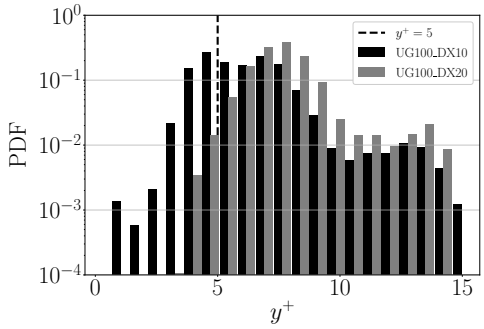

Figure 5.20: PDF of y^+ at the nozzle walls for high Weber cases

A cut on the $y = 0$ plane with a view on the nozzle region is displayed in Figure 5.21. For $x < 0$ the element size field Δx in the fine resolution simulation is shown, while the coarse one is displayed for $x > 0$. The interface outside the injector is highlighted by the white contour, and the band limits are denoted by the black contour. The metric within the band is smaller for the fine resolution, which is straightforward since this is the region with imposed Δx_{min}. The band attaches inside the injector and refines the wall in this region, producing a better wall resolution for the fine simulation as it was shown in Figure 5.19. Below the band reattachment location, the nozzle walls are not refined but the rest of the injector is, due to the transition from the cell size Δx_{min} to the baseline cell size (see Figure 2.7). The refinement is found to extend upstream the straight section of the injector: the fine simulation contains smaller elements that the coarse one in this region, while both meshes then show similar element sizes in the tapered section of the nozzle as shown by the zoomed-in region of Figure 5.21.

The improved resolution inside the last section of the nozzle as shown by Figure 5.21 might have an impact on the development of turbulence in this region. Further insight is given in Figure 5.22, where TKE is displayed in two planes perpendicular to the flow direction at two vertical locations: $z = -0.35$ mm (in the middle of the injector, outside the levelset band refined region) and $z = 0$ mm (the nozzle exit, where cells are refined within the levelset band). The TKE values are low at the center of the injector and high around the walls: in fact, the liquid Reynolds numbers Re_l in the operating points considered (see Table 5.2) indicate laminar flow within the injector, hence the freestream liquid flow does not transition into a turbulent state and the turbulent content is null at the center of the injector. TKE increases then at the walls due to the presence of the boundary layer. As observed in Figure 5.22, the coarse case displays low values of TKE with respect to the fine simulation, where $TKE \sim 1$ closer to the walls around all its azimuthal perimeter. The differences in the turbulent state are seen both at $z = 0$ mm and at $z = -0.35$ mm due to the nozzle refinement from the levelset band location up to the tapered section.

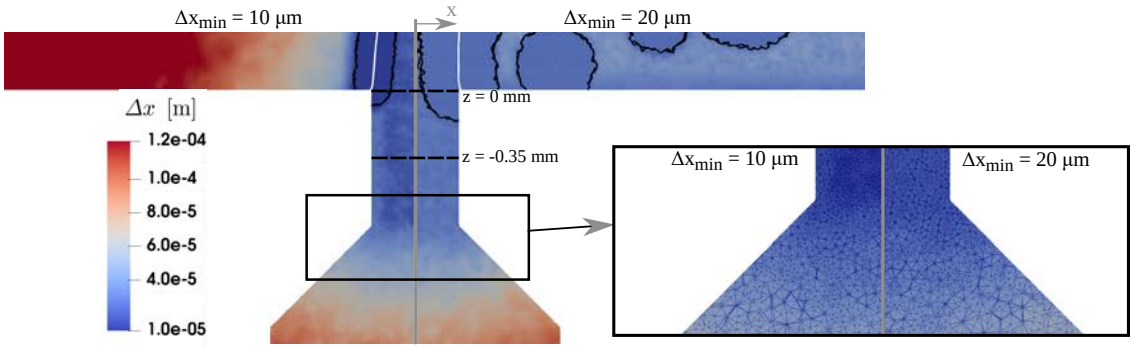

Figure 5.21: Mesh element size Δx shown at plane $y = 0$ for instantaneous simulations of cases UG100_DX10, UG100_DX20

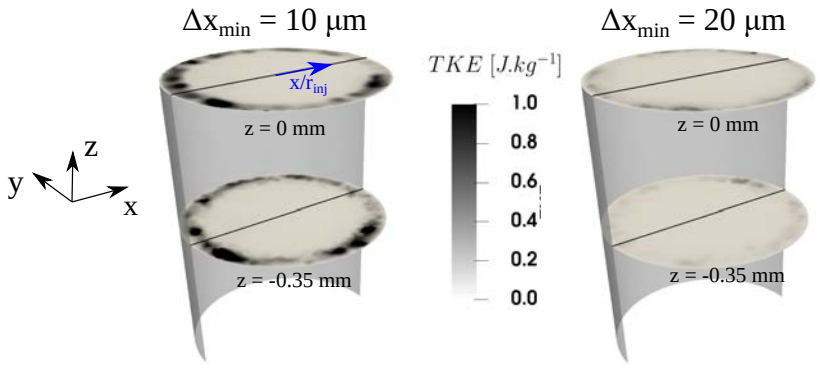

Figure 5.22: Planes within the injector showing TKE at locations $z = 0, -0.35$ mm for the high Weber case

The profiles of mean vertical velocity $\overline{w}$, TKE and mean vorticity magnitude $|\overline{\omega}|$ obtained at the black lines from Figure 5.22 are plotted in Figure 5.23. Due to symmetry, only the first half has been shown. The boundary layer thicknesses δ are obtained as the points where $\overline{w}$ decrease to 99 % of its value at the center ($x = 0$ mm). The $\overline{w}$ graph shows that δ and velocity profiles depend on the resolution $\Delta x_{\min}$ employed: the fine case shows a thinner boundary layer and a steeper $\overline{w}$ profile, specially at $z = 0$ mm. Both TKE and $|\overline{\omega}|$ profiles show higher contents within the boundary layer in the fine case: in the case of TKE, case UG100_DX20 shows a peak of 0.2 $J.kg^{-1}$ magnitude while case UG100_DX10 retrieves 0.57 $J.kg^{-1}$, which is almost three times larger. This higher liquid turbulent state within the injector for the fine resolution could cause the initial interface perturbations that develop into the surface instabilities observed in the fine case. Nevertheless, it is not clear whether the differences in the turbulent state are significant to trigger instabilities: even though there is a ratio of 3 between the maximum TKE found among resolutions, the relation $TKE/\left(0.5u_l^2\right)$ (i.e. TKE againt bulk liquid kinetic energy) is of 0.075 % for UG100_DX20 and of 0.2 % for UG100_DX10, while turbulent liquid jets where the turbulence within the injector is thought to create the instabilities (Xiao et al. 2013) yield ratios of the order of $TKE/\left(0.5u_l^2\right) \sim 2\%$ (Tretola et al. 2021). The ratio TKE - bulk kinetic energy found in this work is one order of magnitudes lower than the ratios reported in literature: this could mean that liquid turbulent fluctuations do not reach the threshold level to overcome surface tension forces, meaning that they would not be the cause of the instabilities (Lee et al. 2007). Nevertheless, this TKE threshold is not known (more research would be needed to ellucidate this value, as literature on the topic is scarce to the knowledge of the author) and such conclusion cannot be drawn from the analysis here presented.

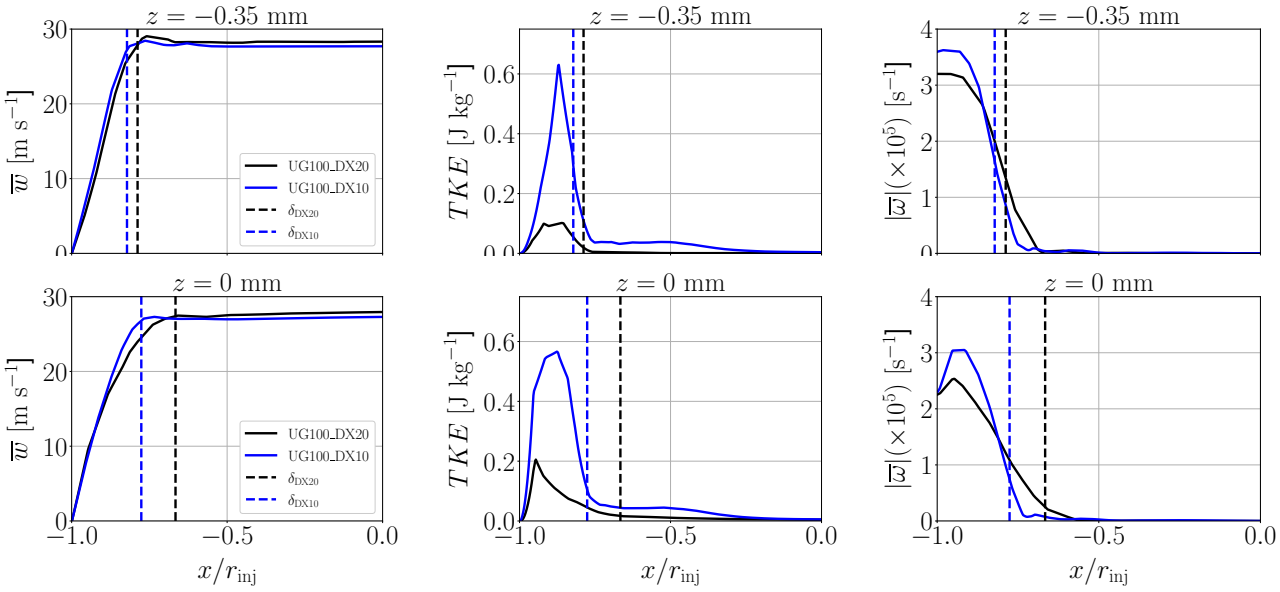

Figure 5.23: Profiles of mean vertical velocity, TKE and mean vorticity magnitude at lines located at $y = 0$ along the planes $z = -0.35,\ 0$ mm

3) Gaseous field perturbed by the jet

The third hypothesis on instabilities is that a finer cell size resolves better the gaseous field perturbed at the vicinity of the liquid interface. Indeed, the liquid conditions within the injector are laminar, and Xiao et al. (2013) suggested that for laminar jets the liquid turbulence does not play a paramount role (while it does for turbulent liquid conditions) and instabilities are instead triggered by shear caused by the incoming gaseous crossflow. The influences of the interface mesh resolution Δx_{min} on the gas phase are then examined in the following lines.

Instantaneous view of the jets and plane $y = 0$ mm from cases UG100_DX10 and UG100_DX20 colored by the vorticity magnitude are shown in Figure 5.24. The fine jet shows high vorticity regions along the interface due to the instabilities formed, as well as high vorticity in the bottom part of the jet at the windward side, which indicates the onset of the instabilities. The coarse jet does not display relevant vortical structures in the jet until column breakup starts taking place downstream the injection point. The zoomed-in views of the plane $y = 0$ close to the wall shows the streamlines and vorticity distribution in the gaseous field upstream the jet. Gaseous vorticity around the interface is much higher for the fine case: roll-up vortices, which are not seen in the coarse simulation, appear and disturb the interface, amplifying the instabilities (they might even be their cause, even though this cannot be fully ensured in this analysis). Horseshoe vortices, englobed by dashed red circles, are also observed at the wall upstream upstream the liquid injector. This vortex, which is a common feature in both gaseous (Kelso et al. 1996, Zhang & Yang 2017) and liquid (Zhou et al. 2020) JICF, is stronger for the coarse simulation and weaker for the fine one (despite the mesh at its location being identical in both simulations), even though it seems not to impose a significant perturbation on the gaseous streamlines, which are on the other hand perturbed by the roll-up vortices.

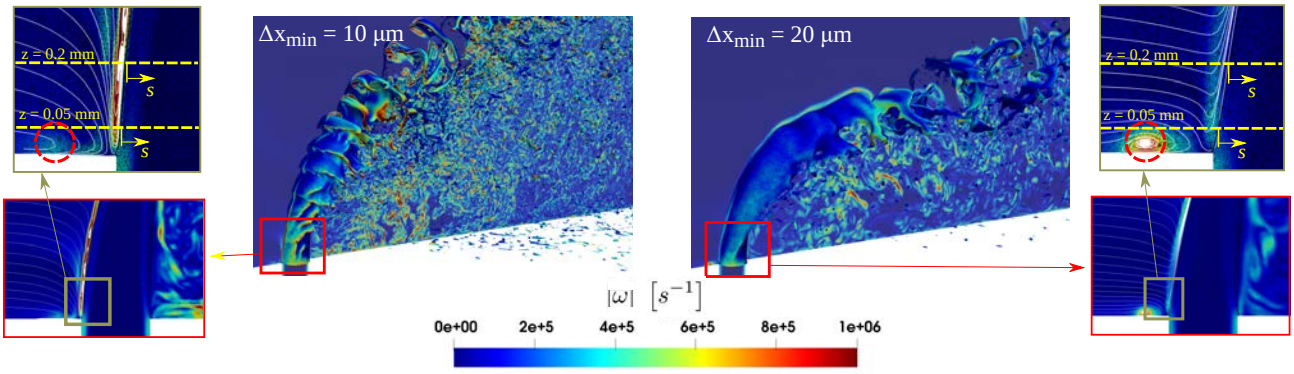

Figure 5.24: Instantaneous vorticity fields for the high Weber operating point. Streamlines are shown in the zoomed-in regions

The vertical velotity profiles along the yellow lines $z = 0.05, 0.2$ mm represented in Figure 5.24 are shown in Figure 5.25. The lines span along the x direction but a change of coordinate has been done to the axial coordinate $s = x - x_{\text{int}}$, where x_{int} is the location of the interface. Closer to the wall ($z = 0.05$ mm), the w profile shows slight differences among resolutions in the vicinity of the interface: the fine case retrieves higher velocity peaks in the liquid and gaseous regions, but still very close to the coarse one. In the liquid region ($s > 0$) the fine simulation reaches faster the freestrem liquid velocity than the coarse one due to a thinner, better resolved boundary layer than in the coarse simulation. In the gaseous phase the velocity profiles are distinct due to the different perturbation of the streamlines as shown in Figure 5.24: the fine case shows negative velocities until reaching the farfield value $w = 0$, while the coarse one presents negative values larger in absolute value than the fine case up to $s \sim -0.15$ mm and then sees a increase to positive values due to the higher perturbation induced by the stronger horseshoe vortex. When looking further from the wall, at $z = 0.2$ mm, the profiles show similar behaviour within the liquid region but significant differences in the gaseous phase: for the fine resolution, the vertical velocity drops quickly with decreasing s from its interface value to below $w = -20$ m s^{-1} and then relatex towards a freestream value close to 0, while the coarse one shows a less sharp gradient. The sharp gradient in the fine case is a possible source of shear force around the interface which can contribute to the development and amplification of the instabilities. Nevertheless, it is yet not clear whether this gradient is the cause of the instabilities, or it is actually caused by other factors such as the turbulence developed within the injector.

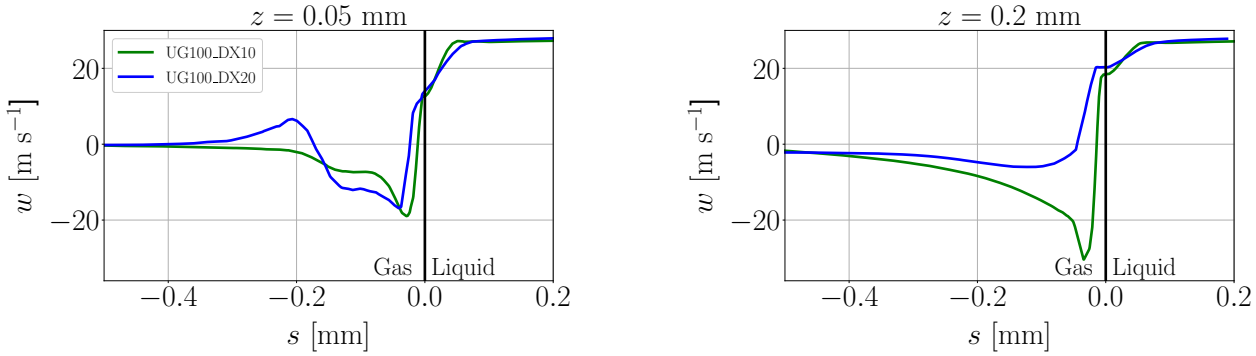

Figure 5.25: Vertical velocity profiles at yellow lines depicted in Figure 5.24. The black vertical line indicates the location of the interface: negative s values are located in the gas phase while positive ones are in the liquid phase

From the analysis performed in this section, it can be stated that refining the mesh at the interface has an effect on both the liquid phase within the injector and the gaseous phase upstream the injection point. Differences have been observed in the liquid nozzle, particularly in relation to the resolution of the boundary layer in the injector walls and the turbulent magnitudes TKE and vorticity: nevertheless, the differences might not be significant in absolute values to be the cause of the instabilities. A proper assessment of this statement should be done by comparing the obtained values with reference values from studies dealing with similar configurations and operating conditions, which are not present in literature nowadays to the knowledge of the authors. Observation of the gaseous phase has shown relevant differences among interface resolutions, particularly in relation to the appearance of vortical structures and shear layers around the interface which are directly linked to interfacial instabilities. However, it is not clear if these features in the gaseous field are the cause of the early development of the instabilities or a consequence of them: this one has been a fundamental question in the field of jets open for a long time (Rayleigh 1878) which requires further study.

5.6.3 Jet trajectories

One of the most important characteristics of a jet in crossflow is its vertical trajectory (see §1.3). This feature determines how far the jet penetrates into the chamber, and has a paramount effect on the latter evaporation and mixing processes, hence affecting flame dynamics in reactive cases. Experimental studies often provide correlations for the trajectory of the windward side of the jet (see Table 1.1). This is the side indicating the furthest vertical location (z) containing liquid for each axial location in crossflow direction (x).

In this section, trajectories from the resolved simulations are analyzed and compared with an experimental correlation. Four post-processing methods for obtaining trajectories are applied to one computation for illustrating their differences. Finally, one method is selected (based on its similarity with the experimental processing methodologies) for comparing the trajectories among simulations. The four methodologies employed (which are thoroughly detailed in Appendix C.1) are grouped into two different families, **mean trajectory methods** or **instantaneous trajectory methods**, according to whether they process the mean or instantaneous ψ field respectively:

- Methods based on processing and averaging **instantaneous trajectories** (hereafter referred as instantaneous methods). These retrieve, at each time instant, the windward contour of the jet by sweeping the z axis and identifying the points with $\psi = 0.5$ at the plane $y = 0$. This provides an instantaneous trajectory per timestep, which can eventually be averaged to provide mean trajectories. If when sweeping the vertical axis, only liquid points that produce an increasing trajectory of z with x are retrieved (rejecting points in the dispersed spray that belong to droplets downstream the windward side), the resulting trajectory is **monotonic**. If, on the other hand, points that produce a trajectory which does not increase continuously along the x axis are also sampled, then the trajectory is **non-monotonic** (see Appendix C.1 for a more graphical explanation).
- Methods based on the **mean levelset function** ($\overline{\psi}$). On one hand, trajectories can be obtained as the contour defining the maximum gradient of the $\overline{\psi}$ field in the vertical direction for each axial coordinate: $\max\left(\nabla_z|\overline{\psi}|\right)$. On the other hand, trajectories can be directly obtained as an **iso-contour** of the $\overline{\psi}$ function, where the contour chosen in this work is $\overline{\psi} = 0.01$.

Table 5.4 summarizes the nomenclature for the four trajectories postprocessing methods.

Table 5.4: Summary of methods for computing JICF trajectories

Group	Method	Nomenclature
Instantaneous	Non-monotonic	INST_NM
	Monotonic	INST_M
Mean	Maximum gradient	MEAN_GRAD
	Iso-contour	MEAN_CONT

The trajectories obtained from the computations are also compared to the experimental correlation obtained by Becker & Hassa (2002), given by the following expression.:

$$\frac{z}{d_{\text{inj}}} = 1.57\text{q}^{0.36} \ln\left(1 + 3.81\frac{x}{d_{\text{inj}}}\right) \tag{5.5}$$

which is valid for $1 < q < 12$, $90 < We_{\text{ae}} < 2120$ and $x/d_{\text{inj}} < 22$. For the simulations studied, $d_{\text{inj}} = 0.45$ mm and $q = 6$. The authors also present a standard deviation for the correlation of $\sigma = 0.81$. Numerical trajectories can be plotted together with Eq. (5.5) to provide a qualitative comparison of the computations. For further insight, a quantitative measure for the difference between simulations and experiments can be introduced through a L_2 norm:

$$L_2 = \sqrt{\frac{1}{N}\sum_{i=1}^{N}\left(\frac{z}{d_{\text{inj}}}\Big|_{\text{num},i} - \frac{z}{d_{\text{inj}}}\Big|_{\text{exp},i}\right)^2} \tag{5.6}$$

where N is the number of points along the abscissa x in which the difference between curves is evaluated and i refers to the i-th point. The subscript "num, i" indicates the mean value obtained from simulations for the vertical location at point i, while "exp, i" indicates the equivalent measure from experiments. From this definition it follows that the L_2 error is a measure of the deviation from experiments: the lower the L_2, the closer the simulation results are to the experimental ones. The L_2 error can also be monitored with time to determine the convergence evolution of the trajectories.

Results

In first place, the four methodologies are compared by applying them to simulation UG100_DX20, since this is the one that has run for longer physical time. The resulting trajectories are shown in Figure 5.26a. In the vicinity of the injector, all trajectories follow the same tendency up to $x/d_{\text{inj}} \sim 1$. After this point, two different tendencies are observed: mean ψ trajectories keep on following the experimental correlation, while instantaneous ones are located below. The different trends shown by the trajectories from both methodologies are due to their underlying definitions: instantaneous-averaged trajectories intend only to retrieve the outer contour of the jet, while the mean-based methods take the $\overline{\psi}$ field defined in all the domain and then obtain the trajectories at plane $y = 0$. The $\overline{\psi}$ field is diffused as opposed to the $\psi = 0.5$ contour retrieved by the instantaneous methods, so the trajectories obtained as max $\left(\nabla_z|\overline{\psi}|\right)$ (maximum gradient) and $\overline{\psi} = 0.01$ (contour) are located in the regions where $\overline{\psi}$ is close to 0 (i.e. where the mean presence of liquid is low). Consequently, trajectories penetrate further away than the instantaneous averaged ones in the near-injector region (coherent liquid) while they show the opposed tendency downstream after atomization has taken place (dispersed liquid)

The evolution of the L_2 norm calculated with Eq. (5.6) is shown in Figure 5.26b for all methods. The norm is calculated for two ranges in the x axis: $x/d_{\text{inj}} < 10$ and $x/d_{\text{inj}} < 20$. The former (reduced range) considers the trajectories closer to the injector before a full disperse spray is present, and all L_2 norms show convergence. The norms from the instantaneous trajectories show similar values since the trajectories for $x/d_{\text{inj}} < 10$ are always close. The mean field trajectories show noisier signals, with the case MEAN_CONT yielding the lowest errors. When considering the range $x/d_{\text{inj}} < 20$, the signals show different behaviours. Regarding the instantaneous-averaged trajectories, both show the same tendencies as in the reduced range, but with larger norms due to the divergence of both curves in the dispersed phase region. The trajectory

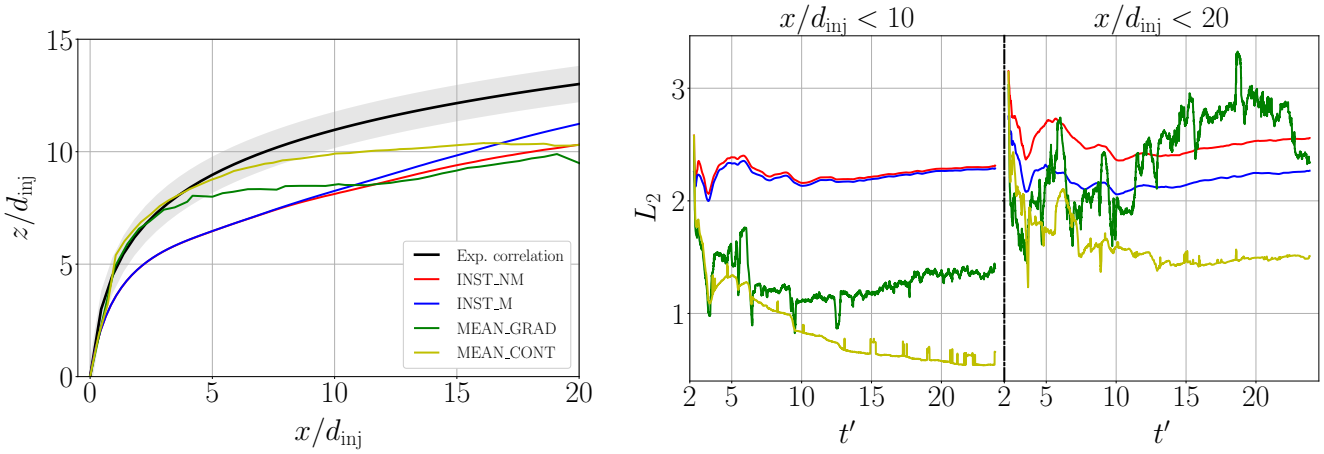

(a) Mean trajectories

(b) L_2 error evolution for two x/d_{inj} ranges

Figure 5.26: Trajectories and L_2 errors obtained with different methods for case UG100_DX20

from method MEAN_CONT shows also convergence in the norm, but with a larger value than for the reduced range. On the other hand, the signal from method MEAN_GRAD does not show convergence with time when the dispersed spray region is included. The reason is that the field $\nabla_z|\overline{\psi}|$ shows a very unstable behaviour with time in the dispersed spray, as opposed to the field $\overline{\psi}$. It is not sure whether this method will yield a converged L_2 if the simulation were run longer. The results from Figure 5.26 show the strong influence that the choice of postprocessing method can have on the resulting trajectory.

For validating experimentally the trajectories from the rest of the simulations, the method MEAN_GRAD is selected due to its similarity with the methodology followed by Becker & Hassa (2002) to obtain the experimental correlation. Results are shown in Figure 5.27 for both operating points, including the case for the high We number without synthetic turbulence injection. The evolution of the L_2 norm displayed has been obtained for the range $x/d_{\text{inj}} < 10$. Additionally, an error along the trajectory ε_i is also defined to indicate the trajectory's accuracy along the crossflow's direction x:

$$\varepsilon_i = \frac{z/d_{\text{inj}}\Big|_{\text{num},i} - z/d_{\text{inj}}\Big|_{\text{exp},i}}{z/d_{\text{inj}}\Big|_{\text{exp},i}} \tag{5.7}$$

Trajectories are shown in Figures 5.27a and b for both operating points. The first remarkable events are the dependence on mesh resolution for both operating points, and the differentiation of two regions with axial distance along the trajectories. From the graphs, the regions can be distinguished as follows:

1. A first near-injector region in which both resolutions coincide with the experimental correlation, showing no dependence on the mesh resolution. This regions extends up to $x/d_{\text{inj}} \sim 5$ for low We and to $x/d_{\text{inj}} \sim 4$ for high We. Here, the dense core is located and primary atomization takes place, resulting in an accurate trajectory prediction.

2. After the near-injector region, trajectories diverge and show different trends: the coarse simulation underestimates the experimental correlation, while the fine one continues within the confidence interval of the experiments until it surpasses it. This is the region where secondary atomization is forming droplets and a dispersed spray starts to be formed, hence mispredicting the experimental correlations.

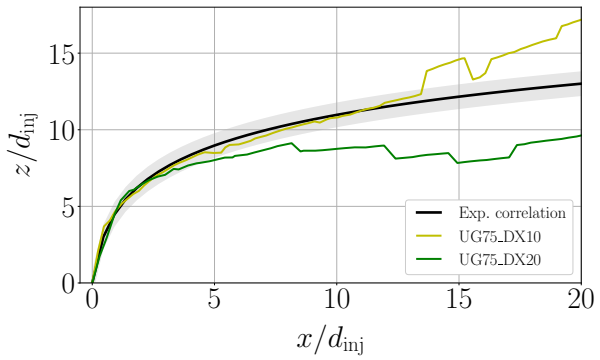

(a) Low We trajectories

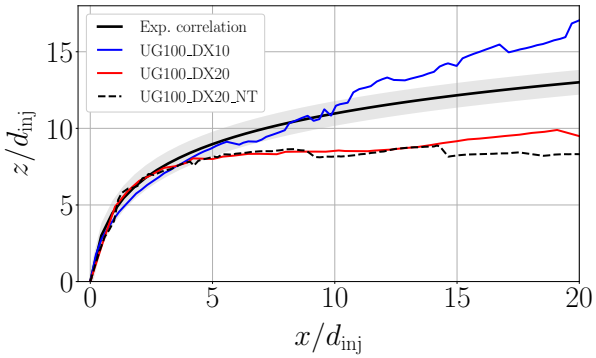

(b) High We trajectories

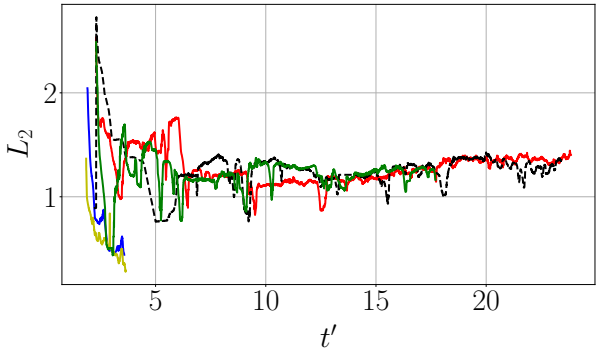

(c) Evolution of L_2 norms with time.

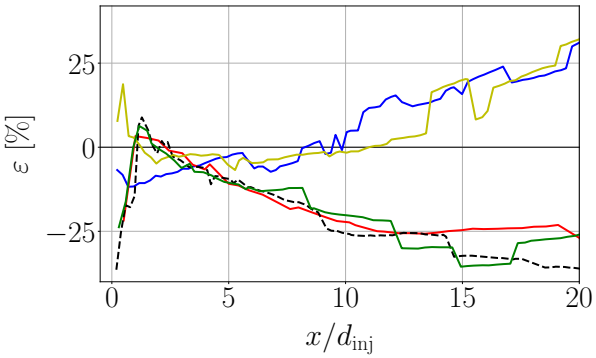

(d) Error ε along trajectory

Figure 5.27: Trajectories and errors obtained with method MEAN_GRAD

The reason why coarse simulations underestimate the trajectory further downstream, while the fine ones overestimate it, is the resolution of instabilities in the windward side of the jet (discussed previously in §5.6.2). Instabilities in the fine simulations create ligaments and droplets with high vertical velocities that penetrate further away than those generated in the coarse simulations. Consequently, their resulting trajectories penetrate further than the coarse ones and the experimental correlation after breakup occurs.

Regarding the effect of injecting turbulence at the gaseous inlet, the red lines of Figure 5.27b show that the mean trajectory is not affected when turbulence is added. The turbulence levels (as calculated in Appendix B) do not have an influence on the formation of instabilities for the case studied. Nevertheless, only the coarse resolution has been simulated without turbulence injection: further studies could include a simulation with a finer resolution in order to determine if the injected turbulence have an effect on the instabilities formed in the windward side of the column.

Figure 5.27c shows the L_2 norm evolution. The coarse cases show convergence while the fine ones are still fluctuating, yet they seem to stabilize (simulations should run longer to confirm this). The final values for the errors are summarized in Table 5.5, confirming that smaller deviations are obtained for fine resolutions. Finally, the relative error along the trajectory ε is displayed in Figure 5.27d. Negative values indicate underestimation of the experimental correlation, while positive ones indicate overestimation. In the vicinity of the injection nozzle ($x = 0$), errors are large because the denominator of Eq. (5.7) is small. Then, deviations are small in the near injector region and start to increase monotonically in absolute value further downstream. Fine simulations present positive erros since they overestimate the experimental correlation, while the coarse ones yield negative ones due to the underestimation. This graph is useful to get an idea on the error commited in the vertical boundary of the spray when placing an SLI. For instance, if an injector is placed at $x = 5$ mm ($x/d_{\text{inj}} \sim 11$), an SLI obtained from the fine resolution would yield low errors (~ 0 % for UG75_DX10 and ~ 10 % for UG100_DX10), but very high ones for a coarse injector (~ -25 %).

Table 5.5: L_2 errors for JICF simulations performed.

Case	UG75_DX10	UG75_DX20	UG100_DX10	UG100_DX20	UG100_DX20_NT
L_2	0.29	1.16	0.44	1.40	1.35

5.6.4 Gaseous perturbations due to liquid core

Resolved simulations capture the liquid dense core, which perturbs the incoming air and creates turbulence downstream the injector. This perturbation effect is illustrated in Figure 5.28. At the left, the instantaneous axial velocity fluctuations u' and the jet interface in the middle plane y = 0 are plotted. The dense core creates turbulence downstream the injection point, as shown by the strong fluctuations. Such perturbations can have a great impact on secondary atomization and spray dispersion once primary breakup has taken place. Therefore, modeling this perturbance effect as accurate as possible is paramount for later performing dispersed-phase simulations (Chapter 6), where the dense core is a priori neglected and a developed spray is injected. A three-dimensional view of the perturbation effect is depicted in Figure 5.28 right, where the gaseous streamlines are visualized. Two main turbulent structures appear: a horseshoe vortex formed at the wall right upstream the liquid jet, widely observed in literature dealing with both gaseous and liquid JICF (Fric & Roshko 1994, Karagozian 2010, Schlegel et al. 2011), and a recirculation zone right downstream the jet. The latter, which is a is characteristic of JICF configurations at high gaseous velocities (Fontes et al. 2019), might entrap droplets emanating from the ligaments formed during column breakup and affect their trajectory and subsequent secondary breakup.

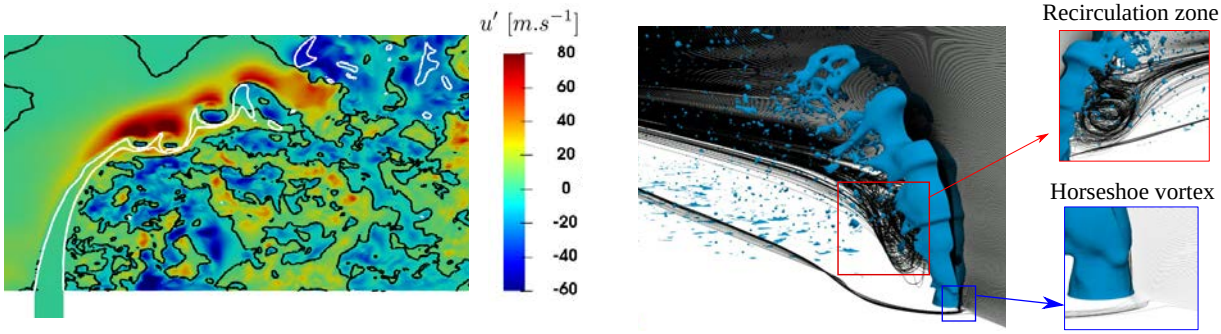

Figure 5.28: Interaction between liquid dense core and gaseous phase. *Left*: Instantaneous u' field in a JICF simulation from case UG100_DX20. The black contours indicate the lines with zero instantaneous fluctuation $u' = 0$, while the white contours denote the location of the interface at the plane. *Right*: 3D streamlines in case UG100_DX20

In this section, the gaseous perturbations created by the presence of the liquid dense core are studied. These results will be used in Chapter 6 to compare with the disturbance effects in the gaseous field modeled in the dispersed phase simulations. The gaseous field is investigated by analyzing the mean axial gaseous velocity field $\overline{u}$ in the planes illustrated in Figure 5.29.

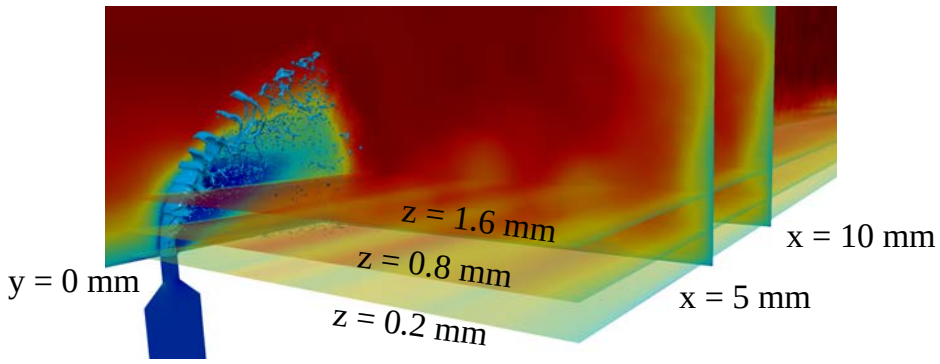

Figure 5.29: Jet from case UG100_DX10 showing planes to study the gaseous phase

Mean axial velocity at the symmetry plane $y = 0$ mm for all cases are shown in Figure 5.30 (case UG100_DX20_NT is not displayed in this section since its mean fields are identical to those of case UG100_DX20). The region with mean liquid obtained as $\overline{\psi} > 0.5$ is denoted in grey, hence the displayed velocities correspond only to the mean gaseous region. Streamlines are also shown to indicate the flow direction. In all cases, a recirculation bubble enclosed by the white solid line is retrieved immediately downstream

the dense core. This recirculation region is fully converged for the coarse cases but not for the fine ones. The effect of this bubble is to push the streamlines below and behind it upwards, hence confering the gas a positive vertical velocity downstream the dense core. Upstream the jet, the streamlines are initially oriented towards the axial direction but then bend vertically due to the presence of the dense core. These streamlines are again directed vertically due to the action of the recirculation bubble. In general, velocities are larger for the high Weber operating point except in the recirculation bubble, where mean negative axial velocities show the same values for both conditions.

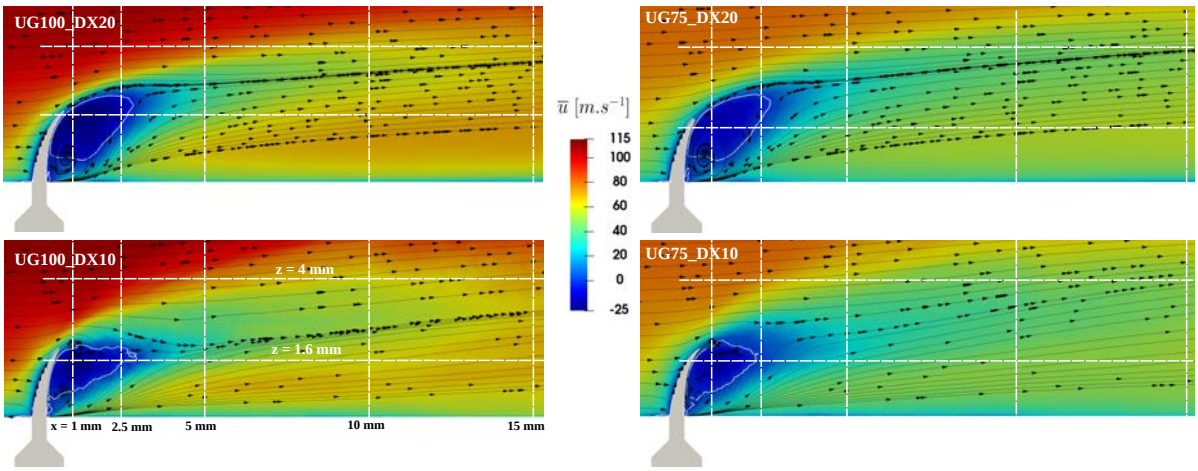

Figure 5.30: Mean axial velocity at plane $y = 0$ mm. Black lines with arrows are in-plane mean streamlines; the white solid line indicates the contour $\overline{u} = 0$ which delimites the recirculation bubble. The grey area indicates the mean liquid region, identifed as $\overline{\psi} > 0.5$

The $\overline{u}$ profiles along the dashed lines from Figure 5.30 are represented in Figures 5.31 and 5.32. Both graphs reveal that perturbations are stronger closer to the bottom wall (line $z = 1.6$ mm in Figure 5.31 traverses indeed the recirculation bubble, since velocities reach negative values). Figure 5.31 shows that velocity profiles stabilize several diameters downstream the injection point to lower values than in the corresponding single-phase simulation (no jet, i.e. dotted line in the figures), which is due to momentum exchanged with the liquid. This gas energy transferred to the liquid has been invested in bending and atomizing the jet. Lines from Figure 5.32 reflect that the recirculation bubble extends up to a location $x = 2.5$ mm, and that this one is actually insensitive to the operating point. This might suggest that the recirculation bubble is not affected by the Weber number and depends only on the q factor, which is identical in both conditions. There is, however, a strong dependent on the interface resolution: profiles crossing the recirculation bubble are not greatly affected by resolution in the regions with the lowest velocities, while the opposite happens outside it, in the deceleration regions. Nevertheless, it is not sure whether the fields from the fine resolutions are fully converged, and hence the profiles depicted might still change if the simulations run for longer time.

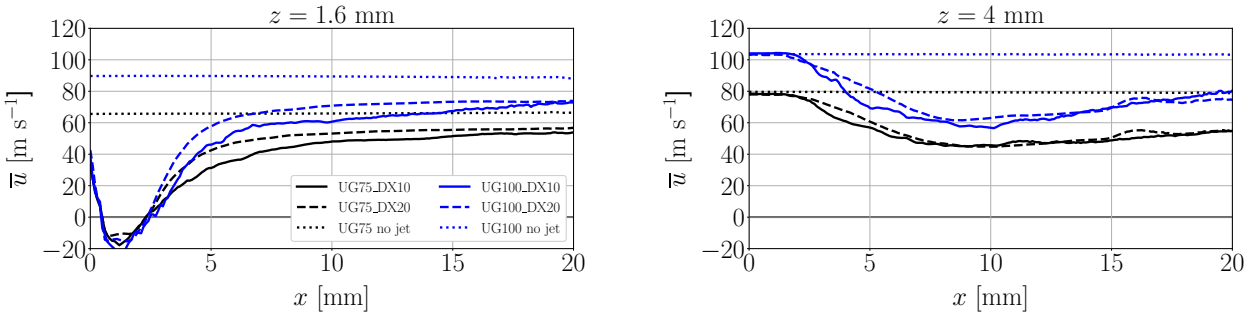

Figure 5.31: Mean axial velocity evolution along axial coordinate at locations $z = 1.6, 4$ mm in plane $y = 0$ (lines of Figure 5.30)

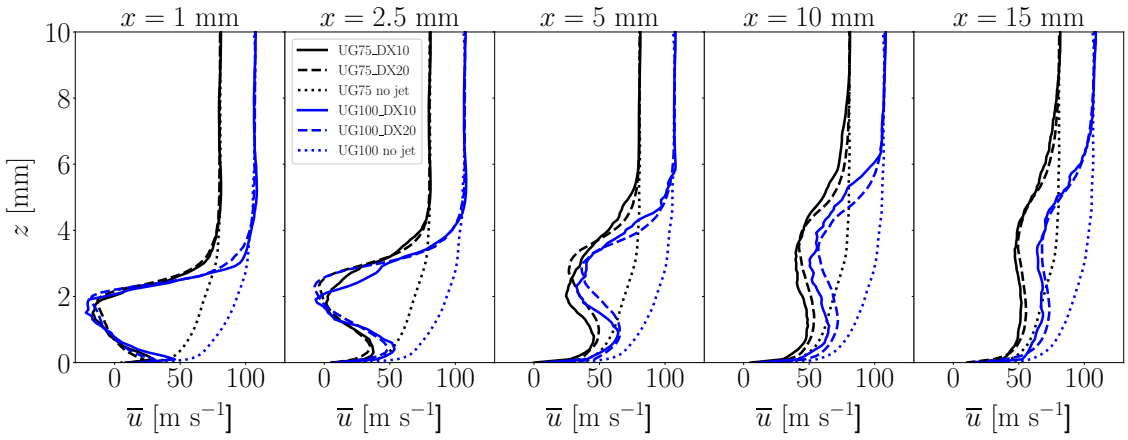

Figure 5.32: Mean axial velocity evolution along vertical coordinate at $x = 1, 2.5, 5, 10, 15$ mm locations of plane $y = 0$ (lines of Figure 5.30)

The mean fields at the liquid sampling planes $x = 5, 10$ mm are shown in Figure 5.33. The perturbation effect of the dense core is observed by the deceleration around the central plane $y = 0$. Lower velocities are found at $x = 5$ mm than at 10 mm, since the perturbance effects are stronger further upstream as previously shown in Figure 5.32. All cases also retrieve vortical structures symmetrical with respect to the $y = 0$ axis, which rotate in counter-clockwise direction for $y > 0$ and in clockwise direction for $y < 0$. These vortical structures in the gaseous phase, known as counter-rotating vortex pair (CVP), are a typical characteristic of the JICF and are found up to several diameter locations downstream the injection nozzle, having a strong effect on droplets dispersion (Arienti et al. 2006). Figure 5.34 shows the mean velocity profiles along the dashed lines from Figure 5.33. All profiles are symmetrical with respect to plane $y = 0$. Decelerations are stronger the closer to the wall ($z = 1.6$ mm) and the closer to the injection nozzle ($x = 5$ mm). All profiles show a dependence on the interface resolution, where larger differences are located at the regions with stronger decelerations.

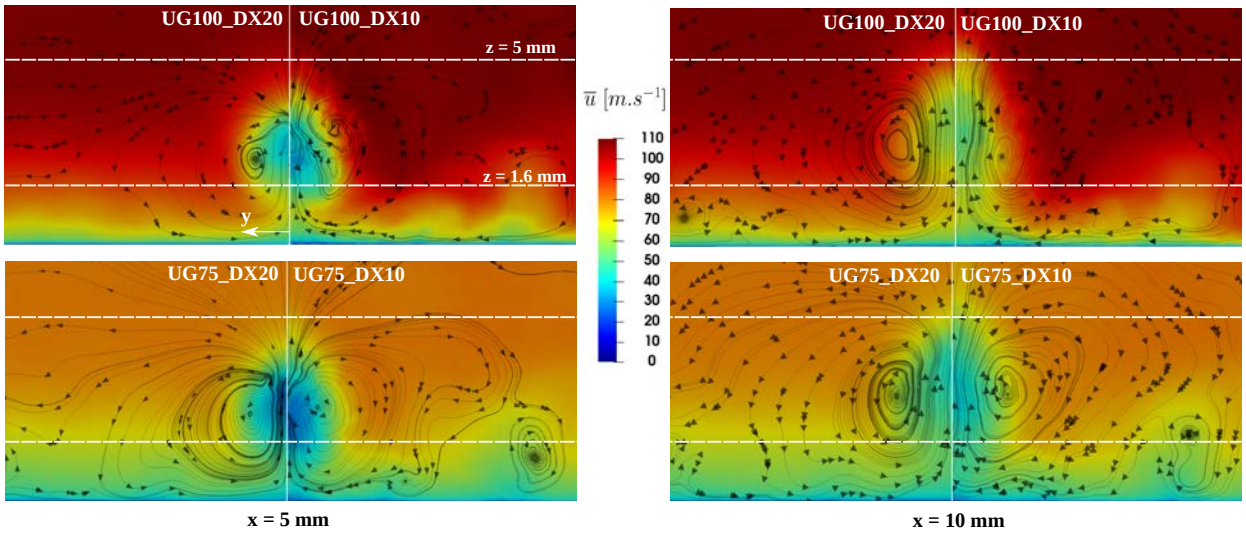

Figure 5.33: Mean axial velocity at planes $x = 5, 10$ mm. Black lines with arrows are in-plane mean streamlines. Fields are symmetric around the $y = 0$, hence each picture shows the mean fields for equivalent operating condition and plane location but different resolution to ease visual comparison

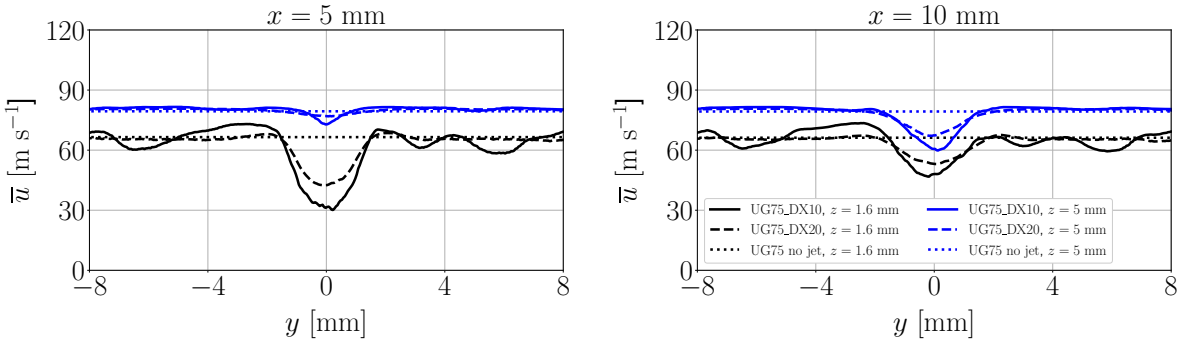

(a) Low Weber operating point

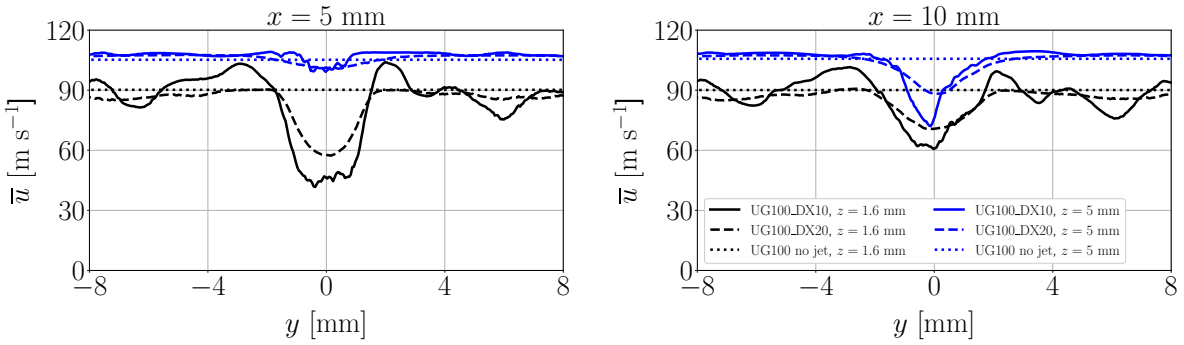

(b) High Weber operating point

Figure 5.34: Mean axial velocity evolution along lateral coordinate at z lines of Figure 5.33

Finally, the mean velocity at the planes perpendicular to the z axis depicted are shown in Figure 5.35. The mean liquid region defined by $\overline{\psi} > 0.5$ is represented in grey. Close to the wall ($z = 0.2$ mm) the dense core has not yet been deformed by the crossflow and its cross-section is circular. As z increases, the column displaces towards the crossflow direction and its cross-section deforms from a circle to a kidney-shape. The recirculation region increases its maximum axial location x with increasing vertical distance z. This is due to the larger deformations of the dense core, since further from the wall the kidney-shape acts like a blunt body. The topology of the fields is similar among operating conditions, yet very sensitive to the interface cell resolution.

All these results show the complex mean features of the turbulent field induced by the crossflow, and the influence that interface cell size play into their resolution. The role of the Actuator Line Method (ALM) will be to retrieve these features as accurately as possible in the dispersed-phase simulations of Chapter 6.

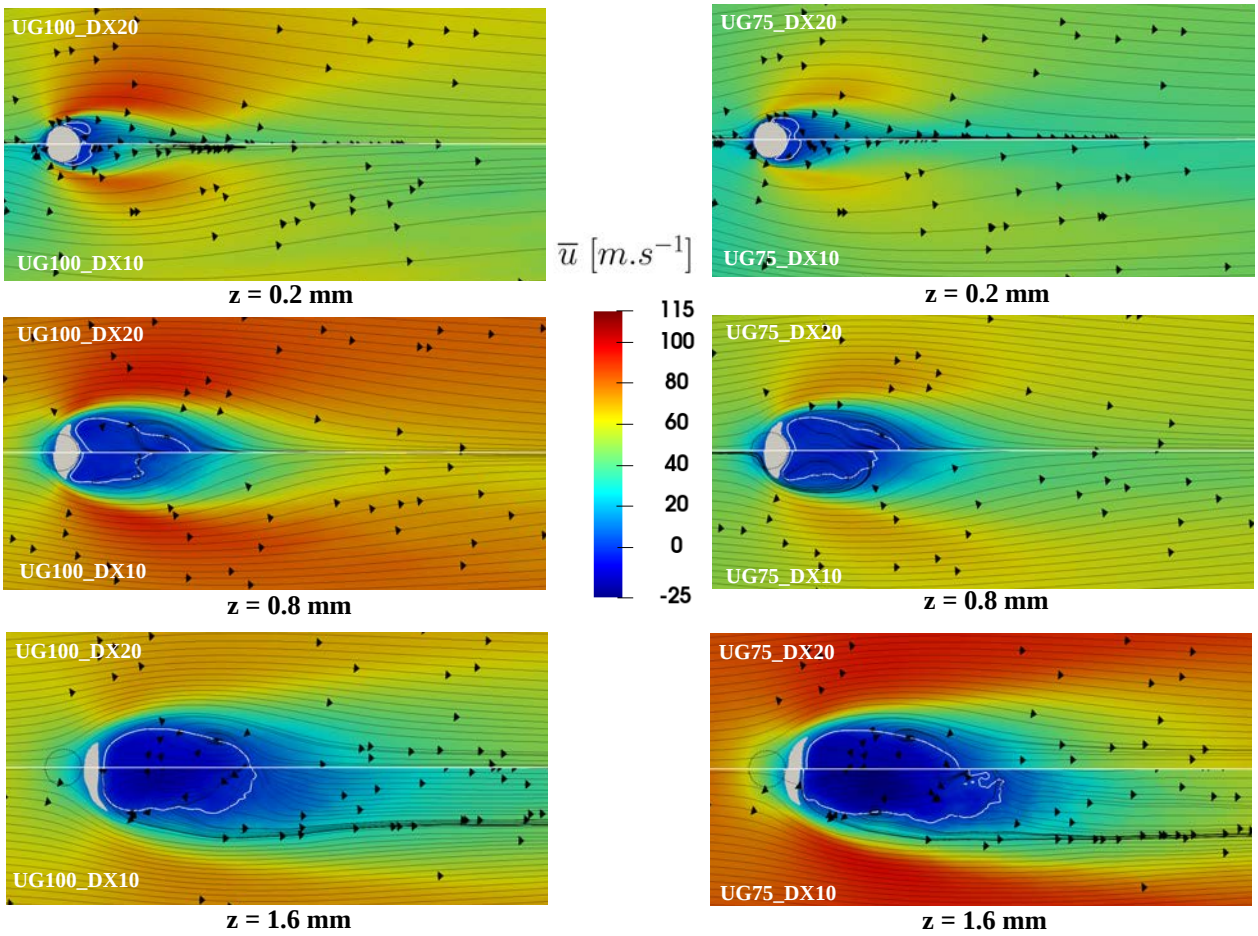

Figure 5.35: Mean axial velocity at planes $z = 0.2, 0.8, 16$. Black lines with arrows are in-plane mean streamlines; the white solid line indicates the contour $\overline{u} = 0$ which delimites the recirculation bubble. The grey area indicates the mean liquid region, identifed as $\overline{\psi} > 0.5$. The black-dotted circle indicates the location of the injection nozzle

5.6.5 Direct measurement of liquid fluxes

Droplet sampling procedure is performed by tracking the center of mass of resolved structures and retrieving droplets when they cross the defined sampling planes by lagrangian projection. With this tool, some droplets are tracked twice and some others might never be tracked. As a consequence, the sampled spray is not the actual spray that crosses the sampling surfaces in the simulations, but an approximation to it. Therefore, the obtained spray size distributions and sampled mass flow rates are also affected. To check the accuracy of the lagrangian projection procedure, the lagrangian mass flow rates will be compared to flow rates measured directly from the resolved simulations (resolved fluxes). The procedure followed to process these resolved fluxes is detailed in Appendix C.2, while here only results are presented.

The first step is to define the spatial regions where liquid rates will be calculated. For comparison with the lagrangian tracking methodology, fluxes are measured in planes perpendicular to the crossflow direction. Figure 5.36. shows a schematic view of the planes, equally spaced at a distance of 5 mm: $x = 5, 10$ and 15 mm. In simulations where liquid is removed at $x = 11$ mm, only the first two planes will be considered (since there is no liquid flux through the third one). Furthermore, three more planes are defined parallel to the bottom wall to quantify the liquid flow rate impinging the channel, phenomenon known as filming: $x < 5, 10$ and 15 mm. Therefore, each combination of sampling and filming surfaces will conform the outlet surfaces of a control volume enclosing the whole liquid jet (no outlet surfaces are located upstream the injection point as there is no liquid flowing in this direction, and the inlet surface corresponds to the liquid nozzle). Each plane where resolved fluxes are calculated will be hereafter referred as interior boundary (IB).

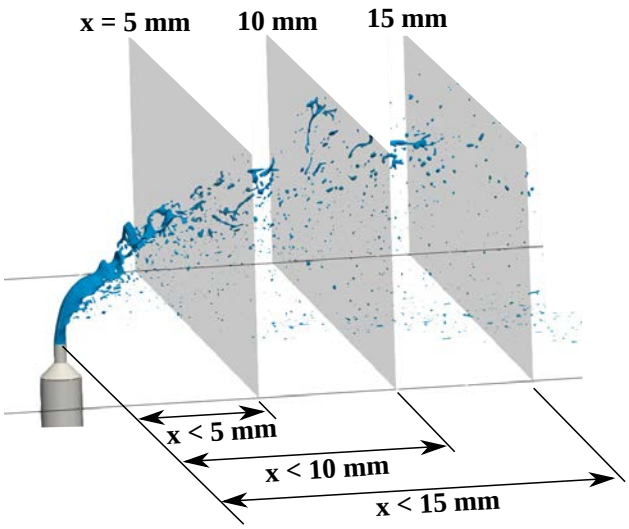

Figure 5.36: Snapshot of a JICF simulation showing the droplets sampling planes (in grey) and the different filming regions

Figure 5.37 shows an example of instantaneous liquid flow rates Q_l from case UG100_DX10. Two IBs perpendicular to the x axis ($x = 5$, 10 mm) are tracked in the left image, and two filming IBs ($x < 5$, 10 mm) are displayed in the right one. The fluxes in Figure 5.37 left show a high variation around the injected flux in both planes. This is due to an intermittent presence of liquid crossing the sampling planes once atomization has started taken place: the liquid phase is no longer a coherent jet but is composed by an ensemble of ligaments and droplets. At some instants there are large clusters of droplets or large ligaments crossing the domain (large fluxes), while in other cases there might only be a few droplets being sampled (low fluxes). Regarding filming, these present lower magnitudes but still display an oscillating behaviour which, in some cases, can descend up to 0 (no liquid impinging the wall).

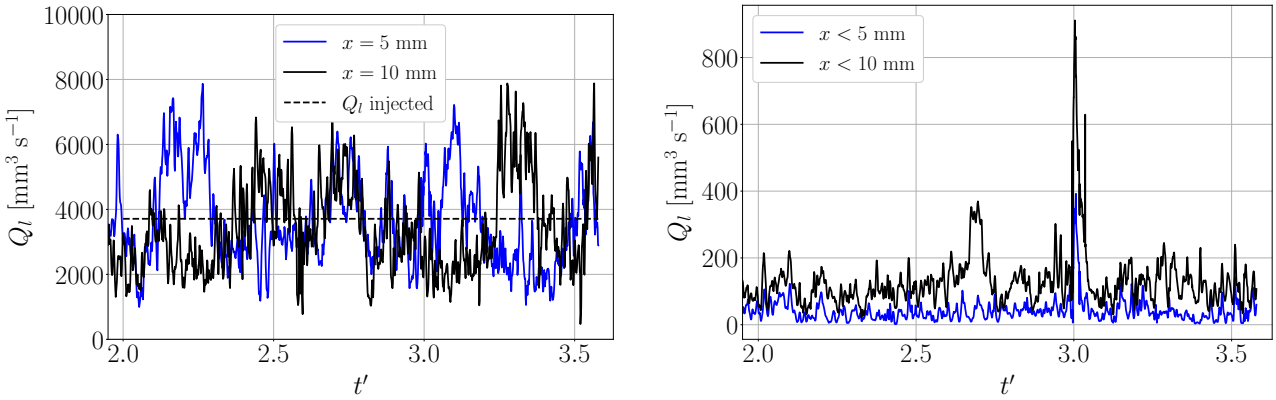

Figure 5.37: Time evolution of instantaneous liquid flow rates Q_l for case UG100_DX10. *Left*: planes normal to crossflow. *Right*: filming planes.

Due to the intermittent behaviour of the jet downstream the injection nozzle, the instantaneous fluxes are not useful to characterize the flow rates in the IBs. Instead, the mean and RMS fluxes provide useful information on the mass conservation in the JICF. The evolution of the mean and RMS values of IBs flow rates with time is shown in Figure 8.19. Statistics have been taken for $t' > 2$ in all cases. The evolution of $\overline{Q_l}$ in the perpendicular IBs (Figure 8.19a) shows that all cases tend towards convergence: the fine cases are shown to be completely converged, while the fine ones show some oscillations at the last timesteps sampled but with a lower amplitude, indicating that they are almost converged. In all cases, the mean values for perpendicular IBS are reduced downstream the crossflow, while the mean filming ones are increased. The RMS values of Figure 8.19b show high magnitudes caused by the high fluctuations in the flow rates as illustrated in Figure 5.37a, which are present in all cases. The steep increases in the RMS at certain times is due to a high volume of liquid crossing the IB at the corresponding instant.

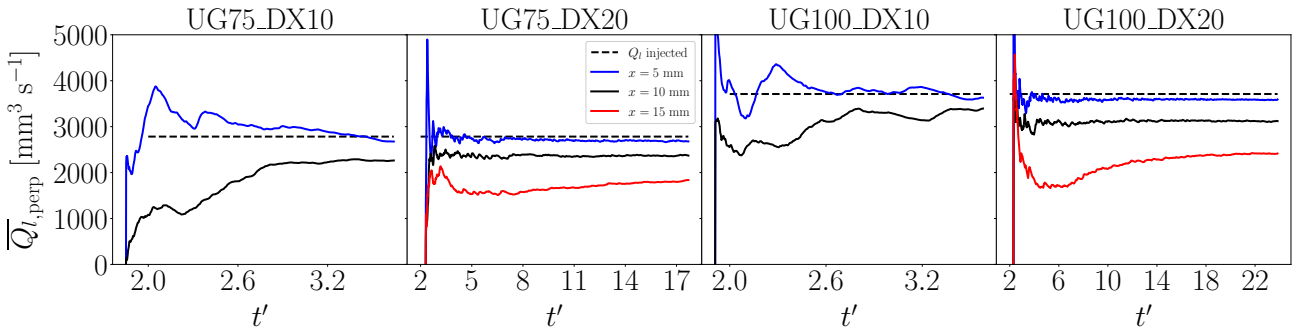

(a) Mean Q_l evolution in IBs perpendicular to crossflow.

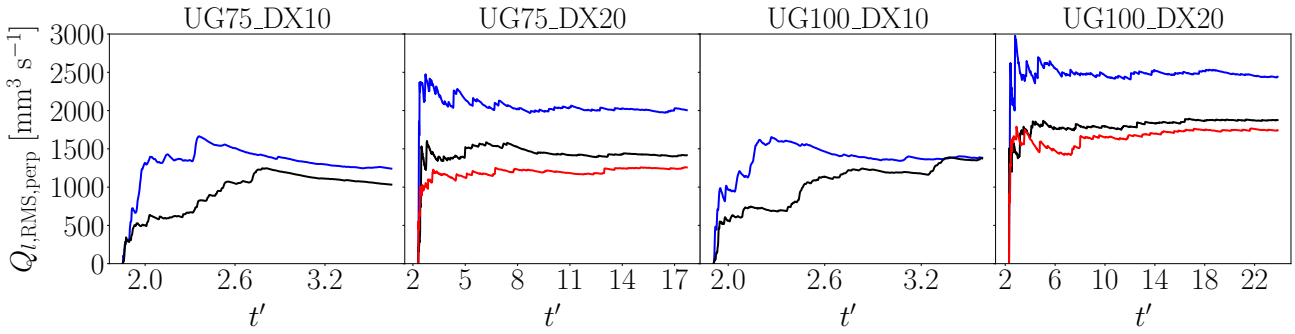

(b) RMS Q_l evolution in IBs perpendicular to crossflow.

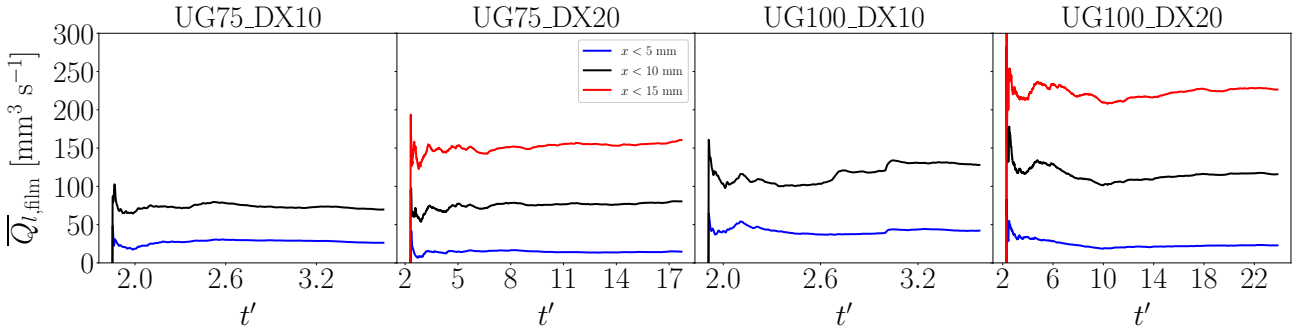

(c) Mean Q_l evolution in filming IBs.

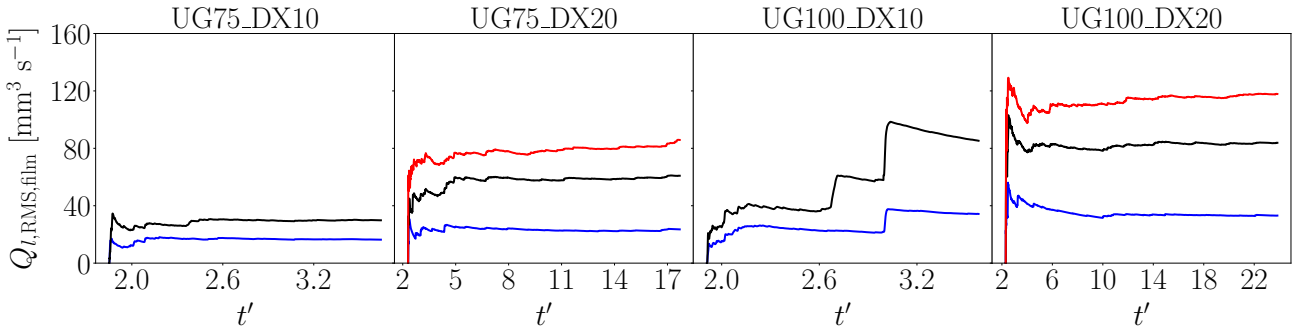

(d) RMS Q_l evolution in filming IBs.

Figure 5.38: Time evolution of mean and RMS values of Q_l in IBs

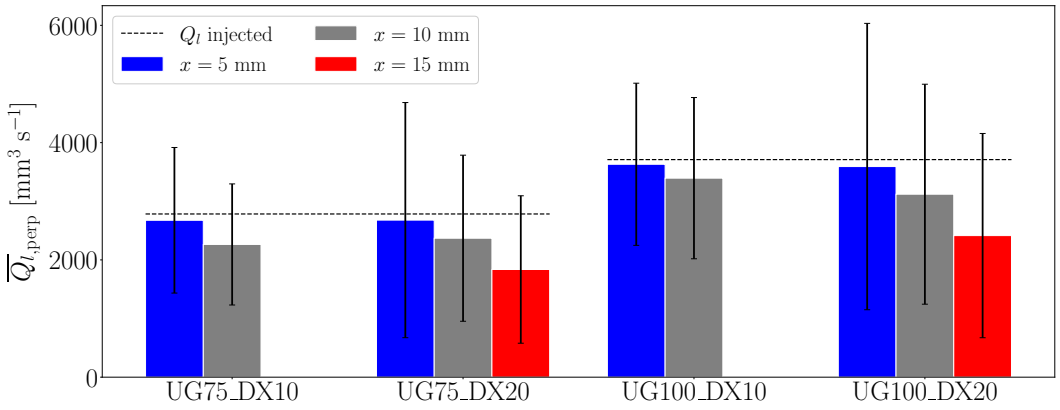

(a) IBs perpendicular to crossflow.

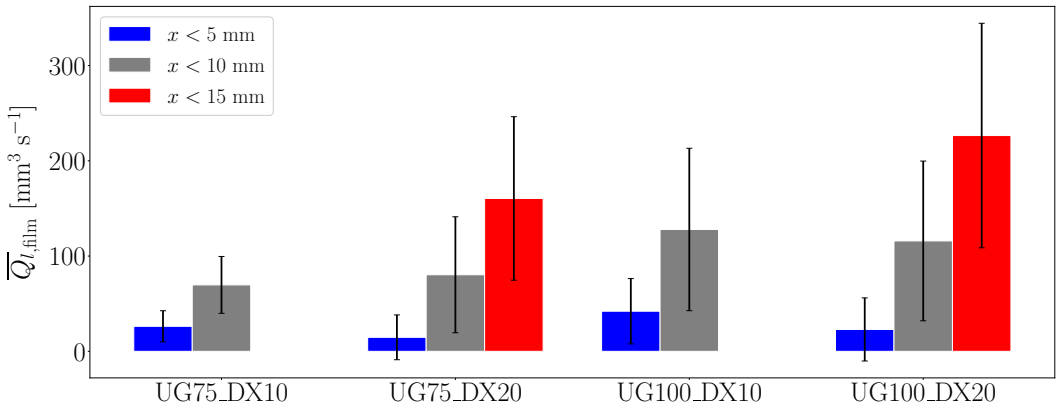

(b) Filming IBs.

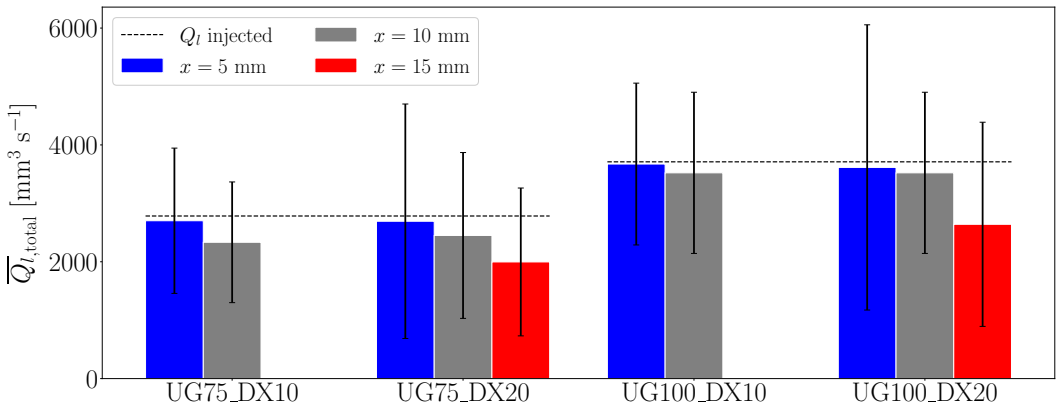

(c) Total (perpendicular + filming) flow rates from IBs

Figure 5.39: Mean flow rates (bars) and RMS (black vertical lines) obtained with IBs for each simulation.

Figure 5.39 shows the final mean and RMS values for the flow rates. Three graphs are represented: (a) the IBs perpendicular to the crossflow direction, (b) the filming IBs and (c) the addition of both filming and perpendicular IBs at each location, named total flux:

$$\overline{Q_l}_{\text{total}} = \overline{Q_l}_{\text{film}} + \overline{Q_l}_{\text{perp}} \tag{5.8}$$

In the JICF configuration studied, if an arbitrary cubic control volume is located englobing the jet and spray, liquid mass can leave this domain only through either the perpendicular or filming surfaces. Since the plenum domain is large enough to avoid liquid impinging the top and side walls, only these two rates comprise the liquid outlets. Therefore, the total flux should ideally equal the injected flow rate.

Figures 5.39a and b show that perpendicular fluxes decrease with axial distance, while filming ones increase. This is coherent, since droplets that cross a perpendicular IB closer to the injector might then reach the wall before reach the following (i.e. the one located 5 mm downstream) perpendicular one, hence contributing to the filming flux instead. Nevertheless, Figure 5.39c shows that the total flow rate is not conserved with axial distance, but actually decreases in all simulations: mass is lost in the simulations. Liquid mass loss can be quantified by substracting the total flow rates from the IBs to the injected flow rate in each simulation. To eliminate this dependence from the operation point, each one with different injected rates, a relative mass loss is defined according to the following formula:

$$\Delta Q_l = \frac{Q_{l,\text{injected}} - \overline{Q_l}_{\text{total}}}{Q_{l,\text{injected}}} \tag{5.9}$$

Results are shown in Figure 5.40. The mass loss is low closer to the injector ($x = 5$ mm), with all values below 3 %, then losses increase further downstream. At the location $x = 15$ mm the relative flow rate loss for the coarse cases is close to 30 %: from $x = 10$ to 15 mm, the mass loss doubles. Indeed, it was found that mass loss is caused by droplets disappearing when reaching a characteristic size of the order of the interface resolution Δx_{min}, since these cannot be further transported by the mesh (see, for instance, droplets generated by surface breakup in Figure 5.16). Then, for $x > 10$ mm the spray is fully disperse and secondary atomization is taking place: droplets generated might reach a small size and vanish. These values of liquid losses show that the location $x = 5$ mm is more suitable for performing lagrangian injection in the dispersed-phase simulations, since the total liquid flow rated injected is closer to the injected one. A more thorough study on the numerical sources of droplet disappearance is reported in Appendix D.

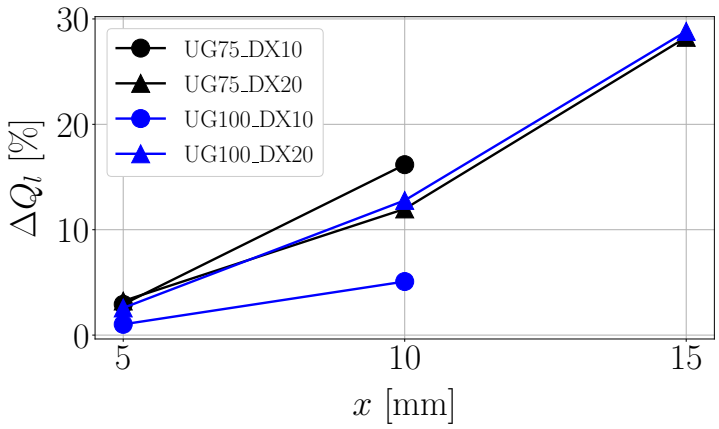

Figure 5.40: Relative loss of total liquid flow rates loss ΔQ_l with axial distance.

Finally, the flow rates obtained for all IBs have been discretized at each timestep and averaged, yielding the spatial maps of Figure 5.41. Each IB has been discretized into squared probes of 1 mm sides, and then the flow rates through each probe have been divided by the probe's surface to give the volume flux q_l according to Eq. (4.14). The flux maps display in all cases a circular distribution of flux of the IBs since there is more liquid concentration in the center part of the spray than at its edges, as also observed in experimental studies (Wu et al. 1998, Becker & Hassa 2002). The spray boundaries become wider in the lateral (y) and vertical (z) directions downstream the injection location due to the spray opening with axial distance. Larger values of maximum q_l are found closer to the jet: this is due to a higher liquid concentration closer to the injector since the spray is less disperse in the lateral and vertical directions, which combined with larger mean fluxes (see Figure 5.39) results in larger values of q_l. These spatial maps show how the resolved atomization simulations can capture a proper spray behavior.

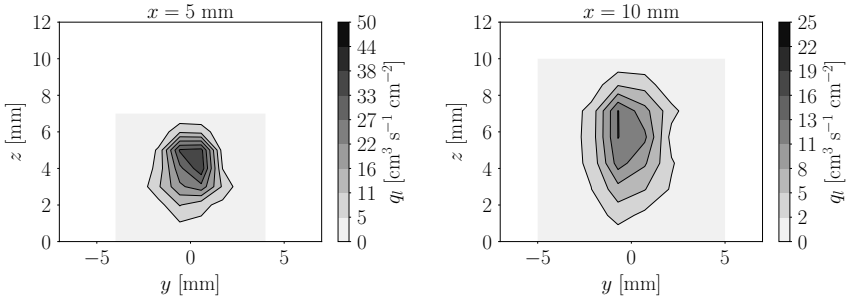

(a) Case UG75_DX10

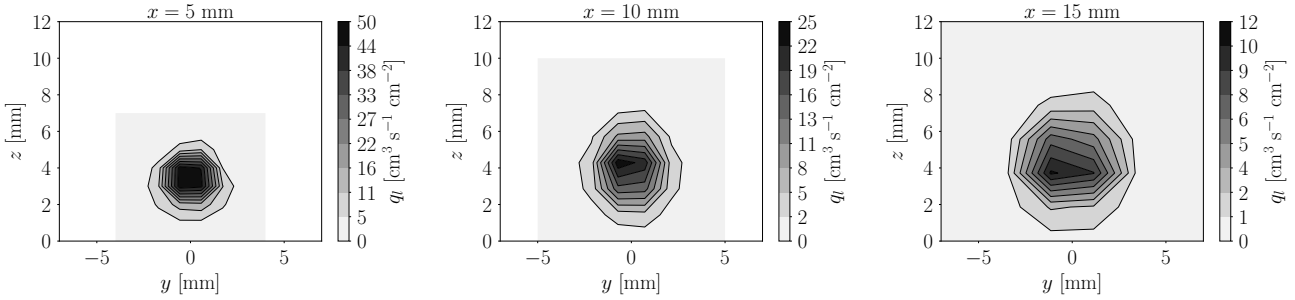

(b) Case UG75_DX20

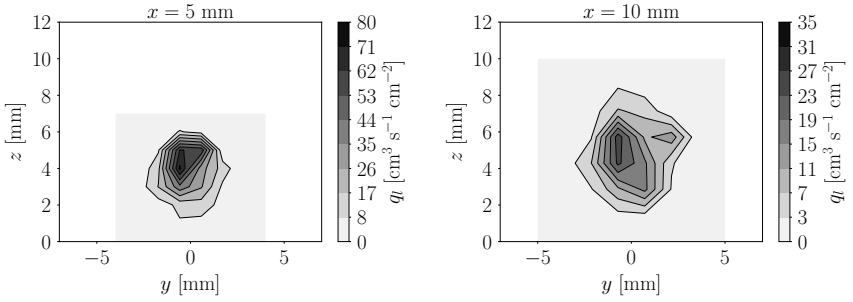

(c) Case UG100_DX10

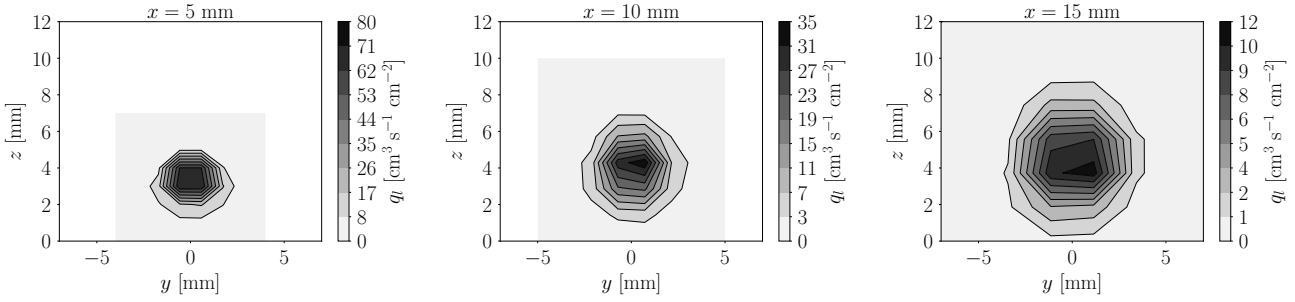

(d) Case UG100_DX20

Figure 5.41: Spatial distributions of volume fluxes obtained from interior boundaries

5.6.6 Computational performances and costs

Table 5.6 shows the numbers of cores, cells and droplets present at $t^* = 12$. At this instant all jets are developed but liquid has not reached yet the sponge layer (i.e. the axial location where it is artificially removed), hence allowing for a comparison among cases. The number of cores evolves in each run as the number of cells increase due to AMR for keeping a ratio $N_{\text{cells}}/N_{\text{cores}}$ between 100,000 and 150,000, which is optimum for parallellization purposes (Trobec et al. 2018). As observed, changing the interface resolution Δx_{min} for a given operating point multiplies the number of droplets by 6. A larger quantity of droplets with a finer interface cell size increases substantially the number of elements, of the order of 5 times. Then, the number of cores rises by the same factor in order to keep the ration $N_{\text{cores}}/N_{\text{cells}}$ within the optimal range for paralellization. A comparison of operating conditions for the fine mesh resolution shows that the number of droplets and cells are larger for the high Weber number than for the low one, which is coherent since the velocities are larger in the former one and more droplets are expected to be formed by surface breakup.

Table 5.6: Computational cores, mesh cells and total number of droplets present at the domain for JICF simulations at $t^* = 12$

Case	N_{cores}	N_{cells} $(\cdot 10^6)$	N_{drops}
UG75_DX10	3840	430	2221
UG75_DX20	768	100	394
UG100_DX10	4224	440	2563
UG100_DX20	768	104	393
UG100_DX20_NT	768	92	326

To assess the computational performances of the performed simulations, a Reduced Computational Time (RCT) can be defined as (Janodet et al. 2022):

$$\text{RCT} = \frac{\text{WCT}\ N_{\text{cores}}}{N_{\text{iter}}\ N_{\text{cv}}} \tag{5.10}$$

where WCT is the Wall Clock Time, N_{cores} the number of cores used by the computations, N_{iter} the number of temporal iterations performed, and N_{cv} the total number of node-based control volumes in the computational domain. RCT, which is expressed in time units, can therefore be used to compare the cost of the different simulations performed independently of the number of cores, iterations and elements they use. The RCT is calculated for each computational routine of the numerical methodology ACLS/AMR, then the different RCTs are added to yield the total RCT of the simulations. These contributions are:

$$\text{RCT} = \text{RCT}_{\text{ACLS}} + \text{RCT}_{\text{AMR}} + \text{RCT}_{\text{NS}} \tag{5.11}$$

Where the subindex ACLS indicates the contribution of the ACLS methodology without mesh refinement (§2.3.4), AMR indicates the contribution of the mesh refinement (§2.3.4), and RCT_{NS} denotes the contribution of the routines devoted to resolution of the Navier-Stokes equation, which in YALES2 employ a linear solver to compute the Poisson equation (Moureau et al. 2011).

Additionally, the CPU time can be computed as follows:

$$t_{\text{CPU}} = \text{WCT}\ N_{\text{cores}} \tag{5.12}$$

which expresses the computational cost in hours of a simulation. Table 5.7 reports the RCT values and the ratio t_{CPU}/t^*. In all simulations, the fastest routine is the NS while the slowest one, and therefore the most expensive, is AMR. For cases UG75_DX20 and UG100_DX20, the reduced time spent in the routines ACLS, AMR and NS is similar. Comparing cases with and without turbulence injection shows that there is a reduction of the RCT in the AMR for the latter case due to a lower degree of atomization which produces less droplets (see Table 5.6) and, therefore, less surface of liquid interface to remesh. The largest differences are found among resolutions: in the fine cases, all the RCT contributions increase from 2 to 3 times with respect to their homologues from the coarse simulations. This increase is mainly due to AMR, which is therefore the most time-consuming and computationally expensive routine.

Table 5.7: Computational performances from JICF simulations at $t^* = 12$

Case	RCT [μs]	RCT_{ACLS} [μs]	RCT_{AMR} [μs]	RCT_{NS} [μs]	t_{CPU}/t^* [h]
UG75_DX10	1549.7	192.0	1182.6	175.1	5252
UG75_DX20	494.1	88.8	362.3	43.0	440
UG100_DX10	1643.6	162.5	1369	112.1	5580
UG100_DX20	517.5	105.8	361.1	50.6	414
UG100_DX20_NT	444.0	105.0	295.0	44.0	342

Figure 5.42 reports the computational cost in CPU hours (t_{CPU}) for of the simulations to reach the physical times reported in Table 5.3 (which yield converged SLIs, as shown in the next section), and the ratio between CPU hours and physical time simulated ($t_{\text{CPU}}/t_{\text{ph}}$). As expected, more CPU hours are devoted to the fine simulations, both in absolute value and per milisecond simulated. Reducing the interface cell size by two increases the cost by a larger extent through two contributions:

- Lower timesteps Δt in the fine simulations due to smaller cell sizes. The latter is estimated from the CFL number (which is equal in all simulations) according to the following expression:

$$\Delta t \leq \min\left(\frac{\text{CFL}\ \Delta x}{|\mathbf{u}|}\right) \tag{5.13}$$

- A larger number of cells in the fine simulations due to more droplets being resolved.

Figure 5.42 also shows that high Weber simulations are more expensive than the low Weber one. The reasons are the two same ones as aforementioned. The higher Weber cases have larger velocities, which for identical resolution yield lower timesteps according to Eq. (5.13). Then, these simulations also contain a larger amount of droplets due to higher shear, which in turn increase the number of cells with respect to the low Weber computations.

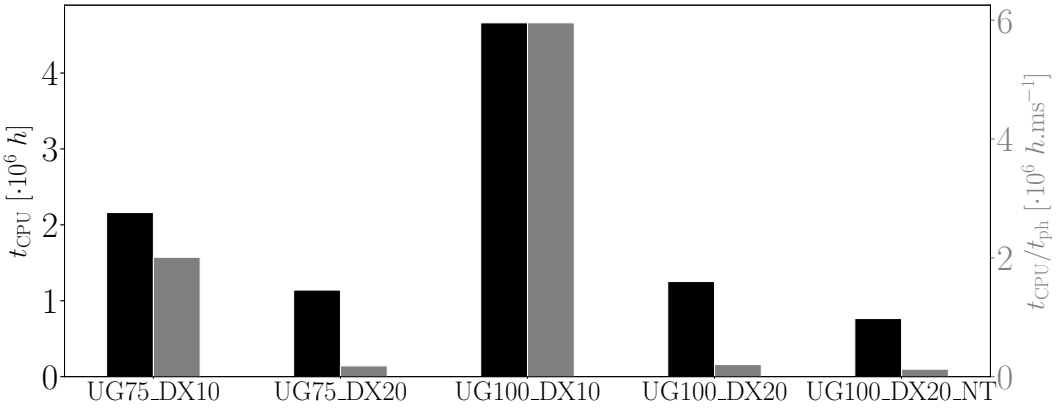

Figure 5.42: Cost of the JICF simulations in CPU time and CPU per physical times simulated

From these analyses, it can be concluded that augmenting the resolution twice will increase the cost of the simulations by a larger factor, and that most of the computational resources are devoted to AMR. Nevertheless, it is thanks to the AMR methodology that such computations become possible. Performing resolved simulations with such fine resolutions in unstructured grids would be unfeasible if the interface cell size Δx_{min} had to be specified in all the domain.

5.7 SLI building

This section reports the results from post-processing data from the resolved simulations for creating a Smart Lagrangian Injector (SLI). Firstly, the dense core topology and momentum parameters to obtain its net force are provided. Next, the spray sampled through lagrangian tracking is postprocessed and spatially discretized. The process sprays will serve as boundary conditions for the liquid phase in dispersed-phase simulations.

5.7.1 Dense core characterization for ALM

The dense core (DC) of a JICF is the focus of numerous studies, since it creates an important blockage effect in the incoming air. Pioneer JICF experimental studies (Wu et al. 1997) focused on obtaining the **breakup point** of the DC by studying side shadowgraphs from the JICF. More recent works (Patil & Sahu 2021) tried also to determine its width and its lateral opening angle. Nevertheless, experimental and numerical studies of the DC topology in JICF are scarce nowadays, specially at operating conditions where surface breakup predominates (since the visualization of the jet is hindered by a large number of small droplets generated).

In this work, the DC topology is determined and studied from the resolved atomization simulations in order to provide input parameters to the Actuator Line Method (ALM) for modeling the gaseous field disturbances in dispersed-phase computations. The dense core is obtained as the largest liquid structure in the domain, and its breakup point is estimated as the point at the symmetry plane $y = 0$ located further downstream from the injection location. The procedure followed to process the DC topology is more thoroughly detailed in Appendix C.3, while here only results are presented.

In first place, the time evolution of the breakup point coordinates and width are shown in Figure 5.43. Time has been non-dimensionalized according to Eq. (5.3). All signals display a sawtooth shape that reflects the dynamic behaviour of the dense core: increasing values correspond to ligaments being formed from the dense core (i.e. the breakup point $x_\mathrm{b}, z_\mathrm{b}$ moves further downstream and upwards, while the width w increases due to the deformation of the dense core cross-section), then they suffer an abrupt decrease when the ligaments are dettached from the jet, and the process repeats once and again. This periodic behaviour has been previously observed in several experimental studies (Wang et al. 2011, Prakash et al. 2018).

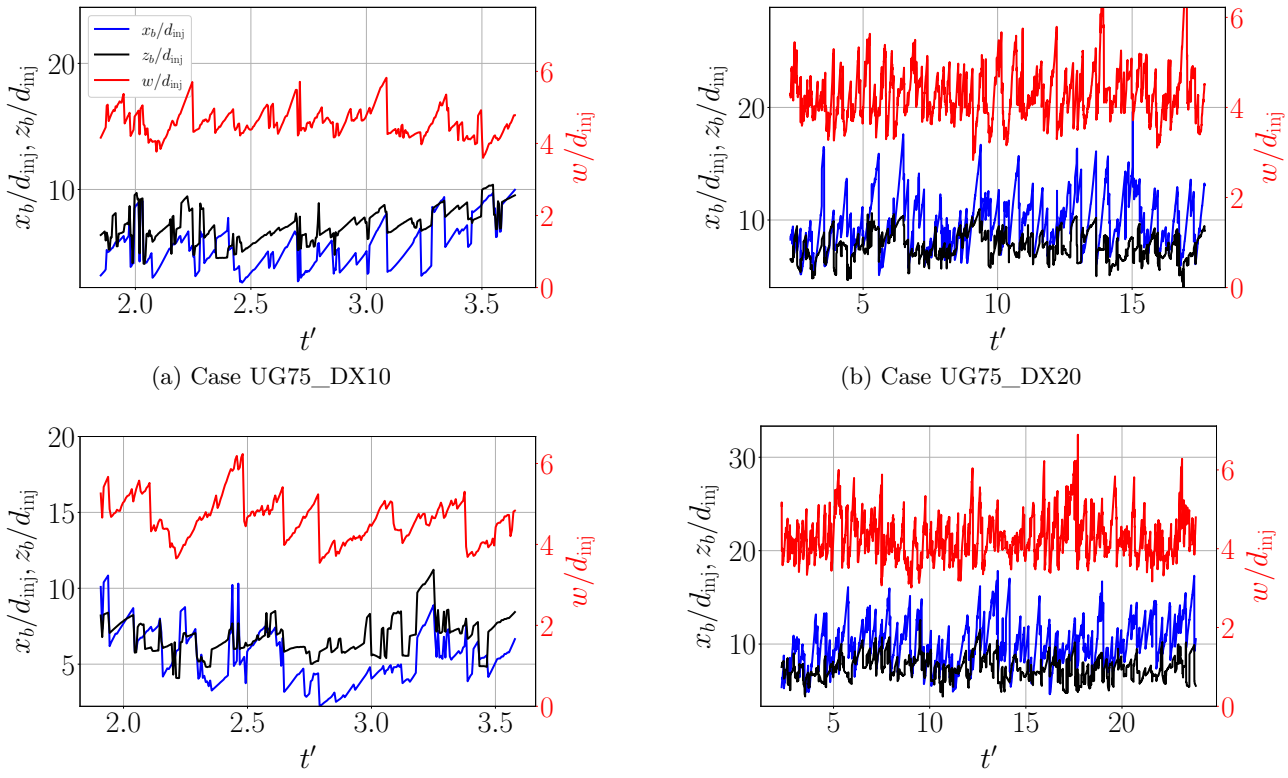

(a) Case UG75_DX10

(b) Case UG75_DX20

(c) Case UG100_DX10

(d) Case UG100_DX20

Figure 5.43: Variation with time of the dense core breakup point coordinates $x_\mathrm{b}, z_\mathrm{b}$ and width w.

To define an actuator representing the dense core in dispersed phase simulations, the mean values of the breakup point coordinates and width will be used. Hence, the mean value of the signals from Figure 5.43 are calculated. The evolution of the mean values with time (i.e. convergence with time) is shown in Figure 5.44. As observed, the simulations performed with the coarse interface cell size $\Delta x_{\min} = 20\ \mu m$ are converged for the three parameters x_b, z_b and w (except for z_b in case UG75_DX20, as this parameter seems the one taking longer time to achieve convergence). The fine resolutions $\Delta x_{\min} = 10\ \mu m$ have not yet achieved full convergence.

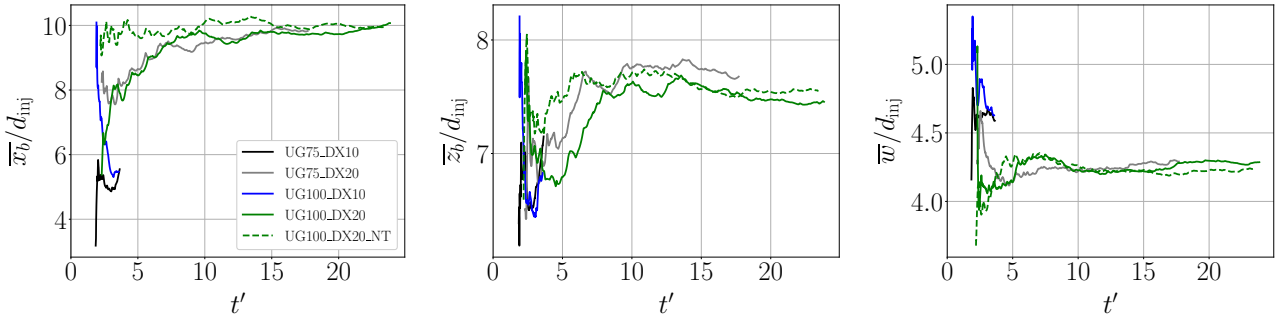

Figure 5.44: Evolution of mean geometric parameters of the dense core

The final mean values obtained for the geometrical parameters are shown in Figure 5.45. The bars in the figures denote the standard deviation of the instantaneous signals. Figure 5.45a shows that the mean values for the coarse resolution are below the $\overline{z_b} = \overline{x_b}$, indicating that the dense core penetrates further along the streamwise direction x than in the vertical z. On the contrary, the points for the fine resolution are located above this line, which shows that the dense core is elongated along the vertical direction. This graph also show iso-lines of the dense core length L_{DC}. Lengths are similar for identical resolutions regardless the operating condition, but present significant differences among resolutions. Fine simulations present a shorter dense core than the coarse ones; in other words, fine simulations capture an earlier breakup than the coarse ones. This is due to the resolution of instabilities in the fine resolution, which foster an earlier breakup of the liquid dense core (Xiao et al. 2014, Prakash et al. 2018, Crialesi-Esposito 2019).

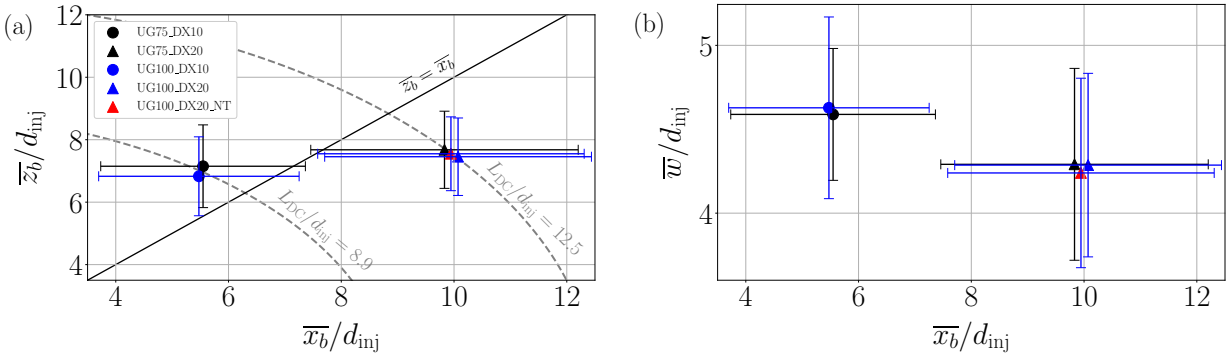

Figure 5.45: Mean values for the dense core geometric parameters

Figure 5.45 reveals also a slight dependendency of the mean parameters with respect to the operating conditions. For the coarse simulations, the breakup coordinates $\overline{x_b}$ ($\overline{z_b}$) are slightly lower (higher) for the low We operating point: increasing aerodynamic gas forces pushes the breakup point further downstream and upwards. This is coherent with the experimental results from Patil & Sahu (2021), who obtained a correlation for the axial breakup point which varies with the gas Weber number as $x_b \propto We_g^{0.1}$. The dependency with We_g is however very weak, as also found in Figure 5.45a since the changes in mean values are not actually very significant. This experimental study also includes a correlation for the width w which depends solely on the q factor, also coherent with the results from Figure 5.45b for the coarse resolution. It is to bear in mind that these experiments do not correspond to the operating points studied here, thus the actual dependencies and their intensities (i.e. exponent constants from the correlations) might be different at these conditions. The present computational study shows, however, similar qualitative trends.

Table 5.8 shows a summary of all the relevant parameters for characterizing the dense core topology and its net force (momentum) in all simulations. These values are taken as input parameters to the ALM model for the dispersed-phase simulations of Chapter 6.

Table 5.8: Dense core characterization: geometric and momentum parameters

Case	L_{DC}/d_{inj}	w/d_{inj}	S_{DC} [mm^2]	$p_{windward}$ [Pa]	$p_{leeward}$ [Pa]	$\lvert\boldsymbol{F}_{DC}\rvert$ [N]
UG75_DX10	9.05	4.60	5.1	5,200	-6,100	0.058
UG75_DX20	12.47	4.29	6.7	3,200	-8,000	0.074
UG100_DX10	8.75	4.62	5.0	10,400	-8,800	0.095
UG100_DX20	12.53	4.28	6.7	5,700	-14,000	0.13
UG100_DX20_NT	12.49	4.24	6.6	5,000	-14,000	0.12

5.7.2 Spray characterization

This section presents a characterization of the global spray sampled from the resolved simulations through lagrangian tracking of the liquid structures as described in §4.4.1. The sampling planes perpendicular to crossflow are those shown in Figure 5.36.

Establishment of mean sprays

Droplets are sampled and accumulated with time in order to get a mean-converged spray. Firstly, an establishment time of $t' \sim 2$ for each case is left before droplets start to be accumulated in order to retrieve a representative spray of a established jet. Droplets are then accumulated for a total duration t_{acc} reported in Table 5.9. The total physical times simulated $t_{ph} \sim t_{acc} + 2\tau_{dr_{x=10}}$ are also stated. Both the absolute physical time and the dimensionless time calculated through Eq. (5.3) are shown. From the absolute time, huge differences among coarse and fine simulations can be seen: the former are cheaper and run with a larger timestep than the latter ones, therefore reaching a longer physical time. For the low Weber case, the physical time reached by the coarse simulations goes 10 times beyond the fine ones, while the low Weber case shows a factor of 15 among resolutions. If, on the other hand, the dimensionless times are considered, the ratio of simulated times among resolutions reduce to 8.6 and 12.9 for the low and high Weber cases respectively. This is caused by the differences in the timescale τ_{dr} between resolutions, as these values are lower for the fine simulations (see Table 5.3). When looking at the convergence of injectors, the timescale t' is the one to consider since it relates the droplet arrival time to the sampling planes. On the other hand, when discussing physical characteristic among simulations, it is more convenient to use either the absolute physical time or the dimensionless time defined by the relation to the liquid inertia timescale, Eq. (5.2).

Table 5.9: Total physical t_{ph} and accumulation times t_{acc}, absolute and dimensionless with Eq. (5.3), for each JICF simulation

Case	t_{ph} [ms]	t'_{ph}	t_{acc} [ms]	t'_{acc}
UG75_DX10	1.08	3.64	0.53	1.79
UG75_DX20	6.30	17.70	5.48	15.40
UG100_DX10	0.78	3.58	0.37	1.67
UG100_DX20	6.16	23.84	5.57	21.54
UG100_DX20_NT	6.10	23.44	5.53	21.24

The total number of droplets accumulated is shown in Table 5.10. The coarse simulations have sampled more droplets than the fine ones, as they have run for longer physical time. Nevertheless, the number of droplets per milisecond simulated (ratio N_{dr}/t_{acc}) shows that the fine cases generate a larger number of particles, of the order of 5 times more than the coarse simulations. As a consequence, fine simulations need less physical time simulated to produce a converged spray for building lagrangian injectors (more insight is given at the end of §5.7.3).

Table 5.10: Number of droplets sampled in JICF simulations: total amount (N_{dr}) and total amount per accumulation time $N_{\mathrm{dr}}/t_{\mathrm{acc}}$

Case	N_{dr}			$N_{\mathrm{dr}}/t_{\mathrm{acc}}$ [ms^{-1}]		
	$x = 5$ mm	$x = 10$ mm	$x = 15$ mm	$x = 5$ mm	$x = 10$ mm	$x = 15$ mm
UG75_DX10	19384	11823	-	36574	22307	-
UG75_DX20	25036	20399	15979	4569	3722	2916
UG100_DX10	12832	9333	-	34681	25224	-
UG100_DX20	35345	29986	19885	6346	5384	3570
UG100_DX20_NT	33443	27221	-	6048	4922	-

In first place, the establishment of the accumulated sprays is verified by checking the evolution of SMD and liquid flux Q_l, defined respectively by Eqs. (4.12) and (4.13), with time. Figure 5.46 shows the results. As observed, all cases shows stabilization at the end of the sampling period considered. The flow rates show a decrease in the stabilized values with axial distance: the further from the injector, the larger the mass losses, which is coherent with the results obtained from the interior boundaries methodology of §5.6.5. The SMD values show a decrease of the final values with axial distance, which is expected since the atomization process breaks liquid structures into smaller ones. Further comments on the atomization process are given in the next section.

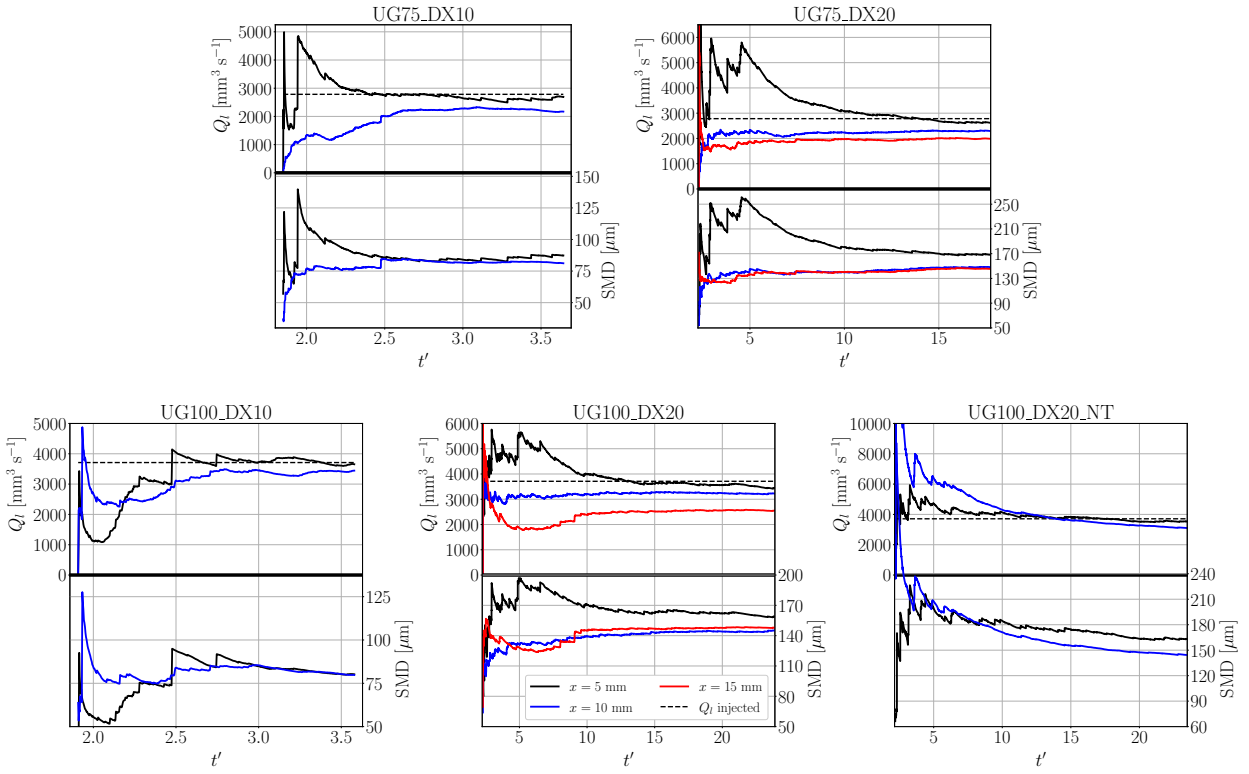

Figure 5.46: Establishment of SMD and Q_l in JICF. The black, blue and red lines represent the sampling planes $x = 5, 10$ and 15 mm respectively. The dashed black line represents the liquid flux injected through the nozzle

Apart from the SMD and mean flux, the spray is also characterized by its mean and RMS velocity components in the three directions and by the deformation parameters α, β. The convergence of these parameters is reported in Appendix E: all these magnitudes show converged values, but are not discussed here.

In order to verify the effectiveness of SLI in terms of liquid mass conservation, the liquid fluxes obtained from lagrangian tracking (i.e. the Q_l values at the last accumulation time instant of Figure 5.46) are compared to their equivalent obtained through interior boundaries, shown in Figure 5.39a. Results are shown in the bar graph of Figure 5.47. As observed, there is a good agreement between the resolved and lagrangian tracked

mass flow rates. Discrepancies arise due to the lagrangian tracking procedure, which assumes droplets to be point particles and projects their center of mass with time to estimate when they cross the sampling plane (this can yield larger errors when deformed liquid structures are sampled and projected as spherical particles). This simplification might lead to some droplets being sampled twice (larger fluxes than in the IBs), or to droplets not being sampled at all (lower lagrangian fluxes). Nevertheless, the lagrangian tracking algorithm provides accurate fluxes plus also statistics on velocities and droplet volumes (which indeed IBs cannot provide), making it a suitable tool to retrieve the spray characteristics.

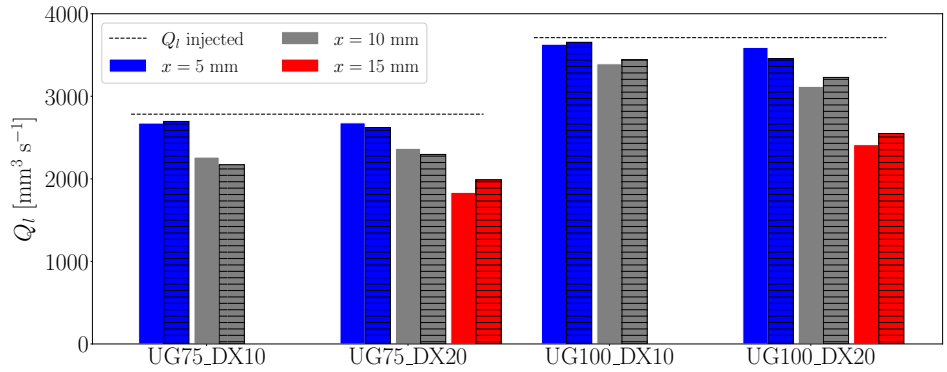

Figure 5.47: Liquid fluxes provided by interior boundaries (solid color bars) and lagrangian tracking (black-dashed color bars).

Granulometry

From the equivalent diameters, information on the droplets sizes can be obtained through either statistical distributions or mean diameters, such as the SMD defined by Eq. (4.12) and whose evolution with time for the sampled sprays was represented in Figure 5.46. In first place, the final SMDs obtained in all simulations are grouped in the graph of Figure 5.48. The first noticeable observation is the high sensitivity of the SMD to resolution, which shows a difference of factor 2: this is expected since the resolutions differ by the same amount. Differences are also found among operating points: in general, the SMDs for the low Weber cases are higher than the ones for the high Weber one, which is expected since high kinetic energy of the gas and fluid phases in the latter foster atomization, generating more and smaller droplets. There are, however, two exceptions: at $x = 10$ mm for the fine resolution, and at $x = 15$ mm for the coarse one. In the former (fine resolutions), both cases present the same SMD at $x = 10$ mm while differ at $x = 5$ mm: in fact, UG75_DX10 shows a reduction in SMD with axial distance (expected behaviour due to atomization) while UG100_DX10 provides the same SMD (unexpected behaviour). Two reasons could explain the constant SMD for UG100_DX10: 1) due to the higher kinetic energies in the gas and liquid phases, atomization is already completed at $x = 5$ mm, or 2) small droplets disappearing in UG100_DX10 when reaching the mesh resolution would not contribute to the SMD, making it larger than its true value in the real spray. This is also the most probable explanation for the almost constant SMDs between $x = 10$ and 15 mm in the coarse simulations.

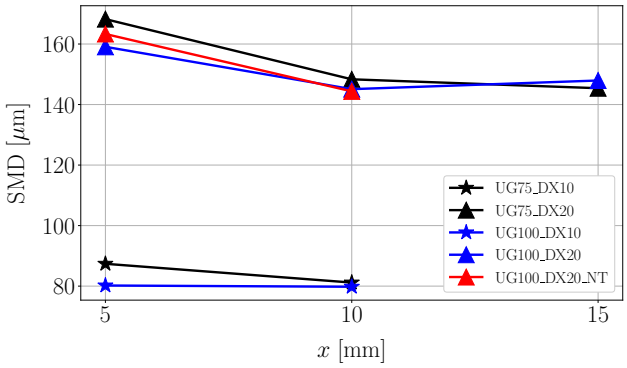

Figure 5.48: Evolution of SMD with axial distance for each simulation.

Droplet size and volume distributions also provide valuable information on the spray. Size distributions are usually represented by the notation $f_0(D)$, while volume distributions are denoted by $f_3(D)$. Two types of distributions are possible: discrete (histograms) or continuous. In the former, the spectrum of droplets size is divided into several range of droplets named bins or classes, and the number of droplets comprised within each class each counted. Histograms are the usual way of representing the granulometry when the size of droplets is directly available, such as in most experimental campaigns and computational studies resolving atomization. Continuous distributions, however, fit discrete distributions obtained experimentally and are used for making simplified models for spray injection in lagrangian simulations, since they can represent the spray by functions depending on few parameters. Examples of function widely used in sprays are the lognormal, Rosin-Rammler and Nukiyama-Tanasama distributions (Lefebvre & McDonell 2017).

Since both volume and equivalent diameters of droplets are known from the resolved simulations, probability histograms can be plotted. Figure 5.49 shows size (black bars) and volume (grey bars) histograms for the sprays from case UG100_DX20. The number of classes has been calculated according to Rice's rule, which estimates this value as $N_{\text{bins}} = \sqrt[3]{2N_{\text{dr}}}$ (Terrel & Scott 1985). The number histograms f_0 show a positively skewed distribution with a lognormal shape where most droplets are smaller than the SMDs. This lognormal behaviour is a common characteristic of sprays resulting from liquid JICF configuration and has been observed in previous numerical (Herrmann 2009) and experimental (Prakash et al. 2018) studies. The volume histograms f_3 shows higher probabilities at larger diameters than in f_0. In the fine simulations, only a small amount of droplets with large diameters are present due probably to their location in the decelerated gaseous phase caused by the crossflow. In the coarse simulations, the quantity of volume at high diameters is more uniform due to larger droplets generated. The fine simulations also show a larger number of droplets than the coarse ones (as shown in Table 5.10) due to the better resolution of surface and column breakup phenomena (see for instance Figure 5.17), which leads to a higher total volume contained in droplets of small diameters with respect to large ones.

Finally, lognormal curves are superimposed to the number histograms to show the trend of the sprays produced. Two lognormal curves are shown: one obtained through a theoretical correlation (red lines), and one obtained through a curve fit (blue lines). Both curves follow the following expression:

$$f_0(D) = \frac{dN}{dD} = \frac{1}{D\sqrt{2\pi \ln(s_g)^2}} \exp\left[-\frac{1}{2}\left(\frac{\ln D - \ln \overline{D}_{ng}}{\ln s_g}\right)^2\right] \tag{5.14}$$

where $\overline{D}_{ng}$ and s_g are the curves parameters. For the fitted lognormals, these parameters were obtained through a differential evolution algorithm which minimises a fitness function representing the deviation between the curve and the histogram (Storn & Price 1997). The other case has been taken from Lefebvre & McDonell (2017), who state that $\overline{D}_{ng}$ is the geometric mean size of the logarithmic droplet size and s_g is the geometric standard deviation. If the spray is assumed to be composed of spherical droplets, these moments can be obtained through the following formulas:

$$\overline{D}_{ng} = \exp\left(\frac{\sum_i \ln D_i}{N_{\text{droplets}}}\right) \quad ; \quad s_g = \exp\sqrt{\frac{\sum_i \ln\left(D_i/\overline{D}_{ng}\right)^2}{N_{\text{droplets}}}} \tag{5.15}$$

As observed in Figure 5.49, both curves present similar shapes in all cases but show larger differences when closer to the liquid injector (especially at the distribution's mode). The fitted lognormal retrieves better the histogram shape than the correlated one: this indicates that the definitions from Eq. (5.15) do not properly represent the spray. As the sampling plane moves downstream, the curves get closer, so the former definitions become more accurate. The reason of the mismatch close to injector and the posterior approach is the deformation of the droplets: closer to the injector more deformed (i.e. less spherical) liquid structures are sampled, while further downstream the spray is more atomized and droplets are generally more spherical. Therefore, Eqs. (5.15) represent better the spray further downstream the injector, where primary atomization is no longer taking place.

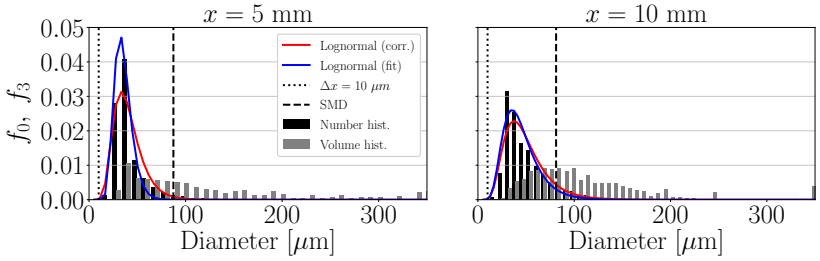

(a) Case UG75_DX10

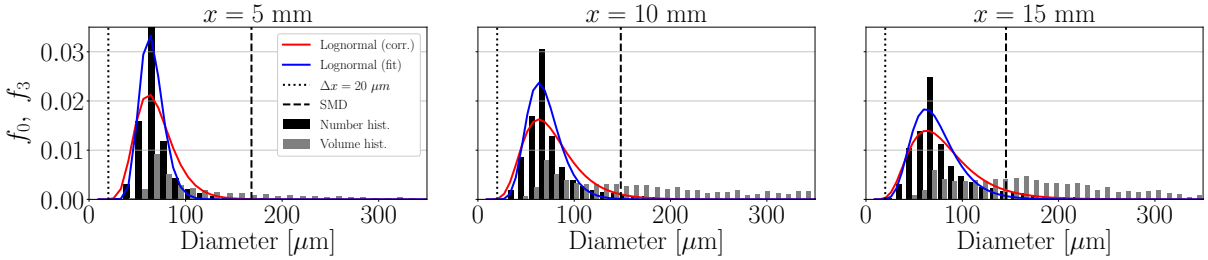

(b) Case UG75_DX20

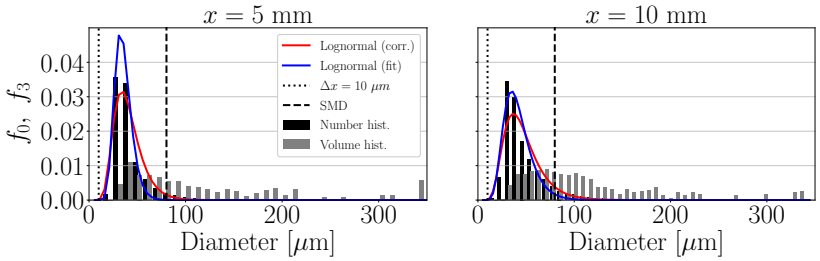

(c) Case UG100_DX10

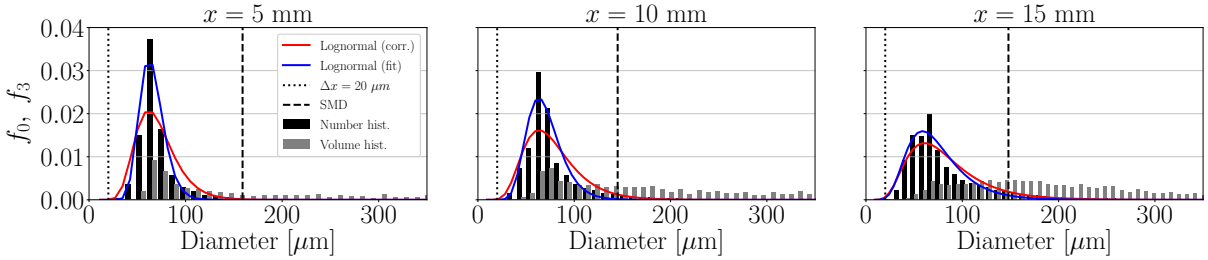

(d) Case UG100_DX20

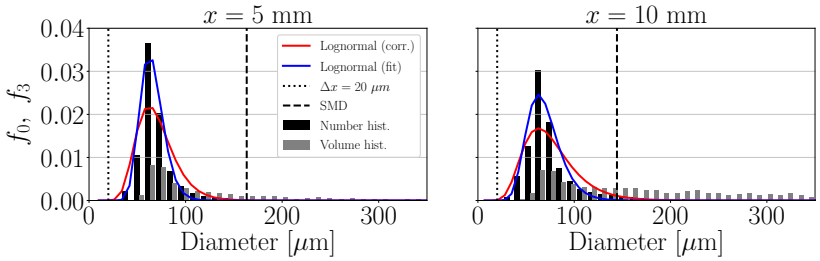

(e) Case UG100_DX20_NT

Figure 5.49: Droplets size (f_0) and volume (f_3) histograms for all cases

Liquid velocities

Final mean liquid velocities in axial and vertical directions for all simulations are shown in Figure 5.50. Lateral mean velocities are not displayed since they are in all cases close to 0 (see Appendix E), which is due to an equal jet opening in both positive and negative lateral directions. Two different mean velocities are shown in the graph of Figure 5.50: the arithmetic mean velocities calculated with Eq. (4.10), given by the solid lines, and the volume-weighted velocities calculated from Eq. (4.11) represented by the dashed lines.

The mean axial velocities are displayed in Figure 5.50a. The dependence on resolution is clearly noticeable: fine simulations show much larger velocities than the coarse ones due to the presence of a large number of finer droplets which relax fast towards the gaseous phase. In all cases, the magnitudes for the low Weber point are lower than for the high Weber one. From $x = 5$ to $x = 10$ mm, both the arithmetic and volume-weighted velocities increase in magnitude, which is a priori expected since the liquid structures are dragged and accelerated towards the crossflow direction. From $x = 10$ to 15 mm, however, the volume-weighted velocities still increase but the arithmetic ones show the opposite tendency. This unexpected decrease is attributed to the small droplets disappearing from the simulation which before their removal, are faster than the larger ones due to faster relaxation towards the gas. Hence, the arithmetic mean will take them into account at $x = 10$ mm (before their disappearance) and not at $x = 15$ mm (after their disappearance), producing a reduction in the mean velocity. The volume-weighted velocities, on the other hand, do not show this reduction since they give more importance to the velocities of the larger droplets: as these also relax towards the gas mean velocity (but slowly due to their large sizes), they show a monotonic increase with axial direction.

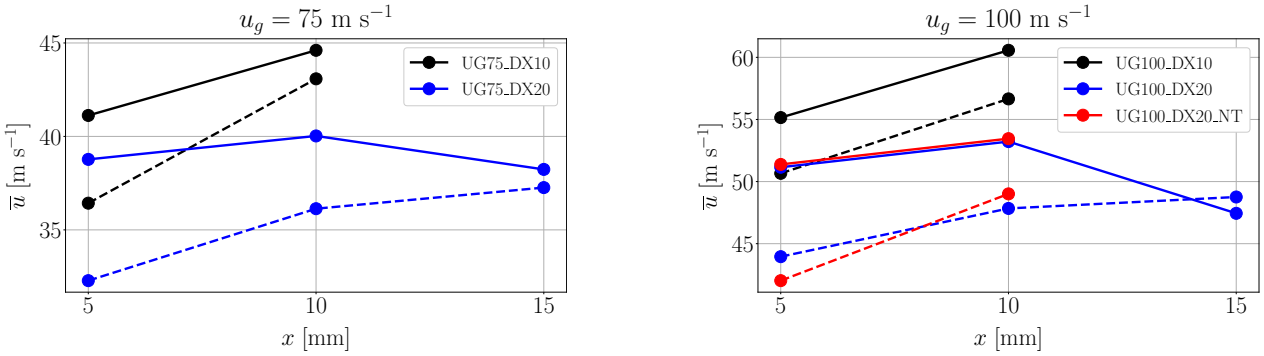

(a) Mean velocities in axial direction.

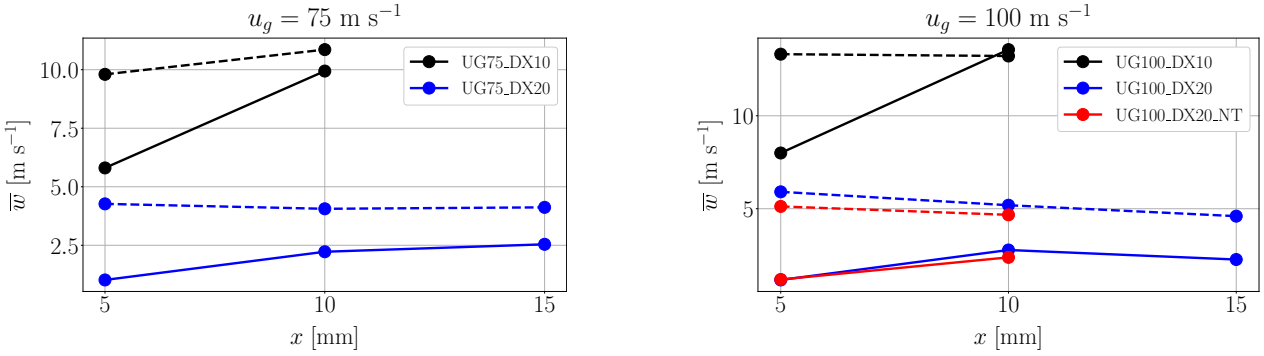

(b) Mean velocities in vertical direction.

Figure 5.50: Mean liquid velocities for all cases. Solid lines indicate arithmetic average velocities, while dashed ones indicate volume-weighted average velocities.

The mean vertical velocities are displayed in Figure 5.50b. Arithmetic velocities increase from $x = 5$ to $x = 10$ mm. The volume-weighted ones show, on the other hand, a constant or even decreasing tendency. In fact, mean vertical velocities are expected to decrease up to 0 with axial distance due to momentum exchange with the crossflow. The point of null vertical velocity has not been reached since it might be much further than $x = 15$ mm, which is unreachable for the simulations considered due to their higher computational cost. Nevertheless, a correct behaviour in terms of non-increasing vertical velocity with axial distance is correctly

captured. It is also worth commenting that fine resolutions show larger mean axial velocities: this is due to the larger vertical velocities generated by the column breakup behaviour, as shown in Figure 5.17. Finally, a last look at the graphs of Figure 5.50 reveals that the differences between arithmetic and volume-weighted velocities decreases with increasing axial distance for all cases: this shows that the spray atomizes along the crossflow direction, breaking large droplets into smaller structures and approaching both velocities. The decreasing difference among velocities indicates a continuing atomization: nevertheless, it is not expected that a fully atomized spray would show equal arithmethic and volume-weighted velocities, since the JICF produces a polydisperse spray with non-uniform velocity distributions (Wu et al. 1998).

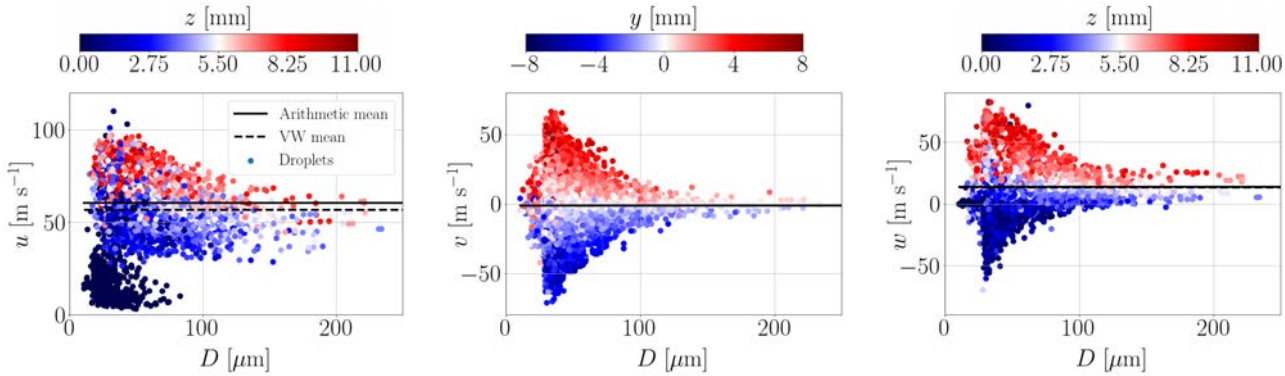

Figure 5.51: Scatterplots velocities - diameters for case UG100_DX10 at plane $x = 10$ mm. The axial velocity is non-dimensionalized with the bulk gaseous velocity, while the lateral and vertical ones have been non-dimensionalized with the bulk liquid velocity

To finish the analysis of velocities, scatterplots of velocities against droplets diameters are shown in Figure 5.51 for case UG100_DX10 at $x = 10$ mm. The black lines show the mean arithmetic (solid) and volume-weighted (dashed) velocities for the spray. The axial velocities show a concentration of droplets with low axial velocity at low vertical distances z: these droplets, smaller than 100 μm, correspond to the liquid structures filming close to the wall, and present also null or negative vertical velocities null. The fastest (axial velocity) droplets are also found for $D < 100$ μm, which correspond to droplets far downstream the liquid nozzle that have exchanged momentum with the crossflow. Larger droplets present lower velocities due to their slower relaxation towards the gas. As the consequence of such a heterogeneous axial velocity distribution, the mean arithmetic and volume-weighted velocities differ by around 10 %, with the latter being lower than the former due to the lower velocities found in the larger droplets. The scatterplot of the lateral velocities display a rotated T shape symmetric with respect to $v = 0$, with the positive velocities for $y > 0$ and negative for $y < 0$. These features indicate that the jet opens equally along the lateral directions, which is an expected behaviour since the freestream gas has no lateral velocity (this will not be the case in swirled configurations, such as the resolved simulations of BIMER shown in Chapter 8). The vertical velocities scatterplot also show a rotated T-shape where the droplets in the top part of the spray have positive velocities, indicating that the spray penetration increases, while the droplets at the bottom part have null or negative values. These droplets are generally small ($D < 100$ μm) and are probably entrained by the gaseous counter-rotating vortices induced by the dense core perturbation (see Figure 5.33). The mean velocities for the ensemble of droplets is positive (as also seen in Figure 5.50), indicating that the spray continues to penetrate vertically.

Deformation of liquid structures

Apart from the equivalent diameters and velocities, the sampled droplets in the resolved simulations are also characterized by their deformation parameters α and β as defined by Eq. (4.9). These magnitudes quantify the deviation of the liquid entity with respect to a perfect sphere: this one would yield $\alpha = \beta = 1$, while deformed droplets present $\alpha > 1$ and $\beta < 1$. Note that the values $\alpha < 1$ and $\beta > 1$ are not possible due to the inherent definitions of both magnitudes.

The mean volume-weighted (VW) values $\overline{\alpha}_{\mathrm{VW}}$ and $\overline{\beta}_{\mathrm{VW}}$ are shown in Figure 5.52. These values have been found to be converged in all simulations (details are given in Appendix E). As shown, $\overline{\alpha}_{\mathrm{VW}}$ decreases with axial distance in all cases, while $\overline{\beta}_{\mathrm{VW}}$ increases: the spray atomizes with axial distance, breaking large liquid structures (ligaments) into smaller droplets which are closer to an spherical shape. The values for $\overline{\alpha}_{\mathrm{VW}}$ are

always larger than 2.5, while $\overline{\beta}_{\mathrm{VW}}$ never exceeds 0.5. However, these criteria are only based on approximated geometrical parameters, hence sphericity needs to be defined by thresholds on α and β: for instance, Zuzio et al. (2018) defines sphericity for liquid structures presenting $\beta > 0.5$, while Herrmann (2010) proposes a sphericity criterion $\alpha < \alpha_{\mathrm{th}}$ where α_{th} should be chosen according to the case.

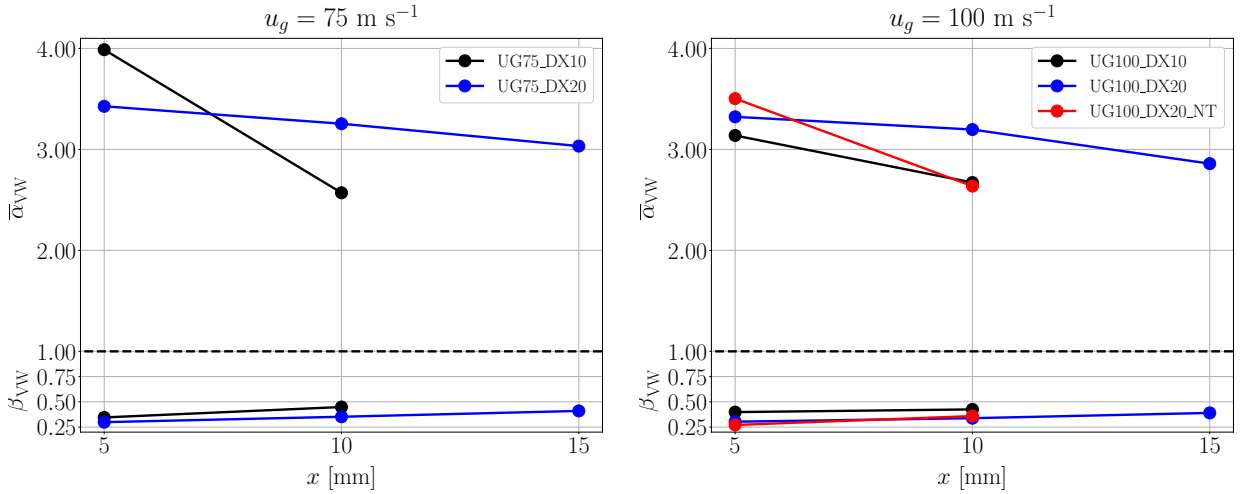

Figure 5.52: Mean deformation parameters for all simulations. Solid lines indicate arithmetic average deformation, while dashed ones indicate volume-weighted average deformation.

The scatterplots $\alpha - \beta$ for cases UG100_DX10 and UG100_DX20 are shown in Figure 5.53. The general trend is that smaller droplets present high values of β and low values of α, meaning that they are closer to a spherical shape. Larger droplets get further away from these values. The black, solid lines denote the sphericity criterion $\beta > 0.5$, $\alpha < \alpha_{th}$ where $\alpha_{th} = 2$ for this study. Hence, droplets within these bounds are considered to be spherical. This yields percentages of 35 % and 15 % spherical droplets in the fine and coarse cases respectively, confirming hence that the fine resolution resolves atomization better and produces more spherical droplets. Such a sphericity criterion could be used to trigger the transformation of droplets into lagrangian point particles for their further transport in the resolved simulations, saving computational resources Janodet (2022). However, the deformation criteria here introduced might not be fine enough to characterize the sphericity of sprays, and more accurate definitions including further information on the droplet's topology should be considered (Canu et al. 2018, Chéron et al. 2019, Palanti et al. 2022).

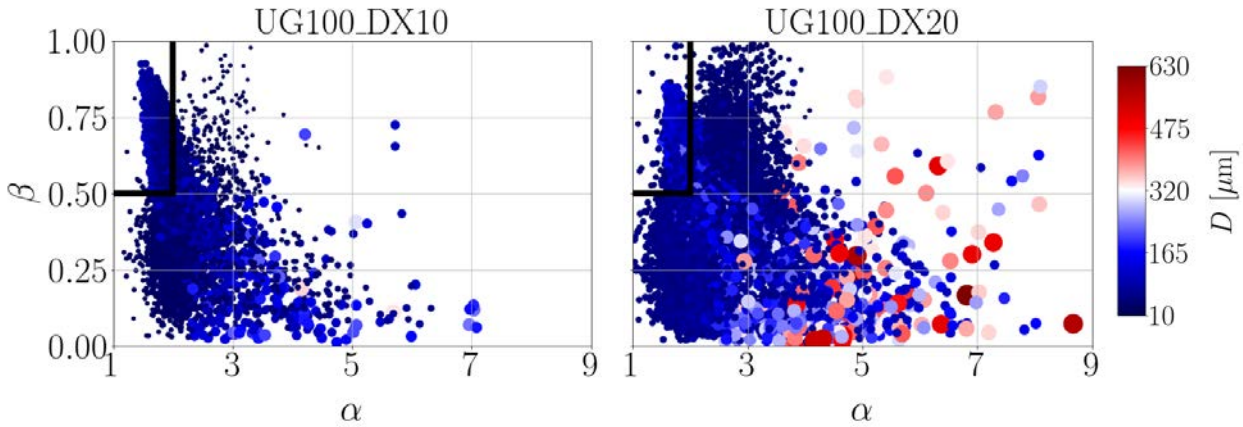

Figure 5.53: Scatterplots of deformation parameters α - β for cases UG100_DX10, UG100_DX20 at plane $x = 10$ mm. Droplets are colored and scaled by their equivalent diameter. Thick, black lines enclose the region where droplets are spherical according to the criteria defined in the text

5.7.3 Sprays spatial dicretization

Once the global spray features have been studied, the discretization process described in §4.4.3 can be applied to produce liquid injectors for dispersed-phase simulations. The resulting SLIs are shown in Figures 5.54 to 5.65. All sprays are discretized in grids composed of square probes, hence the convergence-driven discretization process is not applied here (it will be done in Chapter 6 to illustrate the differences between the convergence-driven and ad-hoc injectors), since the objective here is to describe the spray states for the different sampled sprays. Then, each probe contains a spray represented by the magnitudes from Table 4.2: the magnitudes shown in the figures are the SMD, volume flux q_l, convergence map and mean velocities in axial, lateral and vertical directions (u, v, w respectively). The convergence maps are shown through pixel maps, while the rest of the magnitudes have been interpolated in the grid for generating contour maps. The discretizing grids in each case are displayed in the volume-flux map and convergence maps.

Qualitatively, all maps show similar structures in terms of SMD, flux and velocities. The SMD distributions reveal small droplets at the bottom part (particles generated mainly through the surface breakup phenomenon) and higher values at the top, which correspond to ligaments and large droplets produced by column breakup. A decrease in SMD at the top part of the spray is observed, which is attributed to small droplets being shed from the column ligaments. Flux maps q_l exhibit circular patterns with maxima located at the spray center around the symmetry plane $y = 0$, then flux decreases radially outwards. These fluxes correspond to the same magnitude obtained from the IBs and shown in Figure 5.41: the structures are similar both qualitatively and quantitatively when comparing fluxes obtained with each method, indicating the suitability of the lagrangian tracking algorithm for obtaining spray characteritics from the resolved simulations. The main differences among lagrangian sampling planes and IBs are found when filming is present, which is captured by the former but not by the latter as shown in the flux maps. The mean axial velocity maps $\overline{u}$ exhibit low velocities at the center, bottom part of the spray plume and larger velocities at the sides. The central deceleration corresponds to the wake generated by the presence of the dense core. The higher velocities at the sides are attributed to small droplets accelerated by the crossflow. The lateral velocity $\overline{v}$ shows in all cases a symmetric behaviour with respect to the axis $y = 0$ where positive velocities are found for $y > 0$ and negative ones for $y < 0$, reflecting the spray opening along the lateral direction. Regarding the vertical velocities $\overline{w}$, they show a layered structure with increasing magnitude from the bottom (sometimes negative values are found, which correspond to droplets moving towards the wall that will eventually impinge it) to the top of the spray, indicating that the sprays increases its penetration along the axial direction (as reflected by the trajectories analyzed in §5.6.3). All these structures are characteristic of liquid JICFs which have been similarly observed in several experimental studies (Wu et al. 1998, Becker & Hassa 2002).

The pixel maps show local converged sprays around the maximum fuel flux location. The convergence criterion (introduced in §4.4.2) only takes into account the droplets size distributions and does not consider any other magnitude: areas with large fluxes contain more droplets, hence their distributions are more prone to convergence than probes at the edges which, in some cases, might only have one or two droplets. Furthermore, some cases (such as the spray at x = 15 mm in case UG100_DX20, Figure 5.63) show convergence close to the wall, where filming is present. Their equivalent fluxes maps reveal higher values than the IB fluxes at identical locations (Figure 5.41). Such higher fluxes correspond to filming droplets which are probably sampled twice by the lagrangian tracking algorithm: this one considers all liquid structures to be point particles, while in reality the filming liquid entities are deformed structures which displace along the wall at low velocities. Such structures would be projected through the plane and sampled at several time instants, therefore fostering a faster convergence. The point particle assumption was not done by the IBs methodology, which explains the discrepancies among methodologies at the filming regions. A last important observation is the effect of resolution on the convergence maps: for both operating points, the fine resolution maps show more converged probes (i.e. a more converged local spray) than the coarse ones even though the accumulation times sampled are lower (see Table 5.9). Converged distributions are obtained faster with fine resolutions due to the larger amount of droplets per timestep sampled (despite a lower total amount of droplets sampled in the whole simulation).

Case UG75_DX10

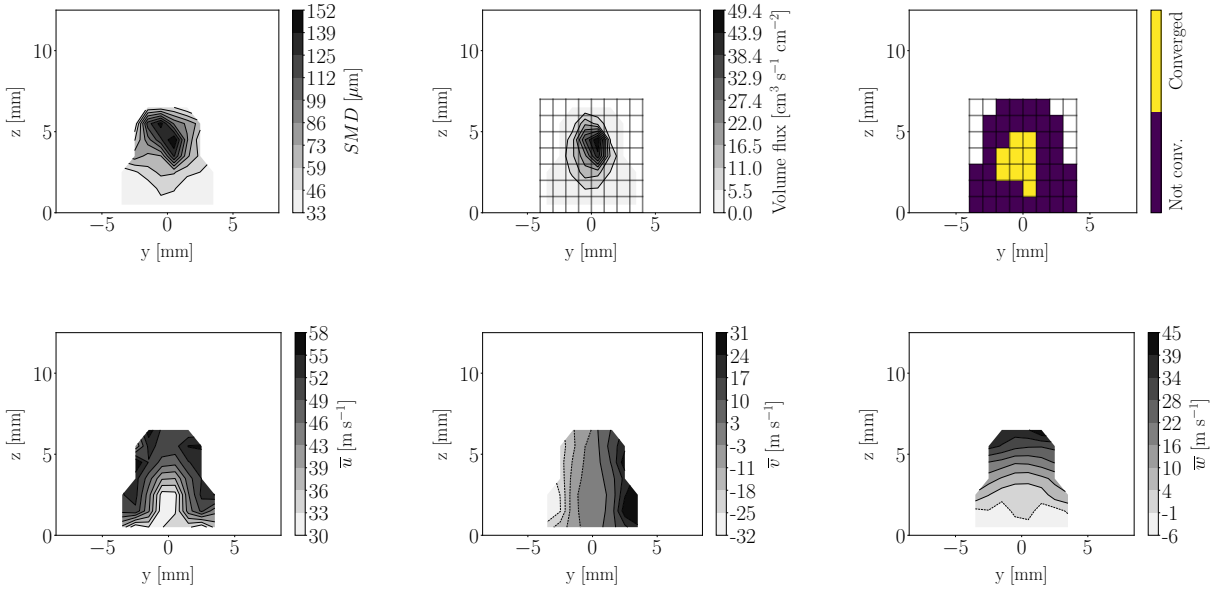

Figure 5.54: Spray states at x = 5 mm for case UG75_DX10

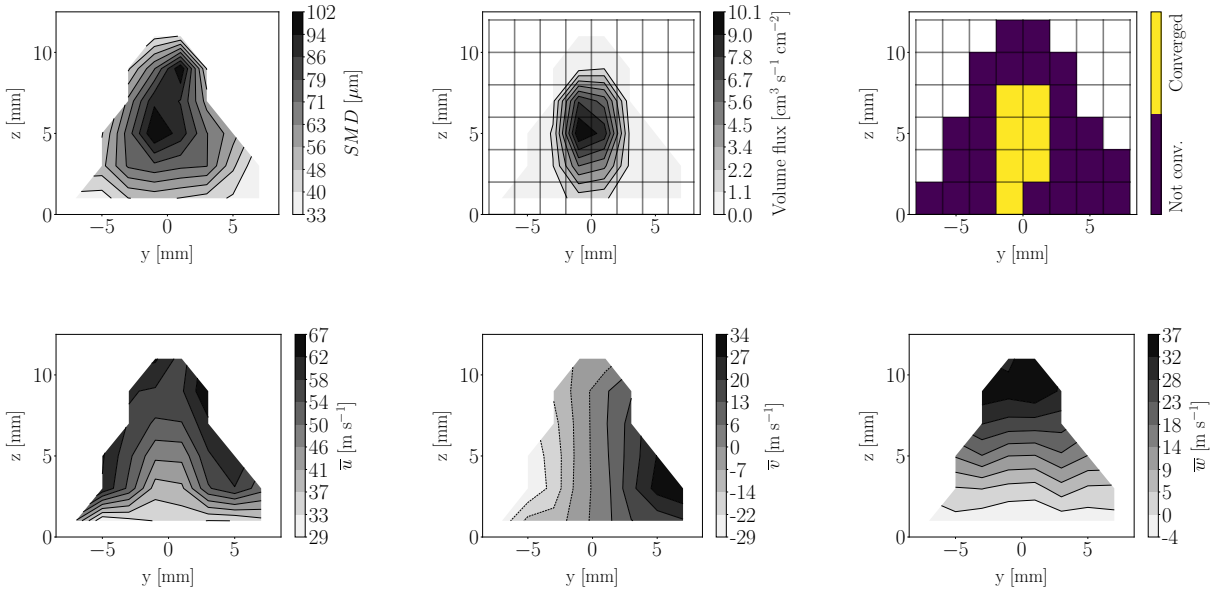

Figure 5.55: Spray states at x = 10 mm for case UG75_DX10

Case UG75_DX20

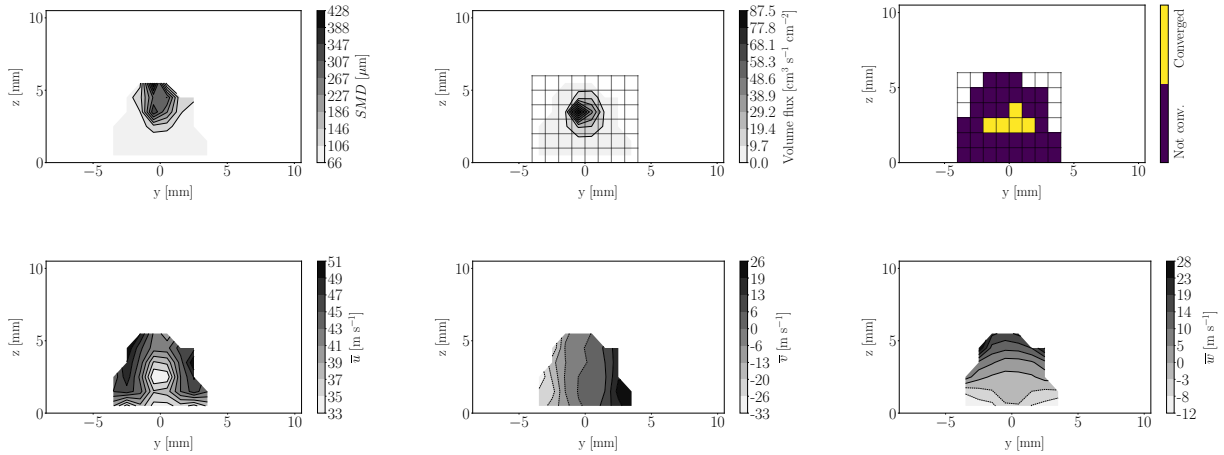

Figure 5.56: Spray states at x = 5 mm for case UG75_DX20

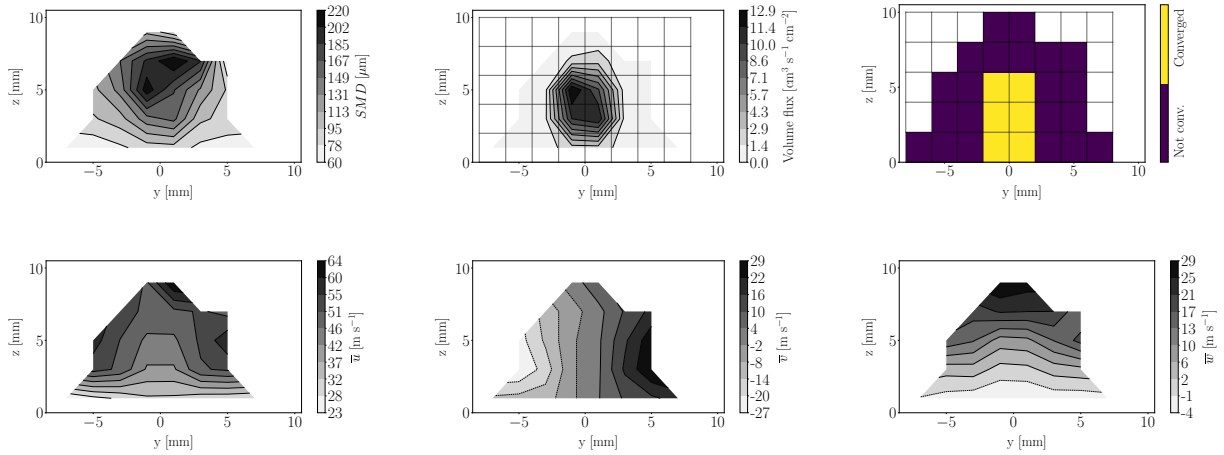

Figure 5.57: Spray states at x = 10 mm for case UG75_DX20

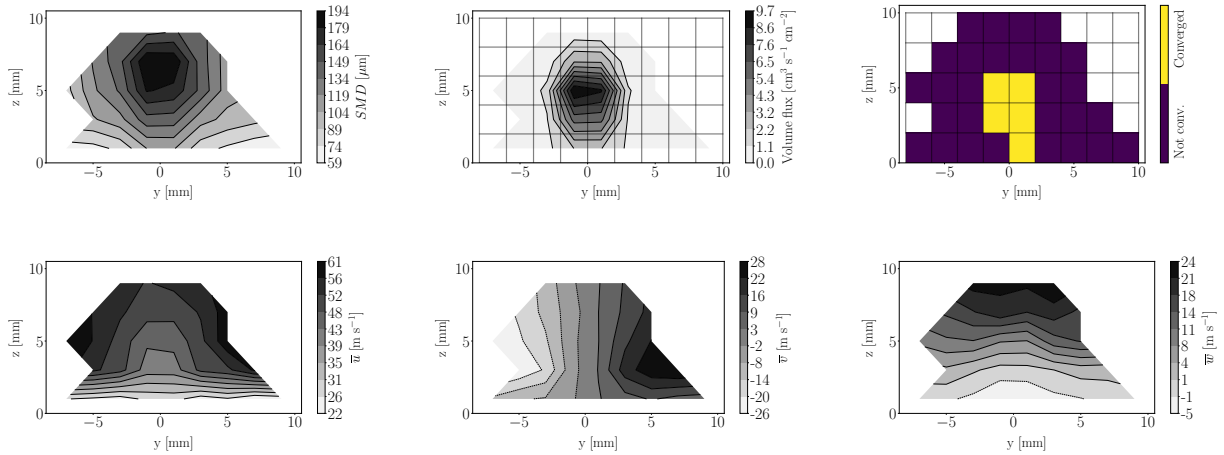

Figure 5.58: Spray states at x = 15 mm for case UG75_DX20

Case UG100_DX10

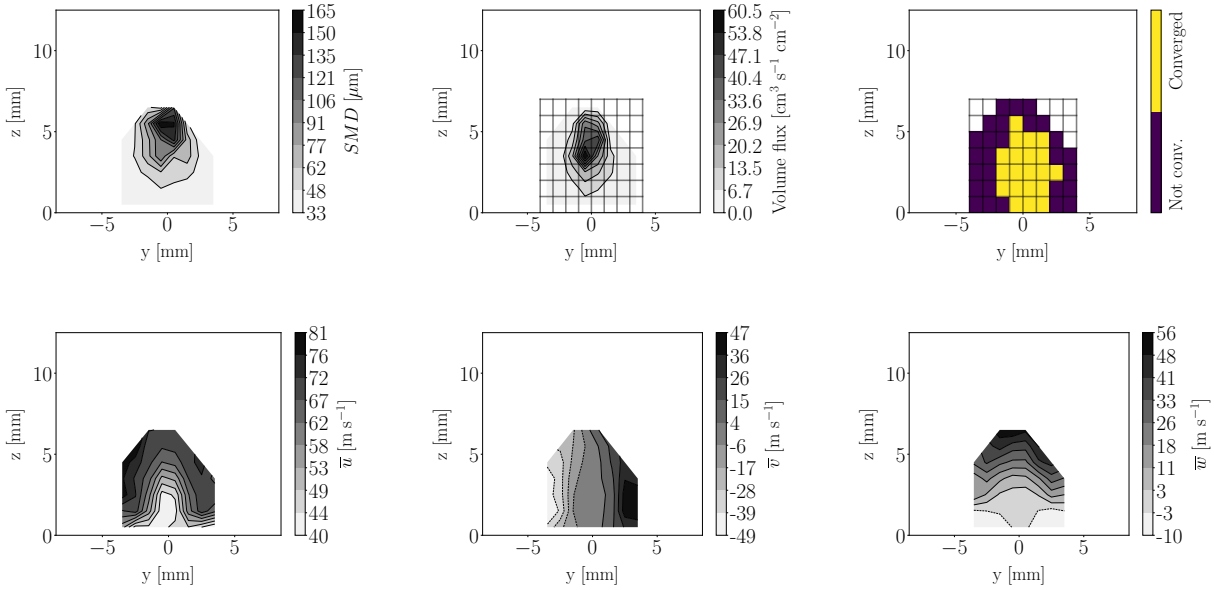

Figure 5.59: Spray states at x = 5 mm for case UG100_DX10

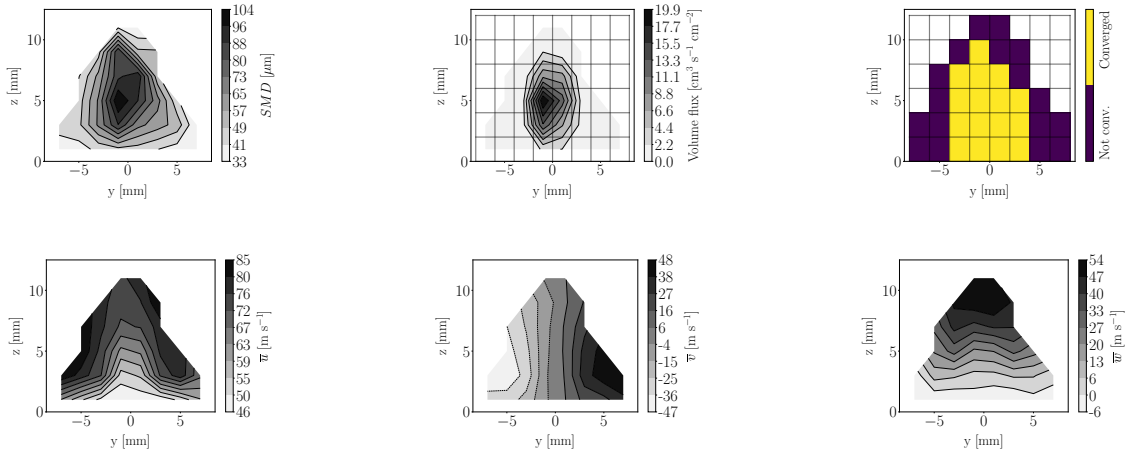

Figure 5.60: Spray states at x = 10 mm for case UG100_DX10

Case UG100_DX20

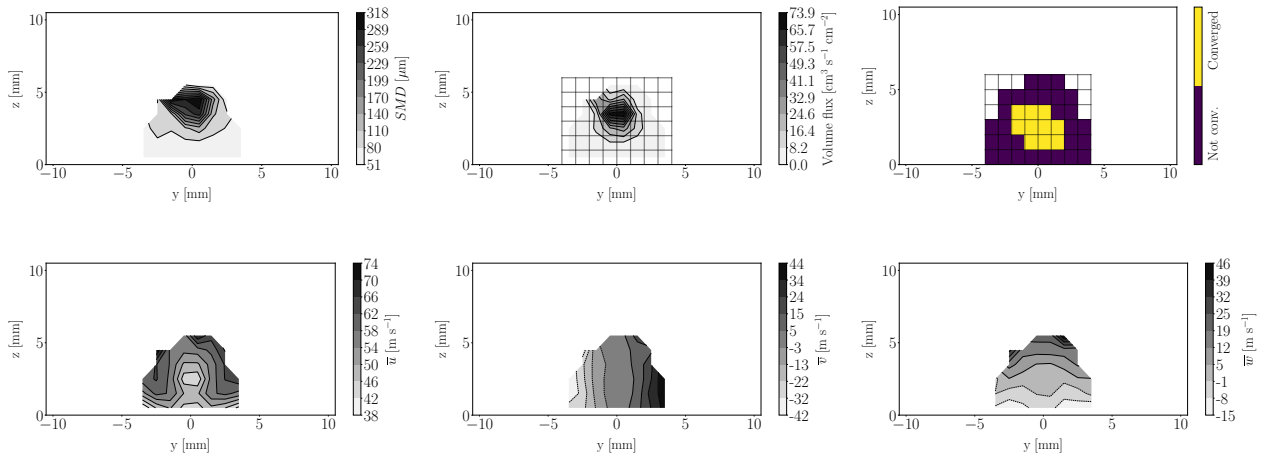

Figure 5.61: Spray states at x = 5 mm for case UG100_DX20

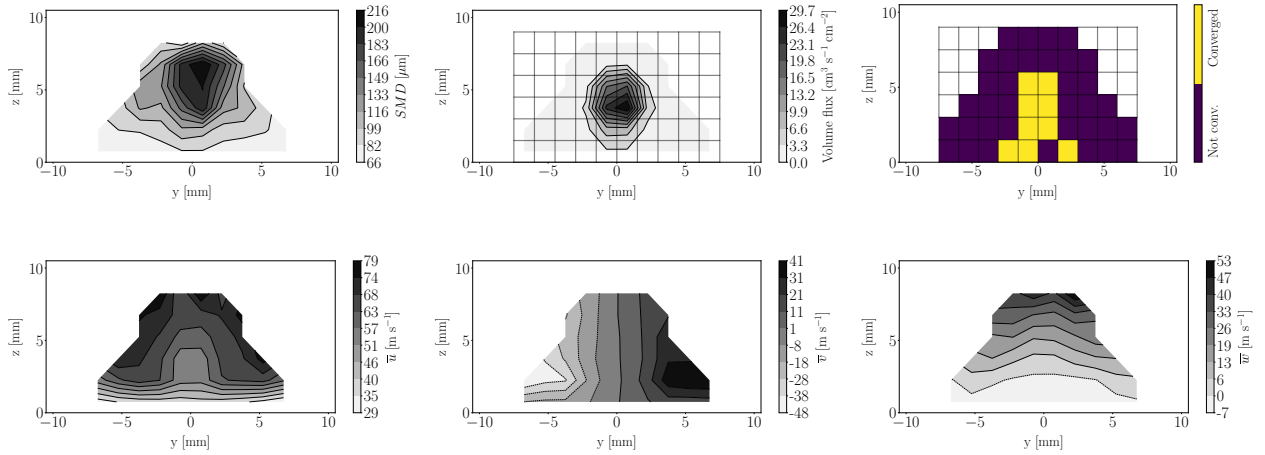

Figure 5.62: Spray states at x = 10 mm for case UG100_DX20

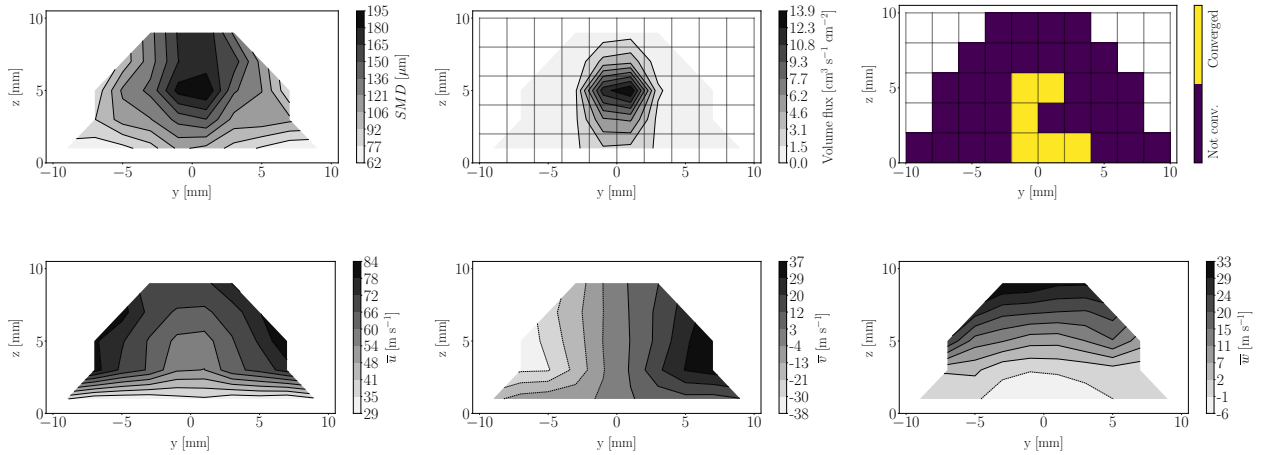

Figure 5.63: Spray states at x = 15 mm for case UG100_DX20

Case UG100_DX20_NT

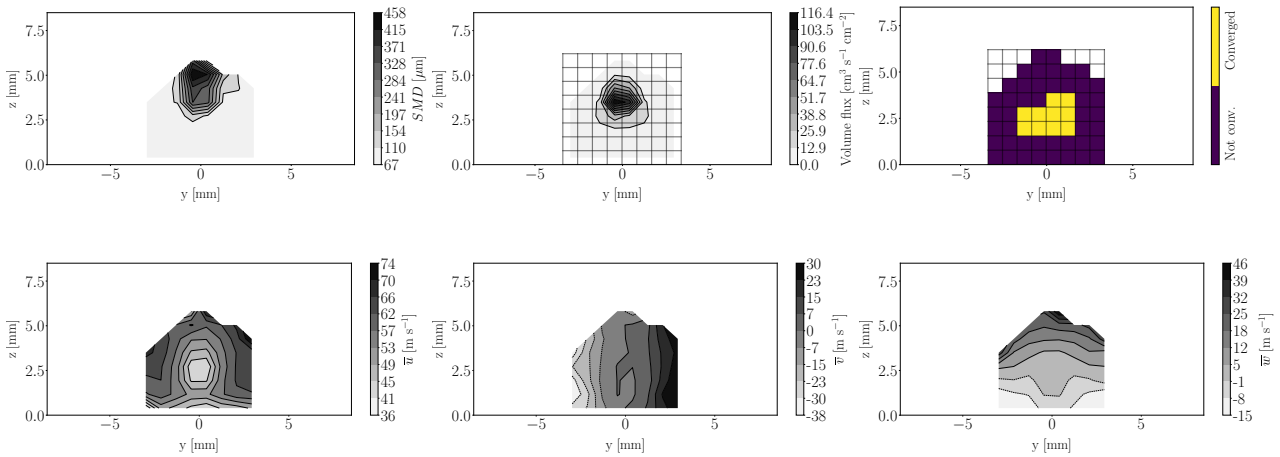

Figure 5.64: Spray states at x = 5 mm for case UG100_DX20_NT

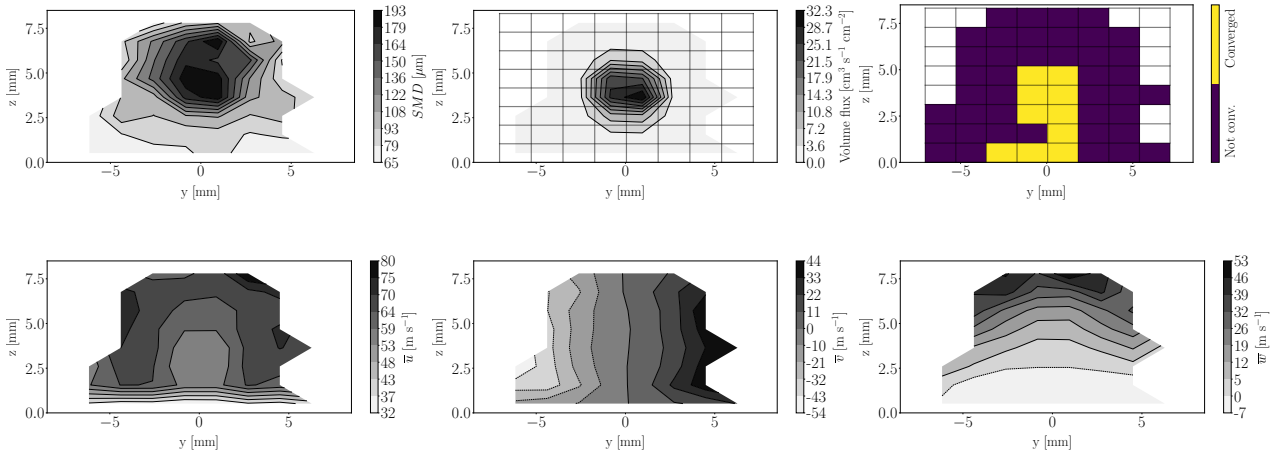

Figure 5.65: Spray states at x = 10 mm for case UG100_DX20_NT

Inhomogeneity of sprays

The resulting spray from a JICF is highly polydisperse and velocity-inhomogeneous, as shown by the previous spatial maps. The proposed SLI approach allows to directly account for these spray characteristics by prescribing spatially discretized statistics in dispersed-phase simulations. This spatial discretization procedure can also be seen as dividing the global in-plane accumulated spray into several individual sprays, each one contained in every discretization probe. Then, each probe will represent a monodisperse spray by accounting only for mean statistics on the diameters (SMD) and velocities. However, the polydispersity and inhomogeneity of each probe's spray should also be taken into account when performing injection.

In order to illustrate this inhomogeneity within the local probes, Figure 5.66 shows the maps of volume flux, arithmetic mean and volume-weighted (VW) velocities at $x = 5$ mm for case UG100_DX10. The probe containing the largest flux is highlighted in blue. The velocity maps show a different spatial distribution of the velocity when considering volume-weighted statistics or not: the VW velocity displays lower magnitudes in all the plane, since actually more importance is given to the large droplets which are slower than the smaller ones. Exceptions are observed where fluxes are the lowest, since the amount of droplets is scarce and the arithmetic mean and VW velocities get closer. The spray at maximum flux probe (i.e. the one with more sampled droplets) is further analyzed by plotting the droplet size D and axial velocity u histograms, as well as the scatterplot $D - u$, in Figure 5.67. In the size histogram the SMD is highlighted: if only the SMD is injected in the dispersed-phase simulations, a wide range of droplets sizes is actually neglected when prescribing the spray. Injection of a spray size distribution f_0 better representing the spray histogram will solvent this issue. The velocity histogram shows also a wide range of droplets velocities with respect to the mean ones: injecting a stochastic velocity given by a law such as the one from Eq. (4.18), which also accounts for the RMS component will then consider the inhomogeneity of the droplets velocities. It is also noticeable the difference between arithmetic mean and VW velocities, 52 against 44 m s^{-1} respectively: such differences at injection could greatly impact secondary atomization of droplets, which is highly dependent on the We based on the relative velocity. These two influences, i.e polydispersity through f_0 and variations in injection velocity through Eq. (4.18), will be investigated in the next chapter. Finally, it is interesting to highlight the dependence of droplets velocities on their sizes as shown in the scatterplot of Figure 5.67 right. The arithmetic mean and VW velocities are represented by the horizontal black lines, while the SMD is given by the vertical green line. The points where curves cross would represent the injection velocity and diameters if a monodisperse spray were to be injected: considering also the RMS through Eq. (4.18) would enlarge the range of velocities to be injected, while also including a f_0 would enlarge the range of droplets sizes injected. The red line represents the mean velocity at diameter intervals when the D axis is discretized into several bins (named sections). As shown, section mean velocities section can highly differ from the constant $\overline{u}$ of $\overline{u}_{\mathrm{VW}}$ ones. Further steps should consider the prescription of this $D - u$ conditioning in dispersed-phase simulations: this strategy is called sectional approach, and has been succesfully tested in lagrangian sprays (Vié et al. 2013).

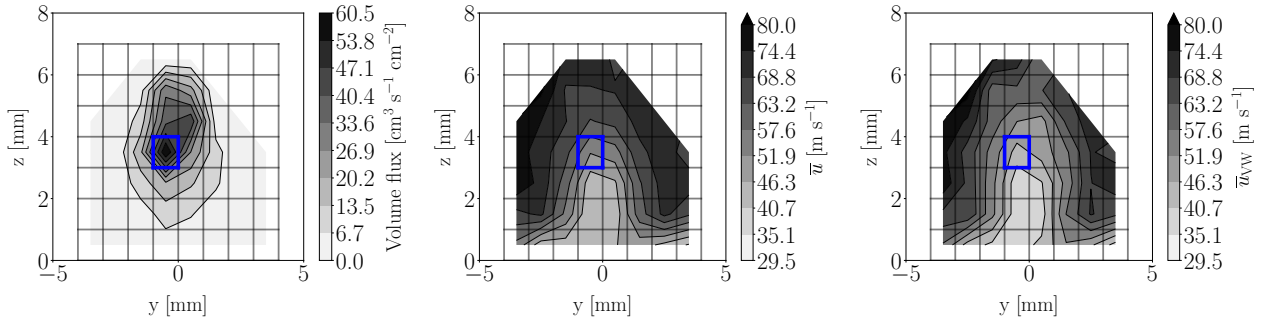

Figure 5.66: Volume flux, arithmetic mean and volume-weighted axial velocities at $x = 5$ mm from case UG100_DX10

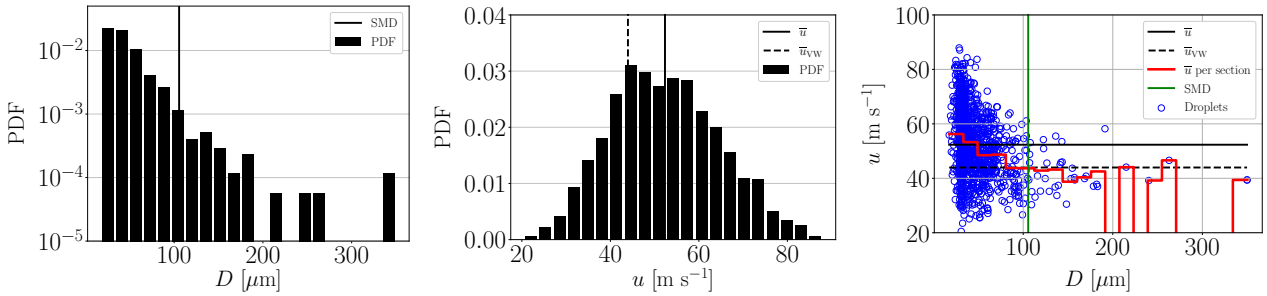

Figure 5.67: Histograms of droplets diameters D (*left*) and axial velocity u (*center*), and scatterplot $D-u$ (*right*) for the spray contained within the highlighted probe of Figure 5.66

On SLI convergenge time with resolution

If obtaining a SLI with a coarse resolution takes a given particle's accumulation time to converge, it is reasonable to assume that a finer resolution also needs to simulate the same accumulation time. This, indeed, has shown not to be true: as illustrated by the convergence maps from Figures 5.54 to 5.65, SLIs obtained with the fine resolution present a greater number of converged local probes than the coarse ones. Even though the accumulation time is lower in the fine resolution simulations, more droplets sampled per timestep and finer liquid structures make injectors converge faster than in the coarse computations. Therefore, increasing the resolution decreases the accumulation time needed to yield a converged spray: producing a final SLI requires less computational resources than a priori thought.

To illustrate the associated cost savings in computational time (named hereafter cost savings), let's consider the high Weber operating condition. The coarse simulation needs $t_{\text{ph}} = 6.16$ ms to produce a converged SLI, while the fine one needs only $t_{\text{ph}} = 0.78$ ms, i.e. 8 times less physical time. Therefore, if only the physical time is considered, it is a priori expected that a fine simulation should also run for $t_{\text{ph}} = 6.16$ ms, increasing the cost from the coarse simulation by 8. Indeed, their actual computational costs are 1.25 and 4.66 million CPU hours for the coarse and fine simulations: the cost to obtain a more locally converged injector rises only 4 times. Figure 5.68 illustrates graphically this difference. The first and second columns show the total CPU hours from Figure 5.42. The third one shows the estimated cost to run a fine simulation as far as the coarse one, which would be of $t_{\text{CPU}} = 36.7 \cdot 10^6$ hours. The cost savings are therefore estimated to be of $30.41 \cdot 10^6$ hours.

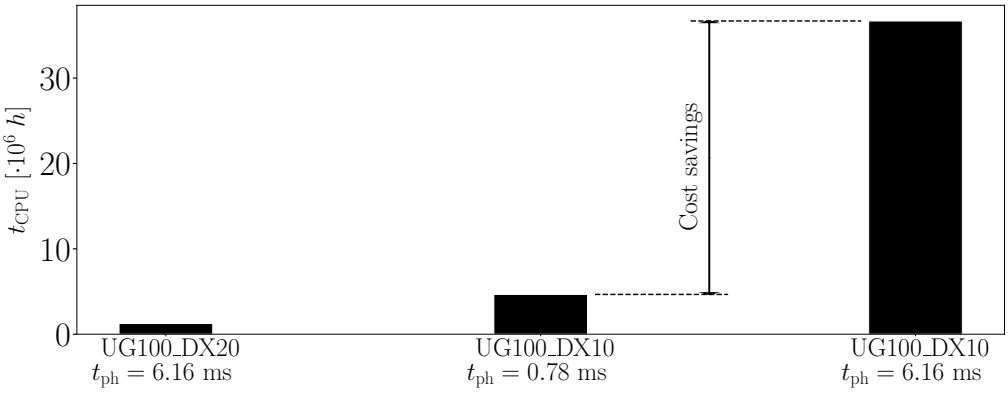

Figure 5.68: Cost savings in SLI development by refining grid resolution

5.8 Conclusions

This chapter has presented resolved simulations of the injection and atomization processes in the academic kerosene jet in crossflow (JICF) configuration tested experimentally by Becker & Hassa (2002). The experimental test case and computational setup chosen to model the former were firstly presented. Two operating conditions at high pressure were simulated with two interface mesh resolutions: a coarse and a fine one, differing by a factor of 2.

Firstly, the physics of the resolved atomization simulationes were studied (§5.6). Studied features and the main results are summarized in the following:

- The jet establishment was measured by the evolution of liquid volume and mesh elements in the domain. These magnitudes showed that the coarse resolution simulations were fully established, while the fine ones were on the verge of it.
- Both column and surface breakup modes are properly retrieved in the simulations, which are the main primary atomization mechanisms observed in liquid JICF configurations. The fine simulations retrieved the windward column instabilities, while the coarse ones did not.
- Trajectories of the jet's windward side were highly sensitive to the postprocessing methodology. Validation with an experimental correlation showed that the computations can accurately predict the trajectory closer to the liquid nozzle. Further downstream, trajectories deviate from the experimental correlation, and the resulting trajectories are dependent on the mesh resolution. This dependency is due to the windward instabilities, which are retrieved only in the fine cases.
- The gaseous field perturbed by the dense core presence was analyzed. The classical turbulent structures appearing in classical JICF configurations (recirculation region and counter-rotaing vortices) were properly captured by the simulations.
- Resolved fluxes in planes perpendicular to the crossflow direction were quantified with the interior boundaries methodology. Flow rates were observed to decrease further away from the liquid nozzle. This is attributed to: 1) mass impinging the wall, and 2) small droplets which reach a characteristic size of the order of the interface resolution and are removed from the simulation.

Finally, the simulations were postprocessed to build a SLI (§5.7). The dense core was characterized and mean values for its breakup coordinates, width and net force applied were obtained. These parameters will be used to define an Actuator Line Model in the dispersed-phase simulations of Chapter 6 for modeling the dense core presence. Sprays were then sampled in planes perpendicular to the crossflow direction. The following global magnitudes were firstly studied:

- Mean liquid fluxes, which yielded close values to the resolved flow rates previously assessed. This proves the suitability of the lagrangian tracking methodology for spray characterization.
- Droplets sizes, which were characterized through 1) the Sauter Mean Diameter (SMD), which shows a decrease with axial distance due to atomization, and 2) droplets size histograms, which show a lognormal shape characteristic of sprays produced in JICF configurations. Convergence of sizes with mesh resolution was not achieved: the smaller SMDs obtained were larger than the experimental SMD for complete atomization. Therefore, finer resolutions would be required to achieve droplets size convergence.
- Mean velocities, which revealed that an adequate spray behaviour is obtained when these are estimated through volume-weighted rather than from arithmetic averages.

Eventually, the sampled sprays were in-plane spatially discretized. The resulting spray structures represented by maps of SMD, velocities and fluxes showed a proper physical behaviour characteristic of liquid JICF configurations. Convergence maps revealed that more converged probes are obtained in regions with higher fluxes and for sprays generated with fine interface resolutions. These simulations produce smaller particles and a larger number of droplets per timestep than the coarse ones: hence, even if their total simulated physical time is lower, their resulting sprays converge faster. These spatially discretized sprays will then serve as the liquid boundary conditions for the computations of Chapter 6.

Chapter 6

Dispersed-phase simulations of JICF

6.1 Introduction

In the previous chapter, resolved simulations of atomization in a liquid jet in crossflow (JICF) configuration were reported. These simulations, which were used to construct a Smart Lagrangian Injector (SLI) for dispersed-phase simulations, could not reach the axial location where Becker & Hassa (2002) provide experimental results on the spray characteristics. In this chapter, dispersed-phase simulations are performed in the same configuration. These simulations prescribe the liquid phase with SLI, and the resulting spray is compared to the experimental results provided far from the liquid nozzle.

In first place, the state of the art is reported in §6.2. The experimental results available for comparison are briefly summarized, as well as an estimation of the experimental uncertainties. A review on previous numerical works on the same configuration is presented, which are compared to results from one of the dispersed-phase computations performed in this thesis. Then, a parametric study on the SLI variables playing a role in the dispersed-phase simulations is performed. This study is divided into three parts:

- Influence of the gaseous phase (§6.4). The Actuator Line Method (ALM) is applied to model the perturbation effect of the dense core. An additional methodology consisting on prescribing statistics of the disturbed gaseous phase on a reduced domain is also proposed and tested.
- Influence of the secondary breakup model (§6.5). The three models implemented in this work (TAB, ETAB and Gorokhovski), which were introduced in §4.6, are assessed.
- Influence of the liquid phase parameters (§6.6). Parameters tested include the injectors produced by each resolution and sampling location, droplets injection velocities and diameters, convergence-driven discretization and the operating condition.

In all cases it is found that, due to secondary atomization, the resulting droplets are smaller than those reported by the experiments. This hypothesis is finally confirmed in §6.7 by deactivating secondary breakup during the first instants after injection, allowing droplets to relax towards the gaseous phase before breakup is triggered again.

Preliminary parts of this chapter have been published in Guillamon et al. (2021).

6.2 State of the art

6.2.1 Experimental results for validation

The study from Becker & Hassa (2002) reports experimental results on SMDs and fluxes in a plane perpendicular to the crossflow $x = 80$ mm downstream the liquid injection point. These results, shown in Figure 6.1 for the high Weber operating point (see nomenclature from Table 5.2), are represented in the form of contour maps. The volume flux shows a circumferential pattern where the largest flux is located at the center and is reduced radially. The SMD shows a layered profile where the largest droplets are located at the top part of the spray (ballistic behaviour).

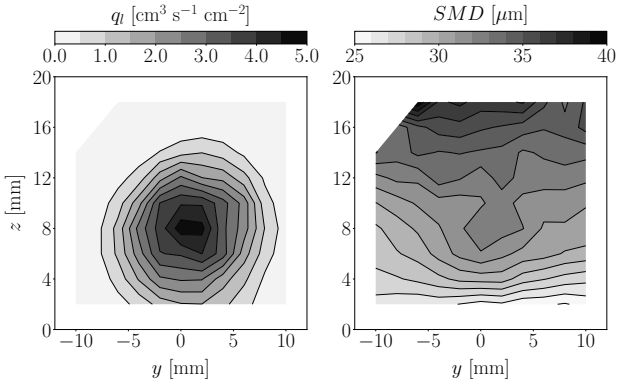

Figure 6.1: SMD and volume flux maps for the high Weber case obtained experimentally by Becker & Hassa (2002) at a location $x = 80$ mm downstream the liquid injector

Apart from the maps, quantitative results are also reported. These ones are given as the integrated profiles of the liquid volume flux and flux-averaged SMD over the z and y directions, which are then respectively dependent on y and z. The expressions used to calculate such measurements are given by Eqs. (6.1):

$$\langle q_l \rangle (z) = \frac{1}{L_y} \int_0^{L_y} q_l (y,z)\, dy \quad ; \qquad \langle SMD \rangle (z) = \frac{1}{L_y \langle q_l (z) \rangle} \int_0^{L_y} q_l (y,z)\, SMD (y,z)\, dy \tag{6.1a}$$

$$\langle q_l \rangle (y) = \frac{1}{L_z} \int_0^{L_z} q_l (y,z)\, dz \quad ; \qquad \langle SMD \rangle (y) = \frac{1}{L_z \langle q_l (z) \rangle} \int_0^{L_z} q_l (y,z)\, SMD (y,z)\, dz \tag{6.1b}$$

Figure 6.2 shows the profiles obtained by applying these expressions to the experimental results. The integrated volume flux over y (Figure 6.2a) shows the maximum flux to be located at $z \sim 8$ mm. Above this location, flux decreases with z until there is no more liquid present. Flux values are generally larger for the high Weber point than for the low Weber one, and liquid penetrates further in the former than in the latter due to its larger liquid velocity at injection. Regarding the SMD profiles, both cases follow a ballistic behaviour. The spray of the low Weber point contains droplets of larger mean size than the high Weber one.

With respect to the profiles integrated over z (Figure 6.2b), both SMD and flux lines follow parabollic profiles with maxima located at $y = 0$. The behaviour of the profiles depending on the operating point follow the same tendencies than in Figure 6.2a: lower fluxes and larger droplets for the low We case.

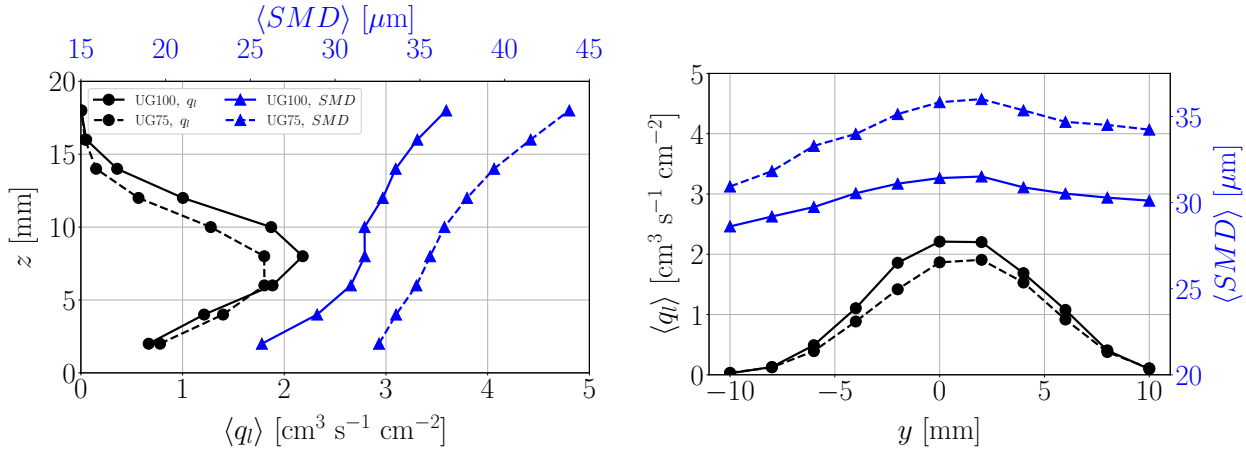

(a) Profiles integrated over y.

(b) Profiles integrated over z.

Figure 6.2: Integrated liquid volume flux and SMD profiles by Becker & Hassa (2002) at a location $x = 80$ mm downstream the liquid injector for both operaing points from Table 5.2

Finally, the overall SMDs estimated from PDA measurements are reported in Table 6.1.

Table 6.1: Experimental SMDs at $x = 80$ mm

Operating point	SMD [μm]
Low Weber	35.2
High Weber	31.0

Sources of uncertainty

The experimental results previously shown were obtained through Phase Doppler Anemometry (PDA) measurements. PDA is built on the assumption that droplets are spherical, hence such measurements can therefore yield considerable errors on droplets sizes and fluxes (Tropea 2011). Several sources of error have been identified in the past. Bachalo (1980) explained that the optical setup plays a paramount role, since it can lead to the misalignment of dual-beam reflected and refracted rays (Gaussian beam Effect) which can pollute the measurements. In this sense, Doublet (2019) showed through an error propagation analysis that the uncertainties in the diameters were actually especially sensitive to the elevation angle of the PDA detectors. Damaschke et al. (1998) discussed the role of the droplet non-sphericity, stating that PDA is prone to size overestimation when particles are deformed or oscillate in a preferential direction. Dullenkopf et al. (1998) identified three main sources of error in fluxes estimation: 1) the particles size measurement (from which the flux is calculated, hence propagating the error), 2) the number count of droplets, and 3) the reference area used for measurements (the smaller the area the better, since it can also avoid counting droplets twice). Brandt et al. (1998) tested an airblast configuration and discussed several possible sources of error in sizes, highlighting the contribution of alignment uncertainties in the setup (~ 1 %), the change in refractive indices due to heating (~ 3.5 %), and the deformation of the sampled particles, which is common at high speed environments (such as the found found in airblast). They estimated a 7 % for the uncertainty on droplets sizes and a 10 % in fluxes if the concencentration of particles was not too high. It is worth mentioning that their test bench is the same one that Becker & Hassa (2002) used later at DLR to test the liquid kerosene JICF dealt in this thesis. The experiments from Becker & Hassa (2002) do not actually provide data on the sizes uncertainties, but do discuss errors on fluxes for which they report mean deviations of 20 % and maximum of 37 %. Tropea (2011) makes a review on experimental methods involving optical techniques to characterize disperse multiphase flows, and states that PDA measurements often show flux uncertainties from 20 % up to several hundreds, while errors in particle size often range ideally between 10 and 30 %.

The objective here is to estimate uncertainties in the experimental measurements of Becker & Hassa (2002) to obtain confidence intervals for validation of numerical results. As mentioned in the previous paragraph, they provide a mean uncertainty of 20 % for fluxes, but do not give any information on sizes. For the same test bench but with different atomizers and operating conditions, Brandt et al. (1998) report errors of 7 % and 14 % for the droplets diameters and fluxes, respectively. Even though the PDA setup is identical in both studies, the provided errors in fluxes differ among each other: this might be due to different operating conditions, the atomizer or misalignments in the optical setup in both experiments. Therefore, to estimate the diameter uncertainty for the study of Becker & Hassa (2002), the relation between droplets sizes and fluxes errors is assumed to be identical as in Brandt et al. (1998), who state uncertaintes for fluxes to be twice larger than for sizes. Applying this factor to Becker & Hassa (2002) yields mean diameter uncertainties of 10 %. It is important to keep in mind that this estimated error in droplets size is only approximative and could greatly vary in the actual experiments.

Since Becker & Hassa (2002) give values on the flux uncertainties and their experimental data are available through the maps, it is possible to estimate the fluxes obtained in the experiments. The flux map ax $x = 80$ mm for the high Weber operating condition is shown in Figure 6.4a. The grid which was used in the experiments to sample the spray and process the data, which is composed of 2 mm sides probes, is also displayed. Each probe contains a volume flux value q_l which is stored at the center of the probe to plot the maps (as done in the SLI injectors of Figures 5.54 to 5.65). The grid is then composed of $N_y = 11$ probes in the lateral direction and $N_z = 9$ in the vertical one. Given an arbitrary probe located at a position (j, k) (where j is the probe index in the lateral direction y and k in the vertical one z) with surface $S_{\mathrm{j,j}}$, the nominal liquid flux through this probe can be calculated by applying Eq. (4.14) to the probe volume flux $q_{l_{j,k}}$:

$$Q_{l_{j,k}} = q_{l_{j,k}} S_{j,k} \tag{6.2}$$

Then, the total liquid flow rate from the map can be calcuated by adding all the nominal fluxes from each probe:

$$Q_l = \sum_{j=1}^{N_y}\sum_{k=1}^{N_z} Q_{l_{j,k}} = \sum_{j=1}^{N_y}\sum_{k=1}^{N_z} q_{l_{j,k}} S_{j,k} = 4062 \text{ mm}^3 \text{ s}^{-1} \tag{6.3}$$

which, as shown, gives a value of 4062 mm^3 s^{-1}. The injected flow rate for this case is $Q_{l,\text{inj}} = 3710$ mm^3 s^{-1}, as given in Table 5.2. Therefore, the PDA measurements report a flux excess of 9.5 % with respect to the injected flow rate. This deviation is comprised within the mean uncertainty of 20 % provided by the authors of the experiments. Nevertheless, it is paramount to consider this flux overestimation when comparing to dispersed-phase simulations, since liquid is injected with SLI in these ones at a rate of $Q_{l,\text{inj}} = 3710$ mm^3 s^{-1}. In reality, if the PDA was exempt of errors, the retrieved experimental flux could not be larger than the injected one (mass is not created in the simulation). Indeed, it should be lower since there is filming in the experiments, as shown in Figure 6.3, that reduces the liquid flux perpendicular to the crossflow. The resolved simulations could capture this filming phenomenon in the jet.

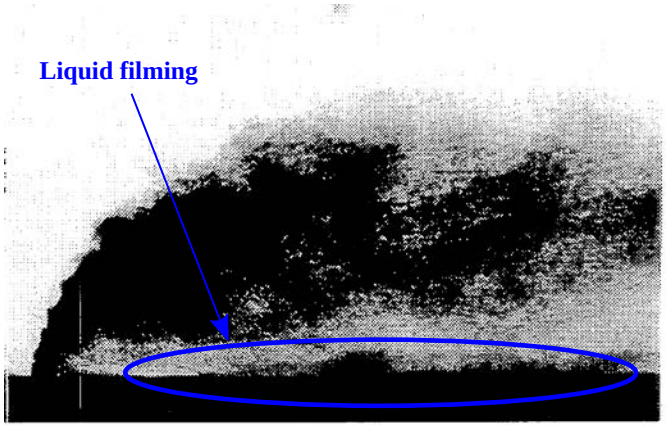

Figure 6.3: Snapshot of instantaneous liquid jet from Becker & Hassa (2002), showing the filming phenomenon

6.2.2 Previous numerical studies

The experimental configuration of Becker & Hassa (2002) has been studied through computations by several authors, all of them simulating the high Weber operating point from Table 5.2. Rachner et al. (2002) simulated the jet in steady crossflow by considering the early liquid as a cylinder deflected by the airflow, which exchanges momentum with a modified drag coefficient, sheds mass and produces droplets whose properties are given from experimental correlations. Later on, Eckel et al. (2016) extended this model to account for shear breakup of ellipsoids and flattened liquid jets (to account for more realistic JICF dense core effects) in both steady and unsteady crossflows, by using semi-empirical correlations. Independently of these studies, Jaegle (2009) and Senoner (2010) also developed models with this configuration: the former injected a developed spray at the liquid nozzle while accounting for a modified drag law in the near-nozzle region to mimic the liquid column momentum exchange, and the later injected big blobs at the nozzle but accounting for secondary atomization. All these models (except for Rachner et al. (2002) since it was more recently improved by Eckel et al. (2016)) are summarized in the diagram of Figure 3.3.3 and detailed in §3.2.

In order to position the current work into the state of the art, it is worth to compare it to the previous studies performed. All the works aforementioned use data shown in Figure 6.1 to validate the computations. Nevertheless, not all the numerical studies previously mentioned use all these data for validation, but only display a few of them. Table 6.2 shows a summary of the validation data directly available in the previous works. None of the papers referred present data on the SMD map, while only Eckel et al. (2016) give data on the global SMD obtained. Most of the works give data on the flux and SMD profiles integrated over y, while only Rachner et al. (2002) provides profiles integrated over y.

In first place, the flux maps from all the previous works that provide these information are shown in Figure 6.4. The experimental map is also show for visual comparison. In general, all maps show a circular

flux shape and an overestimation of the maximum flux location in the vertical direction (the integrated maps discussed in the following lines confirm this observation). Since the data belonging to the the maps of the numerical studies were unfortunately not directly available, it was obtained by digitalizing the 2D maps depicted in the papers. The grid used for digitalizion is not shown since it was finer than the experimental grid in order to properly capture all the features of the maps, and showing it together with the maps hinders their visualization. From the digitalized maps, the total flux in the plane can be calculated as done previously for the experimental data applying Eq. (6.3). The results are shown in Table 6.3: even though the fluxes are not exactly equal to the injected flux (the digitalization methodology is not robust enough to retrieve accurately the actual fluxes plotted by the authors, which should be equal to the injected flux and therefore differ from the values obtained), all values are lower than the flux integrated from the experimental map. The only exception is Rachner et al. (2002): in fact, this work does not display neither maps nor nominal rates, but normalized integrated profiles which in this case have been de-normalized with the injected flux (it has been assumed that the flux retrieved at 80 mm is equal to the injected one). The integrated profiles of the fluxes shown in Figure 6.5 confirm these lower flow rates obtained in all simulations performed by each author. These integrated profiles have been obtained through either direct digitalization of the curves when available (Table 6.2) or by applying Eq. (6.1) to the maps when not available. The error bars in the experimental flux profiles of Figure 6.5 correspond to a deviation of 20 % in each point.

Table 6.2: Available data from previous numerical studies on experimental validation in the configuration of Becker & Hassa (2002)

Work	Global SMD	SMD map	Flux map	$\langle SMD\,(z)\rangle$	$\langle q_l\,(z)\rangle$	$\langle SMD\,(y)\rangle$	$\langle q_l\,(y)\rangle$
Rachner et al. (2002)				✓	✓	✓	✓
Jaegle (2009)			✓	✓	✓		
Senoner (2010)			✓	✓	✓		
Eckel et al. (2016)	✓		✓				

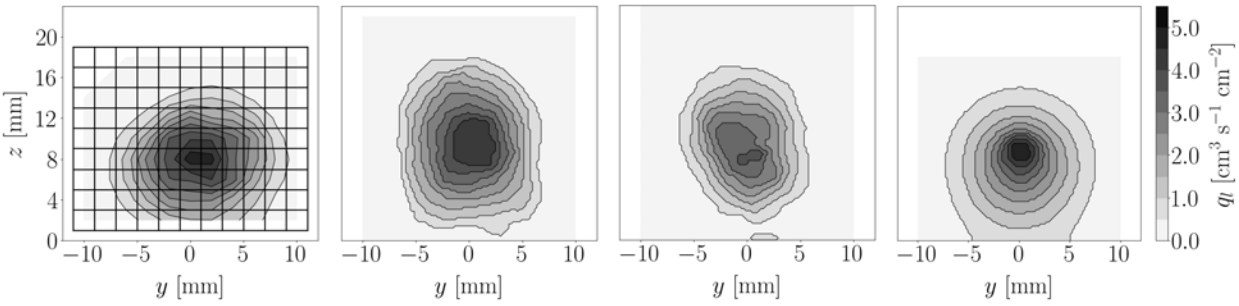

(a) Experimental (b) Jaegle (2009) (c) Senoner (2010) (c) Eckel (2016)

Figure 6.4: Volume flux maps at $x = 80$ mm for the high Weber operating conditions from experiments (Becker & Hassa 2002) and past computational works on the same configuration and operating condition. The experimental map shows the grid composed of the probes through which the spray is characterized

As previously mentioned, none of the previous works display SMD maps. Most of the works report, on the other hand, SMD integrated profiles over y: these are shown in Figure 6.5. The error bars in the experimental SMD profiles correspond to a deviation of 10 % in each point. Furthermore, results from one computation performed with Smart Lagrangian Injectors (SLI) in this thesis are also included for comparison. All cases show a ballistic behaviour in which the SMD increases with vertical distance z. The SMD profiles integrate over z are only present in the present work and in Rachner et al. (2002), who obtained accurate results at the center of the spray (region of maximum flux location) and showed a SMD overestimation when moving away towards the edges. The current results show that fluxes values, the vertical location of maximum flux and the spray ballistic behavior can be properly estimated by SLI. On the other hand, SMDs are always underestimated. As it will be shown later in this chapter, this underestimation is due to secondary atomization which breaks droplets very quickly after they are injected into the liquid channel.

From the SMD integrated profiles over y, a global SMD can be estimated by performing a further integration along the z direction:

$$SMD = \frac{1}{\int_0^{L_z} \langle q_l\,(z)\rangle dz} \int_0^{L_z} \langle q_l\,(z)\rangle \langle SMD\,(z)\rangle dz \tag{6.4}$$

Results are shown in Table 6.3. Eckel et al. (2016) do not provide the integrated SMD profile, yet they give directly the global SMD. Generally, all SMDs show a good agreement with respect to the experimental value of Becker & Hassa (2002). The works of Rachner et al. (2002) and Eckel et al. (2016) perform a calibration of their model to match the experimental size distribution, hence such a good agreement is expected. Similar is the case of Jaegle (2009), who already injected the experimental size distribution at the injector without including any secondary atomization model: then, the flux-weighted SMD is expected to be close to the SMD of this distribution. Senoner (2010) does not inject any distribution but injects droplets at the liquid nozzle with size equal to the nozzle's diameter, drags them with a modified momentum transfer law at the column liquid region and then applies the stochastic secondary breakup model of Gorokhovski (2001), used in this thesis and explained in §4.6.3, to account for further breakup of droplets. The good results in terms of global SMD and integrated profiles obtained in Senoner (2010) denote the suitability of the stochastic breakup model to simulate such configurations.

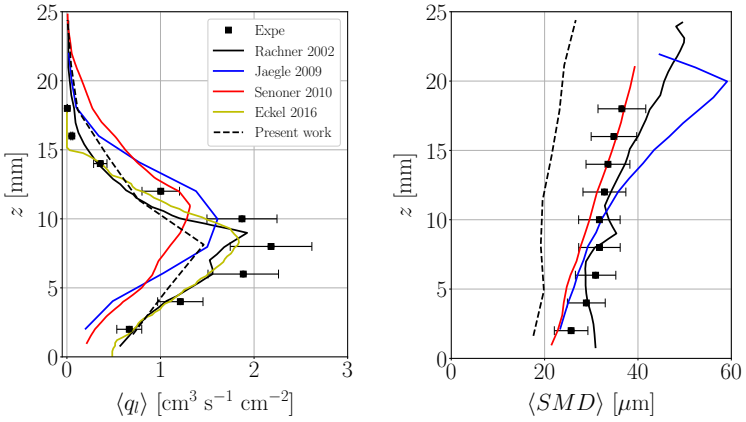

(a) Profiles integrated over y

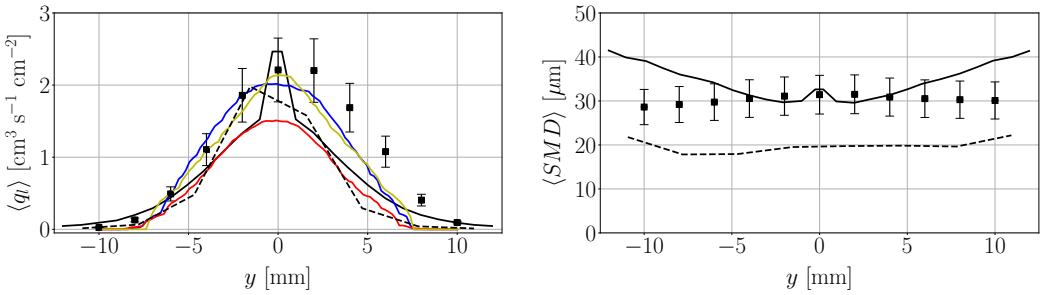

(b) Profiles integrated over z

Figure 6.5: Integrated SMD and volume flux profiles from experiments and past computational works. Computational fluxes have been obtained through digitalization and are hence not fully reliable

Table 6.3: Global data obtained at $x = 80$ mm from experiments, previous computational studies and the present work

Reference	SMD [μm]	Q_l [$\mathrm{mm}^3 s^{-1}$]
Becker & Hassa (2002)	31.0	4062
Rachner et al. (2002)	31.9	3710
Jaegle (2009)	33.2	3693.8
Senoner (2010)	29.6	3573
Eckel et al. (2016)	32.7	3775.9
Present work	19.44	3710

6.3 Procedure for parametric study of lagrangian simulations

With the objective of testing all the parameters involved in the lagrangian computations, a design of experiments process is followed in which each variable is changed in a one-at-a-time basis. The study of dispersed-phase simulations in then divided into three parts, which are enclosed by the dashed-colored lines in Figure 6.6:

1. The **gaseous phase** effect is analyzed in §6.4. Firstly, two methodologies to model the perturbation effects created by the dense core are presented analyzed in gaseous simulations: the Actuator Line Method (ALM), whose modeling was detailed in §4.5, and another approach named prescribed gaseous inlet. Both methodologies are then tested in dispersed-phase simulations, where liquid is injected with the SLIs obtained from the resolved simulation UG100_DX10 at $x = 5$ mm.
2. The different **secondary atomization models** are analyzed in §6.5.
3. The effects of the **liquid phase** parameters from SLI and operating conditions are reported in §6.6.

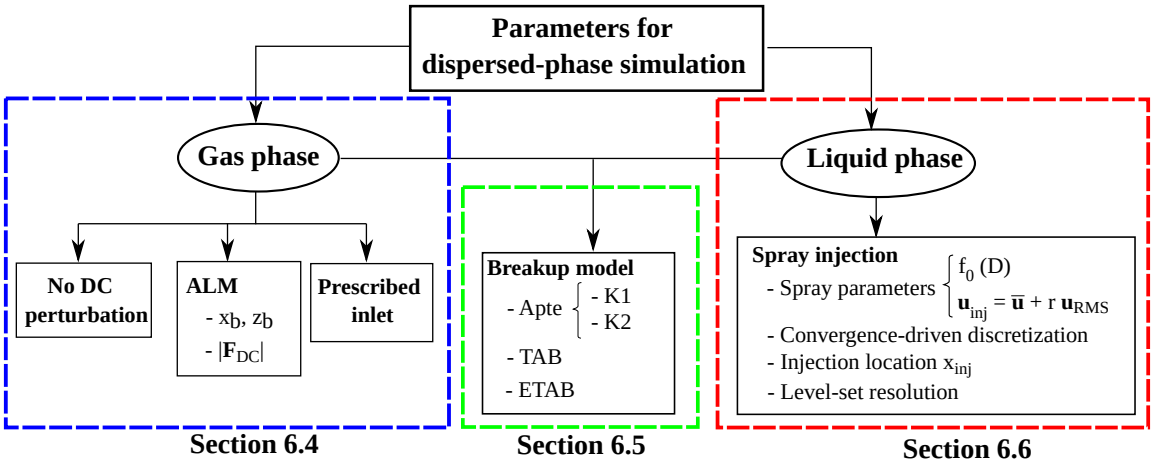

Figure 6.6: Schematic of parameters involved in SLI simulations and their interactions

6.4 Influence of gaseous phase

6.4.1 Computational setups and boundary conditions

In this section, the influence of the gaseous phase in the dispersed-phase simulation is analyzed. Two computational setups with two different modeling methodologies for replicating the perturbed gaseous phase are detailed. The first one employs **Actuator Line Method** (ALM), detailed in §4.5, while the second one consists of **prescribing gaseous phase** statistics on a reduced domain representing the plenum downstream the liquid injection nozzle location. The gaseous fields generated by both methodologies are firstly analyzed, followed by dispersed-phase computations performed with both methodologies.

Actuator Line Method

To mimic the perturbation phase created by the crossflow with ALM, the same computational geometry as the one used by the resolved simulations from Chapter 5 is used (Figure 5.2). In the mesh from these resolved computations, an element size of $\Delta x = 0.5$ mm was prescribed upstream the liquid nozzle, since it could transport the prescribed turbulence (§5.5). In dispersed-phase simulations, the region of interest extends up to a location at $x = 80$ mm downstream the injector, which corresponds to the location where the experiments from Becker & Hassa (2002) report results on fluxes and SMD. Therefore, these simulations use a baseline cell size of $\Delta x = 0.5$ mm in the plenum from the gaseous inlet up to $x = 85$ mm downstream the injector in order to allow for turbulent transport up to the experimental validation plane (located at $x = 80$ mm). The mesh, shown in Figure 6.7, consists of $74 \cdot 10^6$ elements, hence being firstly heavier than the baseline mesh employed for the resolved simulations but eventually lighter due to the lack of AMR. Droplets are injected in this mesh as lagrangian point-particles whose dynamics follow the equations from §3.2.3.

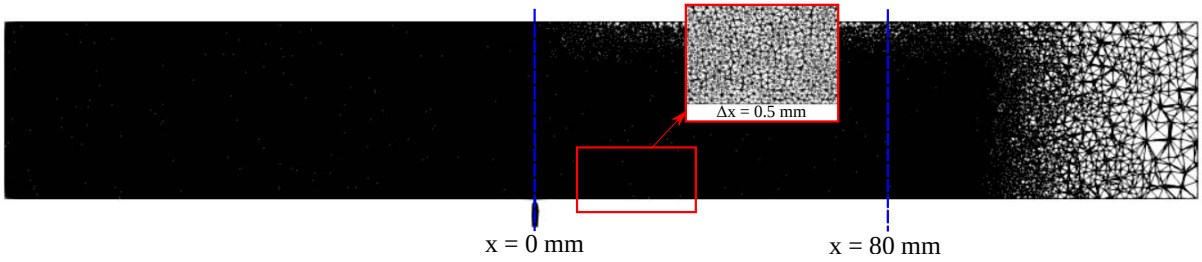

Figure 6.7: Mesh employed for dispersed-phase simulations with ALM

For gaseous phase perturbation, an actuator can be defined in the numerical domain with the control parameters from Table 4.3. An example of an actuator representing the dense core in a gaseous simulations can be seen in Figure 6.8. This one is graphically represented as a cylinder extending from the injection nozzle exit (initial point) up to the dense core breakup point (end point), which is estimated from the resolved simulations. The actuator points (not shown in the figure) are disseminated uniformly along the central line of the cylinder. The discrete forces applied to each point are then mollified in the neighbouring cells in order to avoid flow singularities.

To assess the ALM, the results from the high Weber operating point (Table 5.2) for the fine case (UG100_DX10) are used. The actuator point coordinates x_b, z_b are obtained from the mean values of Figure 5.45, while the force F_{DC} is taken from Table 5.8. These values, summarized in Table 6.4, represent an **initial** actuator. As it will be shown, it was found that the disturbance effect created by this actuator was not optimal to replicate the perturbations from the resolved simulation. Thus, the ALM control variables were tuned until finding an actuator which was found to better match the perturbed gaseous field: this one is summarized as the **optimal** actuator from Table 6.4. Besides from this optimal actuator, two other configurations are also reported to illustrate the influence of the parameters: one which takes the end point of the optimal actuator and the net force of the initial one (**ALM tilted**), and another one which takes the optimal end point but increases the net force (**ALM forced**).

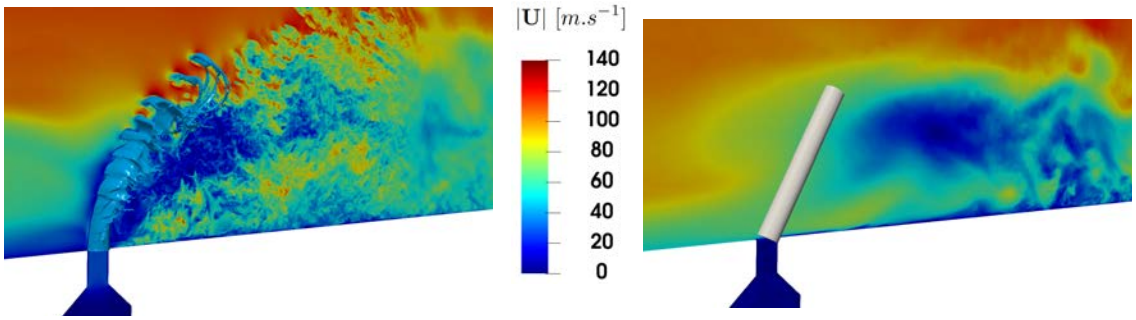

Figure 6.8: Perturbation effect towards the gaseous phase visualized through the instantaneous velocity magnitude in the plane $y = 0$. The snapshots correspond to the resolved simulation UG100_DX10 (*left*) and to a gaseous simulation with the optimal actuator (*right*)

Table 6.4: Parameters of an actuator representing the dense core for the high Weber case

Parameter	Units	ALM Initial	ALM tilted	ALM optimal	ALM forced
x_b	mm	2.46	1.5	1.5	1.5
z_b	mm	3.07	3.0	3.0	3.0
$\lvert\mathbf{F}_{\mathrm{DC}}\rvert$	N	0.095	0.095	0.25	0.30

In first place, the mean axial velocity fields in the symmetry plane $y = 0$ are shown in Figure 6.9. The resolved case UG100_DX10 is also displayed for comparison. As observed, the initial actuator model creates only a slight perturbation downstream the cylinder location, but cannot properly retrieve the recirculation and deceleration captured by the resolved simulation. By changing only the actuator coordinates (tilted configuration), the perturbation effect is intensified and more distributed in space: since the angle θ increases, the imposed drag reduces augments while the lift reduces (Eqs. (4.25)). This effect is also reflected in the mean velocity profiles of Figures 6.10 and 6.11: the tilted profile reduces the gaseous velocity more than the initial one, even though its perturbation is not yet close to the resolved profile. Indeed, the lift force imposed is not large enough and streamlines do not deviate towards the vertical direction as in the resolved case, staying oriented towards the crossflow direction as in the unperturbed case. If the net force is now increased (optimal configuration), Figure 6.9 shows that the axial velocity decreases downstream the ALM region, with an increase also in the lift force as in this case streamlines are deviated upwards. The velocity profiles from Figures 6.10 and 6.11 show this greater perturbation when compared to the previous cases. Nevertheless, the disturbance is still not strong enough to capture the recirculation bubble from the resolved simulation. A further increase in the net force imposed (forced configuration) shows effectively a larger perturbation which can actually capture a recirculation bubble behind the ALM region, even though its location is shifted upwards with respect to resolved simulation. The velocity profiles from Figures 6.10 and 6.11 also reflect this larger perturbation. However, even if the forced configuration case seems to retrieve better the gaseous field a priori, its stronger perturbation was found to greatly affect secondary atomization of the droplets in dispersed-phase simulations, yielding very small droplets. The configuration reported as optimal yielded the best spray results among all the ALM cases tested.

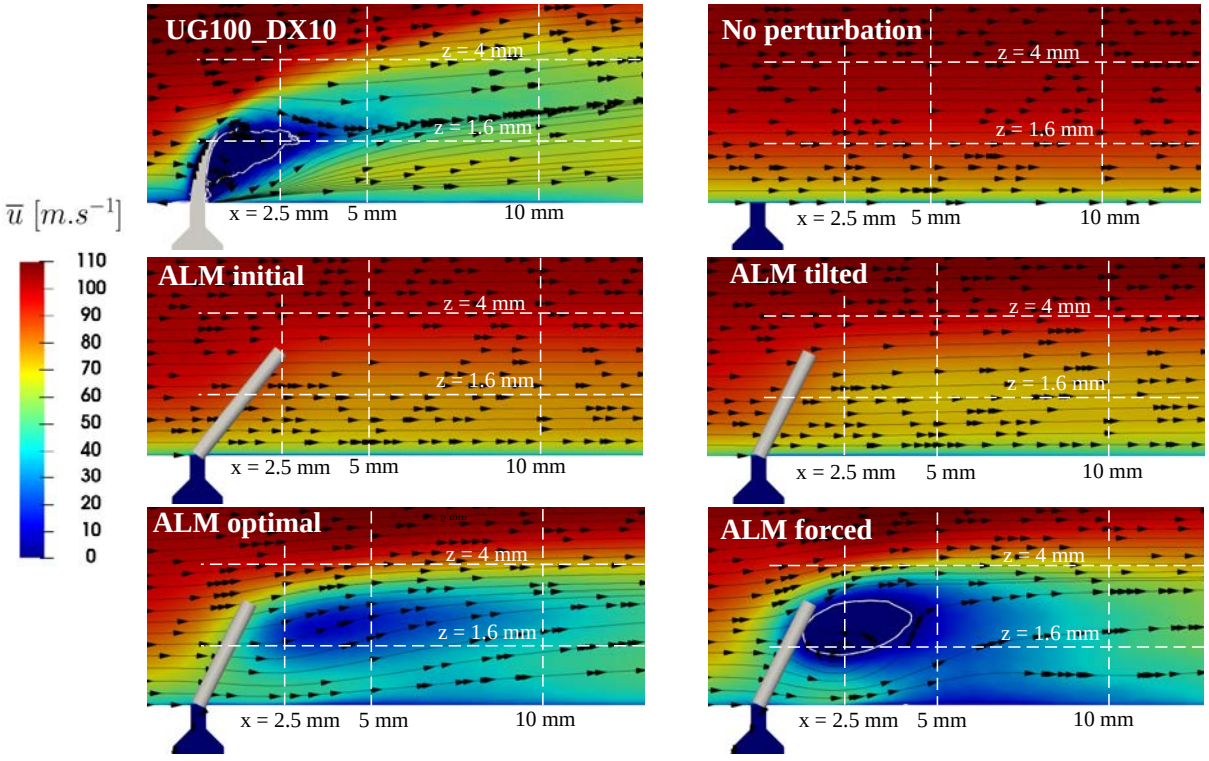

Figure 6.9: Mean axial velocity field at plane $y = 0$ for resolved case UG100_DX10 and the three actuators tested. The grey cylinder represents the actuator, i.e. the location where body forces are applied

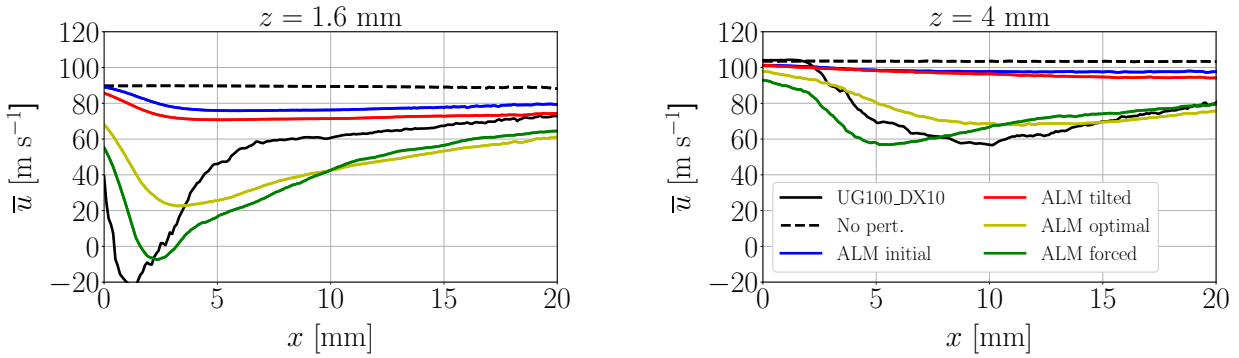

Figure 6.10: Mean axial velocity evolution in ALM and resolved simulations along axial coordinate at locations $z = 1.6, 4$ mm in plane $y = 0$ (lines of Figure 6.9)

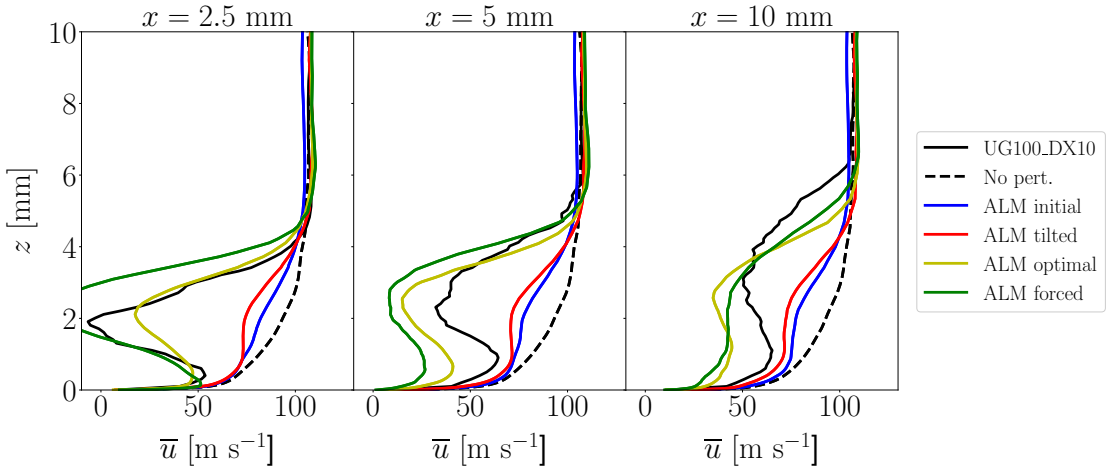

Figure 6.11: Mean axial velocity evolution in ALM and resolved simulations along vertical coordinate at $x = 2.5, 5, 10$ mm locations of plane $y = 0$ (lines of Figure 6.9)

Since the purpose of ALM is to mimic the gaseous perturbations generated by the dense core, it is also of interest to look at the planes perpendicular to the crossflow. Figure 6.12 shows the mean velocity fields at planes $x = 5, 10$ mm compared to the resolved cases. Modifying the actuator ending coordinates and increasing the net dense core reduces further the mean velocities in the flow field. This has also a strong effect in the Counter-Rotating Vortices (CRVs), which can affect the transport and atomization of the droplets. Cases unperturbed and initial ALM do not show CRVs in the flow as shown by the streamlines, while the tilted and optimal ALM cases can retrieve quite accurately the location, intensity and rotation direction of the resolved vortices. Further increasing the net force shows still vortical structures, yet these are small and differ from the shape of the resolved ones.

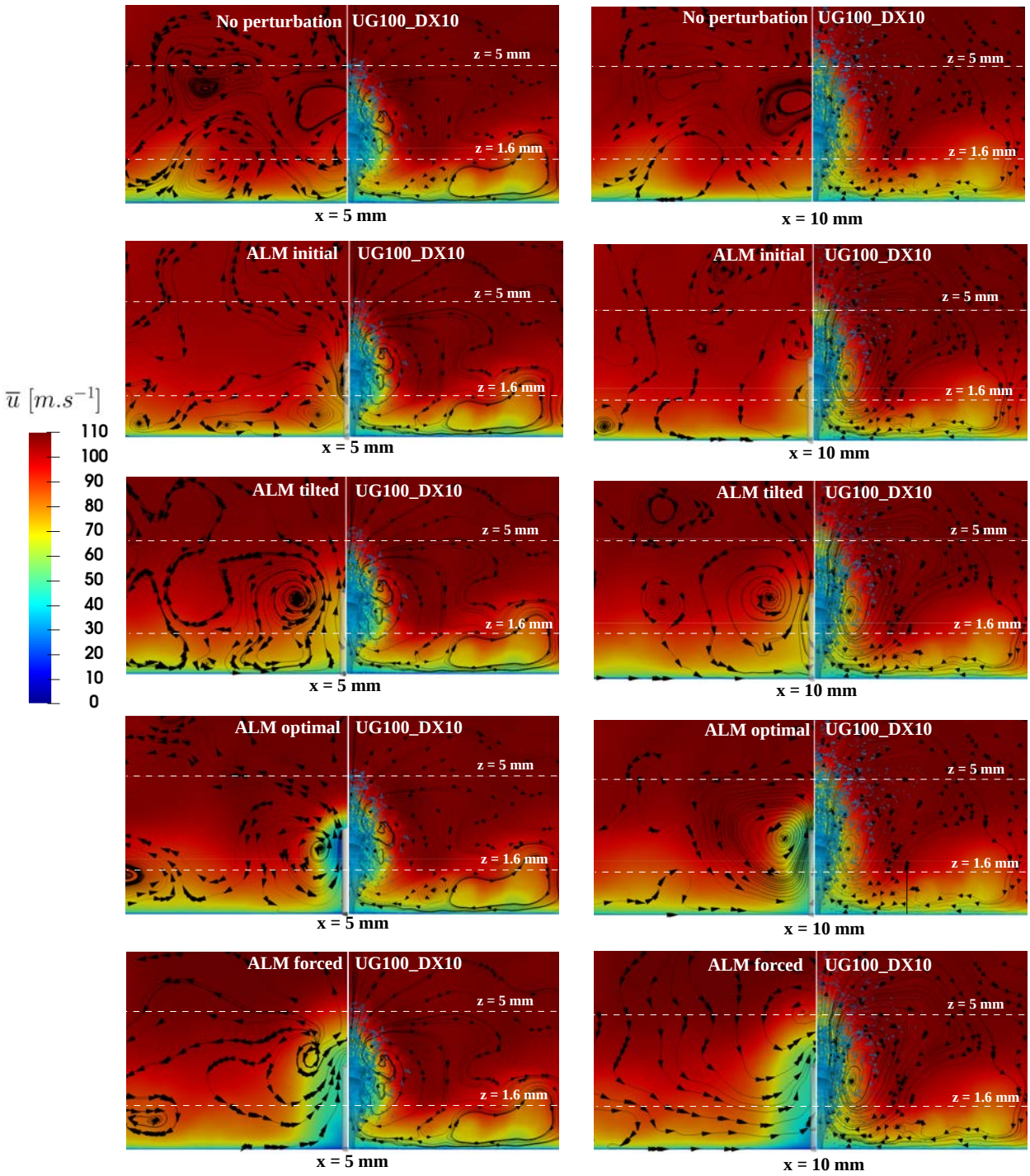

Figure 6.12: Mean axial velocity field at planes $x = 5, 10$ mm for resolved case UG100_DX10 and gaseous cases with and without ALM

Finally, the velocity profiles along the white lines from Figure 6.12 are plotted in Figure 6.13. Again, the initial and tilted ALM do not create in general a noticeable disturbance in the flow field compared to the resolved case, except at $z = 1.6$ mm in plane $x = 10$ mm where the tilted case shows the closest match of all models. Increasing the force approaches the resolved perturbation at plane $x = 5$ mm: the optimal ALM shows a good match at $z = 1.6$ mm, while the equivalent occurs for the forced ALM further away from the wall at $z = 5$ mm. For the profiles at $z = 5$ mm in plane $x = 10$ mm, none of the actuators could achieve the intensity of the resolved perturbation: all actuators create the greatest perturbations downstream the actuator region but has a very limited influence further vertically from its ending point, which is not the case of a resolved dense core since the ligaments created during primary atomization also create perturbations in the gas field away from the dense core.

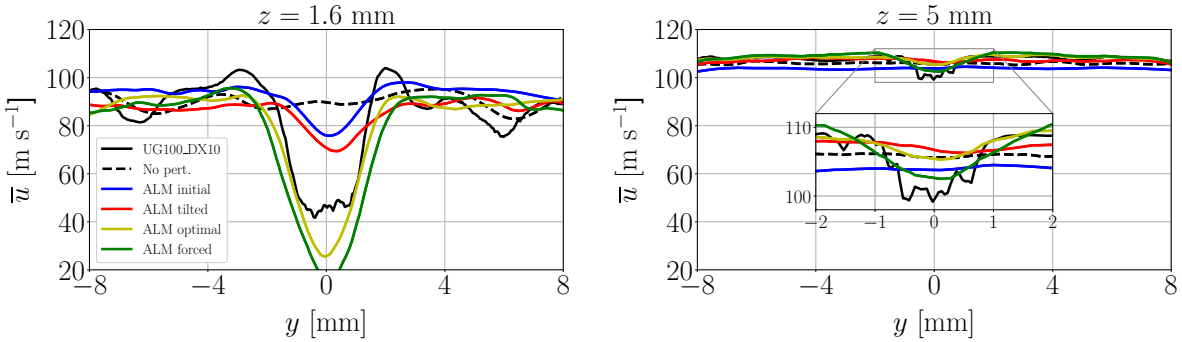

(a) Plane $x = 5$ mm

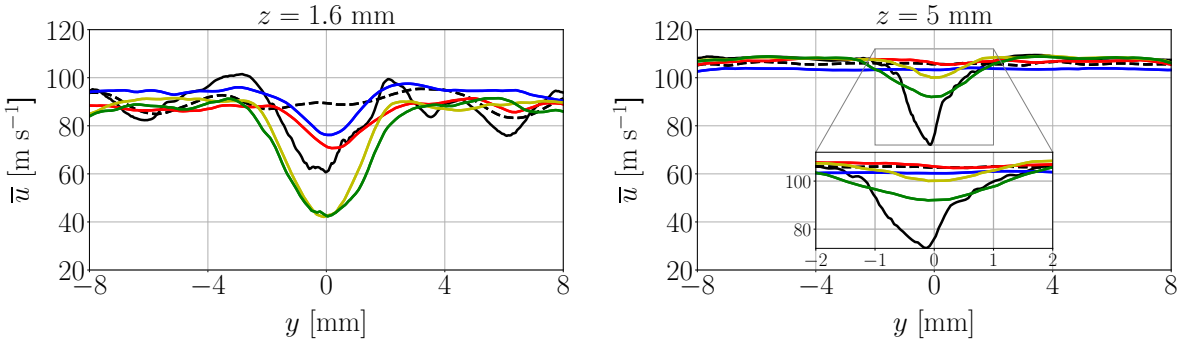

(b) Plane $x = 10$ mm

Figure 6.13: Mean axial velocity evolution along lateral coordinate in ALM and resolved simulations at z lines of Figure 6.12

In general, it can be concluded that ALM can perturb the gaseous field through the application of body forces. With a simplified geometry, a careful choice for ALM parameters allows to retrieve the main structures of the flow perturbed by a liquid dense core. The parameters directly obtained from the resolved simulations did not yield a realistic disturbed phase, and hence were optimized through trial-and-error. A better methodology to find optimal configuration could be through a multivariable optimization where the most suitable ALM parameters were found by minimizing an objective function. Further improvements in the model could also include modifications in the ALM geometry, such as the addition of several actuator models, or the inclusion of frequential effects to better represent the dense core unsteady shape. Such strategies were out of the scope of this thesis and are left for future work.

Prescription of gaseous inlet from resolved simulations

An alternative strategy to obtain gas boundary conditions is proposed in this section. This one consists of obtaining the gaseous field in a plane perpendicular to the crossflow from the resolved simulations, and then prescribing this field as the inlet of a reduced computational computational domain. The gaseous field is characterized by the mean and RMS values of the velocities in the three directions. These statistics are then imposed in a reduced domain consisting of a box with length 150 mm and cross-section 25x40 mm^2 representing the downstream part of the plenum from the full JICF configuration. Figure 6.14 shows the location of the reduced domain within the geometrical setup from the resolved atomization simulation and the computational grid. The mesh, which contains $12 \cdot 10^6$ elements, has been refined up to a location $x = 40$ mm downstream the inlet to an element size $\Delta x = 0.3$ mm. Further downstream up to $x = 100$ mm, the cell size has been set to $\Delta x = 0.5$ mm. The finer cell size of $\Delta x = 0.3$ mm has been selected with the objective of better capturing the turbulent structures created by the inhomogeneous gaseous velocity profile injected. Nevertheless, this cell size is not resolved enough to capture those: in the resolved simulations of Chapter 5, the cell size in the gaseous field around the liquid regions was of the order of the interface cell sizes ($\Delta x_{\min} = 20, 10$ μm), while such resolutions cannot be imposed into this reduced domain as the mesh size would greatly increase, yielding computations more expensive. Furthermore, a too fine mesh would create large volume fractions which are not in accordance with the application of lagrangian methods to simulate dispersed multiphase flows, since they are applicable to small volume fractions (Murrone & Villedieu 2011).

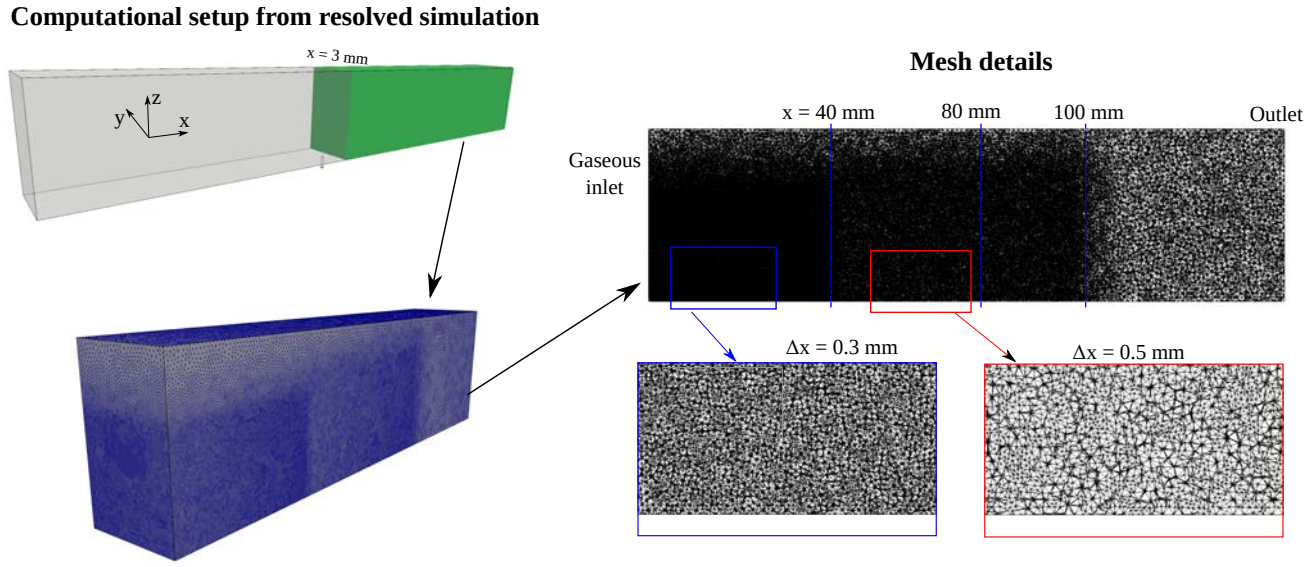

Figure 6.14: Location of the reduced domain within the resolved atomization computational setup (in green) and mesh details

The methodology to obtain and prescribe gaseous boundary conditions in the reduced domain is illustrated in Figure 6.15. Mean and RMS velocity profiles are extracted from the resolved atomization in a plane perpendicular to the crossflow. Then, velocity in the truncated setup is prescribed through the following law:

$$\mathbf{u}(\mathbf{x}, t) = \overline{\mathbf{u}}(\mathbf{x}) + r(t)\, \mathbf{u}_{\mathrm{RMS}}(\mathbf{x}) \tag{6.5}$$

where $\overline{\mathbf{u}}(\mathbf{x})$ and $\mathbf{u}_{\mathrm{RMS}}(\mathbf{x})$ are the mean and RMS velocity distributions. $r(t)$ is a time-varying scalar sampled from a normal distribution with mean 0 and variance 1: $r \sim \mathcal{N}(\mu = 0, \sigma^2 = 1)$. This velocity prescription law, which is based on the weak recycling method of synthetic turbulence injection by Wu et al. (1995), ensures that the injected TKE in the dispersed phase simulations is the same as the one retrieved from the resolved atomization ones. Hereafter, this methodology will be referred as **prescribed gaseous inlet**.

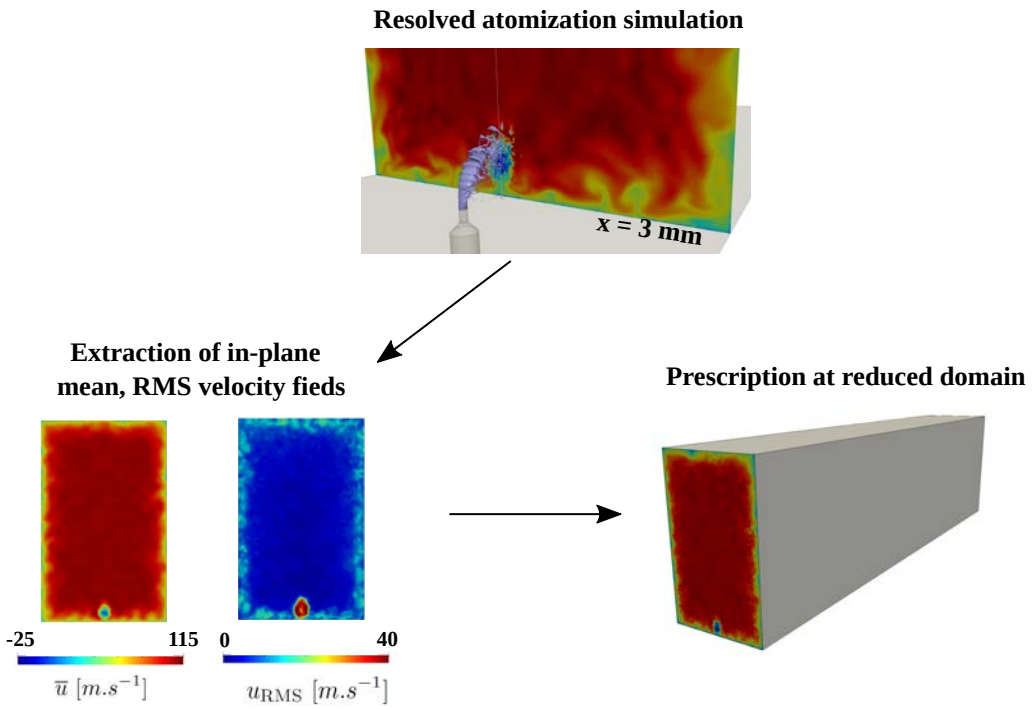

Figure 6.15: Methodology to prescribe mean and RMS velocity fields from resolved simulations in reduced domain for dispersed-phase computation.

The injected in-plane profiles have been obtained at the location $x = 3$ mm downstream the liquid injection nozzle in the resolved atomization simulations. Other plane locations have been tested without observing significant differences in the dispersed-phase simulations. In fact, the range of the possible planes to retrieve gaseous data for prescribing inlet BCs is narrow: upstream $x = 3$ mm the jet dense core is present and mean gaseous profiles would contain velocities corresponding to the liquid phase, while further downstream the lagrangian spray is injected in the dispersed-phase simulations (the earliest injection location is $x = 5$ mm). Hence, the only reported case hereafter corresponds to the location $x = 3$ mm. Since the computational domain is reduced with respect to the full computational configuration, the axial coordinates are shifted by 3 mm and the experimental validation plane, located at 80 mm downstream the liquid injection nozzle in the test bench, correspond indeed to the location $x = 77$ mm. From now on, however, all axial coordinates reported will be expressed in the absolute reference frame of the experimental test bench for easing comparison with the ALM dispersed-phase simulations.

Figure 6.16 shows results for the mean axial velocity at plane $y = 0$ mm. Statistics from the resolved case UG100_DX10 have been used in the reduced domain. Both the resolved atomization simulation and the prescribed gaseous simulation are shown: the former shows the field up to the location $x = 3$ mm (prescription plane), then the gaseous field corresponds to the prescribed gaseous inlet. The velocity field shows good continuity among simulations at the prescription plane, indicating that the resolved field is correctly specified in the gaseous simulation. The perturbation created by the prescribed simulation is very close to the resolved simulation at vertical locations $z < 4$ mm, as shown by the profiles along the white lines plotted in Figures 6.17 and 6.18. For locations further from the wall ($z > 4$ mm), velocities in the prescribed deviates from the profiles of the resolved one, indeed approaching the velocities from the optimal ALM simulation. In the resolved simulations, perturbations far away from the wall are created by ligaments ejected from the dense core, which can be present up to several diameters downstream the liquid nozzle (see for instance Figure 5.29, where ligaments are found up to $x = 5$ mm). In the prescribed simulation, gaseous statistics are specified at $x = 3$ mm and there is no liquid present to perturb the gaseous field as ligaments do in the resolved simulations, hence such disturbances are not captured. As commented before, changing the location of the gaseous inlet at further upstream or downstream (prior to $x = 5$ mm, since lagrangian droplets will be injected at this location) had no influence on the gaseous field.

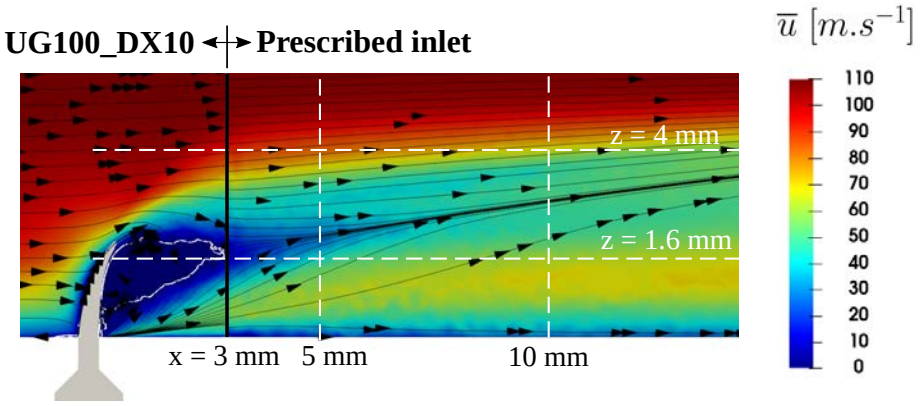

Figure 6.16: Mean axial velocity field at plane $y = 0$ for resolved case UG100_DX10 and prescribed gaseous inlet. The resolved simulation is cut at $x = 3$ mm, location from which the prescribed gaseous inlet simulation starts. Both computations are independent and are shown simultaneously in this figure for visual comparison of the flow fields

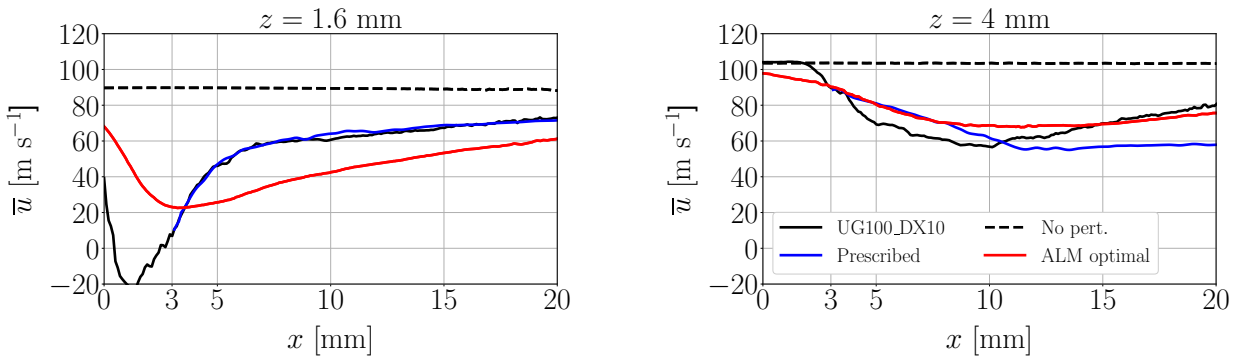

Figure 6.17: Mean axial velocity evolution along axial coordinate at locations $z = 1.6, 4$ mm in plane $y = 0$

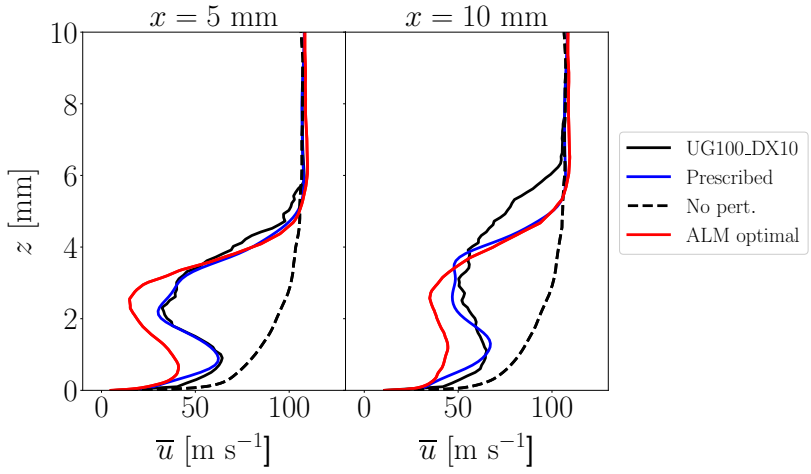

Figure 6.18: Mean axial velocity evolution along vertical coordinate at $x = 2.5, 5, 10$ mm locations of plane $y = 0$ (lines of Figure 6.19)

The flow field at planes perpendicular to crossflow direction $x = 5, 10$ mm are displayed in Figure 6.19. The prescribed gaseous inlet can retrieve the Counter-Rotating Vortices (CRVs) spinning directions in both cases. At $x = 5$ mm the vertical location of the CRV is underestimated with respect to the resolved case, while further downstream it gets closer. The velocity profiles along the white lines are shown in Figure 6.20. Closer to the wall ($z = 1.6$ mm), the prescribed inlet profile coincides with the resolved one in all the range except for the local minima captured at both sides close to $y = 0$, which are not present in the resolved case. Further from the wall ($z = 5$ mm) the prescribed profile does not match the resolved profile due to the reasons aforementioned, and creates flow decelerations with magnitudes similar to the ALM optimal case.

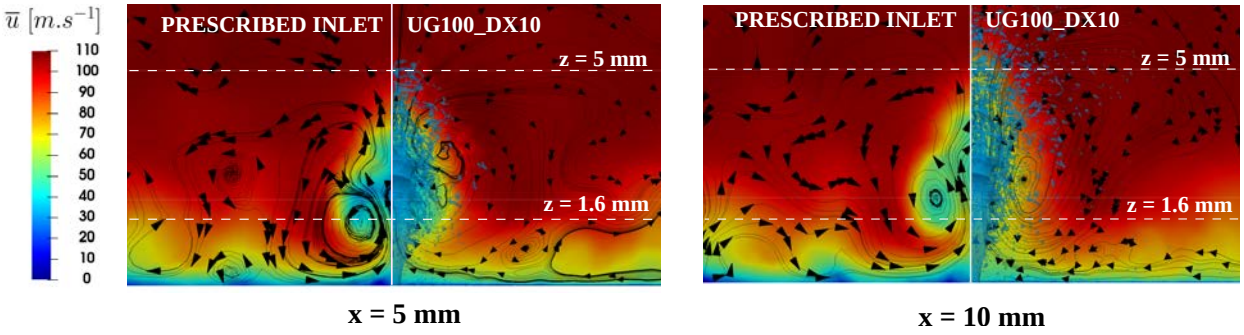

Figure 6.19: Mean axial velocity field at planes $x = 5, 10$ mm for resolved case UG100_DX10 and prescribed gaseous inlet

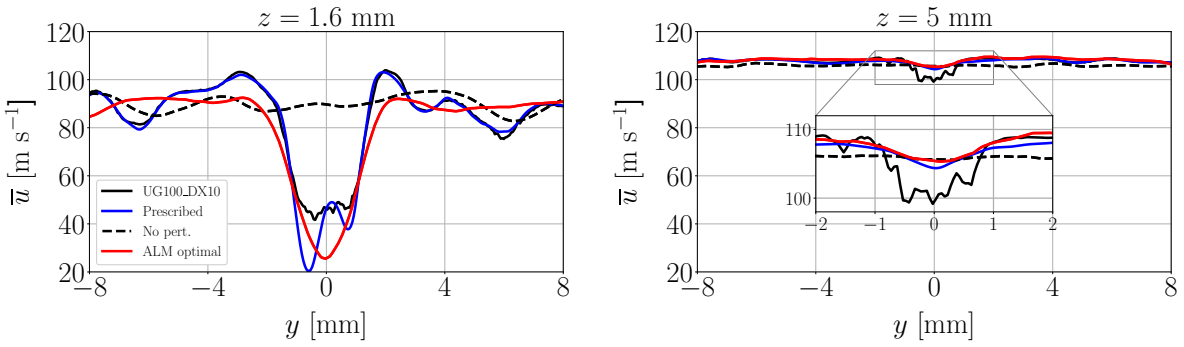

(a) Plane $x = 5$ mm

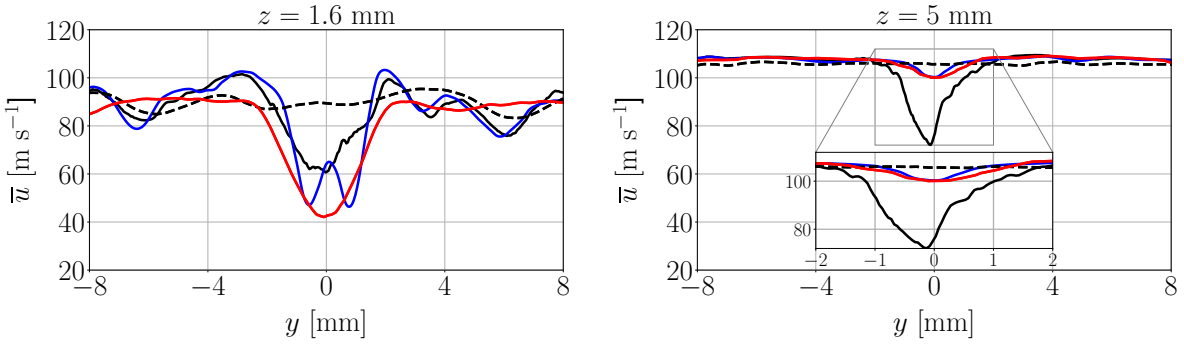

(b) Plane $x = 10$ mm

Figure 6.20: Mean axial velocity evolution along lateral coordinate at z lines of Figure 6.19

It can be concluded that the prescribed inlet captures more accurately the gaseous field than the ALM model. Furthermore, its computational cost is lower, since the reduced domain represents only a fraction of the original computational setup and less mesh elements are used. On the contrary, its main disadvantage is its only applitability to simple geometries such as the academic JICF tested.

6.4.2 Lagrangian jet establishment

The previous gaseous fields are now taken as initial solutions to perform dispersed-phase computations. To initialize the SLI, the injectors used correspond to the resolved simulation UG100_DX10 obtained at $x = 5$ mm are used to prescribed liquid boundary conditions. These are shown in Figure 6.21. Injected mean velocities are Volume-Weighted (VW) within each sampling probe according to Eq. (4.11). The RMS components of the velocities are also considered. The injected velocity $\mathbf{u}_{\text{inj}}$ is the prescribed by the expression $\mathbf{u}_{\text{inj}} = \mathbf{u}_{\text{VW}} + r\mathbf{u}_{\text{RMS,VW}}$, where r is a random number sampled from a Gaussian distribution (more details on velocity prescription in SLI were given in §4.4.5). Secondary breakup is considered through the Gorokhovski's stochastic model.

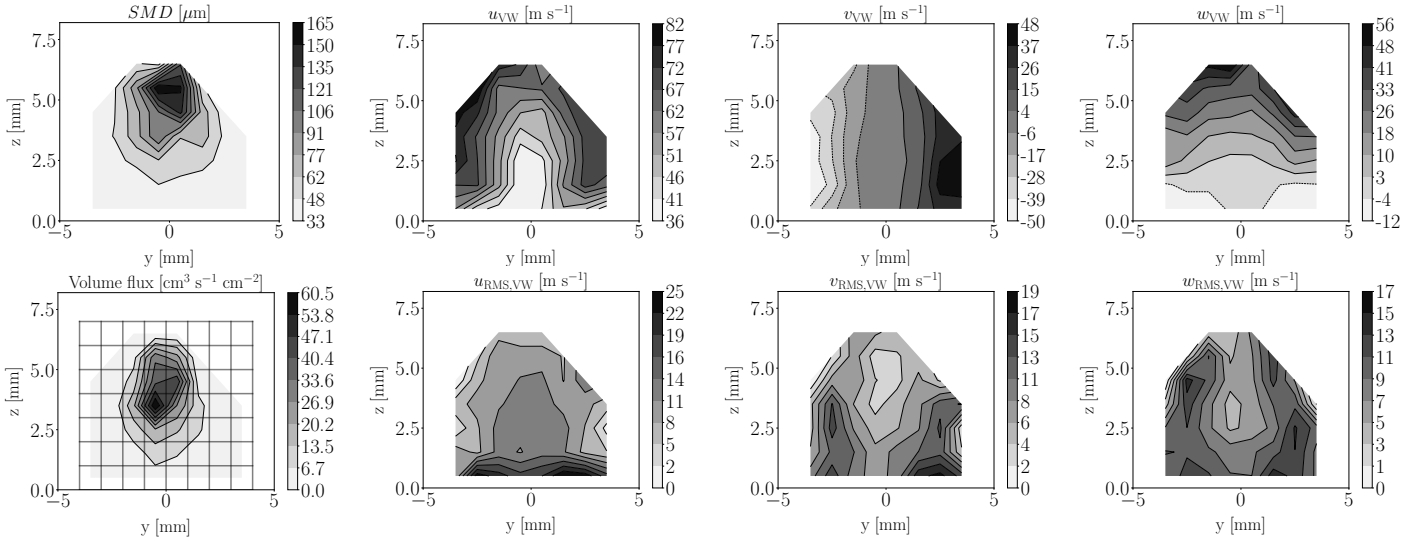

Figure 6.21: SLI mean volume-weighted (VW) and RMS velocity maps from case UG100_DX10 at $x_{\text{inj}} = 5$ mm

The establishment of the dispersed phase for cases ALM optimal and the prescribed inlet are shown in Figure 6.22. In both cases the injection and experimental validation planes, $x = 5$ and $x = 80$ mm respectively, are shown. The black outline at the first plane denotes the injection region. The prescribed inlet simulation includes as well an instantaneous view of the resolved liquid jet from case UG100_DX10 solely for visualization among resolved and lagrangian jets: resolved liquid is not actualy present in the dispersed-phase computations. The time instants are expressed in a dimensionless form with respect to the inertial timescale according to Eq. (5.2).

In both simulations, lagrangian droplets are injected at $x = 5$ mm and then convected downstream. Right after injection, the particles have a finite vertical velocity component which is larger at the spray top than at its bottom. Consequently, the jet's vertical trajectory continues to increase with axial distance. Shortly after injection, droplets are quickly atomized into smaller particles. The liquid-gas relative velocity is large in all simulations, hence the secondary breakup model triggers atomization soon after injection and the droplets sizes are reduced very fast with axial distance. Indeed, the dispersed-phase simulations show a very abrupt decrease in SMD up to a location between $x = 15$ and 20 mm, depending on the case. Further downstream, the dispersed spray is fully atomized and droplets are only convected. As a consequence of such a fast breakup, the smaller droplets generated have a lower relaxation time and are quickly dragged by the gaseous crossflow, increasing their axial velocity and reducing their vertical one, hence stopping penetrating in the vertical direction.

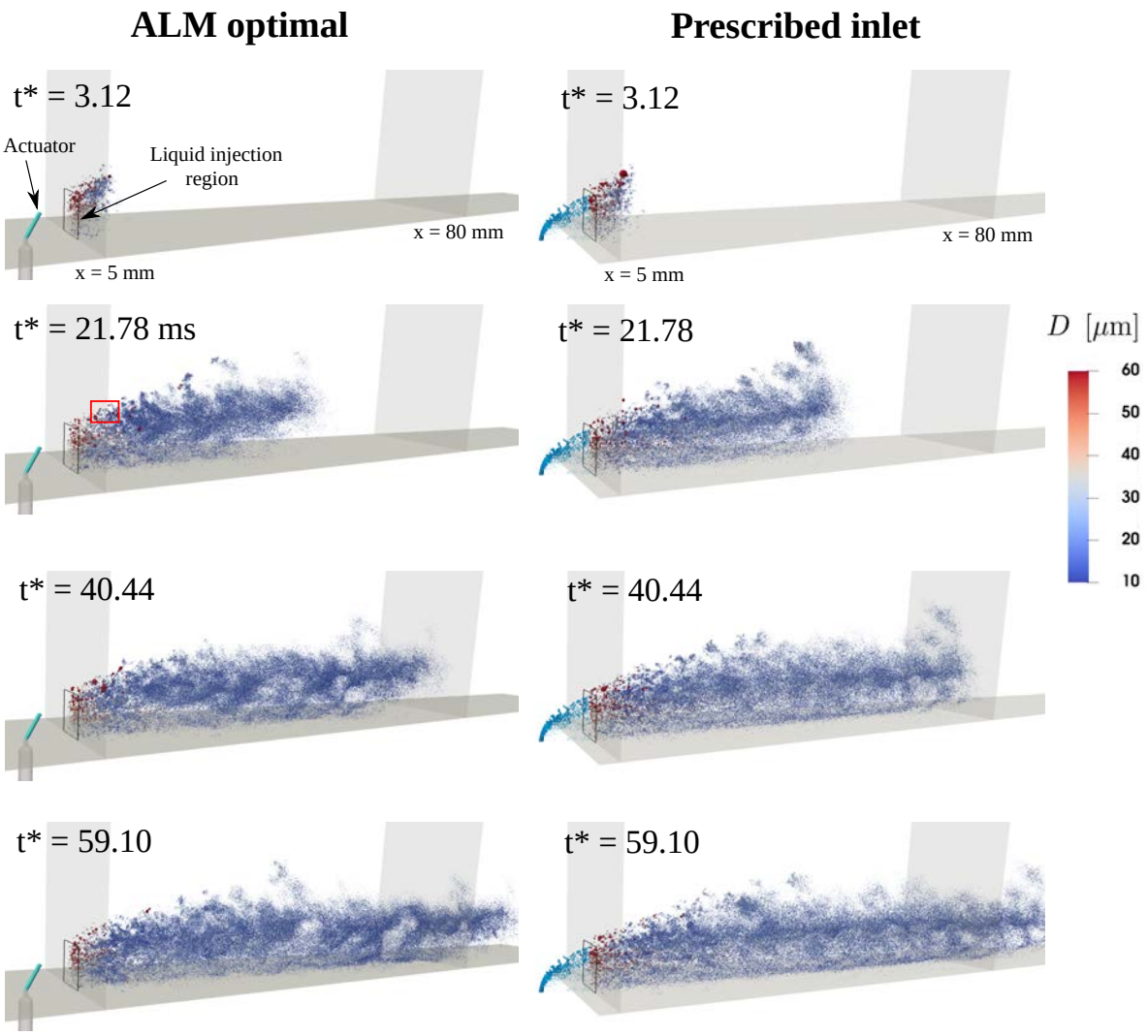

Figure 6.22: Lagrangian jet establishment in the JICF simulation performed for the ALM optimal configuration (*left*) and prescribed inlet (*right*) gaseous phases. The latter displays the liquid jet from the resolved computation only for visual comparison (it is not actually present in the dispersed-phase comptutation). The red rectangle at instant $t^* = 21.78$ in case ALM initial is augmented in Figure 6.23. Each sphere represents a parcel containing three droplets with the displayed diameter. Each sphere is scaled by 3 times its diameter for better visualization

Figure 6.23 shows the secondary atomization of a single lagrangian dropletl. The displayed domain in each figure corresponds to the region enclosed by the red rectangle in Figure 6.22. The original droplet at $t^* = 22.40$, with a diameter of 93 μm, breaks into several droplets of smaller size at $t^* = 23.02$ whose total volume contains the same mass as the original droplet (mass is conserved during secondary breakup). These children droplets have different sizes as a consequence of the statistical sampling from the cumulative distribution Eq. (4.58). Particles are then convected and undergo another breakup event at $t^* = 24.26$, producing a larger number of smaller children particles, where the smallest droplet's diameter was 13 μm. This sequence of subsequent atomization events is referred as the breakup cascade mechanism (Tanner & Weisser 1998). In the particular snapshots shown, the original droplet prior to breakup at $t^* = 22.4$ is located at $x = 5.5$ mm (i.e. 0.5 mm further downstream the injection location), while the droplets at the last instant $t^* = 24.26$ are located at $x \sim 9$ mm. This indicates that the breakup cascade occurs soon after the injection process and gets completed shortly afterwards. For this particular breakup event, the cascade occurs within a region $\Delta x = 3.5$ mm in a timespan of $\Delta t^* = 1.86$, which corresponds to a physical timespan of $\Delta t = 0.036$ ms.

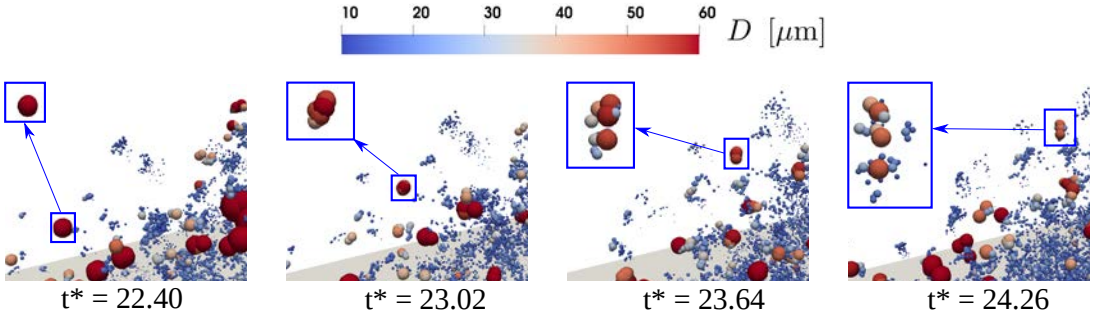

Figure 6.23: Visualization of the breakup cascade from a single lagrangian droplet in case ALM initial illustrating the breakup cascade. Displayed domain at each instant corresponds to the region enclosed in red at Figure 6.22

6.4.3 Analysis of lagrangian spray

Spray establishment

Sprays have been sampled in planes perpendicular to the crossflow direction separated by a distance $\Delta x = 2$ mm from the injection location $x = 5$ mm up to the experimental sampling plane $x = 80$ mm. In order to study established sprays, the time that the first droplet takes to reach the experimental sampling plane $x = 80$ mm, hereafter referred as $\tau_{\mathrm{dr}_{x=80}}$, has been firstly obtained. Then, simulations have been run for a time $t \sim 2\tau_{\mathrm{dr}_{x=80}}$ (establishment time) without lagrangian droplets tracking, and then tracking has been activated to start accumulating droplets and calculating statistics. The times $\tau_{\mathrm{dr}_{x=80}}$ for the gaseous simulations performed, as well as the physical and accumulation times, are summarized in Table 6.5. The convergence of the global spray has then be assessed by monitoring the SMD and the flux Q_l with respect to time, which is expressed in a dimensionless form with respect to $\tau_{\mathrm{dr}_{x=80}}$ as:

$$t' = \frac{t}{\tau_{\mathrm{dr}_{x=80}}} \tag{6.6}$$

Table 6.5: Droplets arrival time to $x = 80$ mm, total physical t_{ph} and accumulation times t_{acc}, absolute and dimensionless with Eq. (6.6), for lagrangian JICF simulations

Case	$\tau_{\mathrm{dr}_{x=80}}$	t_{ph} [ms]	t'_{ph}	t_{acc} [ms]	t'_{acc}
Prescribed inlet	0.7017	4.42	6.3	3.10	4.42
No ALM	0.6936	3.29	4.75	2.00	2.89
ALM initial	0.6959	3.69	5.3	2.10	3.02
ALM tilted	0.6829	3.82	5.6	2.53	3.71
ALM optimal	0.6843	3.45	5.04	2.04	2.98
ALM forced	0.6812	2.08	3.05	0.85	1.25

The evolution of flux and SMD at the plane $x = 80$ mm with time for the simulations are shown in Figure 6.24. The flux shows that all cases tend to wards the injected flow rate, with slight overestimations in some cases possibly due to some lagrangian particles being sampled twice. The SMD profiles show convergence in all cases, but towards different values which in the most extreme cases (prescribed inlet versus ALM forced) differ by a factor of 2. The evolution of SMD along the channel and the dependence of granulometry with the gaseous boundary conditions is analyzed next.

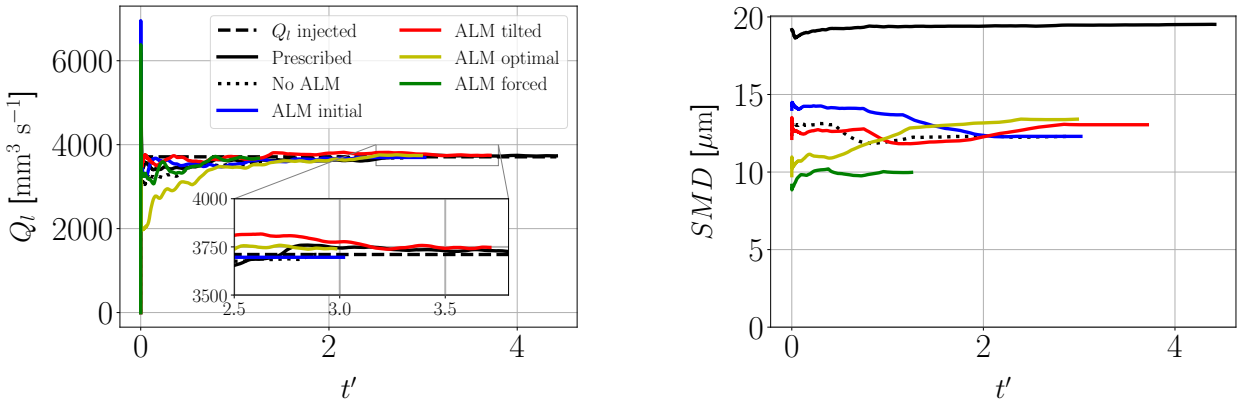

Figure 6.24: Convergence of spray liquid flux (*left*) and SMD (*right*) with time at plane $x = 80$ mm

Spatial evolution of spray

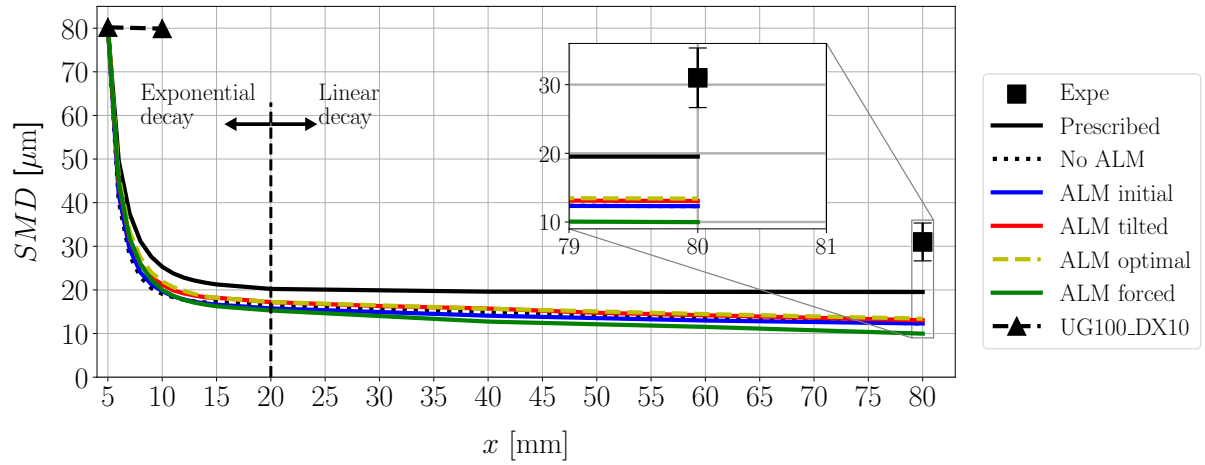

Figure 6.25: Evolution of SMD along axial location x for the different gaseous boundary conditions tested. The SMD at $x = 5$ and 10 mm for the resolved atomization case UG100_DX10 is also added for comparison

Since there is a strong reduction of particles diameters due to secondary atomization, it is of interest to see at which extent atomization acts along the channel. For this purpose, the evolution of SMD with axial distance x along the plenum is plotted in Figure 6.25. The SMD from the resolved simulation UG100_DX10 and the experimental one with its uncertainties are also shown for comparison. As observed, the SMD drops drastically shortly after injection up to $x \sim 20$ mm, then it continues decreasing in a linear way up to $x = 80$ mm. The abrupt decrease in diameter at early axial locations is exponential and shows a similar shape for all cases; however, for the ALM cases, the decaying rate and the final SMD varies. In general, the prescribed inlet provides the largest SMD while the ALM cases result in lower values due to a worse replication of the resolved gaseous phase, thus mispredicting the relative velocity for the lagrangian droplets and affecting breakup. At $x = 10$ mm the deviation with the resolved case is large: 79.9 vs 23.9 μm for the prescribed inlet, which supposes a difference of 70 %. However, the resolved atomization simulation might not be fine enough to retrieve the smallest liquid scales that would be actually present (as discussed in §5.7.2), hence limiting the smallest droplets that can be resolved.

The linear region, which spans from $x = 20$ to 80 mm, reduces the mean diameter slowly along the channel after the disminution in the exponenial region. This is specially noticeable for the cases with the full computational domain from the resolved simulation (with and without ALM), while in the prescribed gaseous inlet simulation the variation is so small that is not appreciated in the figure. For quantifying this variation, a decay rate λ is calculated as the slope in the SMD-x curve from $x = 20$ mm to $x = 80$ mm:

$$\lambda = \frac{SMD_{x=20\text{mm}} - SMD_{x=80\text{mm}}}{60} \tag{6.7}$$

Table 6.6 summarizes the obtained SMDs and decay rates for all cases. The values for λ are of the same order for all ALM and the unperturbed cases, while it is more than one order of magnitude lower than for the prescribed gaseous inlet spray. The lower decay rate is associated to a more accurate resolution of the gaseous phase with the prescribed inlet (meaning that it matches better the perturbed field of the resolved atomization simulation), which can be seen for instance in the gaseous profiles of Figure 6.17. The decay rates for the ALM cases show similar orders of magnitude, yet the values also differ and affect the final SMDs obtained: the lowest value (which results in a higher final SMD) corresponds to the optimal case, while the highest decay rate has been obtained for the ALM forced. In general, the lower the decay rate (or in other words, the larger the final SMD), the better, since as observed in Figure 6.25 the SMDs found in the simulations underestimate the experimental results.

Table 6.6: SMD values at $x = 20, 80$ mm and decay rates λ in the linear region

Case	$SMD_{x=20\text{mm}}$ [μm]	$SMD_{x=80\text{mm}}$ [μm]	λ [μm mm^{-1}]
Prescribed inlet	20.23	19.52	$8 \cdot 10^{-3}$
No perturbation	16.42	12.30	$128 \cdot 10^{-3}$
ALM initial	15.77	12.30	$128 \cdot 10^{-3}$
ALM tilted	17.20	13.05	$116 \cdot 10^{-3}$
ALM optimal	17.225	13.41	$110 \cdot 10^{-3}$
ALM forced	15.280	9.98	$167 \cdot 10^{-3}$

Experimental comparison

The sprays at $x = 80$ mm can be compared with the experimental results reported at the same locations. In first place, the global SMDs shown graphically in Figure 6.25 are also summarized in Table 6.7, where where the error with respect to experiments ε_{SMD} is calculated as:

$$\varepsilon_{SMD} = \frac{SMD_{\text{simu}} - SMD_{\text{expe}}}{SMD_{\text{expe}}} \tag{6.8}$$

where SMD_{simu} and SMD_{expe} are the numerical and experimental SMDs at $x = 80$ mm respectively. Results show that (as already mentiones in the previous section) the gaseous prescribed inlet provides the better experimental match for global SMD, while the ALM forced case provides the largest deviation.

Table 6.7: SMD values at $x = 80$ mm and deviation with the experimental value for different gaseous conditions

Case	SMD [μm]	ε_{SMD} [%]
Experiments	31	-
Prescribed inlet	19.52	-37.03
No perturbation	12.30	-60.31
ALM initial	12.30	-60.31
ALM tilted	13.05	-57.90
ALM optimal	13.41	-56.75
ALM forced	9.98	-67.82

The spray at $x = 80$ mm is then discretized to yield the spatial maps of SMD and flux in Figure 6.26. These spatial magnitudes can also be integrated in each direction with Eqs. (6.1) to yield the spatially integrated profiles of Figure 6.27. The experimental maps and profiles are also displayed for comparison.

Flux maps show an elliptical pattern elongated along the vertical direction, while experiments show a circular shape. Simulations show a larger concentration of droplets in the center, which is reflected in higher local maximum fluxes whose vertical location agrees fairly well with the experiments. The prescribed gaseous inlet simulation captures accurately this location, while the ALM ones underestimate it slightly, as it is also reflected in the vertical profiles of Figure 6.27. The numerical spray vertical boundaries, observed both in the

maps and in the vertical flux profiles of Figure 6.27, show that these penetrate further than the experiments. Nevertheless, the overestimated upper boundary corresponds to areas with large SMD and low liquid fluxes ($q_l < 0.5$ cm^3/cm^{2}s), corresponding then to a few large droplets with a more ballistic behaviour (due to a larger Stokes number) that travel further away in the vertical direction. Indeed, the boundaries for the regions with larger fluxes ($q_l > 0.5$ cm^3/cm^{2}s) match their experimental equivalent ones. Similarly, lateral boundaries show droplets up to the channel walls, although these regions (generally for $|y| > 6$ mm) contain low fluxes. The vertical boundaries where $q_l > 0.5$ cm^3/cm^{2}s are located closer to the central plane than in the experiments, yielding the elliptical pattern in the computations. This might be caused by an underestimation of the lateral trajectory in the resolved atomization simulation, although this characteristic of the JICF has not been addressed in this work and a definitive statement cannot be performed. The flux profiles integrated along the lateral direction $\langle q_l \rangle (y)$ shows good experimental agreement for $y < 0$ but underestimation of flux for $y > 0$, which might indicate that experiments overestimate the flux at this region. In general, it can be said that the dispersed-phase computations retrieve quantitatively the patterns of the flux with similar vertical boundaries, yet there are a small quantity of large droplets penetrating further away than in the experiments. Simulations also show vertical locations of the maximum fuel flux close to experiments: the prescribed case can accurately retrieve this location, while the ALM ones generally underestimate it.

The numerical SMD maps show layered profiles with droplets sizes increasing from the bottom to the top, which is the characteristic ballistic behaviour of JICF sprays. This ballistic profile is also confirmed by the increasing SMD along z in the profiles from Figure 6.27. As shown both in the maps and profiles, all cases underestimate the experimental values (which agrees with the previous discussions on the global granulometry of the sprays). Most maps also reveal an increase in SMD towards the lateral edges, which is also reflected at the integrated profile $\langle SMD \rangle (y)$ in Figure 6.27 right (convex profile). Such behaviour, which is not observed in experiments but was also retrieved numerically by Rachner et al. (2002) (Figure 6.5), is caused by large droplets following their own direction rather than being entrained by the flow, which reach the walls of the plenum and do not undergo further atomization. This lateral increase is clearly noticeable for the prescribed inlet simulation and less pronounced for the ALM ones: as secondary atomization acts faster for the latter, the larger droplets are quickly disintegrated and smaller droplets are obtained. Actually, the lateral profiles become flatter as the cases underestimate the SMDs, producing even a concave profile in the ALM forced simulation.

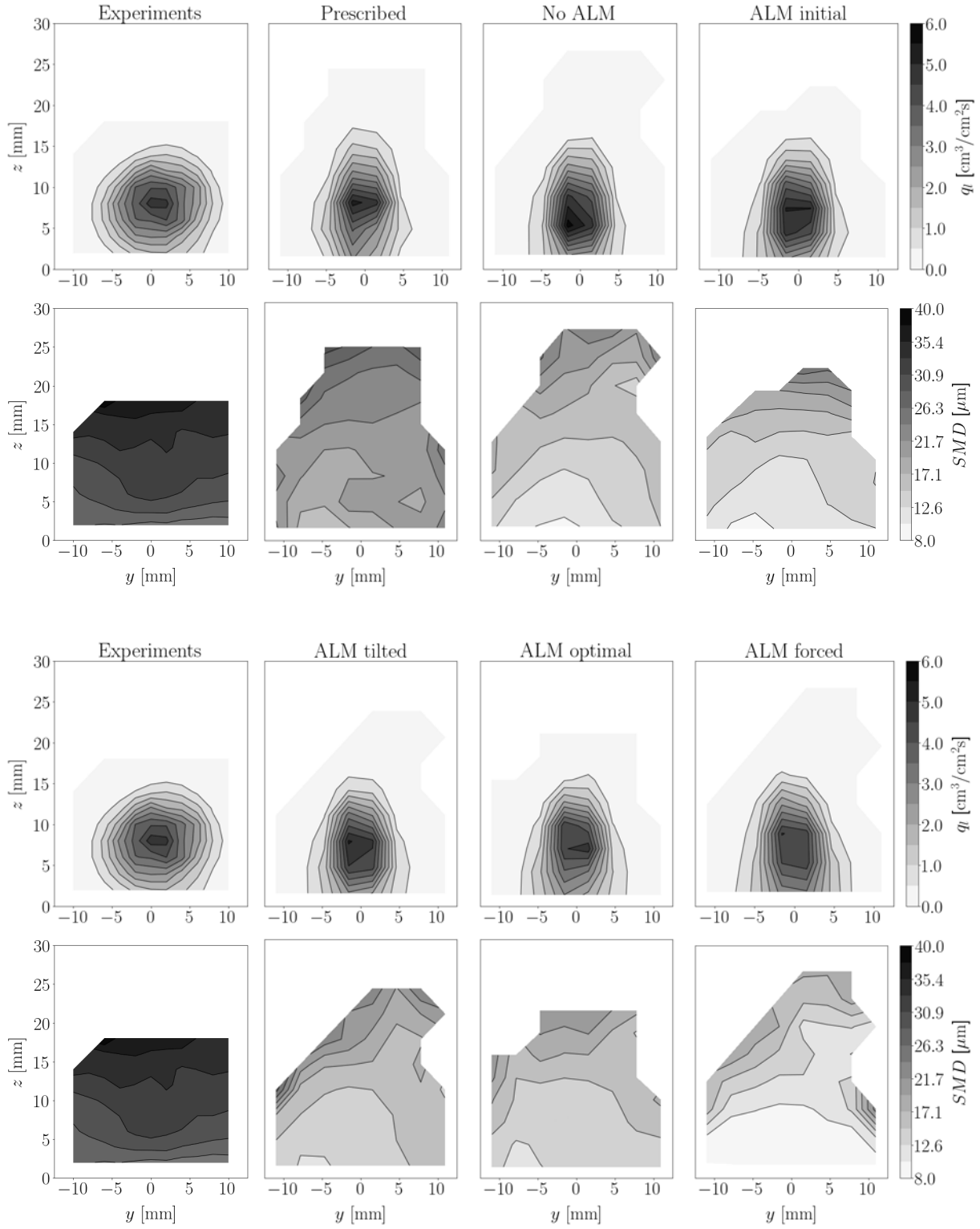

Figure 6.26: Flux and SMD maps for numerical simulations comparing the effect of gaseous phase modeling with the experimental results

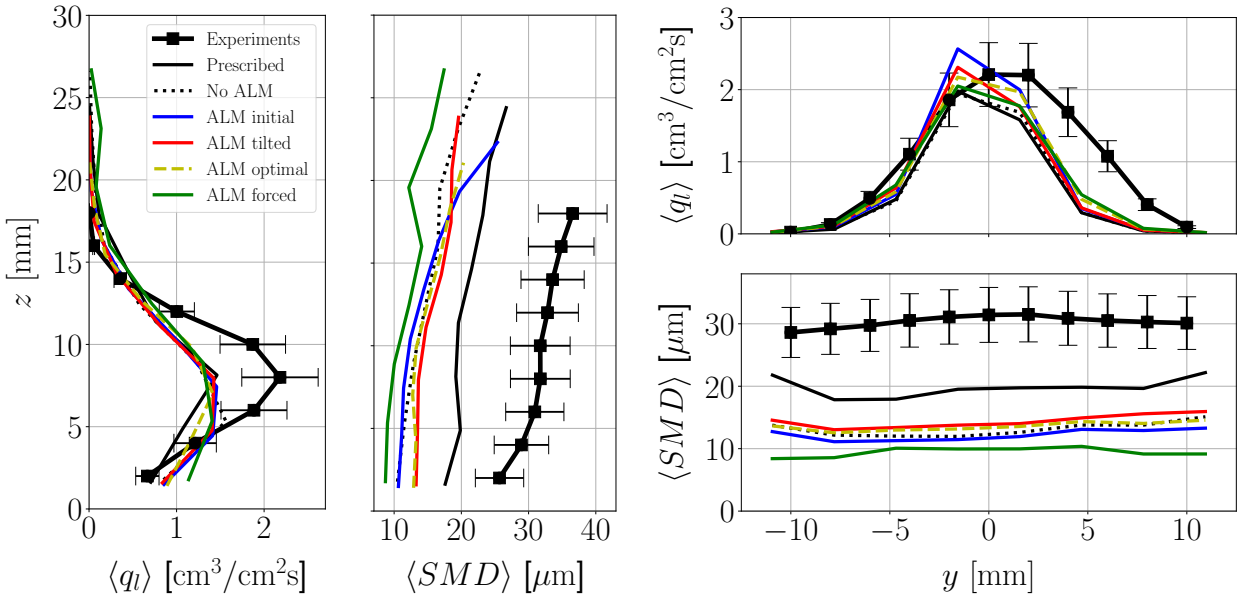

Figure 6.27: Integrated profiles of flux and SMD maps for numerical simulations comparing the effect of gaseous phase modeling with the experimental results

The analysis from this section has shown that the imposition of accurate boundary conditions for the gaseous phase is paramount for a proper modeling of JICF dispersed-phase simulations, as the gaseous flow field will affect the secondary atomization of the droplets through the liquid-gas relative velocity. The **prescribed gaseous inlet** methodology has found to retrieve more accurately the experimental results, and therefore it will be kept for the subsequent studies in this chapter.

6.5 Influence of secondary atomization model

To consider the secondary breakup of lagrangian droplets in dispersed-phase simulations, three atomization models are available (§4.6): TAB, ETAB and Gorokhovski. All these models estimate breakup according to the Weber based on the relative velocity, which is the known parameter to control secondary atomization. Then, the exact instant of breakup and the size and number of children droplets are calculated differently by each model. The TAB and ETAB models belong to the same family and provide fixed values for the parameters controlling the model, while the Gorokhovski's stochastic model presents two constants (K_1, K_2) that can be chosen by the user. These constants were calibrated to better match the experimental results: the values $K_1 = 0.05$, $K_2 = 1.0$ were retrieved since they yield the lowest error in SMD with respect to experiments (results from the calibration analysis are provided in Appendix G). In this section, all the three models are compared in three different dispersed-phase simulations.

The SMD maps are displayed in Figure 6.28, and their corresponding integrated profiles in Figure 6.29. Both TAB and ETAB models produce similar circular patterns for the fluxes. Spray from TAB model overpredicts the vertical maximum flux location, also condensing a large part of the spray in this region as shown by the larger local fluxes. The ETAB model, on the other hand, predicts this location accurately and shows a good spatial repartition of the spray. This model also retrieves properly the experimental vertical bounds as reflected both in the map and the integrated profile $\langle q_l \rangle (z)$. The SMD maps and profiles show a proper ballistic behaviour for both TAB and ETAB sprays but an underestimation of the diameters, those being specially small for the TAB model. Underprediction of particles sizes by the TAB model is a known downcome of this model (Tanner 1997), and solving this issue was the reason why the ETAB model was developed. Indeed, the figures show that the latter model produces larger droplets than the former: the SMDs at $x = 80$ mm, summarized in Table 6.8, yield errors of -55.07 % and 43.59 % for the TAB and ETAB models respectively. The closest is then obtained for the Gorokhovski model.

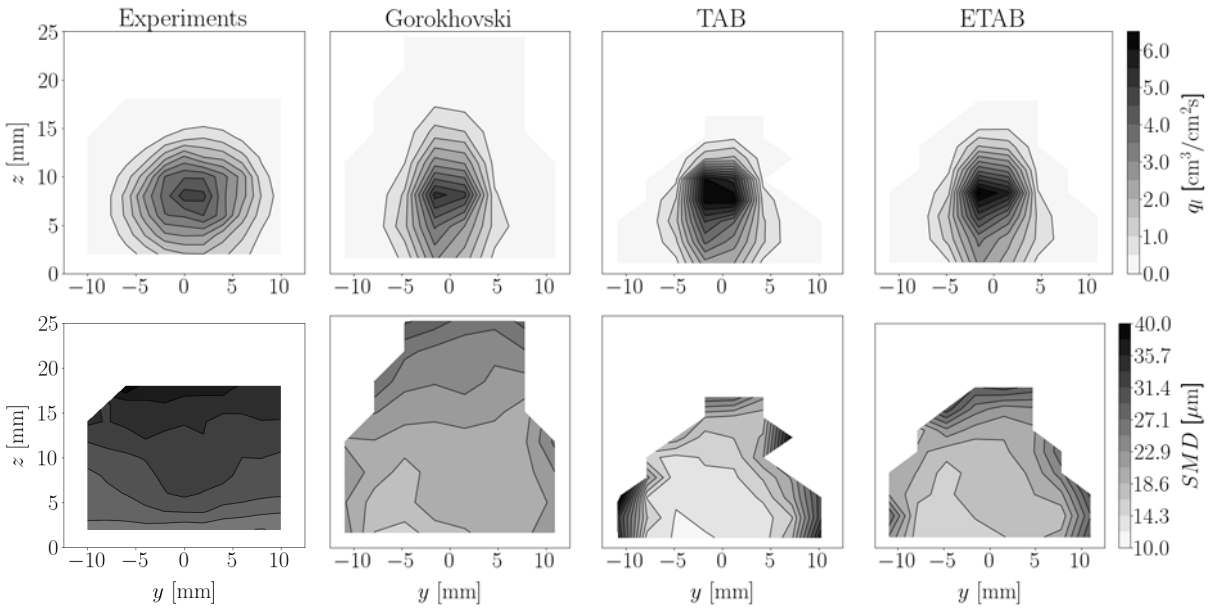

Figure 6.28: Flux and SMD maps for numerical simulations comparing the effect of secondary atomization models with the experimental results

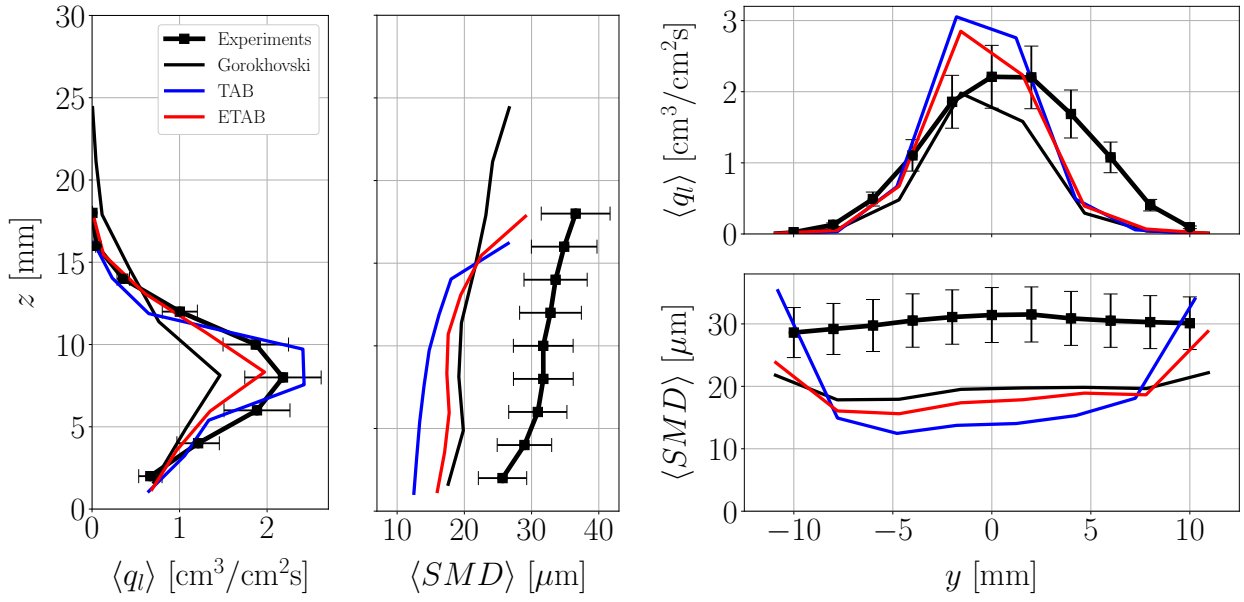

Figure 6.29: Integrated profiles of flux and SMD maps for numerical simulations comparing the effect of secondary atomization models with the experimental results

Table 6.8: SMD values at $x = 80$ mm for simulations with the different secondary atomization models

Case	SMD [μm]	ε_{SMD} [%]
Experiments	31	-
Gorokhovski	19.44	-37.29
TAB	13.93	-55.07
ETAB	17.49	-43.59

Evolution of the SMD along the channel is plotted in Figure 6.30. The SMD shows also a sharp reduction close to injection, with a faster decay for the TAB than for the ETAB and Gorokhovski models. The models from the TAB family stabilize at $x \sim 15$ mm, earlier than Gorokhovski. From this graph, it is demonstrated that the earliest instants are crucial for the atomization process, since the lowests SMDs are always obtained for the largest decay rates close to injection. Such abrupt decay rates very close to injection occur due to large relative velocities, as momentum exchange between the liquid and the gas has not occured yet. Momentum exchange is assessed later in §6.7 by introducing an artificial delay from injection to the onset of atomization.

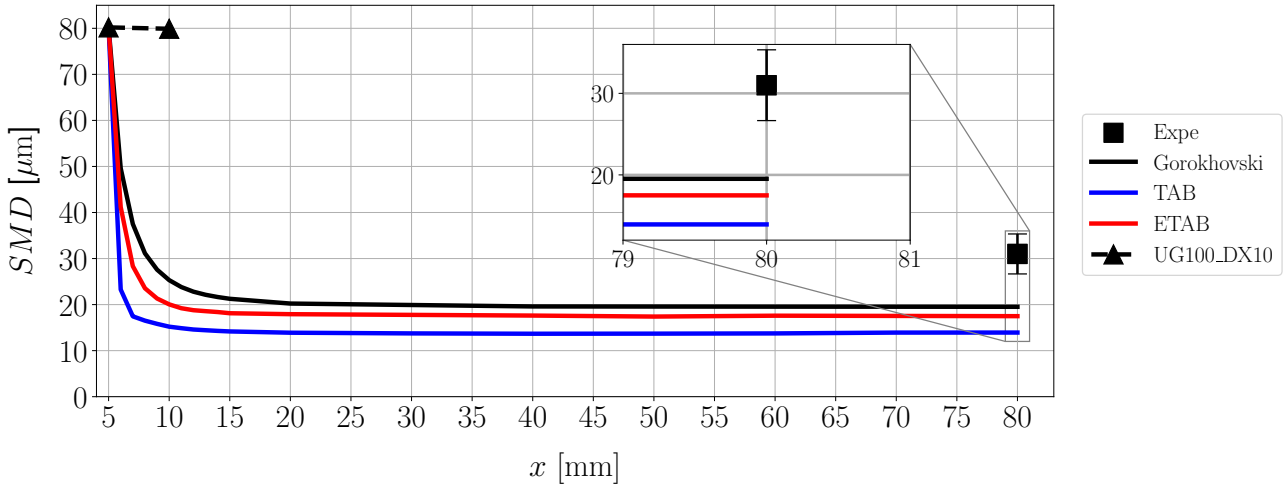

Figure 6.30: Evolution of SMD along axial location x for the three atomization models. The SMD at $x = 5$ and 10 mm for the resolved atomization case UG100_DX10 is also added for comparison

In general, it has been observed that the secondary atomization model has a great influence on the resulting lagrangian spray. The **Gorokhovski model** shows the best agreement in terms of spray sizes, and hence it is retrieved for further analyses. Even so, all models tested do not yield particles sizes within the experimental range. Nevertheless, these atomization models are general and have not been developed for particular conditions: the high pressure, highly turbulent environment found in the studied case might require atomization models more fitted to these conditions (indeed, both Rachner et al. (2002) and Eckel et al. (2016) employed an ad-hoc atomization model particular for this operating condition). Furthermore, this work has not considered the coalescence of lagrangian droplets, which in reality could produce larger diameters after the atomization process.

6.6 Influence of spray injection variables

In this section, the sensitivity of the dispersed-phase simulations to the parameters that can be prescribed with SLI is assessed. These parameters are summarized in the corresponding block of Figure 6.6. For performing these simulations, the prescribed gaseous inlet is chosen as boundary condition for the gas phase, and the Gorokhovski model is applied, as justified by the analyses performed in the last sections.

6.6.1 Level-set resolution and injection location

Firstly, the influence of the injection location and the level-set resolution are assessed. For the former one, the SLIs obtained at $x = 10$ mm shown in Figure 5.60 are injected in the prescribed inlet which replicates the gaseous field for case UG100_DX10. For the latter, the SLIs at $x = 5$ and 10 mm from case UG100_DX20 (respectively Figures 5.61 and 5.62) are plugged into an aerodynamic field obtained by prescribing the gaseous phase statistics from this resolved case. Each case is named as its corresponding resolved atomization simulation plus its injection location: for instance, the baseline case is named UG100_DX10_x05 since it uses the SLI from resolved simulation UG100_DX10 at the location $x = 5$ mm.

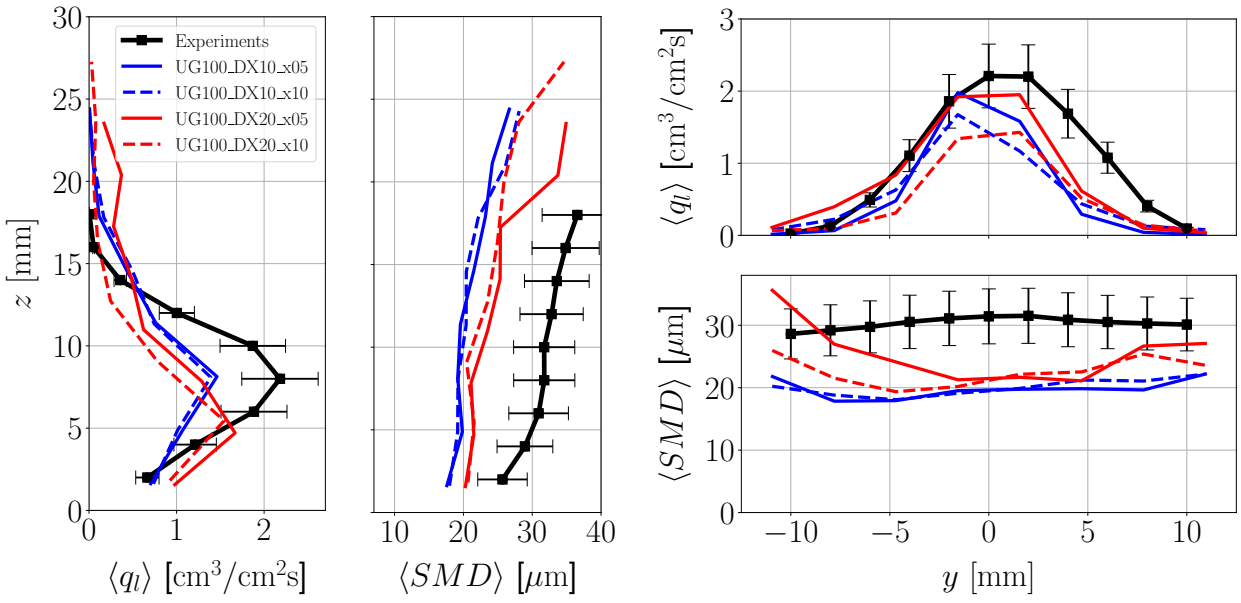

Figure 6.31: Integrated profiles of flux and SMD maps for numerical simulations comparing the effect of SLIs obtained with different resolutions and at several injection locations with the experimental results

Profiles for the integrated SMD and flux are shown in Figure 6.31. The effect of the level-set resolution on the dispersed-phase spray is clearly remarkable: vertical flux profiles shows their maximum flux location in the coarse cases (UG100_DX20) at a position closer to the wall, which does not agree with the experiments (the fine simulations UG100_DX10 capture it accurately). This is a consequence of the lower vertical penetration from the resolved jets with the coarse resolution (see trajectories in Figure 5.27). The vertical boundaries for the coarse SLIs are similar to the fine ones, and even higher for case UG100_DX20_x10. This is attributed to big particles being injected in these computations: droplets with larger diameters will travel along the vertical direction for longer than the smaller ones from the fine simulations until they atomize and relax towards the crossflow direction. Yet, such droplets are located in very low flux regions and do not represent a large portion of the spray.

Particles are generally larger for the coarse SLI simulations than for the fine one. The vertical SMD profiles show a more pronounced ballistic behaviour for case UG100_DX20_x05, caused by larger droplets sampled at the top part of the spray. These droplets, which can be seen in the snapshot of Figure 6.32, are very large particles injected at $x = 5$ mm which are convected along the channel without undergoing atomization. They were found to be surrounded by a cluster of smaller particles that might affect the gaseous phase in ensemble, preventing them from atomizing. Furthermore, since these particles are introduced from

the beginning of the simulation, the SMD evolution along the channel will also be affected. This is shown in Figure 6.33: simulation UG100_DX20_x05 captures a SMD decay with different rates compared to the rest of the cases. On the other hand, computation UG100_DX20_x10 does not show over-estimated ballistic profiles, and its SMD evolution along the channel shows a profile such as the ones previously observed: a clear exponential decay right after injection followed by a linear decrease afterwards. This demonstrates that for the coarse case it is better to inject downstream, since the spray from the resolved simulation is better atomized. In terms of global size, the SMDs at $x = 80$ mm summarized in Table 6.9 show that the coarser simulations produce larger droplets, which approach the experimental results. Nevertheless, this is a consequence of larger droplets being injected, which atomize through a breakup cascade into smaller and smaller particles, and end up reaching equilibrium with the ambient gas at larger diameters than in the fine simulations. The results for the vertical flux profiles from Figure 6.31 shows that, indeed, the coarse simulations do not capture accurately the vertical location of maximum flux, and hence it is better to initiate lagrangian computations with the finer injectors.

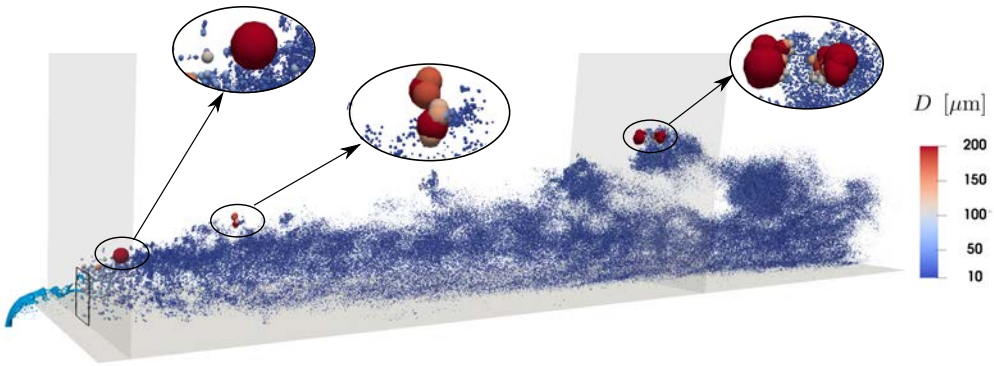

Figure 6.32: View of the dispersed spray in simulation UG100_DX20_x05, showing three regions with large droplets along the channel

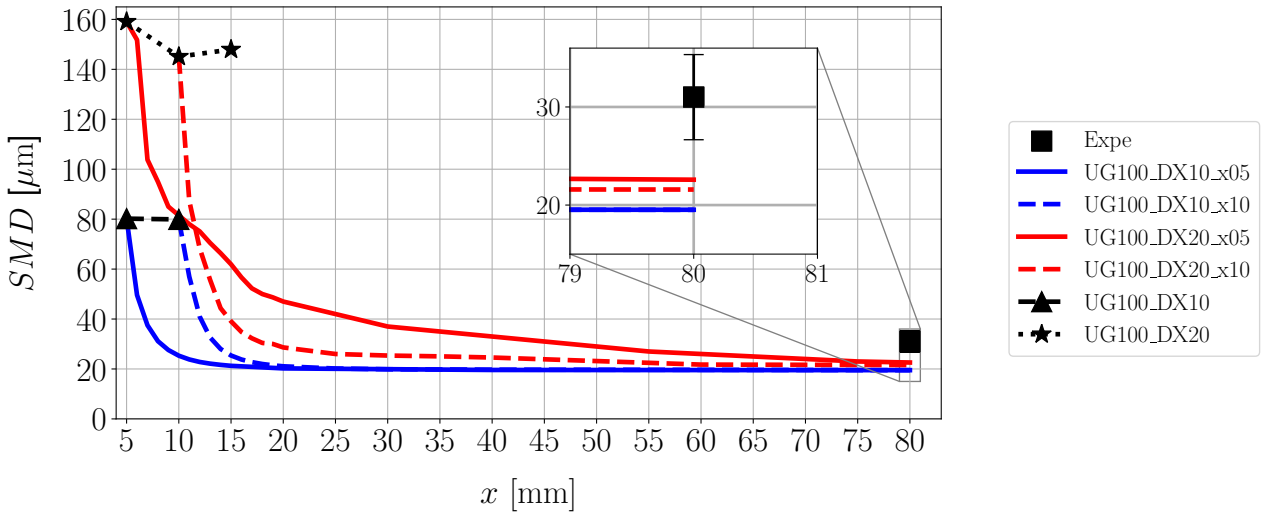

Figure 6.33: Evolution of SMD along axial location x with SLIs from two level-set resolution at two injection locations $x = 5, 10$ mm. The SMD at $x = 5$ and 10 mm for the resolved atomizations are also added for comparison

With respect to injection location, the differences for the SLIs for the coarse simulations have already been discussed, showing greater differences in profiles and SMD evolution along the channel. Regarding the SLIs from the fine simulations, the corresponding dispersed-phase computations do not show relevant dependencies on the injection location: all integrated profiles are similar in shape and in values, and the global SMDs obtained are practically identical. This might suppose that injecting droplets through SLIs obtained from the fine resolutions at different locations would make no difference in the lagrangian spray at

$x = 80$ mm. In such case, a resolved simulation could provide a SLI with cheaper computational costs than the ones reported in the previous chapter (Table 5.42), as the liquid removal sponge layer could be placed further upstream, for instance at $x = 6$ mm than at 11 mm, while retrieving an almost identical lagrangian spray in the dispersed-phase computation. This analysis reaffirms the idea that it is better to build a SLI with finer resolved atomization simulations: not only the particle's granulometry is better resolved than in an equivalent coarser simulation, but also a SLI can be built with a more reduced spatial domain due to a better atomization of the resolved droplets. Therefore, the **SLIs from case UG100_DX10_x05** (i.e. obtained for the fine interface resolution closer to the liquid nozzle) are retrieved for the subsequent analysis. It would be interesting to continue this study with even finer interface cell sizes in the resolved simulations, which has not been possible in this thesis due to the higher computational costs required.

Table 6.9: SMD values at $x = 80$ mm for simulations with different SLIs

Case	SMD [μm]	ε_{SMD} [%]
Experiments	31	-
UG100_DX10_x05	19.44	-37.29
UG100_DX10_x10	19.51	-37.05
UG100_DX20_x05	22.59	-27.14
UG100_DX20_x10	21.58	-30.38

6.6.2 Spray velocities

Prescribed velocities through SLI are investigated here by using different combinations of the parameters in Eq. (4.18). For the previous cases, the mean velocity was volume weighted (VW) and the r law for prescribing the RMS component was Gaussian (SLIs from Figure 6.21), injecting then into each SLI probe a stochastic component representing the normal dispersion of the droplet's velocities. Here, the effect of mean velocity is seen by injecting the arithmetic mean velocity ($\overline{u}$) while keeping constant the r law to follow a Gaussian distribution. Then, the effect of RMS is assessed by changing the r law to a uniform distribution and by removing the RMS component of the velocity (zero law), these two modifications performed with volume-weighted mean velocity being injected. Figure 6.34 shows the SLIs from simulation UG100_DX10 at $x_{\text{inj}} = 5$ mm with the arithmetic mean and VW velocities for visual comparison. Larger differences are found at the central and top parts of the maps, which are respectively the regions with larger flux and with larger droplets.

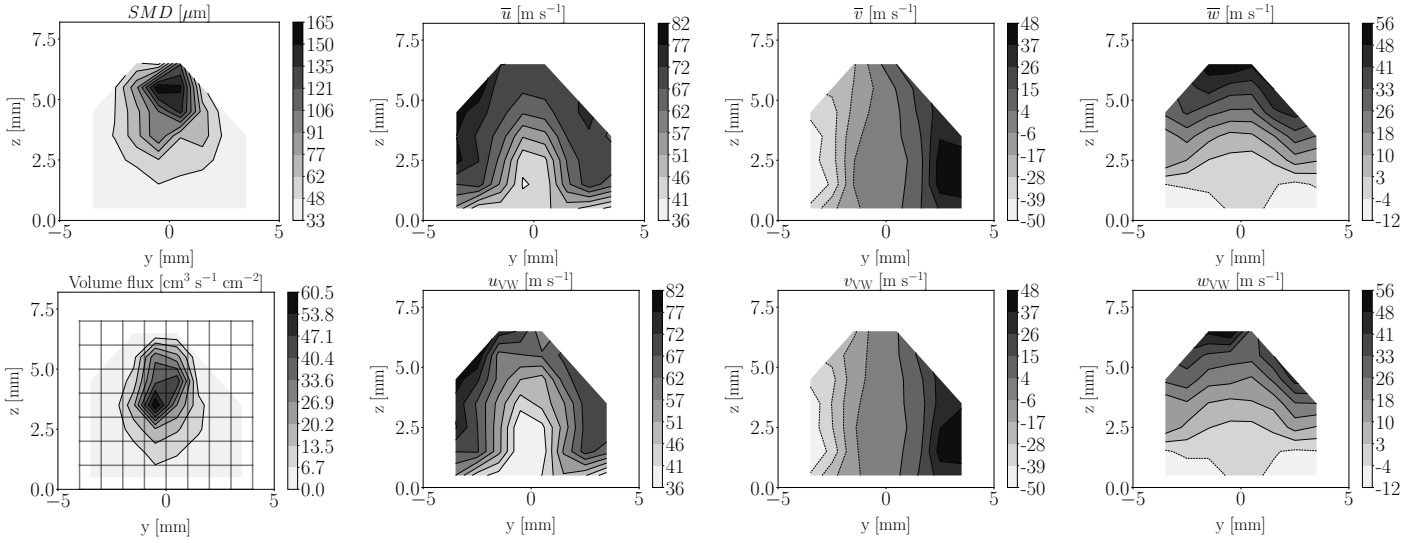

Figure 6.34: SLI mean arithmetic and VW velocity maps from case UG100_DX10 at $x_{\text{inj}} = 5$ mm

Results are shown in Figure 6.35, where the integrated SMD and flux profiles are plotted. The largest differences are observed for the treatment of the average velocities, since the vertical profiles change drastically when either arithmetic mean or VW averages are considered. By prescribing the arithmetic mean, droplets penetrate further away than for VW. The reason is the larger vertical velocities injected with arithmetic means: as shown in Figure 6.34, droplets at the top of the spray are injected with faster vertical velocity, and since these droplets are larger, they travel further along the vertical direction. The imposition of a different liquid velocity field also affects secondary atomization, since as observed in the SMD vertical profile from Figure 6.35 the droplets at the top part of the spray are smaller than at the bottom one, creating then a counter-ballistic behaviour which is not physical in such a JICF configuration. The flux profile also shows a flatter shape in the center of the spray instead of a peaky one, indicating concentration of droplets in a wide region around the spray center. Therefore, a proper prescription of accurate mean velocities is crucial for dispersed-phase simulations when using SLI.

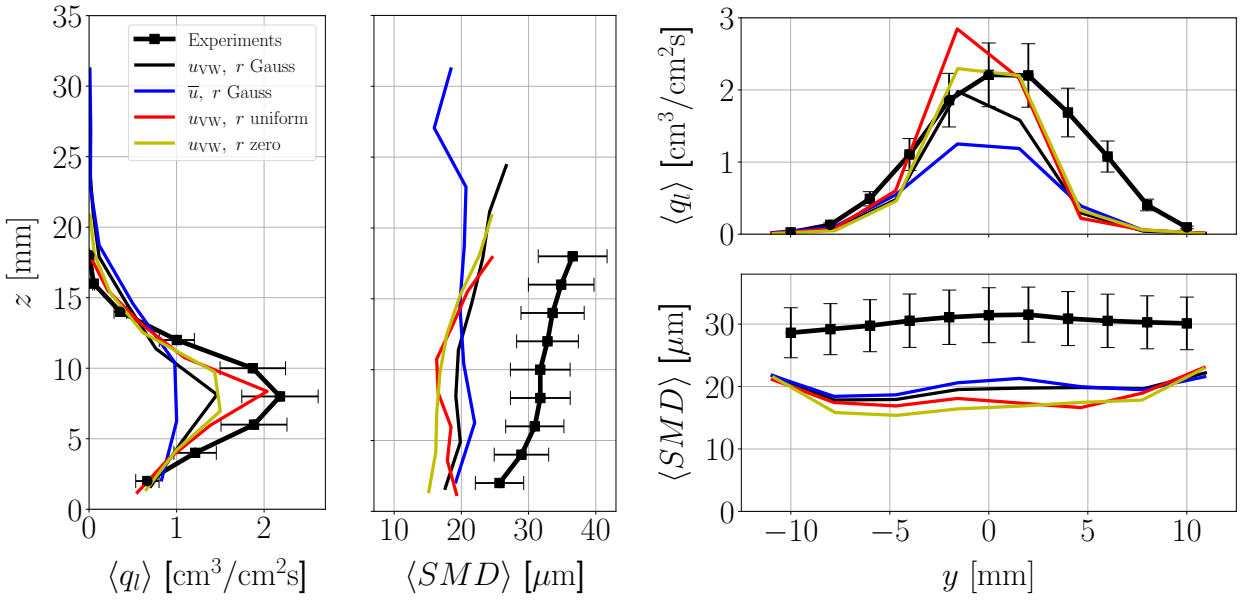

Figure 6.35: Integrated profiles of flux and SMD maps for numerical simulations comparing the effect of spray velocities with the experimental results

Regarding the effect of the r law governing the RMS component, the results show that the imposition of one distribution or another affects the spray penetration: the minimum upper vertical bound is found for the uniform law, while the maximum one is obtained for the gaussian one. All cases show a correct ballistic behaviour of the spray, which indicates that the counter-ballistic shape observed for the blue curve is due to the average velocity imposed to the droplets. However, the droplets obtained with the uniform and zero laws are smaller than for the gaussian one. Table 6.10 shows that the final SMD obtained is effectively lower for these two cases. The vertical location of maximum flux is properly retrieved by the gaussian and uniform laws, while the zero one shows a flat shape extending from $z = 5$ to 10 mm. This behaviour is again due to a similar concentration of droplets in this area: the zero law removes the RMS component of the droplets, injecting only the mean, hence increasing particle's concentration. It is therefore recommended to use the gaussian law for prescribing RMS velocities. Indeed, the sampled velocities distributions in the resolved simulations showed a normal distribution (see Figure 5.67), hence the Gaussian r law replicates this physical behaviour better than the other distributions. Different configurations, however, might require other prescribing laws more representative of their actual sprays.

From the results presented in this section, the **volume weighted average velocities** and a **gaussian r law for prescription of RMS components** are then chosen for the subsequent analyses.

Table 6.10: SMD values at $x = 80$ mm for simulations with different prescribed velocities

Case	SMD [μm]	ε_{SMD} [%]
Experiments	31	-
u_{VW}, r Gauss	19.44	-37.29
$\overline{u}$, r Gauss	20.44	-34.05
u_{VW}, r uniform	17.66	-43.05
u_{VW}, r zero	16.56	-46.57

6.6.3 Droplets diameters

In all previous cases, the diameters injected within each SLI probe $f_0\,(D)$ follow a lognormal law with a mean diameter given by the SMD and a standard deviation as given by s_g from Eq. (5.14). This parameter can be studied by performing a simulation where the prescribed diameters are constant and equal to the SMD within each probe (but they differ among probes, hence still injecting a polydisperse spray). The results for this simulation are given in Figure 6.36, and the global SMDs are reported in Table 6.11. Prescribing droplets with a constant SMD produce a lagrangian spray with lower vertical bounds and with slightly smaller droplets. Nevertheless, no significant differences are found when injecting with one f_0 or another, so the f_0 **lognormal law** is kept for further analyses.

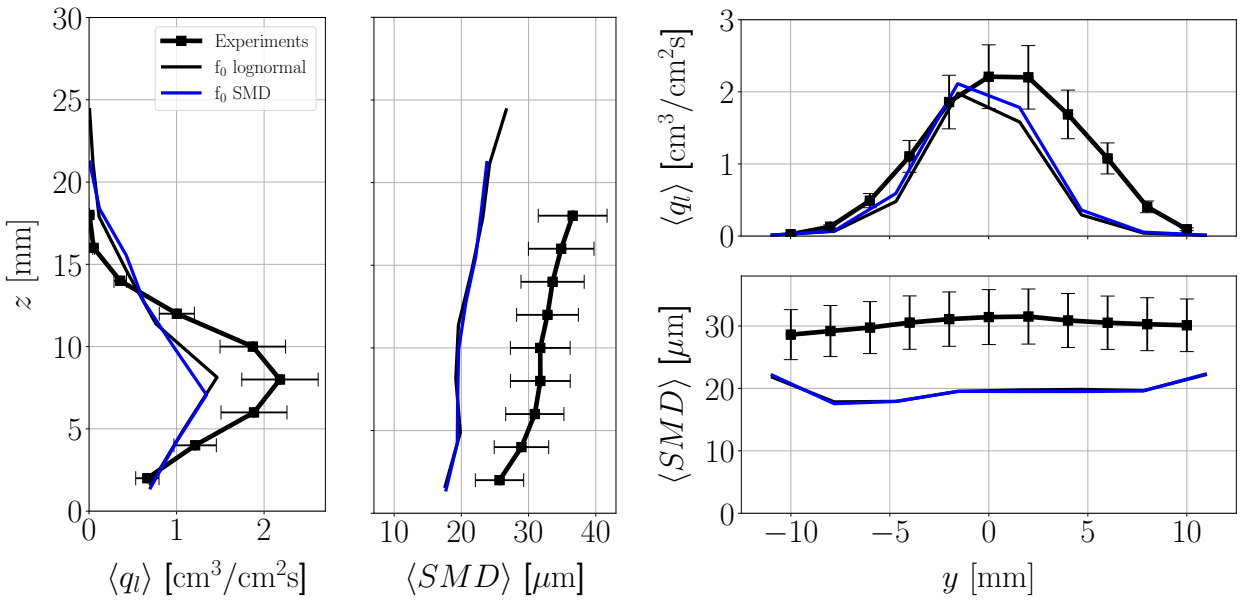

Figure 6.36: Integrated profiles of flux and SMD maps for numerical simulations comparing the effect of injection diameters $f_0\,(D)$ with the experimental results

Table 6.11: SMD values at $x = 80$ mm for simulations with different f_0 laws

Case	SMD [μm]	ε_{SMD} [%]
Experiments	31	-
Lognormal	19.44	-37.29
Constant	19.32	-37.68

6.6.4 Convergence-driven discretization

The effect of SLIs obtained through the convergence-driven discretization procedure (described in §4.4.4) is assessed in this section. This strategy has been applied to the spray obtained for case UG100_DX10 at $x_{\text{inj}} = 5$ mm. Three levels of refinement have been performed. The resulting SLI is shown in Figure 6.37, where the ad-hoc SLI for the same case is also added for comparison. It is directly observed how the convergence-driven discretization acts in order to preserve a fully converged spray in all the spatial domain.

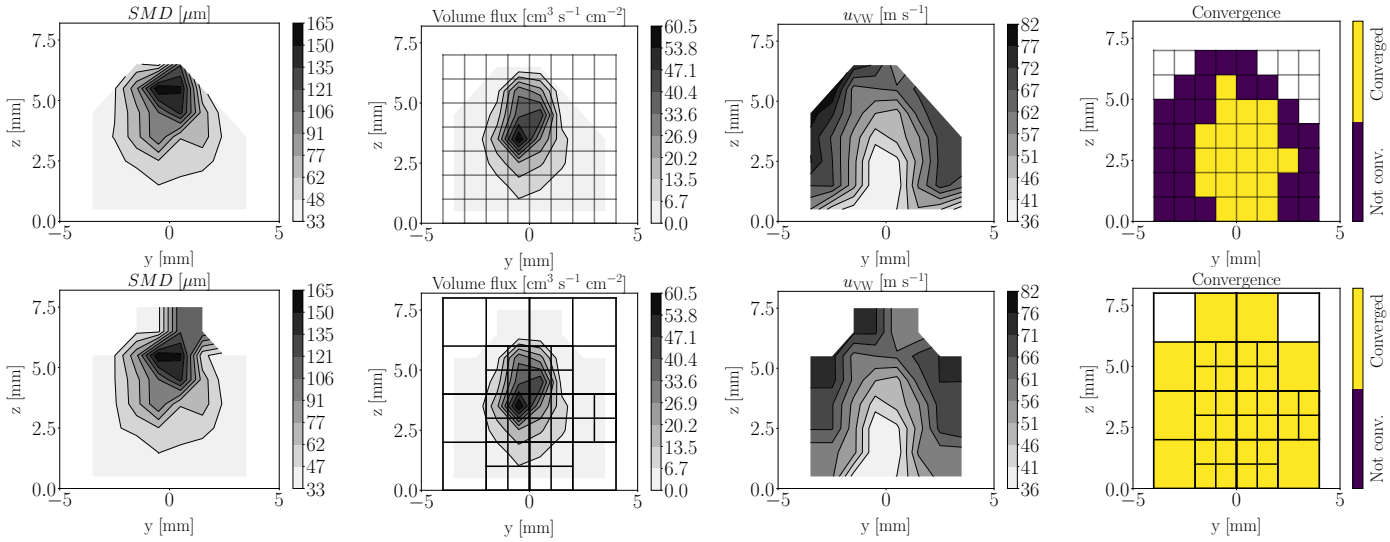

Figure 6.37: SLI maps from case UG100_DX10 at $x_{\text{inj}} = 5$ mm with and without convergence-driven discretization applied

Results for the spatially-integrated profiles of flux and SMD at $x = 80$ mm are shown in Figure 6.38. As observed, by using this discretization strategy, the vertical penetration of the spray is lower, matching the actual experimental limits. The vertical location of maximum fuel flux also agrees pretty well with experiments. The vertical SMD profile shows a correct ballistic behaviour, yet it yields underestimated values for most of the range. Lateral profiles of SMD and the global SMDs from Table 6.12 also show this tendency to diameter underestimation. This behaviour seems contradictory, since actually it is expected that a better spatial refinement yields better results. Such reduction in particles sizes with convergence-driven discretization might be be caused by the different velocities imposed, since by looking at Figure 6.37 these seem to be the magnitude differing the most with respect to the ad-hoc SLIs (flux and SMD profiles are very alike). The reasons for this behaviour are not yet fully understood, therefore **the discretization without quadtrees is retained**.

Table 6.12: SMD values at $x = 80$ mm for simulations with and without quadtrees

Case	SMD [μm]	ε_{SMD} [%]
Experiments	31	-
Without quadtrees	19.52	- 37.29
With quadtrees	16.60	-46.44

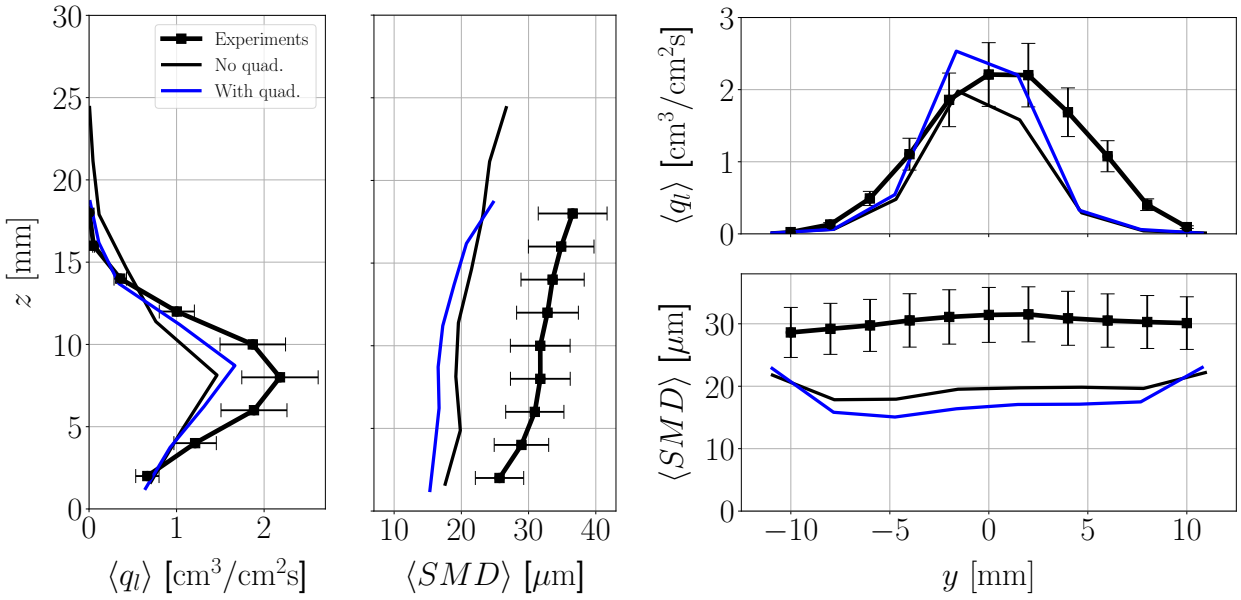

Figure 6.38: Integrated profiles of flux and SMD maps for numerical simulations comparing the effect of convergence-driven discretization with quadtrees with the experimental results

6.6.5 Operating condition

Finally, the influence of the operating condition is tested by injecting the SLIs obtained from case UG75_DX10 at $x = 5$ mm (Figure 5.54) into a reduced channel with the corresponding gaseous statistics as given by the prescribed gaseous inlet methodology. The spatially integrated profiles of SMD and flux are shown in Figure 6.39. Similar features than for the high Weber operating condition are retrieved: vertical bounds are slightly overestimated, and the SMD profile along axis z follows a ballistic profile. The maximum location of vertical flux is slightly overestimated, even though a flat profile for this location is obtained as in the experiments. The SMD profiles seem to be closer to experiments than the previous simulations for the high Weber case: this is confirmed by checking the global SMD in Table 6.13, which shows that it is underestimated by 20.64 % in the simulation. This improves the results from the high Weber point, which in the best case yielded an error of -36.64 %. There are two possible reasons why the SMD might be more accurately resolved in the dispersed-phase simulations: 1) the SLIs from the level-set computations of this operating condition are better resolved, since as the gaseous dynamic pressure is lower the resulting droplets from atomization are larger, and hence can be better captured by the employed mesh, or 2) relative velocities are better approximated in the lagrangian computations for this case due to the a lower velocity gaseous field, hence secondary atomization breaks droplets more smoothly and particles in equilibrium are closer to the experimental values. Given any of these two hypothesis (or both) to be true, this would suppose that actually the SLI methodology could work more accurately for operating conditions involving lower gaseous velocities in the flow.

Table 6.13: SMD values at $x = 80$ mm for simulation of the low Weber operating point

Case	SMD [μm]	ε_{SMD} [%]
Experiments	35.2	-
Simulation	27.93	-20.64

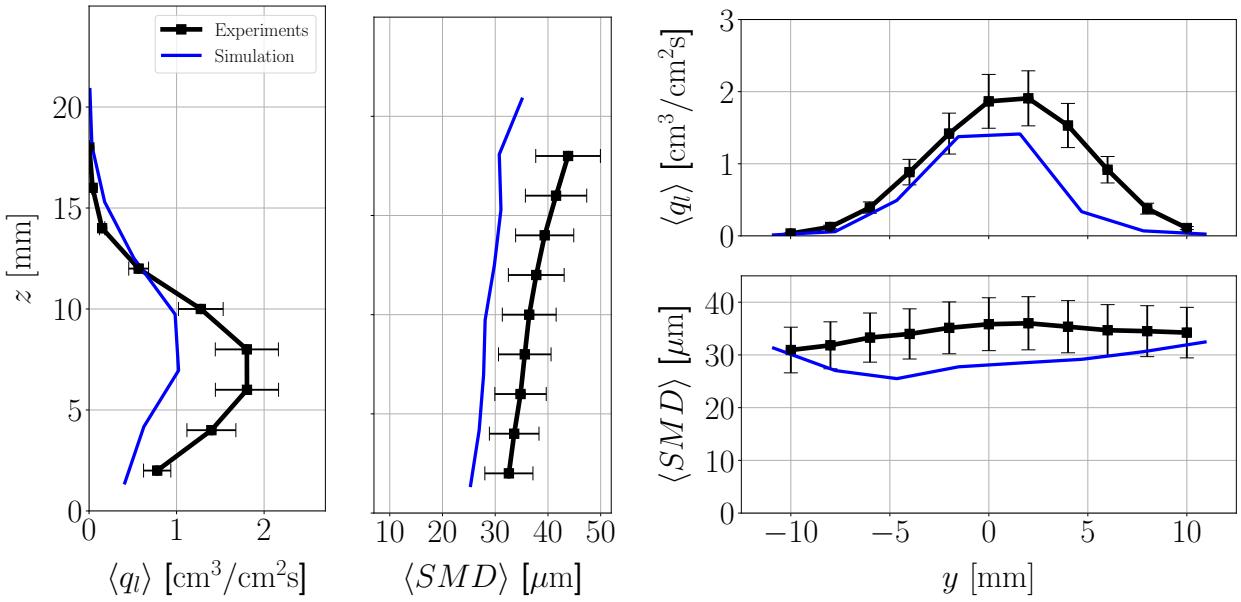

Figure 6.39: Integrated profiles of flux and SMD maps for numerical simulation UG75_DX10 at $x = 5$ mm (low Weber operating condition)

6.7 Artificial delay in secondary breakup

For the high Weber number case, a SMD ballistic profile and a coherent flux distribution were obtained, although the particles sizes produced underestimated the experimental SMD by 37 %. This deviation got reduced to 20 % for the low Weber point. These underestimations are thought to be caused by the secondary atomization model, which breaks droplets shortly after they are injected into the domain as they are not in equilibrium. The gaseous velocity field has a great influence on the granulometry produced, as it directly affects the particles breakup through the relative liquid-gas velocity.

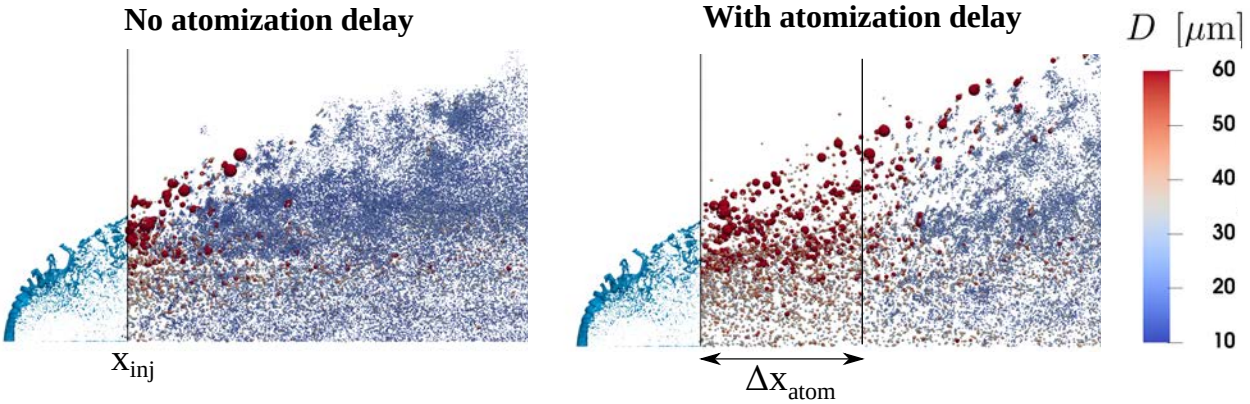

Figure 6.40: Effect of introducing an atomization delay in space Δx_{atom} in the lagrangian field

Since the low sizes obtained are attributed to large relative velocities at injection that enhance breakup, this deviation among velocities is going to be reduced by testing a delay in secondary atomization Δx_{atom}. The effect of this new parameter in the flow field can be seen in Figure 6.40: it consists of deactivating the secondary atomization model during an axial distance of length Δx_{atom} after injection. In this way, the liquid particles exchange momentum with the gas along this spatial region but do not break, accomodating their velocity to the gaseous field. A total of ten extra simulations have been performed, for which Δx_{atom} has been varied from 2 to 20 mm in steps of 2 mm. Note that case $\Delta x_{\text{atom}} = 0$ mm corresponds to the simulation previously reported as the baseline case in all parametric studies.

In first place, the evolution of global SMD along the channel is shown in Figure 6.41. The effect of the atomization delay is clearly seen: size stays constant and equal to the injected one within the region where the breakup model is not activated. Then, once it is triggered, droplets start to undergo a fast break and SMD decreases exponentially. The value at which curves stabilize is dependent on Δx_{atom}, being directly proportional to it. The SMDs at the experimental validation location can be better compared in Figure 6.42, which shows their evolution with Δx_{atom}. This magnitude evolves linearly in the simulations for the range tested, and for $\Delta x_{\text{atom}} > 12$ mm, the SMD enters within the range of experimental uncertainties at $x = 80$ mm. These graphs show then that leaving a relaxation time for the liquid phase to accommodate to the gas has a positive effect on the global sprays produced, as the relaxation of droplets results later in a less aggressive secondary atomization.

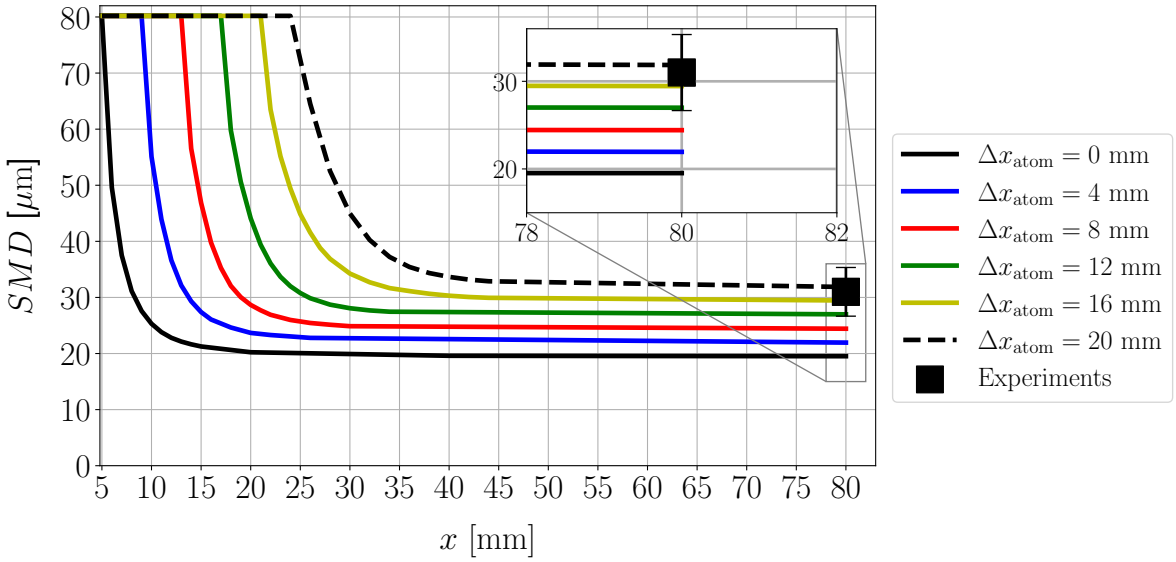

Figure 6.41: Evolution of SMD along axial location x with parameter Δx_{atom}

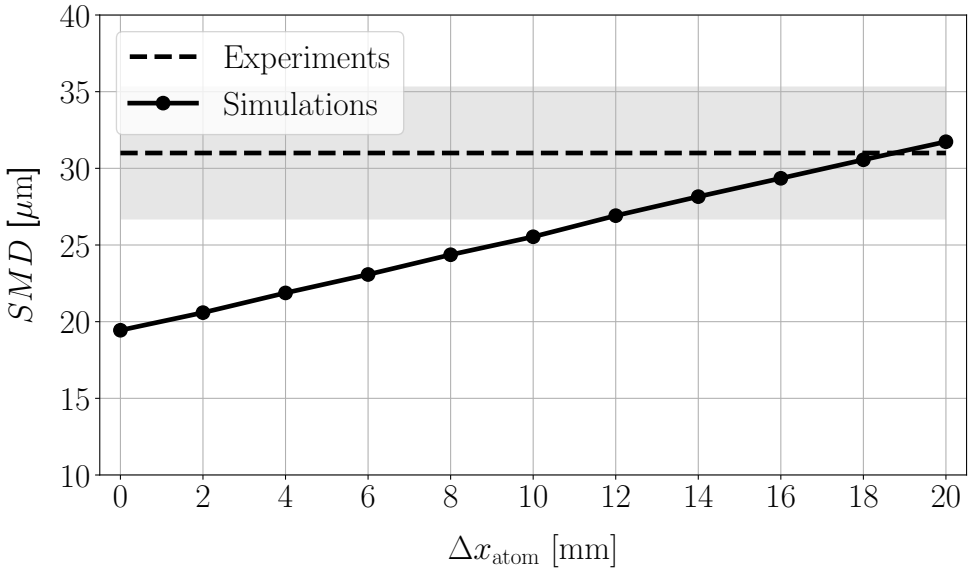

Figure 6.42: SMD at $x = 80$ mm for several values of parameter Δx_{atom}. The grey shaded area indicates the range of experimental SMD uncertainties

At last, the integrated profiles of flux and SMD at $x = 80$ mm are shown in Figure 6.43. Despite the improvements in the global SMD, the inclusion of the secondary atomization delay is detrimental for the spatially distributed sprays. Increasing Δx_{atom} makes the spray penetrate further, increasing its vertical bound, and flattens the volume flux curve. Furthermore, the SMD profiles increase their value with Δx_{atom} at the bottom part of the spray (regions with high flux), but not at the upper part, actually inverting the ballistic behaviour for $\Delta x_{\text{atom}} \geq 12$ mm. Overall, this atomization delay shows that when letting droplets relax to the gas before their breakup, they reach equilibrium at larger diameters, since the relative liquid-gas velocities are lower. This proves that the relative velocity is the parameter governing droplets breakup through the secondary atomization model: further works should consider improvements in this sense by better retrieving the gaseous flow field and by making a better prescription of the liquid velocities, for which the sectional approaches mentioned in §5.7.3 are suggested. Furthermore, it was proved in the previous chapter that sampled droplets are generally deformed while the lagrangian particles in the dispersed-phase computations assume spherical shapes. It is suggested that this non-sphericity should be taken into account in the dispersed-phase computations through a modified drag law for droplet transport, which could affect the momentum exchange and hence the secondary atomization through the relative velocities.

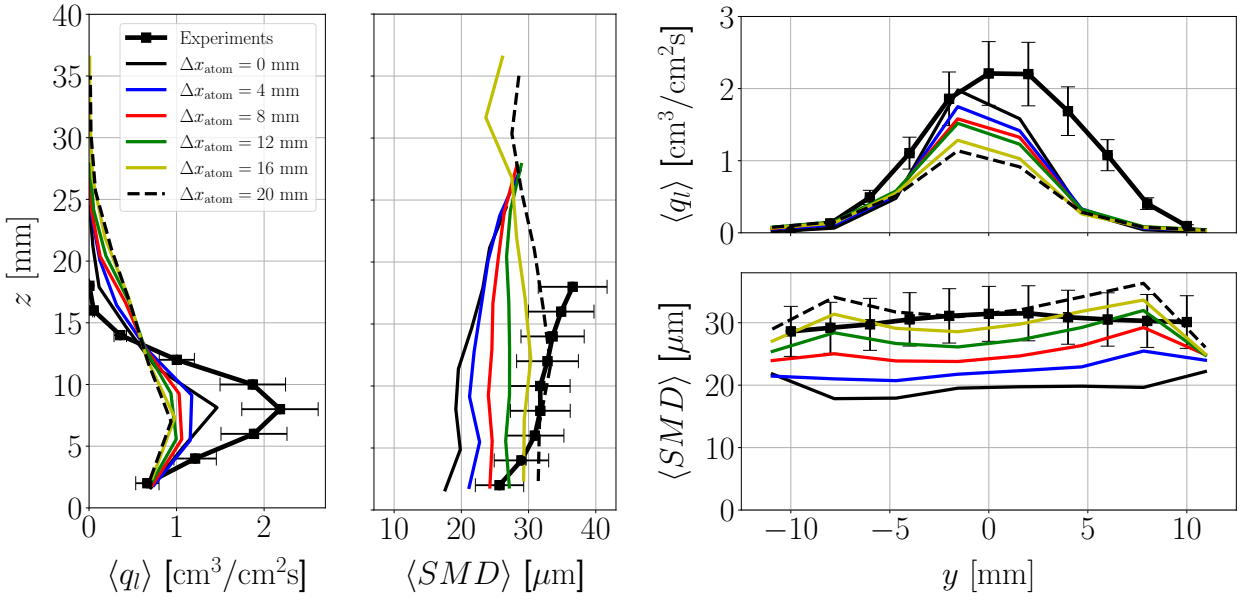

Figure 6.43: Integrated profiles of flux and SMD maps for numerical simulations comparing the effect of Δx_{atom} with the experimental results

6.8 Conclusions

This chapter has discussed dispersed-phase computations performed with the SLI models derived from the resolved atomization simulations. In first place, the state of the art was described. Experimental results were summarized, including an estimation of uncertainties for droplets sizes and fluxes. Previous numerical work were also reported, comparing with the results from one simulation performed in this thesis with Smart Lagrangian Injectors (SLI). Dispersed-phase computations were then performed, with the different parameters involved in SLI being analyzed. The study was divided into three main parts:

- First, the effect of modeling the perturbed gaseous phase was addressed. Two approaches were studied: the Actuator Line Method (ALM) and a methodology based on prescribing gaseous statistics on a reduced domain (prescribed gaseous inlet). The latter could capture more accurately the disturbed flow field, even though ALM also retrieved the main turbulent flow features (such as the recirculation bubble and counter-rotating vortices). Lagrangian simulations verified this observation: droplets from the prescribed gaseous inlet matched better the experimental sizes than the ALM ones. Hence, the prescribed gas inlet methodology was selected for the forthcoming studies.

- Then, the effect of the secondary atomization model was assessed. The three breakup models available (TAB, ETAB and Gorokhovski's stochastic model) were tested. TAB was found to produce the smallest droplets, while the model by Gorokhovski yielded the best experimental match. Hence, Gorokhovski's model was retrieved.

- Finally, the influence of the liquid phase prescription parameters was studied. Resolution from the resolved simulations was found to have a crucial effect, with the injectors from the fine resolution yielding the best results. Injection velocities also had a great influence: it is recommended to prescribe mean injection velocities as volume-weighted from the resolved ones, and set a gaussian r law for the RMS components. Changing the operating condition from a high Weber point to a lower one yields a better match for droplets sizes, probably due to a reduction in the liquid-gas relative velocities (which makes secondary atomization to produce larger droplets).

In all simulations performed, the flux profiles, vertical location of maximum flux and a correct spray behaviour were properly retrieved. Nonetheless, all cases showed an underestimation in droplets sizes, reflected by SMDs lower than in the experiments. It was found that secondary atomization is the main mechanisms creating such small droplets, and a disturbed gaseous field not properly modeled will enhance this breakup as it directly influences the relative velocity of the particles. To finally verify this, an artificial atomization delay after injection was introduced. This one was specified as a spatial region Δx_{atom} after droplet's injection in which the secondary breakup model is deactivated to let droplets exchange momentum with the air. After this delay, atomization was triggered again. It was found that increasing Δx_{atom} produced larger droplets, proving that the misprediction of relative velocities is the cause of size underestimation. On the other hand, such increase have also the effect of creating a counter-ballistic behaviour of the spray, which is not physical: hence, including this additional parameter is not the solution to retrieve a physical spray which matches the granulometry.

As future work, it is suggested to improve the prediction of the relative liquid-gas velocities by 1) a more accurate modeling of the gaseoud field perturbations and 2) improving the prescription of particles liquid velocities, for which the sectional approach described in §5.7.3 is suggested. Furthermore, the inclusion of droplet non-sphericity in dispersed-phase computations through modified drag coefficients might also enhance the results, since a different momentum exchange would also affect the relative velocities and, consequently, the secondary atomization. To finish, this first version of SLI has neglected additional models such as subgrid dispersion terms for the velocities, which could affect atomization, or coalescence, which if present would actually increase the size of the particles. It would be interesting to assess wheter these additional models, or others, could improve the dispersed-phase sprays.

Part III

Application to a multipoint injector

Chapter 7

Description and gaseous flow validation

7.1 Introduction

Part II has been devoted to the development of models for lagrangian injection. The modeling methodology has been detailed in Chapter 4. Firstly, lagrangian injectors have been constructed from resolved atomization simulations of a liquid jet in crossflow. Then, the built models have been applied to perform dispersed phase simulations of the same configuration. The next chapters show the application of the models to a swirled MSFI burner more representative of industrial systems. The same rationale as in Part II is followed: models for lagrangian injection are built from resolved atomization simulations of one multipoint injector hole (Chapter 8), and then applied to dispersed phase simulations of the full take-off stage (Chapter 9).

Prior to the application of the models, this chapter introduces the experimental test bench and the numerical setup replicating this geometry. Non-reactive simulations of the aerodynamic flow field without liquid injection are reported and validated with experiments. Two experimental operating points are simulated: one studied in the thesis of Providakis (2013) for validating the numerical simulations, and another one studied by Renaud (2015) that settles the gaseous field and initial conditions for performing the two-phase flow studies from Chapters 8 and 9.

7.2 Experimental setup

Banc à Injection Multiple pour les Ecoulements Réactifs (BIMER) is a test rig developed at the laboratory EM2C for the study of reactive phenomena in MSFI systems. Originally studied experimentally by Barbosa (2008) with gaseous fuel, its was later extended to liquid fuel in the works of Providakis (2013) and Renaud (2015).

The test bench is shown in Figure 7.1. Air is introduced into a cylindrical plenum where the MSFI burner is located. The injector is then connected to a combustion chamber with a length of 500 mm and a rectangular cross section 150x150 mm^2. The lateral walls are made of quartz to allow for optical access to the interior, while the top and bottom walls are cooled with water. Exhaust gases are evacuated at the end of the chamber through a collector. Two different fuel feeding lines are connected to each stage of the injector. A detailed view of the burner is shown in Figure 7.2. Each stage has a swirler and a liquid injector. The swirlers will give a rotating motion to the air coming from the plenum. The stages are designed as follows:

- The **pilot stage** consists of a swirler with 18 vanes located in a crown with inner and outer diameters of 30 and 45 mm respectively. These vanes have a width of 6 mm and a 42° inclination angle. Fuel injected through the pilot forms a hollow cone.

- The **take-off stage** consists of a swirler with 20 vanes of 35° inclination and 10 mm width spanning between inner and outer diameters of 55 and 75 mm. The swirl number generated is close to 1. For liquid injection, 10 holes of 0.3 mm diameter are equally spaced along the multipoint annulus, with the

same radial distance to the center of the pilot injector. Each hole is aligned with the center of a vane (one hole every two vanes), and the vanes are placed so that the swirls of each stage are co-rotating.

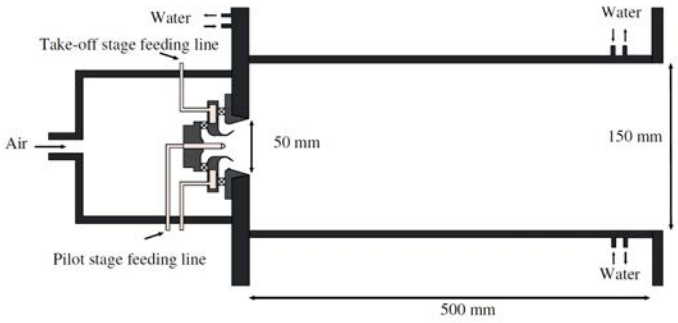

Figure 7.1: BIMER experimental test bench. Source: Cheneau (2019).

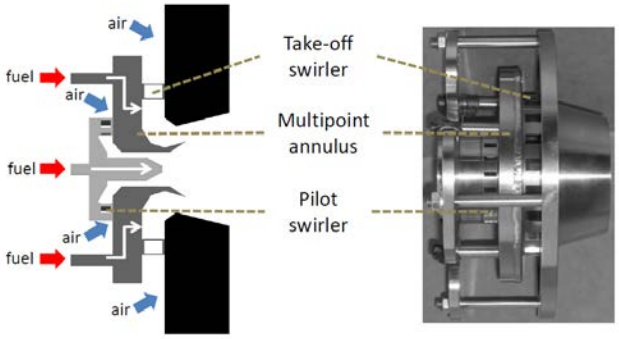

Figure 7.2: Swirled injector of the BIMER test bench. *Left*: schematic cross-section of the injector, indicating air and liquid inlets. *Right*: experimental view of the injector. Source: Renaud (2015).

BIMER is a multi-staged combustor where liquid is introduced through both multi-point and pilot stages. The fuel repartition between stages can be defined by the staging parameter α, which indicates the quantity of fuel going through the pilot stage $\dot{m}_{l,\text{pilot}}$ with respect to the total fuel:

$$\alpha = \frac{\dot{m}_{l,\text{pilot}}}{\dot{m}_{l,\text{pilot}} + \dot{m}_{l,\text{takeoff}}} \tag{7.1}$$

where $\dot{m}_{l,\text{takeoff}}$ is the fuel mass flow rate going through the take-off stage. A factor $\alpha = 0$ % indicates that fuel is injected only through the take-off stage, while $\alpha = 100$ % denotes pilot injection only.

The test bench operates at atmospheric pressure. Air can be preheated up to a temperature of 600 K. The injected fuel is dodecane. Kerosene is not used since at a laboraty scale it can present risk of coking and its complex chemistry hinders the analysis of the flames (Providakis 2013). Hence, dodecane was chosen due to its more simple composition and to its properties being close to kerosene. Dodecane properties of interest for this work are shown in Table 7.1.

Table 7.1: Physical properties of dodecane fuel ($C_{12}H_26$) at 20 °C

ρ [kg m^{-3}]	μ [Pa s]	σ [N m^{-1}]
750	$1.36 \cdot 10^{-3}$	0.022

7.3 Choice of operating points

Gaseous flow simulations of BIMER have been performed for two operating conditions tested experimentally (Providakis 2013, Renaud 2015). One condition is used for validation of the aerodynamic simulations, while the other is used as application to obtain a developed gaseous field for initialising two-phase computations in the next chapters:

- **Validation** of the gaseous simulations is performed with the operating point tested experimentally by Providakis (2013), since this one presents data on the non-reactive aerodynamic field. The simulations are also compared to numerical results obtained for this same operating condition by Cheneau (2019).
- **Application** to the setup condition tested by Renaud (2015). This study shows data on non-reactive spray characteristics, and hence it will be used as the application case to run the full flowchart formerly introduced in Chapter 4.

The parameters corresponding to both operating points are listed in Table 7.2.

Table 7.2: Operating points for performing non-reactive gaseous simulations

Operating condition	$\dot{m}_g$ [g s^{-1}]	T_g [K]	ρ_g [kg m^{-3}]	μ_g [Pa s]	p [atm]	Reference
Validation	53	473	0.75	$2.57 \cdot 10^{-5}$	1	Providakis (2013)
Application	43.1	433	0.82	$2.39 \cdot 10^{-5}$	1	Renaud (2015)

7.4 Numerical setup

7.4.1 Computational geometry

The computational configuration of the BIMER test bench is shown in Figure 7.3. Air is introduced into the plenum through a cylindrical nozzle. The MSFI burner is located at the end of the plenum. This burner is connected to the combustion chamber with a diffusor. A region representing the atmosphere with a coflow of air at low speed (5 m/s) is located at the end of the chamber.

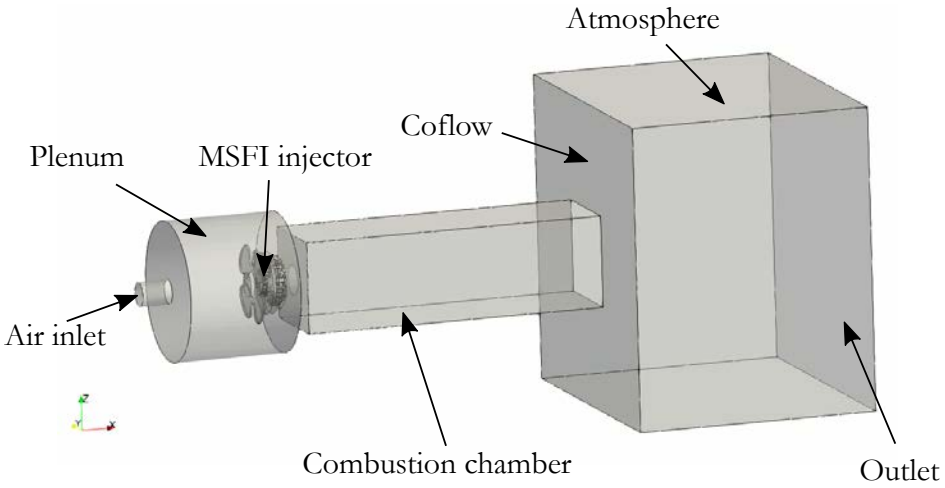

Figure 7.3: Numerical configuration of BIMER test bench

Figure 7.4 gives a detailed view of the MSFI burner. Both the take-off and pilot stages are represented as in the experimental geometry, with the fuel injectors and the gaseous swirlers. Fuel feeding lines and other experimental features have not been modeled due to their geometrical complexity (Cheneau 2019). The flower, whose main function is to attach the burner to the test rig, has been included in the computational domain since it influences the incoming gaseous flow field.

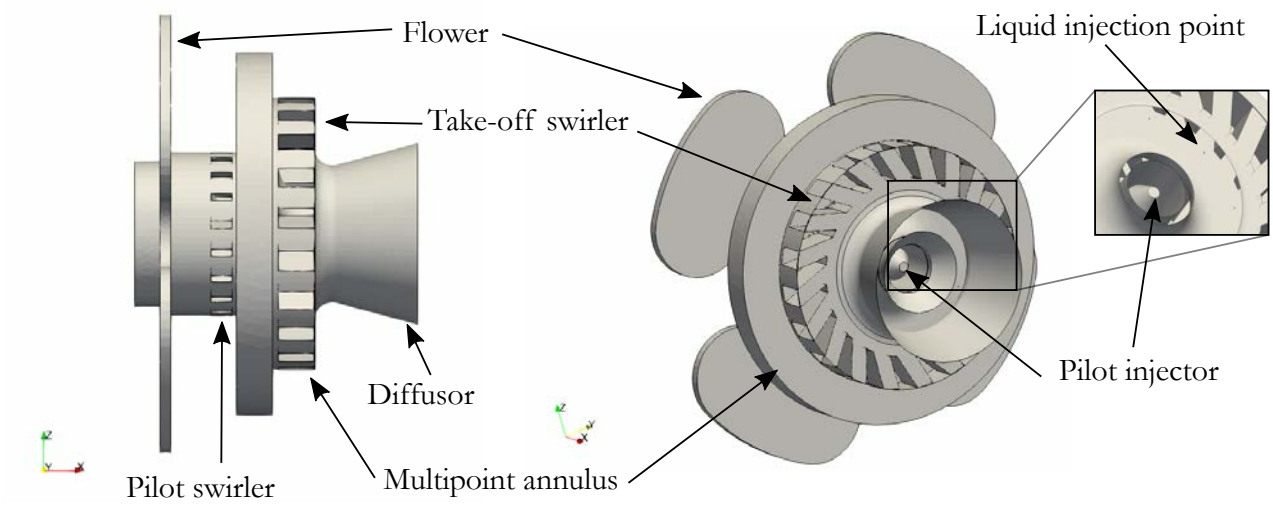

Figure 7.4: Details of multipoint injector from BIMER test bench. *Left*: side view indicating same features of Figure 7.2. *Right*: isometric view of the injector, with a zoom-in region showing the multipoint injector.

7.4.2 Meshes

For the numerical gaseous study of BIMER, two meshes have been simulated. Their characteristics are given in Table 7.3: a grid independence study has been performed with a coarse mesh of 7 million elements and a fine one of 38 million elements.

Table 7.3: Characteristics of meshes employed in BIMER study

Mesh	# elements	# nodes	Minimum cell size Δx [μm]
Coarse	7,356,140	1,891,542	29.82
Fine	37,835,617	9,738,371	5.04

Figure 7.5 provides a view of both grids, with zoomed-in views of the injector where more elements are placed. At the plenum, the baseline cell size is $\Delta x = 3$ mm. Then, the injector region is refined overall with $\Delta x = 0.5$ mm for both meshes. In the coarse mesh, the cell size in the combustion chamber evolves gradually from $\Delta x = 3$ mm at the exit of the injector until $\Delta x = 8$ mm at the inlet of the atmospheric region. The injector walls are not refined in this case. For the fine mesh, on the contrary, the walls of the pilot and take-off have been refined to $\Delta x = 0.25$ mm. At the exit of the injector, a conic region has been placed with a baseline size of $\Delta x = 1$ mm. Downstream the combustion chamber, the cell size evolves from $\Delta x = 1$ mm to $\Delta x = 8$ mm at the inlet of the atmospheric region as in the coarse mesh. Simulations are run using an LES approach where a dynamic Smagorinsky filter is used to model the subgrid turbulent scales (Germano et al. 1991).

7.4.3 Simulated cases

In total, three simulations have been performed: two for the validation operating condition, one with each mesh from Table 7.3, and one for the application operating point with the fine mesh. The nomenclature for 7.4.

Table 7.4: Nomenclature for simulations reported in this chapter

Mesh	Operating condition	Name
Coarse	Validation	VAL_COAR
Fine	Validation	VAL_FINE
Fine	Application	APP_FINE

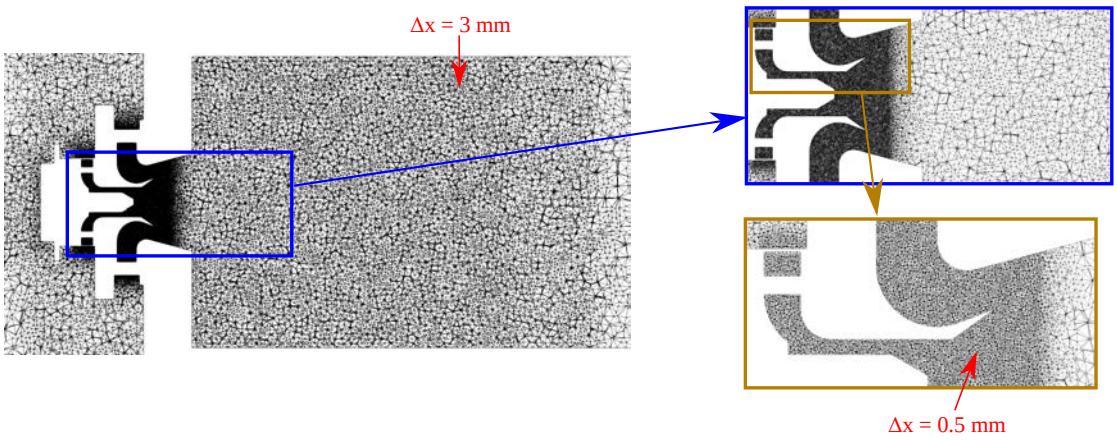

(a) Coarse mesh

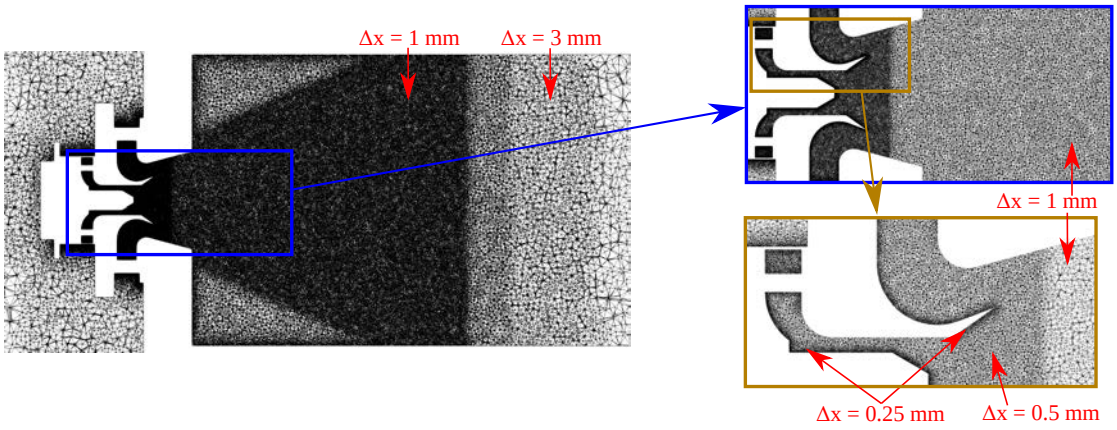

(b) Fine mesh

Figure 7.5: View of the meshes employed for the BIMER study at the central plane of the burner.

7.5 Physical features of swirled flows

7.5.1 Swirl number and vortex breakdown

Swirled flows are characterized by a high rotational flow measured by the azimuthal velocity component u_θ. The relative importance of this component with respect to the axial velocity will determine the characteristics of the gaseous flow. This can also be specified by means of the swirl number S_w, which is calculated as the ratio between the azimuthal and axial momentum fluxes (Huang & Yang 2009):

$$S_w = \frac{G_\theta}{R_{\text{ext}} G_x} = \frac{1}{R_{\text{ext}}} \frac{\int_0^{R_{\text{ext}}} \rho u u_\theta r^2 dr}{\int_0^{R_{\text{ext}}} \rho u^2 r dr} \tag{7.2}$$

where R_{ext} is the outer radius of injection. For swirl numbers over a given critical value, usually 0.6 (Syred & Beér 1974), a phenomenon known as vortex breakdown appears. The later is characterized by the appearance of the recirculation zones and instabilities in the aerodynamic field and in the flame dynamics. A common hydrodynamic instability, present in most swirled burners, is the Precessing Vortex Core (PVC). In the operating points from Table 7.2, the values of S_w are around unity (Providakis 2013, Renaud 2015), which are higher than the threshold $S_w > 0.6$. Hence, in both operating conditions the mentioned phenomena are present. The recirculation regions are shown and discussed for both the validation (§7.6) and application points (§7.7), while the PVC instability is shown only for the latter.

7.5.2 Characteristic time scales

Characteristic time scales of the gaseous flow field can be estimated from the simulations. Their calculation is based on the mean axial and azimuthal velocities, $\overline{u}_x$ and $\overline{u}_\theta$ respectively. For their obtention, the following expressions are applied at the diffusor outlet:

$$\overline{u}_x \approx \frac{1}{R_d}\int_0^{R_d} u_x dl \quad ; \quad \overline{u}_\theta \approx \frac{1}{R_d}\int_0^{R_d} u_\theta dl \tag{7.3}$$

where $R_d = 25$ mm is the diffusor outlet radius. Two time scales are defined:

- Convective time scale τ_{conv}:

$$\tau_{\text{conv}} = \frac{L_{cc}}{\overline{u}_x} \tag{7.4}$$

  where $L_{cc} = 500$ mm is the length of the combustion chamber.

- Swirl time scale τ_{swirl}:

$$\tau_{\text{swirl}} = \frac{\pi R_d}{\overline{u}_\theta} \tag{7.5}$$

The mean velocities and time scales are obtained for both operating points simulated. The results are shown in Table 7.5.

Table 7.5: Gaseous fields time scales for each operating point

Operating condition	$\overline{u}_x$ [m s^{-1}]	$\overline{u}_\theta$ [m s^{-1}]	τ_{conv} [ms]	τ_{swirl} [ms]
Validation	17.1	23.3	29.2	3.4
Application	13.3	18.0	37.6	4.4

7.6 Validation of gaseous field

The numerical setup introduced previously is firstly validated on the operating point tested experimentally by Providakis (2013). This point was also numerically studied in the work of Cheneau (2019) with a mesh of 20.1 million elements and with the software AVBP, developed at CERFACS (CERFACS 2011). Details on the mesh and parameters used in this study can be found in the reference previously mentioned. Regarding the results obtained in this work, two computations have run with YALES2 (one with each mesh shown in Figure 7.5) for a total physical time of 180 ms. For flow establishment, simulations have run first for a total physical time of 60 ms ($\sim 2\tau_{conv}$). At the end of this time, statistics have been accumulated for a physical time of 120 ms ($\sim 4\tau_{conv}$). All the mean values reported in this section have been time-averaged for this duration.

In first place, the meshes employed are assessed by plotting the ratio between the mean turbulent viscosity and the laminar viscosity $\overline{\nu}_T/\overline{\nu}$ in the central plane. $\overline{\nu}_T$ is the turbulent viscosity modeled by the LES subgrid model, in this case the dynamic Smagorinsky model (Germano et al. 1991). A dynamic model has been chosen since it provides values of modeled turbulent viscosity lower than the static ones, hence improving the simulation results in recirculation regions and turbulent boundary layers (Sayadi & Moin 2010). The results are shown in Figure 7.6. In both meshes, the ratio is high upstream the multipoint injector and low within it, since both meshes have similar characteristics in these regions (see Figure 7.5) except for the wall refinement in the fine mesh, which has not a big impact on the viscosity ratio in this case. The biggest differences are located downstream the injector: the values of the viscosity ratio are much smaller in the fine mesh than in the coarse one due to the reduction in element size. In both meshes, there is a transition of $\overline{\nu}_T/\overline{\nu}$ in the central plane. $\overline{\nu}_T$ in the divergent section due to a steep gradient in the cell size, which is more pronounced in the coarse case. In general, the lower values of the viscosity ratio in the fine mesh downstream the injector indicate that the turbulent model contributes to a lesser extent, hence improving the LES quality (making it closer to DNS) in these regions for this resolution.

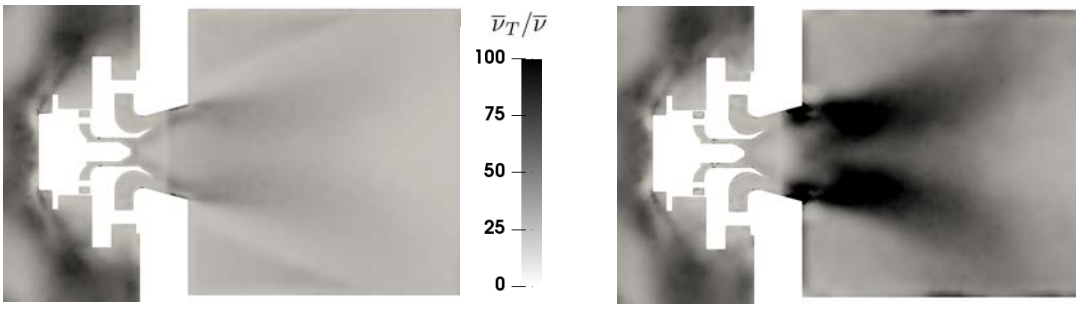

(a) Case VAL_FINE (b) Case VAL_COAR

Figure 7.6: Ratio between turbulent mean viscosity and mean viscosity in central cut of BIMER.

The mean axial field for in the middle plane is shown in Figure 7.7. The white line indicates the contour with zero mean axial velocity, $\overline{u} = 0$. The results obtained by Cheneau (2019) are also shown for comparison. As observed, the range of mean velocity values is the same in the three cases. The flow fields are similar: the topology is typical of swirled burners, containing an Inner Recirculation Zone (IRZ), a Corner Recirculation Zone (CRZ), two Swirled Jets (SWJ) and shear layers with high velocity gradients. These areas are indicated by arrows only in Figure 7.7b, but are present in all the cases. With respect to differences among meshes, the coarse mesh shows a continuous region of negative velocity from the pilot injection point and for the whole domain shown in the figure, while the fine mesh displays a small region of positive velocity between the pilot injector and the tip of the IRZ (stagnation point) as the results of Cheneau (2019) show. Furthermore, the SWJ in the coarse mesh show larger numerical diffusion than in the fine case due to the larger cell sizes.

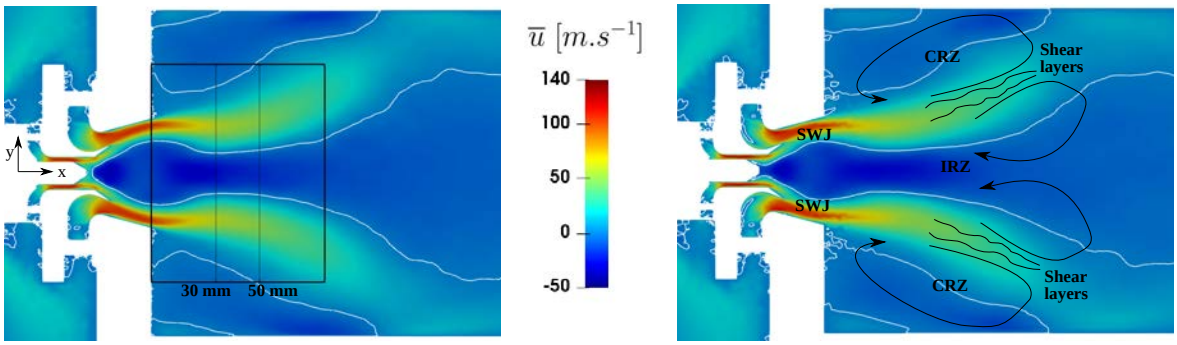

(a) Case VAL_FINE (b) Case VAL_COAR

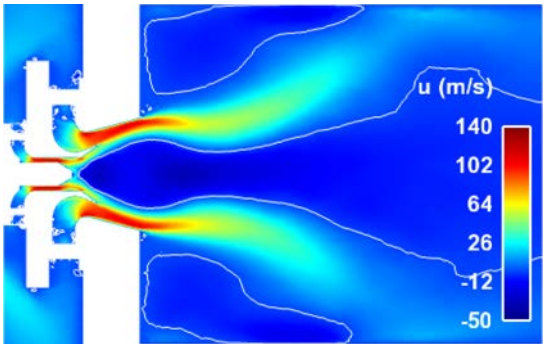

(c) Results from Cheneau (2019).

Figure 7.7: Mean axial velocities at central plane in BIMER. The white line indicates the contour $\overline{u} = 0$.

The pictures from Figure 7.7 show a qualitative view of the mean axial velocity field from only computational results. The numerical results are now validated by comparing with experimental results obtained with Particle Image Velocimetry (PIV) at the probes shown in Figure 7.7a: a qualitative validation is performed by showing mean and RMS velocity maps in the rectangular section, while quantitative results can be compared by plotting the velocity profiles at the lines located at x = 30, 50 mm downstream the diffusor.

7.6.1 Qualitative validation

Experimental validation of the simulations with experimental results is done by comparing the velocity maps at the rectangular probe, see Figure 7.8. The experimental fields from Providakis (2013) are shown in the first column, while the numerical results from Cheneau (2019) obtained with the software AVBP are located in the second one. Mean and RMS axial and vertical velocities are depicted. The black lines denote the contours of zero mean axial velocity, $\overline{u} = 0$.

The results obtained with both fine and coarse meshes show a good flow topology in all cases. The velocities are in the same range as the experiments, with some over(under)estimation of the maximum (minimum) values in the computations. The lines of null axial velocity are properly reproduced in both fine and coarse meshes, with differences in the CRZ probably due to the non-convergence in this regions: these are low-velocity, recirculation areas which take longer to converge than other parts of the domain, and hence the running time of the simulations might not be enough to fully resolve them.

With respect to the axial velocities u, the mean maps from Figure 7.8a show that both IRZ and CRZ are well captured. The shear layers between IRZ and CRZ, where the velocity gradients are high, are also resolved. Symmetry with respect to the central axis is observed. For u_{RMS} (Figure 7.8b), symmetry with respect to this line is also observed. The RMS values are higher at the IRZ and the shear layers, where high velocity fluctuations are present. In general, RMS values are overestimated in the simulations with respect to the experiments. With respect to the vertical velocities v, the mean values from Figure 7.8c far downstream the diffusor match the experiments. Closer, the simulations present two circular pockets of high positive and negative velocities (enclosed by the dashed contours in Figure 7.8c, fine case) that are not present in the experiments. The v_{RMS} values of Figure 7.8d do not fully agree with the experiments. The experimental results for the mean velocity, however, do not present symmetry with respect to the central axis, something which is expected in this type of swirled configurations. Overall, all the numerical results obtained with both fine and coarse meshes match closely the numerical results obtained with AVBP by Cheneau (2019).

By comparing the results from fine and coarse meshes, it is observed that both cases provide values with the same order of magnitude for all velocities. The RMS values obtained with the coarse mesh are lower than for the fine one. Also, it is clearly seen that the fields obtained with the fine mesh are smoother (i.e. present less numerical noise) than the ones with the coarse one. This is attributed to numerical diffusion in the simulations, which is higher for the coarse mesh. The diffusion is more noticeable in the regions with high velocity gradients such as the shear layers of $\overline{u}$ and the velocity pockets of $\overline{v}$, where the numerical noise in the velocity field is visible.

7.6.2 Quantitative validation

The qualitative analyses are complemented with a qualitative experimental validation by showing the velocity profiles at the lines x = 30, 50 mm displayed in Figure 7.7a. The results are shown in Figure 7.9 for the axial velocities u and Figure 7.10 for the vertical ones, v. Once again, the experimental results by Providakis (2013) and the numerical ones by Cheneau (2019) are also shown. The location of maxima and minima peaks in mean velocities are properly captured. Their magnitudes are overestimated in absolute value for $\overline{u}$ at x = 30 mm, while they get closer to the experimental results at x = 50 mm. The RMS values are always overestimated in the simulations, specially in the regions with higher velocity gradients, as also shown in the qualitative images of Figure 7.8. The comparison for the vertical velocities does not fully match the experimental results, but it agrees with the numerical results obtained with AVBP by Cheneau (2019). In general, all results show symmetry with the central axis x = 0.

By comparing the results from the fine and coarse meshes, the same statements as in the previous section for the qualitative validation can be done. The coarse mesh presents noisier signals due to the higher numerical diffusion introduced in this case. The mean values for the axial velocity $\overline{u}$ are quite close in both cases, but the difference is larger for the vertical velocity $\overline{v}$. The RMS values in the coarse mesh are generally underestimated along the z coordinate. Due to the better results obtained with the fine mesh, this case is selected for simulating the application point described in Figure 7.2 (see §7.7) and for performing the subsequents computations shown in Chapters 8 and 9.

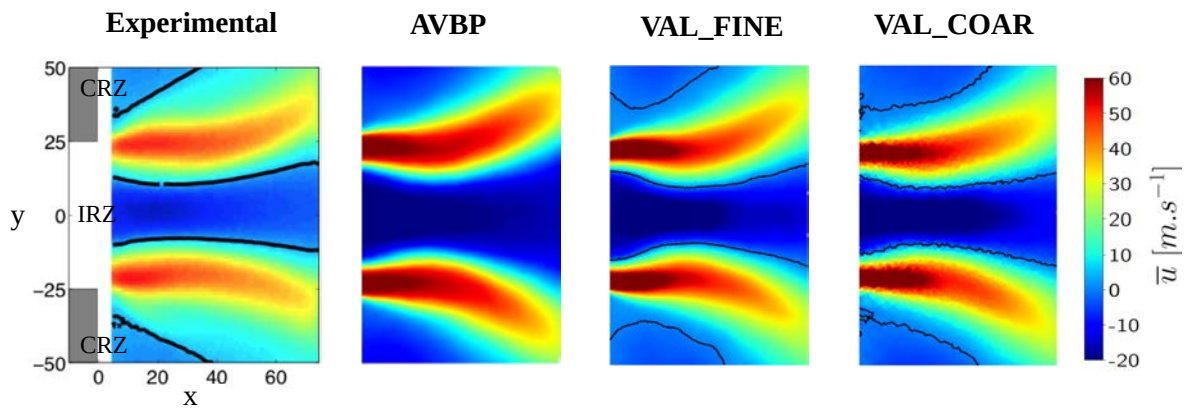

(a) Mean axial velocity

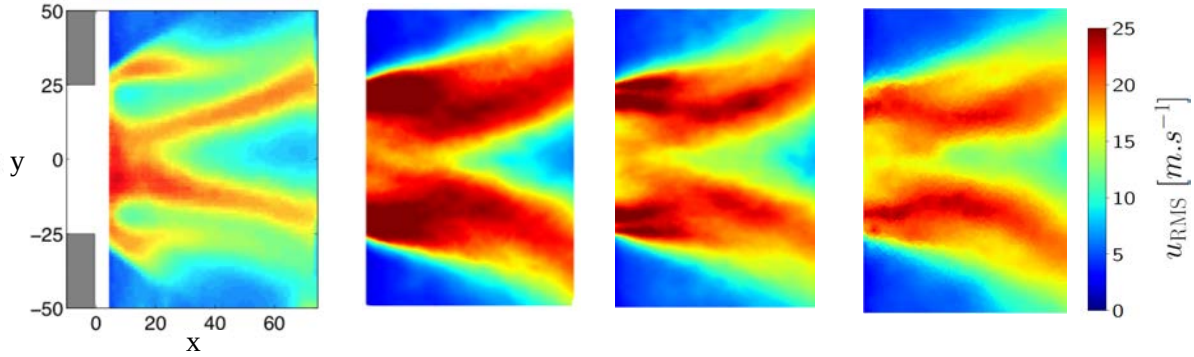

(b) RMS axial velocity

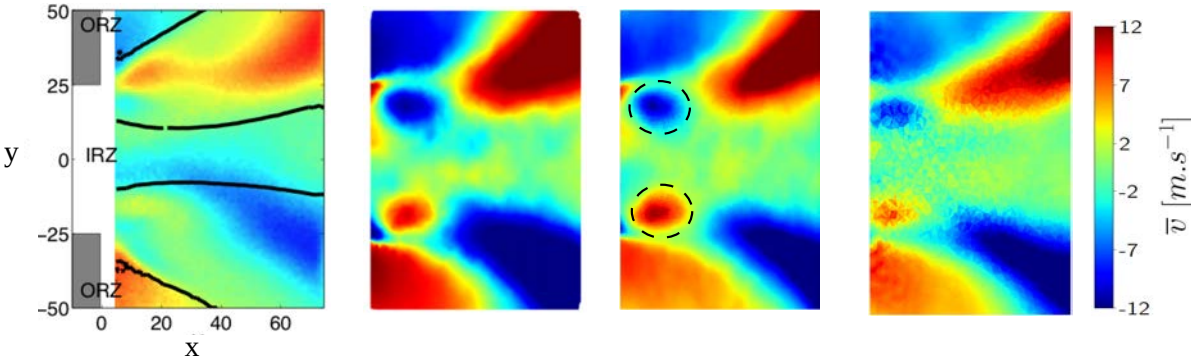

(c) Mean vertical velocity

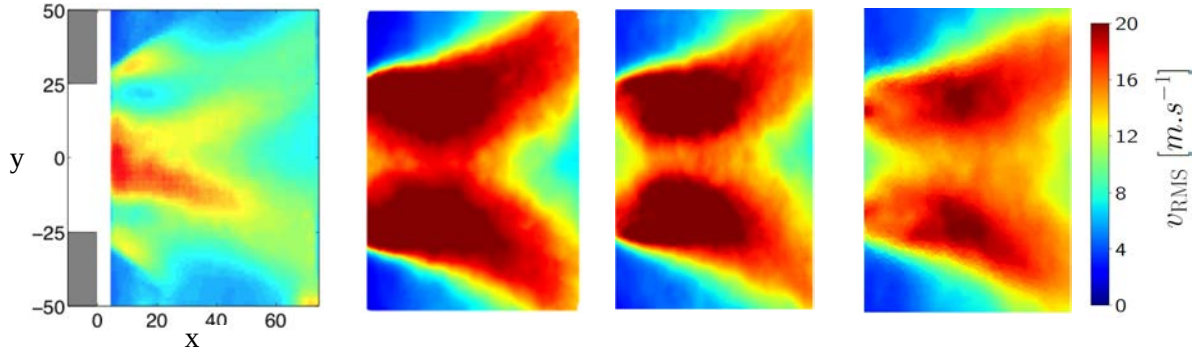

(d) RMS vertical velocity

Figure 7.8: Qualitative experimental validation: velocity fields in enclosed region from Figure 7.7a. The first column denotes the experimental results by Providakis (2013), and the second one the numerical results obtained with AVBP by Cheneau (2019).

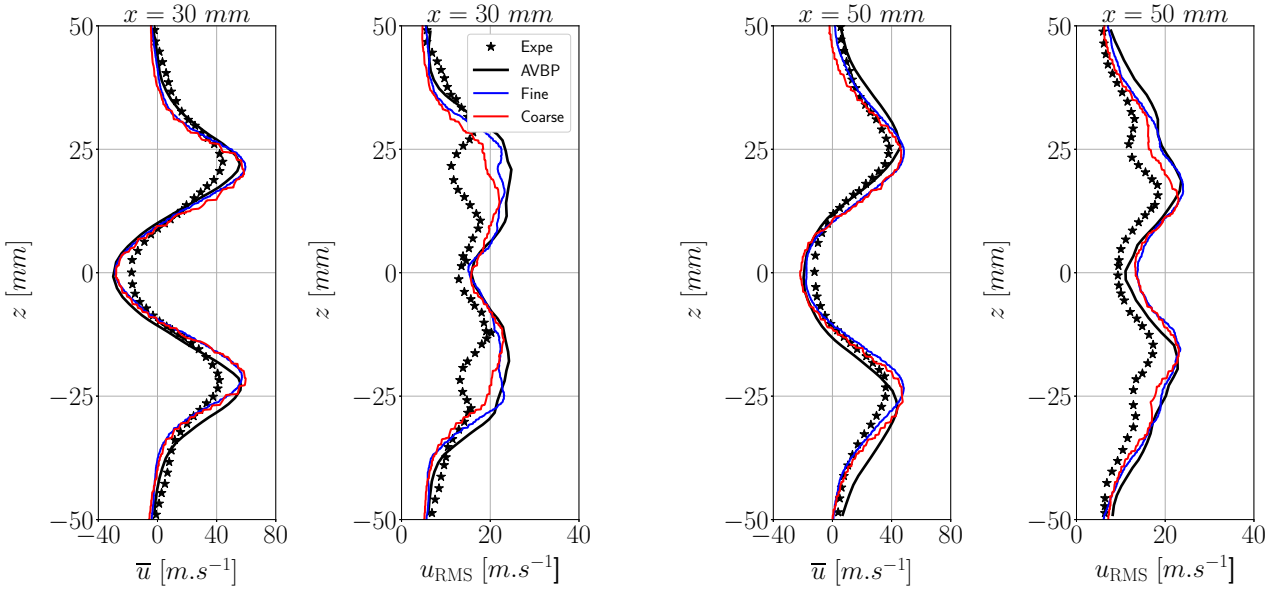

Figure 7.9: Mean and RMS axial velocity profiles along probes lines at x = 30, 50 mm.

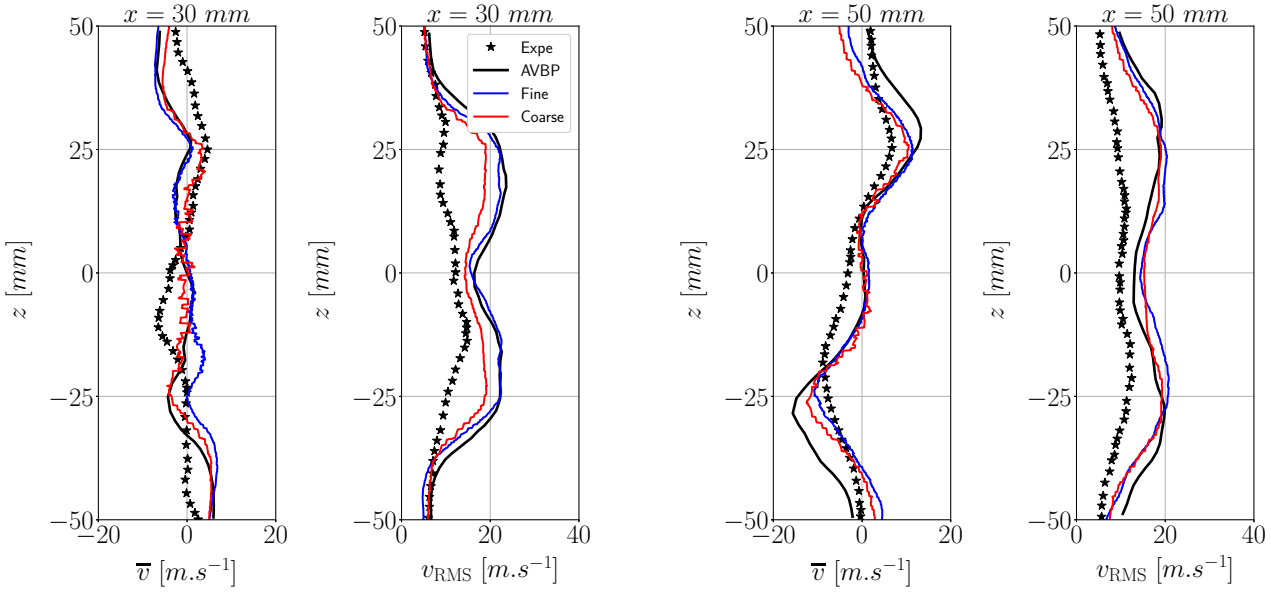

Figure 7.10: Mean and RMS vertical velocity profiles along probes lines at x = 30, 50 mm.

7.7 Application operating point

According to the results obtained for the validation point, the application point from Table 7.2 is simulated with the fine mesh shown in Figure 7.5. In this case, the application operating point by Renaud (2015) (see Table 7.2) has been run for a total physical time of 240 ms: 80 ms ($\sim 2\tau_{conv}$) for flow establishment, and then statistics have been accumulated for 160 ms ($\sim 4\tau_{conv}$). These values have been chosen to keep the same convergence time with respect to the convective characteristic time as in the validation point.

Figure 7.11 shows the mean axial velocity field $\overline{u}$ with the streamlines (black contours). The contours of null mean axial velocity $\overline{u} = 0$ are also shown (white lines). The IRZ and ORZ recirculation zones are clearly observed, as well as SWJ branches and the shear layers. As in the validation point (Figure 7.7), the flow field is typical of gaseous swirled jets for values of $S_w \approx 1$. A stagnation point in the tip of the IRZ, closer to the pilot injector, is also observed. The magnitudes of mean axial velocity are larger than in the application case since the injected mass flow rate is lower.

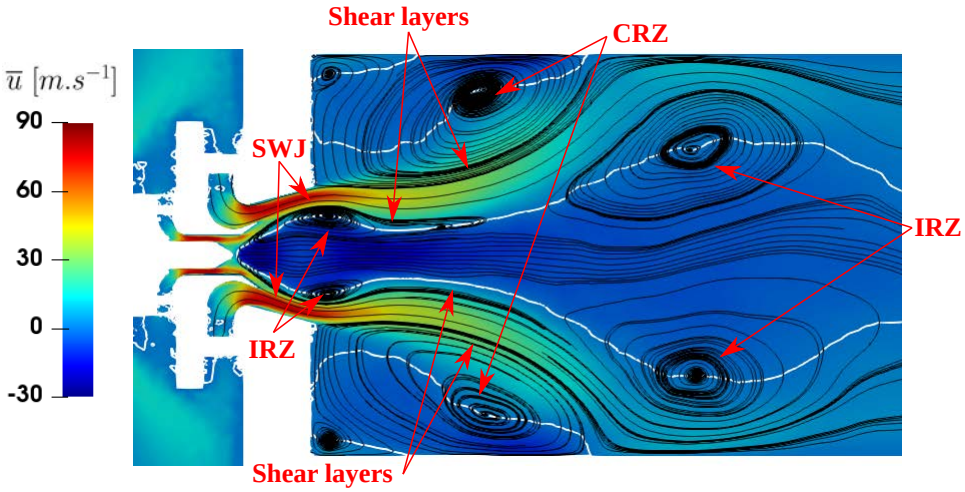

Figure 7.11: Mean axial velocity field with streamlines from case APP_FINE. The white line indicates the iso-contour of $\overline{u} = 0$.

The mean and RMS velocity fields in the axial, vertical and transversal directions are shown in Figure 7.12. The high values of mean vertical velocity $\overline{v}$ in the diffusor indicate the jet opening, and can influence the fuel introduced through the multipoint injector: as shown later in Chapter 9, such high velocities make the injected spray to open and approach the walls of the diffusor, while moving away from the central line $x = 0$. This creates a *hollow cone* of droplets if the pilot injector is not activated. Furthermore, the mean transversal velocity $\overline{w}$ has also a very strong component, which will give a rotational motion to the droplets in the azimuthal direction. The high maximum values of $\overline{w}$, which are of the order of $\overline{u}$, indicate a strong swirl of the jet, being in accord with the value for the swirl number $S_w \sim 1$ as stated by Renaud (2015).

In all cases, the RMS values are really high closer to the injector and decrease further downstream. In the axial velocity field, the highest values are located in the divergent section of the pilot nozzle, probably due to flow detachment in this region. For the vertical and transversal velocities, the highest RMS are found between the pilot injector tip and the stagnation point of the IRZ. This indicates high velocity fluctuations in this region, which can have a strong influence on the spray injected through the pilot nozzle. The fact that the magnitude of the RMS are of the same order as the mean values indicates a highly turbulent flow.

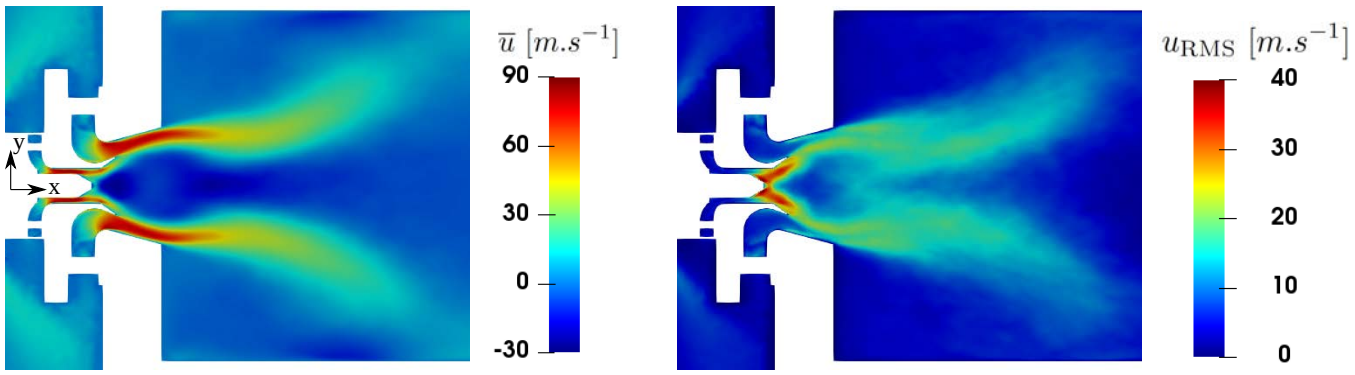

(a) Axial velocity u

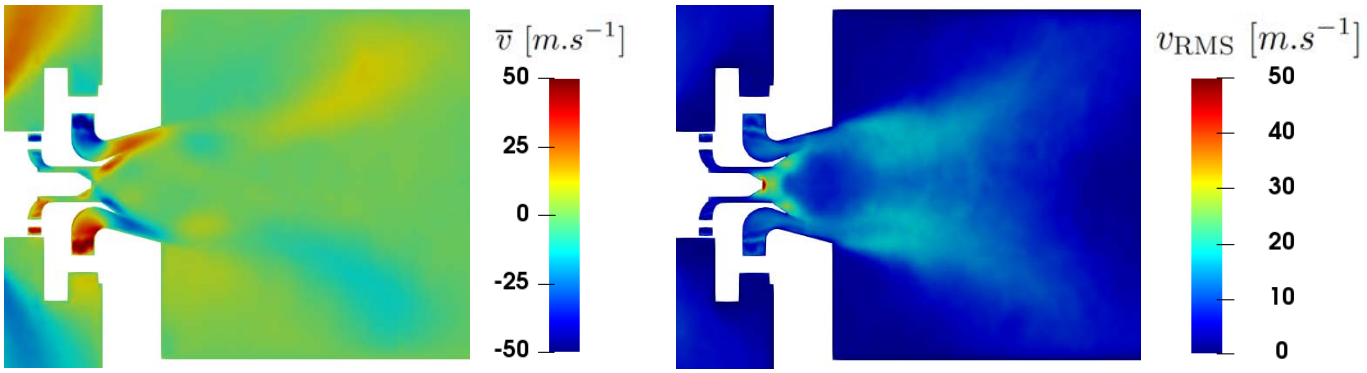

(b) Vertical velocity v

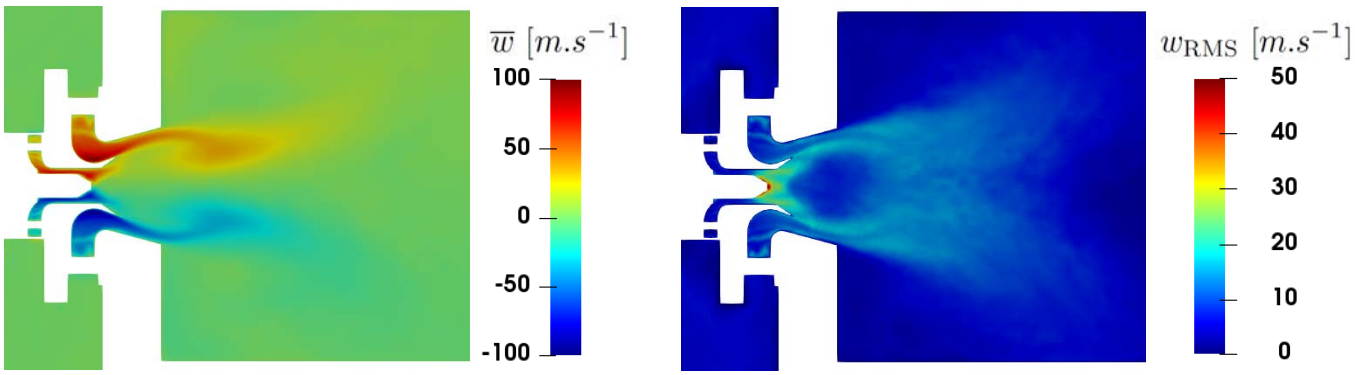

(c) Transversal velocity w

Figure 7.12: Mean and RMS velocity fields at central plane from case APP_FINE

7.8 Conclusion

This chapter has presented non-reactive LES gaseous simulations of the BIMER test bench. In first place, the experimental test rig at EM2C and the operating conditions chosen to perform simulations have been introduced. Two experimental points have been chosen: one studied by Providakis (2013) which presents data on the gaseous flow field, and another one tested by Renaud (2015) which does not show aerodynamic quantities, but studies the spray injection and dispersion. Firstly, simulations with YALES2 have been validated on the former operating condition. From this study, a fine mesh of 38 million elements has been chosen as the baseline mesh for simulating the second operating condition (application case). Results for this case show a good behaviour of the gaseous flow field for swirling jets with high swirl number, in accordance with the flow topologies and velocity fields from literature in similar cases. The simulations of the application case are then used as initial solutions to perform the resolved simulations from Chapter 8 and the dispersed phase computations from Chapter 9.

Chapter 8

Resolved atomization simulations of BIMER

8.1 Introduction

The multipoint burner BIMER was introduced in Chapter 7, where a study of the aerodynamic flow field for two operating conditions of interest was performed. The gaseous field was validated with the aerodynamic data from the operating point tested experimentally by Providakis (2013). Then, one single-phase simulation was performed for the experimental condition by Renaud (2015). The latter provides experimental data on the non-reactive spray state, and hence it is chosen for the studies presented hereafter.

In this chapter, resolved simulations of the atomization process through one injector of the BIMER take-off stage are performed. The numerical setup and liquid injection operating point are described in §8.2 and §8.3 respectively. Two different interface cell sizes are simulated for the same operating condition, hence a total of two simulations are performed. An analysis of the resolved simulations is performed in §8.4. Studied physical features include the evolution of the liquid jet, the jet breakup process, its vertical trajectories, gaseous disturbances due to liquid dense core and computation of resolved fluxes with the interior boundaries methodology. This section concludes then with a few words on the computational performances and cost of the simulations. Finally, the simulations are processed to provide the necessary data for building a Smart Lagrangian Injector (SLI). The dense core of the liquid jet, including its topology and estimated net total force, is studied. Then, the global spray in four sampling planes is characterized, while latter only two planes are chosen to be discretized and provide local sprays. These SLIs will be later used for spray computations of BIMER in Chapter 9.

8.2 Computational setup

The computational geometry for performing the resolved atomization simulations is the one displayed in Figure 7.3. The fine mesh from Figure 7.5b is used, its details provided in Table 7.3. The aerodynamic field described in §7.7 is used as initial condition for the resolved atomization simulations. The boundary conditions are also identical except for the liquid injection point, which for the aerodynamic simulations was specified as solid wall and for the resolved ones is changed to inlet.

The location of the liquid injection point in the take-off stage is shown in Figure 8.1. The injector consists of a nozzle with 8 mm length and a circular cross-section of diameter 0.3 mm. The direction of the incoming air u_g and the liquid injection u_l are detailed, as well as the crossflow direction x_c obtained from the resolved atomization simulations. A cut of the mesh in the injector is appreciated in the left figure: the cell size within the injector has been set to $35 \sim \mu$m, and the walls are refined to $15 \sim \mu$m. The right figure shows the dimensions of the gaseous inlet channel, which yield a hydraulic diameter of $D_h = 7.5$ mm.

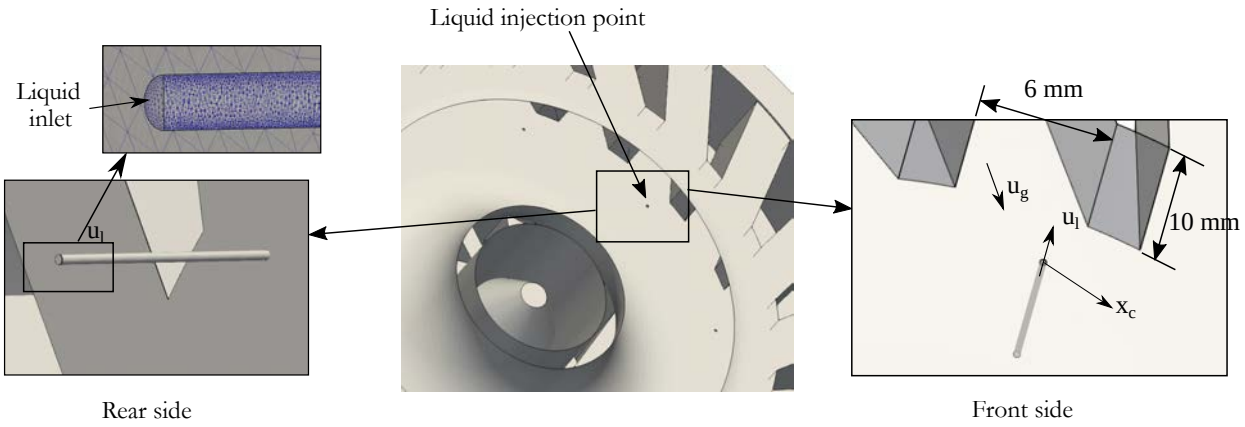

Figure 8.1: View of liquid injection point in BIMER. The central figure shows the multipoint injector previously displayed in Figure 7.4. The rectangular section shows zoomed-in views of the rear (*left*) and front (*right*) sides of the liquid injection nozzle. The front side shows the injection point, the crossflow direction x_c, and the gaseous inlet channel

Sampling planes in BIMER

The purpose of the BIMER resolved simulations is to characterize the spray for creating lagrangian injectors with the SLI methodology. Therefore, the spray must be sampled as it was done in the simulations from Chapter 5, whose sampling planes were shown in Figure 5.36. In that test case, the defined sampling planes were perpendicular to the crossflow axis x, since the jet deviates and atomizes producing a spray that moves in this direction. BIMER presents a more complex geometry representative of real injection systems where the absolute reference system is not aligned with the liquid fuel injection point chosen. Therefore, it is convenient to change the reference system to a local one which is aligned with the jet deviation direction (i.e. the local crossflow direction). This direction is denoted as x_c and is shown in Figure 8.1 right. It has been obtained by performing resolved simulations and checking visually the JICF direction. The local reference system is defined by the orthogonal coordinates $\mathbf{x}_c^T = \{x_c, y_c, z_c\}$ obtained through a transformation from the global coordinate system. This local system, shown in Figure 8.2, is centered at the liquid injection point. The figure also shows the location of the sampling planes, which are perpendicular to the x_c axis and are expressed in relation to the injection diameter d_{inj}. In all simulations performed, a sponge layer where liquid is artificially suppressed has been located at $x_c/d_{\text{inj}} = 12$ to reduce the cost of the computations.

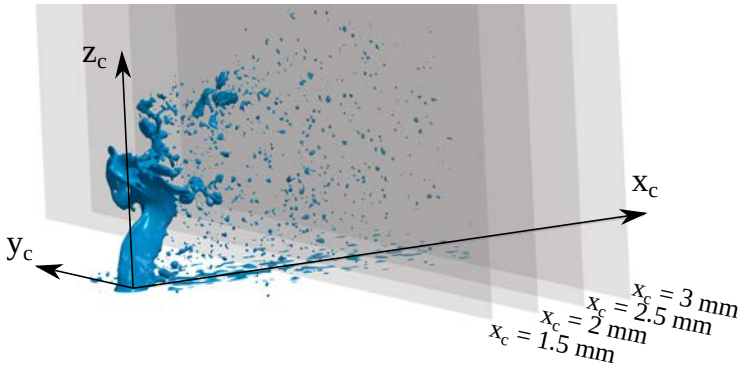

Figure 8.2: Instantaneous snapshot of liquid injection in BIMER shown the local coordinate system and the location of spray sampling planes

8.3 Operating condition

The ambient conditions and inlet gaseous flow rate for the operating point to study were shown in Table 7.2. They characterize the aerodynamic field of the overall burner. To determine now the operating point and classify it into the JICF breakup map, the liquid and gaseous parameters relevant to the single multipoint injector need to be stated.

Gaseous phase

The aerodynamic field inside BIMER for the operating points of interest was discussed in Chapter 7. From this study, a fine mesh consisting of 38 million elements was selected (see Table 7.3). The gaseous field for the application point, which is the chosen one to perform spray simulations, was studied in §7.7. This solution is taken as the initial condition for the resolved atomization simulations.

For characterizing liquid atomization, the relevant gas conditions are those found close to the liquid injection point. In the case of a simple JICF geometry like the one studied in Chapter 5, the gas and liquid flows directions are known, and the gaseous conditions impinging the jet and relevant for liquid breakup are easily determined. For a complex geometry, swirled injector such as BIMER, the crossflow direction is not known a prior and needs to be determined. For such purpose, resolved simulations are a useful tool since they provide all the information regarding the jet. For determining the crossflow reference system $\mathbf{x}_c$, displayed in Figure 8.2, a first simulation was run and the direction in which droplets were convected was taken as the crossflow direction x_c.

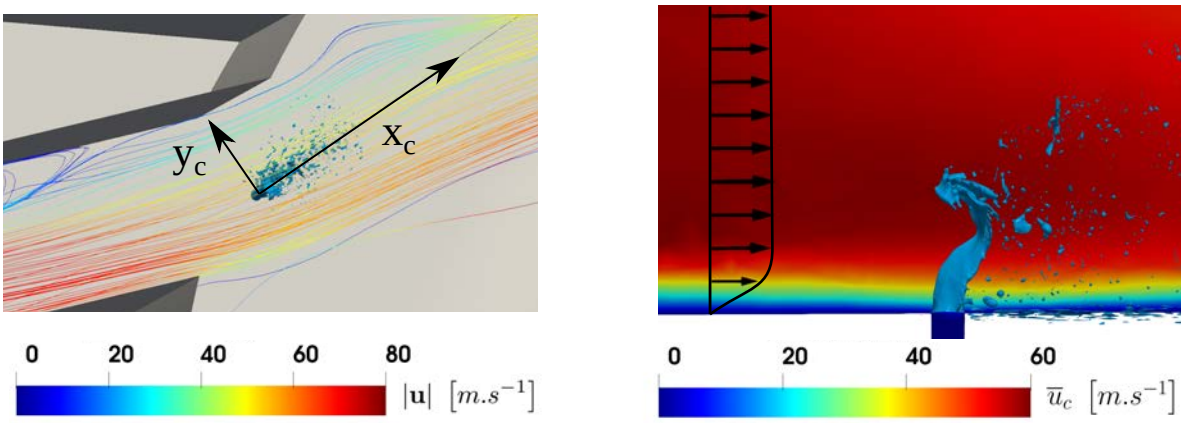

Figure 8.3: Gaseous state at the vicinity of the liquid injection location. *Left*: gas streamlines through the inlet multipoint vane. *Right*: Instaneous BIMER view with mean axial velocity field in plane $y_c = 0$. The mean field corresponds to the gaseous solution without liquid used as an inlet condition, the jet has been added for comparison

Figure 8.3 left shows the gas mean streamlines through the inlet vane of the multipoint stage that impinge the crossflow. An instantaneous view of the jet is shown for visualization, although the streamlines correspond to the gaseous solution without the jet. As observed, the jet is fully immersed within the gas coming through the closest vane, and is not affected by the gas coming from the neighbouring vanes. The streamlines also show a high variation in the velocity magnitude along the vane width, with the highest velocity streamlines being the ones affecting the jet. The jet crossflow direction x_c is also indicated in the view. Figure 8.3 right shows the mean axial velocity field in the middle crossflow plane $y_c = 0$. The velocity coordinates have been transformed from the absolute coordinate system to the crossflow one, hence the mean axial velocity displayed $\overline{u}_c$ is the one in the crossflow direction. The arrows show schematically the mean velocity profile along the crossflow vertical direction z_c at a location $x_c/d_{\text{inj}} = -0.5$, i.e. right upstream the injector (it has been shifted in the figure to allow for visual comparison with the jet). The values for this profile are plotted in Figure 8.4, where the Turbulent Kinetic Energy (TKE) profile along the same line calculated with Eq. (B.5) is also represented. A bulk gaseous velocity $u_g = 56$ m.s^{-1} is obtained as the mean of the gaseous velocity profile. The TKE profile shows high values in general along all the vertical coordinate, which reflects a high turbulent state of the flow created by the swirled injector.

Liquid phase

In the operating point studied, the total liquid mass flow rate injected is $\dot{m}_{l,\text{total}} = 1.64$ g s^{-1}. The staging parameter, defined in Eq. (7.1), is $\alpha = 15$ %, meaning that amount of liquid goes through the pilot stage and 85 % of fuel goes through the take-off. Therefore, $\dot{m}_{l,\text{pilot}} = 0.25$ g s^{-1} and $\dot{m}_{l,\text{takeoff}} = 1.39$ g s^{-1}. This quantity of fuel is injected through 10 injection holes that conform the take-off stage; assuming that fuel repartition is done equally through all the channels, each injector introduces 0.139 g s^{-1} of dodecane fuel,

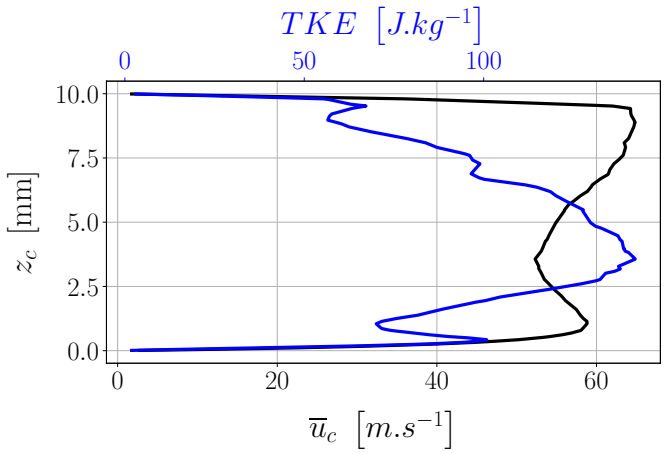

Figure 8.4: Profiles of mean axial velocity $\overline{u}_c$ and TKE along the vertical line right upstream the liquid injector

which is equivalent to a flow rate of $Q_l = 185.3$ mm^3 s^{-1} given the dodecane density from Table 7.1. From this flow rate, the bulk liquid velocity u_l can be estimated with the injection area:

$$u_l = \frac{Q_l}{\pi d_{\text{inj}}^2/4} = 2.6 \text{ m.s}^{-1} \tag{8.1}$$

The velocity profile imposed at the liquid inlet shown in Figure 8.1 is a Poiseuille profile with mean velocity u_l. With the estimate values for bulk liquid and gaseous velocities, the liquid properties given in Table 7.1 and the gaseous properties from Table 7.2, the momentum flux ratio q and the Weber number based on the gaseous phase We_g can now be calculated:

$$q = \frac{\rho_l u_l^2}{\rho_g u_g^2} \approx 2 \quad ; \quad We_g = \frac{\rho_g d_{\text{inj}} u_g^2}{\sigma} \approx 30 \tag{8.2}$$

Figure 8.5 shows the BIMER JICF operating point classified in the breakup diagram of Wu et al. (1997), which is located in the multimode breakup regime. The governing parameters characterizing the BIMER operating point are summarized in Table 8.1. The dimensionless numbers from Eqs. (5.1) are also calculated. Two simulations have been performed with three different element resolutions at the liquid-gas interface $\Delta x_{\min} = 15, 10$ μm, the nomenclature for each case is given in Table 8.2.

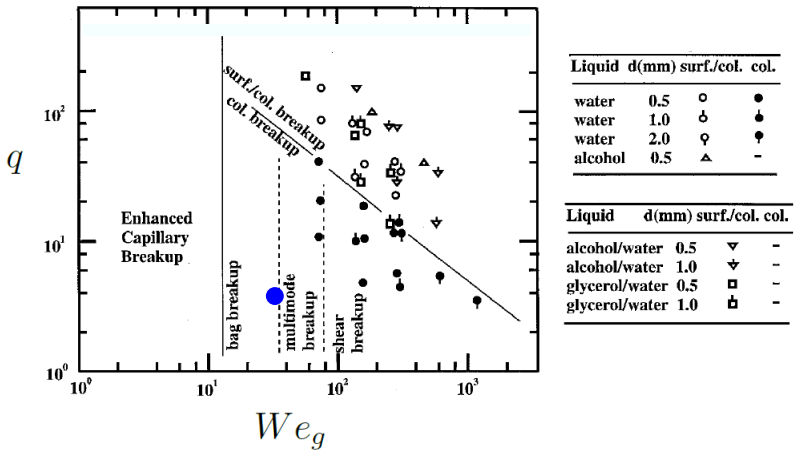

Figure 8.5: Location of simulated operating condition in the breakup map by Wu et al. (1997)

Table 8.1: BIMER operating point to perform resolved atomization simulations

Parameter	**Symbol**	**Units**	**Value**
Nozzle diameter	d_{inj}	mm	0.3
Gas bulk velocity	u_g	m s^{-1}	56
Gas flow rate	Q_g	m^3 s^{-1}	$2.2833 \cdot 10^{-3}$
Liquid bulk velocity	u_l	m s^{-1}	2.6
Liquid flow rate	Q_l	mm^3 s^{-1}	185.3
Ambient pressure	p_{amb}	bar	1
Gas temperature	T_g	K	433
Liquid temperature	T_l	K	293
Gas density	ρ_g	kg m^{-3}	0.82
Liquid density	ρ_l	kg m^{-3}	750
Gas viscosity	μ_g	kg m^{-1} s^{-1}	$2.39 \cdot 10^{-5}$
Liquid viscosity	μ_l	kg m^{-1} s^{-1}	$1.36 \cdot 10^{-3}$
Surface tension	σ	kg s^{-2}	0.025
Gas Reynolds number	Re_g	-	$20 \cdot 10^3$
Liquid Reynolds number	Re_l	-	430
Momentum ratio	q	-	2
Gas Weber number	We_g	-	30
Liquid Weber number	We_l	-	60
Relative Weber number	We_{rel}	-	52
Aerodynamic Weber number	We_{aero}	-	0.067
Ohnesorge number	Oh	-	0.018
Density ratio	r	-	915

Table 8.2: Nomenclature for resolved atomization simulations

Δx_{min} [μm]	Denomination
10	BIMER_DX10
15	BIMER_DX15

8.4 Analysis of BIMER simulations

8.4.1 Jet evolution

The jet evolution at the early instants of the injection process is shown in Figure 8.6. Time is expressed dimensionless as $t^* = t/\tau_{\text{in}}$, with $\tau_{\text{in}} = d_{\text{inj}}/u_l = 115.38$ μs.

Images show the features of a liquid JICF configuration: the jet leaves the injection nozzle and collides with the crossflow, which has the effect of deforming the liquid column and deviating the jet towards the crossflow direction (represented in Figure 8.6 by the black solid line). However, the jet topology is very different from a classical JICF configuration such as the one studied in Chapter 5: both surface and column breakup are present, but in BIMER column breakup creates mainly thin liquid sheets that are quickly disintegrated into small droplets. The jet does not penetrate far and the deviation of the jet column towards the crossflow direction is not highly significant, since breakup occurs close to the injection location. The low penetration is due to the low value of q for this operating point, which is the parameter governing the jet's trajectory. The quick disintegration into small droplets and the instabilities shown along the liquid columns are attributed to the highly turbulent state of the flow, as shown by the TKE profile in Figure 8.4. The interface resolution has also an effect on the jet topology: the coarse case (DX15) penetrates further than the fine one (DX10) and undergoes more deviation due to the action of the crossflow.

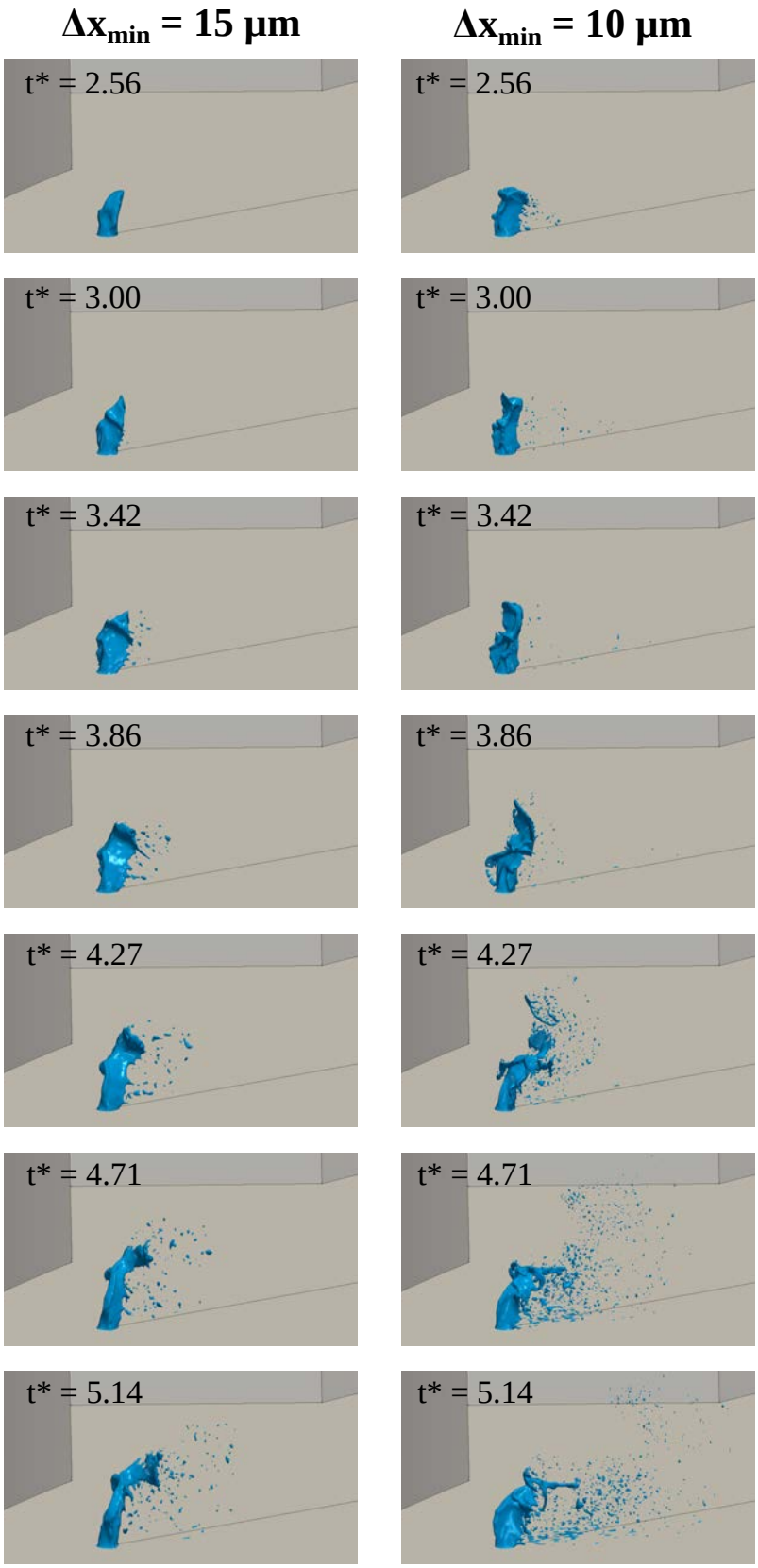

Figure 8.6: Establishment of BIMER resolved atomization simulations at several time instants

Liquid establishment

Establishment of the liquid jet in the BIMER configuration is monitored by quantifying the evolution of the number of mesh elements and the liquid volume inside the domain calculated from Eq. (5.4). Time has been non-dimensionalized with the timescale $\tau_{\mathrm{dr}_{x_c/=3}}$ as given in Table 8.3:

$$t' = t/\tau_{\mathrm{dr}_{x_c/=3}} \tag{8.3}$$

Table 8.3: Characteristic droplet arrival times to sampling planes $\tau_{\mathrm{dr}_{x_c}}$ [μs] in BIMER simulations

Case	$x_c = 1.5$ mm	$x_c = 2$ mm	$x_c = 2.5$ mm	$x_c = 3$ mm
BIMER_DX10	331	354	380	398
BIMER_DX15	511	562	569	582

Results are displayed in Figure 8.7. The graphs show that both simulations are converged, as curves for volume and number of elements stabilize. Volume increase linearly at the early instants of injection due to the constant flow rate injected. At a certain point, the slope of V_l starts to decrease due to droplets being removed from the simulation when reaching the sponge layer. Liquid volume estabilizes at values between $V_l = 0.75$ and 0.8 mm^3. The evolution of the number of elements in the simulation estabilizes quickly for $DX15$ at a value around $60 \cdot 10^6$ elements. Case DX10 presents maximum values around $100 \cdot 10^6$ elements, and shows large magnitude oscillations due to the clusters of droplets resulting from column breakup and reaching the sponge layer at the same time instants, causing large decreases in the number of elements and small ones in the liquid volume evolution. The reduction in the number of elements are specially notorious for case DX10, which shows an abrupt decrease at the end of the simulation time from $125 \cdot 10^6$ to $90 \cdot 10^6$ elements. Establishment is clearly achieved for simulation DX15, which shows small oscillations around constant V_l and N_{elements} values, while case DX10 is on the verge of convergence and might still need some more time to achieve full establishment. The time differences among peaks in the N_{elements} curve might be associated to the frequencies of column breakup sheets/ligament shedding observed in Figure 8.8. Further assessing this hypothesis would need the simulations to run for longer, since these frequencies associated to column breakup are low (which are low when compared to the frequencies of droplets ejected from surface breakup) and larger simulation times would be needed. This has not been done in this work due to constraints in computational resources and since the actual purpose of these simulations is the obtention of data for creating converged SLIs, which has been achieved with the physical times simulated (see §8.5.3)

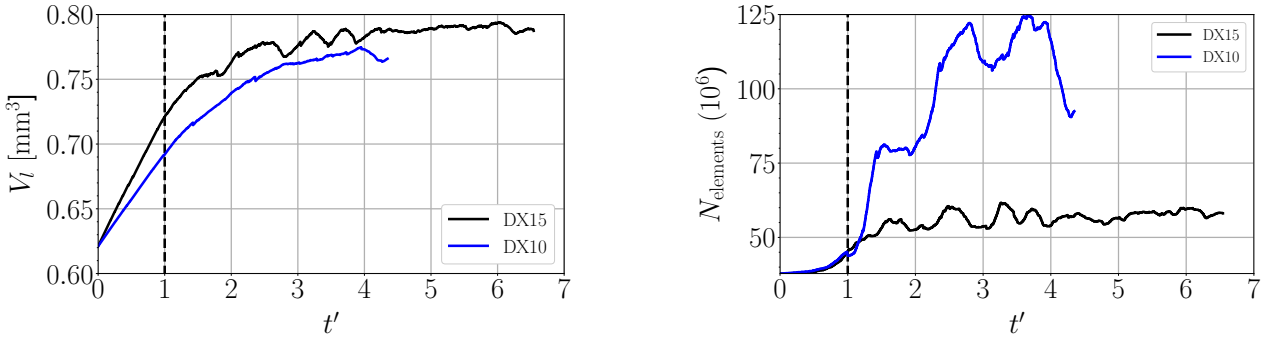

Figure 8.7: Evolution of number of mesh elements (*left*) and number of mesh elements (*right*) with time in BIMER resolved simulations. The dashed, black vertical line corresponds to $t' = 1$, time instant when the first droplet reaches the sampling plane $x_c/d_{\mathrm{inj}} = 10$

8.4.2 Breakup topology

Classification of the BIMER operating point considered in the breakup map of Figure 8.5 estimates the regime to be comprised in the column breakup region, within the multimode breakup regime but very close to bag breakup. This regime is characterized by a mixture of breakup properties from both bag breakup, like enough spacing among column instabilities so that both bags and ligaments can be formed and lead to

breakup, and shear breakup, such as surface stripping (Sallam et al. 2004). As in any traditional JICF, these are also expressed in terms of column and surface breakup features. Figure 8.8 shows these two phenomena observed in BIMER. In the first snapshot of the column breakup series, the red circle denotes the onset of an instability which propagates along the jet vertical and lateral directions. The vertical-propagating instability evolves into a thin sheet (green highlight) that eventually breaks into large liquid ligaments during primary atomization: this is the column breakup phenomenon. As in a classical JICF, these ligaments will propagate further downstream and continue to break. This sheet is followed by a column flattening in the lateral directions that is not typical from a classical JICF configuration (black highlight) and which modifies the ligaments produced later through column breakup. After this flattening, the process repeats again from the beginning. The lateral-propagating instabilities evolve in the surface breakup phenomenon, as illustrated in the bottom snapshots of Figure 8.5. As in the surface breakup of the canonical JICF depicted in Figure 5.16, two different features are highlighted: the generation of very small droplets (green highlight), whose size is of the order of the mesh resolution and will eventually disappear producing mass losses in the simulations, and the generation of small ligaments (red highlight) which break faster into smaller droplets that are later transported. Both column and surface breakup phenomena have been widely observed in traditional JICF configurations and are also captured in BIMER. What has been unexpected, though, is the onset of both phenomena through a central instability that evolves along the column vertical and sides direction, as well as the column flattening in the lateral direction. Both phenomena have been observed in both resolutions simulated and might be associated to the gaseous swirl. Nevertheless, no analysis on the breakup phenomena in liquid JICF with swirl (either in the gas or liquid phases) have been reported in literature to the knowledge of the authors.

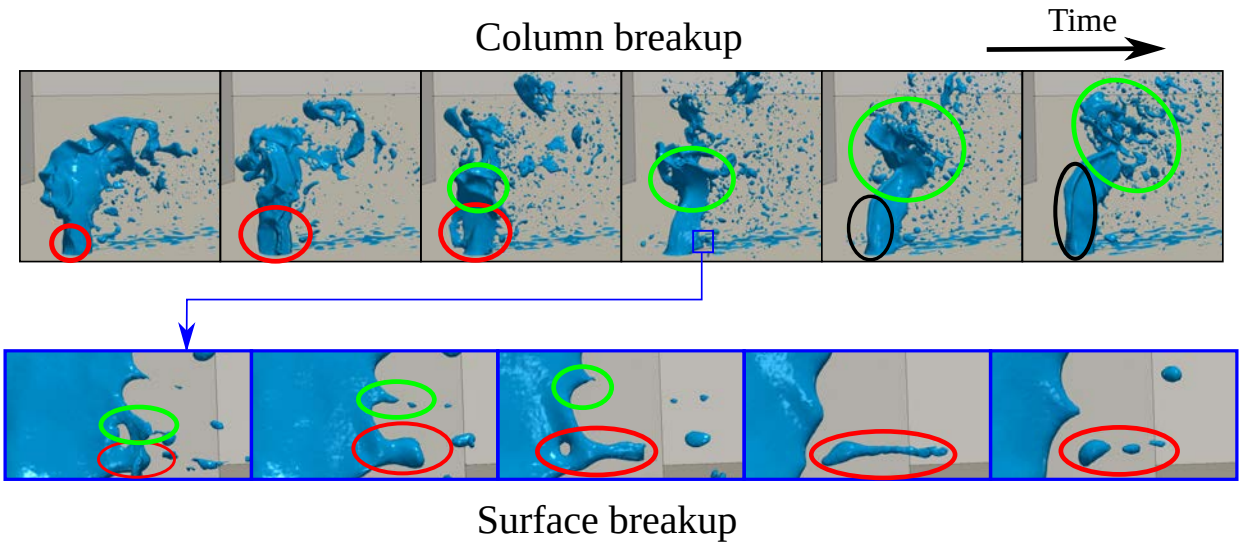

Figure 8.8: Breakup in BIMER, case DX10.

8.4.3 Jet trajectories

Vertical trajectories for quantifying the penetration of BIMER can be obtained by applying the methodologies described in Appendix C.1. The maximum gradient method of the mean levelset function is used. The trajectories obtained are shown in Figure 8.9. There are no experimental data to compare the BIMER resolved simulations: yet, the trajectory given by Eq. (5.5) with $q = 2$, from the study by (Becker & Hassa 2002), is used for comparison. This expression was chosen since it was the only one found in literature (see Table 1.1 for a compilation of several correlations) valid at low q values. The actual comparison with experiments show a good match among the correlation and the experiments closer to injector: numerical trajectories are within the bounds and show a similar deviation trend to the experiments for $x_c/d_{\text{inj}} < 3$ in case DX15 and $x_c/d_{\text{inj}} < 2$ in case DX15, where curves also display a smooth evolution. This confirms again the ability of the ACLS methodology to capture JICF physical features. After the indicated values, however, the numerical trajectories underestimate the experimental correlation and show a peaky behaviour: the jet has undergone atomization and is now in dispersed-phase. Case DX15 shows a smooth curve until

further downstream, while DX10 shows a peakier behaviour which is due to a faster disintegration of the jet (it is later demonstrated in §8.5.1that the obtained dense core lengths are smaller for DX10 than for DX15). The presence of droplets in the dispersed phase region is highly intermitent, which leads to low values of the mean levelset function in this region and to the axial limits in the trajectories found in the figures: no more gradient points are found at x_c/d_{inj} for DX15 and at $x_c/d_{\text{inj}} > 4$ for DX10.

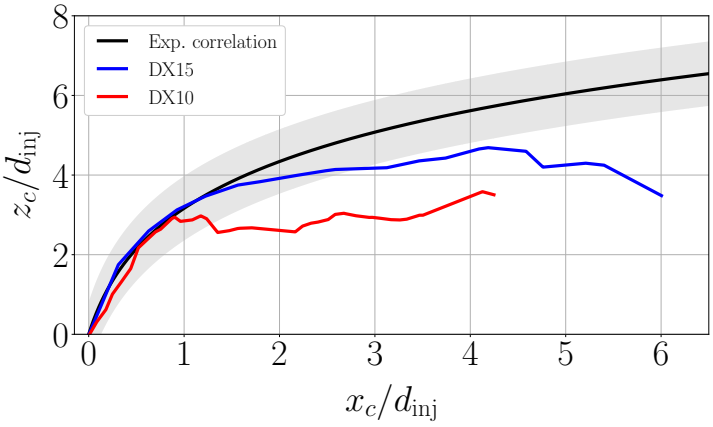

Figure 8.9: BIMER trajectories. The experimental correlation from Eq. (5.5) (Becker & Hassa 2002) is plotted for comparison

8.4.4 Gaseous perturbations due to liquid core

The disturbance effect of the BIMER dense core towards the gaseous phase is analyzed in this section. Figure 8.10 illustrates this perturbation phenomenon. The left picture shows an instantaneous view of the jet perturbation effect in the plane $y_c = 0$, where the axial velocity fluctuation field u_c' is plotted. Large fluctuations are produced downstream the injection point due to the liquid jet. Figure 8.10 right displays 3D streamlines around the jet. Characteristical turbulent structures observed in liquid JICFs, such as horseshoe vortices and recirculation zone behind the liquid column, are also found in BIMER. Both of these features were observed both experimentally and in the JICF simulations of Chapter 5. When compared to those, the recirculation zone in BIMER is located closer to the wall and with a smaller extension. The perturbation effect on the gaseous phase is further analyzed by looking at the planes shown in Figure 8.11.

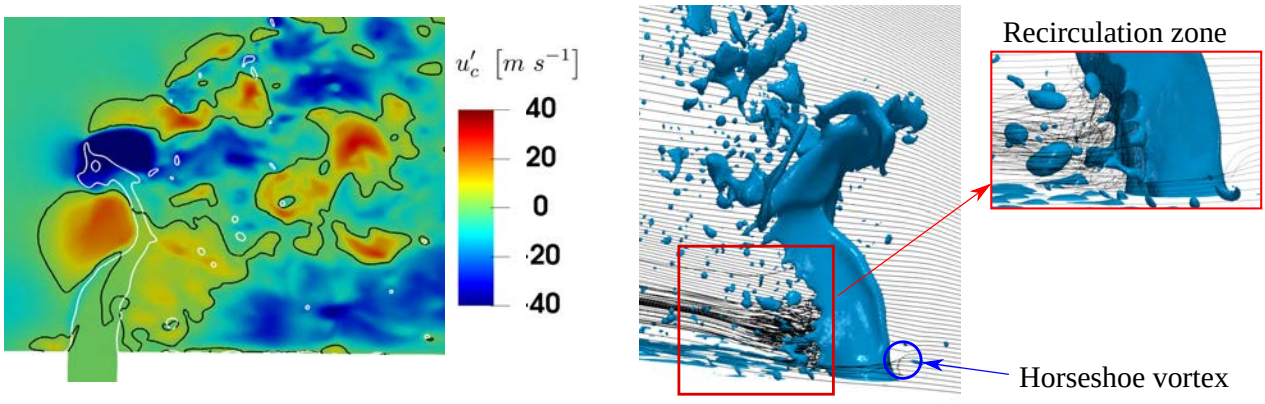

Figure 8.10: Interaction between liquid dense core and gaseous phase in BIMER. *Left*: Instantaneous u_c' field from case DX10. The black contours indicate the lines with zero instantaneous fluctuation $u_c' = 0$, while the white contours denote the location of the interface at the plane. *right* Streamlines in BIMER, case DX10

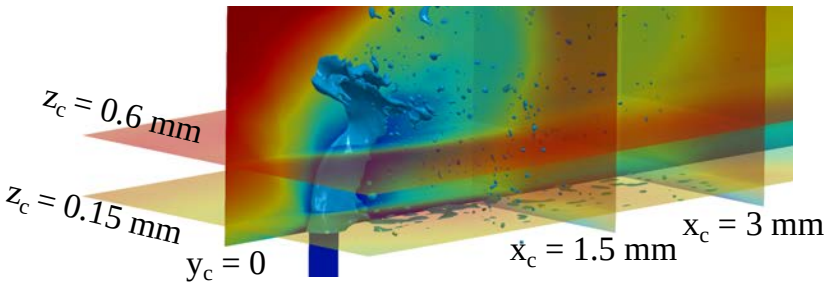

Figure 8.11: Jet from BIMER case DX10 showing planes to study the gaseous phase

The mean axial velocity fields at plane $y_c = 0$ are shown in Figure 8.12. The mean liquid region is denoted by the grey area. This region undergoes a more pronounced deviation in the fine case than in the coarse one, leading to an earlier breakup point (as demonstrated by the shorter dense core lengths from Table 8.6). Regarding the gaseous field, the perturbation effect of the dense core is clearly noticed by the decelerations created by the crossflow. A region with negative velocity is found attached to the wall right upstream the dense core for both resolutions, corresponding to the horseshoe vortex as also visualized in Figure 8.10. Recirculation regions are also observed in the leeward side, being however different in each case: DX10 displays a small vertical region with low thickness in the axial direction, probably not converged with the physical time simulated, while DX15 displays a larger recirculation bubble more inclined along the liquid column due to the jet's deviation and with larger width than the first case. In both cases, however, the recirculation bubbles present small thicknesses in relation to the injection diameter with respect to the recirculation bubbles obtained for the non-swirled in Figure 5.31. This might be attributed to a lower momentum flux ratio in the BIMER case with respect to the previous JICF: $q = 2$ for the former with respect to $q = 6$ for the latter. A lower q reduces the jet penetration, with might lower down the location of the recirculation region and reduce its strength similar to flow behind bluff bodies (Asami et al. 2021). The recirculation zone is also affected by the geometry of the body which, in the case of liquid jets in crossflow, is complex, unsteady and differs among both jets simulated (see the different instantaneous topologies in Figure 5.28 right and 8.10 right). Previous studies about such parametrical influences on JICF recirculation zones have not been performed to the knowledge of the author, and are not ellucidated in this thesis.

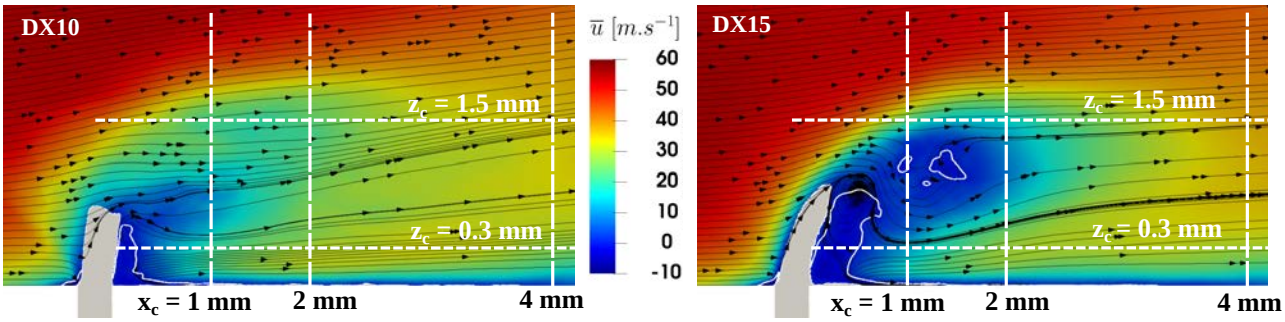

Figure 8.12: Mean axial velocity at plane $y = 0$ mm. Black lines with arrows are in-plane mean streamlines; the white solid line indicates the contour $\overline{u} = 0$ which delimites the recirculation bubble. The grey area indicates the mean liquid region, identifed as $\overline{\psi} > 0.5$

The mean axial velocity profiles along the lines $z_c = 0.3, 1.5$ mm are plotted in Figure 8.13. The dashed black line shows the mean profile for the single-phase simulation without liquid (i.e. undisturbed gaseous phase due to the present of the jet dense core). Near the wall ($z_c = 0.3$ mm), the perturbance effect is strong and the difference with respect to the single-phase case is high. A region with negative axial velocity is observed at the near field region, which corresponds to the recirculation bubble seen in Figure 8.12. The difference with respect to the single-phase decreases further downstream but the gaseous field of the two-phase simulations does not reach the same tendency again, showing low-velocity oscillations with x_c that are maintained further downstream. Further from the wall ($z_c = 1.5$ mm), the disturbance is also close to the jet but the velocity field relaxes quickly and reaches the same tendency as the single-phase simulation further

downstream, at $x_c \sim 11$ mm. For all cases, both resolved atomization simulations recover the same trends in the perturbed fields with quantitative differences observed due to the different jets resolved: the amplitude of the variations with x_c is in general stronger for case DX10. Figure 8.14 plots then the velocity fields along the vertical coordinate z_c represented in Figure 8.12, showing that differences with respect to a pure gaseous simulation are higher in the near-wall region but get closer further upstream, with again differences among resolutions. These differences get lower further dowstream at $x_c = 40$ mm, but still being of the order of 20 m s^{-1} which could greatly affect affect the secondary atomization of the droplets in the dispersed-phase simulations if the gaseous perturbations are not properly modelled. It is worth to note that the sampling planes range from $x_c = 1.5$ to 3 mm (see Figure 8.2), therefore droplets sampled are located within this highly perturbed region. Lagrangian particles injected in the dispersed-phase simulations should ideally *see* a highly perturbed gaseous field right after injection.

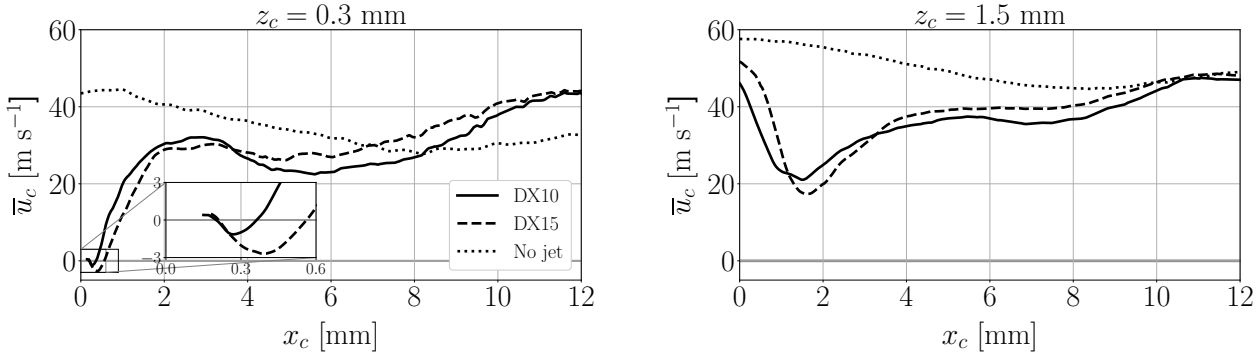

Figure 8.13: Mean axial velocity evolution along axial coordinate at locations $z_c = 0.3, 1.5$ mm at plane $y_c = 0$ (lines of Figure 8.12)

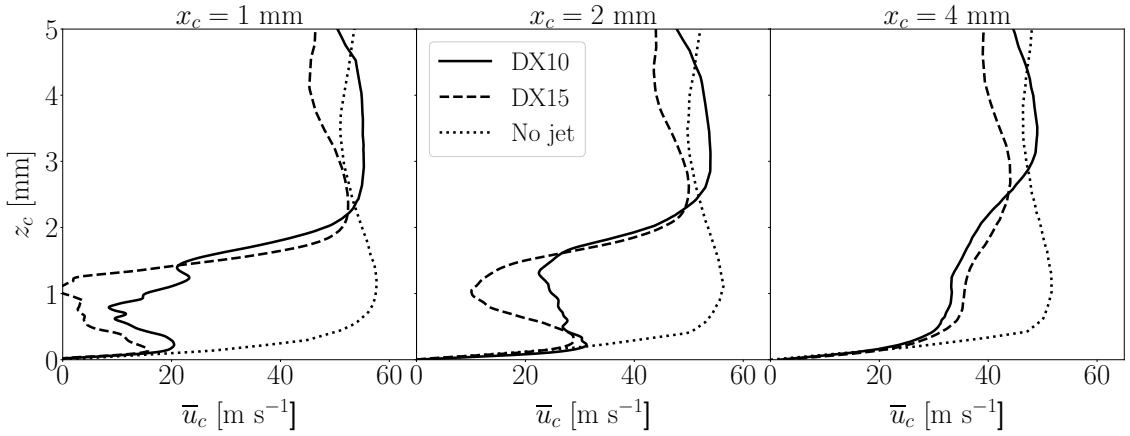

Figure 8.14: Mean axial velocity evolution along vertical coordinate at $x_c = 1, 2, 4$ mm locations of plane $y = 0$ (lines of Figure 8.12)

Planes perpendicular to crossflow $x_c = 1.5, 3$ mm are shown in Figure 8.15. The disturbance effect is clearly seen by the low velocity region at both sides of plane $y_c = 0$. This region is symmetric at plane $x_c = 1.5$ mm for case DX15 but not for the other figures depicted, which show an inclination of the deceleration region towards direction $y_c < 0$. Asymmetry is attributed to the swirl of the jet. This behaviour has been observed in other swirled JICF (Denev et al. 2009, Terzis et al. 2011), while tradicitional configurations without swirl always present symmetric gaseous structures (see for instance Figure 5.33). Another particularity in this configuration is related to the vortical structures, which are not captured in all cases and, when present, are asymmetric with respect to plane $y_c = 0$. Case DX10 at $x_c = 1.5$ mm shows two different vortices that constitute the counter-rotating vortex pair (CVP) as also observed in Figure 5.33. Further downstream at $x_c = 3$ mm the vortex located at $y_c > 0$ has reached the wall and dissipated, while the one at $y_c < 0$ has moved further away from the centerline, resulting in just one vortex. For case DX15, at $z_c = 1.5$ mm only one vertex at $y_c < 0$ is captured while further downstream no vortices are observed. Similar asymmetric vortical

structures and their evolution over the axial coordinate x_c have been observed in previous studies of liquids jet in crossflow where swirl is imposed in the liquid nozzle (Denev et al. 2009, Terzis et al. 2011), which have shown larger asymmetries when the swirl number is increased at low values below 1 (the swirl number in the BIMER configuration is $S_w \sim 1$). Unfortunately, vortical structures in such planes on highly-swirled JICF or configurations where swirl is imposed to the gaseous phase are not available to the knowledge of the author, so a comparison in similar cases cannot be performed.

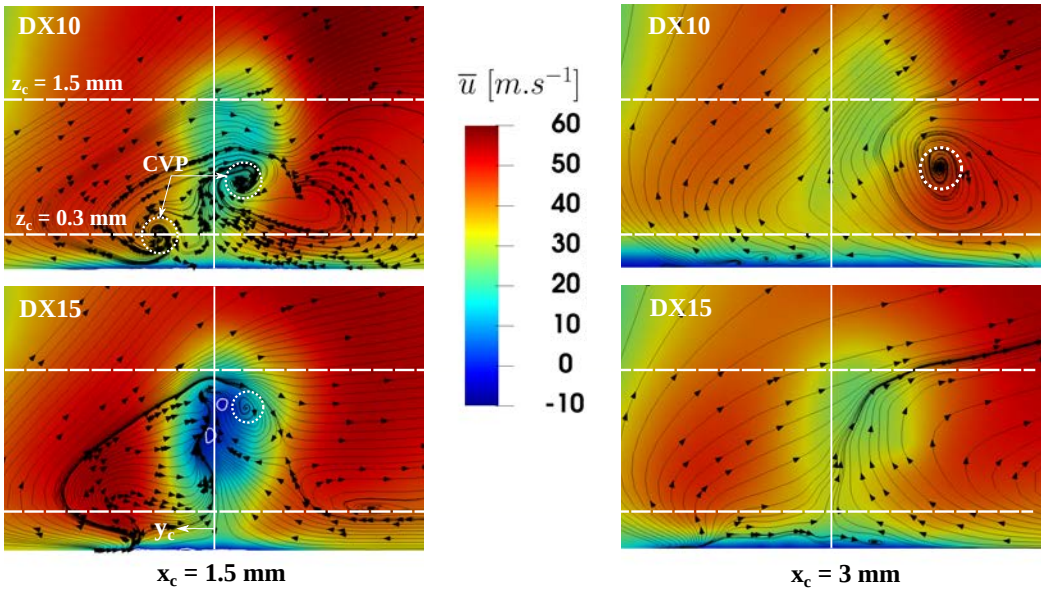

Figure 8.15: Mean axial velocity at planes $x_c = 1.5, 3$ mm, showing in-plane mean streamlines. The vertical, white line corresponds to plane $y_c = 0$

Figure 8.16 shows the quantitative evolution of mean axial velocity along the lines plotted in Figure 8.15. The presence of the liquid jet creates a deceleration region in the gaseous phase at the central region and acceleration of the gas further away. The disturbance is stronger closer to the jet nozzle ($x_c = 1.5$ mm) and weaker further away ($x_c = 3$ mm), where the lines with and without liquid get closer. Asymmetry is also observed as the lowest velocities: while in a traditional jet the largest deceleration is located at the centerline (see for instance Figure 5.34), in BIMER this peak is observed close to it but shifted to the region $y_c < 0$, and moves further away when the axial distance increases, similarly to cases studied in swirled liquids JICF (Denev et al. 2009). Furthermore, as y_c decreases below 0 it is seen that the velocities seem to reach a stable value which is closer to the single-phase simulation for case DX10, while for $y_c > 0$ the gaseous velocities continue decreasing as y_c increases. This is due to the location of the injection point within the multi-staged, the gaseous flow velocity decreases with axial direction due to the presence of the channels walls (Figure 8.3 left).

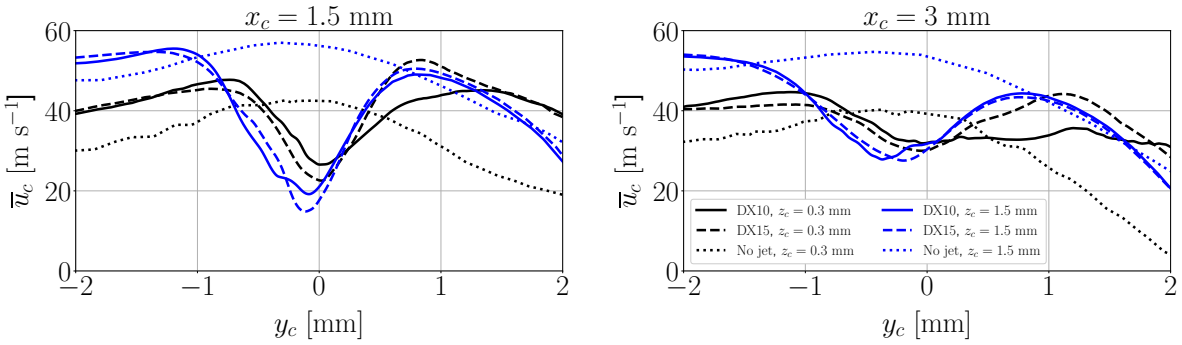

Figure 8.16: Mean axial velocity evolution along lateral coordinate at z_c lines of Figure 8.15. Dotted circles englobe gaseous vortical structures

Finally, the gaseous fields at planes perpendicular to the vertical direction z_c are displayed in Figure 8.17. The recirculation bubble is observed close to the wall $z_c = 0.15$ mm for both cases, and further away ($z = 0.6$ mm) for case DX15 only, while case DX10 at $z = 0.6$ mm shows a high deceleration of the flow which does not reach recirculation. The deceleration fields are symmetric with respect to $y_c = 0$ closer to the wall but asymmetric further away from it: near-wall the freestream velocity is smaller in absolute value since it is within the boundary layer, hence the swirl effect is weakened and the gaseous field is less deviated, resulting in symmetry. Further away from the wall, the freestream is larger and the swirl effects are stronger, hence creating asymmetry. Similar observations have been obtained experimentally in gaseous jets in crossflow where swirl has been imposed to the gaseous phase (Panda et al. 2015).

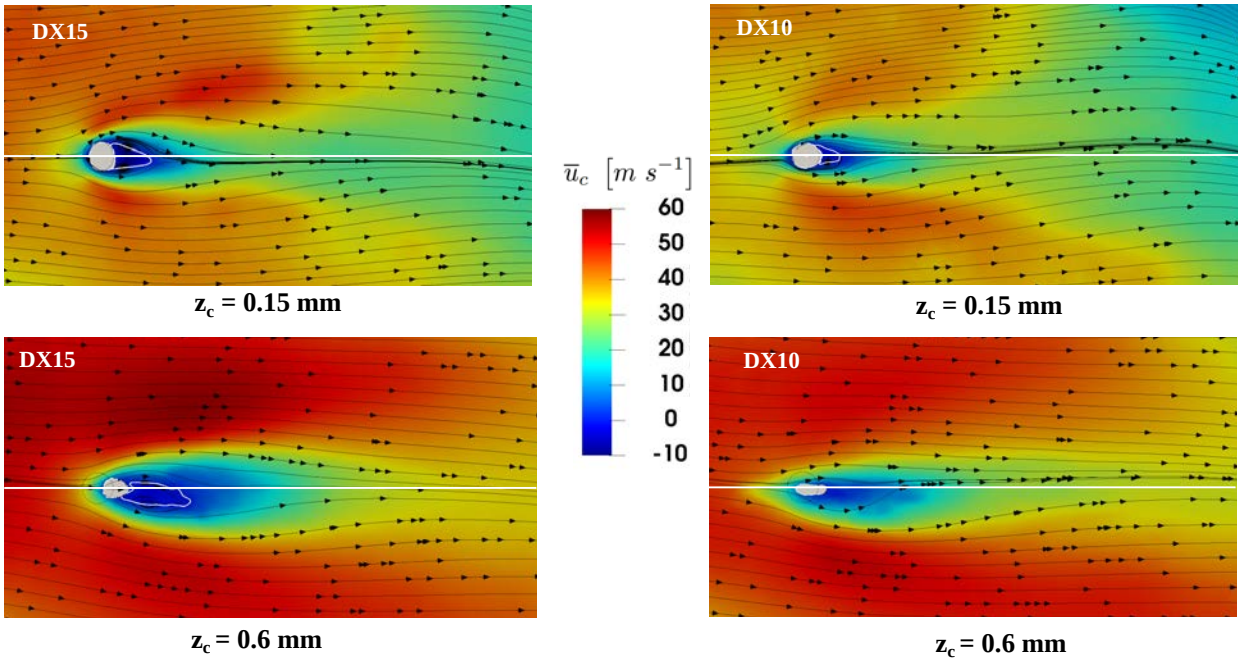

Figure 8.17: Mean axial velocity at planes $z = 0.2, 0.8, 16$. Black lines with arrows are in-plane mean streamlines. ; the white solid line indicates the contour $\overline{u} = 0$ which delimites the recirculation bubble. The grey area indicates the mean liquid region, identifed as $\overline{\psi} > 0.5$. The black-dotted circle indicates the location of the injection nozzle

8.4.5 Direct measurement of liquid fluxes

Resolved liquid fluxes are obtained in interior boundaries (IBs) defined at the same location than the sampling planes from Figure 8.2. The procedure followed to obtain these fluxes is detailed in Annex C.2. Filming planes are not quantified in this case, since these fluxes are not used by the SLI models and not all the mass losses in the planes perpendicular to the crossflow direction were due to liquid filming, but also to liquid structures reaching a characteristic size of the order of the mesh resolution (see Annex D for details).

In first place, the instantaneous flux for simulation DX10 are shown in Figure 8.18 for two sampling planes. In the same way as in the classical JICF (Figure 5.37), the instantaneous fluxes show high oscillations around the injected flow rate due to the intermittent behaviour of the JICF: at certain instants there are cluster of droplets produced by the column breakup mechanism (see §8.4.2) crossing the sampling planes together, which yield instantaneous flux values larger than the injected Q_l (flux overshoots); while at other instants there are only a few droplets being convected.

The evolution of the mean ($\overline{Q}_l$) and RMS ($Q_{\mathrm{l,RMS}}$) flow rates through the IBS for all simulations is shown in Figure 8.19. Mean fluxes (Figure 8.19 left) show oscillations at the early instants and a later stabilization to converged values. Case DX15 is converged while case DX10 still shows oscillations at the last sampling times due to the flux overshoots around $t' \sim 4.2$ shown in Figure 8.18. Such overshoots are also reflected in the step increase in the RMS evolution (Figure 8.19 right) for the same case.

In all simulations, there is a decrease in the mass flux with increasing axial distance x_c as it was also observed in the JICF simulations of Chapter 5. The final mean values of the fluxes, displayed in the bar chart of Figure 8.20, reflect this trend of mass flux reduction in a more visual way. The reason of flux decrease is

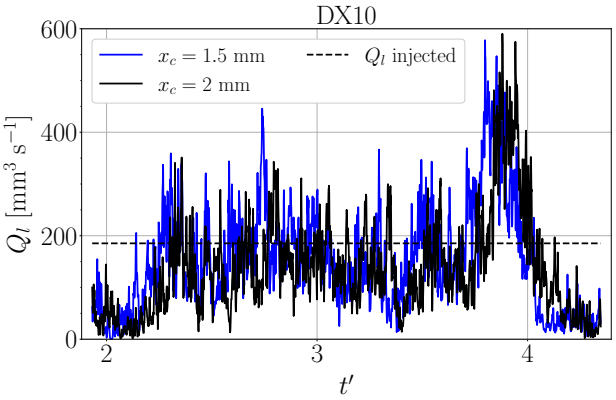

Figure 8.18: Time evolution of instantaneous liquid flow rates Q_l for case DX10

the same as in that chapter: small droplets reach characteristic dimensiones around the order of the interface cell size and are removed from the simulation. The RMS values are also shown in Figure 8.20 by the vertical bars: these ones have large magnitudes, of the order of the mass flow rates obtained (see Figure 8.19b), which indicate the high variance in the instantaneous mass flow rates crossing the sampling planes. Regarding fluxes decreases with axial distance, it is seen that the losses among consecutive sampling planes are larger for the coarse case DX15 than for the fine one DX10, since in the former the resolution limit is more restrictive and there are more droplets disappearing than in the latter. Even so, the mean fluxes show a good evolution with values close to the injected flow rates, with reductions along the axial distance due to filming and vanishing liquid structures when reaching a size of the order of the mesh resolution.

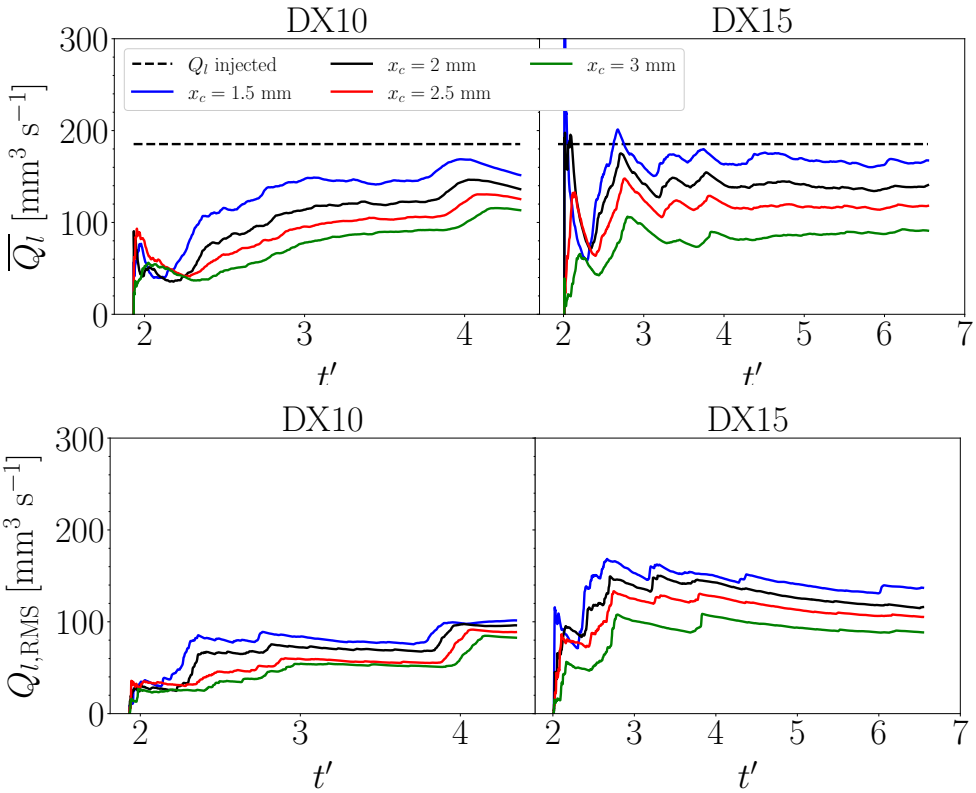

Figure 8.19: Time evolution of mean (*top*) and RMS (*bottom*) fluxes in BIMER IBs

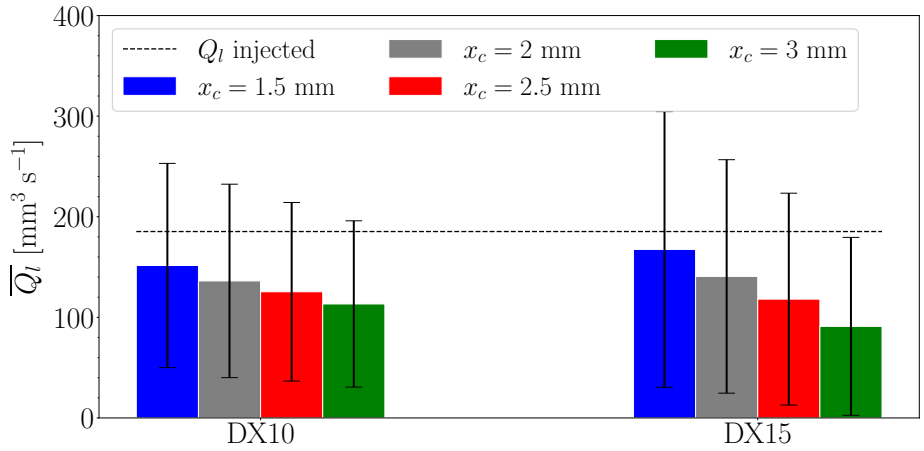

Figure 8.20: Mean flow rates from IBs perpendicular to crossflow in BIMER

8.4.6 Computational performances and costs

Table 8.4 shows the numbers of cores, cells and droplets present at this $t^* = 4.7$. This time instant corresponds to early injection before droplets reach the liquid removal sponge layer, and after the jet has started to develop, hence allowing for a comparison among cases. The fine simulation needs twice the number of cores to run optimally the computation at this time instant (the number of cells is 2.5 larger for the fine case, hence needing the number of cores to evolve of the same order for parallellization purposes). The number of drops in the fine simulation is 6 times larger than in the coarse one, same ratio as between the fine and coarse simulations of Chapter 5. This illustrates again the effect on atomization of reducing the interface size: even though the absolute computational cost per time-step is larger, more droplets are resolved which helps to converge SLIs faster (as illustrated in the convergence maps of §8.5.3).

Table 8.4: Computational cores, mesh cells and total number of droplets present at the domain for BIMER simulations at $t^* = 4.7$

Case	N_{cores}	N_{cells} $(\cdot 10^6)$	N_{drops}
DX10	768	110	963
DX15	384	43	150

The performances for the BIMER simulations at $t^* = 4.7$ are evaluated through the Reduced Computational Tiem (RCT), calculated with Eq. (5.10), in Table 8.5. Results show that the computational time spent in the level-set (ACLS) and Navier-Stokes solver (NS) routines is identical in both simulations, while the actual differences are found for the AMR routine: halving the interface cell size increases the RCT contribution of the AMR by a similar order due to the larger quantity of liquid cells present which need to be refined. Consequently, the total RCT is larger for the fine resolution than for the coarse one.

Table 8.5: Computational performances from BIMER simulations at $t^* = 4.7$

Case	RCT [μs]	RCT_{ACLS} [μs]	RCT_{AMR} [μs]	RCT_{NS} [μs]	t_{CPU}/t^* [h]
DX10	313.9	108.9	160.9	44.1	3.25
DX15	198.4	95.9	67.8	34.7	5.97

The final computational cost of the simulation measured by the total CPU time invested is shown in Figure 8.21. A total of $4.5 \cdot 10^5$ hours have been spent in case DX15, while an amount of $7 \cdot 10^5$ hours (difference factor of 1.5) were used for the resolution DX10. As the latter simulation has run for longer physical time, the ratio of CPU vs physical time simulated is much lower for this one: $1.2 \cdot 10^5$ versus $4 \cdot 10^5$ CPU hours per milisecond. These results show that increasing the resolution from Δx_{min}= 15 to 10 μm increase the cost per milisecond by a factor of almost 4. Nevertheless, the absolute cost needed to yield converge injector (as detailed in the next section) rises only by a factor of 1.5, which proves the advantages of increasing the resolution for producing SLI: a moderate increase in the simulation costs yields more converged injectors in both senses of spray convergence and droplets sizes.

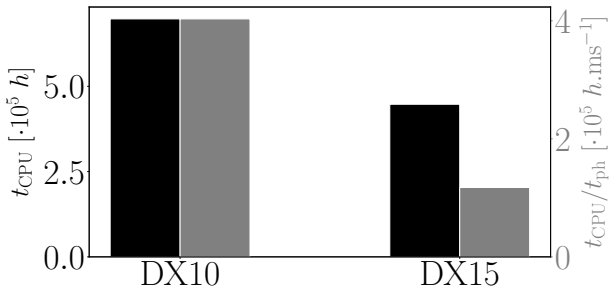

Figure 8.21: Computational CPU costs of BIMER resolved atomization

8.5 SLI building

8.5.1 Dense core characterization for ALM

In order to characterize the dense core topology and net force applied, the methodology detailed in Appendix C.3 is applied. As explained, the dense core is represented by its breakup point coordinates (x_b, z_b) and its width w. The temporal evolution of such coordinates for the simulations performed is shown in Figure 8.22. All temporal signals display a sawtooth shape as in the case of the classical JICF signals from Figure 5.43, with periodic behaviour of the signals associated to the frequencies of ligament stripping. The width signals show a periodic oscillations which in some cases reach a value $w/d_{\mathrm{inj}} < 1$ (i.e. dense core thinner than the injection diameter), corresponding to the time instants where the column flattens as shown, for instance, in the snapshots of column breakup in Figure 8.8. The signal x_b from case DX10 displays at some points a value $x_b < 0$, which indicates that the dense core breakup point has been detected upstream the injection location (as shown, for instance, in Figure 8.10).

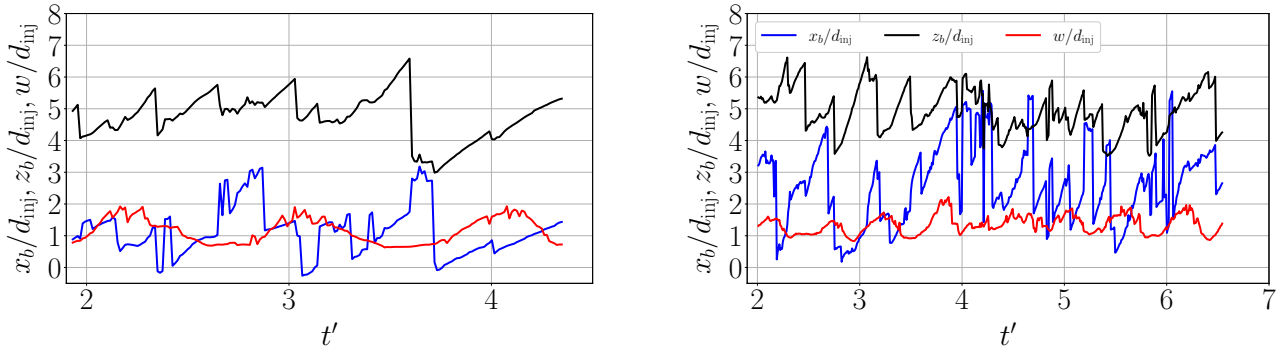

(a) Case DX10

(b) Case DX15

Figure 8.22: Time evolution of the BIMER dense core breakup point coordinates $x_{\mathrm{b}}, z_{\mathrm{b}}$ and width w.

The evolution of mean quantities for all magnitudes are shown in Figure 8.23. All cases are close to convergence. The final mean values are shown in Figure 8.24, where the simulation UG100_DX10 for the JICF from Chapter 5 has been added for comparison. The location of the values in the $\overline{z}_b - \overline{x}_b$ diagram show that $\overline{z}_b > \overline{x}_b$ for both simulations, indicating that the dense core penetrates further vertically than horizontally. There is also a high dependency on resolution: refining the interface cell size does not significantly affect the vertical coordinate $\overline{z}_b$ but reduces considerably the axial breakup location $\overline{x}_b$, reducing hence the dense core length. Similarly, refining the mesh affects the dense core width $\overline{w}$ as shown in Figure 8.23b. When comparing with simulation UG100_DX10, it is seen that both the width and the breakup coordinates are shorter for BIMER. This is coherent with the operating points simulated, since BIMER presents lower values of q and Re_g than the classical JICF which reduces the breakup coordinates and dense core width (Patil & Sahu 2021). The final values for the dense core length $L_{\mathrm{DC}} = \sqrt{\overline{x_b}^2 + \overline{z_b}^2}$, mean width $\overline{w}$, dense core surface S_{DC} and momentum parameters for the net dense force obtention are summarized in Table 8.6.

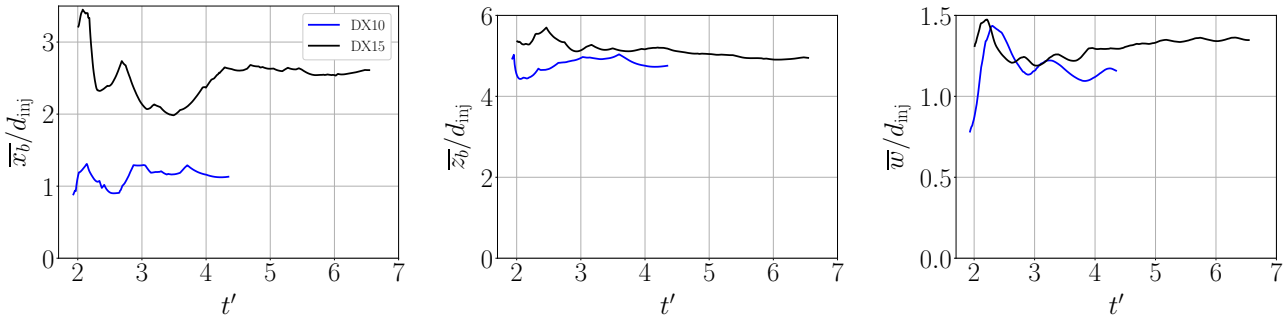

Figure 8.23: Evolution of mean geometric parameters of BIMER dense core

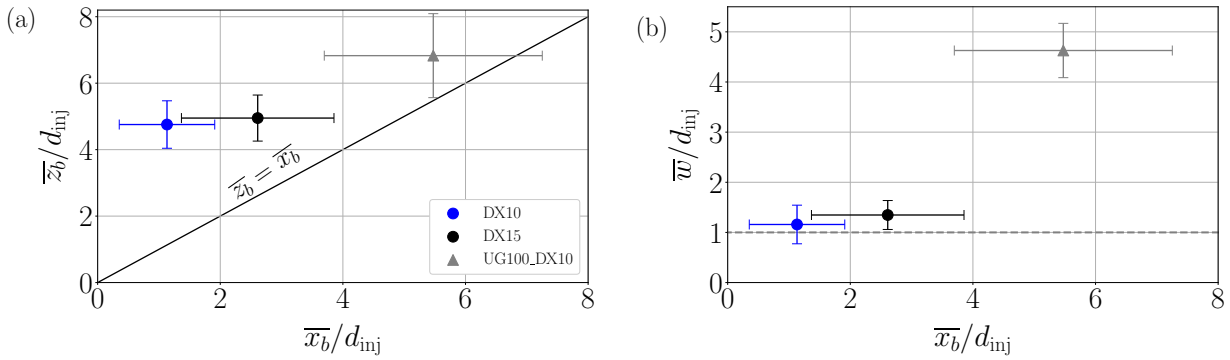

Figure 8.24: Mean values for the BIMER dense core geometric parameters

Table 8.6: BIMER dense core characterization: geometric and momentum parameters

Case	$L_{\mathrm{DC}}/d_{\mathrm{inj}}$	w/d_{inj}	S_{DC} [mm^2]	p_{windward} [Pa]	p_{leeward} [Pa]	$\lvert\boldsymbol{F}_{\mathrm{DC}}\rvert$ [mN]
DX10	4.83	1.04	0.47	2020	1475	0.25
DX15	5.44	1.33	0.59	2340	1550	0.45

8.5.2 Spray characterization

Establishment of mean sprays

Characterization of the spray resulting from atomization in BIMER is obtained through lagrangian tracking of the resulting liquid structures when these cross the sampling planes. The sampling procedure and the droplets properties obtained were described in §4.4.1. The total physical time simulated and time for which statistics and droplets have been accumulated (i.e. after an establishment time of $t' \sim 2$) are summarized in Table 8.7. The total number of droplets accumulated in all sampling planes from each simulation are shown in Table 8.25. Even though the total number of sampled droplets is similar in all cases, the fine case generates more droplets as stated by the higher values of $N_{\mathrm{dr}}/t_{\mathrm{acc}}$. This is in line with the effect of the resolution in the JICF of Chapter 5, where the observations on the effect of resolution in the sampled sprays were identical (see Table 5.10).

Table 8.7: Total physical t_{ph} and accumulation times t_{acc}, absolute and dimensionless with Eq. (8.3)n

Case	t_{ph} [ms]	t'_{ph}	t_{acc} [ms]	t'_{acc}
DX10	1.73	4.89	0.96	2.72
DX15	3.81	6.78	2.64	4.69

Table 8.8: Number of droplets sampled in BIMER simulations: total amount (N_{dr}) and total amount per accumulation time $N_{\mathrm{dr}}/t_{\mathrm{acc}}$

Case	N_{dr}				$N_{\mathrm{dr}}/t_{\mathrm{acc}}$ [ms^{-1}]			
	$x_c = 1.5$ mm	2 mm	2.5 mm	3 mm	$x_c = 1.5$ mm	2 mm	2.5 mm	3 mm
DX10	6214	5674	5183	4701	6463	5901	5390	4889
DX15	6854	6112	5077	3945	2598	2316	1924	1495

Establishment of the global spray in terms of flux Q_l and SMD is shown in Figure 8.25. Flux evolution in all planes show similar trends as the IBs flow rates from Figure 8.19, including a decrease in mean fluxes with axial distance due to liquid structures reaching the mesh resolution and disappearing. The evolution of SMD shows good convergence for all cases for the times simulated. The evolution of other mean quantities which are of interest for SLI are shown in Appendix F.

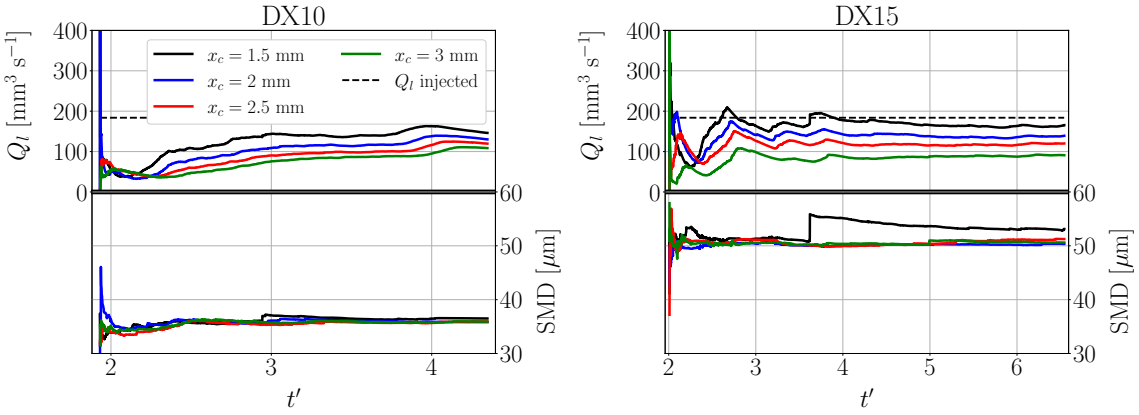

Figure 8.25: Establishment of SMD and Q_l in BIMER sprays

The final fluxes obtained through lagrangian tracking are compared to their equivalent from the IBs in the barchart from Figure 8.26. As in the previous JICF studies (Figure 5.47), there are disparities among both methodologies to obtain fluxes: sometimes the lagrangian fluxes overestimate the IBs ones due to droplets being tracked more than once, while in other cases some droplets might not be detected at all through the lagrangian method and hence the fluxes are underestimated (more details can be found in §5.7.2). Overall, lagrangian fluxes are in the same order as the resolved ones, hence these ones are kept to represent the spray (later on, spatially discretized fluxes to be injected in the dispersed phase simulations from Chapter 9 will be scaled to match the real flux injected in BIMER).

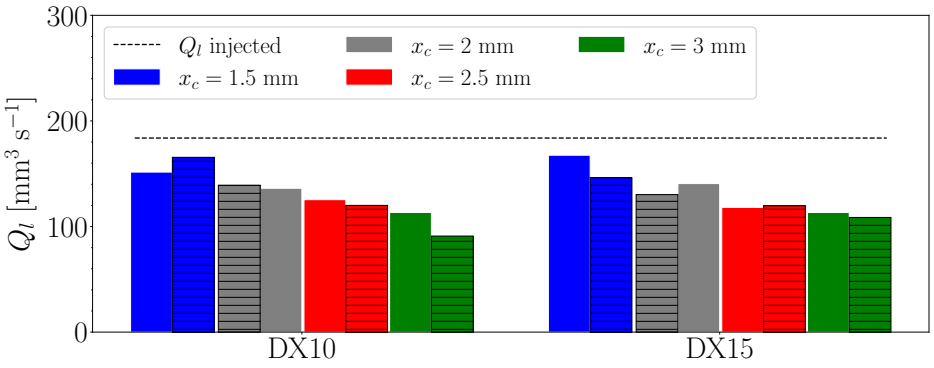

Figure 8.26: Liquid fluxes provided by interior boundaries (solid color bars) and lagrangian tracking (black-dashed color bars).

Granulometry

The final SMDs obtained are shown in Figure 8.27. The SMD has a clear dependency on the resolution: reducing the interface cell size $\Delta x_{\min}$ from 15 to 10 μm (1.5 factor) reduces the SMD from $\sim$ 50 to $\sim$ 35 μm, which is a reduction of the same order. SMD decreases with axial distance for both simulations. This variation is larger for DX15, where SMD decreases from 53 to 50 μm, than in DX10, where the reduction if from 36 to 35 μm. The variations are very low for both cases, indicating that either 1) the mesh resolution limit is reached or 2) atomization is complete and the smallest droplets can be captured with the interface resolutions employed. To assess both hypothesis it is of interest to look at the droplets size histograms in Figure 8.28. The size and volume distributions are shown, as well as relevant sizes and the lognormal distributions (Eq. 5.14) where the parameters have been obtained either by fit or through the correlations given by Eq. (5.15). The histograms from the coarse case DX15 show a clear lognormal distribution which is well fit by the blue curve. The smallest droplets sampled have a diameter $\sim$ 30 μm, which corresponds to $2\Delta x_{\min}$. This means that the smallest droplets in the simulation are resolved with 2 mesh cells: the number of cells to properly resolve a droplet is a subject of discussion, but authors generally agree that it is comprised between 2 (Herrmann 2009) and 5 (Fuster et al. 2009). Therefore, in the case DX15 where smallest droplets are $2\Delta x_{\min} = 30$ μm the smallest droplets simulated are limited by the grid, meaning that a finer resolution would be needed to resolve the smallest physical droplets that would exist in the actual configuration (unfortunately, there are no experimental data available to compare). When refining the mesh from $\Delta x_{\min} = 15$ to 10 μm the histograms show that, actually, the smallest droplets obtained collapse also at around $\Delta x_{\min} = 30$ μm, which in this case corresponds to $3\Delta x_{\min}$. Since the smallest droplet sizes are similar in both simulations, it is suggested that the atomization process is completed at this stage. Lower SMDs obtained in the fine simulation could be caused by smaller liquid structures resulting from column breakup, which shows different topologies in each simulation. For assessing the complete atomization hypothesis, a critical diameter below which secondary atomization would not occur can be approximated by inverting Eq. (4.35) and considering $We_{\text{cr}} = 6$:

$$d_{\text{cr}} = \frac{2\sigma We_{\text{cr}}}{\rho_g \left(u_l - u_g\right)^2} = 128\ \mu m \tag{8.4}$$

where the velocities are taken from Table 8.1. As observed, the critical diameter is much larger than the droplets sizes obtained from both simulations: most droplets produced by primary breakup in the BIMER configuration are below the critical diameter and do not undergo further secondary atomization. This is actually confirmed by the convergence of SMD with axial distance shown in Figure 8.27 and by the histograms from Figure 8.28, which do not change significanly further downstream than $x_c = 2$ mm. Hence, atomization is completed in the simulations performed at this axial location.

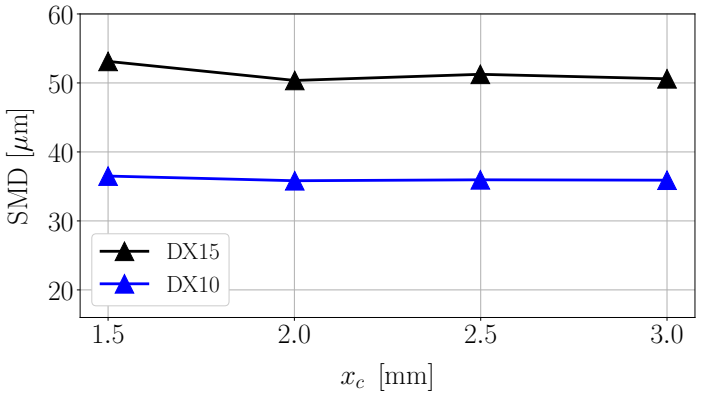

Figure 8.27: Evolution of SMD with axial distance for each simulation.

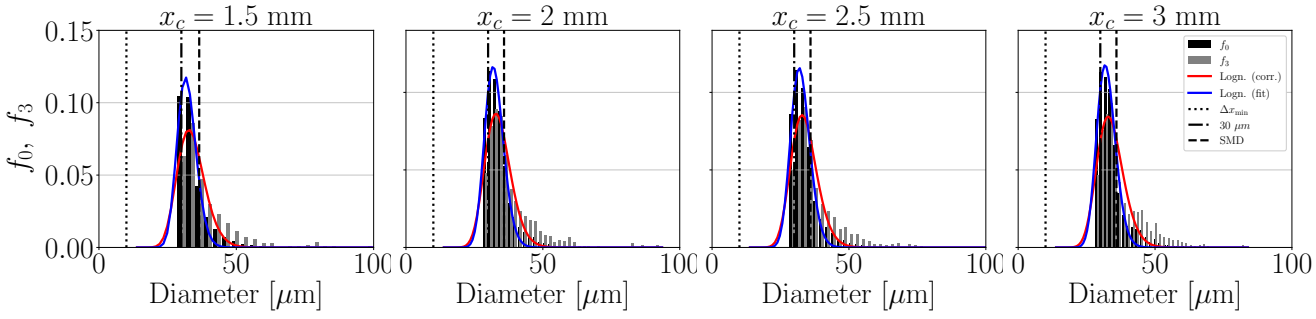

(a) Case DX10

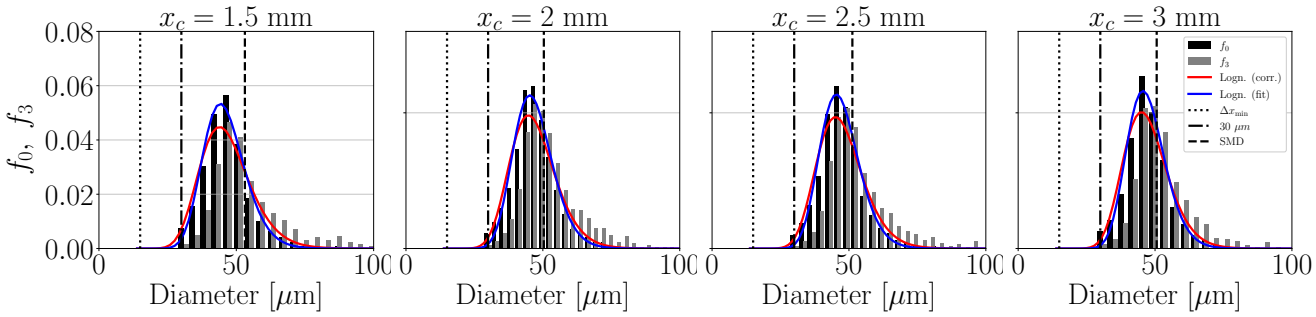

(b) Case DX15

Figure 8.28: Droplets size (f_0) and volume (f_3) histograms for all BIMER cases

Liquid velocities

Mean spray velocities, arithmetic and volume weighted, in axial and vertical directions are shown in Figure 8.29. As observed, establishment in axial velocity is reached at $x = 2$ mm, while the vertical velocities are stable from the first sampling plane. The mean axial velocities do not stabilize at the bulk velocity $u_g = 56$ m s^{-1} since the gaseous field is perturbed due to the presence of the crossflow for the whole range of sampling planes axial locations, as shown in Figure 8.13. Due to these disturbances, the gaseous field is heterogeneous in space as shown in §8.4.4 and droplets relax towards values differing from those found upstream the jet, resulting in mean velocities lower than u_g. Regarding mean vertical velocities, these are stabilized in values other than 0, indicating that the spray continues to open vertically with increasing axial distance rather than reach a constant penetration height. This is also attributed to the jet perturbation, since gas streamlines are diverted downstream the jet vertically as displayed in Figure 8.12. This figure also shows that the vertical component of streamlines for case DX10 is larger than their equivalent in case DX15, which results in larger mean vertical velocities for case DX10 as confirmed by Figure 8.29.

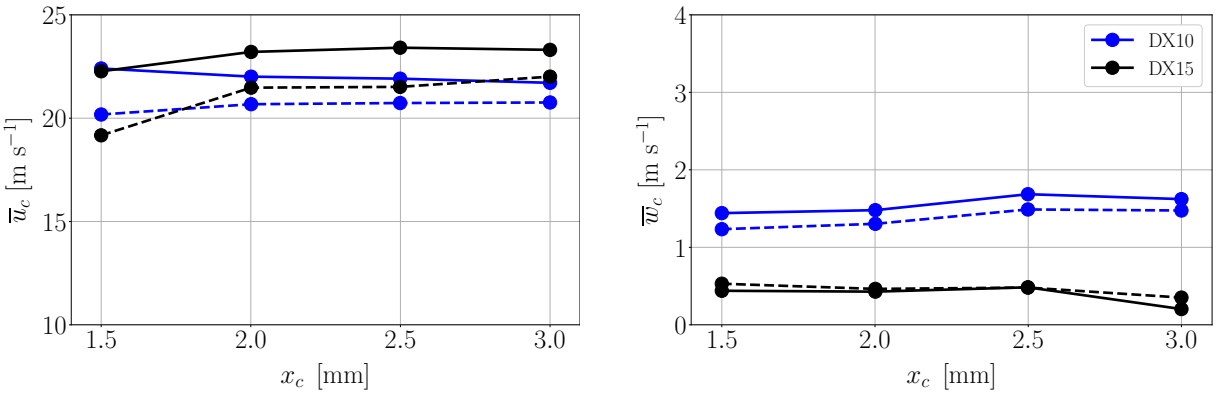

Figure 8.29: Mean velocities in axial, lateral and vertical crossflow directions. Solid lines indicate arithmetic average velocities, while dashed ones indicate volume-weighted average velocities.

Deformation of liquid structures

Figure 8.30 shows the evolution of volume-weighted averages of deformation parameters for all cases. Establishment with axial distance is obtained at $x_c = 2$ mm, as for the other previous magnitudes discussed. Considering the sphericity criteria to be for droplets presenting $\beta > 0.5, \alpha < 2$, it is seen that mean values estabilise outside the sphericity range. A look at the $\alpha - \beta$ scatterplots in Figure 8.31 shows that most droplets are located outside this sphericity region (enclosed by the thick black lines): the percentages of spherical droplets is 5 and 13 % for DX15 and DX10 respectively at plane $x = 2$ mm . Such percentage does not vary considerably further downstream, indicating that transported droplets are mostly deformed.

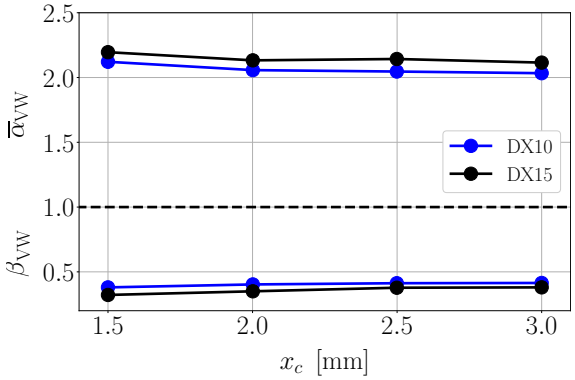

Figure 8.30: Mean deformation parameters for BIMER simulations

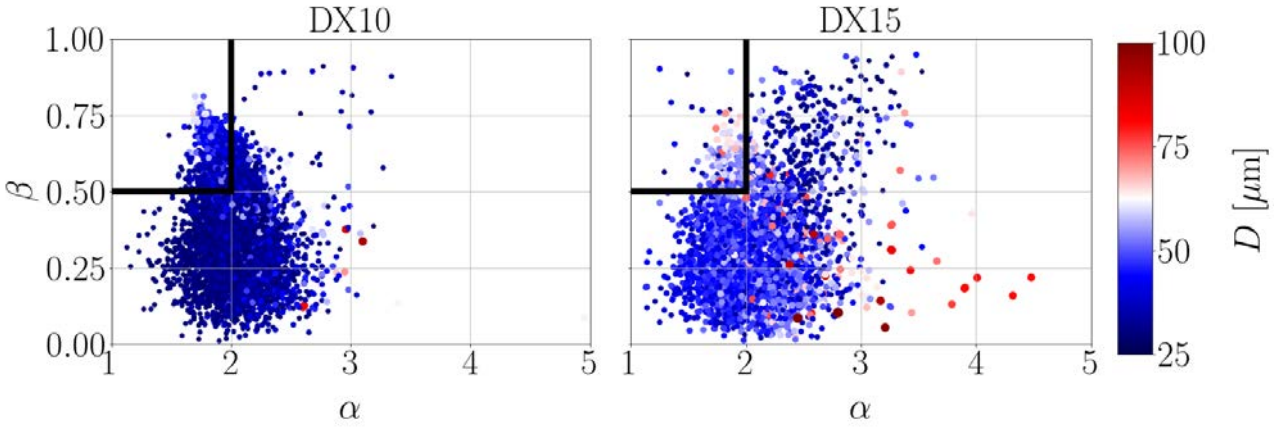

Figure 8.31: Scatterplots of deformation parameters α - β for cases DX10, DX15 at plane $x_c = 2$ mm. Droplets are colored and scaled by their equivalent diameter. Thick, black lines enclose the region where droplets are spherical according to the criteria defined in the text

8.5.3 Sprays spatial discretization

SLIs are obtained by applying the discretization process described in §4.4.3 to the previously shown sprays. Since it was shown in the former section that convergence was achieved for most magnitudes at $x_c = 2$ mm, SLIs are shown here only for the sampling planes at $x_c = 1.5, 2$ mm. Results are shown in Figures 8.32 to 8.35. The SMDs maps show a circular structure in which large values are obtained at the center of the spray and diameters are reduced further away. Fluxes maps exhibit a circular structure which is typical from all liquids JICF. These maps show maximum flux values located at around $y_c = 0$ and symmetry with respect to this axis for case DX10, which indicates that the crossflow direction has been properly chosen. Axial velocity maps show a classical low-velocity region in the bottom part, central region of the spray which corresponds to the disturbance effect of the spray, while the vertical velocity maps display the classical layered structure with increasing velocity along the vertical direction z_c, hence indicating that the spray continues to penetrate further away as it is convected downstream. Large differences with respect to the classical JICF of Chapter

5 are observed for the lateral velocity v_c, since in this case the profiles are not symmetric with respect to the $y_c = 0$ axis due to the swirl component of the air. With respect to the convergence maps, it is shown that more converged probes are obtained for the fine resolution than for the coarse one even though the total physical time simulated is lower. The same observation was done for the classical JICF as detailed in §5.7.3: it can be concluded then that a finer mesh makes SLI converge with lower physical time simulated. It is worth noting that convergence has only been defined according to the droplet size distribution as indicated by Eq. (4.15): further research includes testing other MSE functions accounting for other magnitudes such as velocities. Nevertheless, the SMD and velocity maps obtained for the coarse resolution (Figures 8.34 and 8.35) seem *less converged* than their equivalents for the fine case (Figures 8.32 and 8.33) due to the less smooth contours obtained. This might indicate that the resolution DX15 is too coarse to simulate BIMER, and therefore only the SLI obtained for case DX10 will be used to perform the dispersed phase simulations from Chapter 9.

Case DX10

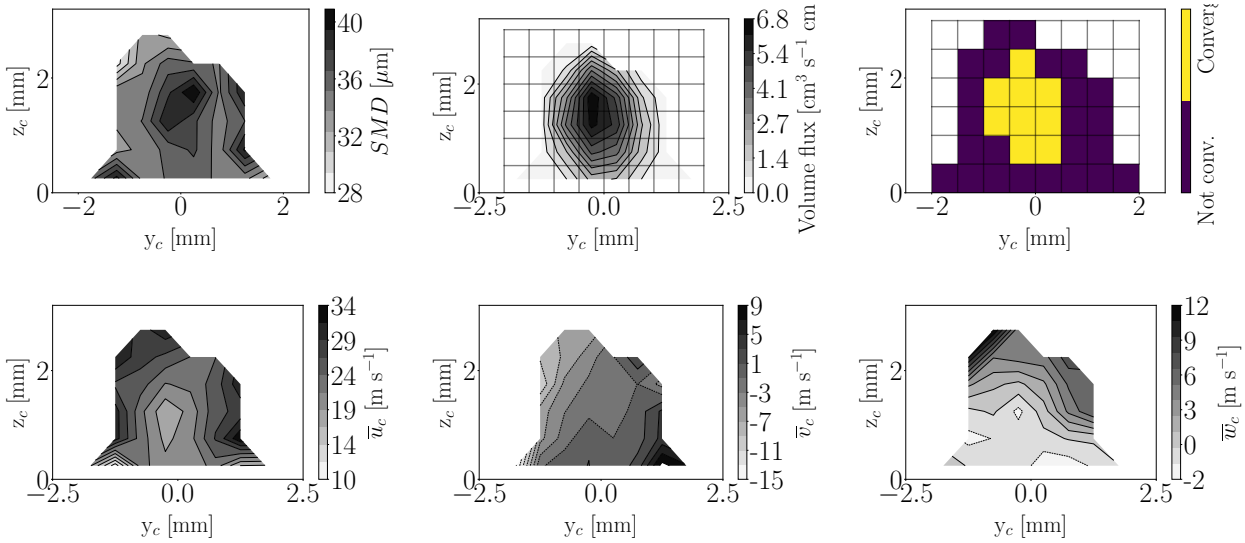

Figure 8.32: Spray states at $x_c = 1.5$ mm for case DX10

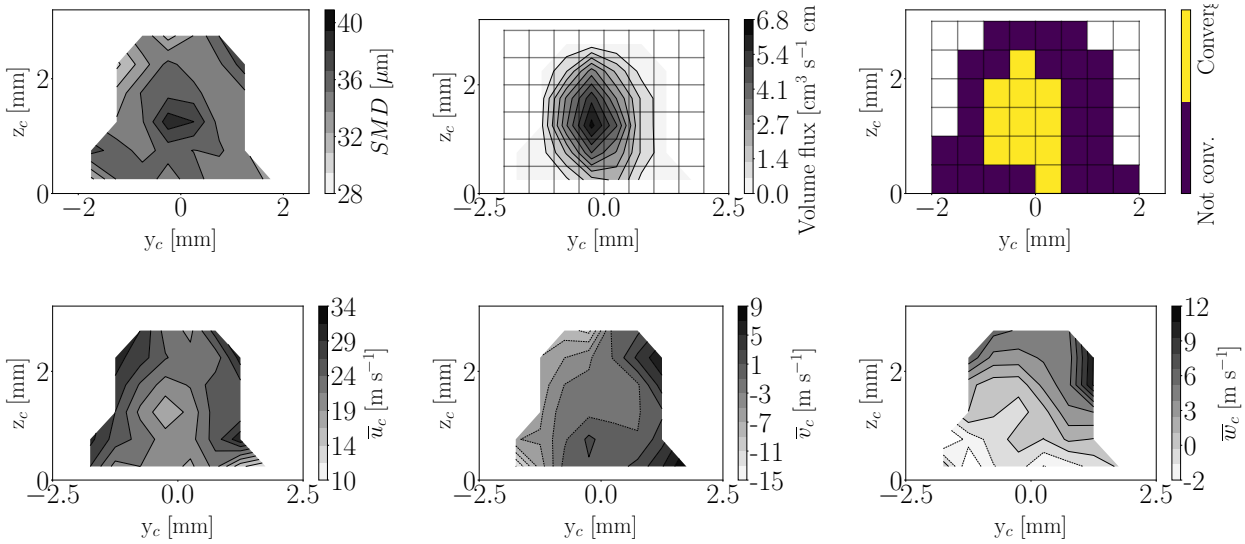

Figure 8.33: Spray states at $x_c = 2$ mm for case DX10

Case DX15

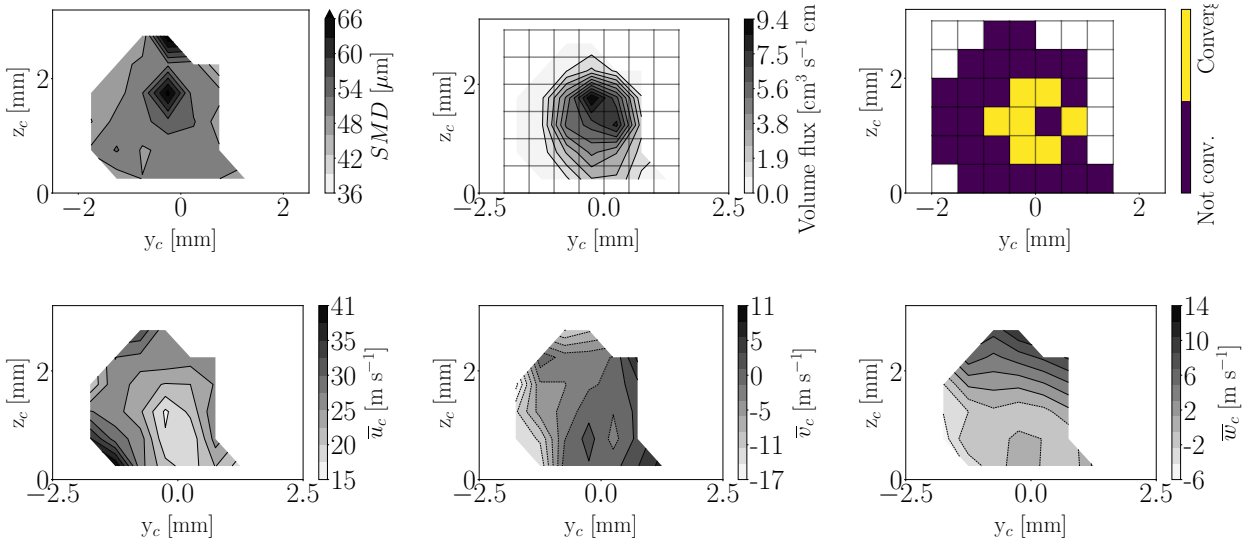

Figure 8.34: Spray states at $x_c = 1.5$ mm for case DX15

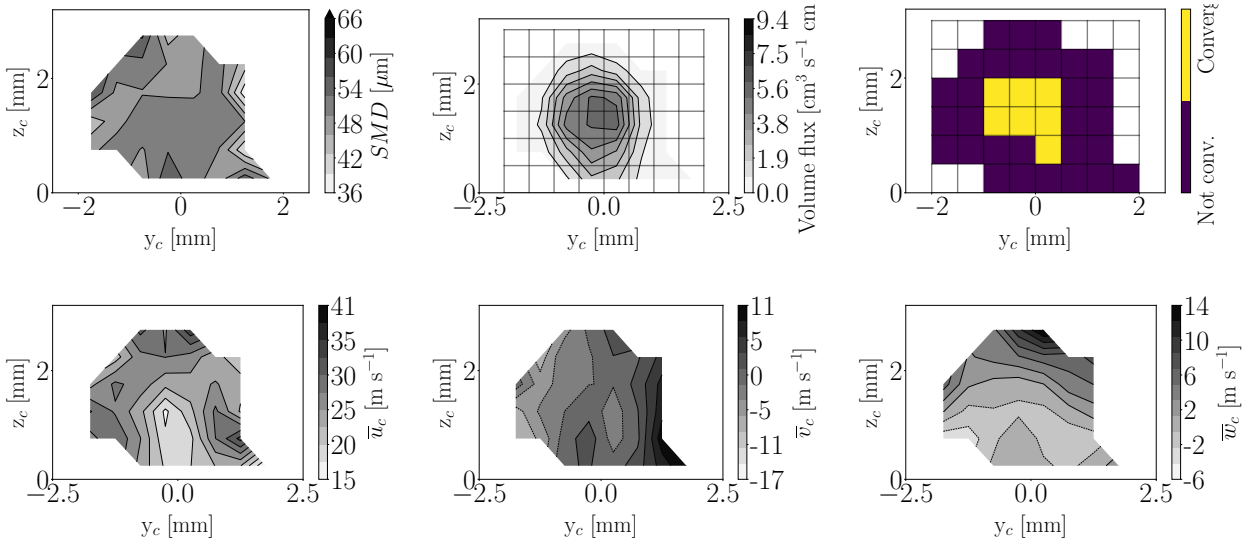

Figure 8.35: Spray states at $x_c = 2$ mm for case DX15

On SLI convergence with resolution

As illustrated by the convergence maps from Figures 8.32 to 8.35, SLIs obtained with the fine resolution present a greater number of converged local probes than the coarse one, even with a lower simulated physical time. This agrees with the findings of Chapter 5. The SLI strategy allows therefore to obtain converged injectors with a lower physical time simulated when finer resolutions are used. The cost savings of the simulation, which are estimated as the difference between 1) the computational time that resolution DX10 would take to reach the same physical time simulated as case DX15 and 2) the actual cost of simulation DX10, are shown in Figure 8.36: $7 \cdot 10^5$ versus $15.4 \cdot 10^5$ CPU hours, which supposes a difference of $8.4 \cdot 10^5$ CPU hours (more than double the actual cost).

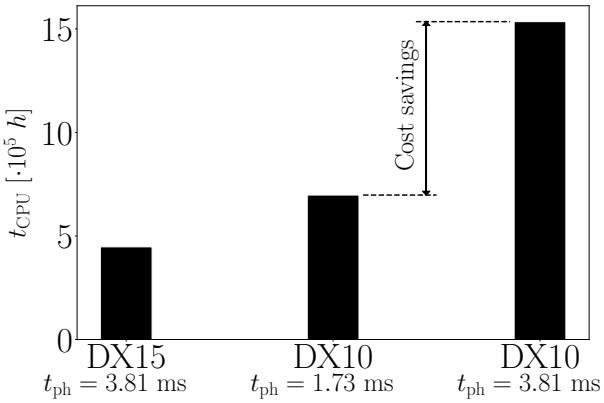

Figure 8.36: Cost savings in SLI development

8.6 Conclusion

This chapter has presented resolved simulations of the injection and atomization processes in the academic multipoint configuration BIMER. The numerical setup, which was presented and studied for single-phase conditions in Chapter 7, was adapted to account for liquid injected through a single point of the multipoint injector. Due to symmetry in the injector's take-off stage and to the multipoint holes being far enough separated from each other (thus avoiding interactions among liquid jets), it was enough to simulate injection through a single injection point to characterize the atomization process and build an Smart Lagrangian Injector (SLI). One operating condition was simulated with two different interface cell sizes.

In first place, the physics of the resolved atomization simulationes were studied (§8.4). Analysis of the breakup process showed that both column and surface breakup modes are present in BIMER as in a classical liquid JICF. Instabilities leading to breakup are very different to the ones from canonical cases: in BIMER they are generated at the nozzle exit and propagate in both the jet streamwise and lateral directions, while in a classical configuration these instabilities evolve only along the former one. Postprocessing of the jet trajectories and comparison with respect to an experimental correlation (from a classical JICF configuration) have shown a good near-field behaviour but an underestimation further downstream: the jet undergoes prompt atomization and atomized droplets are quickly dragged towards the air direction. Analysis of the turbulent gaseous structures has shown that the perturbation effect of the jet is still noticeable several diameters downstream the nozzle. The vortical structures, identified as the counter-rotating vortices pairs in the planes perpendicular to the crossflow direction, have been found (when they were actually present) to be asymmetrical with respect to the axis $y_c = 0$: this is an effect of the swirl, and has also been observed in previous experimental and numerical studies. Computation of the resolved liquid fluxes at planes perpendicular to crossflow direction yields identical conclusions as in the other JICF studied in this thesis: flow rates close to the injected one are retrieved near the injector, then these are progressively reduced further downstream.

In second place, the simulations were postprocessed to obtain the necessary data for building SLI (§8.5). An analysis of the liquid dense core has shown that its topology for this case is very different from the classical JICF (in relation to the injection diameter): the mean breakup point location is shorter and its mean width is smaller, almost of the order of the injection diameter. Characterization of the spray has shown: 1) good

agreement in terms of fluxes with respect to interior boundaries, 2) lower secondary atomization in BIMER, with convergence in both SMD and histograms at location $x_c = 2$ mm, and 3) different histogram shapes with resolution, with the ones from the coarse case showing a lognormal shape while in the fine case they display also a similar trend but with droplets collapsing at $d \sim 30$ μm. All global spray parameters, including mean velocity and deformations, are converged at $x_c = 2$ mm in BIMER. The SLI structures analyzed showed similar spray spatially-distributed structures as in classical liquid JICF, including circular flux structure and deceleration in the axial crossflow velocity caused by the dense core perturbation. A different behaviour was obtained for the lateral velocity, since this was not symmetrical with respect to axis $y_c = 0$ but asymmetrical due to the swirl component of the gas, which drags droplets along its direction. The convergence maps showed that more converged local probes were obtained for the fine resolution. From these results and an analysis of the computational costs it is concluded that, for the purpose of SLI building, performing resolved atomization simulations with a finer interface is more convenient since 1) finer cell sizes provide more reliable results, 2) more converged injectors are obtained, and 3) less physical time simulated is needed which, yet the total computational expenses being higher for a finer resolution, makes such simulations cheaper than expected a priori: eventually, both computations remain in a similar order of CPU costs.

Chapter 9

Dispersed phase simulations in BIMER

9.1 Introduction

The previous chapter has reported the resolved atomization simulations performed through one multipoint injector of the BIMER configuration. The lagrangian injector learning process was applied to get a in-plane, spatially distributed spray. This spray conforms a lagrangian injector that is used in the dispersed-phase simulations in this chapter. The dense core was also characterized: these information can be used in this chapter to impose an actuator with the ALM method that perturbs the gaseous phase similarly to a jet dense column. Due to rotational symmetry in the multipoint stage, the obtained SLI and actuator can be extrapolated to the remaining multipoint holes to perform liquid injection and gaseous phase perturbation in the full configuration. This chapter reports the results of dispersed-phase simulations in BIMER with the SLI methodology.

In first place, the computational setup is explained in §9.2. Experimental qualitative results obtained for the same operating point obtained by Renaud (2015), which can be used for validating the simulations, are reported in §9.3. Then, the liquid boundary conditions for both the multipoint and pilot stages are described in §9.4. Boundary conditions for the gaseous phase obtained with the ALM methodology are then discussed in §9.5, showing that in this case the perturbed gaseous field cannot be properly retrieved. Finally, results for the simulations performed are reported in §9.6. A total of three simulations have been computed: one with evaporation and without perturbance of the gaseous field; and two without evaporation, considering the ALM disturbances in one but neglecting them in the other. It is shown that the ALM has no significant contributions to the dispersion of droplets, which is mainly attributed to the absence of secondary atomization in these simulations. All cases show a good experimental validation with the experimental spray in terms of SMD and axial velocity maps. The results greatly improve when adding evaporation, specially the sizes of the lagrangian droplets, whose mean global SMD shows only a deviation of 5 % with experiments.

9.2 Computational setup

For performing dispersed phase simulations, the operating point defined in Table 9.1 is simulated. The staging factor is $\alpha = 15$, meaning that 15% of the total liquid flow rate is injected through the pilot stage and the remaining liquid through the multipoint. For total flow rate of $\dot{m}_l = 1.64$ g s^{-1}, the take-off stage injects a mass flow rate of $\dot{m}_{l,\text{takeoff}} = 1.39$ g s^{-1} (hence 0.139 g s^{-1}, corresponding to $Q_l = 185.3$ mm^{3}s^{-1}, per injector), and a mass flow rate of $\dot{m}_{l,p} = 0.25$ g s^{-1} is introduced through the pilot stage. The global equivalence ratio of this operating point is $\phi_g = 0.6$.

Evaporation

Due to the high gas ambient temperature inside BIMER combustion chamber ($T_g = 433$ K while $T_l = 293$ K, see Table 9.1), evaporation of lagrangian droplets should be considered. For assessing this influence, the evaporation model of Spalding (1954) is used in one simulation, which is compared to two other simulations

where mass and heat transfer are not taken into account. Details on the hypothesis and implementation of this evaporation model in YALES2 can be found in Domingo-Alvarez (2019).

Table 9.1: Operating point to perform gaseous and two-phase simulations tested by Renaud (2015)

Air properties			
$\dot{m}_g$ [g s^{-1}]	T_g [K]	ρ_g [kg m^{-3}]	μ_g [Pa s]
43.1	433	0.82	$2.4 \cdot 10^{-5}$
Liquid properties			
σ [N m^{-1}]	T_l [K]	ρ_l [kg m^{-3}]	μ_l [Pa s]
$25 \cdot 10^{-3}$	293	750	$1.36 \cdot 10^{-3}$
Burner staging			
α [%]	$\dot{m}_{l,\text{pilot}}$ [g s^{-1}]	$\dot{m}_{l,\text{takeoff}}$ [g s^{-1}]	ϕ_g [-]
15	0.25	1.39	0.6

9.3 Experimental results from literature

The operating point tested experimentally by Renaud (2015) has been chosen to test the SLI methodology because it presents non-reactive experimental results for validation. These ones, shown in Figure 9.1, consist of qualitative maps of SMD and axial velocity. From the SMD map at the left, the global SMD in the disclosed region is 16.58 μm. These ones are the only experimental results provided in non-reactive conditions, and hence a quantitative validation is not possible to this date.

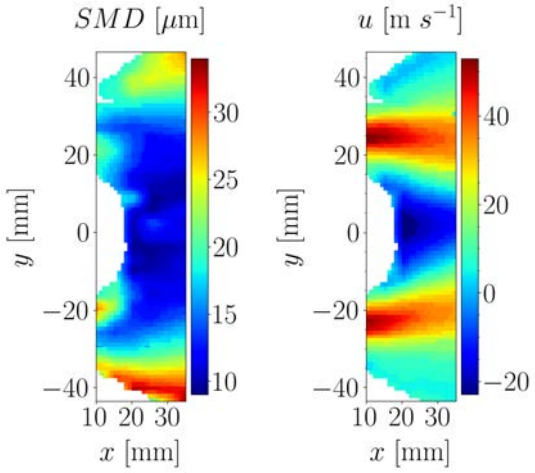

Figure 9.1: Experimental maps for for SMD and axial velocity u from Renaud (2015)

9.4 Boundary condition for liquid phase

9.4.1 Multipoint stage injection

For the multipoint stage, the SLI obtained from the resolved atomization simulations in Chapter 8 are used. Since the objective of this simulation is to prove that SLI can be used to perform dispersed-phase computations in a full multipoint injector, only the SLI obtained from the fine simulation with $\Delta x_{\text{min}} = 10$ μm at the location $x_c = 2$ mm is used. This injector is chosen since 1) it has been obtained with the finest interface resolution simulated and 2) it has been obtained at an axial location along the crossflow direction x_c where all the global spray mean magnitudes (SMD, velocities, deformation parameters) are converged with axial distance (see §8.5.2). This SLI is shown in Figure 8.33: these maps, without convergence-driven discretization, are injected as shown in the dispersed phase simulation. The flux spatial distribution in the SLI is scaled so

that the total mass flow rate injected in one multipoint hole is equal to the actual mass flow rate injected in the experimental configuration. Injected velocities are volume-weighted and RMS following a gaussian r velocity law. For secondary atomization, all the three models have been tested but none of them has shown to actually predict any breakup event throughout the simulations: the injected droplets from both multipoint and pilot stages are considered to already be in equilibrium with the surrounding gas.

For performing injection in the 10 multipoint holes, the SLI from the single liquid injector simulated are replicated in the remaining liquid injectors. The injectors location are translated and the vectorial magnitudes (crossflow normal direction, velocities) are rotated so that the crossflow local direction stays identical in all multipoint holes. Each single injector delivers a mass flow rate of $\dot{m}_{l,i} = 0.139$ g s^{-1} (equivalent to a flow rate of $Q_l = 185.3$ mm^3 s^{-1}), hence making a total liquid flux injected of $\dot{m}_l = 1.39$ g s^{-1} for the take-off phase as indicated in Table 9.1. A schematic view of the injectors location through which lagrangian droplets are introduced can be seen in Figure 9.8.

9.4.2 Pilot stage injection

The operating point simulated injects fuel through both a take-off stage (which has been modeled with the SLI) and a pilot stage. Since pilot stage has not been simulated with the methodology developed in this thesis, another approach must be employed. Given that the pilot of BIMER injects fuel following a hollow cone configuration, the LISA model introduced in §3.3.1 will be used (Guedot 2015). The input parameters for the LISA model to inject a hollow cone spray are summarized in Table 9.2. For the mean opening angle, a value $\theta_s = 30°$ is taken from experiments (Renaud 2015). Regarding the droplet's diameter, previous studies using lagrangian approaches on the same configuration have introduced directly droplets size distributions extracted from experimental data (Mesquita et al. 2018). In this case, since for the operating condition simulated there is not experimental size distributions available, droplets injected will have a constant diameter given by the following experimental correlation (Lefebvre & McDonell 2017):

$$SMD = 2.25\,(\sigma \dot{m}_f \mu_l)^{0.25}\,\rho_g^{-0.25}\,\Delta P^{-0.5} \tag{9.1}$$

where $\Delta P = 2.6$ MPa is the pressure drop in the pilot nozzle (Renaud 2015). Applying the previous correlation with the magnitudes given in Table 9.1 results in a diameter $SMD = 15$ μm imposed constant to the pilot cones particles. As for the multipoint injection, secondary atomization models were applied to particles introduced by the pilot stage without triggering any breakup effects. Hence, pilot droplets with a diameter of 15 μm will not be reduced into smaller children particles due to secondary breakup, and will be solely transported for cases without evaporation.

Table 9.2: LISA model setup for pilot injection

Parameter	Units	Value
Mass flow rate $\dot{m}$	g s^{-1}	0.25
Injector radius R_0	mm	0.125
Mean angle $\overline{\theta}_s$	°	30
SMD	μm	15

9.5 Boundary condition for gaseous phase

The perturbation effect of the liquid dense core, which is be directly accounted for by the lagrangian droplets, can also be modeled in BIMER. In this case, the direct prescription of a perturbed gaseous inlet in a reduced domain as performed in the classical JICF configuration (§6.4.1) is not performed due to the complex geometrical features of the swirl injector. Therefore, only the ALM methodology (§4.5) is applied for this purpose. In a first step, the input parameters to the model are taken from the results of the resolved atomization simulation DX10: dense core topology from the results shown in Figure 8.24 and net force from Table 8.6. These parameters are referred as the initial ones in Table 9.3. As for the ALM model applied to the traditional JICF in §6.4.1, these initial parameters do not capture the actual momentum exchange between the gas and the liquid in the resolved simulation, and are hence tuned to find a better match between the turbulent gaseous structures in the resolved and dispersed-phase computations. Indeed, the initial actuator was found to not create any perturbations, yielding a gaseous field identical to the unperturbed case. Therefore, in this

section only the results obtained with the final actuator are reported. The parameters used for this model are summarized in Table 9.3.

Table 9.3: Parameters of an actuator representing the BIMER dense core

Parameter	Units	Initial	Final
x_b	mm	0.34	0.34
z_b	mm	1.43	0.78
$\lvert\mathbf{F}_{\mathrm{DC}}\rvert$	mN	0.25	3

The mean axial velocity fields at plane $y_c = 0$ mm (using the crossflow local coordinate system from Figure 8.2) are shown in Figure 9.2, where the resolved case DX10, unperturbed and final ALM are displayed. The ALM has the potential to create perturbation in the gaseous phase that are not present when no perturbations are added: in this case, the deceleration close to the wall creates a region with negative axial velocity, which looks like a flat recirculation bubble which attaches at the wall at axial locations far upstream and downstream the liquid injection nozzle when compared to the resolved case. The vertical recirculation bubble from the resolved simulations downstream the jet cannot be retrieved by the ALM configuration shown. Downstream the sketched cylinder from ALM, the gaseous field is disturbed up to several diameters downstream the actuator, and streamlines are slightly deviated vertically with respect to the unperturbed case but eventually return to an axial orientation.

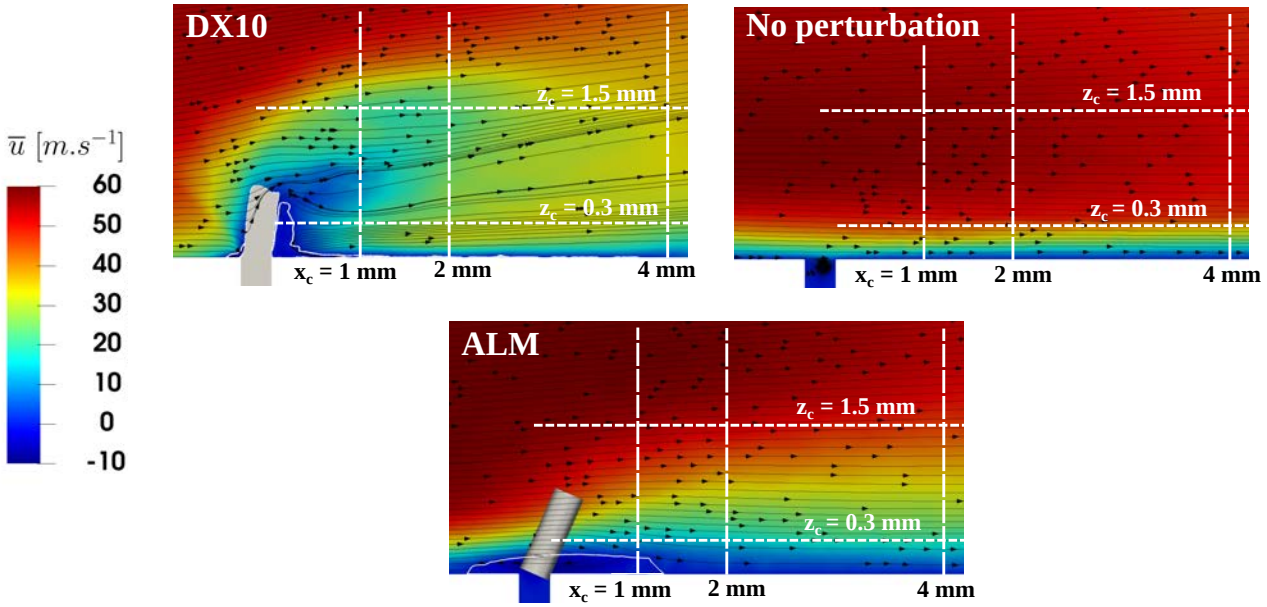

Figure 9.2: Mean axial velocity at plane $y = 0$ mm for resolved DX10, gaseous unperturbed and gaseous ALM cases. The white solid line indicates the contour $\overline{u} = 0$ which delimites the recirculation bubble. The grey area indicates the mean liquid region, identifed as $\overline{\psi} > 0.5$

Mean velocity profiles along lines $z_c = 0.3, 1.5$ mm plotted in Figure 9.3 show that the ALM match close to the wall does not resemble the resolved profiles from $x_c = 2$ to $x_c = 5$ mm, but it gets closer further downstream. The ALM profile further from the wall shows even larger differences: for $x_c < 4$ mm the velocity is similar to the unperturbed case, indicating that ALM has not a big effect in this region, but for $x_c > 4$ mm the actuator perturbations overestimate both the unperturbed and resolved cases, yielding unphysical results. Such overestimation by ALM is due to the deviation of the streamlines: in the bottom part of the actuator, flow deviates towards the wall and decelerates, while in its upper part the stronger forces bend the streamlines upwards. Due to mass conservation, axial velocity increases. The velocity profiles along

lines $x_c = 1, 2, 4$ mm from Figure 9.4 also show a wrong prediction of the gaseous perturbations by ALM. Since droplets are injected at $x_c = 2$ mm, the deviations observed could have strong effects in the particles's transport due to momentum transfer. Such deviations could also affect the secondary breakup of the particles in case it would occur (which could be the case in other operating conditions not studied in this thesis), as it was demonstrated in §6.4.

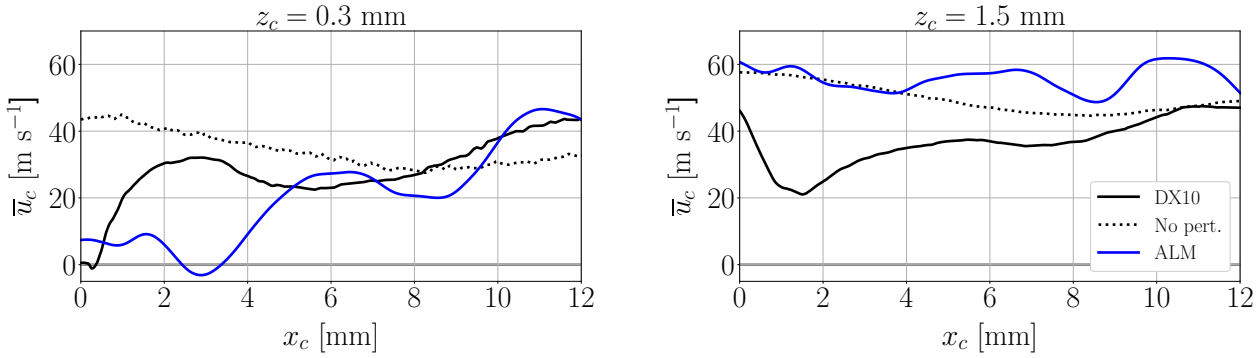

Figure 9.3: Mean axial velocity evolution along axial coordinate at locations $z_c = 0.3, 1.5$ mm at plane $y_c = 0$ (lines of Figure 8.12)

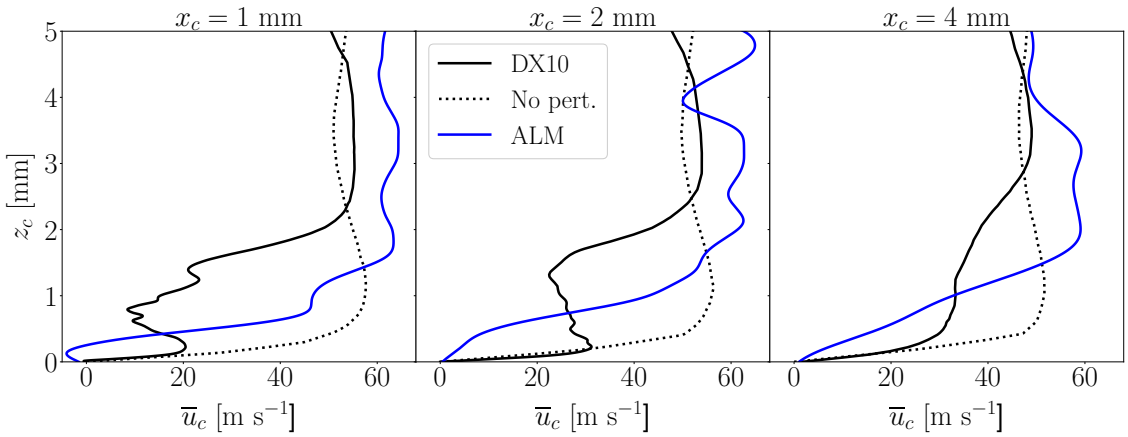

Figure 9.4: Mean axial velocity evolution along vertical coordinate at $x_c = 1, 2, 4$ mm locations of plane $y = 0$ (lines of Figure 8.12)

The planes perpendicular to crossflow direction $x_c = 1.5, 3$ mm are also analyzed in Figure 9.5. As discussed in Chapter 8, the resolved simulations capture vortices which are not symmetrical along the $y_c = 0$ plane due to the presence of a swirl component in the gas. The unperturbed case actually shows strong single vortices which are caused by this swirl component, which demonstrates how swirl can affect the gaseous flow. ALM seems to affect the location and strength of the vortex at $x_c = 1.5$ mm, while it does not have a relevant effect on the one at $x_c = 3$ mm. In any case the actuator can retrieve the CVPs which are seen in the resolved simulation (at plane $x_c = 1.5$ mm, while further downstream a single vortex is captured). On the other hand, the ALM affects the gaseous field by creating a deceleration region, which at $x_c = 1.5$ mm also reflects the recirculation bubble. It is interesting to note that the recirculation bubble does not reach plane $y_c = 0$, which agrees with Figure 9.2 as recirculation in this plane attaches above this axial location. This indicates that the recirculation bubble is not symmetrical with respect to axis $y_c = 0$, which again is attributed to the presence of swirl. The fact that swirl has such a strong effect in this operating point (it is worth reminding that the swirl number is $S_w = 1$, as discussed in §7.5.1) might then create a lateral force in the BIMER dense core which is not modeled by the ALM methodology proposed in this thesis. The velocity profiles along lines $z_c = 0.3, 1.5$ mm at the iso-x_c planes from Figure 9.6 show that effectively the ALM cannot capture the perturbations along the lateral directions: close to the wall the mean velocity is

underestimated, and far from it it is overestimated for $y_c > 0$ mm. For a proper modeling of the gaseous phase perturbations within BIMER and other swirl injectors, ALM should then be extended to account for three-dimensional swirl effects.

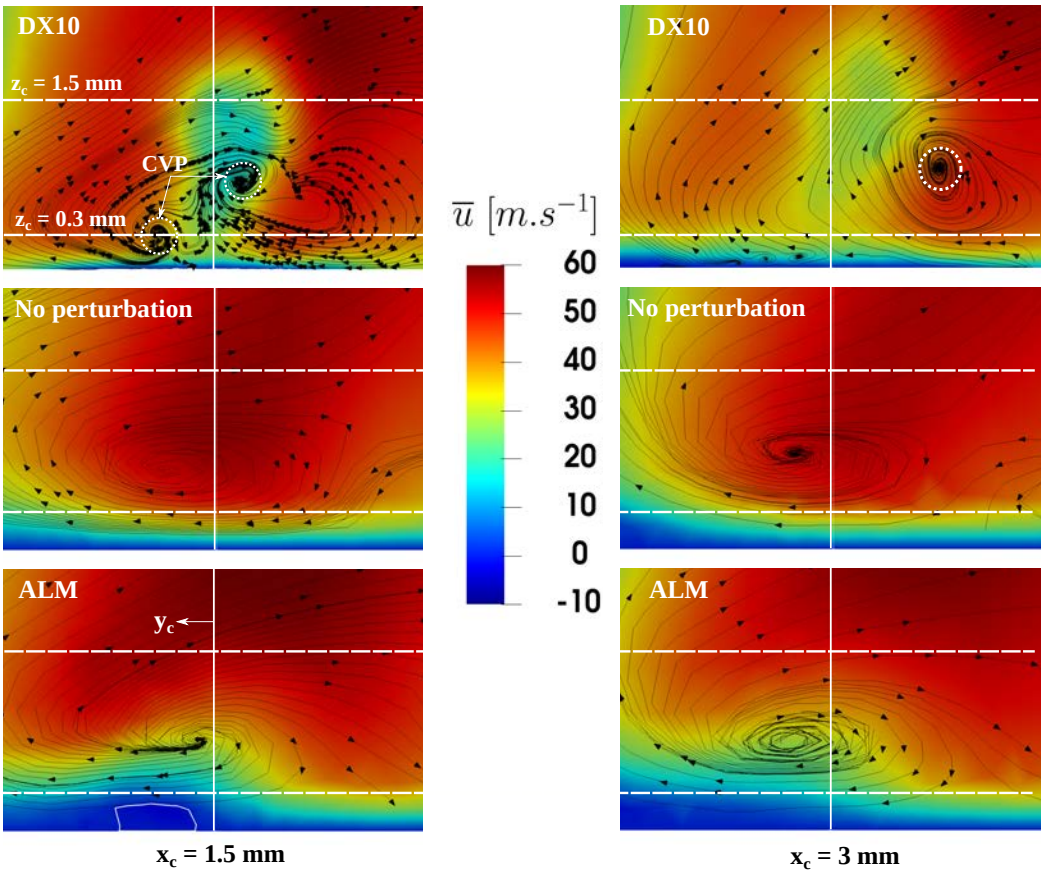

Figure 9.5: Mean axial velocity at planes $x_c = 1.5, 3$ mm for resolved DX10, gaseous unperturbed and gaseous ALM cases. The vertical, white line corresponds to plane $y_c = 0$

The perturbations induced by ALM discussed previously have only been analyzed for the gaseous field at the surroundings of one liquid injection nozzle from the multipoint stage. Since in BIMER there are 10 points for this stage, perturbations also need to be added in those. This can be done by adding actuator body forces in the crossflow local coordinate systems at each point, and then transforming the coordinates and forces directions into the global coordinate system. In this way 10 actuators will be located, one per injection point, each one imposing forces with identical magnitude but different directions due to the different locations of the points around the take-off stage. An example of these multiple perturbations is shown in Figure 9.7, where the mean velocity magnitude in planes $y_c = 0$ at two different injection points are shown.

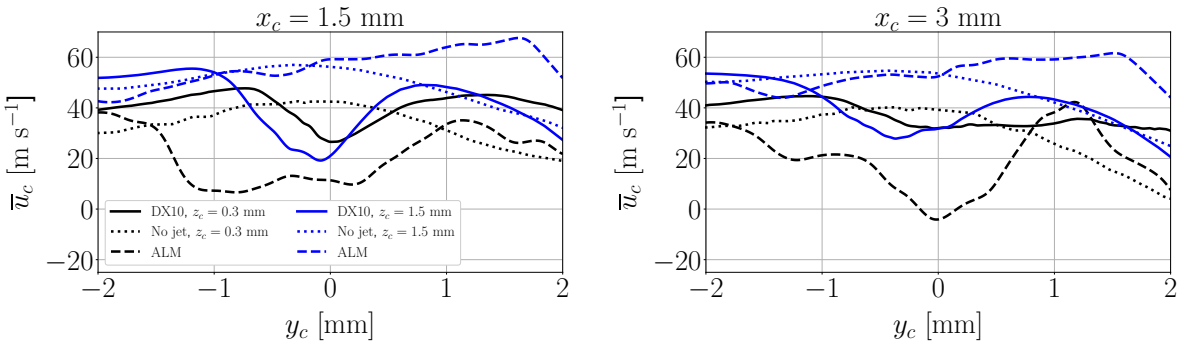

Figure 9.6: Mean axial velocity evolution along lateral coordinate at z_c lines of Figure 8.17. Dotted circles englobe gaseous vortical structures

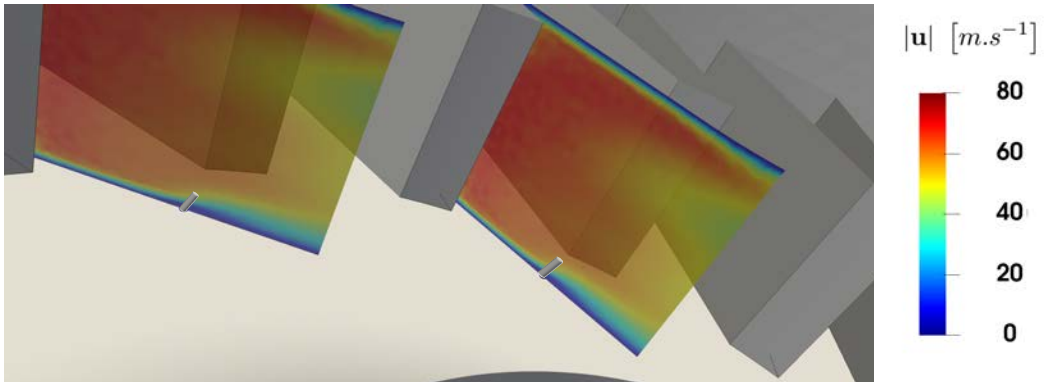

Figure 9.7: Application of the ALM model to two adjacent injectos in BIMER

9.6 Simulations and results

Three dispersed-phase simulations are performed for the BIMER configuration. All of them use the same boundary conditions for the liquid phases in the take-off (SLI model) and the pilot (LISA model) stages. They differ in the inclusion of the perturbation effect in the gaseous phase through ALM and the consideration of evaporation. For the simulation with evaporation, the full domain is preheated to $T_g = 433$ K as in the experiments, and droplets are then injected at a temperature $T_l = 293$ K. The computations performed are summarized in Table 9.4, where a total of three simulations are reported. A baseline simulation is performed without neither ALM nor evaporation. Then, both ALM and evaporation contributions are studied separately in two distinct simulations. A simulation with both ALM and evaporation was not performed in this thesis since the different numerics of both contributions were not coupled, and is left for future work.

Table 9.4: Dispersed-phase simulations performed for BIMER

Case	ALM	Evaporation
Baseline	No	No
ALM	Yes	No
Evap	No	Yes

Characteristic liquid times

As in the resolved atomization simulations of one multipoint injector, characteristic liquid times can be defined for the liquid phase in the dispersed-phase computations. The interest here is to link the physical simulation time to a characteristic time scale related to the magnitudes to be studied. In this case, these magnitudes are the SMD and droplets velocities in the spatial region downstream the combustion chamber where experimental PDA results have been obtained (Figure 9.1). Since this region spans up to a downstream coordinate $x = 35$ mm, droplets characteristics time will be estimated as the time in which the first particle reaches this axial location: $\tau_{\mathrm{dr}_{x=35\mathrm{mm}}}$. Therefore, the dimensionless simulated time t' is defined according to Eq. (9.2):

$$t' = t/\tau_{\mathrm{dr}_{x=35\mathrm{mm}}} \tag{9.2}$$

Table 9.5. summarized the characteristic times obtained in the simulations performed. As observed in this table, the characteristic times chosen are of the order of the gaseous swirl time scale τ_{swirl} for this operating point (Table 7.5) while they differ of one order of magnitude with respect to the liquid characteristic times of the resolved atomization simulations (Table 8.3).

Table 9.5: Characteristic times for droplets to reach location $x = 35$ mm in the pilot and take-off stages

Case	$\tau_{\mathrm{dr}_{\mathrm{pilot}}}$ [ms]	$\tau_{\mathrm{dr}_{\mathrm{takeoff}}}$ [ms]
Baseline	1.65	2.45
ALM	1.52	2.32
Evap	1.48	2.25

9.6.1 Lagrangian field establishment

The three simulations summarized in Table 9.4 are performed with identical liquid dispersed-phase injection boundary conditions and with their corresponding boundary conditions for the gaseous phase. In all cases, liquid has been injected into a established single-phase gaseous solution which was previously run for $2\tau_{\mathrm{conv}}$, being $\tau_{\mathrm{conv}} = 37.6$ ms the convection time scale described in Chapter 7. Running for such time corresponds to $\sim 8\tau_{\mathrm{swirl}}$, which ensures a established gaseous field within the injector for all simulations.

The establishment of the dispersed-phase liquid field is shown in Figure 9.8 for the Baseline case. Time has been expressed non-dimensionally with Eq. (5.2), where the inertia timescale $\tau_{\mathrm{in}} = d_{\mathrm{inj}}/u_l = 115.38$ μs has been used. The figures show droplets being injected through all the SLI located at the vicinity of each multi-point hole and through the pilot stage. Particles delivered through the take-off have different sizes due to the poly-disperse nature of SLI, which injects droplets from 20 to 40 μm of diameter (see Figure 8.33). These particles travel within the injector in the azimuthal direction, transported by the air swirl, and eventually are convected through the diffuser towards the combustion chamber. Simultaneously, the pilot stage introduces a mono-disperse spray with an imposed size of 15 μm with a hollow-cone type injection. The hollow cone shows then an oscillatory behaviour due to the interaction among the rotation of the air that arrives from the pilot swirler (schematically shown in Figure 7.2) and an azimuthal component imposed to the particles by the LISA model (Eq. 3.16). Pilot particles are then directly transported downstream the diffuser and arrive in the plenum before the droplets injected by SLI, as reflected by the characteristic times of Figure 9.5.

Figure 9.9. shows a lateral view of established sprays for the three simulations performed. The experimental region for the SMD and axial velocity maps is outlined by the black rectangle. The first row shows the full spray: once the spray is established, particles from both pilot and multipoint stages are found in the diffuser and further downstream. The baseline and ALM cases do not show any significant differences. The evaporation simulation, on the other hand, reveals that smaller particles are already found within the diffuser, indicating that mass transfer from the SLI particles starts to take place prior being introduced into the diffuser. Overall, all cases show a good topology of the particles field within the injector and at the upper part of the plenum, similar to other particles fields performed in other multipoint configurations with dispersed-phase simulations (Jaegle et al. 2011).

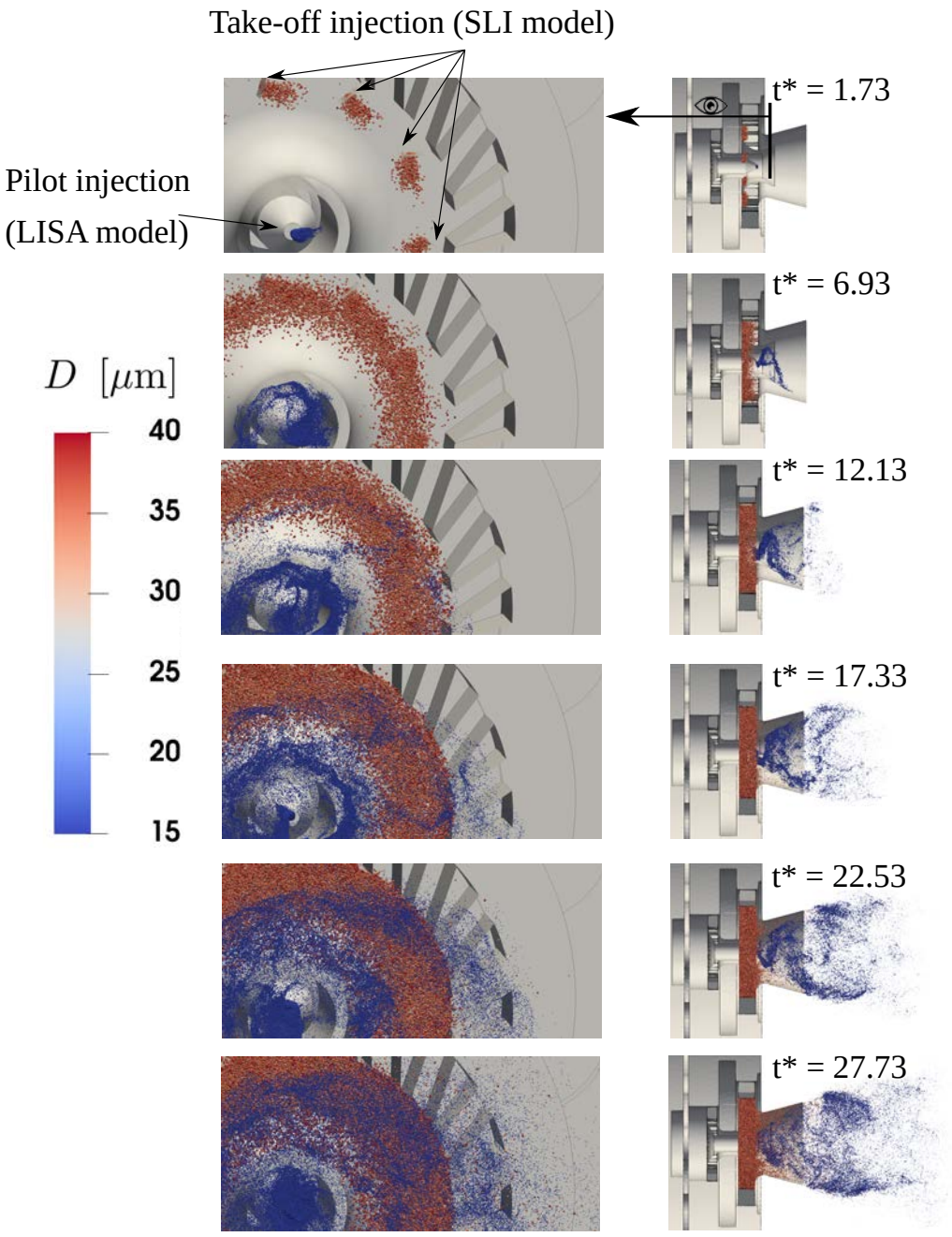

Figure 9.8: Several instants of liquid fuel injection through both pilot and take-off stages for baseline case. Droplets are scaled by 10 times their diameter for visualization purposes

Particles within a slab of 1 mm thickness centered at plane $z = 0$ are also shown in Figure 9.9. The full spray and the contribution of each separate phase are visualized. The pilot particles open with an angle corresponding to the imposed one of 30 ° from the LISA model. Such particles are highly concentrated within the slab close to the injection point and then show empty pockets further downstream: pilot droplets are injected at a low axial velocity and with an imposed rotational component, then they are convected and exchange momentum with the swirl, relaxing towards the gaseous velocity which also has both an axial and an azimuthal component. Therefore, the observed pockets are caused by particles leaving the slab due to the rotational movement; these particles will later enter the slab further downstream, as visualized in the figure. The multipoint particles enter the diffuser and the vicinity of the walls, with a high number of particles filming along the diffuser walls in all cases. There are no particles injected through the multipoint found within the central region of the spray downstream the diffuser, as it is shown later through the maps in Figure 9.11.

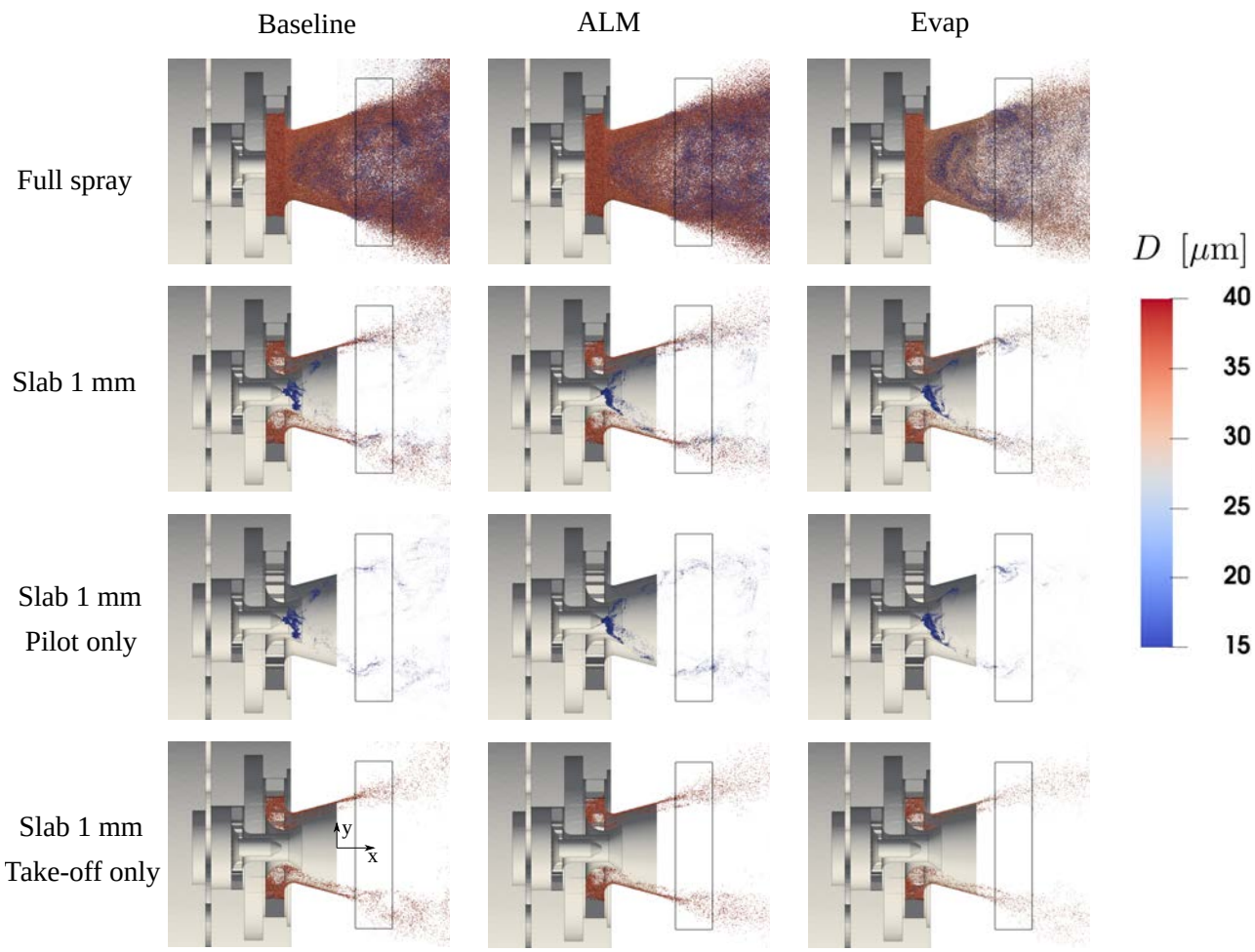

Figure 9.9: Instantaneous views with a established spray for the three disperse-phase computations. In the first row the full lagrangian field is shown, while the second row displays the spray contained within a slab of 1 mm thickness centered at the center of the injector. The third and fourth rows show the droplets from the pilot and take-off stages respectively, contained in the 1 mm thick slab.

9.6.2 Qualitative results and experimental comparison

Simulations can be compared with experiments by sampling lagrangian droplets crossing the region outlined in Figure 9.8, which corresponds to the area from the experimental results shown in Figure 9.1. SMD and droplets axial velocities maps are given in Figure 9.10. In general, the computations capture the topology of the fields accurately and show symmetry with respect to axis $y = 0$. The effect of the evaporation is clearly noticed by the lower values of SMD found with respect to the other computations, approaching the experimental values qualitatively. Numerical SMD maps show a central region with low sizes produced by the pilot stage, with larger droplets than in the experiments. The baseline and ALM case show similar sizes, while the evaporation simulation captures smaller diameters which are closer to the experimental values. The experiments show a pocket of empty droplets with a circular shape with center at ($x = 10$ mm,$y = 0$) and a radius of ~ 20 mm that is not present in the simulations, since these show droplets produced by the hollow cone; and two regions of local high SMDs at $y = \pm 25$ mm that are quantitatively captured by the simulations, even if their size is slightly underestimated and the axial extension of this area is overestimated in the computations. The opening angle of the spray is properly captured by the simulations, although this angle is determined by the presence of the diffuser as Figure 9.8 shows droplets attaching and filming along the diffuser walls. Diameters at the outer part of the spray show larger values than at the center as in the experiments, yet their magnitude is generally overestimated. This outer part, also captured by the experiments, is characterized by a gradient of SMD from lower (green colors) to larger (red colors) values along the vertical direction. The computations predict its beginning closer to the spray center than in the

experiments, and overestimate the SMD values at the edges for both the baseline and ALM cases. The evaporation case shows good experimental match for SMD values in this region, except for the outer part at side $y > 0$ (yet this part is symmetrical in the computations, which is expected for a symmetrical swirl case as BIMER, but is asymmetrical in the experiments).

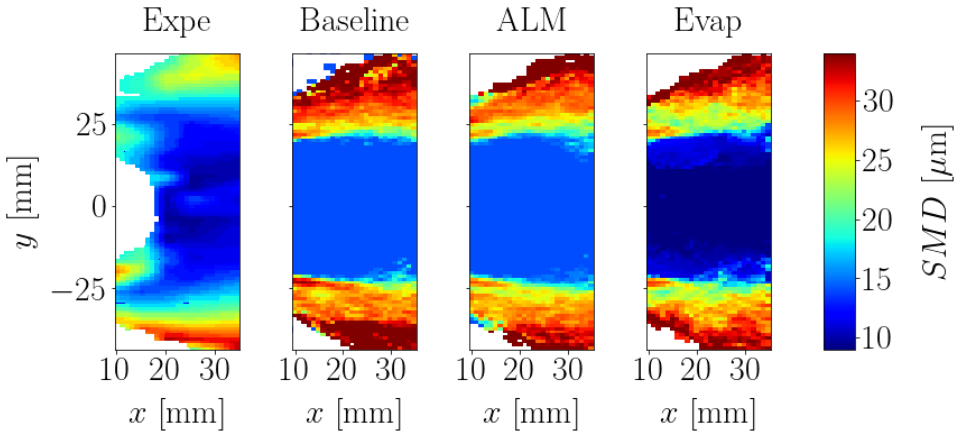

(a) SMD maps

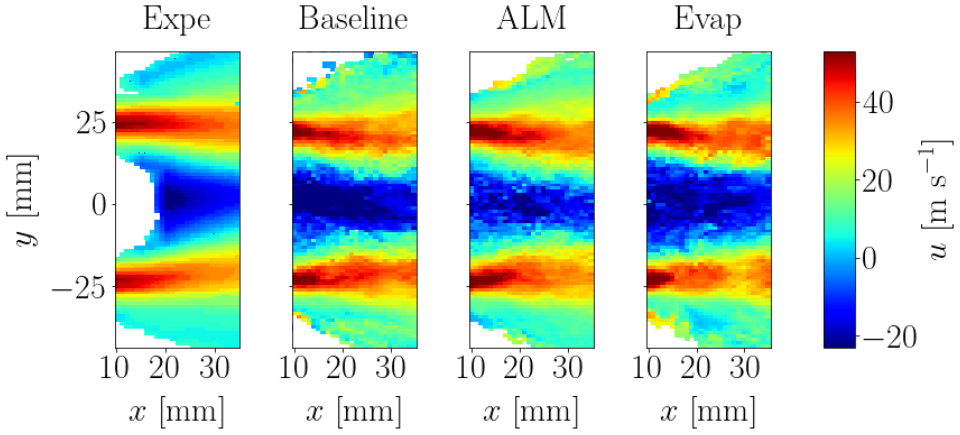

(b) Mean axial velocity maps

Figure 9.10: Qualitative experimental validation in the region enclosed in Figure 9.8. SMD and mean velocity fields from experiments by Renaud (2015) and the three simulations performed

From the analysis of Figure 9.10, it can be generally said that the topology of the lagrangian field in terms of SMD and axial velocity is, despite a few minor features, quite close to the experimental one. It is now of interest to look at the contributions of the droplets from each stage to the sampled sprays, which is done in Figure 9.11. The spatial distribution of both stages is clear from the figures: the pilot spray extends through all the region with a hollow cone shape, while the take-off spray is concentrated at the edges of this hollow cone. No multipoint droplets are then present at the center of the spatial domain, agreeing with the observations of Figure 9.9 where the take-off droplets from SLI stick to the outer part of the diffuser, near the walls. Comparing the baseline and ALM cases shows no differences among those, hence confirming that ALM has no influence in the spray entering the chamber in this BIMER's operating condition.

The contribution of each stage to the full spray can be elucidated in Figure 9.11. In all cases, the velocity field from the pilot spray has a very similar topology to the full one, with exceptions at the edges due to the contribution of the take-off stage. However, this influence of the take-off to the velocity is limited. The opposite occurs, on the other hand, for the SMD: the pilot shows low values (constant for the baseline and ALM simulations, varying for the evaporation case) for all the spatial region, while the take-off shows larger ones: hence in the regions where pilot and take-off coexist, the full spray reveals an average size among both.

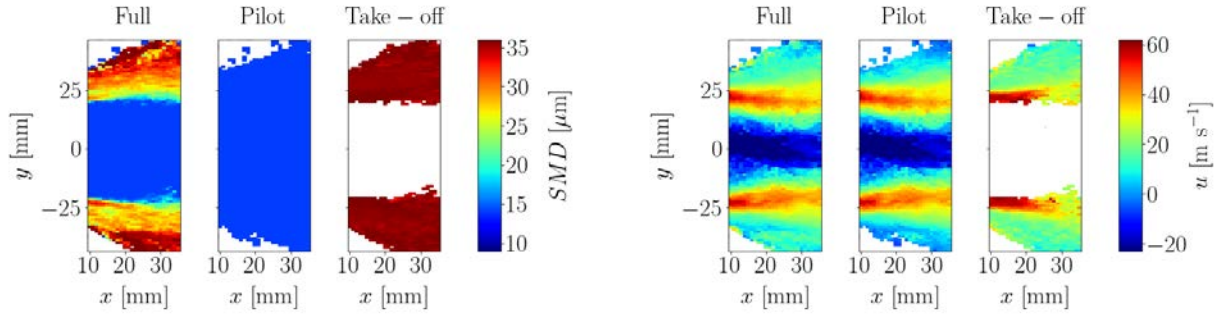

(a) Baseline case

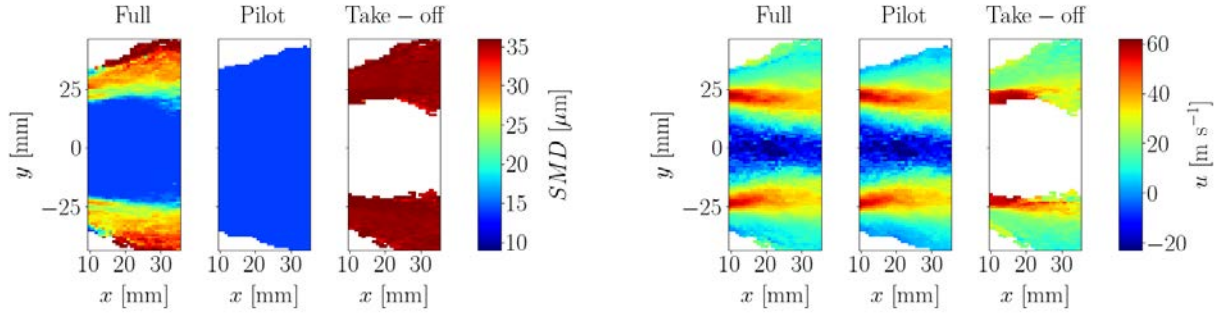

(b) ALM case

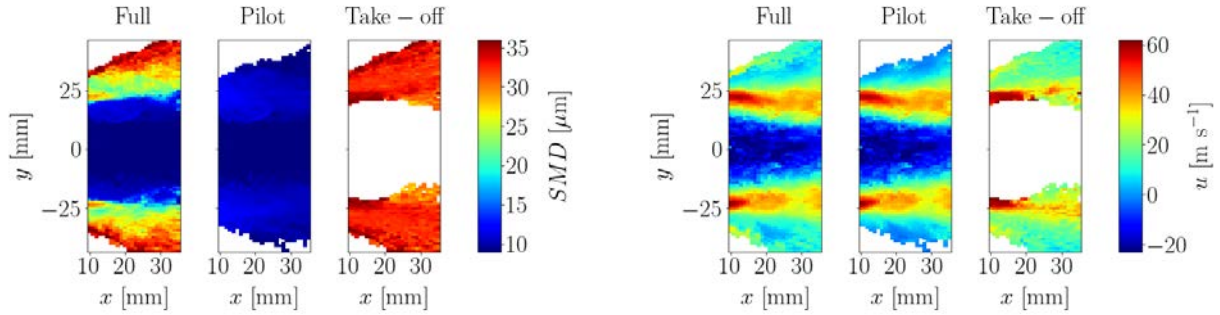

(c) Evap case

Figure 9.11: Contribution of pilot and take-off stages to the resulting spray in the experimental validation region outlined in Figure 9.8

The calculated global SMD of the droplet contained within the experimental region are summarized in Table 9.6. The first SMD shown corresponds to the full case (pilot + take-off sprays), while the global SMD for each separate phase in the computations is also reported. The error with respect to the experiments ε_{SMD} has been calculated with Eq. (6.8), with $SMD_{\text{expe}} = 16.58$ μm. Only the deviation in the SMD of the full spray can be quantified, since from the experimental results the SMDs for each separate phase cannot be obtained. The results show that the baseline and ALM cases provide similar values larger than the experiments, with errors of the order of 30 %. The SMDs for these cases are practically identical for the full, pilot and take-off sprays. Indeed, the pilot spray yields the value prescribed for the injected droplets of 15 μm since these droplets do not change their size due to the absence of secondary atomization and evaporation. In combination with the previous analysis, it can then be concluded that, in this BIMER's operating point:

- The actuator model tested **has not a significant influence in the spray**, even if it perturbs the gaseous phase around the injection nozzles of the take-off stage.
- Such lack of influence is due to the **nonexistent secondary atomization**, which was not present whatsoever in any BIMER simulation. As Chapter 6 showed that secondary atomization was strongly affected by ALM, in BIMER this perturbation model has not a relevant effect due to the absence of breakup.

Table 9.6: SMDs obtained compared to experimental one

Case	SMD [μm]	ε_{SMD} [%]	SMD_{pilot} [μm]	SMD_{takeoff} [μm]
Experiments	16.58	-	-	-
Baseline	21.41	29.13	15.00	35.81
ALM	21.17	27.68	15.00	35.71
Evap	17.53	5.73	9.41	32.67

More relevant results are obtained when including evaporation. As Table 9.6 shows, addition of evaporation reduces the pilot SMD from 15 to 9.41 μm, and the corresponding one for the take-off stage from 35.81 to 32.67 μm. In consequence, the global SMD obtained is 17.53 μm which supposses an error of 5.73 %, showing a very good experimental agreement. However, it can be observed from the SMD maps of Figure 9.10 that the evaporation case seems to underestimate the SMD in all the pilot region and overestimate it in the take-off one: then, both effects compensate and the resulting global SMD for the whole spray shows a value in between which agrees with the experimental one. Nevertheless, overall it can be seen that the spray fields look much closer to experiments when including evaporation. Therefore, including evaporation physics into the dispersed-phase simulation contributed to improve the results of the simulations, and demonstrated the need to properly account for heat transfer physics in this configuration relevant to industrial burners.

The effect of evaporation in both pilot and take-off phases separately can be further analyzed through the droplets histograms from the spray contained within the experimental region, in Figure 9.12. The take-off and pilot stages can be directly distinguished by the difference in the range of droplets sizes obtained: the largest pilot droplets have diameters of 15 μm, while the smallest particles produced by the take-off are slightly below 30 μm. The spray for the baseline case shows a single diameter for pilot at 15 μm, and a distribution for the take-off ranging from $\sim$ 35m to $\sim$ 42 μm. Adding evaporation shifts each histogram to the left. The pilot distribution shows then a polydisperse spray negatively skewed, with the largest diameters at 14 μm and the smallest ones close at 1 μm, while the take-off stage moves towards a lognormal-like distribution but without large differences among density values.

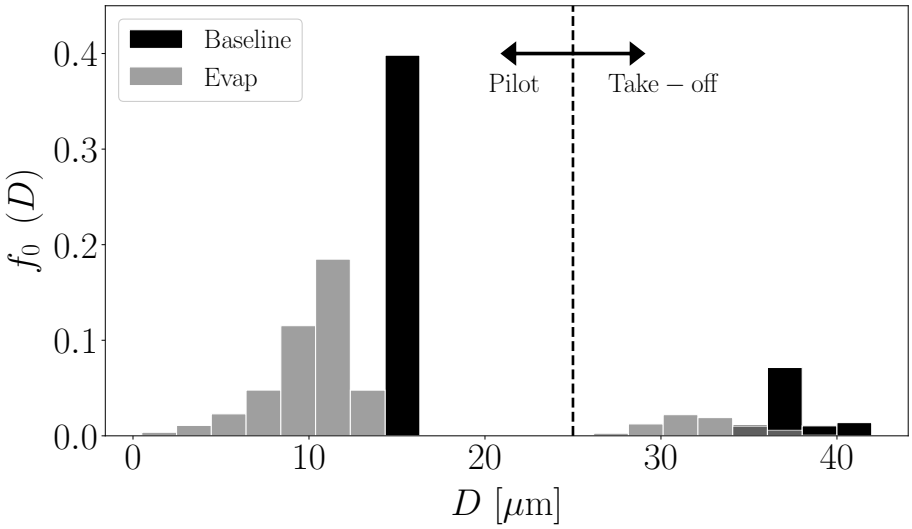

Figure 9.12: Histograms of droplets sizes from Baseline and Evap simulations

In conclusion, the addition of evaporation, which can be accounted for in dispersed-phase simulations, is necessary to accurately capture the dispersed-phase within the plenum in BIMER due to the high ambient temperature. In future works, it would be interesting to study the influence of other evaporation models, such as the one by Abramzon & Sirignano (1989), on the results here presented.

It is not known a priori how evaporation would influence the droplets sizes in the resolved atomization simulations: if it had a relevant effect, this could affect the SLIs obtained and the subsequent results of the dispersed-phase simulations. Nevertheless, the time-scales of the droplets convection, in Tables 8.3 and 9.5 for the resolved and dispersed-phase simulations respectively, show that a resolved droplet takes 0.354 ms

to reach the sampling plane located 2 mm away from the take-off injection nozzle, and a lagrangian droplet needs 2.25 ms (in the evaporation case) to reach the axial location $x = 35$ mm in the plenum. Therefore, in the dispersed case droplets travel for more than 35 mm (without accounting for the path followed by the droplet within the injector due to the air swirl) after injection and see a reduction in SMD from 35.81 to 32.67, while in the resolved simulations the droplet travels only for less than 2 mm (since actually the droplet is first atomized from the dense core, which could hardly evaporate due to its large volume and low surface-to-volume ratio). Therefore, it is expected that evaporation would not have enough time to act and it would not affect the SLIs from the resolved atomization simulation, providing robustness to the results presented in this chapter.

9.7 Conclusions

This chapter has shown the application of SLI for dispersed liquid phase in the academic multipoint injector BIMER. The methodology has been applied to the take-off stage by using the SLI constructued from the resolved atomization simulations of Chapter 8. The SLI obtained from one injection hole has been extrapolated to the rest of the multipoint to prescribe liquid boundary conditions in all the take-off stage. This has been possible thanks to the symmetry of the multipoint injector. The pilot stage, which produces a hollow cone-type injection, has been approximated with the LISA model. For the gaseous phase, the ALM methodology has been applied to model the perturbation of the BIMER dense core in the aerodynamic field. The proposed actuator does not capture accurately the perturbed gaseous field from the resolved simulations: it is thought that the ALM methodology does not work properly in a complex aerodynamic field like BIMER. Suggested further work regarding the ALM methodology would include the addition of forces in the lateral direction, the addition of frequential effects to better retrieve the influence of the dense core dynamics observed at the resolved simulations, and also a better estimate of ALM parameters through multiparameter optimization rather than in-hand tuning.

Dispersed-phase simulations have then been settled for the operating point considered. The multipoint stage has been modeled with the SLIs obtained from the fine simulation, while in the pilot stage the LISA model has been used due to the absence of SLI for the hollow cone injection. Three simulations have been performed: one with evaporation and without perturbance of the gaseous field; and two without evaporation, considering the ALM disturbances in one but neglecting them in the other. Secondary atomization did not take place in any case, hence the droplets were only transported in the cases without evaporation and the injected sizes were maintained throughout the simulation. The ALM was shown not to have any effect on the spray topology in the plenum and in the experimental comparison, probably due to the absence of secondary breakup, since in Chapter 6 it was found that the gaseous phase boundary conditions played a fundamental role in particles breakup due to their influence in the relative velocities. Considering evaporation modified the spray maps of SMD, making it closer to experimental results, and reduced the resulting global SMD of the spray, also approaching it to the experimental results: a deviation in SMD of 30 % with experiments was obtained for the baseline and ALM cases, while when adding evaporation this deviation was substantially reduced to 5 %. This demonstrates the importance of evaporation in BIMER and, more importantly, demonstrates the capabilities of SLI to initialize dispersed-phase computations in configurations similar to industrial multipoint burners. Further work would require to extend the SLI methodology for including the modeling of hollow cone sprays from resolved simulations, and to perform reactive computations of BIMER.

Part IV

Conclusions and perspectives

Chapter 10

Conclusions and perspectives

Conclusions

In this dissertation, a novel methodology to model liquid fuel injection in multi-staged systems has been proposed. In particular, the focus has been placed on liquid jet-in-crossflow (JICF) atomizers. These injection models, named Smart Lagrangian Injectors (SLI), are able to first learn spray features from resolved atomization simulations, and then to process them for prescribing the liquid phase in dispersed-phase computations. In addition, perturbation effects in the gas phase created by the liquid dense core and secondary breakup of lagrangian particles are also accounted for. Two configurations have been studied: an academic JICF which served as the validation case, and a multi-staged injector named BIMER as the application case, which is a configuration more representative of industrial injection systems. The most significant results from each case are summarized next.

Kerosene jet in crossflow

The models have been developed and validated in an academic, non-reactive kerosene JICF studied experimentally by Becker & Hassa (2002). Resolved atomization simulations were performed with the software YALES2. Firstly, the physical behaviour of the jet was studied. Simulations could correctly capture the two classical breakup modes (column and surface breakup) observed experimentally in liquid JICF. The jet penetration was quantified and compared to an experimental correlation, showing good agreement near the injection nozzle (dense core region) and deviations further downstream (dispersed spray region). Secondly, the dense core topology and the spray features were postprocessed to build the SLI model. The former estimates the liquid core breakup point coordinates, width and net force applied. These parameters serve as inputs to the Actuator Line Method (ALM) for modeling the dense core perturbation effect in dispersed-phase simulations. Finally, the spray was analyzed by sampling particles crossing planes perpendicular to the crossflow direction. These sprays were then in-plane spatially discretized and represented through local maps of droplets sizes, velocities and fluxes. Such spatially distributed sprays conform the liquid injectors to prescribe lagrangian droplets in dispersed-phase simulations.

In a second step, lagrangian simulations were performed with SLI. Firstly, two methodologies for modeling the dense core disturbance effect in the gaseous field were assessed: ALM and the prescription of gaseous statistics extracted from the resolved computations into a reduced domain. The former captured relevant flow features such as recirculation and deceleration regions, although it could not retrieve all the characteristics of the resolved flow field. The latter could better capture the gas flow features, yet this methodology cannot be generalized to more complex geometries. Dispersed-phase computations on a high Weber operating point showed that the second methodology yielded droplets sizes closer to experiments, hence it was retrieve for the subsequent studies. The effect of the secondary atomization model was then studied, with the Gorokhovski's stochastic model showing a better performance over the TAB and ETAB ones. Finally, the different liquid phase parameters were analyzed. The most influential ones were the resolution of resolved simulations and the injection velocities. The lagrangian computations performed could properly capture experimental spray features such as the flux profiles, maximum flux location and the ballistic behaviour. On the other hand, droplets sizes were always underestimated, with an experimental deviation of 37 % for the global SMD. Computations on a lower Weber number operating conditions reduced these deviations to 20 %. These results

indicate that secondary breakup is the most influential mechanism when SLI is applied to this configuration, and that size underprediction arises due to a misprediction of relative velocities. This hypothesis was verified by deactivating secondary breakup in a spatial region after droplet injection. Droplets sizes increased, proving the hypothesis to be true, although sprays showed a counter-ballistic spray behaviour which is unphysical. Further work should be devoted to improve prediction of relative velocities in dispersed-phase simulations. Nevertheless, these computations have shown the capability of SLI to prescribe liquid boundary conditions in dispersed-phase simulations of JICF atomizers, paving the way to a realistic modeling of liquid injection in multi-staged injectors relevant to gas turbine combustion systems.

Swirled injector BIMER

In the last part of this thesis, the SLI strategy was applied to the take-off stage of the BIMER buner, tested experimentally by Renaud (2015) at EM2C laboratory. Resolved atomization simulations were performed with two interface resolutions on a single injection point. The liquid jets captured the column and surface breakup modes often observed in liquid JICF. Vertical trajectories showed good agreement with an applicable experimental correlation in the near-nozzle region. Sprays were also analyzed in planes perpendicular to the crossflow, revealing that droplet size convergence is reached for interface resolution (smallest droplets captured have a diameter of 30 μm) and for axial distance (constant SMD and invariant histograms are obtained at 2 mm downstream the injection nozzle, indicating complete atomization). These sprays were then spatially discretized to yield SLI for liquid fuel injection in lagrangian computations.

Dispersed-phase computations were finally performed for the full multi-staged injector. The pilot stage was simulated with the hollow-cone model FIM-UR. The take-off stage was modeled with the SLI built from the resolved atomization simulations. Even if only one liquid injection point was resolved, the full take-off stage (composed of 10 injectors) could be simulated by applying the same SLI to each injector. Three lagrangian computations were performed: one with ALM to model the gaseous phase perturbations, another one where evaporation physics were accounted, and another one without any of both. It was found that secondary atomization did not act in any computation, since all injected droplets were in equilibrium with the surrounding gas. The ALM simulation showed that the actuator proposed could not retrieve the complex gaseous field from the resolved simulations. Nevertheless, comparison with experimental results showed no difference when ALM was included or not, which is due to the absence of secondary atomization. These two simulations showed good experimental agreement qualitatively on the SMD and axial velocity maps, and quantitatively on the global SMD, with differences slightly lower than 30 %. Adding evaporation physics improved results, reducing the SMD deviation up to 5 %. These simulations are, to the author's knowledge, the first lagrangian computations of a complete multi-staged injector where the full multipoint stage is addressed through a realistic injection model. The results presented hence demonstrate the capability of the SLI model to simulate multi-staged systems. Further works should apply these models to more operating points for investigating its range of application, and to compare with more experimental data on sprays when available for further validation.

Perspectives

This thesis has contributed to the modeling of liquid injection in multi-staged fuel injectors. For this purpose, the Smart Lagrangian Injectors (SLI) methodology has been developed and applied. While showing its capability for learning the spray behaviour from resolved simulations and prescribing boundary conditions for dispersed-phase simulations, further efforts should be devoted to improve its reliability.

In first place, the different modeling blocks from SLI should be addressed to improve the accuracy of dispersed-phase computations. The Actuator Line Method (ALM) could be extended to consider complex geometries and net force laws more representative of the jet dense core, and to include unsteady effects for replicating the dense core dynamic behaviour. Obtention of ALM parameters could also be improved through the employment of multiparameter optimization methods or machine learning tools, such as neural networks. Regarding the liquid injection parameters, more realistic physics could be included for their prescription. In particular, it is suggested to address the following aspects:

- Accounting for droplet non-sphericity through modified drag coefficients for lagrangian particles (Bagheri & Bonnadonna 2016). This would increase the momentum transfer after injection for highly deformed structures (such as those corresponding to ligaments in the resolved computations), hence making a more realistic spray transport prior to secondary atomization.

- Prescribing droplets velocities conditioned on their sizes through sectional approaches (Vié et al. 2013). This could lead to a better estimation of liquid-gas relative velocities and, therefore, to a more realistic breakup of lagrangian particles through secondary atomization.
- Consider transient flow rates for prescription of lagrangian droplets, to better mimic the unsteadiness in the dispersed phase region of liquid jets in crossflow.

Secondly, this work has built SLI from resolved atomization simulations. Future works could consider the construction of SLI models from extended databases. Current works are focusing on an Eulerian-Lagrangian coupling to convert the droplets from resolved simulations into Lagrangian Point Particles (LPP) that are later transported in the same simulation (Janodet 2022). Thus, the SLI methodology could be applied in these coupled simulations to generate liquid injectors from both lagrangian and levelset particles in locations further downstream the dense core. Another possibility to be considered is to feed SLI with experimental data on particles when available, since experiments do not often provide limitations on particles sizes as the resolved computations do.

Finally, the impact of the injection models in reactive simulations should be studied. This thesis has shown the possibility to perform lagrangian simulations with SLI in realistic multi-staged injectors, while also accounting for relevant physical mechanisms such as secondary atomization and evaporation. Therefore, SLI is an adequate tool to further analyze the effect of liquid injection in reactive phenomena such as ignition, flame topology, flame-turbulence interaction, thermoacoustic instabilities and pollutant formation. Since BIMER is a reactive test bench which also presents experimental results on combustion simulations (Renaud 2015), the SLI developed in this thesis could be used as starting point for such studies.

Bibliography

Abramzon, B. & Sirignano, W. (1989), 'Droplet vaporization model for spray combustion calculations', *International Journal of Heat and Mass Transfer* **32**(9), 1605–1618. Number: 9.

ACARE (2017), Strategic Research and Innovation Agenda, Executive summary.

Adelberg, A. (1968), 'Breakup Rate and Penetration of a Liquid Jet in a Gas Stream', *AIAA Journal* **6**, 1134–1147.

Albrecht, H.-E., Borys, M., Wenzel, M. & Wriedt, T. (1994), 'Influence of the Measurement Volume on the Phase Error in Phase Doppler Anemometry. Part 1: Reflective mode operation', *Particle & Particle Systems Characterization* **11**(4), 339–344.
URL: *https://onlinelibrary.wiley.com/doi/10.1002/ppsc.19940110410*

Albrecht, H.-E., Wenzel, M. & Borys, M. (1996), 'Influence of the Measurement Volume on the Phase Error in Phase Doppler Anemometry. Part 2: Analysis by extension of geometrical optics to the laser beam; Refractive mode operation', *Particle and Particle Systems Characterization* **13**(1), 18–26.
URL: *https://onlinelibrary.wiley.com/doi/10.1002/ppsc.19960130105*

Anderson, T. W. (1962), 'On the distribution of the two-sample Cramér-Von Mises criterion', *Annals of Mathematical Statistics* **33**(3), 1148–1159. Number: 3.

Andreini, A., Bianchini, C., Puggelli, S. & Demoulin, F.-X. (2016), 'Development of a turbulent liquid flux model for Eulerian-Eulerian multiphase flow simulations', *International Journal of Multiphase Flow* (81), 88–103.

Anez, J., Dabonneville, F., Duret, B., Reveillon, J. & Demoulin, F.-X. (2019), 'Multi-scale spray atomization model', p. 8.

ANSYS, I. (2018), ANSYS Fluent User's Guide, Release 19.0, Technical report.

Apte, S. V., Gorokhovski, M. & Moin, P. (2003), 'LES of atomizing spray with stochastic modeling of secondary breakup', *International Journal of Multiphase Flow* **29**, 1503–1522.

Araneo, L. & Tropea, C. (2000), Improving Phase Doppler Measurements in a Diesel Spray, pp. 2000–01–2047.
URL: *https://www.sae.org/content/2000-01-2047/*

Arienti, M., Madabhushi, R. K., van Slooten, P. R. & Soteriou, M. C. (2006), 'Aerodynamic blockage effect on the spray characteristics of liquid jet atomized by crossflowing air', *ASME Turbo Expo 2006* .

Asami, M., Kimura, A. & Oka, H. (2021), 'Improvement of a Diagnostic Urban Wind Model for Flow Fields around a Single Rectangular Obstacle in Micrometeorology Simulation', *Fluids* **6**(254), 20.

Bachalo, W. D. (1980), 'Method for measuring the size and velocity of spheres by dual-beam light-scatter interferometry', *Applied Optics* **19**(3), 363–370.

Bagheri, G. & Bonnadonna, C. (2016), 'On the drag of freely falling non-spherical particles', *Powder Technology* **301**.

Balachandar, S. (2009), 'A scaling analysis for point-particle approaches to turbulent multiphase flows', *International Journal of Multiphase Flow* **35**, 801–810.

Barbosa, S. (2008), Etude expérimentale de la dynamique de combustion d'un injecteur pauvre pré-mélangé étage swirlé, PhD Thesis, Ecole Centrale Paris, France.

Barbosa, S., Scouflaire, P. & Ducruix, S. (2009), 'Time resolved flowfield, flame structure and acoustic characterization of a staged multi-injection burner', *Proceedings of the Combustion Institute* **32**, 2965–2972.

Batten, P., Goldberg, U. & Chakravarthy, S. (2004), 'Interfacing statistical turbulence closures with large-eddy simulation', *AIAA Journal* **42**, 485–92.

Becker, J. & Hassa, C. (2002), 'Breakup and atomization of a kerosene JICF at elevated pressure', *Atomization and Sprays* **11**, 49–67.

Becker, J. & Hassa, C. (2004), 'Experimental investigation of spatial and temporal aspects of the liquid fuel placement in a swirl cup at elevated pressure', *Proceedings of ASME Turbo Expo* .

Behzad, A., Ashgriz, N. & Karney, B. W. (2016), 'Surface breakup of a non-turbulent liquid jet injected into a high pressure gaseous crossflow', *International Journal of Multiphase Flow* **80**, 100–117.

Behzad, M., Mashayek, A. & Ashgriz, N. (2010), 'A KIVA-based model for liquid jet in cross flow', *ILASS Americas* .

Benard, P., Viré, A., Moureau, V., Lartigue, G., Beaudet, L., Deglaire, P. & Bricteux, L. (2018), 'Large-Eddy Simulation of wind turbines wakes including geometrical effects', *Computers and Fluids* **173**, 133–139.

Bittlinger, G. & Brehm, N. (1999), 'High Pressure Combustion Test of Lean Premixed Prevaporised (LPP) Modules in an Axially Staged Combustor Using a Multisector Rig', *Air breathing engines* **5**.

Boniou, V. (2022), On the numerical simulation of evaporating two-phase flows using sharp interface capturing methods, PhD thesis, Ecole Centrale Paris, Paris, France.

Brandt, M., Gugel, K. O. & Hassa, C. (1997), 'Experimental Investigation of the Liquid Fuel Evaporation in a Premix Duct for Lean Premixed and Prevaporized Combustion', *Journal of Engineering for Gas Turbines and Power* **119**, 815–821.

Brandt, M., Rachner, M. & Schmitz, G. (1998), 'An experimental and numerical study of kerosine spray evaporation in a premix duct for gas turbine combustors at high pressure', *Combustion Science and Technology* **138**, 313–348.

Broadwell, J. E. & Breidenthal, R. E. (1984), 'Structure and mixing of a transverse jet in incompressible flow', *Journal of Fluid Mechanics* **148**, 401–412.

Cahn, J. W. & Hilliard, J. E. (1958), 'Free energy of a nonuniform system. I. Interfacial free energy', *Journal of Chemical Physics* **28**(2), 258–267. Number: 2.

Canu, R., Puggelli, S., Essadki, M., Duret, B., Menard, T., Massot, M., Reveillon, J. & Demoullin, F. X. (2018), 'Where does the droplet size distribution come from', *International Journal of Multiphase Flow* **107**, 230–245.

Carmona, J. (2021), Modélisation des phénomènes diphasiques dans des injecteurs aéronautiques de type Airblast, PhD thesis, INP Toulouse, Toulouse, France.

Ceman, D. L., Rader, D. J. & O'Hern, T. J. (1993), 'Calibration of the Phase Doppler Particle Analyzer with Monodisperse Droplets', *Aerosol Science and Technology* **18**(4), 346–358.
URL: *http://www.tandfonline.com/doi/abs/10.1080/02786829308959609*

CERFACS (2011), *The AVBP Handbook*.

Chapman, S. & Cowling, T. (1970), *The Mathematical Theory of Nonuniform Gases: An Account of the Kinetic Theory of Viscosity, Thermal Conduction and Diffusion in Gases*, cambridge mathematical library edn, Cambridge University Press.

Chaussonnet, G. (2014), Modeling of liquid film and breakup phenomena in Large-Eddy Simulations of aeroengines fueled by airblast atomizers, PhD Thesis, Institut National Polytechnique de Toulouse, Toulouse, France.

Chaussonnet, G., Vermorel, O., Riber, E. & Cuenot, B. (2016), 'A new phenomenological model to predict drop size distribution in Large-Eddy Simulations of airblast atomizers', *International Journal of Multiphase Flow* **80**, 29–42.

Cheneau, B. (2019), Étude numérique de la dynamique de combustion dans un brûleur diphasique turbulent à deux étages, PhD thesis, CentraleSupelec, Universite Paris-Saclay.

Chiodi, R. & Desjardins, O. (2017), 'A reformulation of the conservative level set reinitialization equation for accurate and robust simulation of complex multiphase flows', *Journal of Computational Physics* **343**, 186–200.

Chiu, P. H. & Lin, Y. T. (2011), 'A conservative phase field method for solving incompressible two-phase flows', *Journal of Computational Physics* **230**, 185.

Chou, W.-H., Hsiang, L.-P. & Faeth, G. M. (1997), 'Temporal properties of drop breakup in the shear breakup regime', *International Journal of Multiphase Flow* **23**(4), 651–669. Number: 4.

Chéron, V., Brändle de Motta, J. C., Vaudor, G., Ménard, T. & Berlement, A. (2019), 'From droplets to particles: Transformation criteria', *ILASS-Europe 2019, 29th Conference on Liquid Atomization and Spray Systems* .

Collado, F. J. (2007), 'Reynolds transport theorem for a two-phase flow', *Applied Physics Letters* **90**.

Cousin, J., Berlemont, A., Ménard, T. & Grout, S. (2012), 'Primary breakup simulation of a liquid jet discharged by a low-pressure compound nozzle', *Computers and Fluids* **63**, 165–173.

Crialesi-Esposito, M. (2019), Analysis of primary atomization in sprays using Direct Numerical Simulation, PhD thesis, Universitat Politecnica de Valencia, Valencia.

Dahms, R. N. & Oefelein, J. C. (2013), 'On the transition between two-phase and single-phase interface dynamics in multicomponent fluids at supercritical pressures', *Physics of Fluids* **25**(9). Number: 9.

Dahms, R. N. & Oefelein, J. C. (2016), 'The significance of drop non-sphericity in sprays', *International Journal of Multiphase Flow* **86**, 67–85.

Damaschke, N., Gouesbet, G., Gréhan, G. & Tropea, C. (1998), 'Optical techniques for the characterization of non-spherical and non-homogeneous particles', *Measurement Science and Technology* **9**, 137–140.

Denev, J. A., Fröhlich, J. & Bockhorn, H. (2009), 'Large eddy simulation of a swirling transverse jet into a crossflow with investigation of scalar gransport', *Physics of Fluids* **21**.

Desclaux, A., Thuillet, S. & Zuzio, D. (2020), 'Experimental and Numerical Characterization of a Liquid Jet Injected into Air Crossflow with Acoustic Forcing'.

Desjardins, O., Moureau, V. & Pitsch, H. (2008), 'An accurate conservative level set/ghost fluid method for simulating turbulent atomization', *Journal of Computational Physics* **227**, 8395–8416.

Domann, R. & Hardalupas, Y. (2003), 'Quantitative Measurement of Planar Droplet Sauter Mean Diameter in Sprays using Planar Droplet Sizing', *Particle & Particle Systems Characterization* **20**(3), 209–218. **URL:** *https://onlinelibrary.wiley.com/doi/10.1002/ppsc.200390027*

Domingo-Alvarez, P. (2019), High-pressure combustion large-eddy simulation for an a priori optical diagnostics validation, PhD thesis, INSA Rouen.

Doublet, P. (2019), Effet de la presion et de la température de l'air et du carburant sur les caractéristiques du spray délivré dans une chambre de combustion, PhD thesis, Institut Supérieur de l'Aéronautique et de l'Espace (ISAE), Toulouse, France.

Drew, D. & Passman, S. L. (1999), *Theory of Multicomponent Fluids*.

Dukowicz, J. (1980), 'A particle-fluid numerical model for liquid sprays', *Journal of Computational Physics* **35**, 229–253.

Dullenkopf, K., Willmann, M., Wittig, S., Schöne, F., Stieglmeier, M., Tropea, C. & Mundo, C. (1998), 'Comparative mass flux measurements in sprays using a patternator and the Phade-Doppler technique', *Particle and Particle Systems Characterization* **15**, 81–89.

Dunn-Rankin, D. (2008), *Lean Combustion. Technology and Control*.

EASA (2019), European Aviation Environmental Report, Technical Report.

Eckel, G., Rachner, M., le Clercq, P. & Aigner, M. (2016), 'Semi-empirical model for the unsteady shear breakup of liquid JICF', *Atomization and Sprays* **26**(7), 687–712. Number: 7.

Eggers, J. & Villermaux, E. (2008), 'Physics of liquid jets', *Reports on progess in physics* **71**.

El-Asrag, H., Ham, F. & Pitsch, H. (2007), 'Simulation of a lean direct injection combustor for the next high speed civil transport (HSCT) vehicle combustion systems', *Center for Turbulence Research. Annual Research Briefs 2007* .

Esclapez, L. (2015), Numerical study of ignition and inter-sector flame propagation in gas turbines, PhD thesis, INP Toulouse, Toulouse, France.

Fan, X., Wang, J., Zhao, F., Li, J. & Yang, T. (2018), 'Eulerian–Lagrangian method for liquid jet atomization in supersonic crossflow using statistical injection model', *Advances in Mechanical Engineering* **10**(2), 1–13. Number: 2.

Fedkiw, R. P., Aslam, T., Merriman, B. & Osher, S. (1999), 'A Non-oscillatory Eulerian Approach to Interfaces in Multimaterial Flows (the Ghost Fluid Method)', *Journal of Computational Physics* **152**(2), 457–492. Number: 2.

Fontes, D. H., Vilela, V., Souza Meira, L. & Souza, F. J. (2019), 'Improved hybrid model applied to liquid jet in crossflow', *International Journal of Multiphase Flow* **114**, 98–114.

Foust, M. J., Thomsen, D., Stickles, R., Cooper, C. & Dodds, W. (2012), 'Development of the GE Aviation Low Emissions TAPS Combustor for Next Generation Aircraft Engines', *50th AIAA Aerospace Sciences Meeting including the New Horizons Forum and Aerospace Exposition* .

Freitag, S. & Hassa, C. (2008), 'Spray characteristics of a kerosene jet in crossflow of air at elevated pressure', *ILASS-Europe* .

Fric, T. F. & Roshko, A. (1994), 'Vortical structure in the wake of a transverse jet', *Journal of Fluid Mechanics* **279**, 1–47.

Fuller, R. P., Wu, P.-K. & Kirkendall, K. A. (2000), 'Effects of injection angle on atomization of liquid jets in transverse airflow', *AIAA Journal* **38**(1), 64–72. Number: 1.

Fuster, D., Bagué, A., Boeck, T., Le Moyne, L., Leboissetier, A., Popinet, S., Ray, P., Scardovelli, R. & Zaleski, S. (2009), 'Simulation of primary atomization with an octree adaptive mesh refinement and VOF method', *International Journal of Multiphase Flow* **35**, 550–565.

Garcia, M. (2009), Développement et validation du formalisme Euler-Lagrange dans un solveur parallèle et non-structuré pour la simulation aux grandes échelles, PhD Thesis, INP Toulouse, Toulouse.

Gepperth, S., Guildenbecher, D., Koch, R. & Bauer, H.-J. (2010), 'Pre-filming primary atomization: Experiments and modeling', *Proceedings of ILASS Europe 2010* .

Germano, M., Piomelli, U., Moin, P. & Cabot, W. H. (1991), 'A dynamic subgrid-scale eddy viscosity model', *Physics of Fluids A: Fluid Dynamics* **3**(7), 1760–1765. Number: 7.

Ghassemi, H., Baek, S. W. & Khan, Q. S. (2006), 'Experimental study on evaporation of kerosene droplets at elevated pressures and temperatures', *Combustion Science and Technology* **178**, 1669–1684.

Ghods, S. (2013), Detailed Numerical Simulation of Liquid Jet In Crossflow Atomization with High Density Ratios, PhD thesis.

Goldman, R. (2005), 'Curvature formulas for implicit curves and surfaces', *Computer Aided Geometric Design* **22**(7), 632–658.

Gorokhovski, M. A. (2001), 'The stochastic lagrangian model of drops breakup in the computation of liquid sprays', *Atomization and Sprays* **11**, 505–520.

Gorokhovski, M. A. & Saveliev, V. L. (2003), 'Analyses of Kolmogorov's model of breakup and its application into Lagrangian computation of liquid sprays under air-blast atomization', *Physics of Fluids* **15**, 184–192.

Gosman, A. D. & Ioannides, E. (1983), 'Aspects of computer simulation of liquid-fueled combustors', *Journal of Energy* **7**(6), 482–490. Number: 6.

Gréhan, G., Gouesbet, G., Naqwi, A. & Durst, F. (1993), 'Particle Trajectory Effects in Phase Doppler Systems: Computations and experiments', *Particle & Particle Systems Characterization* **10**(6), 332–338. **URL:** *https://onlinelibrary.wiley.com/doi/10.1002/ppsc.19930100607*

Guedot, L. (2015), Développement de méthodes numériques pour la caractérisation des grandes structures tourbillonnaires dans les brûleurs aéronautiques : application aux systèmes d'injection multi-points, PhD Thesis, INSA de Rouen, Rouen.

Guillamon, C., Janodet, R., Voivenel, L., Mercier, R. & Moureau, V. (2021), 'Building Lagrangian injectors from resolved primary atomization simulations. Application to jet in crossflow fuel injection', *International Conference on Liquid Atomization and Spray Systems (ICLASS)* .

Hanna, S. R., Hansen, O. R. & Dharmavaram, S. (2004), 'FLACS CFD air quality model performance evaluation with Kit Fox, MUST, Prairie Grass, and EMU observations', *Atmospheric Environment* **38**, 4675–4687.

Hansen, M. O. (2015), *Aerodynamics of Wind Turbines*, Taylor and Francis.

Herrmann, M. (2003), 'Modeling primary breakup: A three-dimensional Eulerian level set/vortex sheet method for two-phase interface systems', *Annual Research Briefs. Center for Turbulent Research* pp. 185–196.

Herrmann, M. (2009), 'Detailed Numerical Simulations of the Primary Atomization of a Turbulent Liquid Jet in Crossflow', *Journal of Engineering for Gas Turbines and Power* **132**.

Herrmann, M. (2010), 'A parallel Eulerian interface tracking/Lagrangian point particle multi-scale coupling procedure', *Journal of Computational Physics* **229**, 745–759.

Herrmann, M., Arienti, M. & Soteriou, M. (2011), 'The impact of density ratio on the liquid core dynamics of a turbulent liquid jet injected into a crossflow', *Journal of Engineering for Gas Turbines and Power* **133**.

Hesse, H. (1922), *Siddhartha*, New Directions Publishing.

Hirt, C. W. & Nichols, B. D. (1981), 'Volume of fluid (VOF) method for the dynamics of free boundaries', *Journal of Computational Physics* **39**(1), 201–225. Number: 1.

Houtin-Mongrolle, F., Bricteux, L., Benard, P., Lartigue, G., Moureau, V. & Reveillon, J. (2020), 'Actuator line method applied to grid turbulence generation for large-Eddy simulations', *Journal of Turbulence* **21**(8), 407–433. Number: 8.

Huang, Y., Wang, S. & Yang, V. (2006), 'Systematic Analysis of Lean-Premixed Swirl-Stabilized Combustion', *AIAA Journal* **44**(4). Number: 4.

Huang, Y. & Yang, V. (2009), 'Dynamics and stability of lean-premixed swirl-stabilized combustion', *Progress in Energy and Combustion Science* **35**(4), 293–364. Number: 4.

Ivey, C. B. & Moin, P. (2017), 'Conservative and bounded volume-of-fluid advection on unstructured grids', *Journal of Computational Physics* **350**, 387–419.

Jaegle, F. (2009), Large Eddy Simulation of evaporationg sprays in complex geometries using Eulerian and Lagrangian methods, PhD Thesis, Institut National Polytechnique de Toulouse, Toulouse.

Jaegle, F., Senoner, J.-M., Garcia, M., Bismes, F., Lecourt, R., Cuenot, B. & Poinsot, T. (2011), 'Eulerian and Lagrangian spray simulations of an aeronautical multipoint injector', *Proceedings of the Combustion Institute* **33**, 2099–2107.

Janodet, R. (2022), Numerical simulation of primary atomization in aeronautical injectors using a massively parallel adaptive mesh refinement technique, PhD Thesis, Normandie Université.

Janodet, R., Guillamón, C., Moureau, V., Mercier, R., Lartigue, G., Bénard, P., Ménard, T. & Berlemont, A. (2022), 'A massively parallel accurate conservative level set algorithm for simulating turbulent atomization on adaptive unstructured grids', *Journal of Computational Physics* **458**(111075).

Janodet, R., Vaudor, G., Lartigue, G., Benard, P., Moureau, V. & Mercier, R. (2019), 'An unstructured conservation level-set algorithm coupled with dynamic mesh adaptation for the computation of liquid-gas flows', *ILASS-2019* .

Jeong, J. & Hussain, F. (1995), 'On the identification of a vortex', *Journal of Fluid Mechanics* **285**, 69–94.

Jofre, L., Lehmkuhl, O., Castro, J. & Oliva, A. (2014), 'A 3-D Volume-of-Fluid advection method based on cell-vertex velocities for unstructured meshes', *Computers and Fluids* **94**, 14–29.

Jofre, L. & Urzay, J. (2021), 'Transcritical diffuse-interface hydrodynamics of propellants in high-pressure combustors of chemical propulsion systems', *Progress in Energy and Combustion Science* **82**.

Johnston, A. J. (1984), 'An investigation into the interfacial shear stress contribution in two-phase stratified flow', *International Journal of Multiphase Flow* **10**(3), 371–383. Number: 3.

Karagozian, A. (2014), 'The jet in crossflow', *Physics of Fluids* **26**.

Karagozian, A. R. (1986), 'An analytical model for the vorticity assiciated with a transverset jet', *AIAA Journal* **24**(3), 429–436.

Karagozian, A. R. (2010), 'Transverse jets and their control', *Progress in Energy and Combustion Science* **36**, 531–553.

Kelso, R. M., Lim, T. T. & Perry, A. E. (1996), 'An experimental study of round jets in cross-flow', *Journal of Fluid Mechanics* **306**, 111–144.

Kolmogorov, A. (1941), 'On the log-normal distribution of particles sizes during breakup process', *Dolk. Akad. Nauk SSSR* **31**.

Kraichnan, R. H. (1970), 'Diffusion by a Random Velocity Field', *Physics of Fluids* **13**(1), 22–31. Number: 1.

Lancien, T. (2018), Etude numerique de l'allumage diphasique de foyers annulaires multi-bruleurs, PhD Thesis, Université Paris-Saclay, Paris.

Laurent, F. & Massot, M. (2001), 'Multi-fluid modeling of laminar poly-dispersed spray flames : origin, assumptions and comparison of sectional and sampling methods', *Combustion Theory and Modelling* **5**, 537–572.

Lee, K., Aalburg, C., Diez, F. J., Faeth, G. M. & Sallam, K. A. (2007), 'Primary breakup of turbulent round liquid jets in uniform crossflows', *AIAA Journal* **45**(8), 1907–1916.

Lefebvre, A. H. (1980), 'Airblast atomization', *Progress in Energy and Combustion Science* **6**(3), 233–261. Number: 3.

Lefebvre, A. H. & Ballal, D. R. (2010), *Gas Turbine Combustion*, third edn.

Lefebvre, A. H. & McDonell, V. G. (2017), *Atomization and Sprays*, second edn.

Leparoux, J., Mercier, R., Moureau, V. & Musaefendic, H. (2018), 'Primary atomization simulation applied to a jet in crossflow aeronautical injector with dynamic mesh adaptation', *ICLASS 2018. 14th Triennal International Conference on Liquid Atomization and Spray Systems* .

Li, X. & Soteriou, M. (2018), 'Detailed numerical simulation of liquid jet atomization in crossflow of increasing density', *International Journal of Multiphase Flow* **104**, 214–232.

Lieuwen, T. C. (2012), *Unsteady Combustor Physics*, first edn.

Liu, J., Piomelli, U. & Spalart, P. R. (1996), 'Interaction between a spatially growing turbulent boundary layer and embedded streamwise vortices', *Journal of Fluid Mechanics* **326**, 151–179.

Lucca-Negro, O. & O'Doherty, T. (2001), 'Vortex breakdown: a review', *Progress in Energy and Combustion Science* **27**, 431–481.

Lund, T. S., Wu, X. & Squires, K. D. (1998), 'Generation of inflow data for spatially-developing boundary layer simulations', *Journal of Computational Physics* **140**, 233–258.

Luo, K., Shao, C., Chai, M. & Fan, J. (2019), 'Level set method for atomization and evaporation simulations', *Progress in Energy and Combustion Science* **73**, 65–94.

Mashayek, A., Jafari, A. & Ashgriz, N. (2006), 'On the jet trajectory of a liquid jet in crossflow', *Proceedings of ICLASS 2006* .

Maxey, M. R. & Riley, J. J. (1983), 'Equation of motion for a small rigid sphere in a nonuniform flow', *The Physics of Fluids* **26**, 883.

Mayinger, F., Feldmann, O., Mewes, D. & Mayinger, F., eds (2001), *Optical Measurements*, Heat and Mass Transfer, Springer Berlin Heidelberg, Berlin, Heidelberg.
URL: *http://link.springer.com/10.1007/978-3-642-56443-7*

McCaslin, J. O. & Desjardins, O. (2014), 'A localized re-initialization equation for the conservative level set method', *Journal of Computational Physics* **262**, 408–426.

McKee, S., Tomé, M. F., Ferreira, V. G., Cuminato, J. A., Castelo, A., Sousa, F. S. & Mangiavacchi, N. (2008), 'The MAC method', *Computers and Fluids* **37**, 907–930.

McKinley, G. H. (2005), Dimensionless groups for understanding free surface flows of complex fluids., Technical report.

Mesquita, L. C. C., Vié, A. & Ducruix, S. (2018), 'Large Eddy Simulation of a two-phase staged swirling burner using an Euler-Lagrange approach: validation of the injection strategy', *Proceedings of the ASME Turbo Expo 2018* .

Michaelides, E., Crowe, C. & Schwarzkopf, J. (2017), *Multiphase Flow Handbook*, second edn.

Mirjalili, S., Ivey, C. B. & Mani, A. (2019), 'Comparison between the diffuse interface and volume of fluid methods for simulating two-phase flows', *International Journal of Multiphase Flow* **116**, 221–238.

Mirjalili, S., Ivey, C. B. & Mani, A. (2020), 'A conservative diffuse interface method for two-phase flows with provable boundedness properties', *Journal of Computational Physics* **401**.

Mirjalili, S., Jain, S. S. & Dodd, M. S. (2017), 'Interface-capturing methods for two-phase flows: An overview and recent developments', *Center for Turbulence Research. Annual Research Briefs 2017.* .

Moin, P. & Apte, S. V. (2006), 'Large-eddy Simulation of Realistic Gas Turbine Combustors'.

Moureau, V., Domingo, P. & Vervisch, L. (2011), 'Design of a massively parallel CFD code for complex geometries', *Comptes Rendus Mécanique* **339**(2-3), 141–148. Number: 2-3.

Murrone, A. & Villedieu, P. (2011), 'Numerical Modeling of Dispersed Two-Phase Flows', *AerospaceLab* pp. 1–13.

Nayigizente, D. (2021), Unsteady simulations of liquid/gas interfaces in real gas flows using the Second Gradient theory, PhD thesis, Université Paris-Saclay, Paris, France.

Novick, A. & Troth, D. (1981), Low NOx Heavy Fuel Combustor Concept Program, Technical Report, NASA.

Odier, N. (2006), Simulation numerique de jets liquides cisailles par une phase rapide : dynamique de battement a grande echelle et interaction avec les structures tourbillonnaires, PhD Thesis, Universit\'e de Grenoble, Grenoble.

Olsson, E., Gunilla, K. & Wahedi, S. (2005), 'A conservative level set method for two phase flow I', *Journal of Computational Physics* **210**, 224–246.

Olsson, E., Gunilla, K. & Wahedi, S. (2007), 'A conservative level set method for two phase flow II', *Journal of Computational Physics* **225**, 785–807.

O'Rourke, P. J. & Amsden, A. A. (1987), 'The Tab Method for Numerical Calculation of Spray Droplet Breakup', *SAE Technical Paper 872089* .

Osher, S. & Fedkiw, R. (2003), *Level Set Methods and Dynamic Implicit Surfaces*, 1 edn, Springer, New York.

Pai, M. G., Bermejo-Moreno, I., Desjardins, O. & Pitsch, H. (2009), 'Role of Weber number in the primary breakup of liquid jets in crossflow', *Center for Turbulence Research. Annual Research Briefs 2009.* pp. 145–158.

Pairetti, C. I., Marquez-Damian, S., Nigro, N. M., Popinet, S. & Salezki, S. (2020), 'Mesh resolution effects on primary atomization simulations', *Atomization and Sprays* **30**(12), 913–935.

Palanti, L., Puggelli, S., Langone, L., Andreini, A., Reveillon, J., Duret, B. & Demoulin, F. (2022), 'An attempt to predict spray characteristics at early stage of the atomization process by using surface density and curvature distribution', *International Journal of Multiphase Flow* **147**, 103879.
URL: *https://linkinghub.elsevier.com/retrieve/pii/S0301932221002949*

Pamiès, M., Weiss, P.-E., Garnier, E., Deck, S. & Sagaut, P. (2009), 'Generation of synthetic turbulent inflow data for large eddy simulation of spatially evolving wall-bounded flows', *Physics of Fluids* **21**.

Panao, M. R. O. (2012), 'Assessment of measurement efficiency in laser- and phase-Doppler techniques: an information theory approach', *Measurement Science and Technology* **23**(125304), 8. Number: 125304.

Panao, M. R. O., Moita, A. S. & Moreira, A. L. (2020), 'On the Statistical Characterization of Sprays', *Applied Sciences* **10**(6122), 18. Number: 6122.

Panda, P. P., Roa, M., Szedlacsek, P., Laster, W. R. & Lucht, R. P. (2015), 'Structure and dynamics of the wake of a reacting jet injected into a swirling, vitiated crossflow in a staged combustion system', *Experiments in Fluids* **56**(21).

Patil, S. & Sahu, S. (2021), 'Liquid jet core characterization in a model crossflow airblast atomizer', *International Journal of Multiphase Flow* **141**.

Pehanhoat, O. (2006), 'Low emissions combustor technology developments in the European programmes LOPOCOTEP and TLC', *ICASS 2006* .

Pilch, M. & Erdman, C. A. (1987), 'Use of Breakup Time Data and Velocity History Data to Predict the Maximum Size of Stable Fragments for Acceleration-Induced Breakup of a Liquid Drop', *International Journal of Multiphase Flow* **13**, 741–757.

Piomelli, U. (2018), 'Large Eddy and Direct Simulation of Turbulent Flows. Lecture Series on Large Eddy Simulation: Theory and Applications, 2018-05. von Karman Institute for Fluid Dynamics.'.

Pirozzoli, S., Di Giorgio, S. & Iafrati, A. (2019), 'On algebraic TVD-VOF methods for tracking material interfaces', *Computers and Fluids* **189**, 73–81.

Pope, S. B. (2000), *Turbulent Flows*, Cambridge University Press.

Popinet, S. (2003), 'Gerris: a tree-based adaptive solver for the incompressible Euler equations in complex geometries', *Journal of Computational Physics* **190**, 572–600.

Prakash, R. S., Sinha, A., Tomar, G. & Ravikrishna, R. V. (2018), 'Liquid JICF - Effect of liquid entry conditions', *Experimental Thermal and Fluid Science* **93**, 45–56.

Providakis, T. (2013), Etude de la dynamique de flamme swirlé dans un injecteur diphasique multipoints étagé, PhD thesis, Ecole Centrale Paris.

Qiu, H. & Hsu, C. T. (1999), 'Method of phase-Doppler anemometry free from the measurement-volume effect', *Applied Optics* **38**(13), 2737.
URL: *https://opg.optica.org/abstract.cfm?URI=ao-38-13-2737*

Rachner, M., Becker, J., Hassa, C. & Doerr, T. (2002), 'Modelling of the atomization of a plain liquid fuel jet in crossflow at gas turbine conditions', *Aerospace Science and Technology* **6**, 495–506.

Ragucci, R., Bellofiore, A. & Cavaliere, A. (2007), 'Trajectory and momentum coherence breakdown of a liquid jet in high-density air cross-flow', *Atomization and Sprays* **17**, 1–24.

Ranger, A. A. & Nicholls, J. A. (1968), 'Aerodynamics shattering of liquid drops', *AIAA Journal* **7**(2), 285–290. Number: 2.

Rayleigh, L. (1878), 'On the instability of jets', *Proceedings of the London mathematical society* **10**, 4–13.

Reitz, R. D. (1987), 'Modeling Atomization Processes in High-Pressure Vaporizing Sprays', *Atomisation and Sprays Technology* **3**, 309–337.

Renaud, A. (2015), High-speed diagnostics for the study of flame stabilization and transient behaviour in a swirled burner with variable liquid-fuel distribution, PhD Thesis, CentraleSupelec, Universite Paris-Saclay, Chatenay-Malabry.

Rezayat, S., Farshchi, M. & Berrocal, E. (2021), 'High-speed imaging database of water jet disintegration Part II: Temporal analysis of the primary breakup', *International Journal of Multiphase Flow* **145**.

Rizk, N. K. & Lefebvre, A. H. (1985), 'Internal Flow Characteristics of simplex swirl atomizers', *Journal of Propulsion and Power* **1**(3), 193–199. Number: 3.

Sallam, K., Aalburg, C. & Faeth, G. (2004), 'Breakup of round nonturbulent liquid jets in gaseous crossflow.', *AIAA Journal* **42**(12), 2529–2540. Number: 12.

Sanjose, M., Senoner, J. M., Jaegle, F., Cuenot, B., Moreau, S. & Poinsot, T. (2011), 'Fuel Injection Model for Euler-Euler and Euler-Lagrange Large Eddy Simulations of an evaporating spray inside an aeronautical combustor', *International Journal of Multiphase Flow* **37**(5), 514–529. Number: 5.

Saurel, R. & Pantano, C. (2018), 'Diffuse-Interface Capturing Methods for Compressible Two-Phase Flows', *Annual Review of Fluid Mechanics* **50**, 105–130.

Sayadi, T. & Moin, P. (2010), 'A comparative study of subgrid scale models for the prediction of transition in turbulent boundary layers', *Center for Turbulence Research. Annual Research Briefs 2010* pp. 237–247.

Scardovelli, R. & Zaleski, S. (1999), 'Direct numerical simulation of free-surface and interfacial flow', *Annual Review of Fluid Mechanics* **31**, 567–603.

Schiller, L. & Naumann, A. (1935), 'A drag coefficient correlation', *VDI Zeitung* **77**, 318–320.

Schlegel, F., Wee, D., Marzouk, Y. M. & Ghoniem, A. F. (2011), 'Contributions of the wall boundary layer to the formation of the counter-rotating vortex pair in transverse jets', *Journal of Fluid Mechanics* **676**, 461–490.

Senoner, J.-M. (2010), Simulation aux Grandes Echelles de l'ecoulement diphasique dans un bruleur aeronautique par une approche Euler-Lagrange, PhD Thesis, Institut National Polytechnique de Toulouse, Toulouse.

Shepherd, J. E., Nuyt, C. D. & Lee, J. J. (2000), Flash Point and Chemical Composition of Aviation Kerosene (Jet A), Technical report, Caltech, Pasadena, California.

Shinjo, J. & Umemura, A. (2010), 'Simulation of liquid jet primary breakup: Dynamics of ligament and droplet deformation', *International Journal of Multiphase Flow* **36**, 513–532.

Shukla, R. K., Pantano, C. & Freund, J. B. (2010), 'An interface capturing method for the simulation of multi-phase compressible flows', *Journal of Computational Physics* **229**, 7411–7439.

Smagorinsky, J. (1963), 'General circulation experiments with the primitive equa-tions. I. The basic experiment', *Monthly Weather Review* **91**, 99–164.

Sánchez, A. L., Urzay, J. & Liñán, A. (2015), 'The role of separation of scales in the description of spray combustion', *Proceedings of the Combustion Institute* **35**, 1549–1577.

Soedarmo, A., Pereyra, E. & Sarica, C. (2018), 'A Simplified Model for Steady-State Pseudo-Slug Flow', *Offshore Technology Conference* .

Sorensen, J. N. & Myken, A. (1992), 'Unsteady actuator disc model for horizontal axis wind turbines', *Journal of Wind Energy and Industrial Aerodynamics* **39**(1), 139–149. Number: 1.

Spalart, P. R. (1988), 'Direct simulation of a turbulent boundary layer up to R$_\theta$ = 1410', *Journal of Fluid Mechanics* **187**, 61–98.

Spalding, D. B. (1954), 'The Combustion of Liquid Fuels', *Proceedings of the Fourth Symposium on Combustion* pp. 847–864.

Sørensen, J. N. & Shen, W. Z. (2002), 'Numerical Modeling of Wind Turbine Wakes', *Journal of Fluids Engineering* **142**, 393–399.

Stenzler, J. N., Lee, J. G. & Santavicca, D. A. (2003), 'Penetration of liquid jets in a crossflow', *41st AIAA Aerospace Sciences Meeting and Exhibit* .

Storn, R. & Price, K. (1997), 'Differential Evolution - a simple and efficient heuristic for global optimization over continuous spaces', *Journal of Global Optimization* **11**, 341–359.

Subramanian, S. (2000), 'Statistical representation of a spray as a point process', *Physics of Fluids* **12**(10). Number: 10.

Sussman, M., Smereka, P. & Osher, S. (1994), 'A Level Set Approach for Computing Solutions to Incompressible Two-Phase Flow', *Journal of Computational Physics* **114**(1), 146–159. Number: 1.

Syred, N. & Beér, J. M. (1974), 'Combustion in swirling flows: A review', *Combustion and Flame* **23**(2), 143–201. Number: 2.

Tacina, R. (1983), Autoignition in a premixing prevaporizing fuel duct using three different fuel injection-systems at inlet air temperatures to 1250 K, Technical Report NASA Technical Memorandum 049909320. Issue: NASA Technical Memorandum 049909320.

Tacina, R. (1990), Low NOx potential of Gas Turbine Engines, NASA Technical Memorandum 102452. Issue: 102452.

Tanner, F. X. (1997), 'Liquid Jet Atomization and Droplet Breakup Modeling of Non-Evaporating Diesel Fuel Sprays', *SAE Technical Paper 970050* .

Tanner, F. X. & Weisser, G. (1998), 'Simulation of Liquid Jet Atomization for Fuel Sprays by Means of a Cascade Drop Breakup Model'.

Teigen, K. E., Song, P., Lowengrub, J. & Voigt, A. (2011), 'A diffuse-interface method for two-phase flows with soluble surfactants', *Journal of Computational Physics* **230**, 373–393.

Terrel, G. R. & Scott, D. W. (1985), 'Oversmoothed Nonparametric Density Estimates', *Journal of the American Statistical Association* **80**(389), 209–214. Number: 389.

Terzis, A., Kazakos, C., Zachos, P., Kalfas, A. & Ott, P. (2011), 'Swirl Jet and Crossflow Interaction at Low Velocity Ratios and Incompressible Flows', *9th European Conference on Turbomachinery* .

Tretola, G., Vogiatzaki, K. & Navarro-Martinez, S. (2021), 'Effect of the Density Ratio Variation on the Dynamics of a Liquid Jet Injected into a Gaseous Cross-Flow', *Physics of Fluids* **33**.

Trobec, R., Slivnig, B., Bulić, P. & Robić, B. (2018), *Introduction to Parallel Computing. From Algorithms to Programming on State-of-the-Art Platforms*, Undergraduate Topics in Computer Science, first edn, Springer.

Tropea, C. (2011), 'Optical Particle Characterization in Flows', *Annual Review of Fluid Mechanics* **43**, 399–426.

Tryggvason, G., Bunner, B., Esmaeeli, A., Juric, D., Al-Rawahi, N., Tauber, W., Han, J., Nas, S. & Jan, Y.-J. (2001), 'A front-tracking method for the computations of multiphase flow', *Journal of Computational Physics* **169**, 708–759.

Vié, A., Jay, S., Cuenot, B. & Massot, M. (2013), 'Accounting for Polydispersion in the Eulerian Large Eddy Simulation of the Two-Phase Flow in an Aeronautical-type Burner', *Flow, Turbulence and Combustion* **90**(3), 545–581. Number: 3.

Vié, A., Pouransari, H., Zamansky, R. & Mani, A. (2016), 'Particle-laden flows forced by the disperse phase: Comparison between Lagrangian and Eulerian simulations', *International Journal of Multiphase Flow* **79**, 144–158.

Wang, Q., Mondragon, U. M., Brown, C. T. & McDonell, V. G. (2011), 'Characterization of trajectory, break point, and break point dynamics of a plain liquid jet in a crossflow', *Atomization and Sprays* **21**(3), 203–219.

Wei, X. & Yong, H. (2014), 'Improved Semiempirical Correlation to Predict Sauter Mean Diameter for Pressure-Swirl Atomizers', *Journal of Propulsion and Power* **30**(6), 1628–1635.

White, F. M. (2005), *Viscous Fluid Flow*, third edn, McGraw Hill.

Williams, F. A. (1958), 'Spray Combustion and Atomization', *Physics of Fluids* **1**(541-545). Number: 541-545.

Wu, P.-K., Kirkendall, K. A. & Fuller, R. P. (1997), 'Breakup Processes of Liquid Jets in Subsonic Crossflows', *Journal of Propulsion and Power* **13**(1), 64–73. Number: 1.

Wu, P.-K., Kirkendall, K. A. & Fuller, R. P. (1998), 'Spray structures of liquid jets atomized in subsonic crossflows', *Journal of Propulsion and Power* **14**(2). Number: 2.

Wu, P.-K., Miranda, R. F. & Faeth, G. M. (1994), 'Effects of Initial Flow Conditions on Primary Breakup of Nonturbulent and Turbulent Liquid Jets', *AIAA 32nd Aerospace Sciences Meeting and Exhibit* .

Wu, X. (2017), 'Inflow Turbulence Generation Methods', *Annual Review of Fluid Mechanics* **49**, 23–49.

Wu, X., Squires, K. D. & Lund, T. S. (1995), 'Large Eddy Simulation of a spatially-developing boundary layer', *Supercomputing 95: Proceedings of the 1995 ACL/UEEE conference on Supercomputing* .

Xiao, F., Dianat, M. & McGuirk, J. J. (2013), 'Large Eddy Simulation of Liquid-Jet Primary Breakup in Air Crossflow', *AIAA Journal* **51**(12), 2878–2893.

Xiao, F., Dianat, M. & McGuirk, J. J. (2014), 'LES of turbulent liquid jet primary breakup in turbulent coaxial air flow', *International Journal of Multiphase Flow* **60**, 103–118.

Yang, X. & Sotiropoulos, S. (2017), 'A new class of actuator surface models for wind turbines', *Wind Energy* pp. 1–19.

Yokoi, N., Aizu, Y. & Mishina, H. (2001), 'Unidirectional phase-Doppler method for particle-size measurements', *Applied Optics* **40**(7), 1049.
URL: *https://opg.optica.org/abstract.cfm?URI=ao-40-7-1049*

Zhang, L. & Yang, V. (2017), 'Flow dynamics and mixing of a transverse jet in crossflow - Part I: steady crossflow', *Journal of Engineering for Gas Turbines and Power* **139**.

Zhou, Y.-Z., Xiao, F., Li, Q.-L. & Li, C.-H. (2020), 'Simulation of elliptical liquid jet primary breakup in supersonic crossflow', *International Journal of Aerospace Engineering* .

Zuzio, D. (2010), Direct numerical simulation of two phase flows with adaptive mesh refinement, PhD thesis, Ecole Nationale Superior de l'Aeronautique et de l'Espace, Toulouse.

Zuzio, D., Estivalèzes, J.-L. & di Piero, B. (2018), 'An improved multiscale Eulerian-Lagrangian method for simulation of atomization process', *Computers and Fluids* **176**, 285–301.

Part V

Appendices

Appendix A

Setup of JICF gaseous inlet profile

This appendix describes the mathematical derivations to impose a gaseous inlet velocity profile in the JICF simulations presented in Chapter 5. The modeled geometry representing the experimental test bench is shown in Figure 5.2. The gaseous inlet consists of a rectangular channel of section 25x40 mm^2. The experiments (Becker & Hassa 2002) report a gaseous boundary layer thickness δ_{exp} of between 4 and 5 mm at the lip of the liquid injector, so a profile aiming at obtaining this thickness is developed. The computational domain of the JICF (Figure 5.2) is a reduced portion of the experimental test rig (Figure 5.1), so an artificial velocity profile with a boundary layer is imposed at the gaseus inlet. The gaseous inlet boundary and the repartition performed to impose boundary layer profiles is shown in Figure A.1.

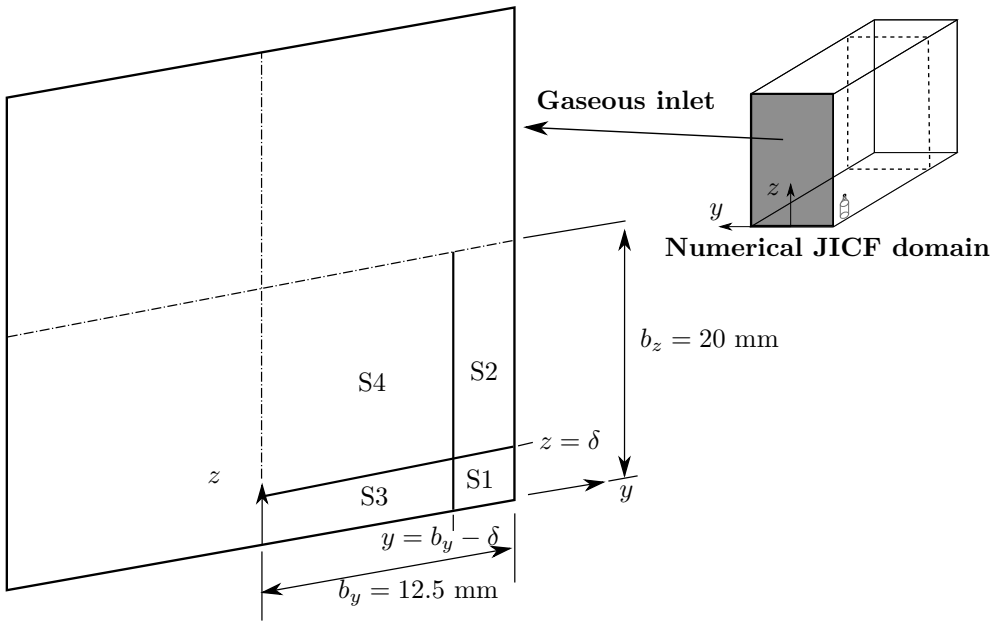

Figure A.1: Inlet domain and partition into sections for calculation of the gaseous velocity profile in JICF simulations

Due to symmetry in both y and z directions, only one fourth of the domain is considered to derive the equations. In this part of the domain, the volumetric flow rate given by the bulk velocity u_g is the following one:

$$Q = u_g b_y b_z \tag{A.1}$$

where $b_y = 25/2 = 12.5$ mm and $b_z = 40/2 = 20$ mm, so the total volumetric flow rate is $4Q$ which agrees with the volumetric flow rate shown in Table 5.2. For deriving the equations, the domain is divided in 4 sections as shown in Figure A.1, where different profiles are imposed:

1. Section 1 (**S1**): Boundary layer profile in both lateral (y) and vertical (z) directions.
2. Section 2 (**S2**): Boundary layer profile in y; outer, constant velocity in z.
3. Section 3 (**S3**): Outer, constant velocity in y; boundary layer profile in z.
4. Section 4 (**S4**): Outer, constant velocity in both y and z.

The boundary layer profiles will follow a 1/7th law, while the outer profile is flat as reported in the experiments (Brandt et al. 1997) and since it corresponds to a turbulent profile as given by the high Reynolds from the operating conditions simulated (Table 5.2).

From mass conservation, it must be fulfilled that the total flow rate from all sections is equal to the total flow rate in this quarter of channel section. The balance then reads:

$$Q = \sum_{i=1}^{4} Q_i = Q_1 + Q_2 + Q_3 + Q_4 \tag{A.2}$$

where Q is given by Eq. (A.1). Hereafter, the expressions for each Q_i and the velocity profile in each section are developed.

Velocity profiles at inlet

Section 1

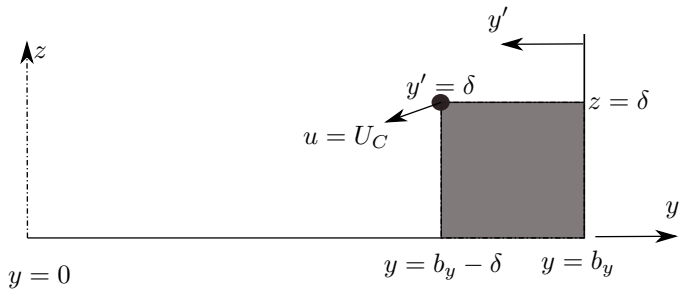

Figure A.2: Parametrization of section 1 (shaded).

To make calculations easier, the following change of variable is introduce in the y direction (Figure A.2):

$$y' = b_y - y \tag{A.3}$$

In this region, there are boundary layers being developed in both y and z directions. The BL is given by the 1/7th velocity profile of White (2005). Hence, the velocity profile in section 1 is given by the following expression:

$$\boxed{u_1\left(y', z\right) = U_c \left(\frac{z}{\delta}\right)^{1/7} \left(\frac{y'}{\delta}\right)^{1/7}} \tag{A.4}$$

where U_c is the velocity at the outer layer, which is constant. This velocity needs to be determined.

The volumetric flow rate at this section is given by the following expression:

$$\begin{aligned} Q_1 &= \int_{y'=0}^{y'=\delta} \int_{z=0}^{z=\delta} u_1\left(y', z\right) = \int \int U_c \left(\frac{z}{\delta}\right)^{1/7} \left(\frac{y'}{\delta}\right)^{1/7} dydz = \\ &= \frac{U_c}{\delta^{2/7}} \int z^{1/7} dz \int y'^{1/7} dy = \frac{U_c}{\delta^{2/7}} \frac{7}{8} \delta^{7/8} \frac{7}{8} \delta^{7/8} = U_C \left(\frac{7}{8}\delta\right)^2 \end{aligned} \tag{A.5}$$

So the volumetric flow rate for region 1 is:

$$\boxed{Q_1 = U_C \left(\frac{7}{8}\delta\right)^2} \tag{A.6}$$

Section 2

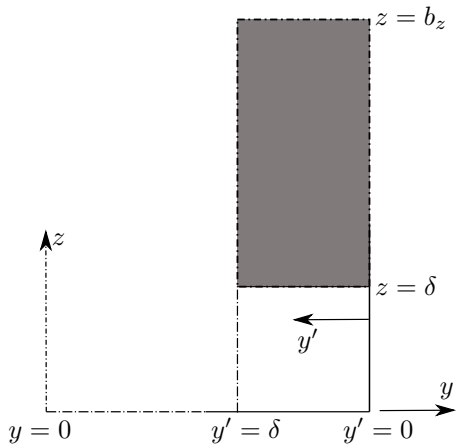

Figure A.3: Parametrization of section 2 (shaded).

In Section 2 there is a boundary layer developing in y' direction and a constant velocity along coordinate z. The velocity in this region is given by the following equation:

$$\boxed{u_2\left(y', z\right) = U_c \left(\frac{y'}{\delta}\right)^{1/7}} \tag{A.7}$$

The volumetric flow rate is given by the following expression:

$$\begin{aligned} Q_2 &= \int_{y'=0}^{y'=\delta} \int_{z=\delta}^{z=b_z} u_2\left(y', z\right) = \int\int U_c \left(\frac{y'}{\delta}\right)^{1/7} dy'dz = \\ &= U_c \int \left(\frac{y'}{\delta}\right)^{1/7} dy' \int dz = U_c \frac{7}{8}\delta\left(b_z - \delta\right) \end{aligned} \tag{A.8}$$

So Q_2 is:

$$\boxed{Q_2 = U_c \frac{7}{8}\delta\left(b_z - \delta\right)} \tag{A.9}$$

Section 3

Section 3 is similar to section 2, except that the boundary layer profile is developed along direction z and the velocity is constant along y. Then, the velocity profile is:

$$\boxed{u_3\left(y, z\right) = U_c \left(\frac{z}{\delta}\right)^{1/7}} \tag{A.10}$$

The volumetric flow rate is given by the following expression:

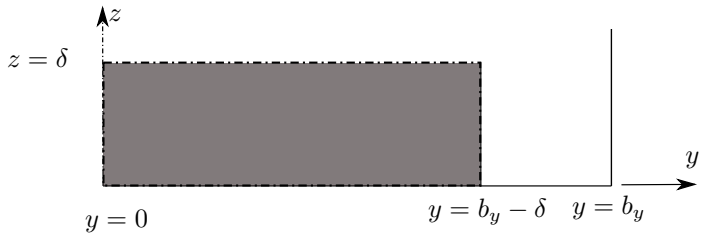

Figure A.4: Parametrization of section 3 (shaded).

$$Q_3 = \int_{y=0}^{y=b_y-\delta} \int_{z=0}^{z=\delta} u_3(y,z) = \int\int U_c \left(\frac{z}{\delta}\right)^{1/7} dydz = \\ = U_c \int dy \int \left(\frac{z}{\delta}\right)^{1/7} dz = U_c \frac{7}{8}\delta\,(b_y - \delta) \tag{A.11}$$

Section 4

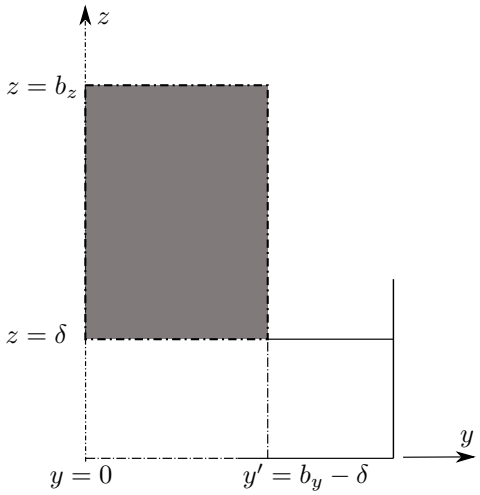

Figure A.5: Parametrization of section 4 (shaded).

The velocity profile at section 4 is flat and constant, equal to the value U_c:

$$\boxed{u_4(y,z) = U_c} \tag{A.12}$$

The volumetric flow rate is:

$$\boxed{Q_4 = U_C\,(b_y - \delta)\,(b_z - \delta)} \tag{A.13}$$

Determining unknowns of velocity profile

The velocity profiles previously derived ensure continuity of velocity in the intersection between sections. These expressions depend on two parameters: the constant velocity of the outer layer U_c and the boundary layer thickness δ of the 1/7th law. This section describes how to estimate analytically these two magnitudes for a given operating point.

Boundary layer thickness from flat plate assumption

The boundary layer thickness δ at the gaseous inlet is calculated assuming that the BL develops as in a flat plate. Figure A.6 shows a general sketch of a BL along a flat plate, showing both the laminar and turbulent profiles. u_g denotes the freestream velocity. The thickness laminar BL grows with the axial coordinate x at a given rate and then transitions to a turbulent one, whose thickness grows steeper with x. The virtual origin of the turbulent BL is shown, which is the point located at the flat plate where the turbulent layer would theoretically start to grow (White 2005).

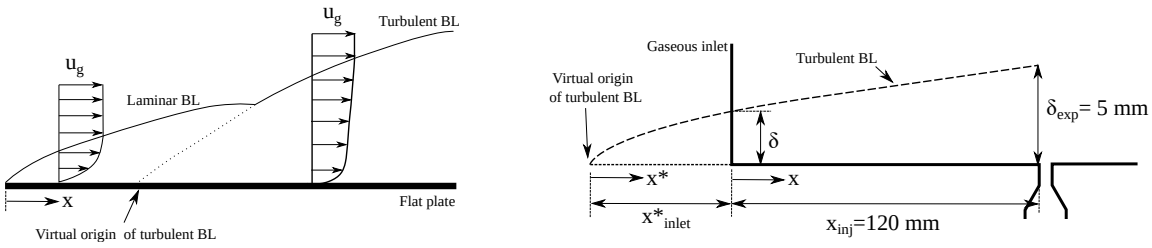

Figure A.6: Boundary layers in flat plates. *Left*: laminar and turbulent boundary layers in a flat plate. *Right*: development of turbulent boundary layer in the JICF computational domain used to calculate the inlet velocity profile layer thickness.

Given the operating conditions from Table 5.2, the gaseous boundary layer at the JICF channel is assumed to develop according to a turbulent profile. Figure A.6 right shows the evolution of the BL in the numerical domain of the JICF simulation (Figure 5.2). At the gaseous inlet, this BL has a thickness δ which is calculated in order to recover the experimental thickness of $\delta = 5$ mm at the liquid nozzle inlet located 120 mm downstream.

In order to estimate the thickness δ, first the virtual origin of the turbulent BL needs to be calculated. As depicted in Figure A.6 right, this point is located outside the numerical domain at a distance x^*_{inlet} upstream the gaseous inlet. To estimate this value, the turbulent BL evolves along the axial direction x^* according to a turbulent Blasius profile (White 2005):

$$\delta = 0.37 \frac{x^*}{Re_x^{1/5}} = 0.37 \frac{(x^*)^{4/5}}{(u_g/\nu_g)^{1/5}} \tag{A.14}$$

where $\nu_g = \mu_g/\rho_g = 1.8162 \cdot 10^{-5}/7.21 = 2.52 \cdot 10^{-6}$ m^2 s^{-1} is the kinematic viscosity. This expression can be applied to obtain x^*_{inlet} knowning that $\delta_{\text{exp}} = 5$ mm:

$$\delta_{\text{exp}} = 0.37 \frac{(x^*_{\text{inlet}} + 120 \text{ mm})^{4/5}}{(u_g/\nu_g)^{1/5}} \quad \rightarrow \quad x^*_{\text{inlet}} = \left(\delta_{\text{exp}}/0.37\,(u_g/\nu_g)^{1/5}\right)^{5/4} - 120 \text{ mm} \tag{A.15}$$

And then, it can be applied again to estimate δ to impose at the gaseous inlet:

$$\boxed{\delta = 0.37 \frac{(x^*_{\text{inlet}})^{4/5}}{(u_g/\nu_g)^{1/5}}} \tag{A.16}$$

Outer layer velocity from flow rate conservation

U_c is determined from flow rate conservation, knowing that the addition of the injected flow rates in each section, Eq. (A.2), needs to equal the total flow rate obtained from the bulk velocity u_g given by Eq. (A.1). Therefore, both expressions are equivalent and can be combined to yield:

$$u_g b_y b_z = U_C \left[\left(\frac{7}{8}\delta\right)^2 + \frac{7}{8}\delta\,(b_z - \delta) + \frac{7}{8}\delta\,(b_y - \delta) + (b_y - \delta)\,(b_z - \delta) \right] \tag{A.17}$$

So the outer layer velocity can be solved:

$$\boxed{U_c = u_g \frac{b_y b_z}{\left(\frac{7}{8}\delta\right)^2 + \frac{7}{8}\delta\left(b_z - \delta\right) + \frac{7}{8}\delta\left(b_y - \delta\right) + \left(b_y - \delta\right)\left(b_z - \delta\right)}} \tag{A.18}$$

Resulting velocity profiles

Velocity profiles are then obtained for each operating condition of Table 5.2 by calculating first the BL profile thickness with Eq. (A.16) and the velocity U_c with Eq. (A.16), and then the profile with Eq. (A.4), (A.7), (A.10) and (A.12). For the two conditions studied, the obtained parameters δ and U_c are reported in Table A.1 and the resulting imposed profiles are shown in Figure A.7.

Table A.1: Parameters obtained characterizing the gaseous inlet velocity profiles

Parameter	$u_g = 75$ m s^{-1}	$u_g = 100$ m s^{-1}
δ [mm]	3.531	3.638
U_c [m s^{-1}]	79.50	106.19

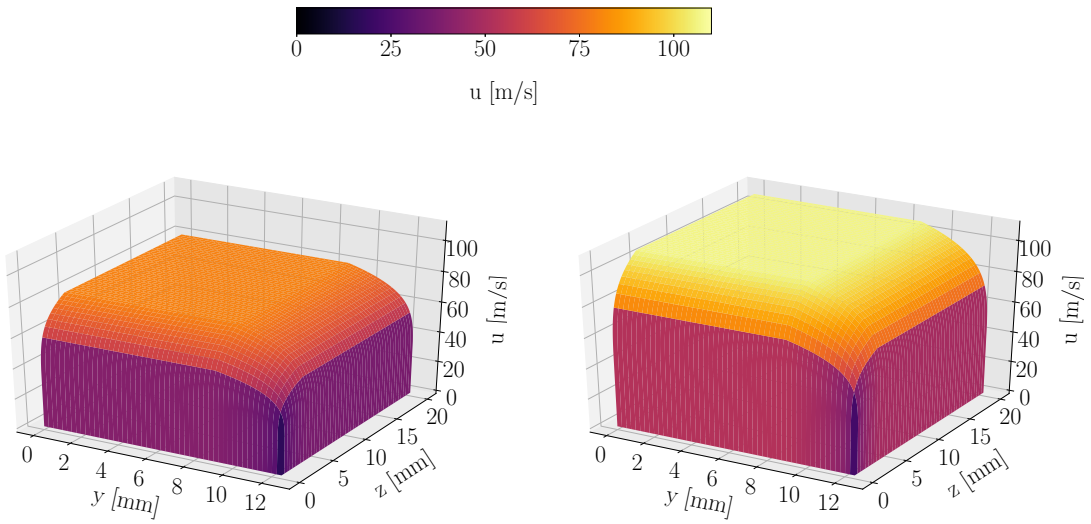

Figure A.7: Gaseous inlet velocity profiles imposed. One quarter of the domain is shown, the profile is then symmetric in both y and z axes. *Left*: $u_g = 75$ m s^{-1}. *Right*: $u_g = 100$ m s^{-1}.

Appendix B
Gaseous initial conditions for JICF

Injection of synthetic turbulence

Prescription of inlet velocity profiles should take into account the contribution of large energy-containing eddies. For this purpose, fluctuations can be added to the mean profiles by specifying either their energy spectrum or their characteristic length scales and their magnitude. These fluctuating components can be obtained by several means. One of the first methods developed consisted of using periodic boundary conditions to reintroduce the outlet velocity field at the inlet in DNS simulations of channels (Spalart 1988, Liu et al. 1996). Such methods rely either on the presence of self-similarity in the channels, which does not always occur, or on adding a forcing term at the outlet to reconvert the boundary layer thickness to its value upstream for reintroducing it into the inlet. To circumvent these issues, the recycling method was proposed by Lund et al. (1998). This technique consists of obtaining the turbulent data at several planes downstream the inlet, compare the velocity fields and correct the inlet conditions accordingly to match the desired data. Recycling methods have been extended and can be divided in weak and strong methods. Other families of techniques include the generation of synthetic turbulence by for superposition of sinusoidal waves (Kraichnan 1970, Batten et al. 2004) or by moments' determination (Pamiès et al. 2009). A review of these and other turbulence generation methodologies can be found in Wu (2017).

In this work, homogeneous synthetic turbulence is injected through the inlet by specifying the integral length scale of the flow L_T and the fluctuating velocity components u'. Since experimental data on the fluctuating field for the configuration of (Becker & Hassa 2002) is not available, both magnitudes are estimated with the following formulas (ANSYS 2018):

$$u' \approx I u_g \quad ; \quad L_t \approx 0.07 D_h \tag{B.1}$$

where I is the turbulent intensity can be obtained from the following correlation:

$$I = 0.16 Re_g^{-1/8} \tag{B.2}$$

For each operating point shown in Table 5.2, the estimated parameters for specifying turbulent profiles are shown in Table B.1.

Characteristic flow-through time

With the inlet velocity specified with a mean profile and turbulence fluctuations, gaseous simulations can be run to generate initial conditions for the liquid simulations. The initial solution needs to be an established velocity profile where the mean and rms values of velocity components are converged. To get an idea of the flow establishment, the flow-through time in the channel τ_{ft} is defined:

$$\tau_{\text{ft}} = \frac{L}{u_g} \tag{B.3}$$

where $L = 120$ mm is the distance from the gaseous inlet to the liquid injector (see Figure 5.2). This quantity represents the time that a gas particle takes, in average, to reach the liquid injector location from the inlet of the domain. Flow-through times for each operating point are shown in Table B.1.

Table B.1: Parameters characterising inflow turbulent fields and flow-through time τ_{ft} in JICF simulations

Operating point	L_t [mm]	I [%]	u' [m s^{-1}]	τ_{ft} [ms]
Low Weber	3	2.88	2.5	1.6
High Weber	3	2.78	3.0	1.2

Mesh independence study with high Weber operating point

In first place, a mesh independence study has been performed with single-phase simulations (without fuel injection) to capture correctly the gaseous turbulent features that can affect the liquid field. For this purpose, 3 grids are tested with the high Weber operating condition. The inlet velocity profile includes the mean velocity profile and the turbulence fluctuations as defined in Table B.1. The meshes differ in the baseline cell size at the region upstream the liquid injection nozzle, which measures 120 mm (see Figure 5.2). This is the region of interest for turbulence development, since it is the gaseous field upstream the injection nozzle the one that will affect the liquid jet. Three meshes are used with baseline mesh sizes of values $\Delta x_{\text{ups}} = 1,\ 0.5,\ 0.3$ mm, summarized in Table B.2. The three refinement levels tested in this section are shown in Figure B.1, where a magnified view of the red rectangle from Figure 5.3 is displayed. The mesh elsewhere is not refined and maintained to the values given previously in §5.3.

Table B.2: Configurations tested for the mesh independence study

Mesh	Δx_{ups} [mm]	# elements	# nodes
Coarse	1.0	59,664,589	10,510,540
Fine	0.5	66,264,433	11,641,585
Very fine	0.3	94,192,955	17,155,591

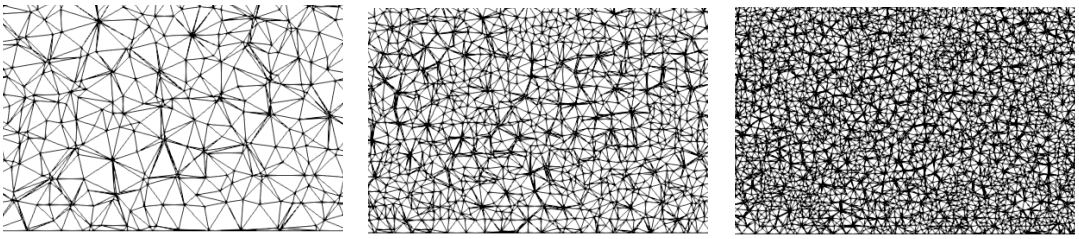

Figure B.1: Baseline meshes in the region spanning from the inlet to the nozzle injector. Zoom-in the red rectangle of Figure 5.3. From left to right: $\Delta x_{\text{ups}} = 1, 0.5, 0.3$ mm.

A total of four simulations have been performed: one simulation per mesh with the imposed turbulent fluctuations at the inlet, and one without injecting synthetic turbulence for the resolution $\Delta x_{\text{ups}} = 0.5$ mm. For flow establishment, the simulations are firstly run for a total physical time of 6 times the flow-through time, i.e. 7.2 ms. From this stage on, statistics are collected. To check the convergence of the simulations, the mean axial velocity u and mean Turbulent Kinetic Energy (TKE) have been integrated along a vertical line upstream the injection point in the middle plane of the domain, shown in Figure B.3 right. These line-integrated magnitudes can be defined as follows:

$$\langle u \rangle = \frac{1}{h}\int_0^h \overline{u\,(z)} dz \quad ; \quad \langle \text{TKE} \rangle = \frac{1}{h}\int_0^h \frac{1}{2}\left(\overline{u'\,(z)^2} + \overline{v'\,(z)^2} + \overline{w'\,(z)^2}\right) dz \tag{B.4}$$

where $\overline{u(z)}$ is the time-averaged, or mean, velocity at each z location; h is the line length, which corresponds to the height of the channel; and u', v' and w' are the fluctuating components of the velocity in the x, y and z directions respectively. The chosen line is located right before the liquid injector, so velocity and TKE profiles in this section are the ones seen by the liquid jet which affect its deviation. The integrated values for these magnidues are shown in Figure B.2. Profiles of both $\langle u \rangle$ and $\langle TKE \rangle$ reach a steady state in all simulations after a simulation time of 30 times the flow-through time τ_{fl}, so statistics are considered to be converged after this value. Therefore, all statistics shown hereafter will refer to statistically-converged results obtained for $t/\tau_{\text{fl}} > 30$. Regarding the mesh effect (considering turbulence injection), $\langle u \rangle$ shows a change for the coarse mesh $\Delta x_{\text{ups}} = 1$ mm with respect to $\Delta x_{\text{ups}} = 0.5, 0.3$ mm, which has the same value, indicating proper mesh convergence for $\langle u \rangle$ at the selected integration line. Surprisingly, $\langle TKE \rangle$ shows the same value for the three mesh resolutions employed: the mesh seems to have no effect in $\langle TKE \rangle$. Regarding the influence of turbulence injection (with $\Delta x_{\text{ups}} = 0.5$ mm), both magnitudes show statistically-converged values lower than the case with turbulence. This is coherent with TKE, since it means that injecting turbulent fluctuations at the inlet increase the turbulent state further downstream. However, no explanation is found of why adding turbulence with the selected methodology changes the value of $\langle u \rangle$ (although the deviations with respect to case with turbulence represents is of less than 1 %). Nevertheless, it is to be noted that these line-integrated values are used only to obtain an idea of the time the flows take to establish, and do not represent magnitudes that can be used for a proper assessment of the mesh independence. As it will later be shown, the TKE profiles represented along here-called integration line are very dependent on the mesh resolution employed.

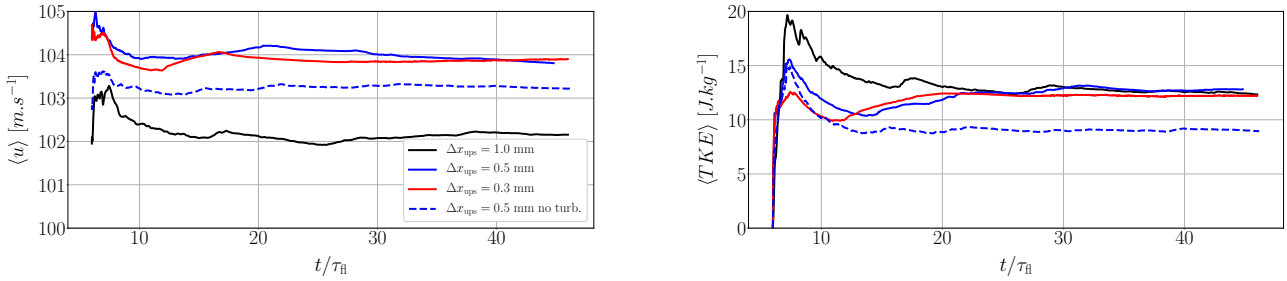

(a) Mean axial velocity

(b) Turbulent Kinetic Energy

Figure B.2: Convergence of line-integrated mean axial velocity and TKE with mesh resolution

Instantaneous snapshots of the fluctuating axial component u' in the middle plane are shown in Figure B.3. Adding turbulence at the inlet introduces fluctuations that are transported downstream the domain. When no turbulence is added, fluctuations are not present (the black contours at the inlet are due to small numerical fluctuations of u') except close to the walls, since they are created inside the boundary layer where flow is intrinsically turbulent. It is also observed that the characteristic length of the eddies changes when refining the mesh: for the coarsest mesh ($\Delta x_{\text{ups}} = 1$ mm), these structures are generally large, while refining the mesh to $\Delta x_{\text{ups}} = 0.5$ and 0.3 mm reduced their size.

In order to compare quantitatively the difference between meshes, the signals of u' have been monitored with time at the probes shown by the white crosses in the top of Figure B.3. Two probes are located: one at 50 mm upstream the liquid inlet (x = 70 mm, probe A) and another one 1 mm upstream the liquid injection nozzle (x = 119 mm, probe B), both at a height of 8 mm from the bottom wall. The capability of the meshes to transport the resolved turbulent scales is then verified by comparing the fluctuations and spectra obtained with Fast Fourier Transform (FFT) at both probes in Figure B.4. Time has been normalised with the flow-through time τ_{fl}, and the signals are shown for one passage of τ_{fl} for easiness of visualization. For the coarsest mesh $\Delta x_{\text{ups}} = 1$ mm (Figure B.4a), the u' signal sampled closer to the nozzle (Probe B) shows similar magnitudes and frequencies to the signal sampled upstream (Probe A). Despite the characteristic peaks at frequencies of 8, 17 and 25 kHz with decreasing intensity for both probes, low frequencies below 10 kHz are excited. The spectrum at Probe B shows a higher relative intensity at these low frequencies with a peak at 3 kHz not observed at probe A. This indicates that for this resolution, turbulent energy is not properly transported to the liquid injector. Furthermore, characteristic frequencies larger than 25 kHz cannot be captured, which is not the case for the rest of resolutions. When the mesh is refined to $\Delta x_{\text{ups}} = 0.5$ mm (Figure B.4b), the small dominant frequencies are no longer relevant and dominant frequencies are properly captured, as the match in the peaks of the spectra indicates. In this case, the frequencies 8 and 25 kHz have

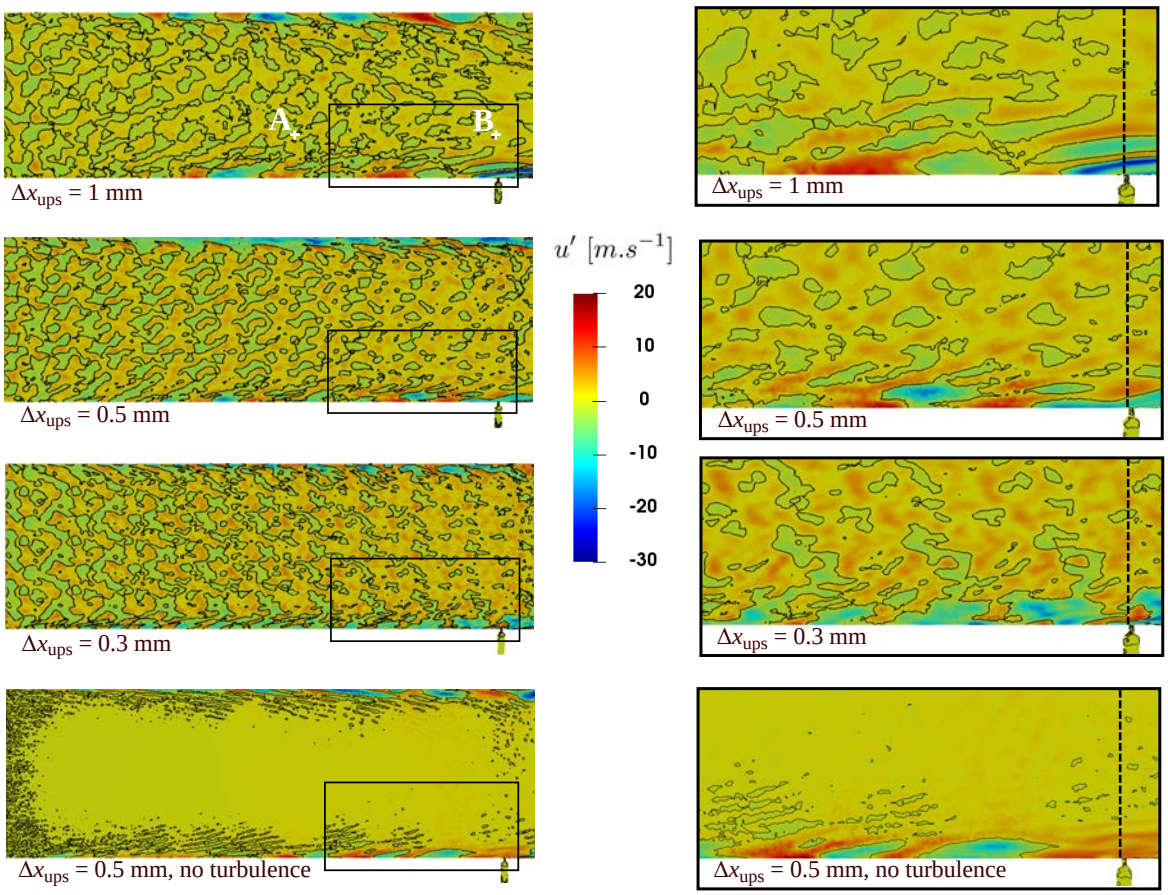

Figure B.3: Instantaneous u' fields from gaseous simulation for the high Weber case. The right column shows a zoomed-in view of the dashed rectangle from the left column. Black contours indicate the lines with zero instantaneous fluctuation $u' = 0$. From top to bottom $\Delta x_{\text{ups}} = 1, 0.5, 0.3$ mm.

larger intensity than 17 kHz. Refining the mesh to $\Delta x_{\text{ups}} = 0.3$ mm (Figure B.4c) has no longer effect neither in the magnitude of the fluctuations nor in the spectrum.

The fluctuations and FFT of the simulation performed without turbulence injection for the resolution $\Delta x_{\text{ups}} = 0.5$ mm are shown Figure B.4d. As expected, the magnitude of the fluctuations is lower than in the cases with synthetic turbulence. The spectrum shows that the energy content at low frequencies is high and that no clear dominant frequencies are found.

A final verification on the mesh capability to transport turbulent energy is done by calculating the Turbulent Kinetic Energy (TKE) at the probes A and B for simulation where turbulence is transported. TKE is defined as follows:

$$TKE = \frac{1}{2}\left(\overline{u'^2} + \overline{v'^2} + \overline{w'^2}\right) \tag{B.5}$$

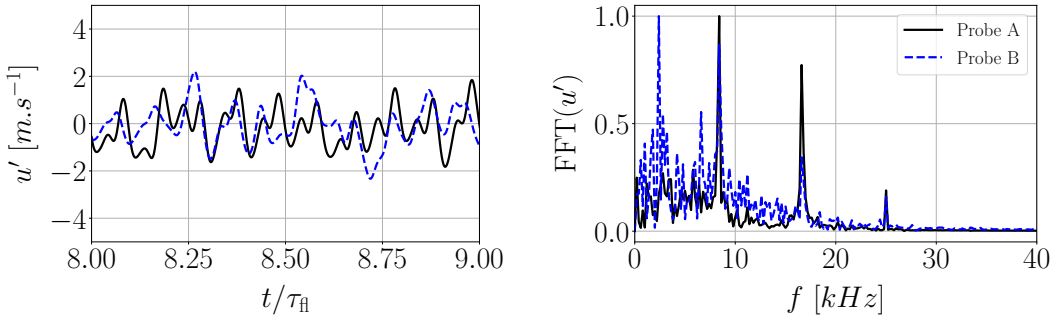

(a) Mesh $\Delta x_{\text{ups}} = 1$ mm

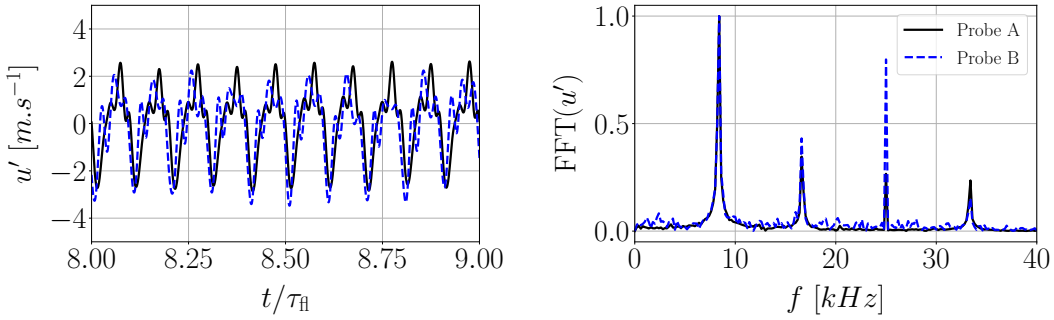

(b) Mesh $\Delta x_{\text{ups}} = 0.5$ mm

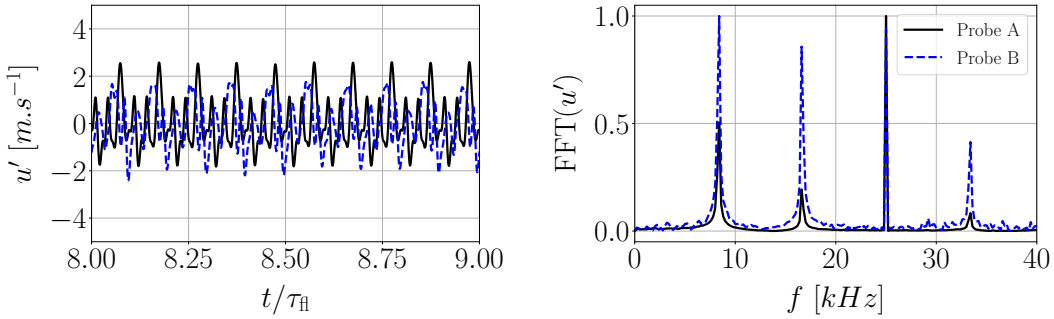

(c) Mesh $\Delta x_{\text{ups}} = 0.3$ mm

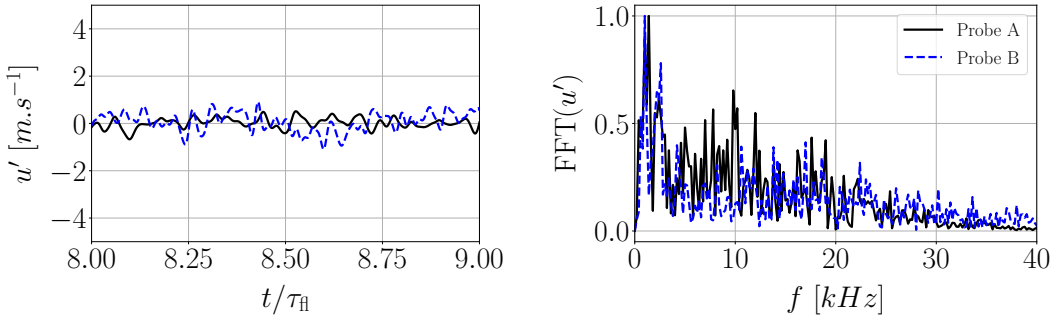

(d) Mesh $\Delta x_{\text{ups}} = 0.5$ mm without turbulence injection

Figure B.4: Axial velocity fluctuations and associated frequencies at the sampling probes for the simulations at high Weber number. *Left*: u' fluctuations. *Right*: spectra of the fluctuations obtained through FFT.

Note that, unlike in Eq. (B.4), the TKE is not line-averaged but represents the resolved energy contained in the eddies at the probes location. Figure B.5 gives the results. The coarser mesh with $\Delta x_{\text{ups}} = 1$ mm provides different values of TKE in both probes with a difference of 34 %: TKE is lost from point A to point B and this mesh cannot transport turbulence properly. Refining to $\Delta x_{\text{ups}} = 0.5$ mm improves the transport capability of the mesh and both probes show similar values of TKE: 4.17 $J\ kg^{-1}$ for probe A against 4.14 $J\ kg^{-1}$ at probe B, making a difference of 0.7 %. Finally, the mesh with $\Delta x_{\text{ups}} = 0.3$ mm provides values of 4.2 and 4.19 $J\ kg^{-1}$ in probes A and B respectively, yielding a difference of 0.24 % and making this mesh more suitable for transporting the turbulence. Nevertheless, the mesh with $\Delta x_{\text{ups}} = 0.5$ mm already yields small errors in the TKE transport while providing TKE values very close to those of the mesh with $\Delta x_{\text{ups}} = 0.3$ mm: it provides also good turbulent transport capabilities with smaller computational cost than the finest mesh due to its smaller number of elements (see Table B.2).

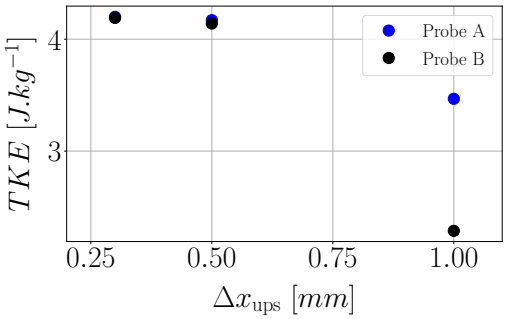

Figure B.5: Variation in Turbulent Kinetic Energy in probes A and B with upstream mesh resolution.

Finally, Figure B.6 plots the profiles of mean axial velocity $\overline{u}$ and TKE along the vertical line from in Figure B.3 right. $\overline{u}$ is properly captured for all meshes, despite slight variations within the boundary layer where it evolves from 0 to the velocity in the outer layer, which is constant and equal in all cases (despite some fluctuations due to numerical noise). The boundary layer thickness (observed in the evolution of both $\overline{u}$ and TKE) is around 5 mm, which is consistent with the experimental values reported in Becker & Hassa (2002). TKE profiles in turbulent cases show that the turbulent energy in the outer layer (z > 5 mm) is similar for resolutions $\Delta x_{\text{ups}} = 0.5$ and 0.3 mm, but lower for the thicker resolution of 1 mm. Within the boundary layer, however, convergence with resolution is never achieved. Effectively, Kolmogorov length-scales for the studied case, which correspond to the length of the smallest eddies in the boundary layer, are of the order of $\eta \sim 0.5$ μm (see Table B.3 for estimations), which cannot be captured with any resolution employed. A proper resolution at this region would require a DNS study, which is nowadays unfeasible for the operating point studied and which justifies the use of LES for these simulations. Nevertheless, the values of TKE for z > 2 mm, including the energy decrease from this point up to the freestream, is converged for the resolution $\Delta x_{\text{ups}} = 0.5$ mm.

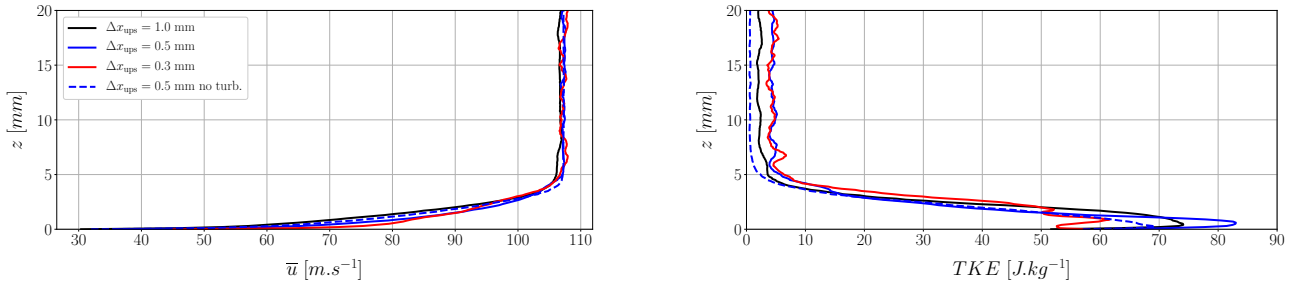

(a) Mean axial velocity

(b) Turbulent Kinetic Energy

Figure B.6: Profiles of $\overline{u}$ and TKE along the line right upstream the injector.

From these results, the simulation with the mesh resolution $\Delta x_{\text{ups}} = 0.5$ mm is chosen as initial solution for performing the two-phase simulations. This mesh size allows for a proper turbulent transport (frequencies and energy content) with a moderate cost: Table B.2 shows that decreasing resolution from 0.5 to 0.3 mm adds up to 28 million more elements. The turbulent content in the inner part of the turbulent layer is not

properly resolved, which could have an effect on the jet atomization and has not been checked in this work. It, however, does not have an effect on the trajectory, as it is shown in §5.6.3. A local refinement in the boundary layer (inflation layer) could help to converge the TKE profiles, but would greatly increase the cost of the simulations due to the length of the domain upstream the liquid injector and to the small cell size required to capture accurately the Kolmogorov scales.

Turbulent scales estimation

In fluid mechanics, the largest and the smalles lengthscales are named respectively the integral and Kolmogorov scales. These ones represent the size of the largest and smalles eddies found within the flow: the largest eddies are the ones containing more energy which is then transferred to the eddies of smaller size up to the Kolmogorov eddies, where viscosity is important and turbulent dissipation takes place (energy cascade).

The size of integral eddies and their associated time scales can be obtained from the geometry and the mean flow characteristics. For the JICF simulations of Chapter 5, the integral scale of the gas phase L_I is estimated as half of the hydraulic diameter (configuration of Figure 5.2), and its timescale τ_I and characteristic frequency is obtained by considering the mean gas velocity u_g:

$$L_I = \frac{D_h}{2} \sim 15 \text{ mm} \qquad \tau_I = \frac{L_I}{u_g} \qquad f_I = \frac{1}{\tau_I} \tag{B.6}$$

At the smallest scales, dissipation takes place and both viscosity ν and dissipation rate ϵ govern these eddies. The characteristic length and time scales, η and τ_η respectively, can then be calculated as:

$$\eta = \left(\frac{\nu^3}{\epsilon}\right)^{1/4} \qquad \tau_\eta = \left(\frac{\nu}{\epsilon}\right)^{1/2} \qquad f_\eta = \frac{1}{\tau_\eta} \tag{B.7}$$

Since the Kolmogorov eddies are isotropic, the dissipation rate can be estimated as $\epsilon \sim u_g^3/L_I$ (Piomelli 2018). Then, the Kolmogorov scales can be expressed in relation to the integral ones and the Reynolds number as:

$$\frac{\eta}{L_I} \sim Re_g^{-3/4} \qquad \frac{\tau_\eta}{\tau_I} \sim Re_g^{-1/2} \tag{B.8}$$

From these expressions, the characteristic flow scales for the gaseous phase in the JICF simulations of Chapter 5.2 can be estimated. Results are shown in Table B.3.

Table B.3: Estimation of characteristic length and time scales for gaseous phase in JICF simulations

Parameter	$u_g = 75$ m s^{-1}	$u_g = 100$ m s^{-1}
L_I [mm]	15	15
τ_L [ms]	0.20	0.15
f_L [kHz]	5	6.5
η [μm]	0.5	0.4
τ_η [μs]	0.20	0.15
f_η [kHz]	5000	7000

Appendix C
Postprocessing methods for JICF

C.1 Jet trajectory

Experimentally, researchers have used different approaches to obtain trajectories based on the different optical techniques employed. Many works (Becker & Hassa 2002, Stenzler et al. 2003, Freitag & Hassa 2008) take instantaneous images of the jet with shadowgraphy techniques and then MIE scattering or emboss-filter operations to obtain binary images where liquid and gas phases can be clearly distinguished. Then, images are averaged and the vertical penetration is obtained by detecting the coordinates where the light intensity gradients are maximum. Image averaging can be performed before or after the filtering operations. Such methods obtaining trajectories from average images are hereafter denoted as **mean trajectory methods**. Figure C.1 shows an illustration of such experimental methodology from the work by Stenzler et al. (2003). Other works (Ragucci et al. 2007) use the same principles of filtering and binarization, but obtain the trajectories from instantaneous jet images. Then, instantaneous trajectories are averaged to yield the mean trajectories. These methods are hereafter denoted as **instantaneous trajectory methods**.

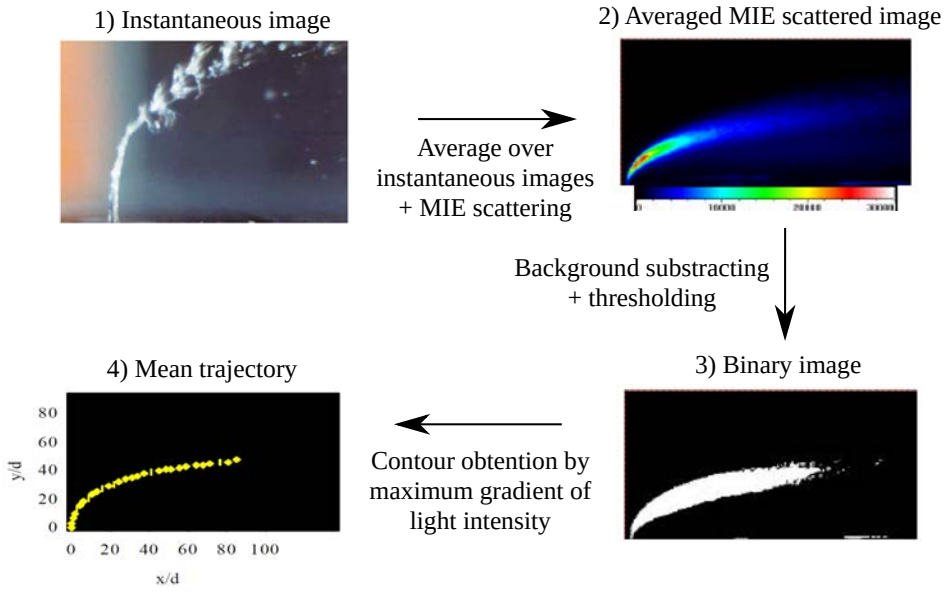

Figure C.1: Illustration of experimental procedure to obtain trajectories. Figures taken from Stenzler et al. (2003)

From a computational perspective, similar methodologies can be applied to obtain the jet trajectories from simulations. The same sequence of operations from Figure C.1 for processing experimental images could be applied to numerical snapshots of the JICF. Nevertheless, the ACLS methodology presents the advantage

that the interface is clearly defined with the ψ function, and hence trajectories can be obtained with different methods without the need to use MIE scattering and binarization (steps 2 and 3 from Figure C.1). In this work, four methodologies to obtain the numerical trajectories from JICF resolved simulations are presented. As in the experimental classification previously suggested to obtain trajectories, these methodologies are also distinguished as **mean trajectory methods** or **instantaneous trajectory methods**, depending on whether they use the mean or instantaneous ψ field respectively. Two methods for each category are detailed in this section.

Mean trajectory methods

One possibility to obtain mean trajectories is by using the mean field of the levelset function, $\overline{\psi}$. An example of a converged $\overline{\psi}$ field is shown in Figure C.2 left. This requires the accumulation of statistics over a certain time (instantaneous trajectories do not need statistics accumulation as long as the instantaneous ψ field is available), but presents the advantage that the jet trajectory can be obtained with one single $\overline{\psi}$ field once convergence is achieved. In this category, two different methods are used: the **maximum gradient method** and the **iso-contour method**:

- The **maximum gradient method** consists to obtain the maximum gradient of $\overline{\psi}$ in the vertical direction for each x coordinate: $\max\left(\nabla_z|\overline{\psi}|\right)$. Figure C.2 center shows an example of a $\max\left(\nabla_z|\overline{\psi}|\right)$ contour. This method is more similar to the experimental methods presented in Becker & Hassa (2002), Stenzler et al. (2003) and Freitag & Hassa (2008): in these works, the jet trajectory is obtained as the contour of the maximum intensity gradient in the vertical direction of the mean jet (see Figure C.1).
- Trajectory as **iso-contour** of mean levelset field $\overline{\psi}$. This approach has been used to obtain JICF trajectories with simulations using a VOF methodology (Desclaux et al. 2020). In this work, several values for the iso-contour have been tested, and it has been found that the mean trajectories obtained are very sensitive to this value. Finally, a value of $\overline{\psi} = 0.01$ has been identified as the best contour to compare the resulting trajectories with the ones obtained with the rest of methods. Figure C.2 right shows an example of a an example of a $\overline{\psi} = 0.01$ contour.

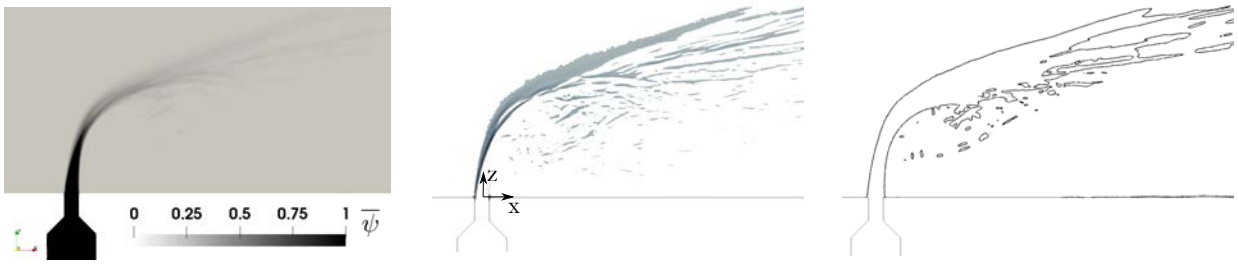

Figure C.2: Methods based on mean trajectories. *Left*: $\overline{\psi}$ field. *Center*: $\max\left(\nabla_z|\overline{\psi}|\right)$ contour. *Right*: contour $\overline{\psi} = 0.01$.

Instantaneous trajectory methods

Instead of using the mean levelset field, the averaged numerical trajectories can be obtained from instantaneous solutions of the jet by firstly getting the instantaneous trajectories and then averaging them. Figure C.3 shows the procedure to extract the interface contour that is later used to obtain the trajectories. First, the liquid-gas interface is plotted in the domain as a surface of iso-contour $\Gamma : \psi = 0.5$ (Figure C.3 left), and then this contour is extracted at the central plane $y = 0$, as indicated by the black line of Figure C.3 right.

Once the interface is obtained at $y = 0$, the outer contour of the trajectory must be obtained. This is the one corresponding to the windward side of the jet, and hence the one defining the instantaneous trajectory. For its obtention, the z axis is swept and the points belonging to the trajectory are obtained as follows:

1. The z axis is discretized in intervals with constant thickness.
2. For each interval, the contour point with minimum x coordinate is obtained.
3. Points are sorted according to their x coordinate, defining the trajectory.

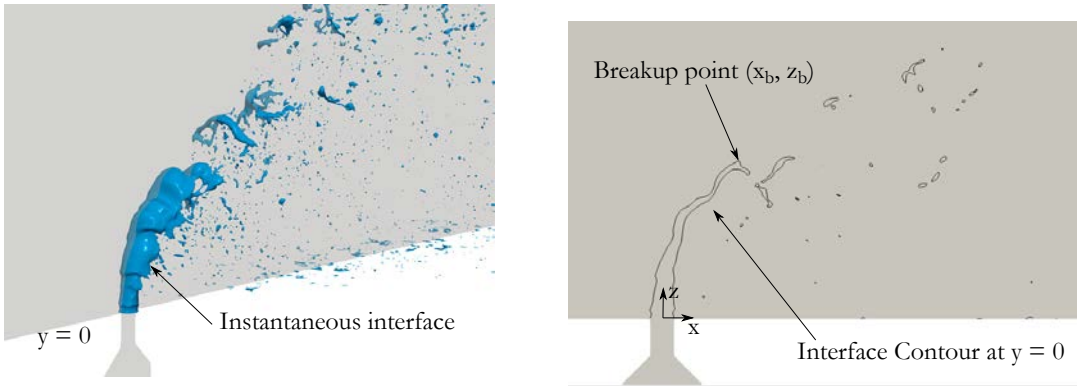

Figure C.3: Procedure to process instantaneous trajectories. *Left*: instantaneous jet interface. *Right*: contour of instantaneous interface at plane y = 0

This procedure is repeated at every instantaneous snapshot of the jet to obtain the corresponding trajectories. Then, all trajectories are interpolated in the same axial locations and averaged to yield mean trajectories which can be compared to experimental correlations. This method is similar to the experimental methodology employed by Ragucci et al. (2007), and was used by Leparoux et al. (2018) to simulate their experimental configuration and validate the computations. However, it differs from the methodology employed by Becker & Hassa (2002), whose experimental test rig is simulated in this work and who obtained the trajectories with a methodology more similar to the mean trajectory methods (see next point). Still, it is worth to investigate the instantaneous methodologies and to compare them with the mean methods to illustrate the effect that the post-processing methodology can have on the jet trajectories when treating the same simulations.

The procedure previously described works properly in the dense core, where the interface contour is continuous up to the breakup point z_b. After this location, atomization takes place and the detected interface contours belong to ligaments or droplets. In this case, the definition of *outer trajectory* does not hold as clearly as in the dense core: some contours detected might belong to satellite droplets or to drops originated from surface breakup, and could modify the final average trajectory by lowering it down. With this consideration, two different trajectories are distinguished in the instantaneous methodologies: **non-monotonic** and **monotonic** trajectories:

- **Non-monotonic instantaneous trajectories** can be obtained by applying the methodology as explained in the previous lines, accounting also for the contours which a priori do not pertain to the instantaneous trajectory. This procedure is illustrated in Figure C.4: the different points of the trajectory are obtained when sweeping the z axis, and the instantaneous trajectory is obtained by joining these points. Then, sorting all the sampled points along the x axis creates a non-monotonic trajectory since some contour points belong to liquid structures further downstream, see Figure C.4 right.
- **Monotonic instantaneous trajectories** are obtained similarly to non-monotonic ones but with one fundamental difference: when sorting along the x axis, only points with increasing z coordinate are considered. In this way, a monotonic trajectory is obtained, see Figure C.5 right.

Table 5.4 shows a summary of the four methodologies presented, and the names used in §5.6.3 to display the results.

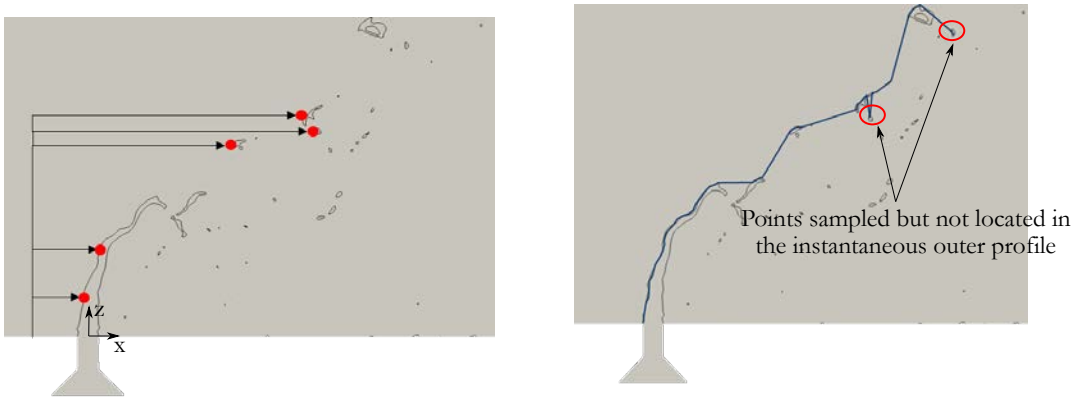

Figure C.4: Obtention of non-monotonic instantaneous trajectory. *Left*: sweep process along z axis of interface points. *Right*: instantaneous trajectory.

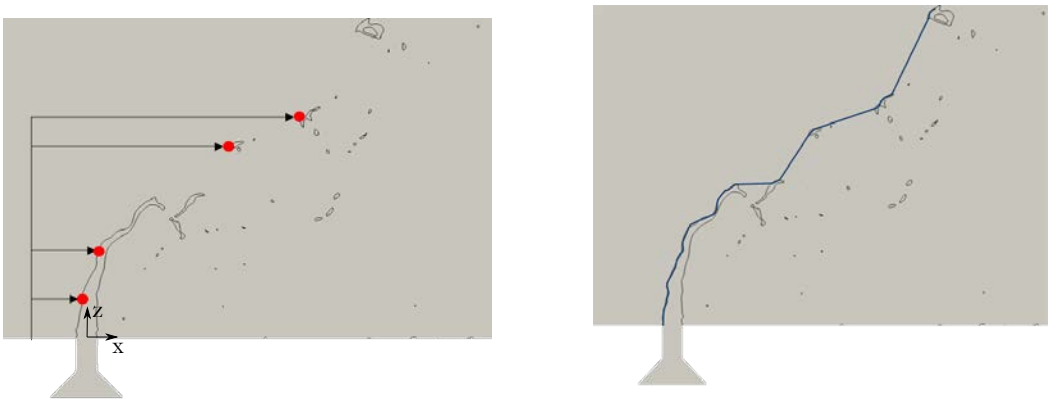

Figure C.5: Obtention of monotonic instantaneous trajectory. *Left*: sweep process along z axis of interface points, excluding points whose vertical location is lower than the vertical location of the previous ones. *Right*: instantaneous trajectory.

C.2 Direct measurement of liquid fluxes

While for obtaining lagrangian quantities the droplets are tracked through the sampling planes when they cross their axial locations x, direct measurement of the fluxes requires the integration of the level-set function ψ in all the mesh elements conforming the plane. Therefore, it is necessary to consider all the mesh elements that intersect with the defined sampling plane for the numerical computation of the fluxes. Figure C.6 shows an example of a plane perpendicular to the crossflow with all the 3D elements intersecting this plane. This geometrical entity where fluxes are directly integrated will be hereafter referred as **interior boundary** (IB).

Liquid flow rates can be calculated in the IBs from the levelset function ψ by applying directly Eq. (2.23) divided by the density, with $\phi = \psi$:

$$Q_{l,\mathrm{IB}} = \int_{\mathrm{IB}} \psi \left(\mathbf{u} \cdot \mathbf{n}\right) dS \tag{C.1}$$

For evaluating this integral, firstly the liquid flux through each mesh element belonging to the IB is needed. As depicted in C.6 right, each surface element is defined by a normal n_e and by three nodes $N_{\mathrm{no}} = 3$. Physical quantities are stored at the nodes, so the liquid flux passing through each single element is calculated as:

$$Q_{l,e} = \frac{1}{N_{\mathrm{no}}} \sum_{i=1}^{N_{\mathrm{no}}} \psi_i \mathbf{u}_i \mathbf{n}_e \tag{C.2}$$

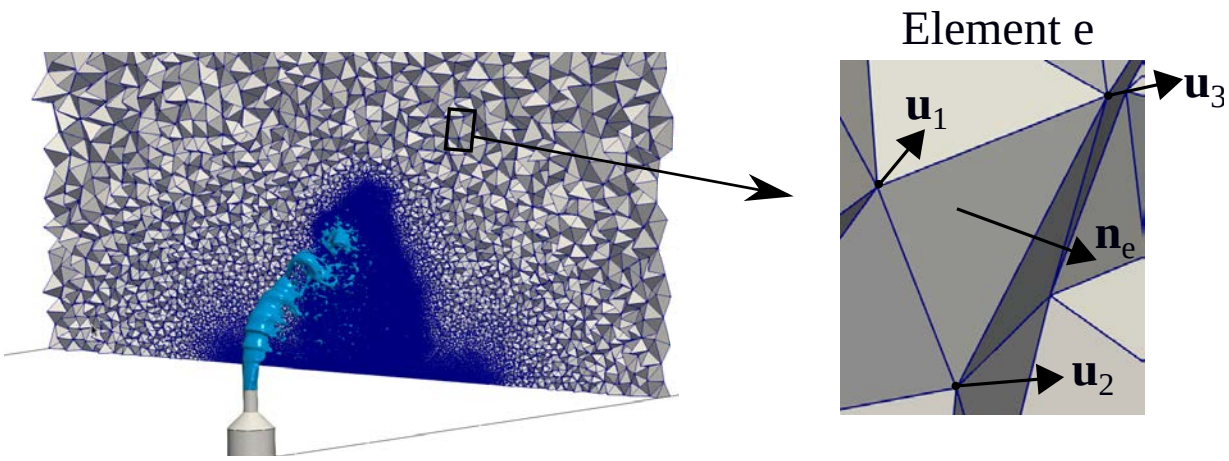

Figure C.6: Interior boundaries discretization for obtention of liquid flow rates.

Then, all elements are summed up to yield the liquid flux at the IB:

$$Q_{l,\mathrm{IB}} = \sum_{e=1}^{N_e} Q_{l,e} = \sum_{e=1}^{N_e} \frac{1}{N_{\mathrm{no}}} \sum_{i=1}^{N_{\mathrm{no}}} \psi_i \mathbf{u}_i \mathbf{n}_e \tag{C.3}$$

With this procedure, the instantaneous liquid flow rates at a given IB is obtained. Fluxes are then monitored with time and statistics (mean and RMS quantities) can be obtained.

In the same way as the sampled lagrangian spray can be in-plane characterized (see §4.4.3), liquid fluxes can also be spatially discretized in the IBs. The procedure is shown in Figure C.7: a grid composed of rectangular probes can be defined in the IB, so that all elements comprised by the probes are contained. However, it is observed that the rectangular mesh does not fully match the elements distributed in the IB, since the CFD mesh is not uniform and is comprised of tetrahedral elements. Therefore, the requested rectangular probes cannot be obtained in the IB, as it often crosses elements (red line in Figure C.7 right). Instead, the probes used for calculation of spatially distributed fluxes are adjusted to take into account the elements that are crossed by the requested mesh, as indicated by the green line in Figure C.7 right. Therefore, the actual probes used for calculation are not rectangular, but fitted to the actual mesh in order to properly retrieve fluxes.

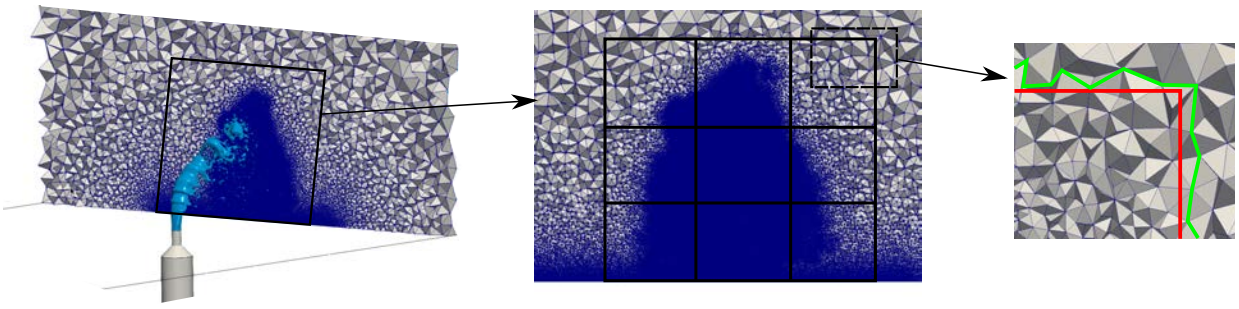

Figure C.7: Interior boundaries discretization for obtention of bounded flow rates.

C.3 Dense core breakup point

Topology processing methodology

The procedure to extract the DC, depicted in Figure C.8, works as follows:

1. **DC identification and isolation**. The DC is identified at a given time instant as the liquid structure with largest volume in the simulation. This can easily be done with YALES2 since each liquid structure has a unique tag, named droplet number, which helps to differentiate it from the others. The droplet number with the associated largest volume in the domain is isolated from the others, so the coordinates of the liquid nodes belonging to the dense core are obtained.

2. **Topology characterization**. Once the DC has been obtained, its topology is characterized through its **breakup point** and **width**:

   - The breakup point (x_b, z_b) is obtained as the point at the symmetry plane $y = 0$ which is located further away from the injection location in the vertical direction z.
   - The width w is obtained by sweeping the DC along the x axis and discretizing it into segments of size Δx. For each segment, the maximum and minimum points in the y direction are calculated, i.e. the points which are located further away from the symmetry plane at both sides of the jet in a $x - y$ plane. The difference between this maximum and minimum denote the local width at each segment: the DC width is obtained as the maximum value of all the local widths obtained.

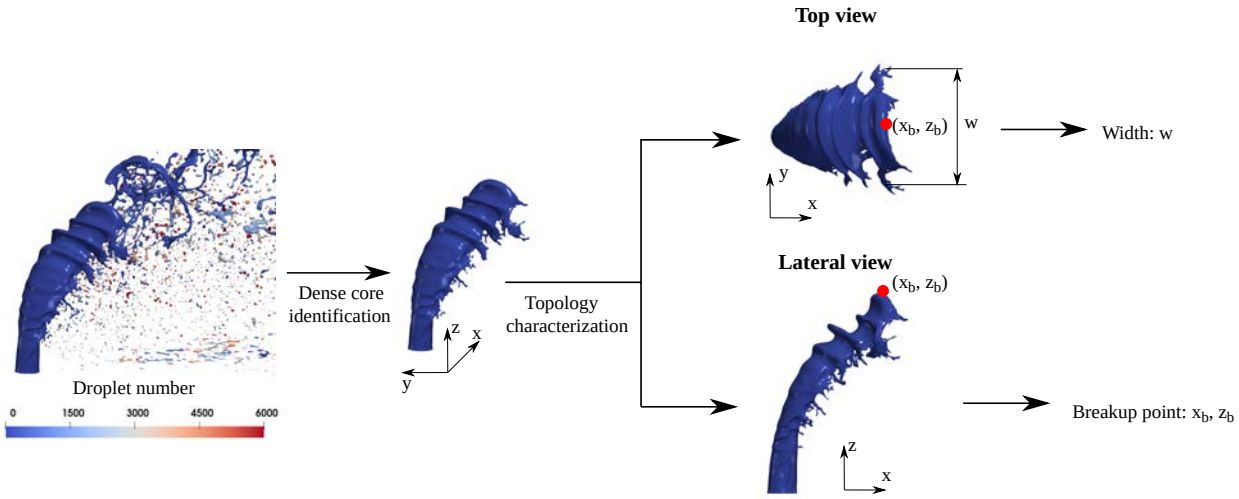

Figure C.8: Extraction of dense core from resolved atomization simulations.

The DC is then characterized by its breakup point coordinates (x_b, z_b) and its width w. These values are time-dependent, and therefore statistics will be obtained from them. It is also important to note that the procedure employed to extract the DC from YALES2 simulations is ad-hoc and is not based on any methodology employed in experimental works to characterize the DC. This is justified by the fact that there are not many experimental studies on the JICF topology and not one single one of them applies to the operating conditions studied in this work. Therefore, no proper experimental validation can be performed for the DC characteristics. Instead, the main purpose of this analysis is to obtain input values for the ALM employed in lagrangian simulations.

Net force obtention

Besides the dense core geometry, the net force $|\mathbf{F}_{\mathrm{DC}}|$ needs also to be provided as input parameter to the ALM model. As explained in §4.5.3, the model considers only the contribution of the pressure momentum term and the force is calculated through Eq. (4.28). Two parameters are therefore needed: the dense core surface S_{DC} and the mean pressures in the windward and leeward sides. The surface is estimated through the mean values of the geometric dense core parameters, assuming that this one is a trapezoid with bases d_{inj}, $\overline{w}$ and length $L_{\mathrm{DC}} = \sqrt{\overline{x_b}^2 + \overline{z_b}^2}$:

$$S_{\mathrm{DC}} = \frac{(d_{\mathrm{inj}} + \overline{w})\, L_{\mathrm{DC}}}{2} \tag{C.4}$$

For estimating the mean pressures, the procedure schematized in Figure C.9 is followed. First, the mean dense core is extracted from the resolved simulations as an iso-surface of the mean levelset surface: $\overline{\psi} = 0.5$. Then, the gradient vector $\nabla\left(\overline{\psi}\right)$ field is calculated on this surface, which points towards the direction of increasing values: that is, towards the inner part of the dense core, where $\overline{\psi} = 1$ in the areas where there is always liquid. The windward side of the mean dense core is then obtained as the region with a positive normal component of the gradient in the x direction: $\nabla_x\left(\overline{\psi}\right) > 0$. Equivalently, the leeward side is defined by the points where $\nabla_x\left(\overline{\psi}\right) < 0$. Then, the mean pressure at both the windward and leeward sides, p_{windward} and p_{leeward} respectively, are calculated and taken as inputs to Eq. (4.28).

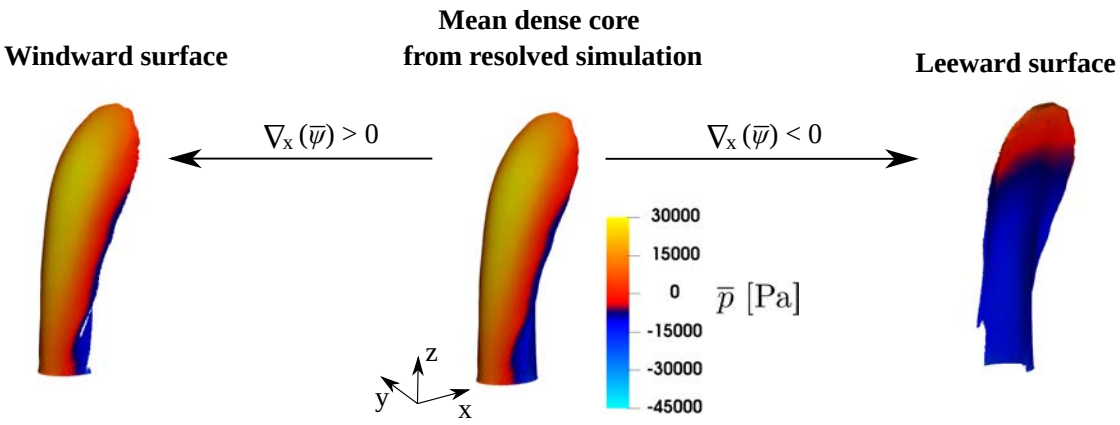

Figure C.9: Methodology to obtain windward and leeward surfaces of mean dense core from resolved atomization simulations. The displayed dense core corresponds to case UG100_DX10.

Appendix D
Mass conservation in ACLS

It was shown in Section 5.6.5 that liquid fluxes decrease downstream the injection point in the planes perpendicular to crossflow. Quantifiying the filming fluxes that reach the wall has also shown that actually the total mass flow rate is not conserved, as the addition of the mean perpendicular and filming fluxes up to a given x location downstream injection does not amount to the injected flow: there is liquid loss with the x distance.

The ACLS/AMR methodology was described in §2.3.4. Two sources of mass loss were identified in this numerical strategy:

- **Flagging the levelset band**. The levelset band needs to be flagged at each iteration in order to define the region where to compute interface features such as signed distance, normals, curvature and reinitialization fluxes (Janodet et al. 2022). When encountering cell-size gradients, it has been observed that some liquid structures diffuse in the mesh and dissappear. The amount of liquid lost by this source is quantitied and discussed in this section.

- **Mesh adaptation**. Adaptive Mesh Refinement (AMR) is automatically triggered at a reasonable frequency for AMR which is neither too low (adaptation triggered very often, yielding high computational costs) nor too high (adaptation barely happens and the advected interface finds cell size gradients). Nevertheless, regions in the mesh containing small droplets with size close to mesh resolution or which are travelling fast might sometimes be difficult to adapt, and liquid might disappear there when triggering AMR. The quantity of liquid lost in these computational rotuines has not been directly quantified, but can be estimated by substracting the quantity lost by the band flagging to the total volume of levelset in the domain.

In order to retrieve the quantity of lost liquid due to band flagging, the ψ function has been clipped before the flagging step is performed. This function is then denoted as ψ^-. Then, the ψ function after flagging is done is also clipped and denoted as ψ^+. Therefore, a field determining the spatial and temporal distribution of levelset loss due to band flagging process can be defined as:

$$\Delta\psi\left(\mathbf{x},t\right)=\psi^{-}\left(\mathbf{x},t\right)-\psi^{+}\left(\mathbf{x},t\right) \tag{D.1}$$

where the mass loss regions is defined for values $\Delta\psi\left(\mathbf{x},t\right)>0$. From the levelset function ψ, the amount of liquid volume present in the domain can be obtained at each iteration from Eq. (5.4). The ψ field in this expression corresponds to the one after performing the band flagging process, i.e. ψ^+, hence the liquid volume at each iteration could be denoted as V_l^+. For simplicity reasons, it will be simply denoted as V_l in the graphs that follow. In the same fashion, liquid volume before the band flagging operation can also be obtained with ψ^-, which yields then a volume V_l^-. From these two quantities, the amount of loss liquid at each time instant t_i due to the band flagging (BF) process can then be easily obtained as their difference:

$$\Delta V_{l,\mathrm{BF}}\left(t_i\right)=V_l^{-}\left(t_i\right)-V_l^{+}\left(t_i\right) \tag{D.2}$$

And hence, the total liquid volume loss at one simulation due to the band flagging process can be monitored in time t as follows:

$$\Delta V_{l,\mathrm{BF}}(t) = V_l^-(t) - V_l^+(t) + \int_{t_0}^{t} \Delta V_{l,\mathrm{BF}}(\tau)\, d\tau \tag{D.3}$$

Where t_0 is the first time instant at each simulation run. The last integral term has been added so that ΔV_l represents the accumulated liquid volume lost throughout a run. This quantity can now be added to the total volume at the end of each iteration to provide the liquid volume that would be present at the domain if there was no mass loss due to band flagging, named $V_{l,\mathrm{NF}}$:

$$V_{l,\mathrm{NF}}(t) = V_l(t) + \Delta V_{l,\mathrm{BF}}(t) \tag{D.4}$$

Finally, the total amount of liquid volume injected in a simulation run can be quantified with the following expression:

$$V_{l,\mathrm{inj}}(t) = V_{l,0} + \int_{t_0}^{t} Q_{\mathrm{injected}}\, d\tau = V_{l,0} + Q_{\mathrm{injected}}(t - t_0) \tag{D.5}$$

where $V_{l,0}$ is the liquid volume present at the beginning of every simulation run. $V_{l,\mathrm{inj}}$ represents therefore the quantity of liquid volume that would be present in the domain if there was not mass loss of any kind,i.e. neither through levelset band flagging nor to mesh adaptation. Then, the total volume loss can be computed as:

$$\Delta V_{l,\mathrm{total}}(t) = V_{l,\mathrm{inj}}(t) - V_l(t) \tag{D.6}$$

With Eqs. (D.1) and (D.6), the amount of volume lost can be fully characterized: the former provides an instantaneous field of the location in which liquid disappears due to the band flagging process, and the latter yields the instantaneous amount of levelset loss. Then, the losses due to the band flagging process are calculated with Eq. (D.4). Finally, the difference of Eqs. (D.6) and (D.4) provides the mass loss which is not due to the band flagging process, and which is thought to be caused by the AMR process as shown later. This magnitude is denoted as $\Delta V_{l,\mathrm{NBF}}$:

$$\Delta V_{l,\mathrm{NBF}} = \Delta V_{l,\mathrm{total}} - \Delta V_{l,\mathrm{BF}} \tag{D.7}$$

Evaluation of mass loss is performed in two simulations for the two resolutions of the high Weber case: UG100_DX20, UG100_DX10 (see Table 5.1,).. Computations are run for a short time ($\Delta t^* = 0.6$) without artificial liquid removal at the end of the domain, otherwise the application of Eqs. (5.4) (D.4) would also account for this artificial loss. The parameters from the ACLS methodology that can have an influence on the ψ loss are the interface thickness ε from Eq. (2.48) and the number of reinitiation steps N_{reinit} of the reinitialization equation (2.55). These two parameters are tested hereafter with case UG100_DX20; case UG100_DX10 is only studied with one configuration to evaluate the influence of interface resolution. The four simulations performed are shown in Table D.1, where Case 1 is the baseline case.

Table D.1: Simulations performed to evaluate mass loss due to ACLS

Case	Δx_{min} [μm]	N_{reinit}	ε
1	20	3	0.5
2	20	6	0.5
3	10	3	0.5
4	20	3	0.7

Case 1: Baseline

Figure D.1 shows a instantaneous snapshot of the jet. The black field denotes the regions with $\Delta\psi(\mathbf{x}, t) > 0$ for the whole duration of the simulation. Losses are distributed right downstream the jet dense core due to the droplets coming from surface breakup that reach a size of the order of the mesh resolution and disappear (see §5.6.2), and also further downstream along the jet as the ligaments from column breakup form small droplets that eventually vanish. The further downstream the injection point, the more liquid is lost, which explains the reduction in mean flow rates with increasing axial distance from Figure 5.39. The evolution of the liquid volumes calculated from Eqs. (5.4), (D.4) and (D.5) are shown in Figure D.2a by the black, blue

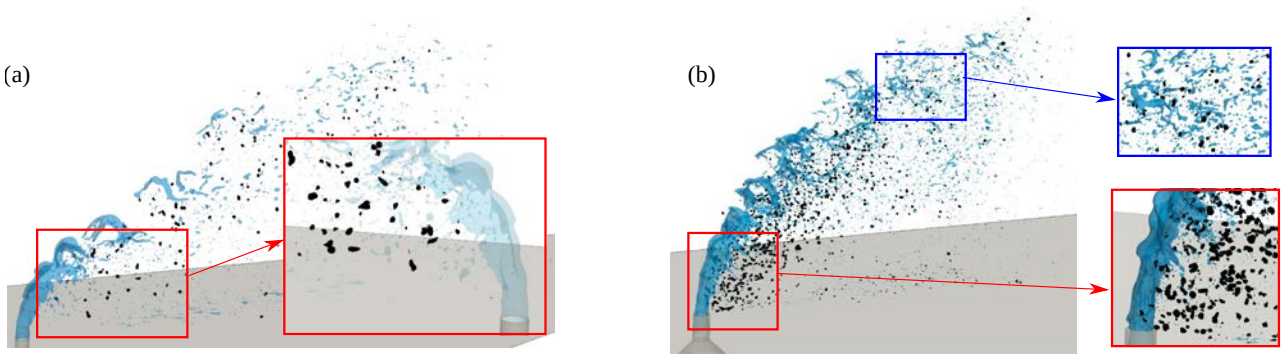

Figure D.1: Regions of mass loss at the end of simulation for (a) case 1 (baseline) and (b) case 3 ($\Delta x_{\min} = 10\ \mu$m).

and red lines respectively. The iterations at which mesh adaptation is performed are denoted by the dashed grey lines. As observed, $V_{l,\text{inj}}$ evolves linearly with time as the injected flow rate is constant. From the early instants of the simulation, the curve given by V_l starts to diverge from $V_{l,\text{inj}}$ due to the mass lost in the band flagging process. On the contrary, the line for $V_{l,\text{NF}}$ follows the same trend as $V_{l,\text{inj}}$ until the first adaptation iteration in the simulation, where a slight mass decrease is observed. As the simulation runs, the $V_{l,\text{NF}}$ line keeps the same slope as $V_{l,\text{inj}}$ but sees step reductions at several AMR iterations. The line V_l, on the other hand, suffers volume losses at certain AMR iterations but also among adaptation iterations: in particular, a strong gradual decrease has been captured between the adaptation iterations 4 and 5. This demonstrates that the losses not due to band flagging are observed only at the adaptation iterations, while the ones due to band flagging are also present outside the adaptation procedure.

The mass losses at the end of the run are shown in Figure D.2.: graph (a) shows the absolute losses, while graph (b) shows the pertentual contribution of the each source to the total volume loss. As observed from Figure D.2(b), most of the liquid suppression is caused by the band flagging process (88 %) while only a small percentage happens outside this routine. This demonstrates that, with the parameters from case 1, the band flagging is the main source of liquid loss in the simulations.

Case 2: Effect of N_{reinit}

The effect of the number steps to perform the steps of the levelset reinitialization equation (2.55), N_{reinit}, is increased increased from 3 to 6. Increasing the number of steps helps to better maintain the hyperbolic tangent profile of the levelset, to avoid numerical and to reduce spurious oscillations around the interface in flows where the interface is highly deformed (McCaslin & Desjardins 2014), as it is the case of the JICF operating conditions studied in this chapter. Consequently, the interface location $\psi = 0.5$ is better determined and the levelset transport is more accurate. Figure D.3b shows that the V_l curve gets closer to the $V_{l,\text{NF}}$ for all the simulation; in other words, the amount of loss $\Delta V_{l,\text{BF}}$ is reduced. The absolute amount of liquid loss ΔV_l as given in Figure D.3a is reduced with respect to Case 1, and the percentual contribution of the band flagging to the total loss, given in Figure D.3b, is also reduced: 35 % for $\Delta V_{l,\text{BF}}$ with respect to 65 % obtained for $\Delta V_{l,\text{NBF}}$. It is therefore demonstrated that increasing N_{reinit} has a positive effect on mass conservation.

Case 3: Effect of $\Delta x_{\min}$

Figure D.1b shows an instantaneous snapshot at the end of the simulaton performed with $\Delta x_{\min} = 10\ \mu$m. It is seen that liquid disappearance is more distributed in space than Case 1, which is due to a higher amount of droplets generated by surface and column breakup with a size close to the mesh resolution. At a first glance at the figure, it might seem that the total amount of liquid lost is larger than for case 1: nevertheless, Figure D.3a shows that the total volume loss is in fact of the same order than in Case 1, while the percentual contribution of $\Delta V_{l,\text{BF}}$ is lower than for Case 1 (78 % with respect to 88 %) as given in Figure D.3b. Effectively, by increasing the mesh resolution from $\Delta x_{\min} = 20$ to 10 μm, the droplets disappearing have a characteristic size of the order of this value and therefore, each individual droplet contains less volume than one droplet disappearing with a size of 20 μm. Even if there are more droplets disappearing, the total volume being removed by band flagging is lower than in Case 1. There is on the other hand, according to Figure D.3a, an increase in the absolute loss produced outside the band flagging process. by looking at Figure D.2c, one can

see that the reductions in $V_{l,NF}$ also occur during the adaptation iterations. The increase in $\Delta V_{l,\mathrm{NBF}}$ could be due to the fact that by reducing the interface cell size, the adaptation process needs to locate more cells around the interface and finds more difficulties to adapt its neighbouring elements within the levelset band so that their size increases progressively from $\Delta x_{\min}$ to the baseline mesh resolution. This will also suppose an important increase in the cost of the simulations, as it will be later shown in §5.6.6. Nevertheless, Figure D.2c shows that, as in Case 1, the mass loss in the AMR process does not occur at every adaptation iteration but only at a few of them, and also that more AMR iterations have been performed in Case 3 than in Case 1 (for the same time period simulated). If the same number of AMR iterations had been performed, the value of $\Delta V_{l,\mathrm{NBF}}$ might be different: however, the frequency of AMR iterations is calculated automatically and its possible influence has not been addressed in this study.

Case 4: Effect of ε

Finally, the effect of the levelset profile thickness ϵ is tested by modifying its value from 0.5 (case 1) to 0.7. An increase in ϵ supposes a wider band region and a more diffuse levelset profile. A decrease from 0.5 to 0.3 was also tested and showed no significant differences with the losses obtained for the former one, therefore it has not been reported in this document. As observed in Figures D.2, and D.3a the effect of increasing ε is catastrophic: the amount of volume lost by the band flagging process is huge, and the volume lost during the AMR iterations has also widely increased. For the timespan simulated, the total volume lost adds up to almost 0.25 mm^3 compare to less than 0.02 mm^3 in the rest of the cases. The relative losses in Figure D.3b do not show a big difference with respect to Cases 1 and 3 however: increasing ε has a negative effect on both sources of volume loss.

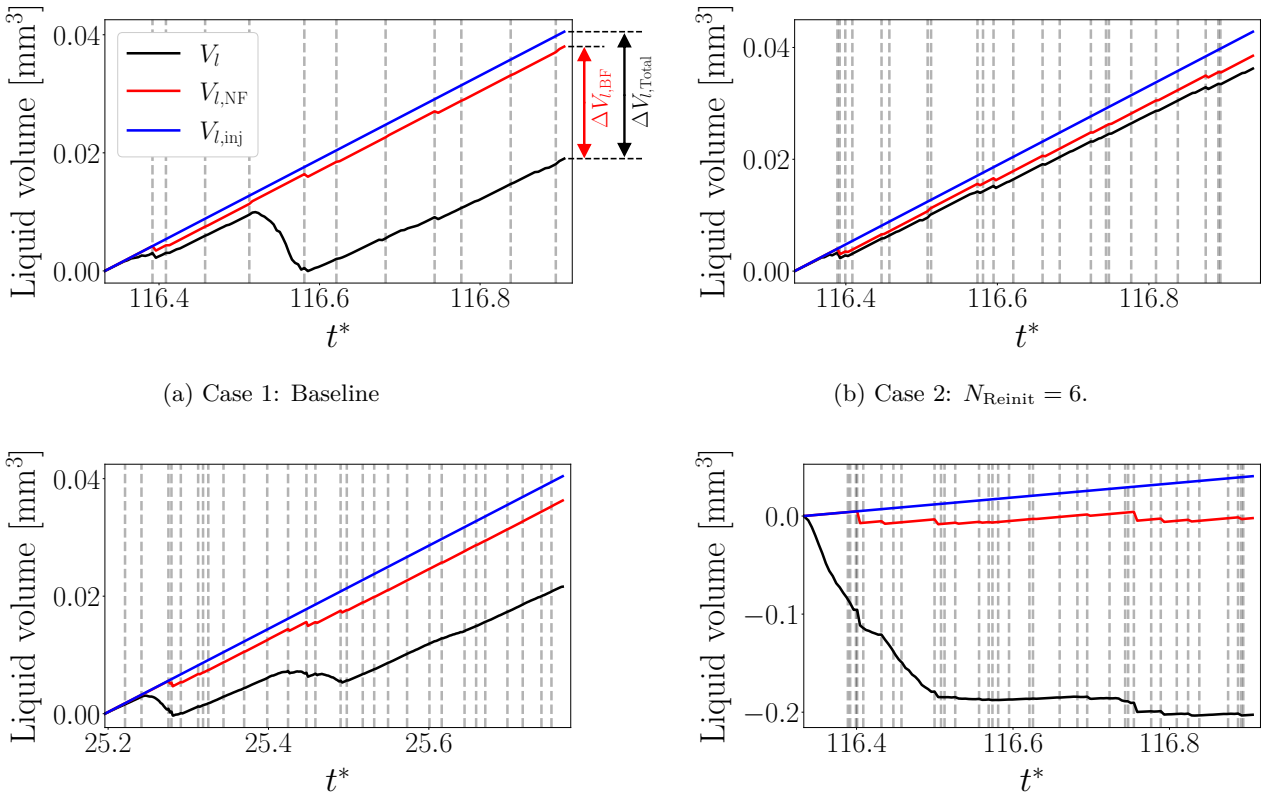

(a) Case 1: Baseline

(b) Case 2: $N_{\mathrm{Reinit}} = 6$.

(c) Case 3: $\Delta x_{\min} = 10$ μm.

(d) Case 4: $\varepsilon = 0.7$.

Figure D.2: Evolution of liquid volumes for cases 1 to 4 from Table D.1. The dashed grey lines indicate the iterations of adaptation for each case. In all cases the liquid volume present at the initialization of the runs has been substracted from all the curves, in order to the comparison among cases

These simulations have shown that the band flagging process in the ACLS/AMR simulations contributes to the liquid volume loss that causes reductions in the liquid flow rates downstream the injection point. These

losses can be reduced by increasing the number of reinitialization steps N_{reinit} of the levelset equation. An increase in the levelset thickness ε has shown to have a detrimental effect on the volume loss. Therefore, the optimal configuration which reduces mass loss has been found for $N_{\text{reinit}} = 6$, $\varepsilon = 0.5$: all the simulations reported in Chapter 5 were performed with these values.

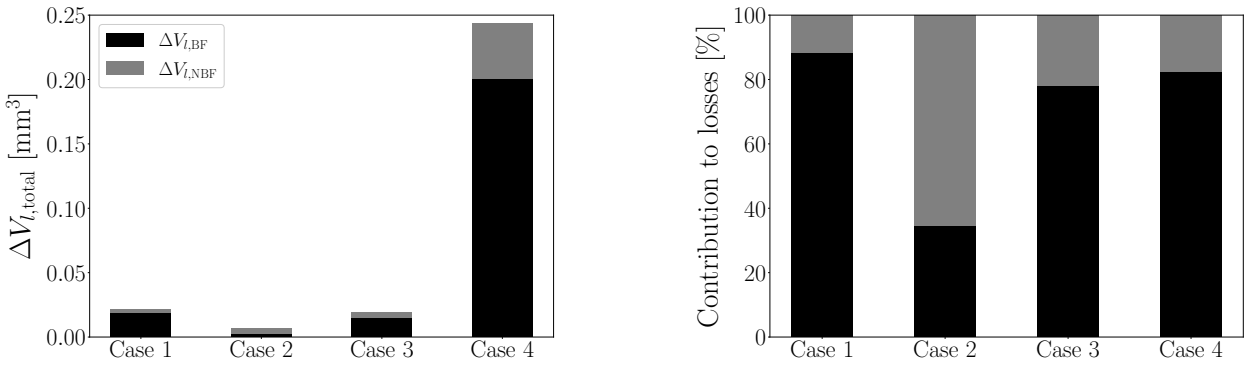

(a) Absolute volume losses from simulations.

(b) Percentual contribution to total volume loss.

Figure D.3: Liquid volume loss at the end of each run and its contributions

Appendix E

Convergence of SLI global parameters in JICF

Spray characterization from the JICF simulations of Chapter has been presented in §5.7.2: the total accumulation times of the simulations are summarized in Table 5.9 and the amount of accumulated droplets in Table 5.10. The establishment of the sprays was shown through the convergence of the global SMD and liquid flux Q_l in Figure 5.46. In this section, the convergence on the remaining parameters not previously shown are displayed: velocities in three directions are shown in Figures E.1 and E.2, and deformation parameters α and β are seen in Figures E.3 and E.4.

Liquid velocities

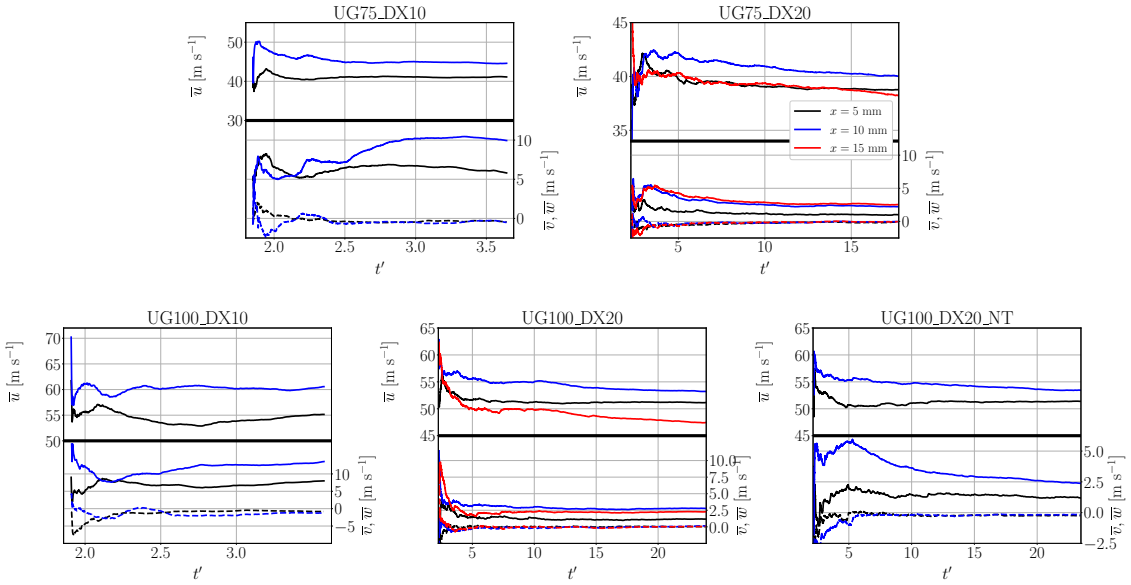

Figure E.1: Establishment of mean liquid velocities for each case.

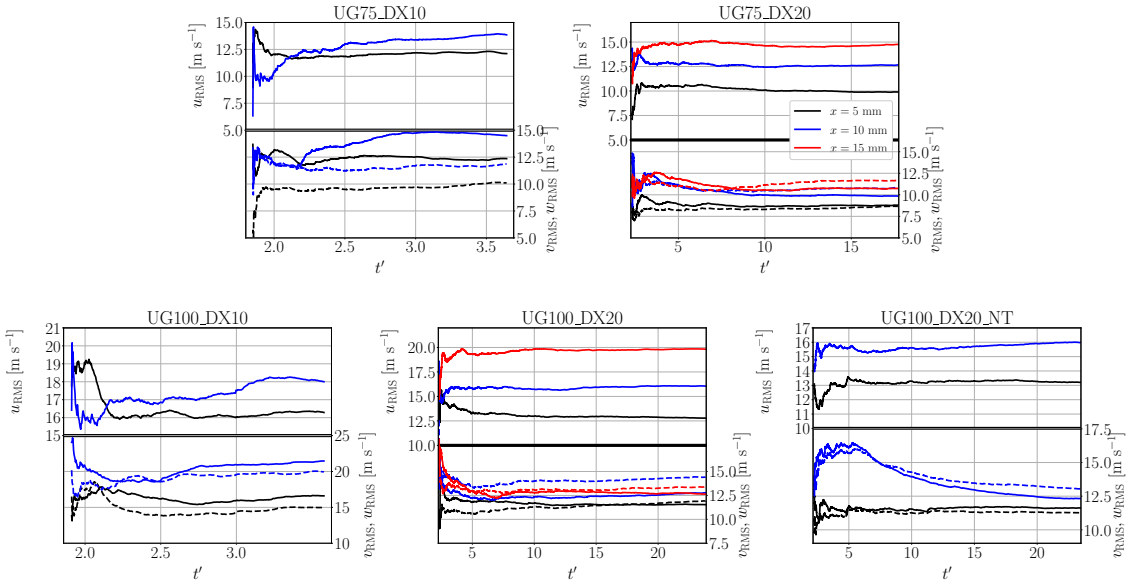

Figure E.2: Establishment of RMS liquid velocities for each case.

Deformation parameters

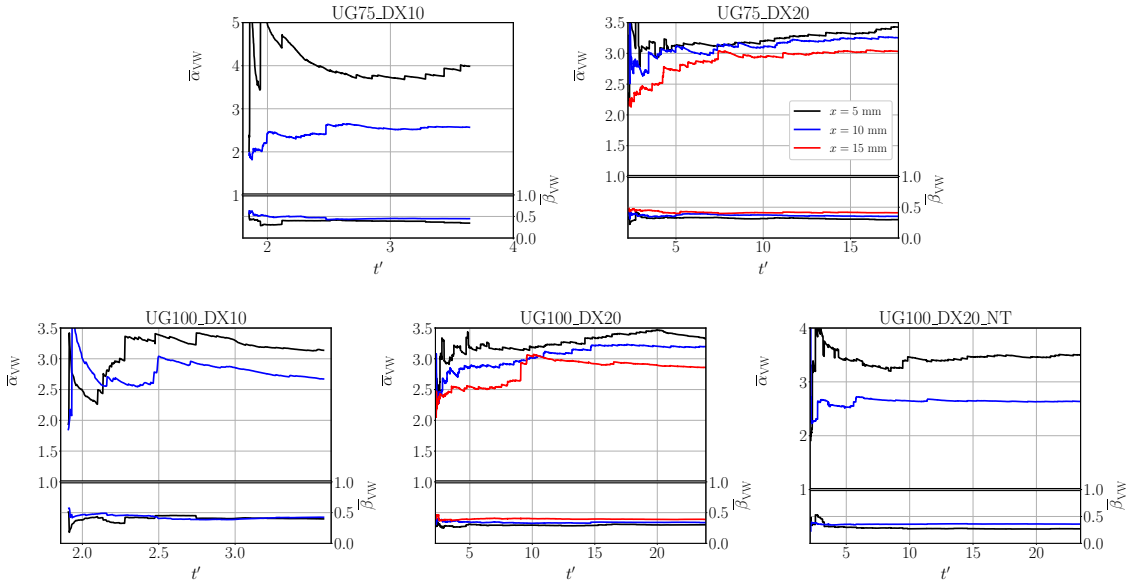

Figure E.3: Establishment of mean deformation parameters for each case.

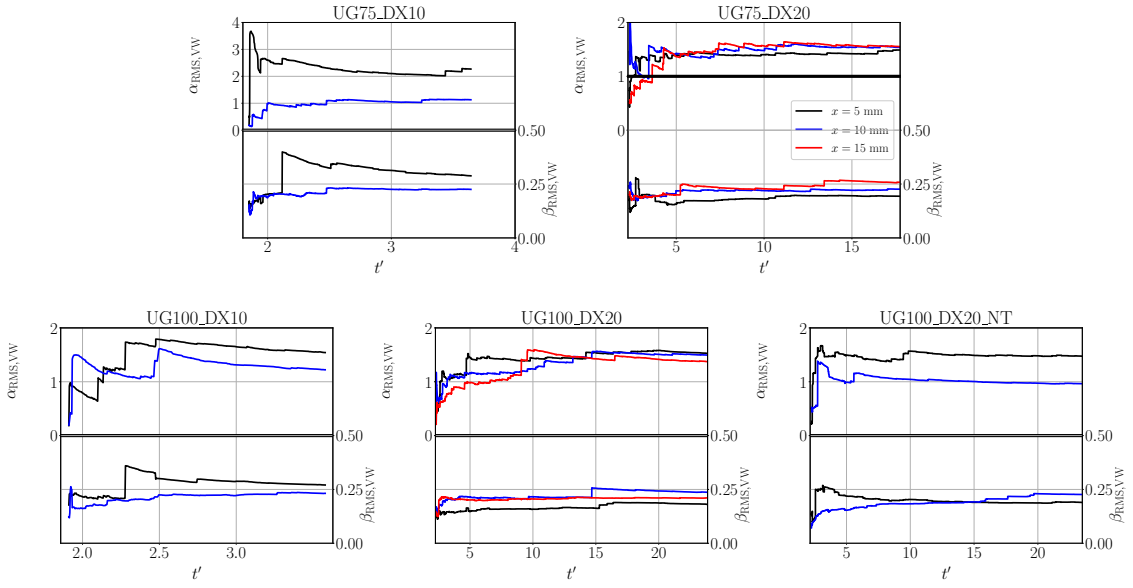

Figure E.4: Establishment of RMS deformation parameters for each case.

Appendix F

Convergence of SLI global parameters in BIMER

Spray characterization from the BIMER simulations of Chapter has been presented in §8.5.2: the total accumulation times of the simulations are summarized in Table 8.7 and the amount of accumulated droplets in Table 8.8. The establishment of the sprays was shown through the convergence of the global SMD and liquid flux Q_l in Figure 8.7. In this section, the convergence on the remaining parameters not previously shown are displayed: velocities in three directions are shown in Figures F.1 and F.2, and deformation parameters α and β are seen in Figures F.3 and F.4.

Liquid velocities

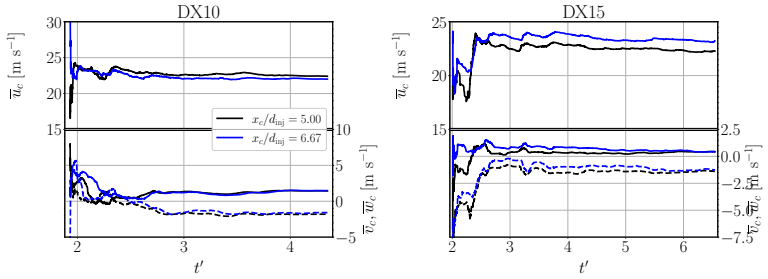

Figure F.1: Establishment of mean liquid velocities for each case.

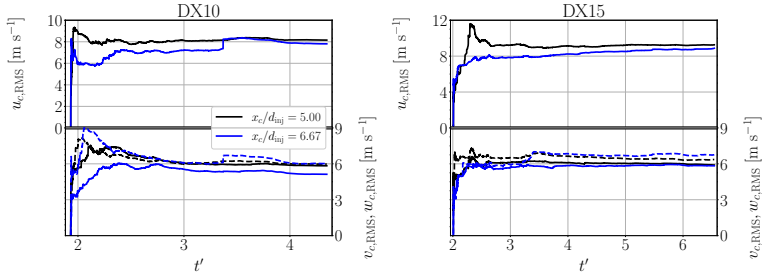

Figure F.2: Establishment of BIMER RMS liquid velocities for each case.

Deformation parameters

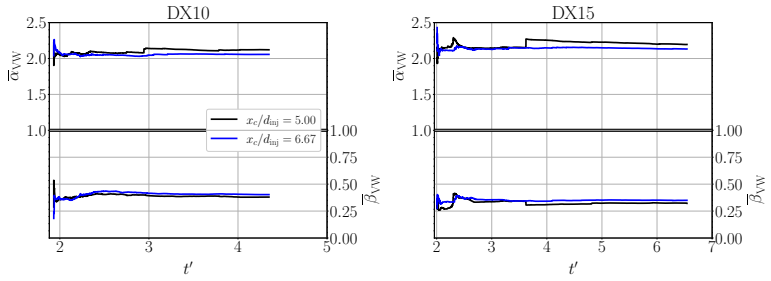

Figure F.3: Establishment of mean deformation parameters for each case.

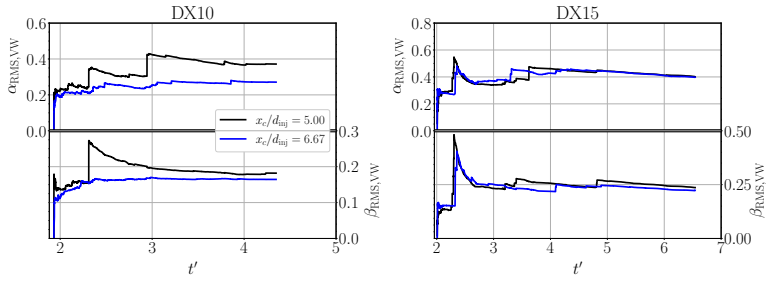

Figure F.4: Establishment of RMS deformation parameters for each case.

Appendix G

Calibration of Gorokhovski's breakup model

The Gorokhovski stochatic model, described in §4.6.3, presents two free constants K_1 and K_2 in Eq. (4.62) which can be tuned for each particular case and which affect the size of the children droplets produced. K_1 affects the mean value of the generated children particles a breakup event, while K_2 controls the deviation from this mean (Senoner 2010). The effect of both constants in the sprays have been investigated by selecting a baseline configuration with $K_1 = 0.05$, $K_2 = 1.0$ (such values provided the best experimental comparison obtained in terms of SMD) and varying both constants independently: first K_1 is increased to 0.1 and 0.2, and then K_2 is decreased to 0.5 and 0.25, making a total of five simulations reported.

Results for global SMD and experimental deviations ε_{SMD}, Eq. (6.8), are given in Table G.1. Maps of SMD and flux are shown in Figure G.1, their integrated profiles in Figure G.2, and the evolution of SMD along the channel is represented in Figure G.3. In general, it can be stated that:

- By increasing K_1, the global SMD decreases. The spray vertical boundary decreases. Hence, maximum local fluxes retrieved are larger, due to a more concentrated spray.
- By increasing K_2, the global SMD increases. Modifications in K_2 lead to bigger differences in the SMD errors as shown in Table G.1, which indicates that this constant has a greater influence on the atomization than K_2. Also, the spray vertical boundary increases.

From this analysis, the constants $K_1 = 0.05$, $K_2 = 1.0$ were chosen for performing the rest of the analyses from Chapter 6 since they yield the lowest error in SMD with respect to experiments.

Table G.1: SMD values at $x = 80$ mm obtained with different constants in the Gorokhovski secondary atomization model

Case	SMD [μm]	ε_{SMD} [%]
Experiments	31	-
$K_1 = 0.05,\ K_2 = 0.25$	16.60	-46.45
$K_1 = 0.05,\ K_2 = 0.5$	18.74	-39.55
$K_1 = 0.05,\ K_2 = 1.0$	19.52	-37.03
$K_1 = 0.10,\ K_2 = 1.0$	18.57	-40.11
$K_1 = 0.20,\ K_2 = 1.0$	17.58	-43.28

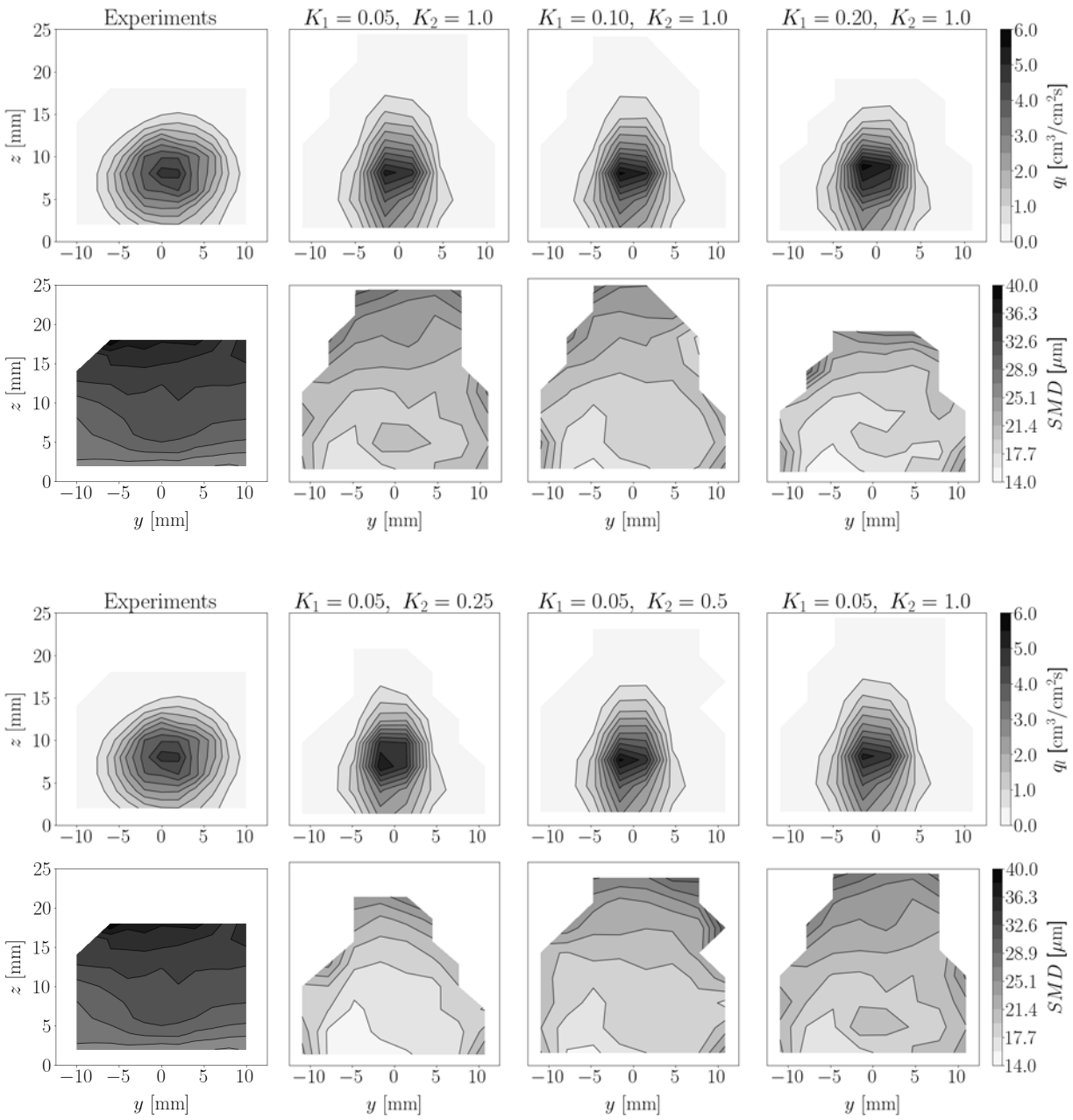

Figure G.1: Flux and SMD maps for numerical simulations comparing the effect of calibrating the constants from the Gorokhovski model with the experimental results

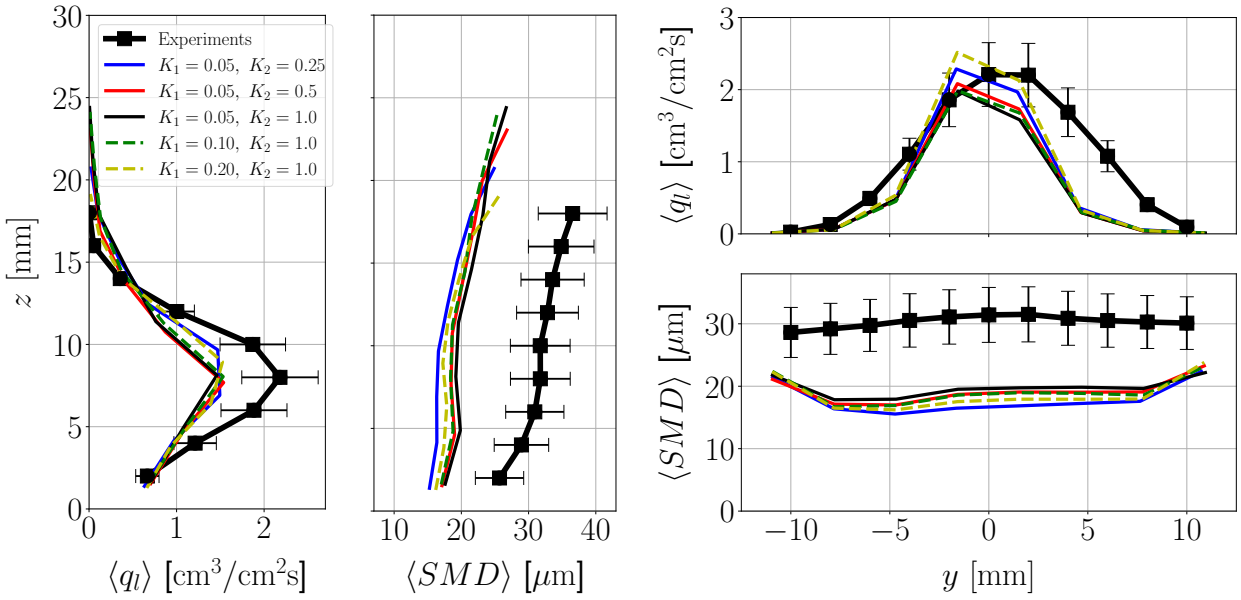

Figure G.2: Integrated profiles of flux and SMD maps for numerical simulations comparing the effect of Gorokhovski's model calibration with the experimental results

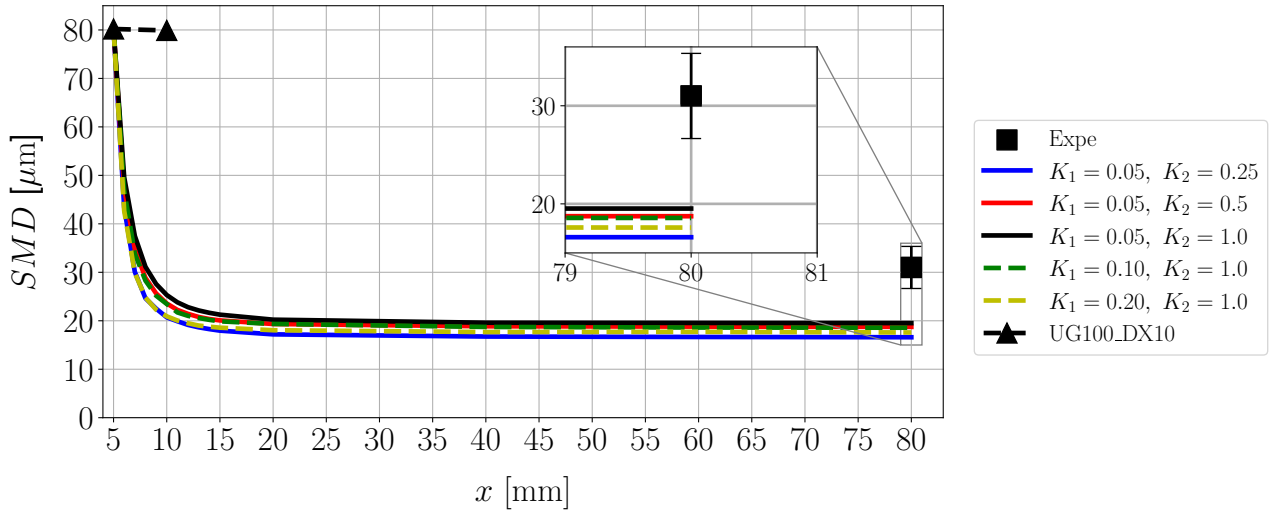

Figure G.3: Evolution of SMD along axial location x for several values of constants K_1, K_2 of the Gorokhovski atomization model. The SMD at $x = 5$ and 10 mm for the resolved atomization case UG100_DX10 is also added for comparison